ty/simplemargins

A PRECISION MEASUREMENT OF THE NEUTRON D_2: PROBING THE COLOR FORCE

A Dissertation
Submitted to
the Temple University Graduate Board

In Partial Fulfillment
of the Requirements for the Degree
DOCTOR OF PHILOSOPHY

---

by
Matthew Posik
January 2014

Examining Committee Members:

Zein-Eddine. Meziani, TU Member, Advisory Chair
C. J. Martoff, TU Member
Andreas Metz, TU Member
Bernd Surrow, TU Member
Leonard Gamberg, External Member, Penn State University-Berks

DEDICATION

for my parents

ABSTRACT

The g_2 nucleon spin-dependent structure function measured in electron deep inelastic scattering contains information beyond the simple parton model description of the nucleon. It provides insight into quark-gluon correlations and a path to access the confining local color force a struck quark experiences just as it is hit by the virtual photon due to the remnant di-quark. The quantity d_2, a measure of this local color force, has its information encoded in an x^2 weighted integral of a linear combination of spin structure functions g_1 and g_2 and thus is dominated by the valence-quark region at large momentum fraction x. To date, theoretical calculations and experimental measurements of the neutron d_2 differ by about two standard deviations. Therefore, JLab experiment E06-014, performed in Hall A, made a precision measurement of this quantity at two mean four momentum transfers values of 3.21 and 4.32 GeV^2. Double spin asymmetries and absolute cross-sections were measured in both DIS and resonance regions by scattering longitudinally polarized electrons at beam energies of 4.74 and 5.89 GeV from a longitudinally and transversely polarized ^{3}He target. Results for the absolute cross-sections and spin structure functions on ^{3}He will be presented in the dissertation, as well as results for the neutron d_2 and extracted color forces.

ACKNOWLEDGEMENTS

I would first like to thank my advisor, Zein-Eddine Meziani, for giving me the opportunity to work on this experiment, and for guiding me through the dissertation process.

I would also like to thank everyone who worked on the Transversity experiment. Specifically, Im particularly grateful to Kalyan Allada, Xin Qian, Chiranjib Dutta, and Jin Huang for helping me learn about the detectors and how to set up and conduct software analysis. I would like to extend my thanks to Yi Qiang, Jin Huang, Yawei Zhang, Lamiaa El Fassi, and Chiranjib Dutta for their valuable help and insight into the experiment's polarized ^{3}He target setup.

Thank you to Brad Sawatzky and Gregg Franklin for the valuable insights that they shared over the course of the experimental analysis, especially with regards to the BigBite sub detectors.

I would like to thank the other graduate students, David Flay and Diana Parno, who worked tirelessly on the E06-014 experiment to make sure it ran as planned, and conducted a majority of the analysis.

I would also like to thank my wife, family, and parents who supported me through this long journey.

CONTENTS

LIST OF FIGURES

LIST OF TABLES

CHAPTER 1

INTRODUCTION AND THEORY

Atoms are the macroscopic building blocks of matter, which are made up of positively charged nuclei and negatively charged point-like electrons that orbit around the nuclei. The nucleus is composed of positively charged protons and electrically neutral neutrons, called nucleons, and are responsible for 99.9% of all visible matter in the universe. The Standard Model provides a fundamental interpretation of nuclear matter through which the nucleons themselves are found to be made up of point-like particles known as quarks and gluons. In addition to the electrical charge, these constituents possess another charge known as the *color* charge. The color charge is responsible for the strong interaction that binds quarks and gluons together, allowing the formation of nucleons and atoms. The fundamental theory for describing the color charge and strong interaction is known as Quantum Chromodynamics (QCD).

1.1 Nucleon Structure

The constituents, or partons, that make up nucleons (such as protons and neutrons) and their dynamical interactions can be described through the Standard Model. In the Standard Model,

there are fundamental spin 1/2 particles known as quarks which come in six flavors: up, down, strange, charm, top and bottom. These six flavors can be further divided into groups of light (up (u), down (d) and strange (s)) and heavy (charm (c), bottom (b) and top (t)) quarks. An up quark u has a fractional charge of $+\frac{2}{3}e$, while a down quark d has a electric charge of $-\frac{1}{3}e$. One of the simplest models used to build up nucleons is the valence quark model. In this model, a proton has a charge +1e, and can thus be built from two up quarks and one down quark (uud); where as the neutron with no electric charge can be formed from two down quarks and one up quark (udd). The three light quarks used to describe the proton and neutron are known as the *valence quarks*.

In addition to carrying an electric charge, each quark also carries a color charge. Unlike the electric charge (e) where there is only one charge, the color charge has three possible charge values which are conventionally labeled as *red, blue* and *green*. Similar to the electric charge having an opposite charge ($\pm e$), the color charge also has a corresponding opposite charge labeled as *anti-red, anti-blue* and *anti-green*. The three valence quarks are bound by the strong force (color charge interaction) in such a way that the nucleon is colorless[1].

Analogous to the photon being responsible for carrying the electromagnetic force, the strong force (also refereed to as the color force) is carried by gluons. Gluons are fundamental particles with spin-1 [2], who also carry a color charge. The quarks within the nucleon constantly interact with each other through gluon exchange, and unlike photons, the gluons within nucleon also interact with one another through the color charge.

The final component that makes up the nucleon is known as the *quark sea*; comprising of many quarks and their anti-matter partners called anti-quarks. Quark and antiquark

[1] Adding all three color charges together produces a colorless charge. This is analogous to effect of adding all the colors of light together to produce white (colorless) light. Additionally, colorless charges can also be formed through the pairing of a particular color charge with its opposite charge, *i.e.* red + anti-red would result in a colorless charge.

[2] Particles comprise of two classes: bosons which possess an integer spin and fermions which possess a non-integer spin.

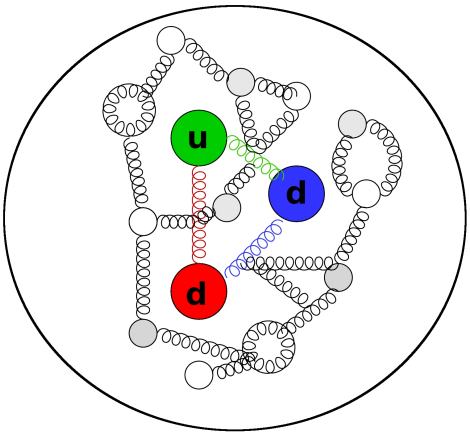

Figure 1.1: A representation of the internal structure of the neutron. Image created with Jaxodraw [1].

pairs form in the nucleon through $(q - \bar{q})$ pair-production and leave the nucleon through annihilation processes. The light quarks are more likely to populate the sea than the heavier quarks, because they require less energy to produce. Of the light quarks, the lightest quark pairs $(u\bar{u})$ and $(d\bar{d})$ are more likely to dominate the sea than the $(s\bar{s})$ quark pair. Figure 1.1 illustrates the internal neutron structure, where the valence quarks are the lager colored circles marked with their flavor, the gluons are represented by the curly lines, and the quark-antiquark pairs represented by the smaller solid and open circles.

1.2 Probing Nucleon Structure

The quark and gluon structure of strongly interacting matter is studied through scattering from quark and gluons at high energies. There are two primary techniques in which to probe the quark and gluon distributions inside nucleons: lepton scattering and the Drell-Yan process.

Lepton scattering involves scattering leptons (such as electrons or muons) from quarks

or anti-quarks that are inside the target nucleon (proton or neutron). The high energy leptons transfer a large fraction of their momentum to the quarks through photon exchange, thus probing the quark substructure of the nucleon. Moreover, scattering a polarized lepton beam from a polarized target would allow one to access the nucleon spin structure. This process has been used primarily to study quark and gluon distributions in nucleons.

The Drell-Yan process involves scattering of two high energy hadrons [3], in which the quark of one of the hadrons annihilates with an anti-quark of the other hadron. This annihilation creates a virtual photon which materializes as pair of oppositely charges leptons (*i.e.* e^+e^- or $\mu^+\mu^-$). This method has been widely used to study the sea quark distributions in the nucleon. However, this process was not used in E06-014 and will not be discussed further.

In the following sections, a general overview of electron scattering will be discussed, followed by the formalism of deep inelastic scattering.

1.3 Electron Scattering

The simplest example of electron scattering is through the one photon exchange (also known as the first Born approximation) shown in Figure 1.2. In this picture an electron with four momentum $k = \left(E, \vec{k}\right)$ interacts with an incoming nucleon with four momentum $p = (E_p, \vec{p})$ through the exchange of a virtual photon with four momentum $q = (\nu, \vec{q})$. In inclusive scattering, only the scattered electron with four momentum $k' = \left(E', \vec{k'}\right)$ is detected at an angle θ, while the final hadronic system with four momentum p' goes unobserved. When $q^2 \neq 0$, the photon exchange between the electron and nucleon is said to be off shell. The emitted photon is not a real photon, but rather a virtual one which

[3] A hadron is a composite particle made of quarks and held together by the strong force, which is analogous to how atoms are held together through the electromagnetic force.

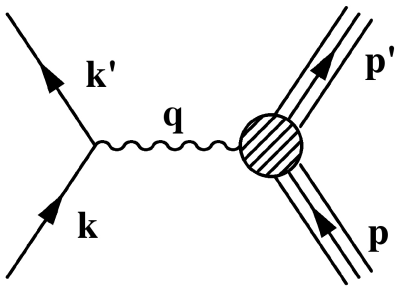

Figure 1.2: Electron scattering through one-photon exchange.

effectively carries borrowed energy for a short time in accordance with the Heisenberg uncertainty principle [2]. For the space-like virtual photon where $q^2 < 0$, the variable $Q^2 = -q^2$ is typically used. The virtual photon acts as a probe to the nucleon structure with Q^2 describing its spatial resolution [3]. In this scattering process energy transfer $\nu = \frac{p \cdot q}{M}$, where M is the nucleon mass, and momentum $\vec{q} = \vec{k} - \vec{k}'$ are transfered to the target. Because only the scattered electron is detected, it is often useful to define the invariant mass of the residual hadronic system $W^2 = (p + q)^2$.

In the laboratory frame, the target is fixed and hence $p = (M, 0)$, which leads to the following kinematic relations [4][4]:

$$\nu = E - E' \tag{1.1}$$

$$Q^2 = 4EE' \sin^2\left(\frac{\theta}{2}\right) \tag{1.2}$$

$$W^2 = M^2 + 2M\nu - Q^2 \tag{1.3}$$

The cross section for electron scattering depends on Q^2 and ν, as seen in Figure 1.3, which shows a typical cross section spectrum plotted as a function of Q^2 and ν. As Q^2 and

[4] $\hbar = c = 1$ (known as natural units), and the electron mass is neglected. This thesis will use natural units unless stated otherwise.

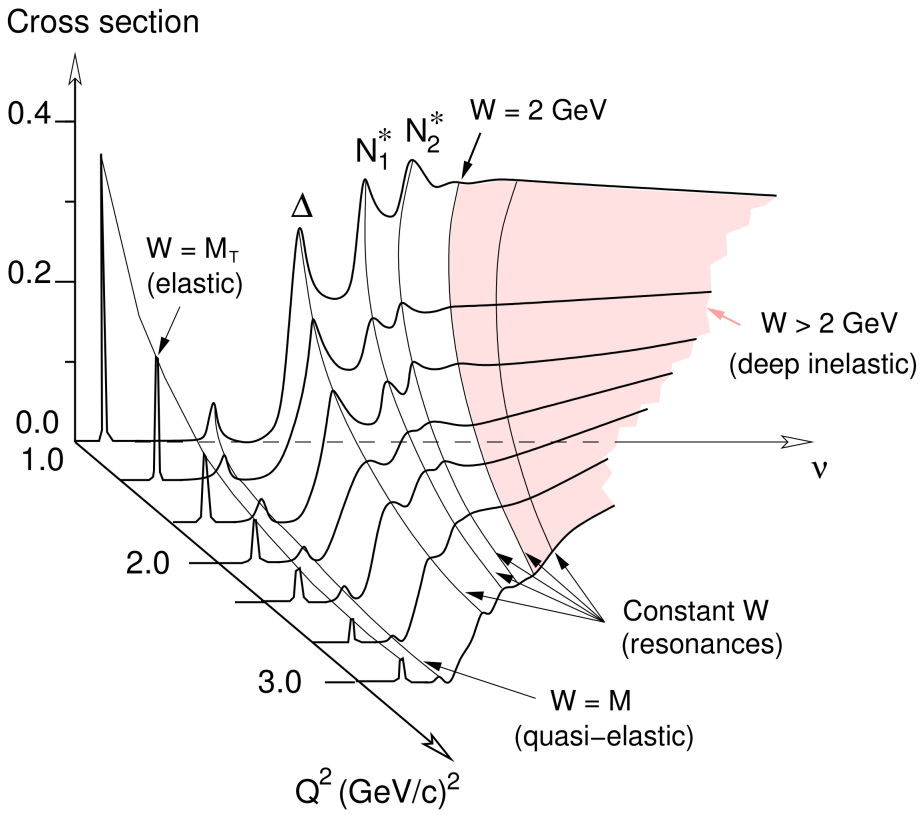

Figure 1.3: Cross section (arbitrary units) as a function of Q^2 and ν for inclusive electron scattering off a light nuclear target. For the elastic peak W is calculated using the target nucleus mass, while for the others the nucleon mass is used. Reproduced from Reference [3].

ν change, different nucleon excitations are seen in the target. The spectrum consists of four distinct scattering regions: elastic, quasi-elastic, resonance and deep inelastic regions [3].

- **Elastic Scattering**

  At low Q^2 and ν, the virtual photon exchanged in electron scattering is unable to resolve any nucleon structure and scatters coherently leaving the target nucleus intact. The invariant mass during elastic scattering can be defined as $W^2 \equiv M_T^2 + 2M_T\nu - Q^2 = M_T^2$, where M_T is the nuclear target mass.

- **Quasi-Elastic Scattering**

  As ν surpasses the nuclear target binding energy (5.49 MeV for two body ^{3}He break up and 7.72 MeV for three body ^{3}He break up) [3], the target breaks up and the nucleus can be viewed as quasi-free nucleons bounded in a mean potential (such as that which is described in the Fermi gas model [5]). In this scattering region, electrons scatter elastically form the quasi-free nucleons, which are not at rest due to Fermi motion and have momenta of 55 $\sim$ 250 MeV [5]. This motion causes a broadening around the quasi-elastic peak $\nu = \frac{Q^2}{2M}$, which is the energy loss due to elastic scattering off a free nucleon. The invariant mass in the quasi-elastic region is defined as $W^2 \equiv M^2 + 2M\nu - Q^2 = M^2$, where M is the nucleon mass.

- **Resonances**

  As Q^2 and ν increase beyond the quasi-elastic region, the electron scattering now enters the resonance region, commonly defined as 1.2 GeV $< W <$ 2.0 GeV, and begins to resolve the nucleon structure. The quarks within the nucleons absorb the emitted virtual photons and cause the nucleons to enter excited states, known as nucleon resonances. In the resonance region, the invariant mass is defined as $W^2 \equiv M^2 + 2M\nu - Q^2 = M_{res}^2$, where M_{res} is the mass of the resonance nucleon res. For the case of inclusive scattering, the $\Delta(1232)$ (M_Δ = 1.232 GeV) resonance is usually the only clearly distinguishable resonance, as higher resonances ($W >$ 1.4 GeV) tend to be heavily convoluted with each other [3].

- **Deep Inelastic Scattering**

  The deep inelastic scattering (DIS) region is typically defined as $W >$ 2 GeV and $Q^2 >$ 1 GeV^2. In this region Q^2 and ν are large enough that the nucleon constituents are resolved, and at large enough Q^2 that electrons can be interpreted as scattering from asymptotically free quarks (and anti-quarks) in the nucleon. At this point it is

useful to define to scalar invariants, the Bjorken scaling variable x_{Bjk} and y

$$x_{Bjk} \equiv x = \frac{Q^2}{2p \cdot q} = \frac{Q^2}{2m\nu} \text{ (for fixed target)} \tag{1.4}$$

$$y = \frac{p \cdot q}{p \cdot k} = \frac{\nu}{E} \text{ (for fixed target).} \tag{1.5}$$

In the infinite momentum frame, that is a frame of reference where the nucleon momentum approaches infinity along the direction of $\vec{q}$, x can be interpreted as the fraction of the nucleon's momentum that is carried by the struck quark [4].

Although some of the data collected in E06-014 was in the resonance region, the majority of it resides in the DIS region. Thus the majority of this dissertation will focus on the DIS region rather than the resonance region.

1.4 DIS Formalism

The formalism of the deep inelastic scattering process will be discussed following the convention established by Reference [6], in which the differential cross section $\frac{d^2\sigma}{d\Omega dE'}$ defines the likelihood of detecting a scattered electron in a solid angle $d\Omega$ and energy range $(E', E + dE')$. Using the process depicted in Figure 1.2, in which the incident electron has an initial four momentum k and spin s, the scattered electron has four momentum k' and spin s'; the incident nucleon has mass M, four momentum p and spin S. The final hadronic state can be ignored because only the electron final state is detected in inclusive scattering. The dynamics at each vertex in Figure 1.2 can be expressed though the lepton tensor $L_{\mu\nu}$ (the left most vertex in Figure 1.2) and hadronic tensor $W^{\mu\nu}$ (the right most vertex in Figure 1.2). The differential cross section can be rewritten in terms of the scattering tensors as

$$\frac{d^2\sigma}{d\Omega dE'} = \frac{\alpha^2}{2Mq^4} L_{\mu\nu} W^{\mu\nu}, \tag{1.6}$$

where α is the fine structure constant and $q = k - k'$. The lepton tensor is well understood from quantum electrodynamics (QED) and can be expressed in terms of the γ matrices, and electron Dirac spinors u and $\bar{u} = u^\dagger \gamma^0$

$$L_{\mu\nu}(k, s; k's') = \left[\bar{u}(k', s')\gamma_\mu u^*(k, s)\right]\left[\bar{u}(k', s')\gamma_\nu u^*(k, s)\right]. \tag{1.7}$$

At this point, it is convenient to separate the lepton tensor into two parts that are symmetric (S) under μ, ν exchange, and two more parts that are anti-symmetric (A) under μ, ν interchange

$$L_{\mu\nu}(k, s; k', s') = L_{\mu\nu}^{(S)}(k; k') + iL_{\mu\nu}^{(A)}(k, s; k') + L'_{\mu\nu}{}^{(S)}(k, s; k', s') + iL'_{\mu\nu}{}^{(A)}(k; k', s'). \tag{1.8}$$

The unpolarized lepton tensor, $2L_{\mu\nu}^{(S)}$ is obtained by summing $L_{\mu\nu}(k, s; k', s')$ over final spin state s' and averaging over the incident spins s.

The hadronic tensor includes information about the structure of the target, as well as QED. Due to the structure contained in the hadronic tensor, it is not as well understood as the leptonic tensor. The hadronic tensor, $W_{\mu\nu}$ can also be defined in terms of symmetric and antisymmetric pieces as

$$W_{\mu\nu}(q; p, S) = W_{\mu\nu}^{(S)}(q; p) + iW_{\mu\nu}^{(A)}(q; p, S). \tag{1.9}$$

Applying conservation laws at the hadronic vertex allows for general expressions of the symmetric and antisymmetric parts of the hadronic tensor

$$W_{\mu\nu}^{(S)}(q;p) = 2M\left(-g_\mu + \frac{q_\mu q_\nu}{q^2}\right) W_1\left(p\cdot q, Q^2\right) + \frac{2}{M}\left(p_\mu - \frac{p\cdot q}{q^2}q_\mu\right)\left(p_\nu - \frac{p\cdot q}{q^2}q_\nu\right) W_2\left(p\cdot q; Q^2\right) \tag{1.10}$$

and

$$W_{\mu\nu}^{(A)}(q;p,S) = 2_{\mu\nu\alpha\beta}q^\alpha\left\{M^2 S^\beta G_1\left(p\cdot q, Q^2\right) + \left[(p\cdot q)\,S^\beta - (S\cdot q)\,p^\beta\right] G_2\left(p\cdot q, Q^2\right)\right\}, \tag{1.11}$$

where the metric tensor $g_\mu\nu$ is given by

$$g_{\mu\nu} = \begin{pmatrix} 1 & 0 & 0 & 0 \\ 0 & -1 & 0 & 0 \\ 0 & 0 & -1 & 0 \\ 0 & 0 & 0 & -1 \end{pmatrix} \tag{1.12}$$

and $\epsilon_{\mu\nu\alpha\beta}$ = 1 if $\mu\nu\alpha\beta$ is an even permutation of 0123, -1 if it is an odd permutation, and 0 if any two indices are the same.

The symmetric hadronic tensor $W_{\mu\nu}^{(S)}$ contains two unpolarized structure functions W_1 and W_2, while the antisymmetric hadronic tensor $W_{\mu\nu}^{(A)}$ contains two spin dependent structure functions, G_1 and G_2. These structure functions are discussed further in Section 1.5. Using the leptonic and hadronic tensors, the differential cross section can be written as

$$\begin{aligned}\frac{d^2\sigma}{d\Omega dE'} &= \frac{\alpha^2}{2Mq^4}\frac{E'}{E}\left[L_{\mu\nu}^{(S)}W^{\mu\nu(S)} + L_{\mu\nu}^{\prime(S)}\left(s,s'\right)W^{\mu\nu(S)}\right] \\ &- \frac{\alpha^2}{2Mq^4}\frac{E'}{E}\left[L_{\mu\nu}^{(A)}\left(s\right)W^{\mu\nu(A)}\left(S\right) + L_{\mu\nu}^{\prime(A)}\left(s'\right)W^{\mu\nu(A)}\left(S\right)\right].\end{aligned} \tag{1.13}$$

Each tensor product in Equation 1.14 is measurable and hence an experiment can select particular pieces by selecting various spin states. For example, the $L_{\mu\nu}^{(S)}W^{\mu\nu(S)}$ term can be accessed by summing over the final spins and averaging the initial spins. This term corresponds to the unpolarized cross section

$$\frac{d^2\sigma^{unpol}}{d\Omega dE'}\left(k,p;k'\right) = \frac{\alpha^2}{Mq^4}\frac{E'}{E}L_{\mu\nu}^{(S)}W^{\mu\nu(S)}. \tag{1.14}$$

Alternatively, taking the difference of cross sections with two opposite target spins, singles out the $L_{\mu\nu}^{(A)}W^{\mu\nu(A)}$ term

$$\sum_{s'}\left[\frac{d^2\sigma}{d\Omega dE'}\left(k,s,p,-S;k's'\right) - \frac{d^2\sigma}{d\Omega dE'}\left(k,s,p,S;k',s'\right)\right] = \frac{2\alpha^2}{Mq^4}\frac{E'}{E}L_{\mu\nu}^{(A)}W^{\mu\nu(A)}. \tag{1.15}$$

1.5 Nucleon Structure Functions

With the general cross section defined in Equation 1.14, it is worthwhile to consider its unpolarized and polarized structure functions, as they are used to compute many physical quantities.

1.5.1 Unpolarized Structure Functions

The Mott cross section, which is defined as

$$\left(\frac{d\sigma}{d\Omega}\right)_{Mott} = \frac{\alpha^2 \cos^2 \frac{\theta}{2}}{4E^2 \sin^2 \frac{\theta}{2}}, \tag{1.16}$$

describes the case for unpolarized relativistic electron scattering from an unpolarized point like spin 1/2 nucleon with infinitely heavy mass. The unpolarized cross section given by equation 1.14 can be factorized into two terms

$$\frac{d^2\sigma^{unpol}}{d\Omega dE'} = \left(\frac{d\sigma}{d\Omega}\right)_{Mott} \left[W_2\left(\nu, Q^2\right) + 2W_1\left(\nu, Q^2\right) \tan^2 \frac{\theta}{2}\right], \tag{1.17}$$

in which one term describes the point like interaction $\left(\text{given by } \left(\frac{d\sigma}{d\Omega}\right)_{Mott}\right)$, and another (containing the unpolarized spin structure functions) which describes the interaction due to the nucleon structure.

The structure functions W_1 and W_2 defined in Equation 1.17, parameterize the manner in which the nucleon deviates from a point like particle, and are usually redefined as $F_1\left(x, Q^2\right)$ and $F_2\left(x, Q^2\right)$ with

$$F_1\left(x, Q^2\right) = MW_1\left(\nu, Q^2\right) \tag{1.18}$$

and

$$F_2\left(x, Q^2\right) = \nu W_2\left(\nu, Q^2\right). \tag{1.19}$$

The cross section defined in Equation 1.17 can then be rewritten in terms of the F_1 and F_2 structure functions

$$\frac{d^2\sigma^{unpol}}{d\Omega dE'} = \left(\frac{d\sigma}{d\Omega}\right)_{Mott} \left[\frac{1}{\nu}F_2\left(x,Q^2\right) + \frac{2}{M}F_1\left(x,Q^2\right)\tan^2\frac{\theta}{2}\right]. \tag{1.20}$$

There are many targets that can be used in an experiment, some of which may have a mass number A. This leads to two conventions for defining the structure functions F_1 and F_2. The definitions given in Equations 1.18 and 1.19 are structure functions over the nucleus. Alternatively, one can define the per-nucleon structure functions $F_1' = F_1/A$ and $F_2' = F_2/A$. This dissertation will adhere to the first convention, where the structure functions are defined over the nucleus.

1.5.2 Polarized Structure Functions

Just as the unpolarized structure functions F_1 and F_2 allowed access to the symmetric part of the hadronic tensor (given in Equation 1.11), the spin dependent structure functions $G_1\left(\nu,Q^2\right)$ and $G_2\left(\nu,Q^2\right)$ allow access to the antisymmetric part of the hadronic tensor (defined in Equation 1.11). As was the case with W_1 and W_2, it is more convenient to express the spin dependent structure functions $G_1\left(\nu,Q^2\right)$ and $G_2\left(\nu,Q^2\right)$ as

$$g_1\left(x,Q^2\right) = M^2\nu G_1\left(\nu,Q^2\right) \tag{1.21}$$

$$g_2\left(x,Q^2\right) = M\nu^2 G_2\left(\nu,Q^2\right). \tag{1.22}$$

As was shown through Equation 1.15, a cross section difference can be obtained by flipping the target spin direction. It turns out the holding the target spin fixed and flipping the electron spin produces the same effect as holding the electron spin fixed and flipping the target spin [6]. If one considers longitudinally polarized electrons, with their spins aligned either parallel ($\uparrow$) or antiparallel ($\downarrow$) to their direction of motion, their spin vector can be

defined as

$$s^{\mu}_{\uparrow} = -s^{\mu}_{\downarrow} = \frac{1}{m}\left(E, \vec{k}\right) \tag{1.23}$$

and a polarized nucleon with arbitrary spin

$$S^{\mu} = \left(0, \hat{S}\right), \tag{1.24}$$

the cross section difference can be written as

$$\begin{aligned} \frac{d^2\sigma^{\uparrow,S}}{d\Omega dE'} - \frac{d^2\sigma^{\uparrow,-S}}{d\Omega dE'} = & - \frac{4\alpha^2}{Q^2}\frac{E'}{E}\left[\frac{\left(\vec{k}' \cdot \hat{S} + \vec{k} \cdot \hat{S}\right)}{M\nu} g_1\left(x, Q^2\right)\right] \\ & - \frac{4\alpha^2}{Q^2}\frac{E'}{E}\left[\frac{2\left(E\vec{k}' \cdot \hat{S} - E'\vec{k} \cdot \hat{S}\right)}{M\nu^2} g_2\left(x, Q^2\right)\right]. \end{aligned} \tag{1.25}$$

The two cases of interest for E06-014 are when the nucleon spins are longitudinal or transverse relative to the electron's momentum. When the nucleon is polarized longitudinally, it has it's spin either parallel ($\Uparrow$) or antiparallel ($\Downarrow$) to the electron's momentum. Taking the parallel spin to be the positive variant of S,

$$\vec{k} \cdot \hat{S} = |\vec{k}| = E \tag{1.26}$$

$$\vec{k}' \cdot \hat{S} = E' \cos\theta \tag{1.27}$$

where θ is the electron scattering angle defined in Figure 1.4. Applying these results to Equation 1.26 one can obtain the longitudinal cross section difference

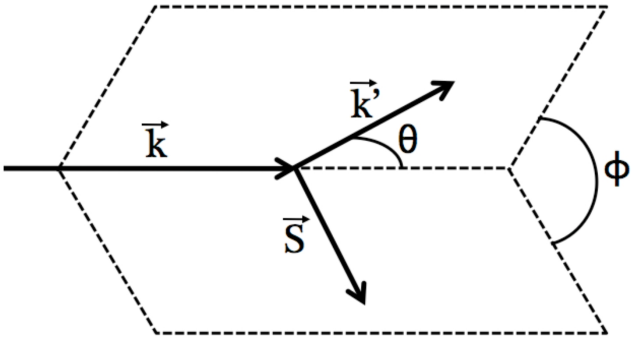

Figure 1.4: Scattering $\left(\hat{k}, \hat{k'}\right)$ and polarization $\left(\hat{k}, \hat{S}\right)$ planes.

$$\frac{d^2\sigma^{\downarrow,\Uparrow}}{d\Omega dE'} - \frac{d^2\sigma^{\uparrow,\Uparrow}}{d\Omega dE'} = \frac{4\alpha^2}{Q^2}\frac{E'}{E}\frac{1}{M\nu}\left[\left(E + E'\cos\theta\right)g_1\left(x, Q^2\right) - \frac{Q^2}{\nu}g_2\left(x, Q^2\right)\right]. \quad (1.28)$$

When the nucleon's spin is perpendicular to the incident electron's momentum, its two spin orientations are denoted as $\Rightarrow$ and $\Leftarrow$. The spin dot products then evaluate to

$$\vec{k} \cdot \hat{S} = 0 \quad (1.29)$$

$$\vec{k'} \cdot \hat{S} = E\hat{k'} \cdot \hat{S} = E' \sin\theta\cos\phi \quad (1.30)$$

where ϕ is angle between the scattering and polarization planes defined in Figure 1.4. Inserting these results into Equation 1.26, the transverse cross section difference is given as

$$\frac{d^2\sigma^{\downarrow,\Rightarrow}}{d\Omega dE'} - \frac{d^2\sigma^{\uparrow,\Rightarrow}}{d\Omega dE'} = \frac{4\alpha^2}{Q^2}\frac{E'^2}{E}\sin\theta\cos\phi\left[\frac{1}{M\nu}g_1\left(x, Q^2\right) + \frac{2E}{M\nu^2}g_2\left(x, Q^2\right)\right]. \quad (1.31)$$

Notice that when the target nucleon spin lies in the scattering plane ($\phi = 0$ or π), the magnitude of the cross section difference is maximum.

Rather than measuring cross section differences, which are time-consuming and more difficult to measure (they are an absolute measurement), the polarized structure functions g_1 and g_2 can be studied through measuring double spin asymmetries (DSA). Asymmetries are easier to measure than cross sections because the are a relative measurement, which results in many experimental limitations and uncertainties canceling each other out. If $d\sigma = \frac{d^2\sigma}{d\Omega dE'}$ denotes the differential cross section, and the unpolarized differential cross section is given as $\sigma_0 = \frac{d^2\sigma^{unpol}}{d\Omega dE'}$, then when the nucleon and electron spins are parallel and antiparallel to each other, the longitudinal double spin asymmetry $A_\parallel$ can be defined

$$A_\parallel \equiv \frac{d\sigma^{\downarrow\Uparrow} - d\sigma^{\uparrow\Uparrow}}{d\sigma^{\downarrow\Uparrow} + d\sigma^{\uparrow\Uparrow}} = \frac{d\sigma^{\downarrow\Uparrow} - d\sigma^{\uparrow\Uparrow}}{2\sigma_0}. \tag{1.32}$$

In the case of a transversely polarized nucleon and longitudinally polarized electron, one can define the transverse double spin asymmetry $A_\perp$

$$A_\perp \equiv \frac{d\sigma^{\downarrow\Rightarrow} - d\sigma^{\uparrow\Rightarrow}}{d\sigma^{\downarrow\Rightarrow} + d\sigma^{\uparrow\Rightarrow}} = \frac{d\sigma^{\downarrow\Rightarrow} - d\sigma^{\uparrow\Rightarrow}}{2\sigma_0}. \tag{1.33}$$

Here the $\Rightarrow$ denotes the target spin in the scattering plane perpendicular to the incident electron's momentum, and is pointing toward the side of the beam where the scattered electron is being detected. The denominators found in Equations 1.32 and 1.33 have the same value, which are given by twice the unpolarized differential cross section, whereas the numerators for the longitudinal and transverse asymmetries are given by Equations 1.28 and 1.31, respectively.

CHAPTER 2

UNDERSTANDING THE STRUCTURE FUNCTIONS

Although Chapter 1 provides an algebraic understanding of the unpolarized and polarized structure functions, it fails to assign any physical meaning. In this section several theories and models will be applied to the nucleon in order to gain insight into the physical meaning of the structure functions.

2.1 Bjorken Scaling and its Violation

When studying an object with a finite size, the resulting measurement will depend on the spatial resolution of the the probe. In the case of electron scattering, the exchanged virtual photon acts as a probe to resolve the structure of the nucleon. The wavelength at which the nucleon is probed depends on the inverse $\sqrt{Q^2}$ of the virtual photon $\left(\lambda \sim 1/\sqrt{Q^2}\right)$. Thus, as Q^2 increases, the virtual photon is able to resolve more subtle features of the nucleon. When Q^2 and ν become large enough, one can think of the electrons as scattering from *free* quarks within the nucleon, such is the case with DIS scattering. Moreover, since quarks are

point-like particles, further increasing the spatial resolution will have no effect, resulting in the loss of the scattering interaction's Q^2 dependence.

Such a phenomenon was predicted by Bjorken and Paschos [7], and is referred to as Bjorken scaling. Bjorken scaling occurs in what is known as the Bjorken limit, where the four-momentum and energy transfer tend to infinity as

$$Q^2 \to \infty \text{ and } \nu \to \infty \text{ with fixed } x = \frac{Q^2}{2M\nu}. \tag{2.1}$$

Structure functions, when considered in the Bjorken limit loose their Q^2 dependence, leading to the Callon-Gross relation [8]

$$F_2(x) = 2xF_1(x). \tag{2.2}$$

However, the scaling behavior of the structure functions is not exact. The one photon exchange that takes place during DIS is actually a first order approximation through which the electron interacts with hadronic matter. In reality, there are higher order interactions that also contribute to this interaction. Two of the higher order processes are shown in Figure 2.1, in which the incident quark or scattered quark emits a gluon. Adding the higher order terms to the first order approximation (shown in Figure 1.2) violates Bjorken scaling and introduces a $\log Q^2$ dependence to the cross section. The Q^2 evolution of the proton structure function $F_2^p(x, Q^2)$ is plotted in Figure 2.2, for a range of fixed x values that which spans four orders of magnitude. Once the size of a structure function has been measured at high Q^2 for some x, its Q^2 evolution can be calculated from QCD.

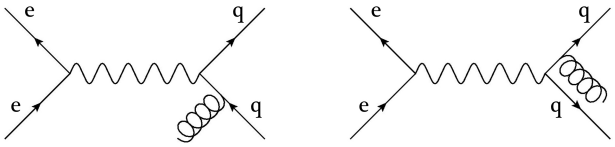

Figure 2.1: Lower order Feynman diagrams for gluon radiation in electron-quark scattering.

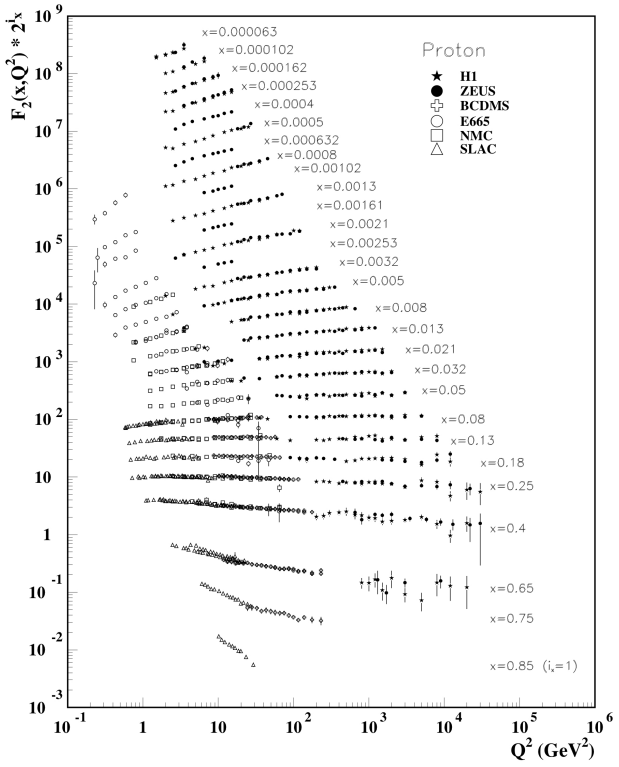

Figure 2.2: Q^2 dependence of $F_2^2\left(x, Q^2\right)$ showing scaling violation, reproduced from Reference [9].

2.2 Quark Parton Model

The quark parton model (QPM) was developed by Feynman [10] and Bjorken [7] in order to aid in the physical understanding of the structure functions. The quark parton model makes two underlying assumptions. First, when viewed in an infinite momentum frame, the transverse momenta and rest mass of the nucleon's constituents (today known to be charged quarks and neutral gluons) are small relative to the constituents longitudinal momenta and can be neglected. The second assumption is that the scattering behave as the incoherent sum of the interactions with each individual parton, with interaction times short enough that they can be viewed as a collection of non-interacting constituents.

One can use the quark parton model to provide an interpretation for the Bjorken x variable [4], by considering the parton's momentum fraction ξ of the nucleon momentum. Within the quark parton model, the parton masses can be neglected leading to

$$(\xi p + q)^2 = \xi^2 M^2 - Q^2 + 2\xi p \approx 0, \tag{2.3}$$

where p is the nucleon momentum and q is the photon momentum. If $M^2 << Q^2$, which is assumed in the quark parton model, then

$$\xi = \frac{Q^2}{2p} \equiv x. \tag{2.4}$$

Hence the Bjorken variable x is given the physical interpretation as being the fraction of nucleon momentum carried by a struck quark.

As a result of the quarks (partons) being non-interacting and free, the cross section for electron-nucleon scattering is simply the weighted sum of cross sections from each individual quark, with the weights computed according to the quark number densities. In the the unpolarized case, the quark spin states ($\uparrow$ and $\downarrow$) are summed over, and the parton

distribution function (PDF) is given as

$$q_i(x) = q_i^{\uparrow}(x) + q_i^{\downarrow}(x). \tag{2.5}$$

In the QPM, $q_i(x)$ is simply the probability that the i^{th} quark within the nucleon has momentum fraction x. One can then define the unpolarized structure function F_1 as

$$F_1(x) = \frac{1}{2}\sum_i e_i^2 q_i(x) = \frac{1}{2}\sum_i e_i^2 \left[q_i^{\uparrow}(x) + q_i^{\downarrow}(x)\right], \tag{2.6}$$

and through the use of the Callon-Gross relation, defined in Equation 2.2, F_2 can be computed

$$F_2(x) = x\sum_i e_i^2 q_i(x) = x\sum_i e_i^2 \left[q_i^{\uparrow}(x) + q_i^{\downarrow}(x)\right], \tag{2.7}$$

where e_i is the electric charge of the i^{th} quark.

To compute the polarized structure functions, the polarized PDF Δq needs to be used and is defined as

$$\Delta q_i(x) = q_i^{\uparrow}(x) - q_i^{\downarrow}(x).$$

The sign of the polarized PDF is determined by letting the $\uparrow$ ($\downarrow$) denote quark spin parallel (antiparallel) to the nucleon spin [6]. Armed with the polarized PDF, the spin dependent structure function g_1 can be defined analogously to F_1 as

$$g_1(x) = \frac{1}{2}\sum_i e_1^2 \Delta q_i(x) = \frac{1}{2}\sum_i e_i^2 \left[q_i^{\uparrow}(x) - q_i^{\downarrow}(x)\right]. \tag{2.9}$$

For as well as the QPM is at ascribing a physical meaning to x, the unpolarized structure functions and spin dependent g_1 structure function, it fails to provide a description of the g_2

spin dependent structure function.

2.3 Operator Product Expansion

A different theoretical approach from the QPM must be considered, if one hopes to assign a physical meaning to the spin-dependent structure function g_2. Such an approach is the operator product expansion (OPE) [11], which provides QCD predictions for moments of the structure functions. The OPE, which has no model dependence associated with it, is derived using only some general results from quantum field theory, and is used to evaluate the non-perturbation part of QCD calculations. First introduced by K. G. Wilson, the OPE allowed the evaluation of operator products, such as the electromagnetic currents $J_\mu(\xi) J_\nu(0)$ in the asymptotic limit, in which ξ is a four dimensional spatial vector. As $\xi \to 0$, the operators can be expanded as [12]

$$\lim_{\xi \to 0} O_a(\xi) O_b(0) = \sum_i C_{abk}(\xi) O_i(0), \tag{2.10}$$

where the coordinate origin was chosen to coincide with the point of application of the second operator (O_b). The Wilson coefficients, $C_{abk}(\xi)$ contain all of the spatial information and can be calculated using perturbative QCD [13]. As long as ξ is small (or equivalently Q^2 is large) enough relative to the mass scale $\left(\Lambda^2_{QCD}\right)$, only the first few terms are expected to make any significant contribution. The quark-gluon operators (O_i), which have dimension d and spin n, represent fundamental fields in QCD. The concept of twist (τ) can now be introduced and defined as $\tau = d - n$. The contribution of any operator to the tensor $L_{\mu\nu} W^{\mu\nu}$ is of order:

$$\left(\frac{M}{Q^2}\right)^{\tau-2}. \tag{2.11}$$

The lowest twist allowed is that of twist-2, while higher twists are suppressed by increasing factors of $\frac{M}{Q^2}$. The physical meaning of the structure functions discussed in Section 2.2 also apply to the OPE, which can be seen through mapping parts of the QPM to the twist two contributions of the OPE [14]. Twist-3 and higher contributions that have no QPM interpretation arise from quark-gluon correlations and non-zero quark masses. Higher-twist processes can be described in terms of coherent parton scattering, in which more than one parton from a particular hadron takes place in the scattering [15].

2.3.1 The g_2 Structure Function

The OPE can be used to study the spin-dependent structure function g_2. A twist expansion via the OPE leads to an infinite set of sum rules [6]. The series expansions for g_1 and g_2, known as the Cornwall-Norton (CN) moments [16], are given as

$$\int_0^1 x^{n-1} g_1\left(x, Q^2\right) dx = \frac{1}{2} a_{n-1},\ n = 1, 3, 5, ... \tag{2.12}$$

$$\int_0^1 x^{n-1} g_2\left(x, Q^2\right) dx = \frac{n-1}{2n}\left(d_{n-1} - a_{n-1}\right),\ n = 3, 5, 7, ... \tag{2.13}$$

where only twist-2 and twist-3 contributions are considered. The quantities a_{n-1} and d_{n-1} represent the twist-2 and twist-3 matrix elements respectively[1]. From Equations 2.12 and 2.13, one can see that the expansions are only over n-odd integers, which is a result of the structure function's symmetry under charge conjugation [13].

[1]The convention used in Reference [6] labels the matrix elements referring to their respective twist n, rather than $n-1$ (i.e. d_n in Reference [6] is equivalent to d_{n-1} as defined in this dissertation). This dissertation will use the $n-1$ convention of the matrix element labeling.

To unravel the meaning of g_2, Equations 2.12 and 2.13 can be combined to give [6]

$$\int_0^1 x^{n-1}\left(g_1\left(x,Q^2\right)+\frac{n}{n-1}g_2\left(x,Q^2\right)\right)dx=\frac{d_{n-1}}{2},\ n\geq 3. \tag{2.14}$$

If one assumes that the twist-3 contribution is negligible compared to that of the twist-2, and that the Burkhardt-Cottingham sum rule [17], which says that $\int_0^1 g_2 dx = 0$, holds; then setting d_{n-1} in Equation 2.14 to zero and $n=1$, g_2 can be expressed entirely in terms of g_1. This relation is known as the Wandzura-Wilczeck relation [18]

$$g_2^{WW}\left(x,Q^2\right)=-g_1\left(x,Q^2\right)+\int_x^1\frac{dy}{y}g_1\left(x,Q^2\right). \tag{2.15}$$

The Wandzura-Wilczeck relation allows the twist-2 contribution of the g_2 structure function to be determined completely by the twist-2 structure function g_1, and can thus be interpreted through the QPM. If the twist-3 term that was initially set to zero in order to derive g_2^{WW} is now considered, then g_2 can be separated into leading twist-2 and higher order twist terms

$$g_2\left(x,Q^2\right) = g_2^{WW}\left(x,Q^2\right)+\bar{g}_2\left(x,Q^2\right), \tag{2.16}$$

$$\bar{g}_2\left(x,Q^2\right) = -\int_x^1\frac{\partial}{\partial y}\left[\frac{m_q}{M}h_T\left(y,Q^2\right)+\xi\left(y,Q^2\right)\right]\frac{dy}{y}. \tag{2.17}$$

Thus from Equation 2.17, it can be seen that up to twist-3 there are three contributions to g_2:

- g_2^{WW}

  The twist-2 contribution, which is determined from the g_1 structure function and has its interpretation explained through the QPM.

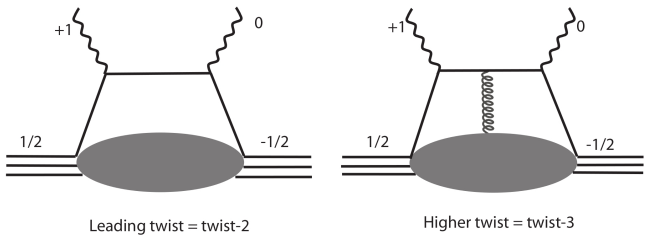

Figure 2.3: Leading twist contributions to the g_2 structure function via virtual Compton scattering [4]. The left diagram shows the twist-two, photon-quark interaction that is described in the QPM. The diagram on the right shows the twist-three contribution in which quark-gluon interactions also take place. Image reproduced from Reference [19].

- h_T

  Known as *transversity*, and describes the quarks transverse polarization distribution. This twist-2 quantity is suppressed by the quark mass, and is expected not to contribute much. This quantity is assumed negligible through out this dissertation.

- ξ

  A twist-3 contribution, which arises from quark-gluon interactions within a nucleon.

With g_2 possessing higher twist contributions at leading order, it serves as an unique opportunity to study higher twist effects.

Another way to see why g_2 contains information about quark-gluon correlations, is to consider virtual Compton scattering [4]. According to the optical theorem, g_2 is the imaginary part of the spin dependent Compton amplitude given by the process [15]:

$$\gamma^* (+1) + N (1/2) \Rightarrow \gamma^* (0) + N (1/2) , \tag{2.18}$$

where γ^* and N represent the virtual photon and nucleon respectively, and the labels contained in the parentheses gives the helicity. QCD allows this helicity exchange to take

place in two ways: first, through single quark scattering in which the struck quark carries one unit of angular momentum through it's transverse momentum; second, through quark scattering with an additional transversely-polarized gluon [15]. Figure 2.3 illustrates the two helicity exchanges that are allowed in the virtual Compton scattering process. The left diagram represents the first helicity exchange process where scattering takes place on a single quark, which is a twist-2 contribution and has an explanation within the QPM. The diagram on the right shows the helicity exchange when scattering involves more than one parton (a quark and gluon), which is a twist-3 contribution in this case and has no interpretation in the QPM. Thus the g_2 structure function is a sum of theses two processes, where the twist-2 contribution can be related to the g_1 structure function (*i.e.* g_2^{WW}) and the higher twist contribution can explained through the use of higher twist expansions via the OPE (*i.e.* $\bar{g_2}$).

The spin-dependent structure function g_2 has a much richer physical interpretation than g_1. It contains higher twist effects at leading order that through the OPE reveal that they originate from quark-gluon interactions, and contain information about one of the most fundamental properties of QCD, confinement[2].

2.4 Probing the Color Force

In Section 2.3.1, g_2 was was seen to contain information about higher twist contributions, which can be used to study the color force of QCD and ultimately provide insight into the phenomenon of confinement.

[2]Confinement is the phenomenon responsible for preventing a color charge, such as a quark, from being directly observed outside of a nucleon.

2.4.1 Color Polarizabilities

When placing an electron cloud, atom or molecule into an external electric field $\vec{E}$, the degree to which the normal charge distribution is distorted is given by the electric charge polarizability α, which results in an electric polarization $\vec{P}$

$$\vec{P} = \alpha \vec{E}. \tag{2.19}$$

Similarly, the magnetic polarizability β describes the response to an external magnetic field. One can measure these quantities through low energy Compton scattering, with a scattering amplitude of [4], [20],

$$T(\nu) = \vec{\epsilon}'^{*} \cdot \vec{\epsilon} f(\nu) + i\vec{\sigma}\left(\vec{\epsilon}'^{*} \times \vec{\epsilon}\right) g(\nu), \tag{2.20}$$

where $\vec{\epsilon}_i$ and $\vec{\epsilon}_f$ refer to the incident and scattered transverse polarizations of the photon respectively, and $f(\nu)$ and $g(\nu)$ are the spin-independent and spin-dependent part of the amplitude defined as

$$f(\nu) = -\frac{e^2}{4\pi M} + (\alpha + \beta)\nu^2 + O\left(\nu^4\right), \tag{2.21}$$

$$g(\nu) = -\frac{e^2\kappa^2}{8\pi M^2}\nu + \gamma_0 \nu^3 + O\left(\nu^5\right), \tag{2.22}$$

where κ is the anomalous magnetic moment and γ_0 is the forward spin polarizability. One can generalize the polarizabilities, at a non-zero Q^2 value by letting $\alpha \rightarrow \alpha(Q^2)$, which can be linked to g_1 and g_2 parton distributions through dispersion relations [21]. It is this connection of g_2 to the electromagnetic polarizabilities at low Q^2, where the photon wavelength is much larger than the nucleon, that has lead to the higher twist

contributions (which have nothing to due with QED) of g_2 being interpreted originally as *color polarizablilities* [22].

If one considers Equation2.14, which is the x^2 weighted integral of a linear combination of g_1 and g_2, one finds the twist-3 matrix element

$$d_2\left(Q^2\right) = \int_0^1 x^2 \left(2g_1\left(x, Q^2\right) + 3g_2\left(x, Q^2\right)\right) dx = 3\int_0^1 x^2 \bar{g}_2\left(x, Q^2\right), \tag{2.23}$$

where the local matrix element, computed in light cone coordinates is given as [20]

$$g\left\langle P, S|\bar{q}\left(0\right) G^{+y}\left(0\right) \gamma^{+} q\left(0\right)|P, S\right\rangle = 2MP^{+}P^{+}S^{x}d_2, \tag{2.24}$$

where g is the QCD coupling constant, P and S the are the nucleon momentum and polarization; q and G^{+y} are the quark and gluon fields. The gluon field can also be written as [20]

$$G^{+y} = \frac{1}{\sqrt{2}}\left(B^x - E^y\right), \tag{2.25}$$

with B^x and E^y being the color magnetic and electric fields respectively, which leads to matrix elements that describe the color electric, χ_E, and magnetic, $_B$, polarizability of the nucleon [22].

$$\chi_E 2M^2\vec{S} = \left\langle P, S|q^{\dagger}\vec{\alpha}\times g\vec{E}q|P, S\right\rangle \tag{2.26}$$

$$\chi_B 2M^2\vec{S} = \left\langle P, S|q^{\dagger}g\vec{B}q|P, S\right\rangle, \tag{2.27}$$

Using Equations 2.26 and 2.27, the d_2 matrix element can be expressed as linear combi-

nation of the color electric and magnetic quark-gluon correlators

$$d_2 = \frac{1}{4}\left(\chi_E + 2\chi_B\right). \tag{2.28}$$

However, at larger values of Q^2, where the wavelength of the virtual photon is smaller than that of the nucleon size, the physical concept of polarizability no longer makes sense, as the twist-3 piece of g_2 is described by a local correlator. Moreover, while the nucleons are polarized they are not distorted, but only spin-aligned. Therefore the higher twist matrix elements are obtained from an undeformed nucleon and can not be interpreted as describing its color polarizability, because a polarizability describes the tendency of a charge or magnetic distribution to be distorted from its normal shape in the presence of an external field. Thus as it will be shown, a better interpretation of these matrix elements is to associate them with a color-Lorentz force rather than color polarizabilities [20].

2.4.2 Color Force

In electromagnetism, a particle with charge e, moving with a velocity near the speed of light in the $-\hat{z}$ direction ($\vec{v} \approx$ (0,0,-1)), will experience a Lorentz force (F^y) in the $\hat{y}$ direction [20]

$$F^y = e\left(\vec{E} + \vec{v} \times \vec{B}\right)^y = e\left(E^y - B^x\right) = -e\sqrt{2}F^{+y}. \tag{2.29}$$

The linear combination of electric and magnetic fields seen in Equation 2.29 matches the same combination that is seen in Equation 2.24 for the color electric and magnetic fields. This suggests that that the d_2 matrix element could be interpreted as a color-Lorentz force experienced by a quark moving near the speed of light.

Furthermore the force like behavior of d_2 can also be seen when comparing the d_2 matrix element to the average transverse momentum of quarks in semi-inclusive deep inelastic

scattering (SIDIS) [23], in which the scattered electron and a scattered hadron are detected in the final state. The average transverse momentum of the ejected quark in SIDIS is given by [24], [20]

$$\langle k_{\perp}^{y} \rangle = -\frac{\sqrt{2}}{2P^{+}} \left\langle P,S|\bar{q}\left(0\right)\int_{0}^{\infty} dtG^{+y}\left(t,z=-t\right)\gamma^{+}q\left(0\right)|P,S\right\rangle , \tag{2.30}$$

which has the physical interpretation of the total color Lorentz force over the ejected quarks entire trajectory, which also plays a role in color *lensing effects* [25]. In particular, the matrix element d_2 can then be interpreted as the transverse color force felt between the remnant di-quark system and the active quark immediately after it is struck by a virtual photon, with the color force given as

$$\begin{aligned} F^{y}\left(0\right) &\equiv -\frac{\sqrt{2}}{2P^{+}}\left\langle P<S|\bar{q}\left(0\right)G^{+y}\left(0\right)\gamma^{+}q\left(0\right)|P,S\right\rangle \\ &= -\sqrt{2}MP^{+}S^{x}d_{2}=-M^{2}d_{2}, \end{aligned} \tag{2.31}$$

where for the last equality is evaluated in the nucleon rest frame, where $P^{+}=\frac{1}{\sqrt{2}}M$ and $S^{x}=1$ [20].

As it can be seen from Equation 2.28, d_2 is a linear combination of the color electric and magnetic components of the color force and another equation is needed to isolate the two force components. It turns out that the x^2 moment of the twist-4 matrix element f_2 provides a different linear combination of the color force components and is given as [26–28]

$$f_{2}M^{2}S^{\mu}=\frac{1}{2}\left\langle P,S|\bar{q}g\tilde{G}^{\mu\nu}\gamma_{\nu}q|P,S\right\rangle , \tag{2.32}$$

where $\tilde{G}^{\mu\nu}$ is the dual gluon field strength tensor. From Equation 2.32, f_2 can be related

to matrix elements of the color electric and magnetic quark-gluon correlators given by Equations 2.26 and 2.27 as

$$f_2 = \chi_E - \chi_B. \tag{2.33}$$

The combination of d_2 and f_2 allows for the decomposition of the color force into its electric and magnetic components $F^y = F^y_E + F^y_B$, where[20]

$$F^y_E(0) = -\frac{M^2}{4}\chi_E \quad F^y_B(0) = -\frac{M^2}{2}\chi_B. \tag{2.34}$$

Equation 2.34 also allows for d_2 and f_2 to be rewritten in terms of the color force

$$d_2 = -\frac{1}{M^2}(F_E + F_B) \tag{2.35}$$

$$f_2 = -\frac{2}{M^2}(2F_E - F_B). \tag{2.36}$$

2.4.3 Extracting the Twist-4 Matrix Element

Section 2.4.2 related d_2 to a color Lorentz force, and showed that in order isolate the color electric and magnetic components, a second matrix element f_2 is needed. Unfortunately f_2 has never been measured and will not for some time. However f_2 can be extracted using the OPE and measured data.

The lowest (unweighted) moment of g_1 can be expanded in an inverse power series of Q^2 using the OPE [26] as

$$\Gamma_1 \equiv \int_0^1 g_1\left(x, Q^2\right) dx = \sum_{\tau=2,4,\ldots} \frac{\mu_\tau\left(Q^2\right)}{Q^{\tau-2}}, \tag{2.37}$$

with the coefficients μ_τ related to nucleon matrix elements with twist greater than or

equal to τ. The twist-2 coefficient μ_2 is determined by matrix elements of the axial vector operator $\bar{q}\gamma_\mu\gamma_5 q$, summed over quark flavors. The twist-2 coefficient can be decomposed into flavor triplet (g_A, measured in neutron β decay), octet (a_8, extracted from weak hyperon decays) and singlet ($\Delta\Sigma$) axial charges to give

$$\mu_2\left(Q^2\right) = C_{ns}\left(Q^2\right)\left(-\frac{1}{12}g_A + \frac{1}{36}a_8\right) + C_s\left(Q^2\right)\frac{1}{9}\Delta\Sigma, \tag{2.38}$$

where C_{ns} and C_s are the non-singlet and singlet Wilson coefficients [29].

The higher twist contributions to Γ_1 can then be obtained by subtracting the leading twist (twist-2) contribution from Γ_1

$$\Delta\Gamma_1\left(Q^2\right) \equiv \Gamma_1\left(Q^2\right) - \mu_2\left(Q^2\right) = \frac{\mu_4\left(Q^2\right)}{Q^2} + \frac{\mu_6\left(Q^2\right)}{Q^4} + O\left(\frac{1}{Q^6}\right). \tag{2.39}$$

The μ_4 term contains the twist-2 (a_2), twist-3 (d_2) and a twist-4 (f_2) matrix elements,

$$\mu_4\left(Q^2\right) = \frac{M^2}{9}\left(a_2 + 4d_2 + 4f_2\right). \tag{2.40}$$

The twist-2 term, a_2, is due target mass corrections [30], and is related to the second (x^2-weighted) moment of g_1.

Therefore with the use of measured results (Γ_1, μ_2, a_2 and d_2) the twist-4 matrix element f_2 can be extracted and the color force components separated as

$$\begin{aligned} F_E &= -\frac{M^2}{6}\left(2d_2 + f_2\right) \\ F_B &= -\frac{M^2}{6}\left(4d_2 - f_2\right). \end{aligned} \tag{2.41}$$

2.5 Target Mass Corrections

Studies of higher twist have traditionally been done using the CN moments, however the exact relation of the CN moments to the dynamical higher twist contributions has recently come into question [16], [31]. The CN moments are argued to only be valid when the terms connected to the finite mass of the nucleon are neglected, these terms are known as target mass corrections. The target mass corrections are related to twist-2 operators and are of order $O\left(\frac{M^2}{Q^2}\right)$. Analogous to the CN moments, the Nachtmann moments (M_1 and M_2) can be used to separate the higher twist contributions from the target mass corrections [32–37], and are defined as [16, 38, 39]

$$\begin{aligned} M_1^n\left(Q^2\right) &\equiv \frac{1}{2}a_{n-1} \equiv \frac{1}{2}\tilde{a}_n E_1^n \\ &= \int_0^1 \frac{\xi^{n+1}}{x^2}\left[\left(\frac{x}{\xi} - \frac{n^2}{(n+2)^2}\frac{M^2 x\xi}{Q^2}\right) g_1\left(x,Q^2\right) - \frac{4n}{n+2}\frac{M^2x^2}{Q^2} g_2\left(x,Q^2\right)\right] dx, \\ n &= 1,3,..., \end{aligned} \tag{2.42}$$

$$\begin{aligned} M_2^n\left(Q^2\right) &\equiv \frac{1}{2}d_{n-1} \equiv \frac{1}{2}\tilde{d}_n E_2^n \\ &= \int_0^1 \frac{\xi^{n+1}}{x^2}\left[\frac{x}{\xi} g_1\left(x,Q^2\right) + \left(\frac{n}{n-1}\frac{x^2}{\xi^2} - \frac{n}{n+1}\frac{M^2x^2}{Q^2}\right) g_2\left(x,Q^2\right)\right] dx, \\ n &= 3,5,..., \end{aligned} \tag{2.43}$$

where a_{n-1} (d_{n-1}) (Appearing in Equations 2.12 and 2.13), and $\tilde{a_n}$ ($\tilde{d_n}$) are the CN and Nachtmann twist-2 (twist-3) matrix elements, respectively; E_2^n and E_3^n are the corresponding Wilson coefficients for the twist-2 and twist-3 matrix elements, and ξ is the Nachtmann scaling variable (analogous to the Bjorken scaling variable x) defined as

$$\xi = \frac{2x}{1 + \sqrt{1 + \frac{4x^2M^2}{Q^2}}}. \tag{2.44}$$

It should be noted that when $Q^2 >> M^2$, $\xi \to x$ and the Nachtmann moments reduce to the CN moments.

CHAPTER 3

D_2: MODELS AND MEASUREMENTS

In this section, the status of the d_2 matrix element before the E06-014 experiment will be presented. This includes first discussing the various models used to compute theoretical values of d_2, followed by an experimental overview of measured d_2 quantities for both proton and neutron targets.

3.1 Models

There are many theoretical and phenomenological models used to try and understand the structure of the nucleon. Rather than give an exhaustive description of the models, a brief summary of a few of the more prominent models are presented.

3.1.1 QCD Sum Rules

In QCD, there are two very distinct limits that exist, the short and long distance limits. At short distances, where particles have high energy and large momentum transfers, the partons are asymptotically free and the degrees of freedom are clearly the quarks and gulons. In contrast, at large distances composite hadrons form the degrees of freedom.

The sum rule approach [40] interpolates between the perturbative (short distance) and non-perturbative (long distance) regimes of QCD, through the use of dispersion relation methods in combination with OPE [4]. The QCD sum rules allow the low and high energy properties of QCD to be related to one another.

3.1.2 Lattice QCD

At large distances in QCD is where the phenomena of confinement takes place. Analytic approaches in this region are difficult due to the non-perturbative nature of QCD. One analytical approach, known as lattice QCD [4, 41–43], is used to discretize space-time allowing QCD to be solved on a lattice. This approach requires a substantial amount of computing power in order to solve the discrete equations on the lattice, and has been a rapidly evolving field since its inception.

3.1.3 Bag Model

In an effort to try and create the confinement mechanism of QCD (which says that no free quarks exist outside of the nucleon), a model was formed where extremely massive quarks were bound in a deep potential, known as the bag model [4]. One of the simplest bag models was developed by Bogoliubov [44], in which the the quark masses m are infinity large and placed in a spherical volume of radius R, within which they felt an attractive scalar field of strength m. Bogoliubov's bag model lead to a simple explanation of the deviation of g_A from the naive SU(6) result.

A more realistic bag model, known as the MIT bag model [45, 46] was constructed in such a way that the model included both the short (quarks are asymptotically free) and long (quarks are confined) range QCD limits. Space was divided into an interior and exterior region. Within the interior region of the bag, quarks had very light masses and felt only

weak fields. Where as the exterior region of the bag prevented the quarks from propagating and had a lower vacuum energy. For the case of a static spherical cavity and in the limit $m \to \infty$, the MIT bag model wavefunctions reduce to those found in Bogoliubov's bag model [4].

3.1.4 Chiral Solitons

In the quark chiral soliton model, the nucleon is viewed as a chiral soliton, which is a non-linear dynamical system in which quarks are bound and localized by their interaction with chiral fields [4].

The fact that chiral symmetry [1] is spontaneously broken in QCD implies that scalar and pion fields should appear in combinations, such that the effective Lagrangian is symmetric under a chiral transformation. This allows one to introduce these fields in a minimal way (with no other scalar fields) and find chiral solitons for the chosen parameters [4].

3.1.5 MAID

The unitary isobar model (MAID) [48] uses phenomenological fits to electro- and photo-production data for the nucleon. These fits cover the region from the single-pion production threshold to the resonance limit, conventionally set at W = 2 GeV. The major resonances are modeled using Breit-Wigner functions to construct the production channels. This model provides helpful comparisons to data (i.e. moments of structure functions, photo-absorption cross sections, etc.) that fall within its defined phase space.

[1] Chiral symmetry is a possible symmetry of the Lagrangian, under which the right- and left-handed Dirac fields transform independently [47].

3.2 Measurements

Experimental measurements of the neutron g_2 structure function began with the SMC [49] and SLAC E142 [50] collaborations. Afterwards the SLAC E143 [51], E154 [52] and E155 [53, 54] collaborations improved upon the measurement, leading up to the most recent measurements performed at Jefferson Lab (JLab) by the E97-103 [55], E94-010 [56], E99-117 [57], RSS [39], E01-012 [58] and E06-014 (the experiment analyzed in this dissertation). The free neutron in nature is unstable, with a life time of about 15 minutes [9]. This results in the neutron information having to be extracted from a non pure neutron target. Experiments typically have two ways to extract the neutron information from the measured quantities. The first is by scattering leptons from proton and deuteron targets, where by using the proton and deuteron wave functions the proton contribution can be subtracted from the deuteron leaving behind the neutron contribution. The SMC, E143, E155 and RSS experiments have successfully extracted polarized neutron quantities via scattering from proton and deuteron targets. The second method in which to access the neutron information is through the use of polarized ^{3}He targets (see Section 6), in which a ^{3}He nucleus is polarized and when detecting target-spin dependent quantities (such as g_1 and g_2) the two protons in the nucleus have opposite spins who cancel each other, effectively leaving only a polarized neutron. The E142, E154, E99-117, E01-012, E97-103 and E06-014 have measured polarized neutron quantities using a polarized ^{3}He target. Figure 3.1 shows the measured g_2^n structure function weighted by x^2 plotted against x for a few selected experiments: E143 [51] and E155 [53, 54], which used proton an deuteron targets; E142 [50], E154 [52], E97-103 [55] and E99-117 [57], which used a polarized ^{3}He target.

In addition to measuring the g_2 structure function, it can be used to extract the twist-3 matrix element d_2. This quantity was first experimentally measured at SLAC, where they combined their E155 results with those from E142, E143 and E154 to determine the proton

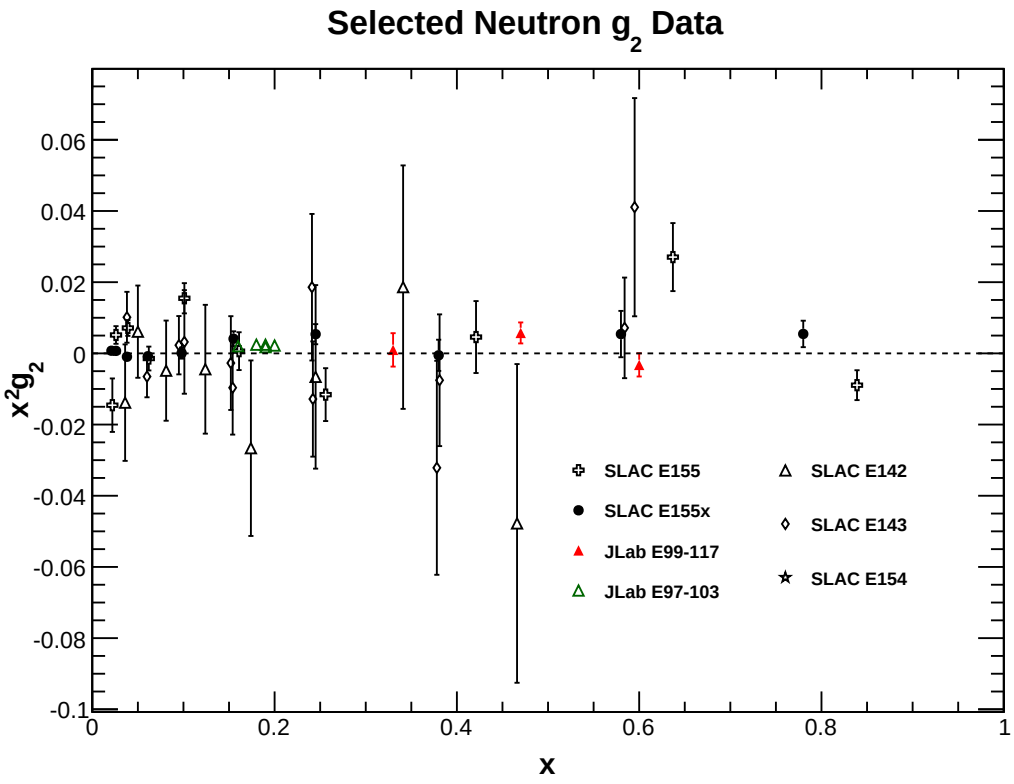

Figure 3.1: The g_2^n structure function weighted by x^2 plotted against x for a few selected experiments: E143 [51] and E155 [53, 54], which used proton an deuteron targets; E142 [50], E154 [52], E97-103 [55] and E99-117 [57], which used a polarized ^{3}He target.

(d_2^p) and neutron (d_2^n) d_2 matrix elements. In combining their data [54], they assumed no Q^2 dependence on g_2 and covered a range of 0.02 to 0.8 in x and 0.7 to 20 GeV^2 in Q^2, resulting in an averaged Q^2 of 5 GeV^2 and measured values of d_2^p = 0.0032 $\pm$ 0.0017 and d_2^n = 0.0079 $\pm$ 0.0048. When these values are compared to theoretical calculations using bag models [59–61], QCD sum rules [62–65], lattice QCD [66] and chiral soliton models [67, 68], the proton d_2 was found to be in fairly good agreement with the majority of the models. The measured neutron d_2 however, was found to disagree with all of the models; but it had a fairly large uncertainty. Later E99-117 [57] combined their measured g_2^n data with E155 [54] to improve the uncertainty of the neutron d_2, however the disagreement between theoretical calculations and the experiment remained. Figure 3.2 shows the comparison of E155 measured d_2^p (top panel) and the neutron d_2 result obtained from combining the E155 and E99-117 data (bottom panel) to theoretical calculations.

Since the SLAC d_2 measurement there have been several complimentary d_2 measurements in the resonance region ($W < 2$ GeV) performed at JLab (E94-010, RSS and E01-012). These experiments generally have a much lower average Q^2 ($\sim$ 0.1 –2.5 GeV^2) than the SLAC results and contain no contribution from the DIS region. These experiments showed that at low Q^2 in the resonance region, that after the subtraction of the elastic contribution at x=1, there is a sizable twist-3 contribution which quickly dies off with increasing Q^2. This trend like the theoretical calculations of d_2^n also disagrees with the measured SLAC neutron d_2, although one needs to keep in mind that the SLAC data and the lattice QCD calculation are in the DIS region and d_2 may not have the same behavior as it does in the resonance region. The top panel of Figure 3.3 shows elastic subtracted ($\bar{d}_2^n = d_2^n - (d_2^n)^{\text{elastic}}$) d_2^n measurements in the resonance region from JLab, along with comparisons of $\bar{d}_2^n$ as a function of Q^2 calculated using MAID [48], the combined SLAC and E99-117 data and lattice QCD calculation (note that the SLAC + E991-117 data and lattice QCD calculation

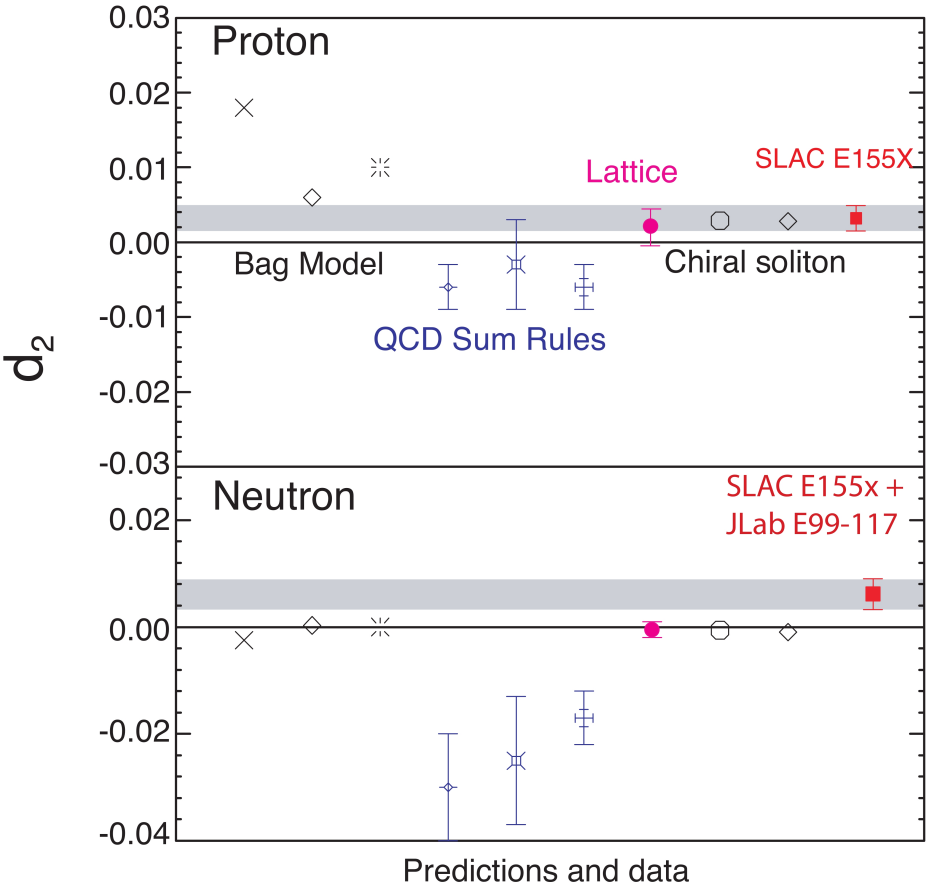

Figure 3.2: Theoretical calculations from: bag models [59–61], QCD sum rules [62–65], lattice QCD [66] and chiral soliton [67, 68];compared to experimental SLAC E155 [54] of the proton d_2 (top panel) and the combined SLAC E155 [54] and JLab E99-117 [57] neutron d_2 (lower panel). Plot reproduced from Reference [19].

are in the DIS region and no elastic contribution has been subtracted [2]). The bottom panel of Figure 3.3 shows the measured d_2^n with the elastic contribution added, and the size of the elastic d_2 obtained from the dipole model parameterized by the Galster fit [69] (also discussed in Appendix G). The elastic contribution clearly dominates the d_2^n matrix element at low Q^2 (< 1 GeV^2).

E06-014 measured d_2^n at two mean Q^2 values of 3.25 GeV^2 and 4.43 GeV^2, in which the data spanned both the DIS and resonance regions, but with the majority of the data collected in the DIS region. These measurements will not only be able to provide a bench mark test for lattice QCD (since most of the data falls in the DIS region), but also provide a more precise measurement of d_2^n to better determine f_2^n via the extract method discussed in Section 2.4.3, allowing for the separation of the color electric and magnetic forces.

[2]The d_2^n elastic contribution at Q^2 = 4 GeV^2 is on the order of 10^-4 and is usually negligible.

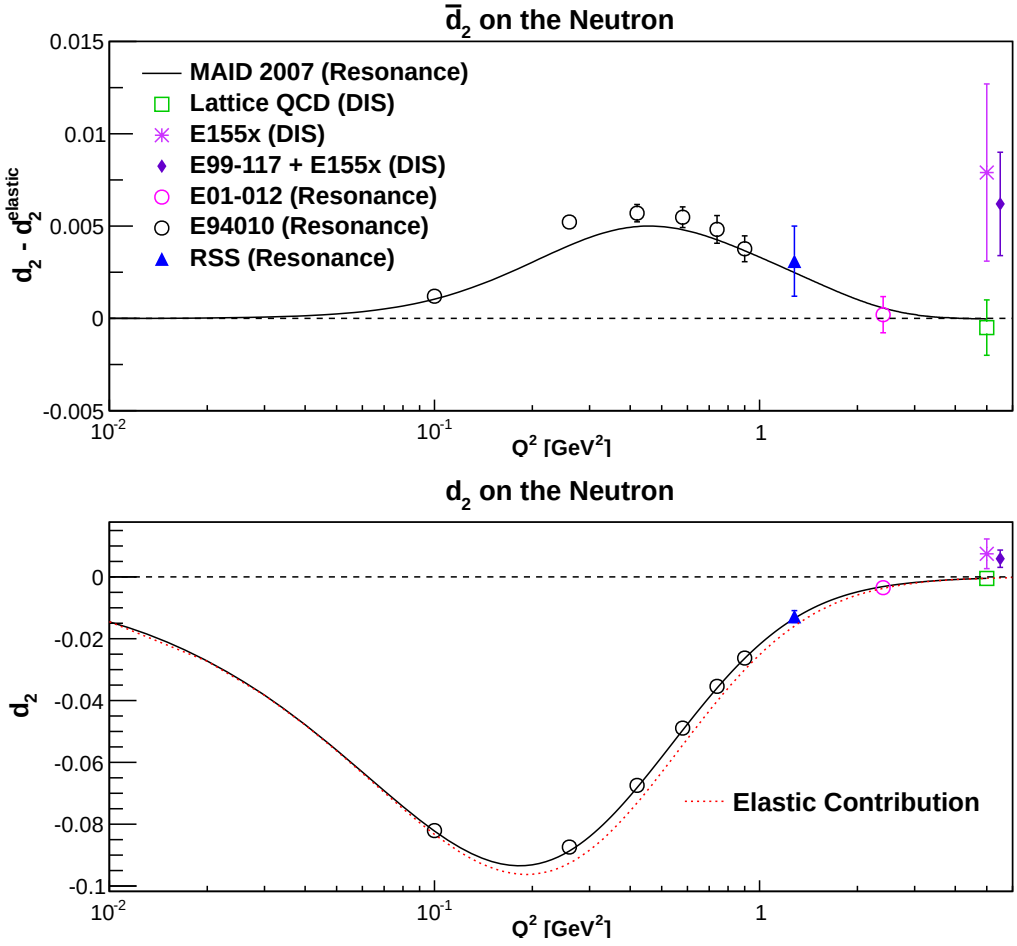

Figure 3.3: World neutron d_2 values in the DIS region from: SLAC E155 [54] (magenta star), combined JLab E99-117 [57] + SLAC E155 [54] data (purple diamond) and lattice QCD calculation [66] (green open square); neutron d_2 values in the resonance region from: JLab E01-012 [58] (magenta open circle), JLab RSS [39] (blue solid triangle) and JLab E94-010 [56] (open black circle), calculation from MAID [48] fit (solid black line). The top panel shows d_2^n with the elastic contribution subtracted ($\bar{d}_2^n$), while the bottom panel shows the measured d_2^n values with elastic contribution added. The elastic contribution to d_2 (red dashed line) was determined from the dipole model parameterized by the Galster fit [69]).

CHAPTER 4

THE E06-014 EXPERIMENT

The data presented in this dissertation were taken during experiment E06-014, which ran at the Thomas Jefferson National Accelerator Facility (JLab) in Newport News Virginia. The primary goal of the experiment was to measure the neutron[1] d_2 matrix element via beam-target double spin asymmetries (DSAs) and absolute scattering cross sections. The measurement was performed in the valence quark region covering $\sim$ 0.2-0.93 in x and $\sim$ 1.73-6.88 GeV^2 in Q^2, which encompassed both the DIS and resonance regions. In this section the setup and tools used during E06-014 to measure d_2^n will be discussed. Section 4.1 will describe the setup and kinematic coverage of E06-014. Section 4.3 will describe the JLab electron accelerator, while Section 4.4 will discuss the hardware and software used in Hall A (the experimental hall were E06-014 took place). Finally in Section 4.5 an overview of E06-014's run history will be presented.

[1] Neutron information is extracted from a polarized ^{3}He target.

4.1 Experiment Overview

Experiment E06-014, which is also known as the d_2^n experiment, ran in Hall A (one of three experimental halls) of JLab from February 7th to March 17th of 2009. The primary goal of the experiment was to provide a dedicated precision measurement of the neutron d_2 matrix element, which was calculated from a x^2 weighting of the polarized spin structure functions g_1 and g_2 given by Equation 2.23. The neutron information was extracted from a polarized ^{3}He target system.

4.2 Setup

For E06-014 to achieve a precision measurement of d_2^n, it ran with a $15\mu A$ polarized electron beam incident on a fixed polarized ^{3}He target (Section 6). The scattering electrons were measured using two of the three spectrometers in Hall A, the BigBite spectrometer (Section 4.4.4) and Left High Resolution Spectrometer (LHRS) (Section 4.4.5). Both spectrometers were positioned at an angle of 45° relative to the beam line and each operated independently of the other.

The BigBite spectrometer, with its large acceptance and ability to handle high counting rates, was chosen to measure the DSA $A_\parallel$ and $A_\perp$. The LHRS was employed to measure the unpolarized total cross section σ_0 because of its small acceptance, which lead to low noise and contamination; in addition to its well understood detector efficiencies and systematic effects.

The asymmetries are formed between fast 30 Hz flipping of the electron beam helicity and periodic changes to the target polarization direction. E06-014 optimized the time spent collecting $A_\parallel$ and $A_\perp$ in such a way that the statistical error on d_2 was minimized, rather than on g_1 and g_2[19]. Combining the measured quantities σ_0, $A_\parallel$ and $A_\perp$, d_2 can be expressed as

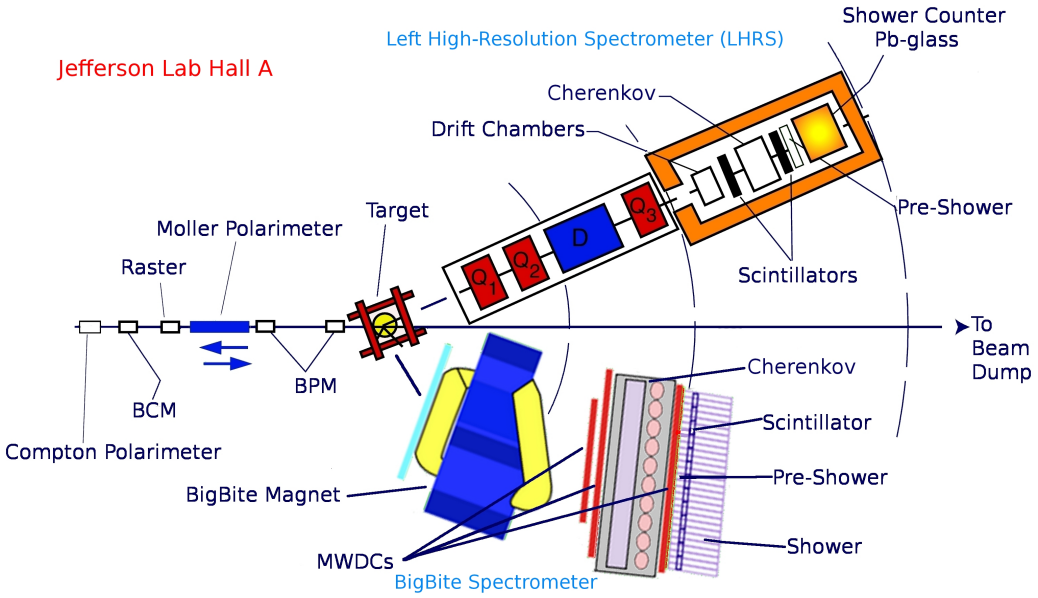

Figure 4.1: Hall A floor layout during E06-014. Spectrometers are both positioned 45° relative to the electron beam.

$$d_2 = \int_0^1 \frac{MQ^2}{4\alpha^2} \frac{x^2 y^2}{(1-y)(2-y)} \sigma_0 \left[\left(3\frac{1+(1-y)\cos\theta}{(1-y)\sin\theta} + \frac{4}{y}\tan\frac{\theta}{2} \right) A_\perp + \left(\frac{4}{y} - 3 \right) A_\parallel \right] dx, \tag{4.1}$$

where M is the neutron mass and θ is the scattering angle in the laboratory frame. It was found that $A_\perp$ contributes the most to the statistical uncertainty on d_2, therefore the majority of data taken during E06-014 was with the target spin polarized transverse to the electron helicity.

Figure 4.1 shows the layout of the Hall A floor during the experiment[2].

[2]The third spectrometer known as the right HRS is not shown in the figure, but was positioned as far to the right as possible to allow the BigBite spectrometer to be at an angle of 45° relative to the electron beam.

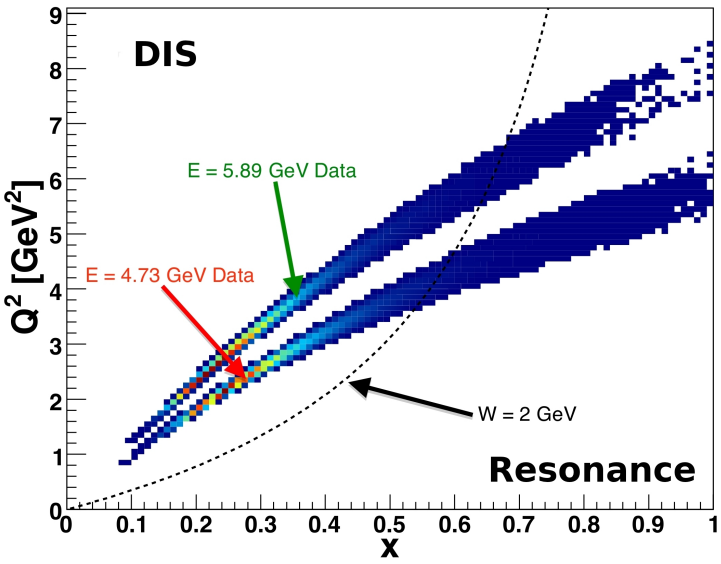

Figure 4.2: Kinematic coverage of E06-014 as measured in the BigBite spectrometer.

4.2.1 Kinematic Coverage

Figure 4.2 shows the kinematic coverage of the experiment measured in the BigBite spectrometer, which spanned both the DIS ($W > 2$ GeV) and resonance ($W < 2$ GeV) regions, which are defined by the $W = 2$ GeV dashed line. Two Q^2 values were measured for each x bin in order to obtain a sense of the Q^2 dependence in the results. This was achieved taking data at a fixed angle of 45° for two electron beam energies of 4.74 GeV and 5.89 GeV. A single BigBite magnetic field setting covered the entire range shown in Figure 4.2, where as the LHRS, with its much smaller acceptance, required twenty magnetic settings (eleven at $E = 5.89$ GeV and nine at $E = 4.74$ GeV) to reach a similar coverage. Tables 4.2.1 and 4.2 list the final LHRS kinematic settings for the two beam energies, with corresponding x and Q^2 values.

Table 4.1: LHRS kinematic settings during E06-014 for a beam energy of 4.73 GeV.

Momentum Setting [GeV]	x	Q^2 [GeV^2]
0.60	0.215	1.67
0.80	0.301	2.22
1.12	0.458	3.10
1.19	0.496	3.29
1.26	0.536	3.49
1.34	0.584	3.71
1.42	0.634	3.94
1.51	0.693	4.19
1.60	0.755	4.43

Table 4.2: LHRS kinematic settings during E06-014 for a beam energy of 5.89 GeV.

Momentum Setting [GeV]	x	Q^2 [GeV^2]
0.60	0.209	2.07
0.70	0.248	2.41
0.90	0.332	3.11
1.13	0.437	3.90
1.20	0.471	4.14
1.27	0.506	4.39
1.34	0.542	4.63
1.42	0.584	4.90
1.51	0.634	5.21
1.60	0.686	5.52
1.70	0.746	5.86

4.3 CEBAF

The Continuous Electron Beam Accelerator Facility (CEBAF) [70], is JLab's source of accelerated, polarized electrons. It is responsible for producing highly polarized electrons and delivering simultaneous beam of varying beam energy and currents to JLab's three experimental halls (known as Hall A, Hall B and Hall C); with Halls A and C getting high current beam, while Hall B gets low current beam. The average polarization of the beam is about 85%, and the maximum total beam current is about 150 μA. This is achieved by forming a beam with electron bunches that have a repetition rate of 499 MHz, the third harmonic of the 1479-MHz fundamental frequency of the accelerator. The bunches are interleaved, resulting in the properties of a given bunch being shared with electrons three bunches ahead and three bunches behind, but not with those in between.

4.3.1 Polarized Electron Source

The source of the polarized continuous wave (cw) electron beam is a photocathode that emits electrons when illuminated by a pulsed laser at a particular energy via the photoelectric effect. The photocathode is made of strained super lattice gallium arsenide (GaAs) [71] [72], which requires a photon energy of 780 nm to emit electrons from the material. The 780 nm photons needed to excite the electrons in the photocathode are produced by a frequency-doubling fiber based 1560 nm laser. Each of the three halls had their own dedicated laser system consisting of a 1560 nm seed laser, ErYb-doped fiber amplifier and periodically poled lithium niobate (PPLN) crystal, used to double the photon frequency [73] [74]. Each laser is then gain-switch so that the pulse rate, and hence the repetition rate of the electron bunches, is 499 MHz and 120° out of phase with the others. Through the use of various optic components, beam splitters, polarizers and dichroic mirrors, the lasers from each hall are directed along a single axis so that they will illuminate the same photocathode [75].

The electrons that are emitted from the photocathode can be linearly polarized by exciting them with circularly polarized laser light. Along the common beam line, Pockel cells (voltage controlled wave plates) operated as quarter wave plates, converting the 780 nm linearly polarized laser light into circularly polarized light. By flipping the sign of the voltage on the Pockel cell, fast helicity flipping (right to left circularly polarized photons and vis versa) of the laser light was achieved, resulting in the fast helicity flipping of the emitted electron helicity states [75].

In order to minimize the helicity correlated charge asymmetry, a couple of controls were put in place. First, before the linearly polarized 780 nm light reaches the Pockel cell that will convert it into circularly polarized light, it passed through another Pockel cell whose voltage, changing according to the fast-helicity-flipping sequence, is set to vary the intensity of the laser light. This cell is part of a feed back loop that also include the Hall A beam current monitor and special data acquisition system developed by the Hall A Proton Parity Experiment (HAPPEX) collaboration, and generally keeps the charge asymmetry below 200 ppm. Another helicity correlated charge asymmetry control is through the use of an insert able half wave plate (IHWP). The IHWP is made of mica, and is placed in the photon beam line and flips the helicity sign produced by the Pockel cells for a given voltage [75, 76].

The electrons that are emitted from the photocathode are aided in their emission through the application of a constant -100 kV electric field that is applied to the photocathode. This results in the electrons having an energy of 100 keV, as they make their way into the injector. Within the 100 keV beam line, a Wien filter [77] is used to rotate the electron spin direction without changing the central beam orbit. Which when combined with knowledge of the electron's spin precession in the accelerator and beam line, allows for the polarization direction to be optimized to each of the three experimental halls.

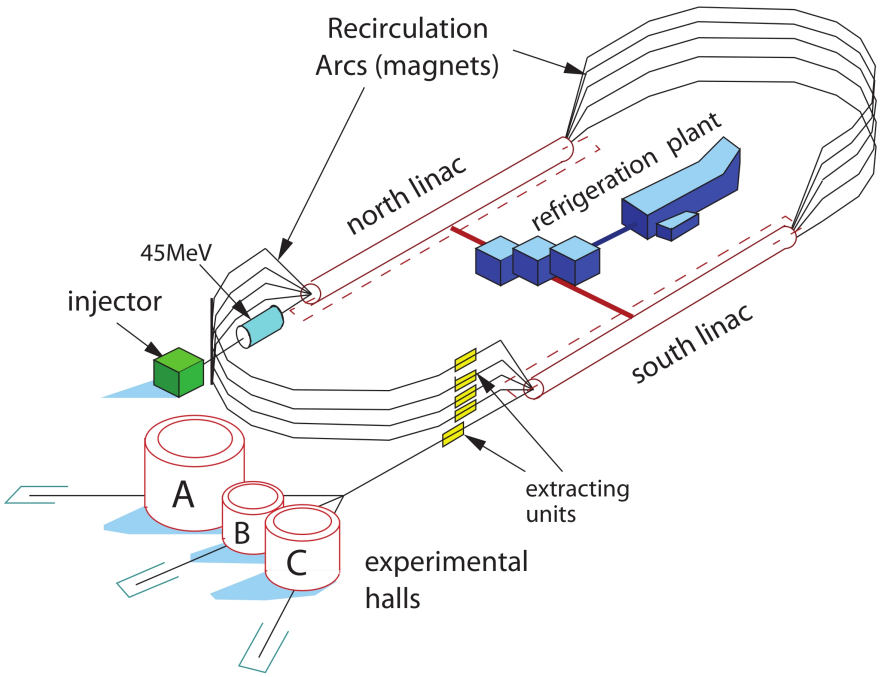

Figure 4.3: The Jefferson Lab Accelerator. Figure is from Reference [3].

4.3.2 The Accelerator

The accelerator consists of an injector, two super-conducting linear accelerators (linacs), and two recirculation arcs. Polarized electrons are accelerated through the linacs and circulated up to five times before being delivered to the experimental Halls. A layout of the accelerator can be seen in Figure 4.3.

The injector is the injection point of the polarized electron beam into the accelerator. The injector consists of 18 accelerating cavities, each giving the initial 100 keV electrons from the electron source an additional 2.5 MeV of energy. Thus as the electrons leaving the injector have an energy of about 45 MeV.

The two linacs, which are refereed to as the north and south linacs, are responsible for responsible for the majority of the electron acceleration. Each of the linacs consist of 20

cryomodules, where each cryomodule has 8 cavities, giving each linac a total of 160 cavities. The cavities are made of niobium, which is superconducting at a temperature of 2.08 K. The cavities are placed in liquid He, which is produced at the Central Helium Liquefier (CHL). The CHL is essentially a large refrigerator that keeps He cooled to about 2.2 K, and sends the cold He at a pressure of 2.8 atm to the cryomodules in the linacs. The cavities are driven by 1497 MHz electromagnetic waves so that the wave crests can be aligned with the electron bunches, causing them to accelerate. The end result is that with each pass through the cryomodules, the electrons gain about 500-600 MeV [70].

Finally, the two recirculation arcs (east and west), which connect to the two linacs, consist of thousands of magnets and are responsible for bending and focusing the electron beam. The more energy an electron has, the harder it is to bend. As a result electrons with low energy (those that take the first pass through the accelerator) are bent the most into the upper pipe, while those with the highest energies are left almost undeviated and travel along the pipe nearest the floor. This energy dependent bending results in electrons traveling through designated pipes that correspond to the number of passes through the accelerator that it traversed. Each of the three halls can independently choose what beam energy they would like, this could result in there being more than one electron energy, and hence a splitting of the electron beam as it enters the recirculation arcs. Thus the different energy electrons are recombined as they exit the recirculation arc via another magnet.

4.3.3 Beam Delivery to the Hall A

Once the electron bunches that correspond to Hall A's beam exit the south linac, it is bent through an angle of 37.5° and enters the hall [78]. The bending is achieved through the use of a series of magnets that make up the Hall A bend arc[3].

[3]Similar systems handle beam delivery to the other two halls.

The fast helicity flipping of the polarized electrons (Section 4.3.1) can be programmed based on the experiment's needs. However since the Pockel cell is in the common photon beam line, all three halls will have the same beam helicity structure. During E06-014, the beam helicity structure followed specifications engineered by the G^0 [79] experiment that took place in Hall C. This helicity scheme subdivided the electron beam into 30 Hz helicity windows, whose boundaries were marked by master pulse signals (MPSes). For each window, the electron has a well defined nominal direction of parallel (+) or anti-parallel (-) to its momentum. Sets of four consecutive helicity windows were arranged in quartets of +,-,-,+ or -,+,+,-. Once the first helicity window is decided, from a pseudo random number generation algorithm, the other three windows are uniquely determined. A signal indicating the helicity direction is then sent to the data acquisition system, along with a signal marking the beginning of the helicity quartet.

4.4 Hall A

E06-014 ran in Hall A of Jefferson Lab and relied on the Hall A apparatuses to carry out the measurement of d_2^n. This section will discuss all of the Hall A equipment and tools used to complete the experiment.

4.4.1 Coordinate Systems

Several coordinate systems are used in Hall A. Two sets of coordinate systems that generally describe events before the electron beam scatters from the target, which are referred to as the accelerator (this system is used in the EPICS data management system) and Hall A coordinate systems. These two systems are defined below:

- **Accelerator Coordinate System:**

  - Positive x is pointing towards beam right
  - y is defined as $\hat{y} = -\hat{z} \times \hat{x}$
  - z is along the beam line, with increasing z in the downstream direction (towards the target)

- **Hall A Coordinate System:**
  - Positive x is pointing towards beam left
  - y is defined as $\hat{y} = \hat{z} \times \hat{x}$
  - z is along the beam line, with increasing z in the downstream direction (towards the target)
  - The origin for this coordinate system is at the target center.

In addition to the two coordinate systems describing events before scattering, there are two coordinate systems, the target and detector coordinate systems, that are used to describe events after the electron beam interacts with the target. They are defined below:

- **Target Coordinate System:**
  - Positive x is pointing vertically downward (with gravity)
  - y is defined as $\hat{y} = \hat{z} \times \hat{x}$
  - z is the nominal direction of the particle passing through the detector
  - The origin for this coordinate system is at the target center.

- **Hall A Detector Coordinate System (BigBite):**
  - Positive x is pointing vertically downward (with gravity)
  - y is defined as $\hat{y} = \hat{z} \times \hat{x}$

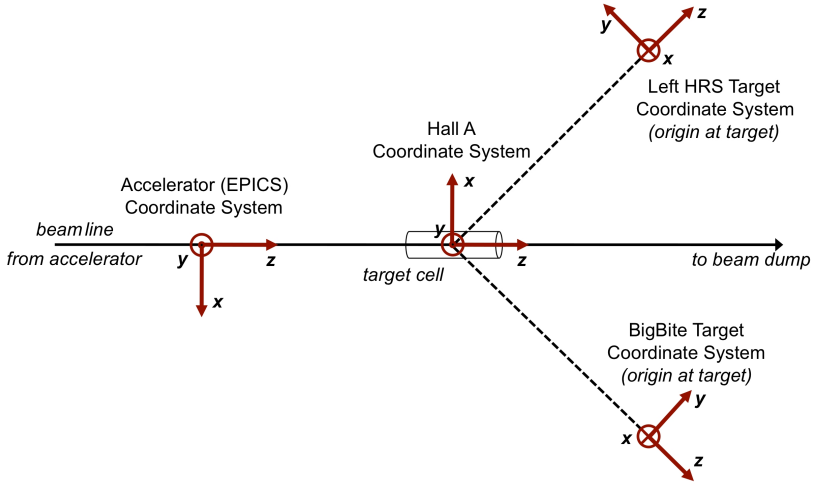

Figure 4.4: Illustration of the four Hall A coordinate systems used during E06-014. Here the beam line is seen from above, with the downstream direction pointing towards the right of the figure. Image taken from Reference [75].

  - z is the nominal direction of the particle passing through the detector
  - The origin for this coordinate system is at the center of the first multi-wire drift chamber plane.

- **Hall A Detector Coordinate System (LHRS):**
  - Positive x is pointing vertically downward (with gravity)
  - y is defined as $\hat{y} = \hat{z} \times \hat{x}$
  - z is the nominal direction of the particle passing through the detector
  - The origin for this coordinate system is at the center of the first vertical drift chamber plane, also known as the focal plane.

All four of the coordinate systems used in Hall A are shown in Figure 4.4.

4.4.2 Beam Line

Upstream of the target there are devices built into the beam line to measure and monitor beam characteristics. There are Møller and Compton detectors, which measure the electron beam's polarization (discussed in Section 5); beam current monitors used to measure the beam current and accumulated charge; beam position monitors and a raster which are used to determine the beam position. In this section the devices and methods used to measure the beam current, accumulated charge, beam position and energy will be discussed.

4.4.2.1 Current and Accumulated Charge

The average beam current used in E06-014 was 15 μA, which was measured through the use of standard Hall A equipment, known as beam current monitors (BCMs). The BCMs consisted of two resonant RF cavities tuned to the electron beam frequency of 1.497 GHz and were located 25 m upstream from the target. One of the cavities was denoted *up stream* (u), and the other *down stream* (d) based on their position relative to the beam line positions. The output voltages of the cavities are proportional to the beam current. The signals from both cavities are then fanned into three copies, which are then sent into three amplifiers possessing three different gain factors (1X, 3X and 10X). The amplified signals (six in all, three for up stream and three for down stream) are then passed through a voltage-to-frequency (V-to-f) converter, resulting in a frequency that is proportional to the beam current, and are then sent to high frequency VME scalers which are read out as counts in the LHRS and BigBite arms. These BCM scalers allow for continuous monitoring of the beam current and charge accumulation; and are labeled as u1, u3, u10, d1, d3, and d10, based on the originating BCM cavity and gain factor [80].

The calibration of the BCM readouts is a two step process and requires dedicated runs, where the beam current was systematically stepped up during each run. The first step of the

Table 4.3: Calibration results for the three up stream and three down stream BCM scalers. Errors on the offsets are on the order of 10^{-2}Hz.

Scaler	Slope [Hz/μA]	Offset [Hz]	Scaler	Slope [Hz/μA]	Offset [Hz]
u1	2101 ± 1	396	d1	2152 ± 1	154
u3	6480 ± 2	453	d3	6658 ± 3	133
u10	19731 ± 11	771	d10	21008 ± 10	293

BCM calibration is to calibrate the OL02 resonant cavity (the cavity used by the accelerator group to measure the beam current) located at the injector through the use of a Faraday cup, a water cooled copper beam dump that can be inserted into the injector beam line to collect all the current [81]. In the second step of the calibration, the OL02 current reading is compared directly to the Hall A BCM readouts. The left panel in Figure 4.5 shows the OL02 current as a function of the absolute measurement taken using the Faraday cup. Using that information, the beam current can be derived and is plotted against the six BCM readouts, shown in the right panel of Figure 4.5. From a linear fit to the scaler readouts between 5 and 30 μA, the slope of the line relating the scaler rates to the beam current can be determined: $\omega_n = \text{offset}_n + \text{slope}_n \cdot I$. Since the fit does not extend down to zero current, because the BCM readouts are known to be nonlinear at low currents, the offset was determined from a Gaussian fit to scaler rates measured with no beam. The results to these fits are listed in table 4.3.

The fit results allow the extraction of beam current and accumulated charge over time t through Equations 4.2 and 4.3 from scaler rate ω_n for the n^{th} beam-current signal.

$$I = \frac{\omega_n - \text{offset}_n}{\text{slope}_n}, \tag{4.2}$$

$$I = I \cdot t = \frac{t\,(\omega_n - \text{offset}_n)}{\text{slope}_n}. \tag{4.3}$$

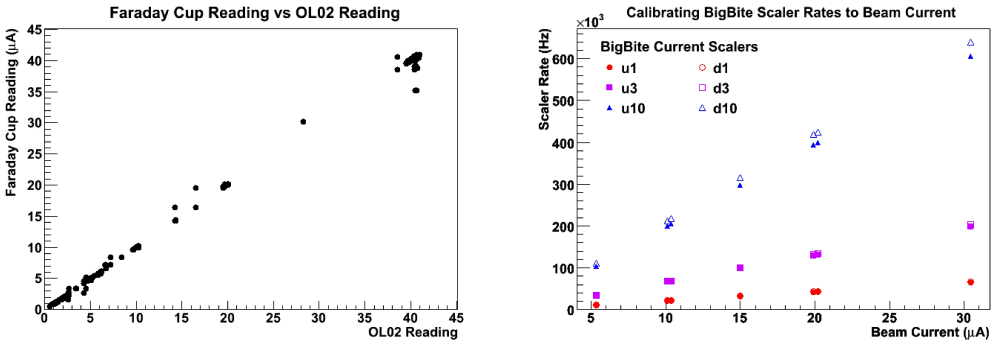

Figure 4.5: Left Panel: Relationship between current reading from the OL02 cavity at the injector, to the current reading measured by the Faraday cup. Right Panel: BCM scaler rates (from BigBite arm) plotted against the calibrated current readings of the OL02 cavity. Plots done by D. Parno [75].

The BCM calibration was done by D. Parno [75] with scalers from the BigBite arm. The LHRS arm recorded the same signal as BigBite and yielded consistent results. Neglecting the uncertainty in the clock rate, the error on the fit corresponds to a systematic error of about 0.03% on the beam current calculated from the u3 scaler rate.

4.4.2.2 Beam Position from the Beam Position Monitors

The beam position is measured using two beam position monitors (BPMs) that located about 7.5 m and 1.3 m upstream of the target. Each BPM has four wire antennae that are parallel to the beam direction and tuned to the RF frequency of the beam. The wires are positioned at $\pm$ 45° relative to the horizontal and vertical direction in the Hall A coordinate system. When the beam passes near a wire, it induces a signal in the wire that is recorded in an ADC. The induced signal is inversely proportional to the distance of the wire from the beam position. Thus the signal difference between two wires determines a relative beam position to a level of about 100 μm.

The BPM signals are usually calibrated using harps (wire scanners) that are situated

adjacent to the BPMs. Harp scans are an invasive procedure, in which wires are scanned across the beam resulting in scattered particles that are detected. The harps are surveyed and so their positions are known, thus enabling their absolute position to be used to calibrate the BPMs. Unfortunately, during E06-014 the harp results were unreliable due to software issues associated with the measurement. As a result, the BPMs were calibrated to the beam-position recorded in the EPICS data stream (see Section 4.4.8). The EPICS readouts reflected results of an earlier calibration that was done using the harp wire scanners, and thus could be used to calibrate the current BPMs [75].

4.4.2.3 Beam Position from the Raster

The electron beam is rastered in order to avoid any local over heating of the target cell. This involves producing small deviations of a few millimeters in the beam position at the target. Deviations in the beam position are achieved through the use of two dipole magnets (horizontal and vertical) positioned 23 m up stream of the target [80]. The magnets produce a small transverse magnetic field which the electron beam passes through, this leads to small deviations in the beam position in both directions at the target location. The magnet currents are recorded in the data stream and can be used to extract the beam position from data. The BPMs are slow in measuring the beam position at the time when the electron hits the target, with delays on the order of microseconds; whereas the raster magnets have a much smaller delay and can be used to determine the beam position directly [82].

The raster size used during E06-014 was 4 x 6 mm^2 and its effect was found to be small compared to the experimental momentum resolution, with the largest momentum deviations due to rastering being < 0.7 MeV [75]. As a result, the rastering effects were neglected in the E06-014 analysis.

Table 4.4: Electron beam energy results via arc measurement and Tiefenback method for E06-010 [85].

Arc Measurement [MeV]	Tiefenback Method [MeV]
$5889.4 \pm 0.5_{stat} \pm 1_{sys}$	$5891.3 \pm 2.5_{sys}$

4.4.2.4 Beam Energy

The electron beam energy can be continuously monitored via the Tiefenback method [83], in which BPM measurements are combined with the field integral of the Hall A arc magnets to compute the beam energy as it enters the Hall. The Tiefenback method is calibrated and kept calibrated by the use of an absolute beam energy measurement, known as an arc measurement. In the arc section of the beam line, shown in Figure 4.6, consists of eight dipole magnets that bend the beam through a nominal angle of 34.3°. Any deviations from the bend angle are measured using SuperHarps, pairs of wire scanners located before and after the row of magnets. The measured bend angle, along with the known magnetic field can be used to compute the beam momentum, and hence the energy

$$p = \frac{k \int \vec{B} \cdot d\vec{l}}{\theta}, \tag{4.4}$$

where k = 0.299792 GeV rad $\mathrm{T}^{-1}m^{-1}$ [80].

Simultaneously with the SuperHarp measurement of the bend angle, the magnetic field integral can also be measured through the use of a ninth magnet, which located outside the vacuum and its field measured directly with a Hall probe [84].

During E06-014, there was no independent arc measurement performed, therefore confidence in the Tiefenback method used during the experiment relies on results of arc and Tiefenback measurements taken during E06-010 shown in Table 4.4.

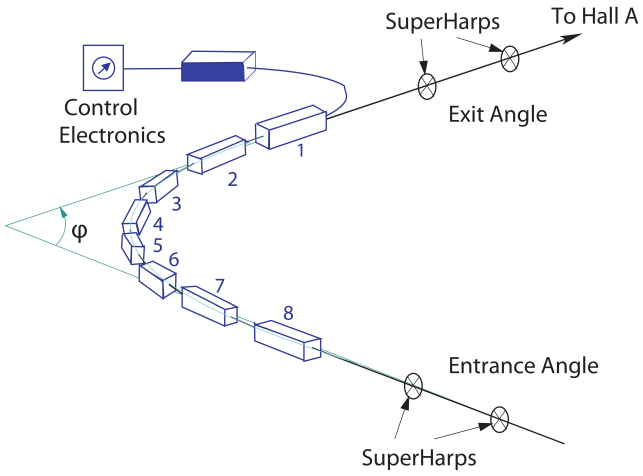

Figure 4.6: Schematic of an arc beam energy measurement. Reproduced from [3]

4.4.3 Target

The standard Hall A polarized ^{3}He target package was use. This packaged allowed the ^{3}He target to be polarized longitudinally (parallel and anti-parallel to the electron's momentum) and transversely (in the electron scattering plane perpendicular to the electron's momentum) relative to the incident electron helicity. The target is discussed in detail in Section 6.

4.4.4 BigBite Spectrometer

The BigBite spectrometer was positioned at an angle of 45° to the right electron beam line, and was used to measure the double spin asymmetry. As the spectrometer's name suggests, the BigBite spectrometer was designed to cover a wide momentum and scattering angle range, resulting in a solid angle of about 64 msr. This large acceptance was obtainable though the use of the BigBite magnet, a non-focusing dipole magnet. The BigBite magnet is located 1.5 m from the target and has a large metal plate installed in the front of it in order to shield the target from its fringe field [86]. In addition to the shielding plate, an insertable

sieve plate can be positioned in front of the magnet, providing a means by which to calibrate the BigBite optics. Detectors used to measure particles passing through the BigBite magnet are stacked horizontally behind it, and are pitched at 10° from the magnet center. Figure 4.7 shows an engineering drawing of the BigBite magnet and the detectors used in E06-014 to measure the scattered electrons. An illustrated layout of the detectors used in the BigBite spectrometer can be seen in Figure 4.8, and consists of: three sets of multi-wired drift chambers (MWDC) for particle tracking, a short gas Čerenkov used for pion rejection, a scintillator plane used for particle identification, and a shower calorimeter (consisting of two layers, a preshower and shower) which is used for particle identification. The Čerenkov detector was installed in between the second and third MWDCs, and the scintillator plane was sandwiched between the preshower and shower calorimeter layers. Additionally, there were two target collimators installed on the BigBite side to shield high energy electrons and photons generated from the two end caps of the target scattering chamber [86]. In the following sections the magnet and each of the detectors making up the BigBite spectrometer used in E06-014 will be discussed.

4.4.4.1 BigBite Magnet

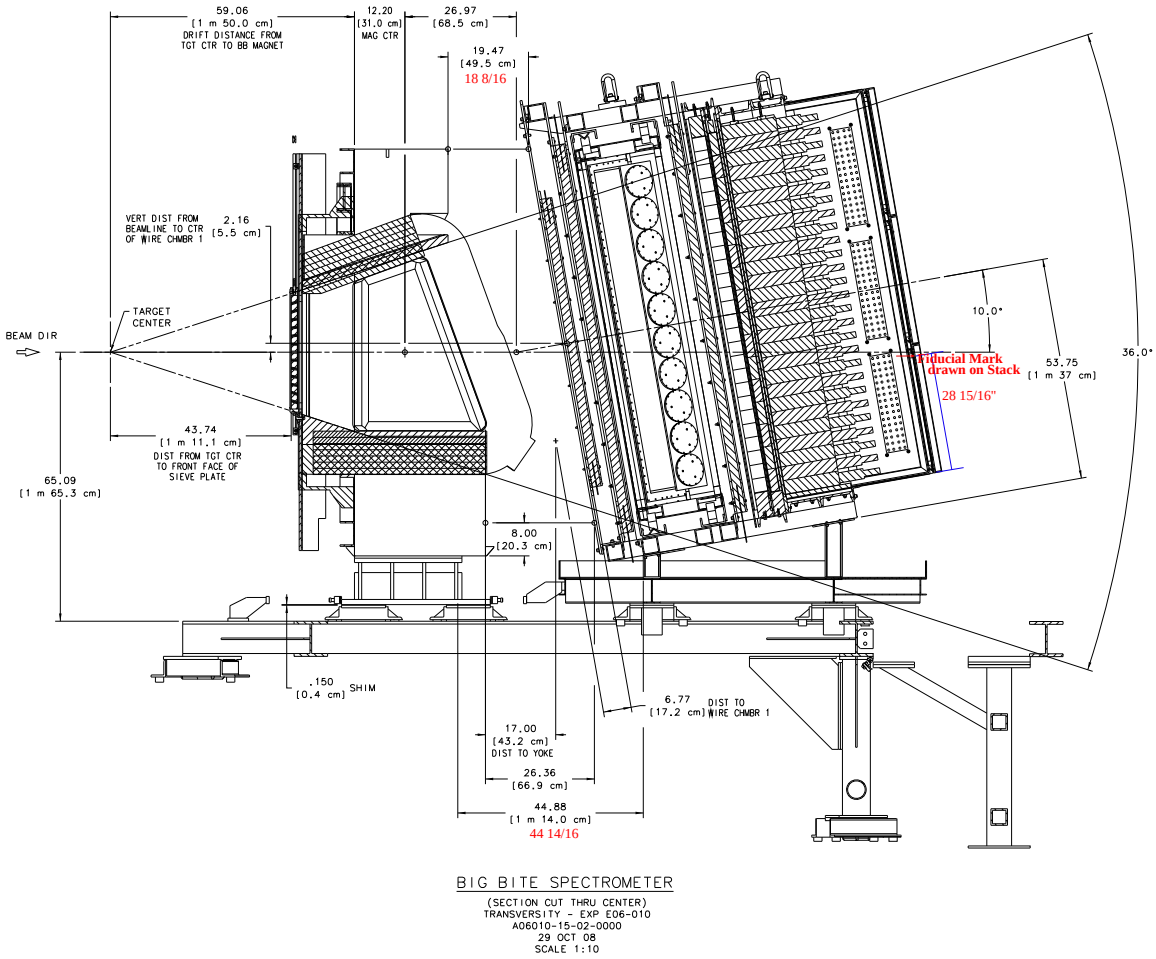

Figure 4.7: BigBite spectrometer engineering drawing; consisting of the BigBite magnet and detectors used in E06-014.

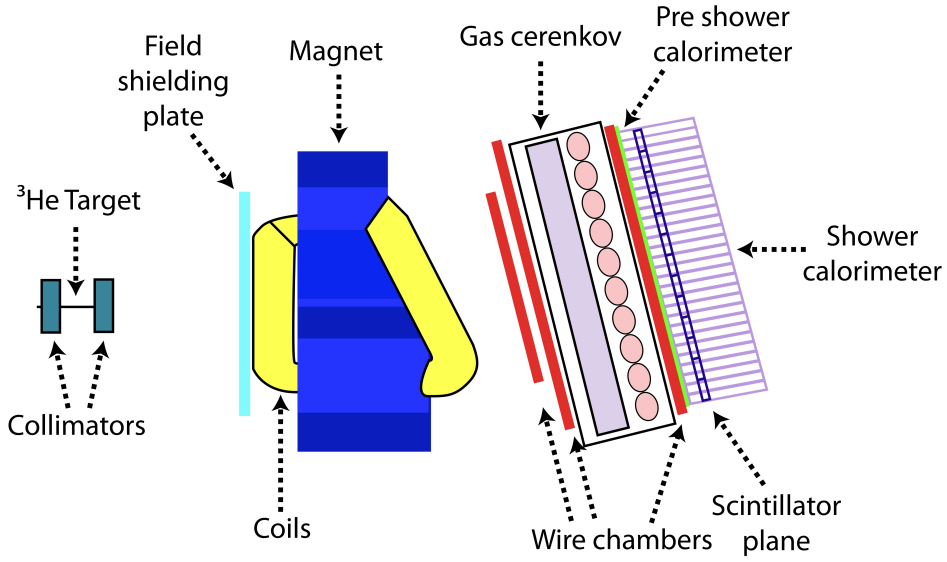

Figure 4.8: An illustration of the BigBite spectrometer package used in E06-014. Image reproduced from Reference [86].

The magnetic field generated by the BigBite magnet is in the horizontal (parallel to the floor and perpendicular to the particle's momentum direction) direction, making the dispersion direction vertical. A central magnetic field of about 1.2 T was used during E06-014, produced from a current of 710 A. Figure 4.10 shows the magnetic field for the larges component, B_y (detector coordinates), plotted against the z direction (the direction of the particle's nominal velocity direction) taken before E06-010[86]. The field mapping results show a uniform magnetic field spanning about 15 cm. The magnet has two polarity settings, positive and negative. When the magnet is set to the negative polarity setting, positively charged particles passing through the magnet will be bent down (toward the floor), while negatively charged particles will be bent up (away from the floor). Switching the polarity of the magnet to positive polarity, results in negatively charged particles being bent down, and positively charged particles being bent up.

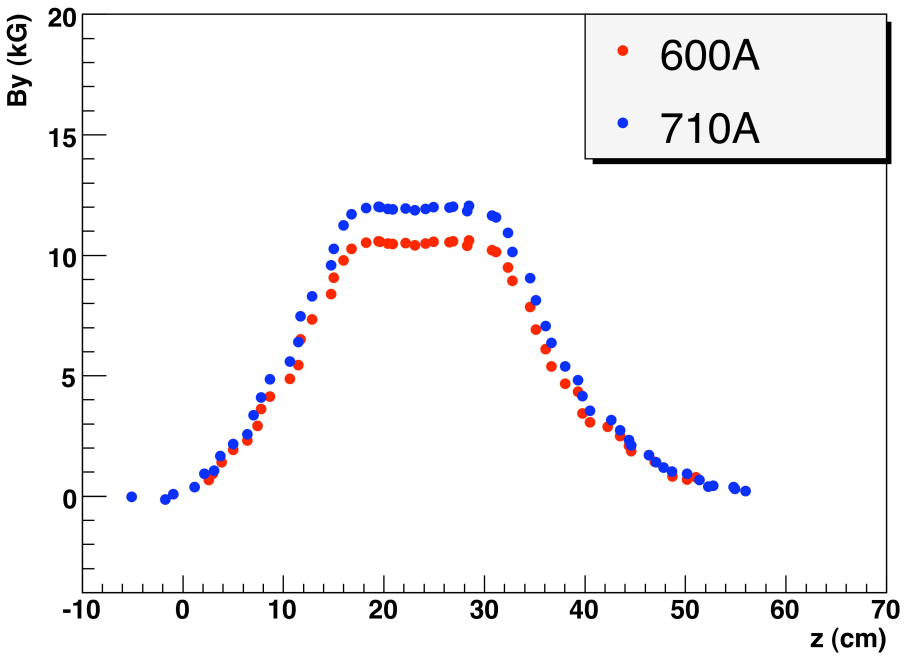

Figure 4.9: BigBite magnetic field (B_y) measurements taken two current settings, reproduced from Reference [86]. The current setting of 710 A (blue points) was used during E06-014.

4.4.4.2 MWDC

Charged particle trajectories were reconstructed using the measurements from three sets of MWDCs. The first chamber had an active area of 140 cm x 35 cm, while the second and third chambers had an active area of about 200 cm x 50 cm. Each chamber is filled with a 50%/50% argon-ethane gas mixture, and contains three pairs of wire planes, for a total of 18 planes across all three chambers. The wire planes are bounded up and down stream by two cathode planes 6 mm apart, which contain a series of alternating field and sense wires halfway between the cathode planes [86] as shown in Figure 4.10. The field wires, separated by 1 cm, are held at a constant high voltage (HV) of about -1600 V, which produces a nearly symmetric potential around the sense wires [75].

The six wire planes making up one chamber were grouped into two sets of three and labeled as x, u, v for the first set and x' (xp), u' (up) and v' (vp) for the second set. The wires in the x plane were horizontal (0°), and were oriented at +30° and -30° respectively from the horizontal direction in the u and v planes, as illustrated in Figure 4.11. The second set of wire planes was identical to the first, with the directions of the x', u' and v' planes matching the orientations of the x, u and v wire planes, except that it was shifted by 0.5 cm (half the wire cell). This offset from the first set of wire planes, allowed the tracking algorithm to determine if a track passed through the chamber left-to-right or right-to-left of the wire that registered a hit in the first set of wire planes.

As a charged particle passes through the MWDC, it ionizes the argon-ethane gas, freeing charges which due to the potential difference between the wires drift to the closest one. The particle's drift time, the time it takes the particle to travel from the point of ionization to the hit wire, is proportional to the distance it traveled. As the ionized particle drifts towards the closest wire, the particle's energy increases due to the electric field, causing additional ionization which in turn leads to more ionization, causing an avalanche. The avalanche

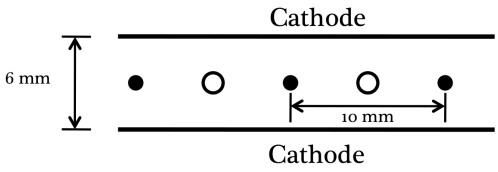

Figure 4.10: Schematic of BigBite MWDC wire plane (side view), reproduced from Reference [75]. The sense wires are represented by open circles, and the field wires by closed circles.

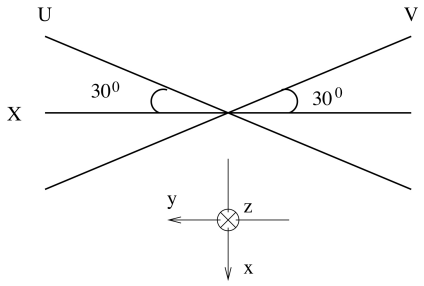

Figure 4.11: Orientation of the u, v and x wire planes in the BigBite wire chambers. Image reproduced from Reference [82].

produces an electric signal in the sense wire that is then read out to other electronics [75].

Signals from each wire of the MWDC were read out by grouping every 16 wires together, except for those close to the edges, and sending it to an amplified A/D card. If the signal passes the threshold set on A/D card, then each wire signal contained within that group is recorded using 1877 TDCs (which have a 0.5 ns resolution) [86].

4.4.4.3 Čerenkov

E06-014 served as the commissioning experiment for the BigBite short gas Čerenkov detector. With rates from pions and protons expected to be much greater than those from electrons [87], and coupled with BigBite being used in single arm mode [4], the BigBite

[4] In coincidence mode, BigBite could be used with one of the HRS detectors to remove pions from the sample, and better understand pion contamination and rates.

Čerenkov was built to remove pions and protons from the online trigger.

Čerenkov counters detect particles by measuring their resulting Čerenkov radiation. Čerenkov radiation occurs when charged particles pass through a dielectric medium at velocities greater than the speed of light in that medium. This velocity is given by $v_C = c/n$, where n is the index of refraction for the dielectric medium. When a particle travels at a speed greater than v_C an electromagnetic shock wave is produced, just as an object traveling faster than sound creates a sonic shock wave. The coherent wavefront of the Čerenkov light is conical in form and has an opening angle of [88]

$$cos_{\theta_C} = \frac{1}{\beta n}, \text{ where } \beta = \frac{v}{c} > \frac{1}{n}, \tag{4.5}$$

and is illustrated in Figure 4.12. Because the Čerenkov effect is sensitive to the particle velocity, it can be used to discriminate between different particle types. The momentum needed for particles to produce Čerenkov radiation is

$$p_{thr} = \frac{m\beta}{\sqrt{1-\beta^2}} = \frac{m}{\sqrt{n^2-1}}, \tag{4.6}$$

where m is the particle's mass. As shown by Equation 4.6, particles of different masses will produce Čerenkov radiation at different momenta based on the dielectric medium used. The BigBite short gas Čerenkov detector used C_4F_8O as the radiator gas, which has an index of refraction of 1.00135, at 1 atm of pressure. Table 4.5 lists the particle momentum, calculated from Equation 4.6, that is needed to trigger Čerenkov radiation for $e^{\pm}$, $\pi^{\pm}$ and protons.

The design of the BigBite Čerenkov was constrained by the space available in the BigBite detector stack, which had to fit in the 60 cm gap between the second and third MWDCs. The resulting Čerenkov detector dimensions were then 60 cm x 80 cm x 200 cm. Although the detector has a physical electron drift distance through the radiator gas of 60 cm,

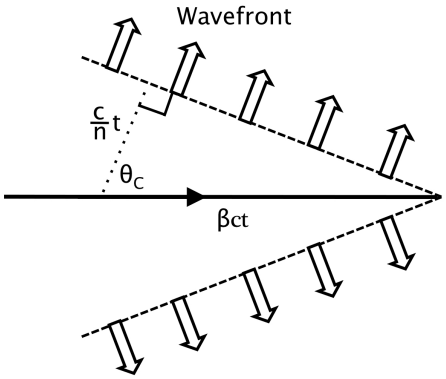

Figure 4.12: Čerenkov radiation. Image reproduced from reference [75].

Table 4.5: Momentum thresholds of different particle types in the BigBite gas Čerenkov. Particle masses are from Reference [9].

Particle	Mass [MeV]	Momentum Threshold [MeV]
$e^{\pm}$	0.510	9.831
$\pi^{\pm}$	139.6	2685
p	938.3	18050

once the mirrors and their support structures were installed, the drift distance was reduced to nearly 40 cm. The Čerenkov consisted of twenty spherical mirrors arranged in two columns of ten at the back of the tank. Each spherical mirror was 31 cm wide x 21 cm tall and had a radius of 116 cm. The spherical mirrors collected the Čerenkov light and reflected it onto flat secondary mirrors (twenty in all) installed at the front of the tank and measured 24 cm wide x 20 cm tall; the Čerenkov light was then directed into the PMT associated with that mirror. A total of twenty 5 in diameter PMTs were used. To accommodate the large acceptance of BigBite, Winston cones [89] were fitted like a collar to the PMTs, effectively extending the area of coverage from 5 to 8 inches. The amplitude response of PMTs are suppressed when exposed to external magnetic fields. Thus in order to shield the PMTs from the extraneous magnetic fields due to the BigBite magnet, they were wrapped in a 0.8 mm layer of mu-metal and then placed in an iron cylinder. It was found that in addition to the magnetic shielding, the PMTs had to be inset by 5 inches with the resulting gap filled with a cylinder of Anomet UVS reflective material in order to remove all significant magnetic field contributions [87] as shown in Figure 4.13. A cad drawing of the Čerenkov detector assembly is shown in Figure 4.14.

The signals were sent from the PMTs into 1877 TDCs (resolution of 0.5 ns) and 1881[5] ADCs (resolution of 50 pC/channel), where the timing information and accumulated charge (produced via photo-electron effect) were recorded. The main BigBite electron trigger, T2 was formed by requiring a coincidence between the signals in the BigBite Čerenkov and shower calorimeter, and is discussed in detail in Section 4.4.6.

[5]During the early commissioning of E06-014, v792 ADCs (resolution of 100 pC/channel) were used, but were soon replaced with the 1881 ADCs due to high rates causing pedestal instability in the signals [87].

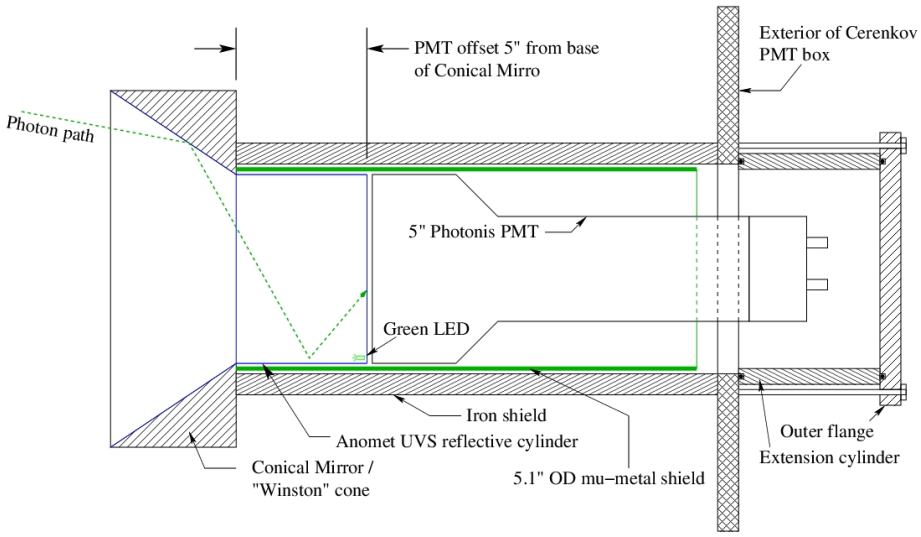

Figure 4.13: Diagram of magnetic shielding used to Čerenkov PMTs. Image reproduced from [87].

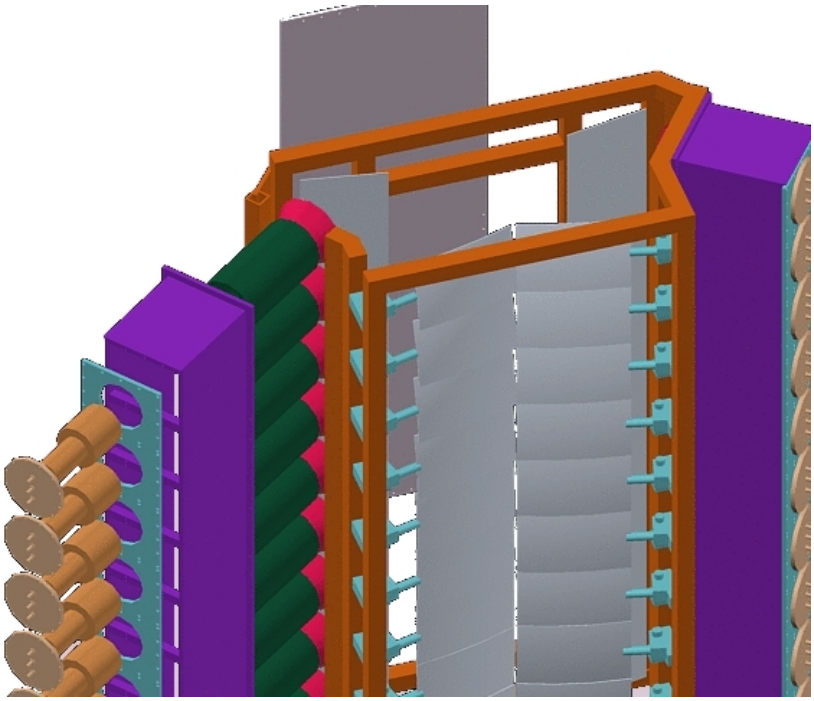

Figure 4.14: Exploded CAD assembly of the BigBite short gas Čerenkov detector.

4.4.4.4 Scintillator

The scintillator plane was installed in between the preshower and shower layers of the BigBite calorimeter, and provided timing and amplitude information. As ionizing particles move through the scintillator, they excite the molecules of the scintillating material, causing a luminescence which is collected by PMTs coupled to the scintillator.

The scintillator plane consisted of 13 plastic scintillating bars, each with dimensions of 17 cm x 64 cm x 4 cm, arranged in a single column. The shortest of the sides (4 cm) was along the longitudinal direction. A geometry of the scintillator can be seen in Figure 4.15. Each scintillator bar was read out by a pair of PMTs attached to both sides of the bar. The signal from each side is amplified by a factor of ten, and then sent to TDCs and ADCs for timing and amplitude information [82]. Because the BigBite spectrometer during E06-014 was used as a single-arm (non-coincidence) detector, the timing information in the scintillators was not extremely useful, however the amplitude signal recorded in the ADCs of the scintillator proved to be effective in providing additional particle identification (see Sections 8.2.2 and 8.2.3).

4.4.4.5 Calorimeter

In addition to the Čerenkov and scintillator detectors, the BigBite calorimeter provided additional particle identification and was also used to from the BigBite triggers (Section 4.4.6). The calorimeter consisted of two layers; the preshower layer, which was positioned before the scintillator plane, and the shower layer, which was located after the scintillator plane. Both the preshower and shower detectors used lead-glass blocks measuring 8.5 cm x 8.5 cm x 34 cm. The preshower used TF-5 lead-glass and had its blocks oriented with the 34 cm side perpendicular to the central particle trajectory. Its blocks were arranged in two columns and twenty-seven rows, giving it an active area of 229.5 x 68 cm^2. Where as the shower

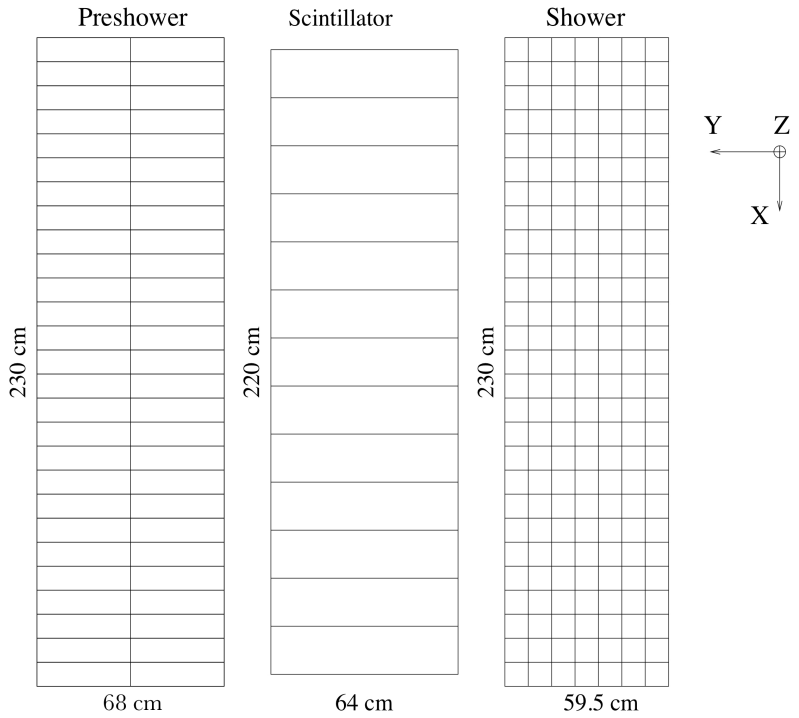

Figure 4.15: Geometry of BigBite preshower, scintillator and shower detectors. Image reproduced from [82].

used TF-2 lead-glass material and had its blocks oriented with the 34 cm side along the central particle trajectory. Its blocks were arranged in seven columns of twenty-seven rows, and filled an active area of 229.5 x 59.5 cm^2.

PMTs were mounted to the end of each block in the preshower and shower detectors where the detected signal, which is proportional to the energy deposited in the block, was read out to 1877 TDCs and 1881 ADCs for timing and energy information. Figure 4.15 shows the preshower, scintillator and shower detector geometries.

The BigBite calorimeter (preshower and shower detectors) measures how much energy a particle deposits into the detector, by measuring the electrical signal resulting from an electromagnetic cascade. As electrons and photons travel through the lead-glass blocks, they will radiate via pair-production and Bremsstrahlung processes. These radiated particles will then radiate themselves through the same processes causing more radiated particles. This chain reaction is known as an electromagnetic cascade (illustrated in Figure 4.16) which is proportional to the initial particle energy deposited in the lead-glass. The cascade stops when the particle's energy falls below the pair-production threshold and bremsstrahlung is no longer the dominate effect. The characteristic amount of matter traversed by these interactions in known as the radiation length, X_0 of the material and is the mean distance over which electrons loose all but $1/e$ of their energy by bremsstrahlung, or $7/9$ of the mean free path for photons by pair-production. The depth of the cascade is given by [9]

$$X = X_0 \frac{\ln\left(\frac{E_0}{E_c}\right)}{\ln 2}, \tag{4.7}$$

where E_c is the critical energy, below which the cascade will begin to dissipate. The critical energy for an electron is about 7 MeV [90] with X_0 on the order of a few centimeters. The preshower blocks, with the 8.5 cm side along the particle's trajectory covers about $3X_0$, while the shower blocks, with the 34 cm side along the particle's trajectory covers about

$13X_0$ [82].

Coulomb scattering during the electromagnetic cascade leads to a transverse contribution. The Molierre radius

$$R_m = \frac{X_0 212 \text{ MeV}}{E_c}, \tag{4.8}$$

defines an area of material that contains 90% of the total deposited energy. A radius of $3.5R_m$ would contain 99% of the total deposited energy [91]. In comparison, the shower blocks used have a radius of only $1.6R_m$, thus blocks are grouped into clusters in order to catch more of the deposited energy.

Heavier particles, such as muons and pions act as minimum ionizing particles (MIPs), which loose a small amount of energy rather than producing a cascade in lead-glass. The energy loss by a MIP is approximately 1.5 MeV per g/cm^2 traveled [92]. If one considers the TF-5 lead-glass of the preshower, which has a density of 4.77 g/cm^3 [93], and neglecting nuclear effects, one would expect a muon or pion to deposit about 60 MeV into the preshower and around 300 MeV into the shower (made of TF-2 lead glass). However during E06-014 there were multiple materials (shown in Figure 9.1 in between the BigBite magnet and the calorimeters. This caused the MIPs to deposit $\sim$ 81 MeV into the preshower and less than $\sim$ 350 MeV into the shower. The densities of the materials used in the MIP energy estimates are listed in Table 4.6, which were obtained from V. Mamyan's GEANT4 simulation. The energy difference between the MIPs and electrons that is deposited into the calorimeter is what makes the preshower and shower an excellent tool by which to remove pions.

4.4.5 Left High Resolution Spectrometer

The Left High Resolution Spectrometer (LHRS) is one of two high resolution spectrometers, the other being the right high resolution spectrometer (RHRS), contained in Hall A. The

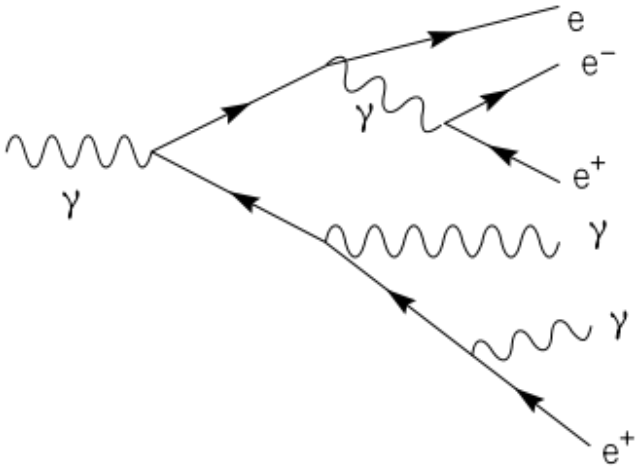

Figure 4.16: Example of an electromagnetic cascade in which the under goes an electromagnetic shower.

Table 4.6: List of material densities used to estimate the MIP energy deposition in the calorimeters. Densities obtained from V. Mamyan's GEANT4 simulation.

Component	Material	Density [g/cm^3]
Scintillator	BC-408	1.032
Preshower	TF-5	4.77
Shower	TF-2	4.09
Shielding	μ-metal	8.25
Shielding	Steel	7.85
Shielding	Acrylic	1.19
Shielding	Aluminum	2.81

LHRS sits to the left of the electron beam line, where as the RHRS sits to the right of the electron beam. During E06-014 the RHRS was not used, while the LHRS was positioned 45° relative to the beam line and was used to measure the unpolarized cross section from the scattered electrons.

The LHRS consists of two super conducting quadrapole magnets, a dipole magnet followed by another quadrapole magnet in order to focus charged particles up into the detector hut, which houses the sub detectors [94]. Figure 4.17 shows the arrangement of magnets and the position of the detector hut. The LHRS is able to reach a momentum resolution of $\sim 10^{-4}$, where the central momentum is selected via the dipole magnetic field. Unlike the BigBite spectrometer, the LHRS has a solid angle of only $\sim$ 6 msr.

The detector hut contains the detector package, whose arrangement is shown in Figure 4.18 and includes the following:

- **Vertical Drift Chambers**

  The tracking information is provided by vertical drift chambers (VDCs). There are two VDC planes which are positioned 23 cm apart from each other. Each plane consists of two wire planes (U and V) that are oriented at +45° and -45° relative to the dispersive and non-dispersive directions. The VDCs lie in the horizontal plane, with particles crossing the wire planes at nominal angle of 45°.

  A gas mixture of 62%/38% argon-ethane (C_2H_6) is used in the VDCs, and a HV of -4kV is applied [94]. Charged particles that pass through the chambers, ionize the gas creating electrons and ions along the its trajectory. The ionized electrons will then drift to the closest wires and trigger a hit in the wire. The drift time of the electron to the wire is proportional to the distance between the initial ionization point and the hit wire position. Combining the information from all of the hit wires, the entire trajectory can be reconstructed [86]. The timing information for the wires were recorded in 1877

TDCs, which provided a resolution of 0.5 ns.

- **Scintillator Planes**

  Two scintillator planes (S1 and S2m), separated by about 2 cm, were used for triggering on charged particles. The S1 scintillator plane was made up of 6 thin plastic scintillators, each containing two PMTs at each end. The scintillators were made thin to minimize particle absorption because it is used in forming the first level of the main LHRS trigger. The total active volume of the S1 plane was 36.0 cm (Length) x 29.3 (width) x 0.5 cm (thickness).

  The S2m plane, consisted of 16 scintillator bars, each containing two PMTs on both ends. The total active volume of the S2m plane was 43.2 cm (length) x 14.0 cm (width) x 5.08 cm (thickness), and provided accurate timing information for charged particles passing through it. The timing information from both the S1 and S2m planes were recorded using 1875 TDCs (with a timing resolution of 50 ps [86]).

- **Gas Čerenkov**

  A gas Čerenkov, which was filled with CO_2 gas (whose index of refraction is 1.00041) at pressure of 1 atm, provided pion rejection with a pion momentum threshold of 4.8 GeV. This detector was 80 cm long and was positioned in between the the two scintillator planes. It consisted of ten mirrors arranged in a 2x10 array, with each mirror having a PMT associated with it in order to collect the radiated Čerenkov light.

- **Lead Glass Calorimeter**

  The lead-glass calorimeter, consisting of two layers, was used to provide additional particle identification and pion rejection by measuring the deposited energy of the electrons. The first layer, also known as the first pion rejection layer, is made up of Pb-glass blocks with dimensions of 14.5 cm x 14.5 cm x 30 cm (with the longest side

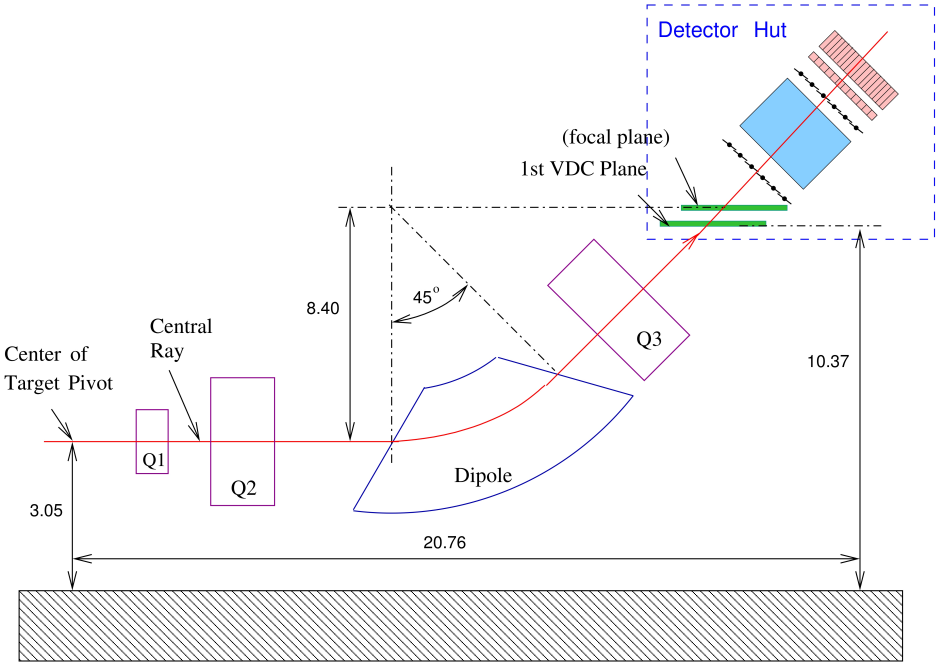

Figure 4.17: Layout of the magnets in the LHRS and position of the detector hut. Units are in meters. Image taken from [3]

perpendicular to the incident electron) which are arranged in a 2 x 17 block array. The second pion rejection layer was also arranged in a 2 x 17 block array, with each block measuring 14.5 cm x 14.5 cm x 35 cm (with the longest side perpendicular to the incident electrons). As it turns out, these layers were not thick enough for the electron to deposit all of its energy, and thus would punch through the layers. However, because pions passing though the calorimeter will leave a distinct minimum ionization signal, while the electrons will leave a larger signal due to the electromagnetic shower, it still served as an effective means to distinguish pions from electrons. Signals deposited in the Pb-glass blocks were collected from PMTs associated with that block and recorded using 1881 ADCs.

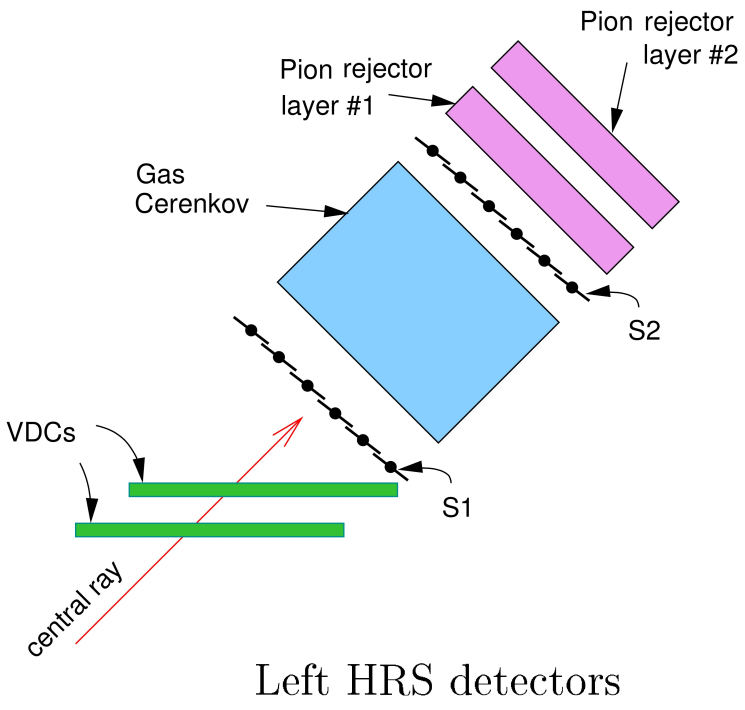

Figure 4.18: Arrangement of the sub detectors that make up the LHRS detector package. Image taken from [3]

4.4.6 Triggers and Trigger Logic

When the electron beam collides with the target there are many potential events generated, so many in fact that not all of them can be recorded. As a result a trigger system was used to record events that satisfy particular parameters, such as whether a detector signal is larger than a pre-programmed threshold. The Hall A data acquisition (DAQ) electronics are equipped to handle up to eight triggers. Each of the triggers contains a prescale factor that can be set by the experiment, which controls the rate at which its associated trigger is written into the data stream. For example when a trigger has prescale factor of n, only n of the total triggers fired (N) will be recorded, effectivly reducing the trigger rate to n/N.

There were several triggers used during E06-014, mostly for trouble shooting and contamination studies. Table 4.7 summarizes the various triggers, which spectrometer they are associated with and a description of how they are formed. The T8 trigger is a 1024 Hz clock signal, which samples mostly background events and was used in determining the BigBite Čerenkov in beam pedestals (Appendix C). The T5 trigger formed a coincidence between the BigBite (T1 trigger) and LHRS (T3 trigger) spectrometers when they were configured in a two arm DAQ mode. This trigger was only used briefly during early low energy calibration runs, and was later disabled when the spectrometers were set to single-arm mode.

4.4.6.1 LHRS Trigger

The T3 was the primary trigger used by the LHRS spectrometer. It was formed when a hit was recorded in both the S1 and S2m scintillator planes. A hit required that both PMTs (left and right) of the affixed paddle record a signal that was above a certain threshold. Thus T3 requires a signal that is above threshold in four PMTs (2 for each scintillator plane). The timing of the T3 was set by the leading edge of the signal in the PMT of the right side of the

Table 4.7: Triggers used in E06-014. The low-threshold triggers select lower-amplitude pulses, whereas high-threshold triggers select higher-amplitude pules.

Trigger	Spectrometer(s)	Description
T1	BigBite	Low shower threshold
T2	BigBite	Overlap between T6 and T7
T3	LHRS	Overlap between S1 and S2m scintillators
T4	LHRS	Overlap between (S1 or S2m) and Čerenkov
T5	BigBite and LHRS	Coincidence between T1 and T3
T6	BigBite	High shower threshold
T7	BigBite	Gas Čerenkov
T8	BigBite and LHRS	1024 Hz clock

S2m paddles.

An additional trigger used in the LHRS was the T4, which was formed by a hit in either the S1 or S2m planes and a hit in the LHRS Čerenkov detector. The T4 trigger was used to determine the efficiency of the T3 trigger (Section 8.3.3.5). The trigger logic for the T3 and T4 triggers can be seen if Figure 4.19.

4.4.6.2 BigBite Trigger

The BigBite spectrometer consisted of four triggers, T1, T2, T6 and T7, all of which (with the exception of T7) are based on the amount of energy deposited in the lead glass calorimeter. The energy in each calorimeter layer that went into forming a trigger was formed via a total hardware sum. The total hardware sum (TSUM) was formed from two overlapping rows in the preshower (2 x 2 = 4 blocks) and the shower (2 x 7 = 14 blocks), which can be seen in Figure 4.20. The signals in the two rows of preshower blocks were summed using LeCroy 428F modules, while the signals in the two rows of shower blocks were summed using a custom built summing module. The signals from the preshower were sent through a 5X amplifier and the shower signal was sent through a 10X amplifier. The

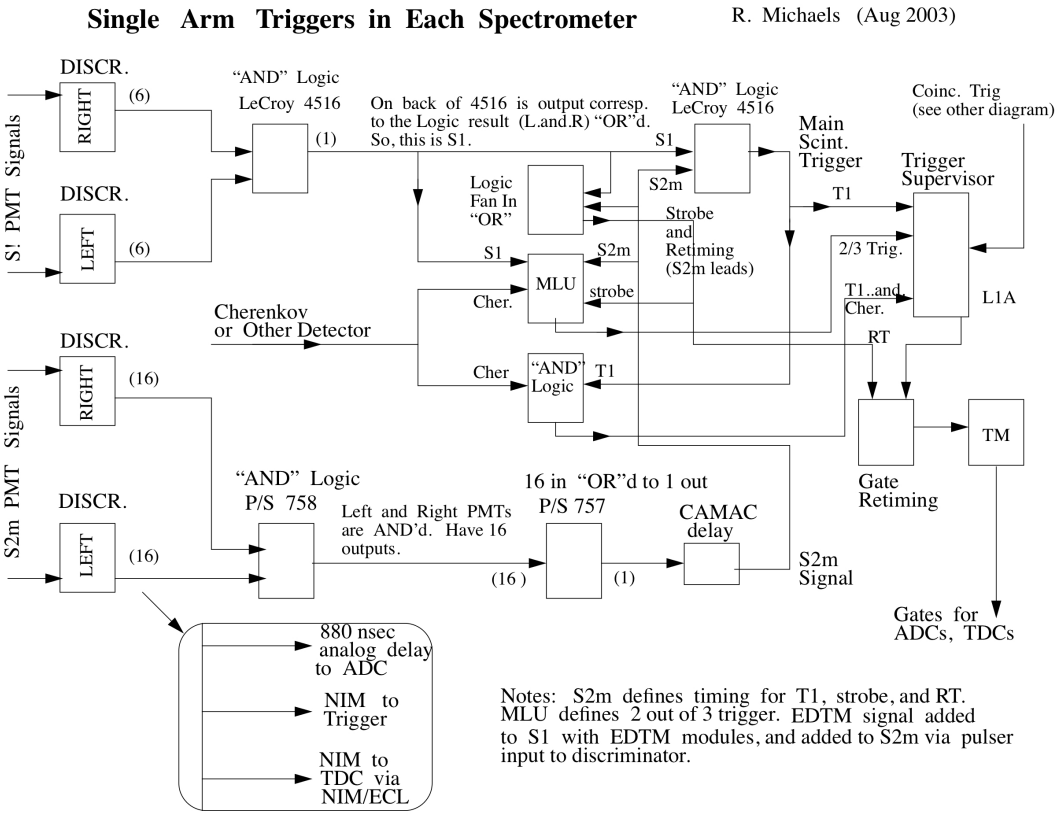

Figure 4.19: Logic diagram for LHRS singles triggers, reproduced from [95]. This is standard wiring for both HRSes; the diagram's T1 corresponds to E06-014's T3, while the 2/3 trigger is E06-014's T4 trigger.

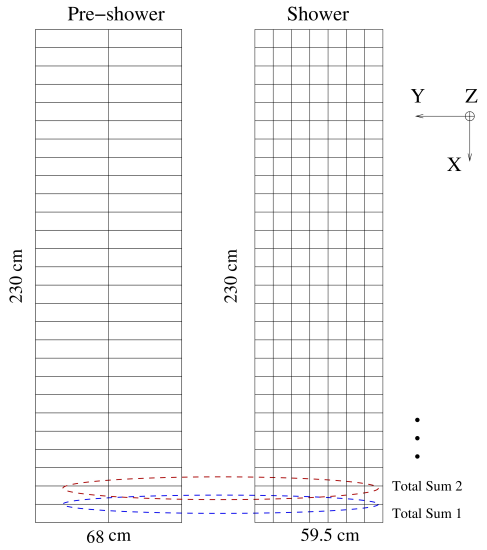

Figure 4.20: Total sum of preshower and shower. Reproduced from [82].

amplified preshower and shower signals were then combined to form the TSUM [82].

Because TSUM is proportional to the energy deposited in the calorimeter, it can be used to form a trigger by passing it through a discriminator with a programable threshold. If any of the 26 TSUMs (the energy deposited in the calorimeter) is larger than the set threshold, then the trigger fires. This describes the T1 trigger. The T6 trigger was identical to the T1 trigger, except that the threshold used to form the T6 was set higher than the T1 threshold. Figure 4.21 shows the electronics diagram that was used to form the T1 and T6 triggers from the BigBite calorimeter.

The T7 trigger was formed in a similar manner as the T1 and T6 triggers, but used the Čerenkov detector rather than the calorimeter. The Čerenkov signals from two adjacent rows of mirrors (four total mirrors) were summed together, resulting in nine overlapping mirror clusters. The sum of each mirror cluster is then passed through a discriminator and compared to pre-programmable threshold. If the sum is larger than the set threshold value, then the T7 trigger fires.

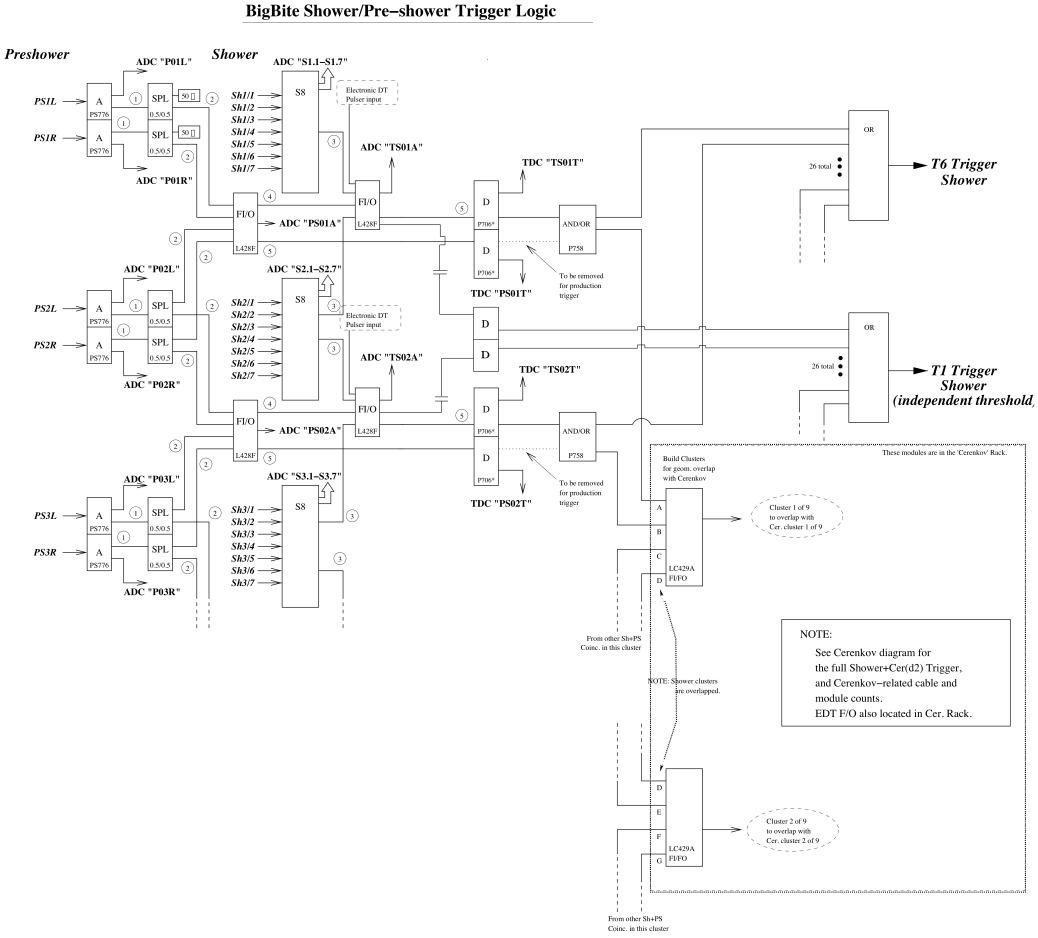

Figure 4.21: Logic diagram for BigBite shower triggers, T1 and T6. Reproduced from [75].

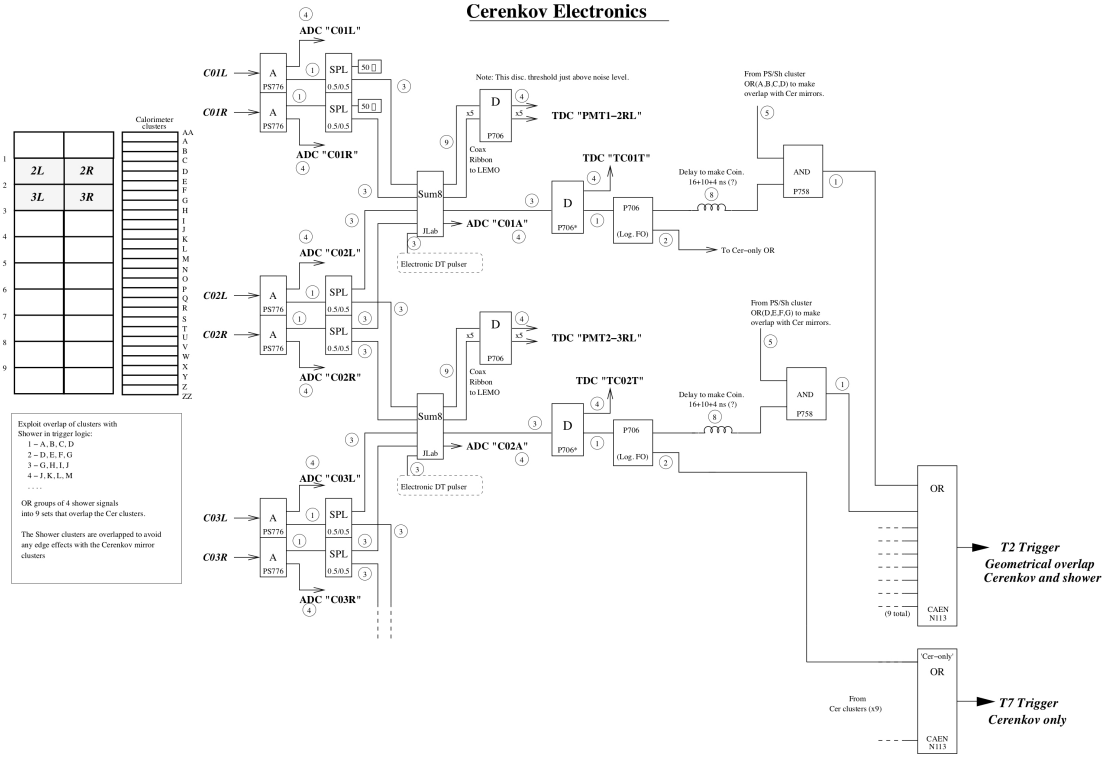

Figure 4.22: Logic diagram for BigBite Čerenkov triggers, T2 (Čerenkov and shower) and T7 (Čerenkov only). Reproduced from [75].

The main electron trigger used in E06-014 was the T2 trigger, which was formed from a geometrical overlap between the calorimeter and Čerenkov detectors. Figure 4.22 shows the trigger logic used to form the T7 and T2 triggers. Being part of an overlap, the thresholds for each of the two detectors needs to be set, in which the calorimeter portion of the T2 trigger is set by the T6 trigger and the Čerenkov portion is set by the T7 trigger. The geometrical overlap of the T2 trigger is shown in Figure 4.23, where there are ten rows of Čerenkov mirrors assigned to 9 overlapping clusters, labeled C1 through C9; and 27 rows of shower and preshower blocks that are assigned to 26 overlapping two-row clusters labeled A-Z. The different colors in each detector represent which Čerenkov clusters overlap with which calorimeter clusters, i.e. Čerenkov rows 2 and 3 (C2) overlap with rows 4-8 of the calorimeter (A,B,C,D and E). The shape of the overlap was chosen based on the paths of the charged particles that pass through the detectors. If a signal passes the threshold of the Čerenkov cluster and the overlapping calorimeter cluster, then the T2 trigger fires.

During E06-014 the T6 threshold was set around 500-600 MeV for most of the experiment, while the T7 threshold was $\sim$ 1-1.5 photoelectrons and had a very large prescale factor, which resulted in no T7 events being written to file. The BigBite energy difference between the three trigger types (T1,T2 and T6) can be seen in Figure 4.25. The T1 and T6 prescales were set relatively large compared to the T2 during data taking, resulting nearly all recorded events being T2 type events. Thus the T1 and T6 histograms in Figure 4.25 needed to be scaled to the T2 histogram, in order to make a comparison to the T2 distribution. The largest difference in the distribution comes from comparing the T1 events to those of the T2 or T6 events, because the TSUM threshold of T1 trigger was much lower than the T2 and T6 triggers; where as the T2 and T6 triggers shared a common TSUM threshold.

Near the end of the experiment running (the very end of the 5.89 GeV data set and all of the 4.74 GeV data set), the preshower hardware sum was also added to the T2 trigger. This meant that in order for the T2 trigger to fire, the conditions previously stated must

be satisfied, in addition to the preshower energy sum, corresponding to the geometrical overlap of the shower and Čerenkov, must also be above a set threshold. The preshower energy inclusion into the T2 trigger resulted in many of the MIP events being rejected in the online trigger. The effect of adding the preshower energy into the T2 trigger can be seen in Figure 8.12.

Since triggers generate gates for ADCs and common stop TDCs, the timing for various triggers must be consistent. The T2 and T6 triggers used the timing of the T6 trigger, which resulted in the need for a retiming circuit that is shown in Figure 4.24. The level one accept (L1A) signal is what gates ADCs and TDCs after the trigger is formed, explained in Section 4.4.8.3.

4.4.6.3 Coincidence Trigger

The T5 tigger is a coincidence trigger in which two particles are detected; one in the BigBite spectrometer and the other in the LHRS. The detected particles share same interaction point, which is determined by the relative timing of the T1 and T3 triggers. Because the particles are being detected in two different spectrometers (two different sets of electronics) and a different particle can be detected in each spectrometer (particles will have different time of flights) care must be taken in determining the timing of the coincidence trigger. This is done by considering the time for the pulser signal to propagate through the trigger logic, and the time of flight for the detected particle, which is determined from the spectrometer geometry and the kinematics of the particle. Delay cables can then be added or removed so the the T1 and T3 trigger signals overlap with each other in time. Figure 4.26 shows the relative timing of the T1, T3, T5 and L1A (triggers the recording of the event) signals used in E06-014. The T3 had a width of 140 ns and defined the coincidence window. The T1 signal, which set the T5 timing, had a width of 40 ns and was designed to arrive 60 ns after the T3 signal.

The T5 trigger was used only briefly in E06-014, during H_2 and ^3He runs for E = 1.23

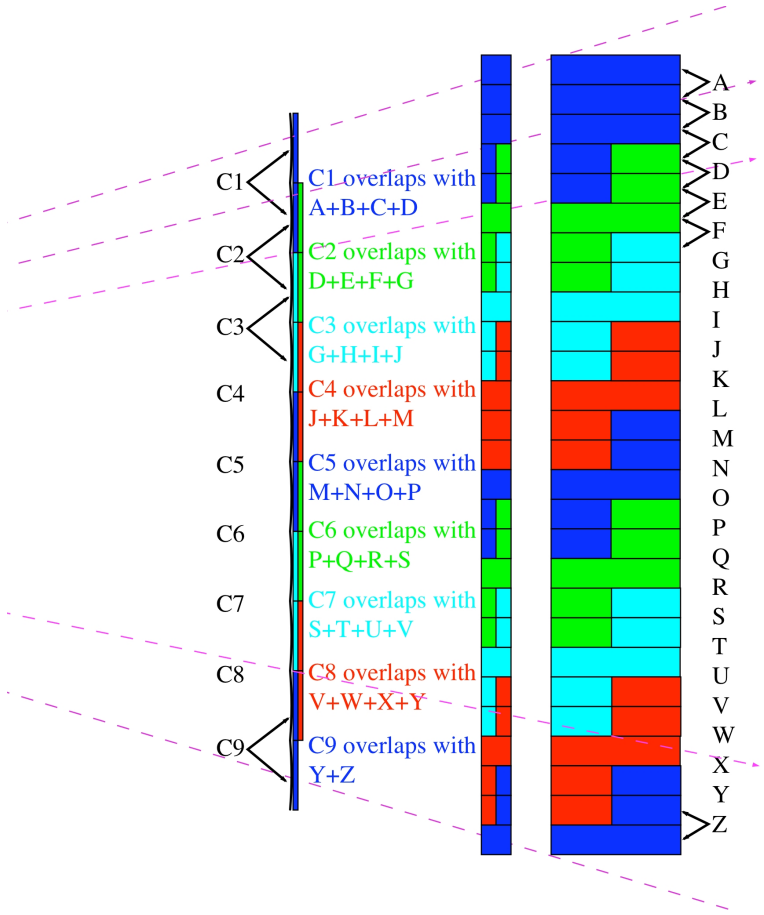

Figure 4.23: Geometric overlap between the gas Čerenkov and shower for the T2 trigger.

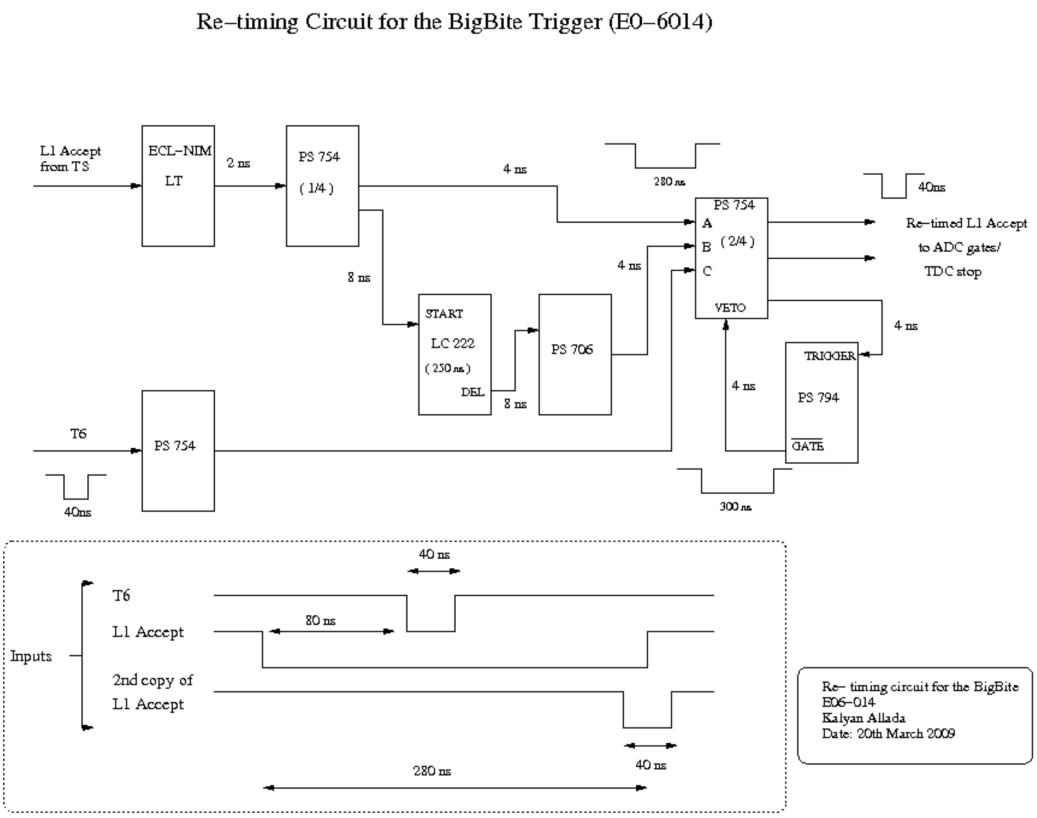

Figure 4.24: Retiming of BigBite trigger from [82]. In timing diagram, the ”2nd copy of L1A Accept” corresponds to the ”Re-timed L1A Accept” from circuit diagram.

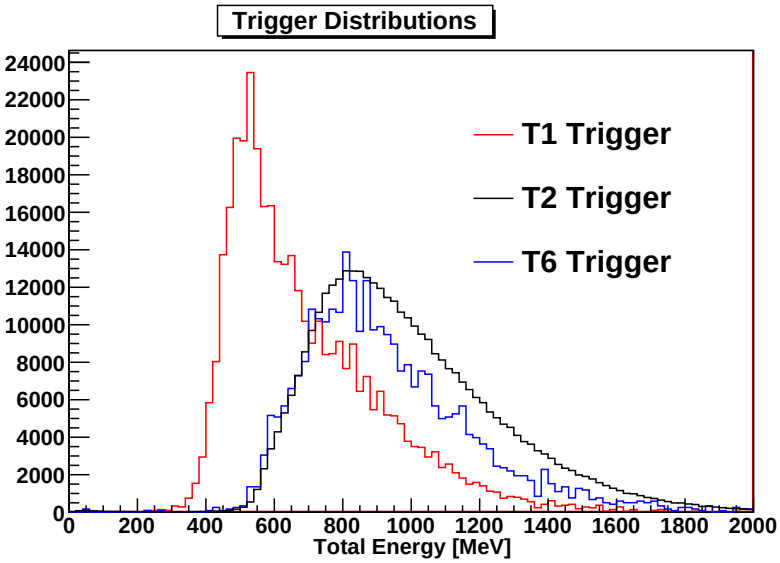

Figure 4.25: Total energy distribution measured in BigBite for T1,T2 and T6 triggers. The T1 and T6 histograms are scaled to the T2 histogram.

GeV incident electrons. During this run period the LHRS and BigBite spectrometer were in the two-arm configuration. Most of the time the LHRS was in positive polarity, where it was detecting protons, while the BigBite spectrometer was in negative polarity in which electrons were being detected. During production running, the LHRS and BigBite spectrometers were both set to the single arm configuration (negative polarity and detecting electrons) and had the T5 trigger disabled in both arms. The LHRS also had the BigBite triggers (T1,T2 and T6) disabled and likewise the BigBite spectrometer had the LHRS triggers (T3 and T4) disabled.

4.4.7 Scaler Setup

Scalers are responsible for counting raw signals from the PMTs without any dead time[6]. From the scalers raw counts and rates can be obtained, which are used for normalization

[6]Dead time is the amount of time that the electronics can not process any new events, because they are busy processing the previous event.

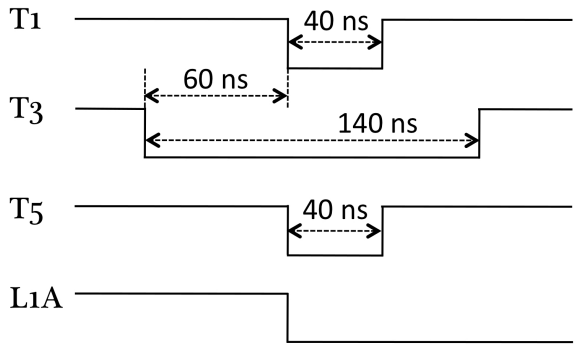

Figure 4.26: Timing of coincidence trigger (T5) relative to BigBite (T1) and LHRS (T3) triggers.

purposes and real time monitoring of various parameters (i.e. beam current, target temperatures and etc.). The BigBite and LHRS spectrometers each had their own scaler setups, which were inherited from E06-010 [82]. The scalers were originally designed to be gated using the target spin and beam helicity, in order to obtain spin-spin dependent scalers. Using target-spin and helicity combinations, four scalers were formed: Tar+ Hel+ (pp), Tar+ Hel- (pm), Tar- Hel+ (mp) and Tar- Hel- (mm). In addition to the four spin dependent scalers, a fifth spin independent scaler was formed. The five scalers were then gated with a run gate, which was obtained from the trigger supervisor (TS), which is responsible for prompting when to acquire and write data, allowing scalers to count only between run start and stops. The scaler gating scheme is shown in Figure 4.27, where the scaler is formed from a logical AND between the run gate, target spin and beam helicity signals. The signals are then sent to the control bit on the S1S3800 scaler for counting purposes [82].

One of the main differences between E06-010 and E06-014 target setups, was that E06-010 flipped their target spin state roughly every 20 minutes, where as during E06-014 the target spin state was flipped every few days. Such an infrequent changing of the target spin state resulted in no need for the scalers gated by the target spin. Therefore the logical signal from the target spin gated scaler was always set to +1. This resulted in two redundant

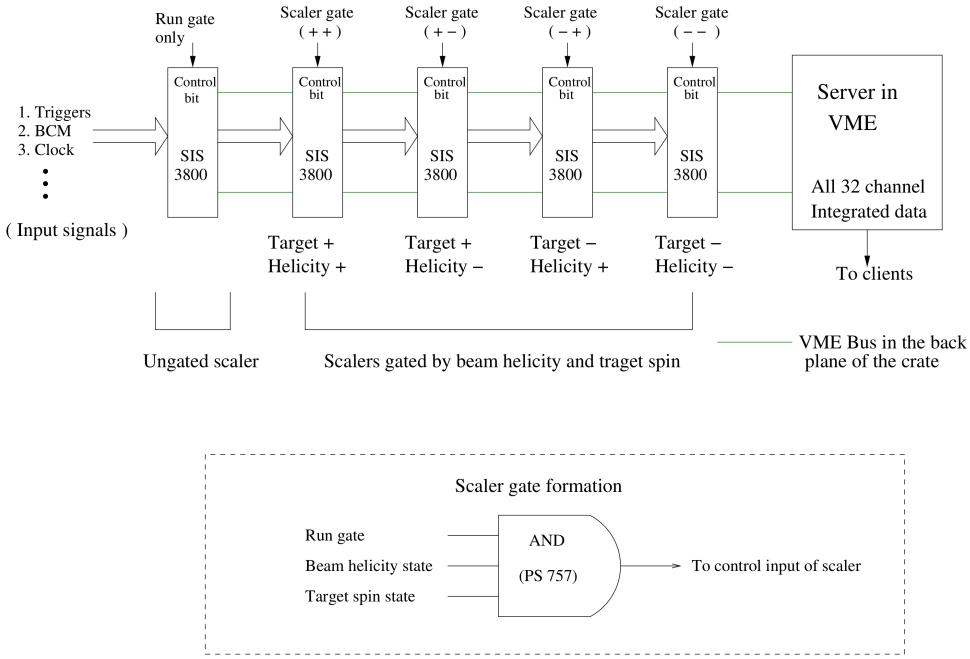

Figure 4.27: Scaler setup and gating scheme. During E06-014 the target spin state logic was set to +1 at all times. Illustration taken from reference [82].

scalers, with the pp and mp (also pm and mm had the same counts) scalers containing the same information.

4.4.8 Data Acquisition

The Data Acquisition (DAQ) system is responsible for storing all of the relevant data and information during a run, including: PMT voltages, target temperatures, timing and analog signals, etc.. At the heart of the DAQ system is the trigger supervisor (TS), which controls the flow of the data acquisition. The data acquisition is done through the use of two software packages known as CODA and EPICS. CODA was written at JLab to handle detector readouts, while EPICS handles the peripheral information and remote controlled devices.

The Versa Module European (VME) bus standard is used by most of the DAQ modules [96].

4.4.8.1 CODA

The CEBAF Online Data-Acquisition (CODA) [97] handles the bulk of the data acquisition and provides an interface to the Read-Out-Controllers (ROCs), which handle the event-by-event retrieval of the data recorded by the detectors. When a L1A signal is received the ROCs process their data and send it to the CODA event builder, which combines the data into one CODA event with a single time stamp and is written to disk.

4.4.8.2 EPICS

Experimental Physics and Industrial Control System (EPICS) [98] is used for device control and the slow read out of scaler parameters, including detector voltages, beam currents, trigger rates, etc.. In Hall A an EPICS script is used to write various EPICS variables to a data file roughly once every 30 s. Additionally a separate list of EPICS variables is logged at the start and end of each run and is written to an electric log book for future reference.

4.4.8.3 Trigger Supervisor

Each spectrometer used in Hall A has its own trigger supervisor associated with it. A trigger supervisor is a VME module with eight inputs corresponding to external triggers formed from the trigger logic defined in Section 4.4.6, and prescales the incoming trigger according to the prescale factor set at the start of the run. When a trigger is accepted, a L1A is generated which prompts the ROCs to process and record their data, as well as gates the ADCs and TDCs. In order to ensure synchronization between all components of the DAQ, no new triggers can be accepted while any crate is busy (still processing information from an accepted trigger) [82].

4.4.9 Analysis Software

All of the detector signals, such as those from ADCs and TDCs, need to be converted into information describing real particles, such as their momentum, energy and trajectory, which are used to derive the final asymmetry and cross section measurements.

The analysis software to do this is written using ROOT [99], a C++ based package developed by CERN to simplify processing and organizing large quantities of particle physics data. The Hall A Analyzer [100], which is an extension of ROOT and was designed by the Hall A collaboration, provides abstract classes for Hall A detectors. The Analyzer's main purpose is to decode and process raw CODA files. Through the use of replay scripts, the Analyzer can be used to combine information into a *tree*, where variables can be computed at the CODA event level.

The Analyzer code is designed to rely on a collection of database files, which contain various hardware features, such as channel, slot and crate information of ADCs and TDCs, as well as calibration constants for the detectors. The data base files are organized in dated directories, making it easy for the Analyzer software to find the correct database needed based on the time stamp of the given run that is being analyzed. This method also provides an easy and efficient way to handle hardware or detector configuration changes.

4.5 Run Summary

E06-014 ran immediately after E06-010[101], which had a very similar setup consisting of a polarized ^{3}He target, LHRS (θ = 16°) and BigBite (θ = 30°) spectrometers with many of the same sub detectors being used. This setup overlap allowed for the two experiments to share a lot of the same software and calibration runs.

E06-014 began by moving both the LHRS and BigBite spectrometers to 45° relative to

the beam line and installing new target cells. BigBite's optics were then calibrated through several elastic ^{2}H and quasi-elastic polarized ^{3}He runs at a beam energy of E = 1.23 GeV. During this time data collection was split between the BigBite magnet being set to negative and positive polarity modes. These calibration runs were taken with the BigBite and LHRS (which was set to positive polarity taking proton data) in coincidence mode. The LHRS optics had been calibrated during E06-010 [102]. After the optics calibrations the LHRS and BigBite spectrometers were both set to negative polarity and single arm modes (nearly the entire experiment ran in this configuration, with brief polarity changes for positron data).

E06-014 saw the commissioning of two new detectors, the BigBite gas Čerenkov and the Compton photon detector [75]. Hall A also saw some of its highest recorded rates of 12 MB/s, as BigBite at 45 saw high event rates. This strain on the network lead to dead time spikes and synchronization gaps, which were alleviated through trigger prescale scale adjustments and at times lowering the beam current from 15 μA to 14 or 13 μA (an average beam current of 15 μA was still achieved).

Early in production running, a vertical hole (about the size of three shower blocks) in the BigBite acceptance was discovered, and a few days later was traced back to an electronics failure. A NIM bin responsible for providing power to a bank of summing modules, was not providing enough power. Upon replacing the NIM bin the BigBite acceptance became more uniform (see Section 8.2.4). Later off-line analysis revealed another hole in the BigBite acceptance (the size of a preshower block) which was traced to a faulty preshower block (see Section 8.2.4). A study of how this gap affected the asymmetries was done and revealed no sizable effects.

The goal of the experiment was to run at two beam energies of E = 5.89 GeV and 4.74 GeV and can be separated into four run periods, each separated by a beam pass change:

1. High polarized 5.89 GeV beam

2. Low polarized ($\sim$ 20% or less) 4.74 GeV beam, due to restrictions set by another Hall.

3. High polarized 5.89 GeV beam

4. High polarized 4.74 GeV beam

On March 1st 2009, JLab experienced power fluctuations during a storm, that eventually lead to contamination of three cryomodules located in the North Linac. The machine control center was able to bring the three cyomodules up to room temperature and bypass them, allowing beam to be delivered at an energy of 4.74 GeV by having the beam make five passes around the accelerator [75]. This unbalanced running of the accelerator only affected one target spin configuration (target spin pointing towards the BigBite spectrometer) of the last 4.74 GeV data set. Due to the Linac issues, E06-014 was able to secure a one week extension and collect about 80% of the proposed statistics.

CHAPTER 5

ELECTRON BEAM POLARIMETRY

The neutron spin structure functions g_1 and g_2 derive from the double spin asymmetries $A_{\parallel}$ and $A_{\perp}$, which are based on the electron beam and target spin orientations. Since neither the beam or target can be completely polarized, a correction factor needs to be applied to the asymmetries in order to account for the imperfect polarization. The methods used to determine the electron beam polarization will be discussed first, followed by the target polarization in Chapter 6.

E06-014 used two independent measurement techniques, based on Møller and Compton scattering to measure the polarization of the electron beam. In this section each of these techniques will be discussed, followed by the final beam polarization achieved during the experiment.

5.1 Møller Polarimetry

Møller scattering ($e^-e^- \rightarrow e^-e^-$) as a polarimetry technique was first proposed by Kresnin and Rozentsveig [103]. They realized that the Møller scattering cross section is sensitive to the polarizations of the electron (P^{beam}) and the atomic electron of the target (P^{target})

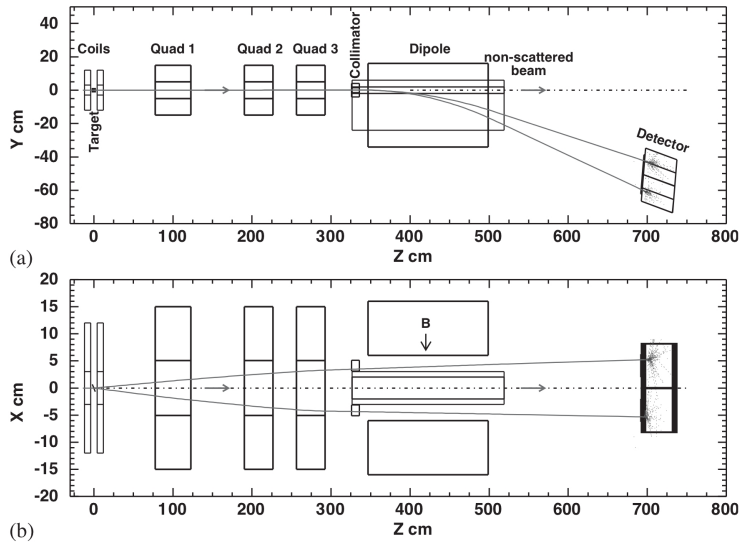

Figure 5.1: Top panel is a side view and bottom panel is a top view of the Hall A Møller polarimeter. This figure shows trajectories from a simulated Møller event (E^{beam} = 4 GeV, θ_{cm} = 80° and ϕ_{cm} = 0°). Figure reproduced from Reference [80].

$$\sigma \propto 1 + \sum_{i=x,y,z} A_i i P_i^{beam} P_i^{target}, \tag{5.1}$$

where $i = x, y, z$ are the axis onto which the polarization is projected, and A is the analyzing power of the Møller measurement.

The Møller polarimeter, in hall A is located in the experimental hall and is part of the standard JLab beam line. Figure 5.1 shows a schematic representation of the Møller polarimeter. The target, a cryogenically cooled 10.9 μm thick iron foil, is located at the upstream end of the detector. The target is polarized to about 7% using a magnetic field of 28 mT produced via Helmholtz coils [75].

The scattered electron passes through three quadrupole magnets and a dipole magnet on its way to a two-arm coincidence lead-glass calorimeter. The longitudinal asymmetry of the beam is measured as the average of the two opposing target angles, resulting in a

Table 5.1: Results for Møller measurements of the electron beam polarization during E06-014 after beam energy fluctuation corrections. Additionally, the insertable half-wave plate status is also shown. The sign of the polarization measurement relates the helicity logic to the helicity of the electron in the hall, which is discussed in Section 8.2.5.1.2.

Date	Energy [GeV]	Polarization	IHWP Status
7 Feb.	5.90	-0.7943 $\pm$ 0.0013$_{stat}$ $\pm$ 0.0159$_{sys}$	in
9 Feb.	1.23	-0.7164 $\pm$ 0.0014$_{stat}$ $\pm$ 0.0143$_{sys}$	in
11 Feb.	5.90	+0.7450 $\pm$ 0.0015$_{stat}$ $\pm$ 0.0149$_{sys}$	out
19 Feb.	5.90	-0.7448 $\pm$ 0.0011$_{stat}$ $\pm$ 0.0149$_{sys}$	in
3 Mar.	5.90	-0.7970 $\pm$ 0.0012$_{stat}$ $\pm$ 0.0159$_{sys}$	in
6 Mar.	4.70	+0.6394 $\pm$ 0.0010$_{stat}$ $\pm$ 0.0128$_{sys}$	out
12 Mar.	4.70	-0.6079 $\pm$ 0.0013$_{stat}$ $\pm$ 0.0122$_{sys}$	out

cancellation of the majority of the transverse polarization contribution [104].

Møller scattering cannot be used during production running or as a way to continuously monitor beam polarization, because of its invasive nature. Another draw back to the Møller polarimeter is that the target foil can only handle a low beam current of about 1.5 μA, whereas during E06-014 the average production current was about 15 μA. However despite these fall backs, the Møller polarimeter with its sub percent statistical uncertainty and $\sim$ 2% systematic uncertainty, provided E06-014 with an accurate and independent method of measuring the beam polarization that complimented the polarization measured using the Compton polarimeter (Section 5.2).

During the experiment, Møller measurements were taken about once every week, and after each major configuration change (e.g. pass change). Table 5.1 lists the results of the seven Møller measurements taken during E06-014.

5.2 Compton Polarimetry

Frederick Lipps and Hendrik Tolhoek [105, 106], were able to show that the Compton scattering cross section is sensitive to the spins of the incoming photon and electron. Taking advantage of the spin sensitivity of the Compton cross section, Charles Prescott [107] proposed an idea to routinely measure electron beam polarization via Compton scattering. Since that time many accelerator facilities such as, SLAC [108], HERA [109, 110] and NIKHEF [111] have all successfully used Compton polarimetry to measure beam polarization. In Compton polarimetry, the electron beam polarization is monitored through Compton scattering between the electron beam and polarized photons. The Compton asymmetry is proportional to the electron beam polarization (P_e) [75]

$$A = \frac{N^+ - N^-}{N^+ + N^-} = \langle A_l \rangle \, P_\gamma P_e, \tag{5.2}$$

where N is the Compton scattering event with longitudinal (+) or anti-longitudinal (-) polarization, P_γ the photon polarization and A_l the analyzing power.

The Compton polarimeter was located upstream of Hall A, and directed the electron beam into a 15.35 cm Compton chicane and then into a photon Fabry-Perot cavity, though the use of two dipole magnets (each with a maximum field of 1.5 T). The scattered electrons and photons along with the unscattered electrons pass through a third dipole magnet, where the scattered photons and electrons are bent into photon and electron detectors respectively; and the unscattered electrons are passed through a fourth dipole magnet. The third and fourth dipole magnets are identical to the first two magnets [75]. Figure 5.2 shows a illustrative representation of the Compton polarimeter.

After leaving the Compton chicane, the electrons involved in the Compton scattering will have less energy than the unscattered electrons, and thus when passing through the third dipole magnet, they will have a lager bend angle missing the fourth dipole magnet and enter

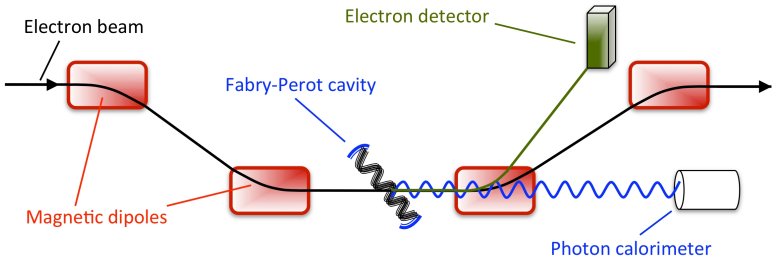

Figure 5.2: Side view illustration of the Hall A Compton polarimeter. The primary electron beam, shown by the black line, enters the magnetic chicane from the left. Compton scattering takes place in the Fabry-Perot cavity located at the center of the chicane; scattered electrons and photons may be detected by appropriately placed detectors, while unscattered electrons continue toward main experimental hall. Reproduced from Reference [75].

the electron detector; photons exiting the chicane will pass though the magnet unbent and enter the photon detector. Prior to E06-014, the electron detector was damaged and not repaired in time to be used in E06-014, thus E06-014 relied entirely on the photon detector to measure the Compton asymmetry.

E06-014 acted as the commissioning experiment for a new installed photon detector, which used a Gd_2SiO_5 (GSO) crystal doped with cerium measuring 6 cm in diameter and 15 cm long. The signal readout was performed using a 12-stage Amperex xp2230 PMT [75]. A more detailed discussion of the Compton polarimeter can be found in Reference [75].

The data recorded using the Compton polarimeter was divided into four run periods, separated by pass changes. All of the Compton runs for a given run period were then combined using an error-weighted average, resulting in a total of four final Compton measurements. The Compton polarimeter was determined to have a systematic uncertainty of 2.49% [75]. This analysis was performed by D. Parno [75].

Table 5.2: Final electron beam polarization, P_e measurements [75]. No Møller measurement was taken during the second run period.

Run Period	Beam Energy [GeV]	Compton	Møller	Combined
1	5.90	0.726 ± 0.018	$0.745 \pm$	0.737 ± 0.012
2	4.74	0.210 ± 0.011	–	0.210 ± 0.011
3	5.90	0.787 ± 0.020	$0.797 \pm$	0.793 ± 0.012
4	4.74	0.623 ± 0.016	$0.628 \pm$	0.626 ± 0.010

5.3 Electron Beam Polarization

The final Compton results for the electron beam polarization have a comparable uncertainty to the Møller results. Since the Compton and Møller techniques have independent systematic uncertainties, the results from each of the techniques can be combined together and reduce the overall uncertainty on the beam polarization. Table 5.2 shows the beam polarization results obtained from the Compton and Møller polarimeters, along with the combined (Compton and Møller) polarization results. The combined systematic uncertainty is 1.56% [75].

CHAPTER 6

POLARIZED HELIUM-THREE TARGET

6.1 Principle of Operation

Information from the proton and neutron are essential in order to form a complete understanding of the structure of the nucleon. However, due to the short life time of the neutron (885.7 ± 0.8 s [9]), it is not possible to perform precision asymmetry measurements on a free neutron target. An effective neutron target must be employed in order to achieve the luminosity required for a precision asymmetry measurement. The ground state of the polarized ^{3}He wave function is dominated by the S wave [112, 113], in which the Pauli exclusion principle forces the spins of the two protons to be anti-aligned relative to each other. This causes the proton spins to cancel, resulting in the neutron carrying all of the spin. In addition to the S state, small components of the S' and D states also contribute to the ground state of ^{3}He [1] as shown in Figure 6.1. The dominant presence of the S wave in the ^{3}He ground state allows polarized ^{3}He to serve as an optimal effective neutron target.

[1] The P state is small enough to be ignored in the ^{3}He ground state.

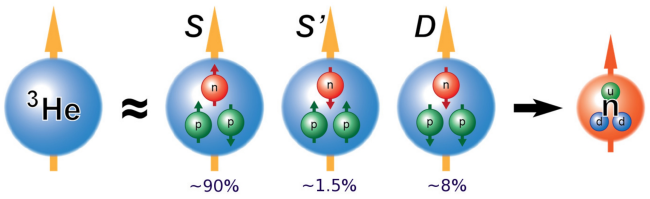

Figure 6.1: Illustration of the components in the polarized ^{3}He ground state. Figure taken from [102]

Polarized ^{3}He targets have been used at MIT-Bates, SLAC, DESY, MAMI, HERMES and JLab to study the electromagnetic and the spin structure of the neutron.

6.1.1 Spin Exchange Optical Pumping

The polarized ^{3}He target used for E06-014 was polarized through spin exchange optical pumping (SEOP). SEOP is a two step process in which alkali metals heated to a vapor are polarized through optical pumping with a polarized laser. The polarized alkali atoms transfer their spins to ^{3}He nuclei, which results in polarizing the the ^{3}He gas.

6.1.1.0.1 Optical Pumping The first step to polarize ^{3}He nuclei is to produce a polarized electron source that can transfer its polarization to the ^{3}He nuclei. Electrons in the outer most shell of vaporized Rb atoms can be polarized through optical pumping of the Rb atom with a circularly polarized 795 nm laser [114]. The polarized Rb atoms then transfer their polarization to the electrons in the outer most shell of the K atoms, which in turn transfer their polarization to the ^{3}He nuclei via spin exchange interactions. If the nuclear spin of Rb is ignored, the principle of optical pumping on the Rb ground state sub levels can be illustrated by Figure 6.2. In a magnetic field ($\sim$ 25 Gauss for E06-014), both the $5S_{\frac{1}{2}}$ and $5P_{\frac{1}{2}}$ ground states split, labeled by m, due to the Zeeman effect. Light from right hand

circularly polarized infrared laser of 795 nm can induce a D1[2] transition, depopulating the electrons occupying the $5S_{\frac{1}{2}}$(m = $-\frac{1}{2}$) ground state sub level and exciting them to the $5P_{\frac{1}{2}}$ (m = $\frac{1}{2}$) sub level. This transition follows the angular momentum selection rule Δm = ± 1. The excited electrons can then decay to the $5S_{\frac{1}{2}}$ (m = $\frac{1}{2}$) or back into the $5S_{\frac{1}{2}}$ (m = $-\frac{1}{2}$) sub level where they can be pumped again. Because electrons decaying into the $5S_{\frac{1}{2}}$ (m = $\frac{1}{2}$) sub level cannot excited again, polarized electrons will accumulate in the $5S_{\frac{1}{2}}$ (m = $\frac{1}{2}$) sub level, resulting in a highly polarized Rb sample. Electrons can emit non-polarized photons, which destroy the Rb polarization when they decay to the $5S_{\frac{1}{2}}$ (m=$-\frac{1}{2}$) state. To counter act the depolarization due to photons, a small amount ($\sim 1\%$ of ^{3}He density) of buffer gas, N_2 is added. N_2, being a diatomic molecule, has vibrational and rotational degrees of freedom to absorb energy from an excited atom, allowing for a radiation-less decay [114, 115].

While this provides a clear description of the optical pumping principle, in reality the Rb atoms of a nuclear spin I = $\frac{5}{2}$ for ^{85}Rb[3]. The introduction of the nuclear spin results in the ground state Hamiltonian operator of the form [115, 116]

$$\hat{H} = A_g \vec{I} \cdot \vec{S} + g_e \mu_B S_z B_z - \frac{\mu_I}{I} I_z B_z, \tag{6.1}$$

the first term describes the coupling of the nuclear spin $\vec{I}$ to the electron spin $\vec{S}$. The second and third terms describe the magnetic-dipole coupling of the electron nuclear spin to the magnetic field B_z, with g_e being the electron g value ($g_e = 2.00232$), μ_B is the Bohr magneton and μ_I is the nuclear magneton for ^{85}Rb ($\mu_I = 4.26426 \times 10^{-12} \frac{MeV}{T}$). Eigenstates for the Rb atom are obtained by solving Equation 6.1, are are labeled with the quantum number $F = I \pm S$ of the total spin $\vec{F} = \vec{I} + \vec{S}$. As with no nuclear spin, the presence of a magnetic field causes the F state to split into $2F + 1$ sublevels

[2]The D1 transition is the transition from the $5S_{\frac{1}{2}}$ state to the $5P_{\frac{1}{2}}$ state.

[3]Rubidium has two isotopes that occur naturally in nature of approximately 72% ^{85}Rb (I=$\frac{5}{2}$) and 28% ^{87}Rb (I=$\frac{3}{2}$). The ^{3}He target at JLab utilized transitions of valance electrons from ^{85}Rb atoms.

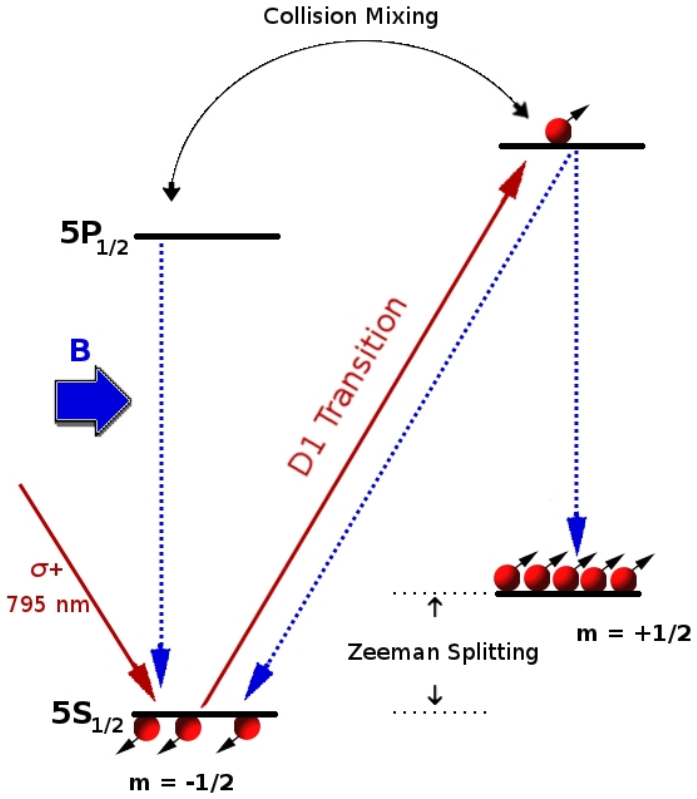

Figure 6.2: Optical pumping of Rb.

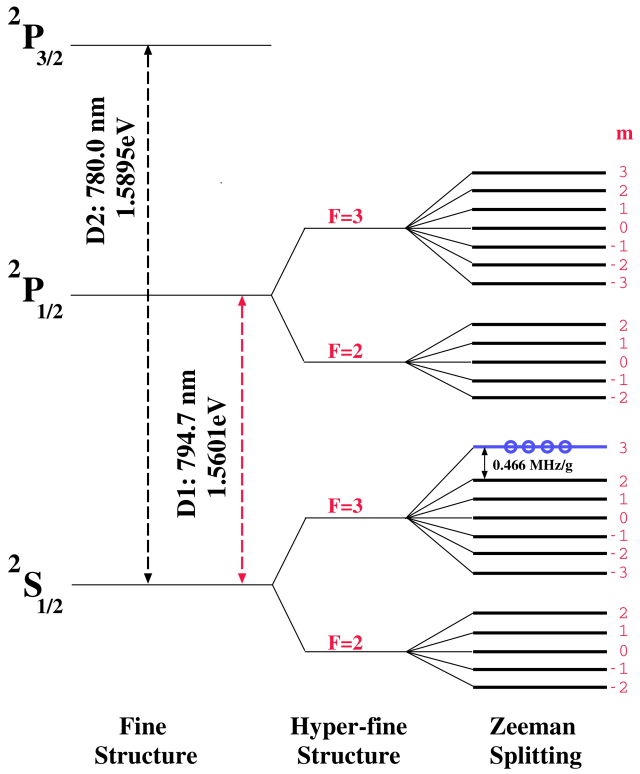

Figure 6.3: Energy level diagram for ^{85}Rb. Image taken from Reference [13].

labeled $m = m_I + m_S$, with $m_I = -I, -I+1, ..., I-1, I$ and similarly $m_S = -S, -S+1, ..., S-1, S$, leading to $m = -F, -F+1, ..., F-1, F$. This energy splitting is shown in Figure 6.3. Similar to the procedure given for no nuclear spin, the valance electrons in Rb are excited with right circularly polarized light through the D1 transition subject to $\Delta m = \pm 1$ selection rules. The excited electrons can then decay by a $\Delta m = 0, \pm 1$ transitions, leading to a majority of electrons occupying the $F = 3, m = +3$ sublevel. The electrons would collect in the $m = -3$ sublevel if left circularly polarized light were used.

6.1.1.0.2 Spin Exchange The polarization of the alkali vapor can be transfered to the ^{3}He nuclei through the process known as spin exchange. Polarization of ^{3}He through spin

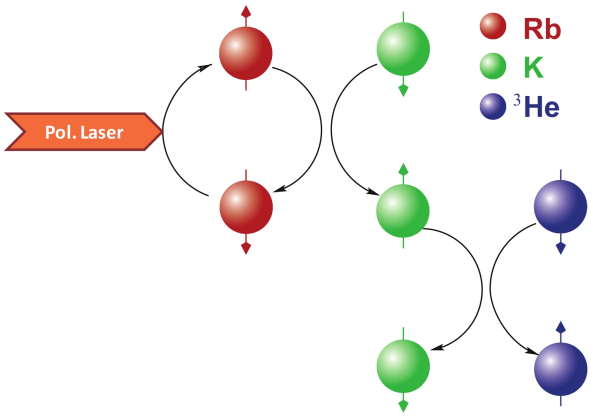

Figure 6.4: Illustration of the spin exchange process for Rb,K and ^{3}He gas mixture. Figure reproduced from [102].

exchange with alkali metal vapor was first demonstrated by Bouchiat [117]. The process of spin exchange is illustrated in Figure 6.4, in which polarized Rb transfers its polarization to K, and K transfers its polarization to ^{3}He through a series of binary collisions. Hyperfine interactions between the alkali electrons and ^{3}He nuclei [118] cause spin exchanges during these collisions, which are given through the spin exchange Hamiltonian

$$H_{SE} = \alpha \vec{I} \cdot \vec{S}, \tag{6.2}$$

where $\vec{I}$ is the nuclear spin, $\vec{S}$ is the electron spin and α is the coupling function which is dependent on the internuclear separation.

The spin exchange efficiency parameter, η, plays an important role in obtaining a highly polarized ^{3}He sample. The spin exchange efficiency is defined as the rate at which angular momentum is transfered to ^{3}He to the rate at which polarization is lost due to various collision channels [119]. Measurements of the spin exchange efficiencies for ^{3}He -Rb and ^{3}He -K gas mixtures as a function of temperature were measured by reference [120], and are shown in Figure 6.5. From Figure 6.5, the K spin exchange efficiency is about ten times

larger than that of Rb. These results suggest that optically pumping directly on K would yield a higher ^{3}He polarization than pumping on Rb. Unfortunately, optical pumping on K directly is not practical due to the lack of commercial lasers with sufficient power and narrow enough line width to polarize K[4] [121]. Although pumping directly on K is not as of yet a practical option, one can take advantage of the higher spin exchange efficiency by using a hybrid target consisting of a Rb, K and ^{3}He gas mixture. Hybrid SEOP relies on polarized Rb atoms rapidly transferring their polarization to K atoms with little polarization loss, resulting in polarized K atoms which then transfer their spin to ^{3}He nuclei (Figure 6.4). The K-Rb spin exchange cross-section is large and the K-Rb spin exchange rate is 200 times faster than typical alkali spin-relaxation rates, leading to the K and Rb atoms having equal electron spin polarization P_A. In the hybrid SEOP, the ^{3}He polarization P_{He} is produced from collisions with both K and Rb atoms [119]:

$$\frac{dP_{He}}{dt} = \gamma_{SE}\left(P_A - P_{He}\right) - \Gamma_{He}P_{He}, \tag{6.3}$$

were Γ_{He} is the rate at which polarization is lost via other processes (discussed further in Section 6.5), $\gamma_{He} = k_K[K] + k_{Rb}[Rb]$, $k_k = (6.1 \pm 0.4) \times 10^{-20}\frac{cm^3}{s}$ and $k_{Rb} = (6.8 \pm 0.2) \times 10^{-20}\frac{cm^3}{s}$ [119] are spin exchange coefficients and $[A]$ is the density of alkali A.

The efficiency of the Rb-K gas mixture was studied in Reference [121] for various K/Rb densities. The E06-014 target (similar to E06-010) took advantage of the K-Rb-^{3}He hybrid gas mixture with a ratio of $\frac{[K]}{[Rb]} \approx 5$[102].

[4]The fine structure splitting of 4s-4p transition in K is 3.4nm, which is comparable to the laser line width ($\sim$2.5 nm) [121].

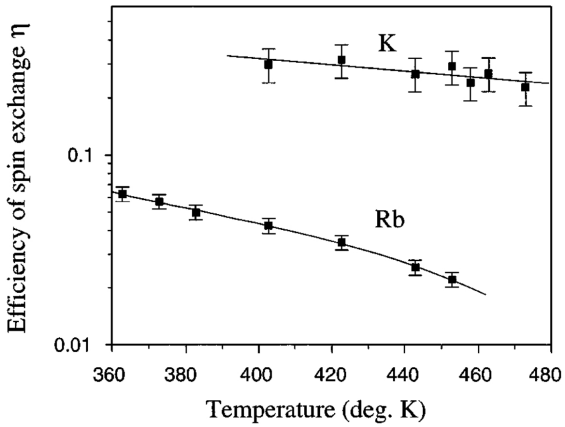

Figure 6.5: Spin exchange efficiencies for ^{3}He -Rb (7.0 amagat of ^{3}He) and ^{3}He -K (6.9 amagat of ^{3}He) versus temperature. Figure reproduced from [120].

6.2 Target Setup

The polarized ^{3}He target system that used in E06-014 consisted of several key components, which can be seen in Figure 6.6. This includes a hybrid Rb-K polarized ^{3}He target cell, Helmholtz coils (which provide a magnetic holding field to align the target spins), pumping lasers (which polarize the ^{3}He gas in the target), an oven and a target ladder (where different target types resided). In this section each of aforementioned components will be discussed.

6.2.1 ^{3}He Target Cell

The polarized ^{3}He gas was contained in a hand blown glass cell made of GE180 aluminosilicate glass. The target cell was sealed with $\approx$ 8 atm of ^{3}He , $\approx 1\%$ of N_2 and a mixture of Rb and K gas [102]. A typical target cell, shown in Figure 6.7, consist of three segments:

1. **The pumping chamber (pc)**, a three inch sphere which contains the Rb, K, N_2 and ^{3}He gas mixture. The pumping chamber was heated to $\approx 265^\circ$ C, and contains two resistance temperature detectors (RTDs) responsible for monitoring the temperature

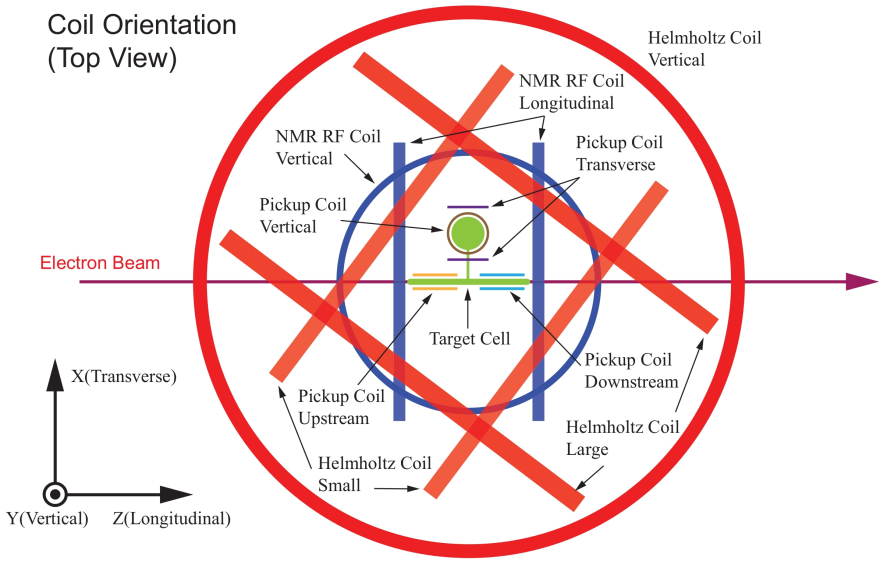

Figure 6.6: Top view of the polarized ^{3}He target setup. $+\hat{X}$ direction is towards the LHRS. The Helmholtz coils are shown in red, the NMR RF coils are shown in blue, the target cell is in green. There are NMR pick-up coils (see Section 6.4) located in the oven and along the target chamber (when the target ladder is at a particular position (see Section 6.2.5)). There are also a pair of pick-up coils at the bottom of the oven that are not shown. Image reproduced from Reference [78].

within the chamber. There is also a *pull off*, about 4 cm long, at the top of the pumping chamber, which was used to seal and detach the cell from the filling apparatus.

2. **The target chamber (tc)** is a 40 cm long cylindrical tube in which the electron beam passes through and interacts with polarized ^{3}He gas contained within the target chamber. During the experiment, the target chamber is cooled to about 70° C by ^{4}He jets on both beam windows [102]. The temperature along the target cell is monitored and recorded using five equally spaced RTDs placed along the length of the target.

3. **The transfer tube (tt)**, extends roughly 9 cm and connects the pumping chamber to the target chamber. Due to the large temperature difference between the pumping chamber and target chamber ($\approx$ 145° C), the polarized ^{3}He gas diffuses from the pumping chamber into the target chamber via the transfer tube, while the the alkali vapor is condensed before exiting the pumping chamber. The transfer tube is at an angle of 42° from the vertical x-axis in the HallA coordinate system, resulting in the pumping chamber and transfer tube lying slightly in beam-left direction (rotation about the beam axis).

More detailed information on the target cell geometry can be found in Appendix D.

6.2.2 Magnetic Holding Field

The ^{3}He target cell was placed in an uniform holding magnetic field of average strength of 25 G produced from a set of Helmholtz coils, which can be seen in Figure 6.6. The holding field had a typical gradient of 10-30 mG/cm [102]. The three sets of orthogonal Helmholtz coils allowed the holding magnetic field to be generated in three directions: longitudinal, transverse or vertical. Table 6.1 shows the characteristics of the Helmholtz coils used to generate the holding field. During E06-014, the holding field was oriented in the transverse[5],

[5] in the electron scattering plane and perpendicular to the nominal beam direction

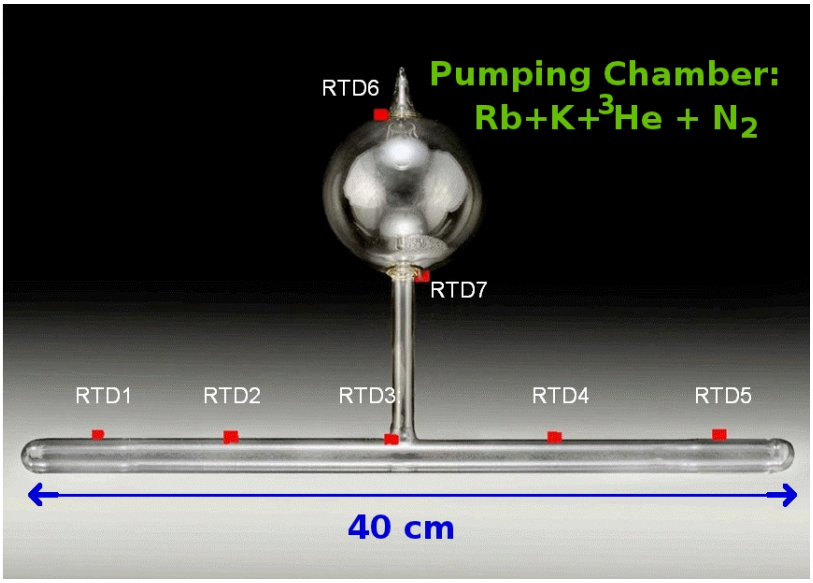

Figure 6.7: Target cell showing three regions: pumping chamber, transfer tube and target chamber.

Table 6.1: Characteristics of Helmholtz coils for target holding field [85].

Coil	Inner Diameter [m]	Number of Turns	Resistance [Ω]
Hori. Small	1.27	256	3
Hori. Large	1.45	272	3
Vertical	1.83	355	4.4

where it was flipped between beam-left (towards LHRS) and beam-right (towards BB), and longitudinal (towards upstream) directions. For all configurations, the holding field was kept anti-parallel to the target spin direction in order to reduce masing[6] [123].

6.2.3 Laser System

E06-014 was able to take advantage of recently installed COMET lasers, which provided a spectral width of about 0.2 nm, a factor of ten improvement over the prior Coherent Fiber Array Package (FAP) system. The narrower line width lead to a significant improvement

[6]The masing effect is a non-linear coupling between the polarization and the coils [122].

in the absorption of light by Rb atoms and the ^{3}He polarization [124]. Three COMET continuous wave (CW) lasers with a wavelength 795 nm and power of 25 W each were installed in an interlock room. The light was transported from the laser source to the target setup via fifteen 75 m long fibers[7]. At the target end, five of the fibers were combined using a five-to-one combiner before entering the optics setup. Three lines of lasers were produced, one for each possible pumping direction: vertical[8], transverse (in electron scattering plane and transverse to the beam) and longitudinal (parallel or anti-parallel to the electron beam). Each of the three laser lines traversed a separate, but similar optics setup designed to circularly polarize laser light and deliver it to the pumping chamber of the ^{3}He cell.

Figure 6.8 shows a schematic of the optics setup was used transverse pumping. A two lens system (L1 and L2) was used to focus the light exiting the five-to-one combiner. The lenses were optimized so the laser spot on the chamber was slightly smaller than three-inches, so that most of the pumping chamber was covered but avoided hitting the edges, which could result in scattering light and depolarization effects. Three six-inch dielectric mirrors (ML1, ML2 and ML3) were used to reflect the laser light to the pumping chamber. In order to preserve the circularly polarized light, the light was incident on each mirror and the mirrors oriented at 45°[9]. ML3 is not shown in Figure 6.8, but is attached to the oven and reflects incident light from ML2 onto the pumping chamber.

The optics components between the lenses and the six-inch mirrors were used to convert the unpolarized laser light into circularly polarized light. After the unpolarized light passed through the lenses (L1 and L2), the light is split by a beam splitting polarization cube (BSPC) into S and P wave components. The P wave component is linearly polarized and transmits through the BSPC. It is then reflected by mirror M2 towards the six-inch mirror

[7]Power loss for light traveling in a 75 m long fiber is about 6% [85].

[8]The vertical pumping direction was not used during E06-014, but was left installed from the previous experiment E06-010.

[9]For longitudinal pumping, the mirrors scattering planes were parallel to each other. A technique that required an additional quarter-wave plate was implemented to recover the laser polarization [102][125].

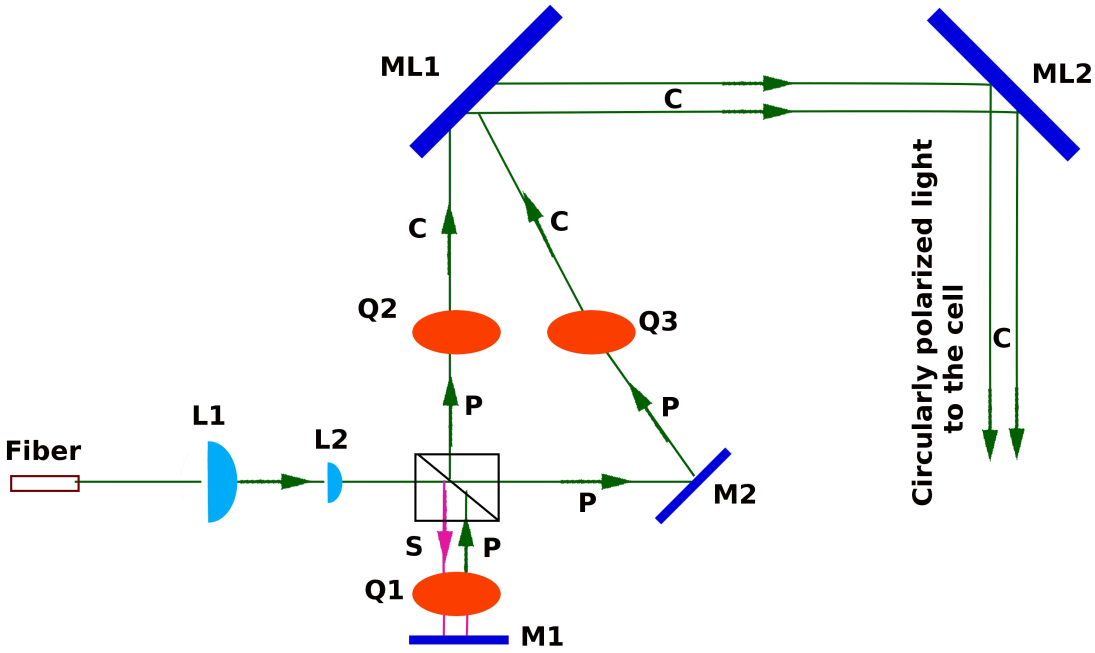

Figure 6.8: Schematic diagram for optics setup for transverse pumping. Light from ML2 is incident on another mirror (not shown) that is attached to the oven. Figure adapted from [78]

ML1. The S wave component of the light is reflected 90° and passes through a quarter-wave plate Q1, then reflected by a flat mirror M1 and again passes through Q1. The two passes through the quarter-wave plate results in converting the S wave into a linearly polarized P wave. The P wave can then transmit through the BSPC and travel towards mirror ML1. There are now two linearly polarized P waves traveling towards mirror ML1. However, before reaching ML1, each P wave passes through a motorized quarter-wave plate, Q2 and Q3. The light wave axises are 45° relative to the laser polarization direction causing the light waves to attain circular polarization. The helicity state of the laser is flipped by rotating the quarter-wave plates by 90°, and therefore flipping the Rb states of $m = \pm 3$ and the pumping spin state of the ^{3}He nuclei [102].

6.2.4 Oven System

The pumping chamber was housed in an oven system made from non-magnetic material CS85, where the cell was heated through hot air to about 240° C producing alkali vapor. Five glass windows were placed on the sides of the oven, allowing the pumping laser light to enter and exit the oven. The temperature of the oven was measured using RTDs. The RTD read back was then inputted into a digital proportional-integral-derivative (PID) controller which controlled the power on the heater and therefore the oven temperature [102]. During the production running, the oven was kept at a stable 240$\pm$ 2° C, except for a brief period where the oven temperature was lowered to 235° C (see Section 6.3).

6.2.5 Target Ladder

Although all production data was taken on polarized ^{3}He target, several other targets were needed for various calibrations and background studies. In order to easily switch between different targets, E06-014 made use of a target ladder, shown in Figure 6.9. The target ladder could be moved vertically via a stepper motor to any of six different positions:

- **Polarized ^{3}He Position**

  This position was used for production data. The cell was glued to the bottom plate of the oven, and could be replaced by a water cell during a water calibration.

- **Solid BeO and Carbon Foil Targets**

  This position consisted of two targets. The first is a solid beryllium oxide target that was used to align and retrieve information of the electron beam position. Downstream of the BeO target were seven carbon foils that were used for optic calibrations (see Section 7.1.2).

- **A "Hole" Target**

The ”hole” target refers to the central carbon foil, which is extended in height relative to the other foils and has a hole in its center to allow the beam to pass through. This target was used to finer beam adjustments.

- **Pick Up Coil Position**

  When at this position the target cell sits between two pairs of pick-up coils, with one pair upstream and the other pair downstream relative to the target center. This resulted in pick-up coils extending the 40 cm length of the target cell. This position was used when measuring the water polarization, which served as a cross-check of the target polarization (Section 6.4) obtained through electron paramagnetic resonance (Section 6.5).

- **Empty Target**

  This position had no target in the path of the beam-line, allowing the beam to pass through. This position was used primarily for beam tuning and performing Møller measurements.

- **Reference Cell Position**

  This was the location of the reference cell, a cell similar in geometry to the production polarized ^{3}He cell. The cell was connected to a gas system allowing it to be filled and vented with several gases: unpolarized ^{3}He , N_2 and H_2. The H_2 target was used with various detector calibrations (Chapter 7) and the N_2 target was used in the analysis of background contaminations (Sections 8.2.6 and 8.3.5).

6.2.6 Enclosure

The target ladder was enclosed in a spherical fiber glass cover, which confined the light from the target laser, as well as provide a containment for radiation in the event of a target cell

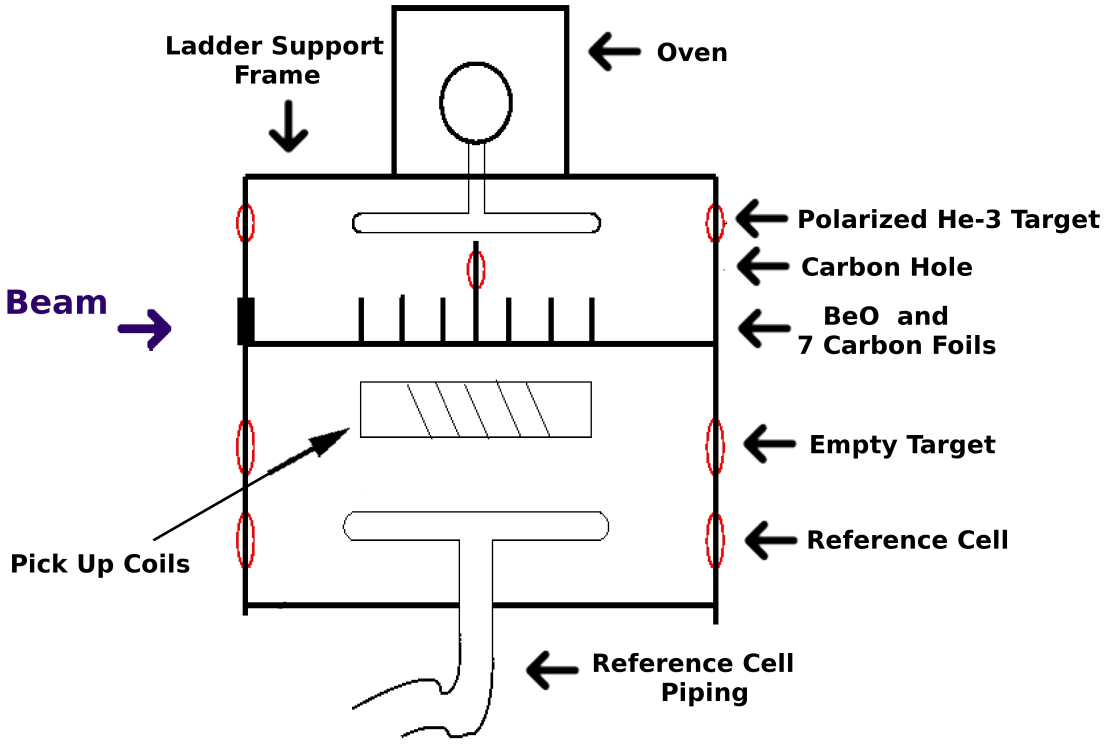

Figure 6.9: Illustration of the target ladder used during E06-014. The red circles represent holes where the electron beam could pass through. Figure adapted from [78].

explosion. In addition to providing safety to workers, the target enclosure also allowed it to be filled with ^{4}He gas, which has a longer radiation length than air. This reduced the energy loss of scattered electrons leaving the target [78]. The target enclosure contained two Be windows that allowed the beam to enter and exit. The entrance window was 0.254 mm thick and the exit window was 0.508 mm thick. Each window was covered on the enclosure side with aluminum foil of 0.076 mm thickness to prevent exposure to air.

6.2.7 Collimator

Target collimators were installed in order to shield from high energy electrons and photons generated from the two beam windows of the target enclosure. The collimators are made of tungsten powder and were $\sim$ 10 cm thick in the nominal particle momentum direction.

6.3 Target Density

A complete understanding of the target density is essential because the calculation of the target polarization depends on the ^{3}He density (Sections 6.4 and 6.5). In this section the analysis of the ^{3}He density in the target and pumping chambers will be presented.

6.3.1 Fill Density

The ^{3}He number density at room temperature, n_0, was extracted by exploiting the fact that collisions with ^{3}He atoms lead to a broadening of the Rb D1 and D2 absorption lines, known as pressure broadening. n_0 can be determined from the D1 and D2 line widths [122, 126]. This measurement was done by L. Fassi [127]. Table 6.2 shows n_0[10] with total systematic uncertainty calculated by Y.-W. Zhang [128].

[10]Densities were calculated in amagats (amg), where 1 amg = 2.687×10^{25} m^{-3}

Table 6.2: Measurement of ^{3}He n_0 density from pressure broadening [127] and relative systematic uncertainty [128].

n_0 amg	Uncertainty [%]
8.099	1.63

6.3.2 Temperature Dependence

The density of a gas is known to have a temperature dependence. When the ^{3}He target cell is placed inside the ^{3}He setup under running conditions, the temperature of the gas will change, resulting in a change in the target density. Due to the pumping lasers and the oven, the gas in the pumping chamber was at a higher temperature than the gas in the target chamber, leading to a different density for each of the chambers. To determine the density in each chamber, one can assume that the ^{3}He gas behaves like an ideal gas and that there is uniform pressure throughout the cell to give,

$$\frac{N_{tc}k_BT_{tc}}{V_{tc}} = \frac{N_{pc}k_BT_{pc}}{V_{pc}}, \tag{6.4}$$

leading to:

$$N_{pc} = \frac{V_{pc}}{V_{tc}}\frac{T_{tc}}{T_{pc}}N_{tc} \tag{6.5}$$

where subscripts tc and pc refer to the quantity in the target chamber and pumping chamber, N is the number of constituents, V is the volume, T is the temperature, and k_B is the Boltzmann constant. N_{tc} can be rewritten in terms of n_0 as

$$N_{tc} = n_0\left(V_{pc} + V_{tc}\right) - N_p, \tag{6.6}$$

where the total target cell volume is $V_{tot} = V_{pc} + V_{tc}$. Combining Equations 6.5 and 6.6 and following similar procedure for N_p, the ^{3}He density in the pumping (n_{pc}) and target

(n_{tc}) chambers can be written as a function of temperature:

$$n_{pc} = n_0 \left[1 + \frac{V_{pc}}{V_{tot}} \left(\frac{T_{tc}}{T_{pc}} - 1\right)\right]^{-1}, \tag{6.7}$$

$$n_{tc} = n_0 \left[1 + \frac{V_{tc}}{V_{tot}} \left(\frac{T_{pc}}{T_{tc}} - 1\right)\right]^{-1}. \tag{6.8}$$

There were two RTDs installed on the pumping chamber and five RTDs installed along the length of the target chamber on the ^{3}He cell to monitor the cell temperature throughout the experiment. The RTD locations can be seen in Figure 6.7. Figure 6.10 shows the average RTD readings from the pumping chamber through out the experiment. The blue markers represent when the ^{3}He target spin state was in the transverse direction, and the red markers represent when the target was in the longitudinal spin state. Ideally the temperature in the pumping chamber would be flat, but due to the pumping laser alignment the pumping chamber temperature was higher when in the transverse orientation compared to the longitudinal orientation. The area between the first two dashed lines marks a run period in which the oven temperature was lowered from 240 °C to 235°C, resulting in a lower pumping chamber temperature. After the red dashed line, the oven temperature was raised back to 240 °C. The last dashed line shows when the oven heaters were replaced, causing a drop in the pumping chamber temperature.

Due to the heat produced from the lasers, the internal temperature of the pumping chamber is higher than the readouts of RTD 6 and RTD 7. To correct for this temperature discrepancy, nuclear magnetic resonance (NMR, see Section 6.4) measurements are done with the lasers on and off. Since the NMR signal is proportional to the ^{3}He density and hence the temperature, the actual temperature can be extracted. The quantity Δ is then defined as the difference between the actual measured temperature and the average temperature read out of RTDs 6 and 7 ($\frac{1}{2}$ (RTD 6 + RDT 7)). The RTD readouts in the pumping chamber can

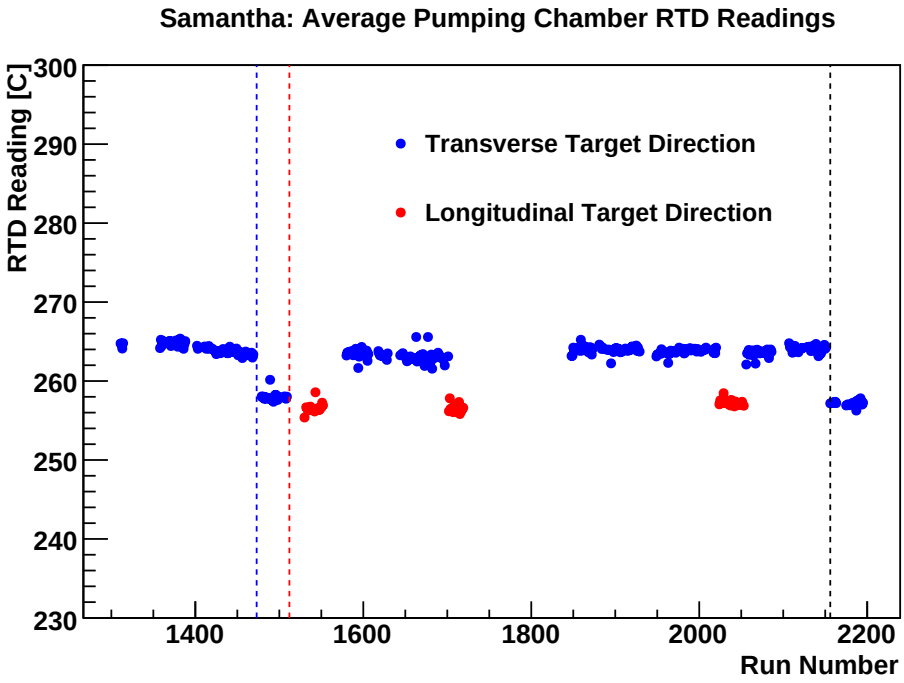

Figure 6.10: Average RTD temperature in the pumping chamber through out the experiment; with blue markers representing the temperature when in transverse pumping configuration, and red markers being the temperature in the longitudinal configuration. The blue dashed line marks where the oven was lowered from 240 °C to 235 °C. The red dashed line marks where the oven temperature was readjusted back to 240 °C. The black dashed line marks when the oven heater were replaced.

Table 6.3: Pumping chamber RTD temperature correction results. [128].

Direction	T (RTD) [°C]	T (Actual) [°C]	Δ [°C]
Longitudinal	257.21	263.39	6.18
Transverse	257.08	264.39	7.31

be corrected once Δ is determined [126]. This correction was carried out by Y.-W. Zhang, with the results summarized in Table 6.3.

Although the temperature in the target chamber is not affected by the pumping lasers, it does need special treatment to extract an average temperature. The temperature at the center of the target chamber was at a higher temperature then the two ends of the target chamber, due to oven and pumping chamber being located near the center of the target chamber. This temperature-position dependence is clearly seen in Figure 6.11 when plotting the readouts from the five RTDs that are along the target chamber. RTD, 3 which is the green marker (at the top of the plot), is the closest to the oven and has the highest temperature readout. RTDs 2 and 4 (red and blue markers located near 70 and 60°C) are positioned roughly the same distance from RTD 5, and have similar temperatures that are lower than RTD 5. Finally, the last two RTDs, RTDs 1 and 5 (black and yellow markers located near 45C), are the furthest from RTD 5 and have similar temperatures and are the lowest of the five RTDs. Several averaging techniques were studied in order to see how different averaging techniques affected the chamber densities. The first method consisted of a non-weighted average

$$\frac{1}{5}\left(RTD1 + RTD2 + RTD3 + RTD4 + RTD5\right). \tag{6.9}$$

The temperature was also computed, by fitting and integrating the temperature *vs.* cell position distributions using several different polynomial functions and then dividing by the distance of the integrand. Figure 6.12 shows an example of the fitting to the temperature-

position distribution with a 2^{nd} order polynomial function. A similar study was done using linear and 4^{th} order polynomial functions. The final method used a weighted average of [129]

$$\frac{6}{40}\left(RTD2 + RTD3 + RTD4\right) + \frac{11}{40}\left(RTD1 + RTD5\right). \tag{6.10}$$

The results of how the various temperature averaging methods affected the target and pumping chamber densities are listed in Table 6.4. The densities were found to be consistent between the various target chamber temperature computations; as a result, the no weight target chamber temperature was used in the analysis. The densities for each chamber were then plotted and fitted (Figure 6.13) for each chamber as a function of run number. The upper two panels are the densities measured in the pumping chamber, and the bottom two panels are the densities measured in the target chamber; with the plots on the left (right) corresponding to the densities when the target spin is transverse (longitudinal). The systematic uncertainty for n_{pc} and n_{tc} was determined by assigning a 5% uncertainty to the each of target cell volumes and varying the temperatures of the chambers by $\pm$ 5 K. The parameters making up n_{pc} and n_{tc} were then varied by the amounts listed in Table 6.5 to assign a systematic uncertainty to the chamber densities. The final density values and their uncertainties can be found in Table 6.6.

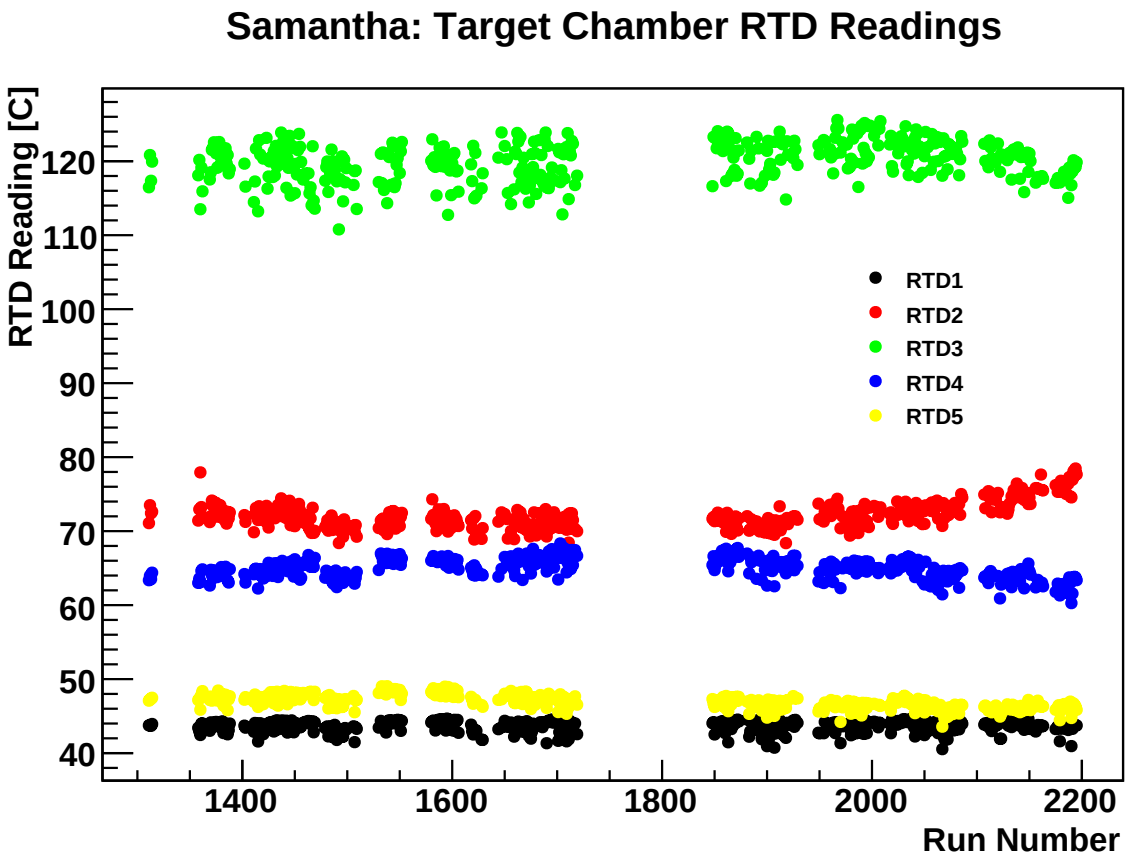

Figure 6.11: Temperature readouts of the five RTDs positioned along the target chamber. The temperature dependence on position due to the oven is clearly seen.

Table 6.4: Results for chamber densities using values of T_{tc} computed by different methods; when the target is in the transverse orientation. $T_{pc} = 543.45K$. Density uncertainties were found using parameter uncertainties found in Table 6.5

Method	$\langle T_{tc} \rangle$ [K]	n_{tc} [amg]	n_{pc} [amg]
No weighting	342.71	10.83 ± 0.41	6.92 ± 0.19
Linear	359.62	10.53 ± 0.38	7.05 ± 0.18
2 Polynomials Func.	345.02	10.79 ± 0.42	6.94 ± 0.19
4 Polynomial Func.	353.91	10.63 ± 0.39	7.00 ± 0.19
weight(Equation 6.10)	336.34	10.95 ± 0.44	6.87 ± 0.20

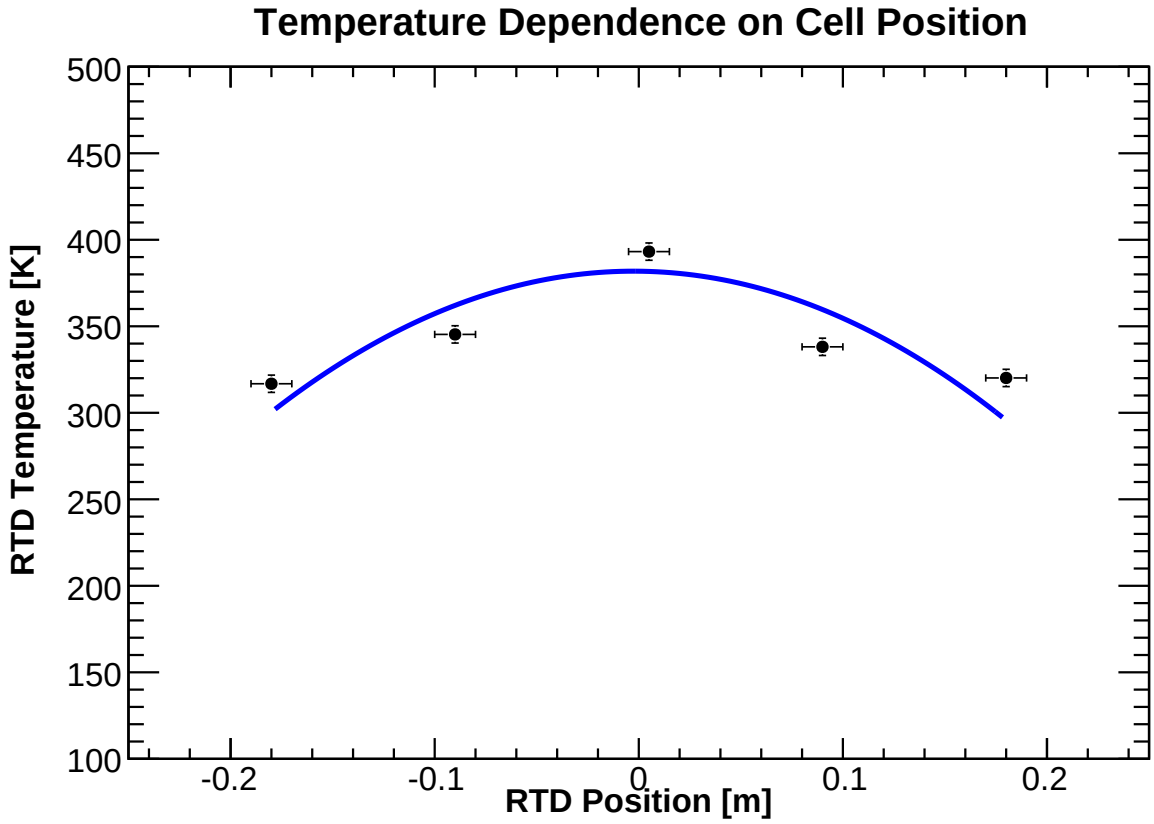

Figure 6.12: Average target chamber RTD readouts vs cell position. The temperature-position distribution is fit with a 2^{nd} order polynomial.

Table 6.5: List parameters and their uncertainties that go into calculating the chamber densities.

Parameter	Value	Unit	Uncertainty [%]
V_{tt}	6.51	ml	5.00
V_{pc}	176.90	ml	5.00
V_{tc}	75.47	ml	5.00
V_{tot}	258.88	ml	8.66
T_{tc} (Transverse)	342.71	K	1.46
T_{pc} (Transverse)	543.30	K	0.92
T_{pc} (Long.)	536.15	K	0.93
T_{tc} (Long.)	342.95	K	1.46
n_0	8.099	amg	1.63

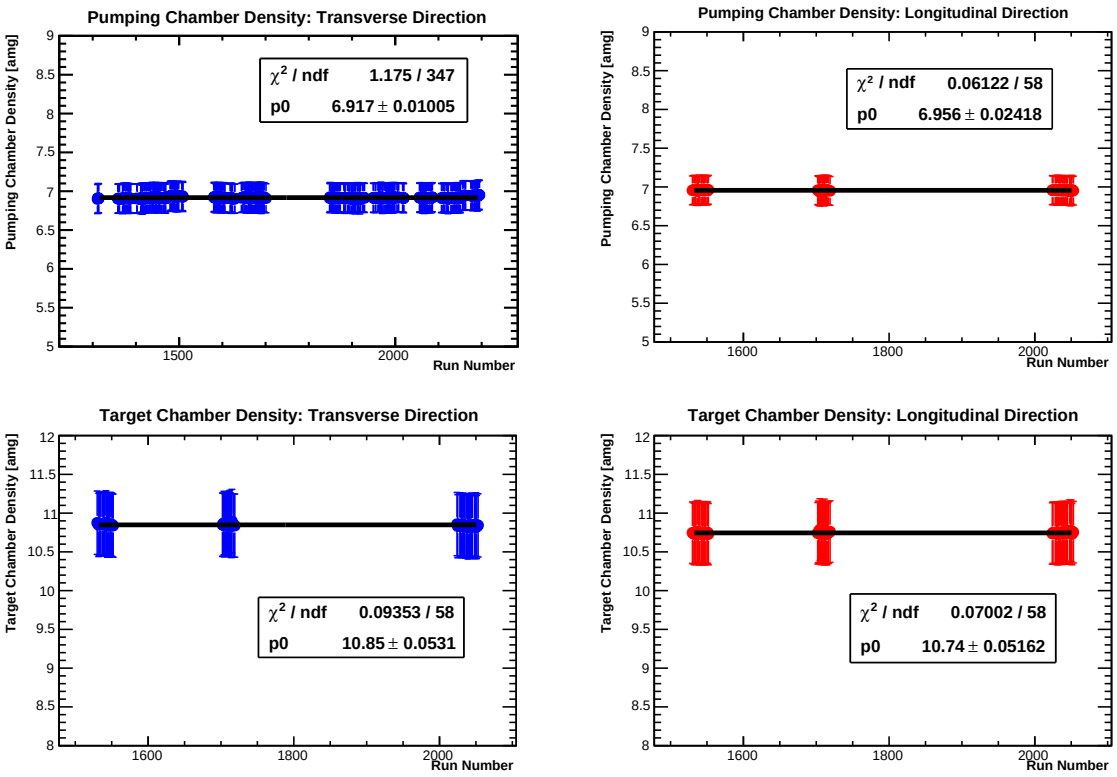

Figure 6.13: Constant fits to the pumping (top two panels) and target (bottom two panels) chambers. The plots on the left (right) refer to density measurements when the target spin was aligned transverse (longitudinal).

Table 6.6: Final density values for the target and pumping chambers when the target is in transverse and longitudinal orientation.

Parameter	Target Direction	Value [amg]	Uncertainty [%]
n_{tc}	Longitudinal	10.74	3.99
n_{pc}	Longitudinal	6.96	2.79
n_{tc}	Transverse	10.85	3.90
n_{pc}	Transverse	6.92	2.74

6.4 NMR Polarimetry

Two types of polarimetry were used to measure the polarization of ^{3}He : nuclear magnetic resonance (NMR) polarimetry using the adiabatic fast passage (AFP) technique [130], and electron paramagnetic resonance (EPR) polarimetry. The NMR signal was calibrated by using EPR and water NMR. In this section the NMR polarimetry and water calibration will be discussed in detail.

6.4.1 Principle

NMR is a phenomenon that takes place when a nucleus with non zero spin is subjected to a static and oscillating magnetic field. The underlying principle of NMR can be explained in a classical framework. Consider a free particle with spin $\vec{I}$ and magnetic moment $\vec{M} = \gamma\vec{I}$, where γ is the gyro-magnetic ratio (3.24 kHz/G for ^{3}He). When the particle is placed in a constant magnetic field $\vec{H}_0$, the particle experiences a magnetic torque whose spin precession in the lab frame follows

$$\frac{d\vec{M}}{dt} = \gamma\vec{M} \times \vec{H}_0. \tag{6.11}$$

An additional RF field $\vec{H}_{RF}$ (perpendicular to $\vec{H}_0 = H_0\hat{z}$) is also present and has the form

$$\vec{H}_{RF} = 2H_1 \cos(\omega t)\,\hat{x} = H_1\hat{e}_+ + H_1\hat{e}_-, \tag{6.12}$$

where $\hat{e}_\pm = \cos(\omega t)\,\hat{x} \pm \sin(\omega t)\,\hat{y}$ are two rotation vectors with frequency $\pm\omega$. At this point, it is more convenient to work in a rotating frame with frequency $+\omega$[11]

[11]The component with frequency -ω was neglected, because it is outside or the resonance.

$$\left(\frac{d\vec{M}}{dt}\right)_{rot} = \gamma\vec{M}\times\left(\vec{H_0}-\frac{\omega}{\gamma}+\vec{H_{RF}}\right) \quad (6.13)$$

$$= \gamma\vec{M}\times\left(H_0-\frac{\omega}{\gamma}\right)\hat{z}+H_1\hat{e}_+. \quad (6.14)$$

Comparing Equations 6.11 and 6.14, it is clear that the effective magnetic field becomes [131]

$$\vec{H_e}\equiv\left(H_0-\frac{\omega}{\gamma}\right)\hat{z}+H_1\hat{e}_+. \quad (6.15)$$

During the NMR measurements, one can either vary the RF field frequency ω, or the holding field H_0 to pass through the resonance condition $H_0=\frac{\omega}{\gamma}$. Moreover, the changing fields must satisfy the two AFP conditions: the fast condition, and the adiabatic condition. To satisfy the fast condition, the field change should be fast enough so that the nucleus spin does not have time to relax. To meet the adiabatic condition, the change in the field needs to be slow enough compared to the resonance condition ($\omega=\gamma H_0$) so that the spin can follow the direction of the effective field.

In the case of the frequency sweep method, the AFP condition can be expressed as

$$\frac{1}{T_2} << \frac{1}{\gamma H_1}\left|\frac{d\omega}{dt}\right| << \gamma H_1, \quad (6.16)$$

where T_2 is the ^{3}He transverse relaxation time which refers to the spin dephasing time constant in the transverse plane. In the case of the field sweep, the AFP condition becomes

$$\frac{1}{T_2} << \frac{1}{H_1}\left|\frac{dH_0}{dt}\right| << \omega. \quad (6.17)$$

During E06-014, NMR measurements were taken approximately once every four hours

via the frequency sweep method. The holding field was fixed at about 25 G and the RF field was swept from 77 kHz to 87 kHz at a rate of 5 kHz/s through a resonance near ω = 82 kHz[12] inducing an electromotive force (EMF) signal, whose height (S) is proportional to the polarization of the sample:

$$S \propto \frac{\left\langle \vec{M} \right\rangle H_1}{\sqrt{\left(H_0 - \frac{\omega}{\gamma}\right)^2 + H_1^2}} \tag{6.18}$$

where $\left\langle \vec{M} \right\rangle = P_{^3\mathrm{He}} \mu_{^3\mathrm{He}} \left[^3\mathrm{He}\right]$, $P_{^3\mathrm{He}}$ is the ^{3}He polarization and $\mu_{^3\mathrm{He}} = 6.706984 \times 10^{-14}$ MeV/T is the ^{3}He magnetic moment. The signal was collected by a pair of pick up coils, which were positioned orthogonal to both the RF and holding fields.

While most of the NMR measurements were performed by changing the RF frequency, several NMR measurements needed as part of the water calibration (Section 6.4.4), were taken by fixing the RF frequency at about 91 kHz and sweeping the holding field from 25 G to 32 G at a rate of 2.1 G/s through the resonance near H_0 = 28 G. Typical NMR signals for both methods are shown in Figure 6.14.

6.4.2 Setup

The ^{3}He target was able to support polarization and polarimetry for three target spin directions: longitudinal, transverse (in the scattering plane) and vertical (transverse out of scattering plane). The first two spin directions were used during E06-014. For each spin direction, the coils were positioned so that the holding field, RF field and pick-up coils were orthogonal to each other. Five pairs of pick-up coils were placed near the pumping chamber and along side of the target chamber. Three pairs of pick-up coils were placed around the pumping chamber (one pair for each spin direction) and two pairs placed along side the

[12]For a nominal holding field of 25 G, one would expect the resonance to occur at ω = 81 kHz. However a slight deviation ($\leq 1\%$) to the nominal holding field will result in a slightly different resonance frequency.

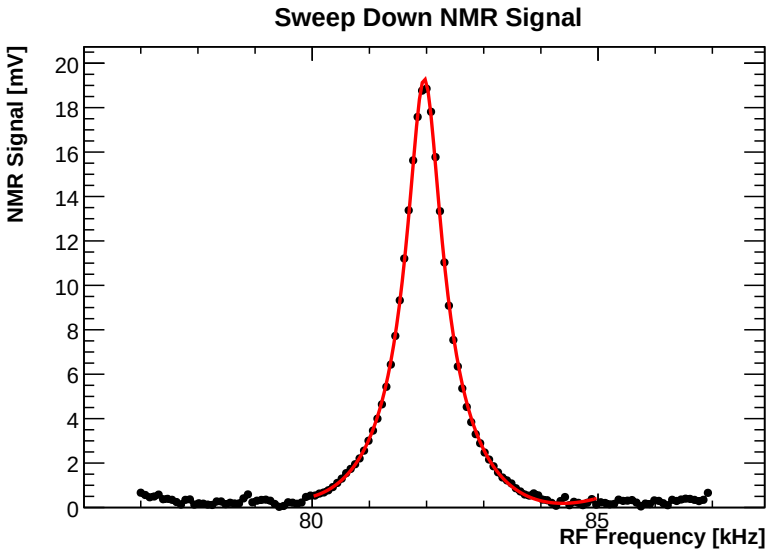

(a) Frequency Field Sweep

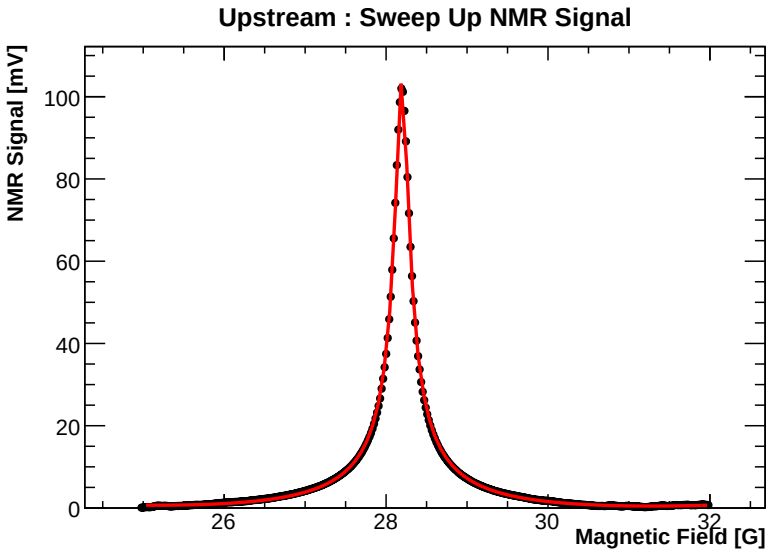

(b) Holding Field Sweep

Figure 6.14: NMR signals from two different sweep methods. Figure 6.14(a) shows a typical NMR signal obtained when sweeping the RF field. While Figure 6.14(b) shows a typical NMR signal obtained by sweeping the holding field.

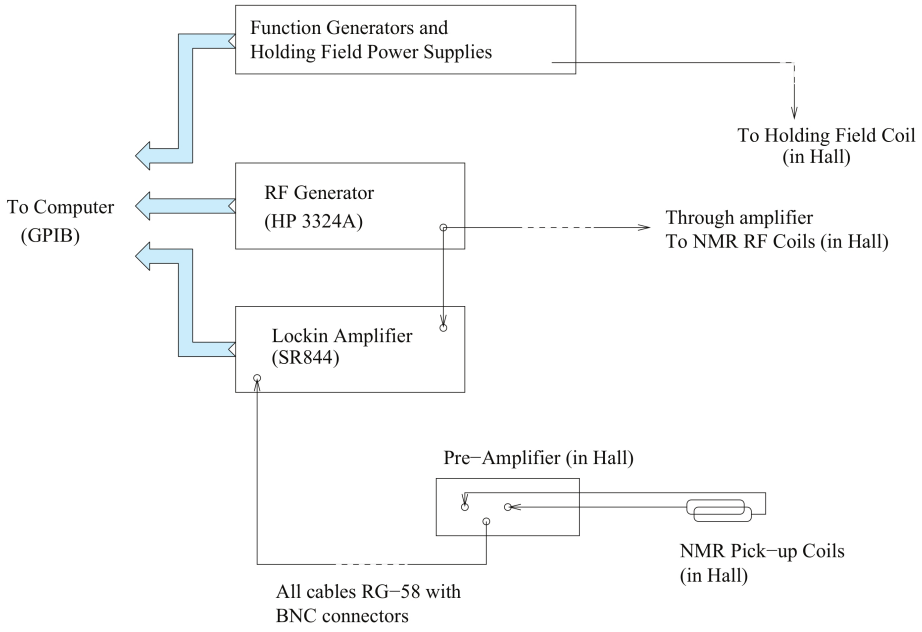

Figure 6.15: The electronic setup for NMR measurements. Figure taken from [102].

target chamber, one pair upstream and the other down stream. Each pick up coil in the pair was installed on opposite sides of the chambers to cancel the background RF signal and double the NMR signal. The arrangement of the pick-up coils can be seen in Figure 6.6. The electronics associated with each spin direction were similar and are shown in Figure 6.15. Power supplies are used to provide current to the Helmholtz coils which produce a constant holding field. A constant or sweeping RF signal is produced using the RF function generator, HP 3324A. The signal is then amplified and sent to the RF coils. The induced NMR signals in both of the pick-up coils was sent into a low-noise pre-amplifier, SR620, inputs A and B. The output (A-B) was then sent to a lock-in amplifier, SR844. The pick-up coils were adjusted such that the background RF signal canceled and the NMR signal doubled in the (A-B) output of the pre-amplifier. The lock-in amplifier picked out the NMR signal, which had the same frequency as the reference RF signal. The data was then sent to the computer via a GPIB (general purpose interface bus) interface.

6.4.3 Analysis

NMR measurements were taken about once every four hours, which allowed for the target polarization to be charted as a function of time. The NMR signals were fitted using the functional form found in Equation 6.18 in addition to a quadratic background

$$f(H) = a\frac{H_1}{\sqrt{\left(H - H_{res}\right)^2 + H_1^2}} + b\left(H - H_{res}\right)^2 + c\left(H - H_{res}\right) + d, \qquad (6.19)$$

where H is the RF field being swept, H_{res} is the resonance RF field, H_1 is the transverse field component, a, b, c and d are scaling constants. Figure 6.14 shows the results of the fit to a typical NMR signal (red line). Signal heights for all NMR measurements were extracted using the fit described above and plotted as a function of time. The NMR signal height, and hence the target polarization, for a given BigBite run can be determined by performing a linear interpolation between two measured NMR heights that occurred before and after the given BigBite run. Figure 6.16 shows the measured (markers) and interpolated (lines) NMR signals as a function elapsed time, where the blue markers are signal heights measured from sweeping with increasing RF frequency (up sweep) and red markers are signal heights measured from sweeping with decreasing RF frequency (down sweep). NMR provides a relative polarization, hence needs to be calibrated in order to obtain an absolute ^{3}He polarization. The calibration of the NMR signals were performed using two methods: water NMR measurements, which will be discussed in the following section, and EPR polarimetry which will be discussed in Section 6.5.

6.4.4 Water Calibration

NMR measurements on a de-oxygenated, de-ionized water sample was used to calibrate the ^{3}He NMR signals. The polarization of the protons in the water, when placed in a known

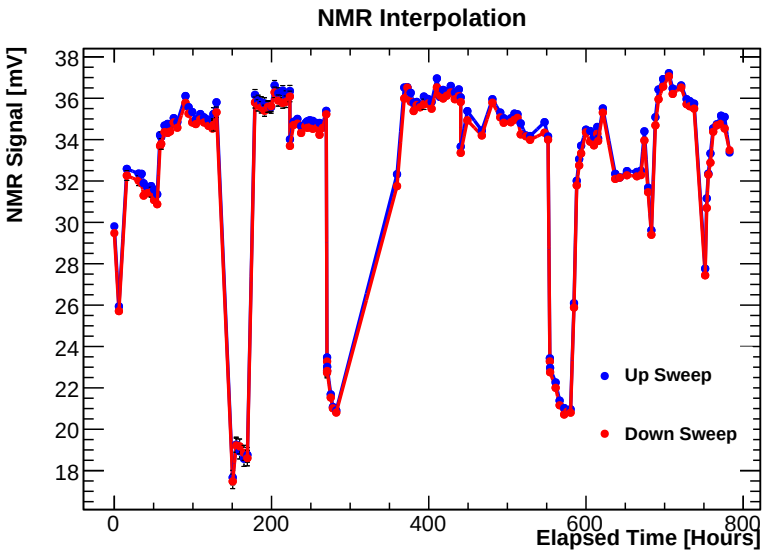

Figure 6.16: Extracted NMR signal heights as a function of time. The connecting lines between two signal heights show the linear interpolation used to acquire a signal height for a given BigBite run. The blue markers represent signals extracted from up sweep NMR measurements and red markers represent signals extracted from down sweep NMR measurements.

magnetic field, can be solved exactly. The water polarization was measured by performing NMR measurements on a target cell filled with water. The water target cell (see Table D.1 in Appendix D) was similar in geometry to the ^{3}He filled cells. The holding field was swept from 18 to 24 G (known as an up-sweep) and from 24 to 18 G (known as a down-sweep) at a rate of 1.2 G/s, while holding the RF frequency fixed at 91 kHz. This resulted in an resonance field of H_0 = 21.37 G. The water NMR signal was detected in two sets of pick-up coils that extended the length of the target on both sides. The ^{3}He NMR measured during production running is proportional to the ^{3}He polarization in the pumping chamber. Since all of the scattering interactions are taking place in the target chamber, the ^{3}He polarization in the target chamber is desired. However, due to the temperature difference ($\Delta T \approx 190^\circ$ C) and distance ($\Delta d \approx 9$ cm) between pumping and target chambers, there is a non-negligible polarization gradient that forms and must be accounted for in order to extract the target chamber ^{3}He polarization. The polarization gradient can be accounted for by two methods: one, by modeling the ^{3}He polarization diffusion from the pumping chamber to the target chamber (which was implemented during the EPR analysis discussed in Section 6.5.), and the second by measuring a NMR cross-calibration factor formed by the ratio of ^{3}He polarization in the target chamber to that in the pumping chamber. The latter method was employed during the water calibration analysis and will be discussed in this section.

The ^{3}He polarization extraction using the known polarization from water can be expressed as

$$P_{^3\mathrm{He}} = C_w \cdot C_{NMR} \cdot S_{^3\mathrm{He}}, \tag{6.20}$$

where C_w is the water constant, C_{NMR} is the NMR cross-calibration factor and $S_{^3\mathrm{He}}$ is the NMR signal height measured during ^{3}He production runs.

6.4.4.1 C_w

Although the water and ^{3}He target cells are similar, they are not identical, therefore in addition to the water NMR signal height and polarization, several other quantities are needed in order to account for the target cell differences. Accounting for these differences

$$C_w = \left(\frac{P_w}{S_w}\right) \cdot \left(\frac{G_w}{G_{^3\mathrm{He}}}\right) \cdot \left(\frac{\mu_p}{\mu_{^3\mathrm{He}}}\right) \cdot \left(\frac{n_p \phi_w}{n^{pc}_{^3\mathrm{He}} \phi^{pc}_{^3\mathrm{He}} + n^{tc}_{^3\mathrm{He}} \phi^{tc}_{^3\mathrm{He}}}\right), \tag{6.21}$$

where the subscripts w corresponds to water, p to the proton and ^{3}He to ^{3}He targets and quantities. The super scripts pc and tc refer to quantities in the pumping and target chambers of the ^{3}He target cell. P_w is the polarization of the protons in the water sample, S_w is the NMR signal height of the water sample, G is the gain setting on the pre-amplifier (these values were fixed at 20x when using the water target and 5x when using the ^{3}He target), μ is the magnetic moment, n_p is the proton density in the water (2482 amg at 22°C) and ϕ is the magnetic flux through the cell.

The first step to calculating C_w is to determine the proton polarization. The thermal polarization of protons in the water sample can be given by Boltzmann statistics

$$P_{thermal} = \tanh\left(\frac{\mu_p H}{k_B T}\right), \tag{6.22}$$

where $\mu_p = 1.4106 \times 10^{-30} J/G$, k_B is Boltzmann's constant ($1.3086 \times 10^{-23} J/K$), T is the temperature of the water cell and H is the holding field. For a holding field of 18 G and target temperature of 294.4 K, $P_{thermal} \sim 6.25 \times 10^{-9}$. While this polarization is small, it can produce a NMR signal large enough to be used to calibrate the ^{3}He NMR signals. Although Equation 6.22 provides a reasonable estimate of the proton polarization in water, the Bloch equations, given by Equations 6.23 through 6.25, can be used to better determine the water polarization. The Bloch equation describe the time evolution of the

three components of the polarization (P_x,P_y,P_z) in a rotating frame [130].

$$\frac{dP_x(t)}{dt} = -\frac{1}{T_2}P_x(t) + \gamma\left(H(t) - H_0\right)P_y(t) + \frac{\chi}{T_2}H_1 \quad (6.23)$$

$$\frac{dP_y(t)}{dt} = -\gamma\left(H(t) - H_0\right)P_x(t) - \frac{1}{T_2}P_y(t) + \gamma H_1 P_z(t) \quad (6.24)$$

$$\frac{dP_z(t)}{dt} = -\gamma H_1 P_y(t) - \frac{1}{T_1}P_z(t) + \frac{\chi}{T_1}H_1 \quad (6.25)$$

where, T_1 is the longitudinal relaxation time, T_2 is the transverse relaxation time, γ is the gyro-magnetic ratio of the proton (26.7515 kHz/G), H_1 is a rotating transverse RF field, H_0 is the resonance field, $H(t) = H_0 + \alpha t$ is the field along the z-axis being ramped at a rate of $\alpha = 1.2$ G/s and $\chi = \frac{\mu_p}{k_B T}$.

Although the Bloch equations can not be solved analytically, they were able to be solved numerically using Mathematica 8.0. In order to solve the Bloch equations values for H_1, temperature, T_1 and T_2 are needed. For the transverse holding field a value of 16 mG was used, based on measurements during E06-010 [102]. RTDs on the water cell were used to measure the average water temperature of 21.25° C. Due to the presence of ^{17}O isotope in natural water, T_2 is slightly smaller than T_1 [132–134]. However, one can first assume a value of $T_1 = T_2 = 2$ s [122] (allowing the Bloch equations to be reduced to one equation) was used as the relaxation times. With these values in place and the condition that the first derivative of the Bloch equations vanish at the start time, the polarization components can be calculated. Figures 6.17, 6.18 and 6.19 show the polarization components P_x, P_y and P_z as a function of time. Figure 6.17 corresponds to the signal shape that is detected by the pick-up coils. One will notice that the signal in Figure 6.18 is much smaller than that detected in the P_x and P_z components. The curve presented in Figure 6.19 begins with the magnetization of the water in the positive z direction. As the field is swept, the

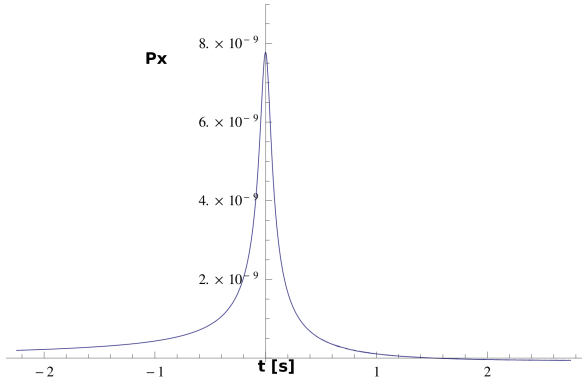

Figure 6.17: Polarization component in the $\hat{x}$ direction. The signal shape that is detected by the pick-up coils.

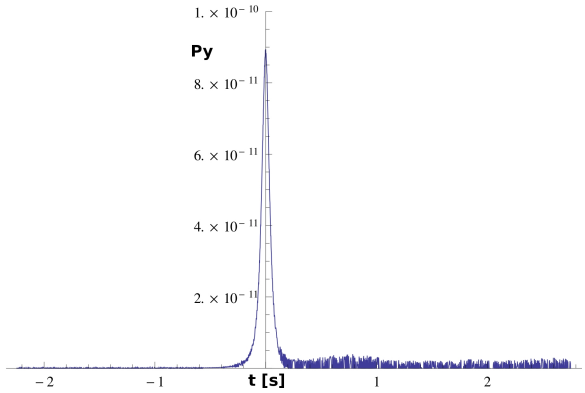

Figure 6.18: Polarization component in the $\hat{y}$ direction.

magnetization becomes zero at the resonance and is then flipped. The spins are in the high energy state, then begin to flip back to the low energy state, approaching the orientation in which the magnetization had at the start of the sweep. The water polarization was found by numerically integrating the Bloch equations and systematic uncertainty was assigned by considering a $\pm 2^{\circ}$C uncertainty in the RTD temperature reading, as well as varying the limits of integration by ± 2 G. Table 6.7 lists the water polarization results.

Fitting and extracting the AFP water signal height is complicated by the fact that the relaxation times T_1 and T_2 are on the same order of magnitude as the sweep time $t_{sweep} \approx$ 5s. Therefore, the Bloch equations, Equations 6.23– 6.25, are used to fit the NMR water signal. In general, there is no analytic solution to the Bloch equations, but in the case where

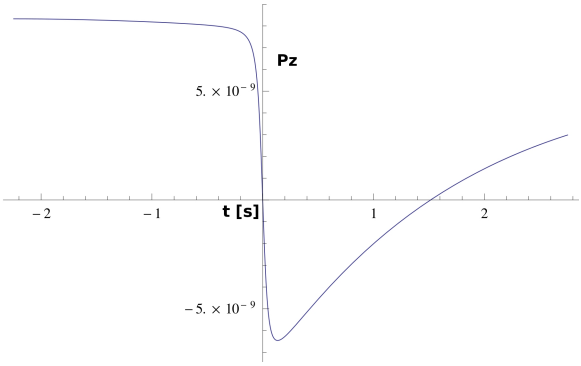

Figure 6.19: Polarization component detected in the $\hat{z}$ direction.

Table 6.7: Water polarization results from Bloch equation integration. The uncertainty is given in relative percent.

Parameter	Value	Uncertainty [%]
Up sweep P_w	6.584×10^{-9}	2.28
Down sweep P_w	7.771×10^{-9}	2.42

$T_1 = T_2$, the three equations can be reduced to one equation for the magnitude of the polarization vector $P_{eff} = \sqrt{P_x^2 + P_y^2 + P_z^2}$, leading to the differential equation

$$\frac{dP_{eff}}{dt} = \frac{1}{T_1}\left[P_{eff}\left(t\right) - P_{eq}\left(t\right)\right], \tag{6.26}$$

where $P_{eq}\left(t\right) = \chi\frac{H_1^2+\alpha t(H_0+\alpha t)}{\sqrt{H_1^2+(\alpha t)^2}}$ is the equilibrium polarization that P_{eff} would relax to if given infinite time. Using the initial condition $\frac{dP_{eff}}{dt}\left(t = t_i\right) = 0$ leads to $P_{eff}\left(t_i\right) = P_{eq}\left(t_i\right)$. The solution to Equation 6.26 is then given by:

$$P_{eff} = e^{-(t-t_i)/T_1}\left(P_{eq}\left(t_i\right) - \frac{1}{T_1}\int_{t_i}^{t} e^{(u-t_i)/T_1} P_{eq}\left(u\right) du\right). \tag{6.27}$$

The signal induced in the pick-up coil is proportional to P_x and can be written as

$$\frac{P_x}{P_{eff}} = \frac{H_1}{\sqrt{H_1^2 + (\alpha t)^2}}. \tag{6.28}$$

Unfortunately, Equation 6.27 has no analytic representation. However, an analytic expression can be approximated by expanding the exponential and square root in the integral in a Taylor series. There exist three regions where a Taylor expansion can be performed:

- If $t_i \leq t < t_a$; $\alpha|t| >> H_1$, then the square root in $P_{eq}(t)$ can be approximated:

$$\frac{H_1^2 + H_0\alpha u + \alpha^2 u^2}{\sqrt{H_1^2 + \alpha^2 u^2}} \approx -(H_0 + \alpha u) + \frac{H_1^2}{2\alpha u} \tag{6.29}$$

  The solution in this region is then given as

$$P_{eff}(t) \approx e^{-(t-t_i)/T_1}\left(P_{eq}(t_i) - \frac{\chi}{T_1}\int_{t_i}^{t} e^{(u-t_i)}\left(H_0 + \alpha u - \frac{H_1^2}{2\alpha u}\right)du\right). \tag{6.30}$$

- If $t_a \leq t < t_b$; $|u| << T_1$, then the exponential in the integral can be expanded

$$e^{(u-t_i)} \approx e^{-t_i/T_1}\left(1 + \frac{u}{T_1} + \frac{u^2}{2T_1^2}\right) \tag{6.31}$$

  which leads to the following solution in this region:

$$\begin{aligned} P_{eff}(t) &\approx e^{-(t-t_i)/T_1}\left(P_{eq}(t_i) - \frac{\chi}{T_1}\int_{t_i}^{t_a} e^{(u-t_i)/T_1}(H_0 + \alpha u)\,du\right) \qquad (6.32)\\ &+ e^{-(t-t_i)/T_1}\frac{\chi}{T_1}e^{-t_i/T_1}\int_{t_a}^{t}\left(1 + \frac{u}{T_1} + \frac{u^2}{2T_1^2}\right)\frac{H_1^2 + H_0\alpha u + \alpha^2 u^2}{\sqrt{H_1^2 + \alpha^2 u^2}}du. \end{aligned}$$

- Finally, if $t_b \leq t < t_f$; $\alpha|t| >> H_1$, then the square root can be approximated as:

$$\frac{H_1^2 + H_0\alpha u + \alpha^2 u^2}{\sqrt{H_1^2 + \alpha^2 u^2}} \approx H_0 + \alpha u\,. \tag{6.33}$$

Then the solution in this region is given as

$$\begin{aligned} P_{eff}(t) &\approx e^{-(t-t_i)/T_1}\left(P_{eq}(t_i) - \frac{\chi}{T_1}\int_{t_i}^{t_a} e^{(u-t_i)/T_1}(H_0+\alpha u)\,du\right) \\ &+ e^{-(t-t_i)/T_1}\frac{\chi}{T_1}e^{-t_i/T_1}\int_{t_a}^{t_b}\left(1+\frac{u}{T_1}+\frac{u^2}{2T_1^2}\right)\frac{H_1^2+H_0\alpha u+\alpha^2u^2}{\sqrt{H_1^2+\alpha^2u^2}}du \\ &+ e^{-(t-t_i)/T_1}\frac{\chi}{T_1}\int_{t_b}^{t} e^{(u-t_i)/T_1}(H_0+\alpha u)\,du. \end{aligned} \tag{6.34}$$

To see how close the approximate polarization is to the exact polarization, Equation 6.27 and the equations representing the approximate solution in all three regions (Equations 6.30, 6.33 and 6.34) were integrated using Mathematica. The difference between the approximate and exact polarization is plotted in Figure 6.20. From that difference, it is clear that the approximated polarization adequately describs the exact polarization with a maximum difference of around the order of 10^{-12}. The analytical expression $f(H)$, from the approximate P_{eff}, that was used to fit the water NMR signal is given as:

$$f(H) = a\frac{g(H-H_0)}{g(0)}\frac{H_1}{\sqrt{(H-H_0)^2+H_1^2}} + b(H-H_0) + c, \tag{6.35}$$

with:

- $g(x) = F_1(x)$ if $t_i \leq t < t_a$, that is $H_{min} \leq H < H_a$,
- $g(x) = F_2(x)$ if $t_a \leq t < t_b$, that is $H_a \leq H < H_b$ and $H_a \leq H_0 < H_b$,
- $g(x) = F_3(x)$ if $t_b \leq t < t_f$, that is $H_b \leq H < H_{max}$,

where $H_a = (H_0 + \alpha t_a)$, $H_b = (H_0 + \alpha t_b)$, $H(t_i) = H_{min}$, $H(t_f) = H_{max}$ and the functions F_i correspond to the solution in region i given by Equations 6.30, 6.33 or 6.34.

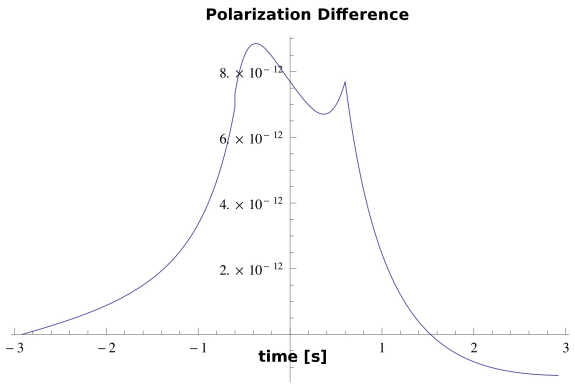

Figure 6.20: Difference between exact and approximated P_{eff} as a function of time.

H is the field value on the $\hat{z}$ axis, the five parameters a, b, c, H_0 and H_1 were determined by fitting the water signal. The time values $t_a = -t_b$ = -0.6 s were used when computing Equation 6.35. The results of the NMR water fits are shown in Figure 6.21. A total of 6,189 sweeps were averaged together and the analytic form of Equation 6.35 was fitted to the up and down sweep NMR signals at the up and down stream pick-up coil positions. The Red markers show the signal induced in the X lock-in channel, the blue line is the signal detected in the Y lock-in channel and the black line is the fit to the water NMR signal in the X channel. Notice that there is very little NMR signal leaking into the Y lock-in channel, as a result no correction was done to account for signal loss. Figure 6.22 shows the residuals of the water fit normalized by the peak signal height, (NMR data - NMR fit)/signal height, in percentage.

The last contribution needed to compute the water constant is the flux through the water and ^{3}He target cells. Due to the fact that the two target cells have slightly different geometries, the flux produced is different and must be divided out [126]. The flux ϕ is defined as

$$\phi = \oint_{coils} \vec{A} \cdot d\vec{l}, \tag{6.36}$$

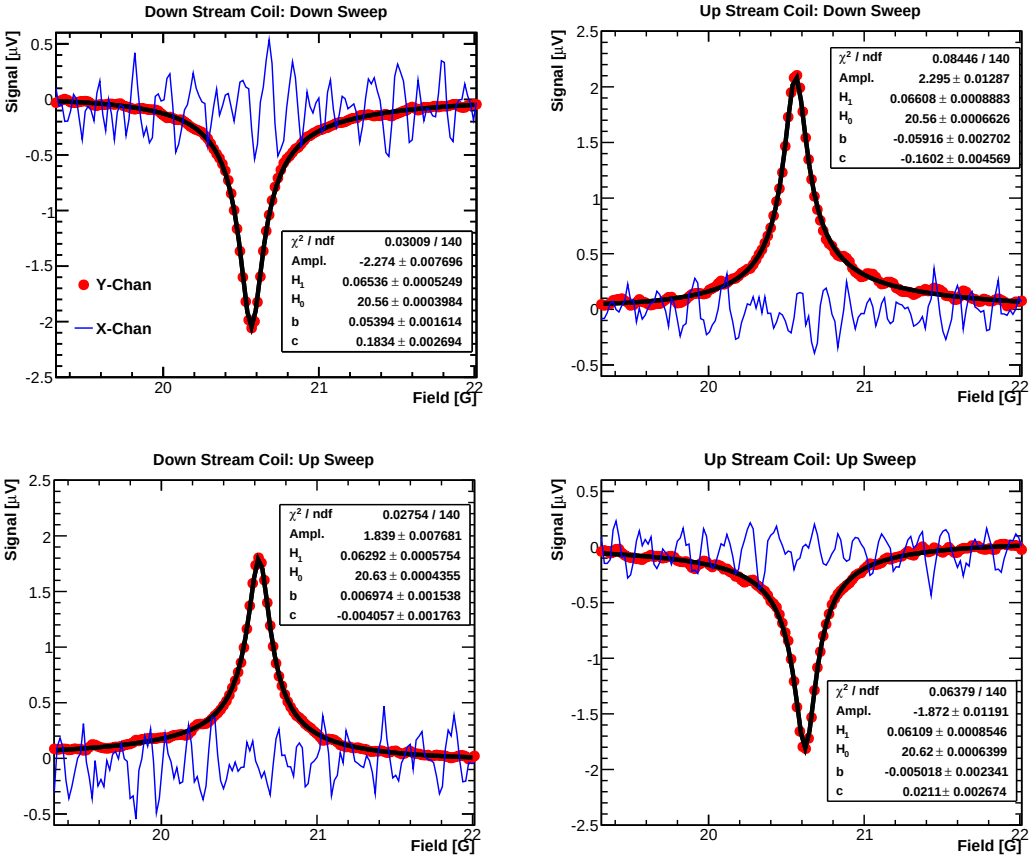

Figure 6.21: Water signal fits to the average of 6,189 up and down sweep signals measured in the up and down stream pick-up coils. Red markers show NMR signal in X lock-in channel, blue line shows NMR signal in the Y lock-in channel and the black line shows the fit to the NMR signal.

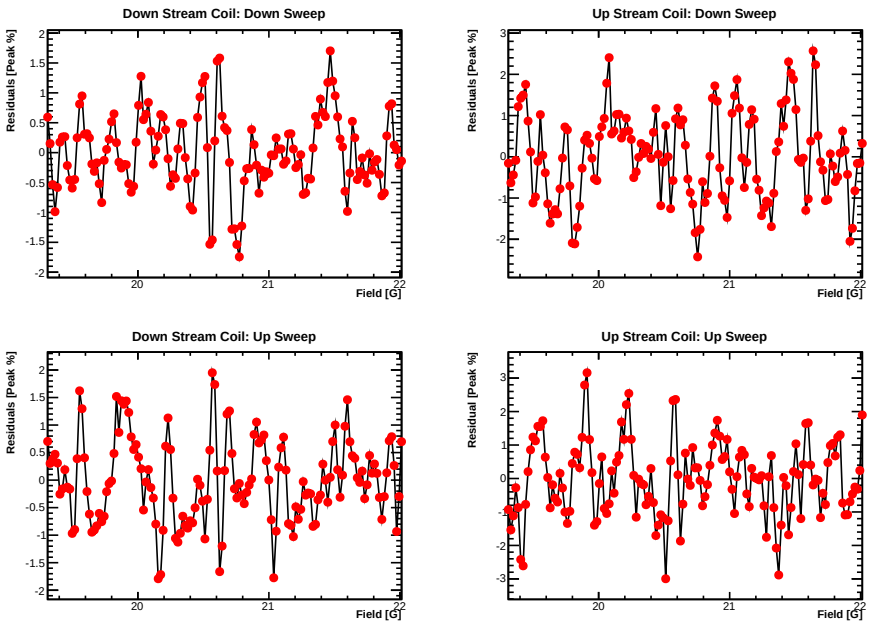

Figure 6.22: Residuals of the NMR water fit. Here the y-axis is 100x(NMR Data - NMR Fit)/Signal Height.

where the integral is around the pick-up coils. The vector potential, $\vec{A}$ is created by magnetized medium in the target cell and is defined as

$$\vec{A}(\vec{r}) = \int_{CellVolume} d^3\vec{r}\,\frac{\vec{z}\times\vec{r}}{|\vec{r}|^3}. \tag{6.37}$$

Figure 6.23 shows the geometry for the flux calculation. The vector potential was calculated, by D. Flay [135], by integrating over the cell volume. For the ^{3}He target, it was found that the transfer tube contributes a negligible amount of flux, while the pumping chamber contributed a significant amount of flux and needed to be included when computing the ^{3}He flux. For the water cell, only the target chamber flux was considered. The main source of uncertainty of the flux calculation was due to not precisely knowing the actual cell position. A total uncertainty of 4% was assigned to each of the flux calculations.

After the flux through the target cells has been calculated, the water constant C_w can now

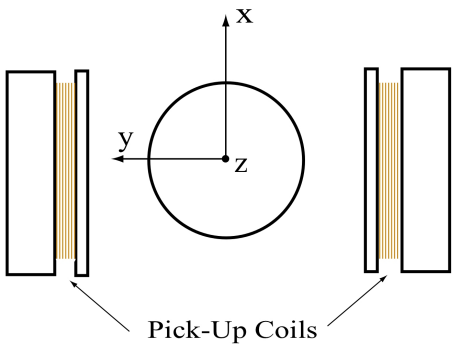

Figure 6.23: Geometry for the flux calculation. Note only the target chamber is shown. Figure reproduced from [126].

be computed using Equation 6.21. Table 6.8 lists all the parameters and their uncertainties that go into computing C_w. Note that the NMR water height, S_w in the table reflects the average of the two up sweeps and down sweeps. The water constant is evaluated at the up and down stream coils for the up and down sweep NMR measurements, resulting in four values of C_w. To combine these water constants into one overall value, the flux weighted average of the water constant is first computed

$$C_w^{(1)} = \frac{\phi^u C_w^u + \phi^d C_w^d}{\phi^u + \phi^d}, \tag{6.38}$$

where u (d) super-scripts represent values at the up (down) pick-up coils and $\phi = \phi_w + \phi_{He}^{pc} + \phi_{He}^{tc}$. Finally, the water constants for the up and down sweeps are combined by taking the weighted average

$$C_w^{final} = \frac{w^{u'} C_w^{u'} + w^{d'} C_w^{d'}}{w^{u'} + w^{d'}}, \tag{6.39}$$

where u' (d') super-scripts represent values for the up (down) sweep measurements and $w = \frac{1}{\delta C_w}$, where δC_w is the uncertainty associated with C_w. Table 6.9 summarizes the final

water constants when the target spin is polarized longitudinal and transversely.

6.4.4.2 C_{NMR}

Table 6.8: Parameters used to compute the water constant C_w.
Uncertainties listed are relative uncertainties.

Parameter	Description	Value	Units	Uncertainty [%]
P_w	up sweep	6.584×10^{-9}	-	2.28
	down sweep	7.771×10^{-9}	-	2.42
S_w	up sweep	1.849	μV	0.349
	down sweep	2.280	μV	0.290
G_w	Gain of pick-up coil pre-amp for water	20	-	-
G_{He}	Gain of pick-up coil pre-amp for ^{3}He	5	-	-
μ_p/μ_{He}	magnetic moment ratio	1.3127	-	-
n_p	proton density in water cell at 22°C	2482	amg	-
ϕ_w	up stream flux through water cell	49.83	cm^2	4.00
	down stream flux through water cell	52.79	cm^2	4.00
ϕ_{He}^{pc}	up stream flux through ^{3}He cell pumping chamber	0.05	cm^2	4.00
	down stream flux through ^{3}He cell pumping chamber	0.005	cm^2	4.00
ϕ_{He}^{tc}	up stream flux through ^{3}He cell target chamber	50.76	cm^2	4.00
	down stream flux through ^{3}He cell target chamber	49.89	cm^2	4.00

Table 6.9: Final C_w values for longitudinal and transverse target spin orientations. The quoted uncertainty is relative.

Target Direction	C_w [%/mV]	Uncertainty [%]
Long.	0.4311	3.30
Trans.	0.4267	3.30

An additional calibration factor,C_{NMR} needed to be included in order to extract the ^{3}He polarization in the target chamber, because of the polarization gradient between the two target cell chambers. C_{NMR} is defined as the ratio of the ^{3}He NMR height produced via magnetic field sweep at the pick-up coil position to the ^{3}He NMR height produced via RF frequency sweep at the production position. This calibration was achieved by measuring the ^{3}He NMR signal at the pick-up coil location, which is proportional to the ^{3}He polarization in the target chamber. The up and down stream NMR signals measured at the pick-up coil position were combined using a flux weighted average. The cell was then raised to the production position and another NMR measurement was taken, which is proportional to the pumping chamber ^{3}He polarization. Unfortunately, there was no way to measure the transverse ^{3}He target spin in the pick-up coil position. Thus the C_{NMR} factor could not be calculated for the transverse orientation, resulting in the water calibration serving only as a cross-check to the longitudinal ^{3}He polarization determined through EPR measurements. Table 6.10 lists the C_{NMR} results for the longitudinal ^{3}He target spin orientation. Figure 6.24 shows a comparison of the ^{3}He polarizations measured in the target chamber via water and EPR calibrations.

Table 6.10: Final C_{NMR} and $C_w \times C_{NMR}$ values for longitudinal target spin orientation. The quoted uncertainty is relative.

Parameter	Value	Uncertainty [%]
C_{NMR}	5.710	0.49
$C_{NMR} \times C_w$	2.462 [%/mV]	3.336

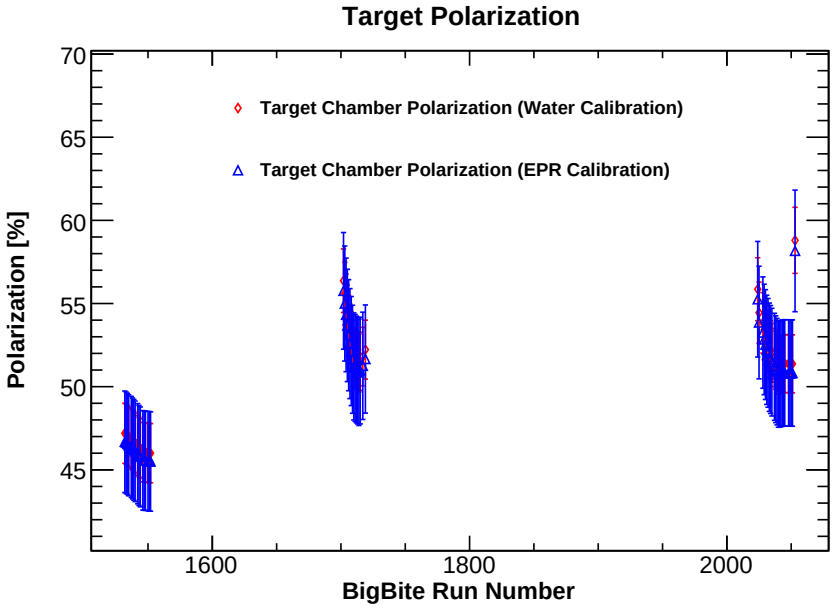

Figure 6.24: Comparison of longitudinal ^{3}He target polarization measured in the target chamber via water and EPR calibrations as a function of production run number.

6.5 Electron Paramagnetic Resonance Polarimetry

6.5.1 Principle

The method of electron paramagnetic resonance (EPR) measures the splitting of different energy levels in alkali atoms due to the presence of polarized ^{3}He nuclei. These energy splittings are caused from two sources, the first being the classical magnetic field (B_M) produced from the polarized ^{3}He gas, and the second being a small effective field arising from spin exchange interactions between alkali-^{3}He atoms (B_{SE}) [122].

When an external magnetic field is applied to the target cell, the alkali atoms in the pumping chamber (^{85}Rb and ^{39}K in this case) will split into 2F+1 energy levels (F = 2, 3 for ^{85}Rb and F = 1, 2 for ^{39}K), as shown in Figure 6.3. In the case of ^{85}Rb, the energy splitting between the m_F = 3 and m_F = 2 states for right circularly polarized light describes the EPR frequency, and the splitting between the m_F = 2 and m_F= 1 energy states describe the

the EPR frequency for ^{39}K. If the polarization of the light were changed to left circularly polarized, the EPR frequency would be described by the splitting between m_F = -3 and m_F = -2 for ^{85}Rb and m_F = -2 and m_F = -1 for ^{39}K.

The eigenvalues of the Hamiltonian given in Equation 6.1 are given by the Breit-Rabi formula [136]:

$$E_{F=I\pm\frac{1}{2},M} = -\frac{\Delta E_{hfs}}{2\left(2I+1\right)} - g_I\mu_N B m_F \pm \frac{E_{hfs}}{2}\sqrt{1+\frac{2m_F}{I+\frac{1}{2}}x+x^2}, \tag{6.40}$$

where $x = \left(g_N\mu_N - g_e\mu_B\right)B/\Delta E_{hfs}$ and ΔE_{hfs} is the hyper fine splitting energy. The EPR frequency ($\nu_{EPR,\pm}$), which corresponds to the energy difference between the $m_F = \pm F$ and $m_F = \pm\left(F-1\right)$ states, where $F = I + \frac{1}{2}$, can be calculated using

$$\begin{aligned} h\nu_{EPR,\pm} &\equiv |E_{F,m_F=\pm F} - E_{F,m_F=\pm(F-1)|} \\ &= -\frac{B}{2}\left(g_N\mu_N + f_e\mu_B\right) \pm \frac{\Delta E_{hfs}}{2}\left(1-\sqrt{1\pm 2\frac{2I-1}{2I+1}x+x^2}\right). \end{aligned} \tag{6.41}$$

The magnetic field as a function of EPR frequency, $B_\pm\left(\nu_{EPR}\right)$, where $\pm$ is determined by $m_F = \pm F$, can be calculated by inverting Equation 6.40.

When the ^{3}He spins are parallel to the holding field, a small additional field is created parallel to the holding field. This results in an effective feild of $B + \delta B$, where $\delta B = B_{SE} + B_M$. However, when the ^{3}He spins are flipped 180° so that they are anti-parallel to the holding field, a small field is generated anti-parallel to the holding field, resulting in an effective field of $B - \delta B$. The effect of flipping the ^{3}He spin states during a typical EPR sweep can be seen in Figure 6.27, where B_0 is the holding field and ν_0 is the frequency of the holding field. Taking the difference of the two spin states, the holding field contribution

drops out and one can write the EPR frequency shift as [136]

$$\Delta\nu_{EPR} = \frac{d\nu_{EPR}}{dB}\left(B_M + B_{SE}\right), \tag{6.42}$$

where $\frac{d\nu_{EPR}}{dB}$ can be computed from Equation 6.40 and

$$B_{SE} = \frac{2\hbar K_{SE} n_{^3\mathrm{He}} \gamma_{SE}}{g_e \mu_B} P_{^3\mathrm{He}}, \tag{6.43}$$

$$B_M = C\mu_{^3\mathrm{He}} n_{^3\mathrm{He}} P_{^3\mathrm{He}}, \tag{6.44}$$

where K_{SE} is the ratio of the imaginary part of the spin-exchange cross section to its real part. γ_{SE} is the alkali-^{3}He spin-exchange rate per alkali atom, and μ_B is the Bohr magnaton. $n_{^3\mathrm{He}}$ is the ^{3}He density and $\mathrm{P}_{^3\mathrm{He}}$ is the polarization. C is a constant that depends on the shape of the cell and $\mu_{^3\mathrm{He}}$ is the ^{3}He nuclear magnetic moment. Combining Equations 6.42 6.43 and 6.44, $\Delta\nu_{EPR}$ can be written as:

$$\Delta\nu_{EPR} = \frac{2}{3}\frac{d\nu_{EPR}}{dB}\mu_0 \kappa_0 n_{^3\mathrm{He}} \mu_{^3\mathrm{He}} P_{^3\mathrm{He}}, \tag{6.45}$$

where κ_0 is a dimensionless constant depending on the cell temperature. Thus, the ^{3}He polarization in the pumping chamber can be determined by measuring the EPR frequency shift $\Delta\nu_{EPR}$.

6.5.2 EPR Setup

The EPR measurement consisted of exciting the EPR transition by sending a RF frequency through a small coil located near the pumping chamber. Using a procedure known as EPR frequency-modulation (EPR FM), the RF frequency was scanned to find the EPR transition. Next, an EPR AFP sweep was performed, which continuously tracked and recorded the

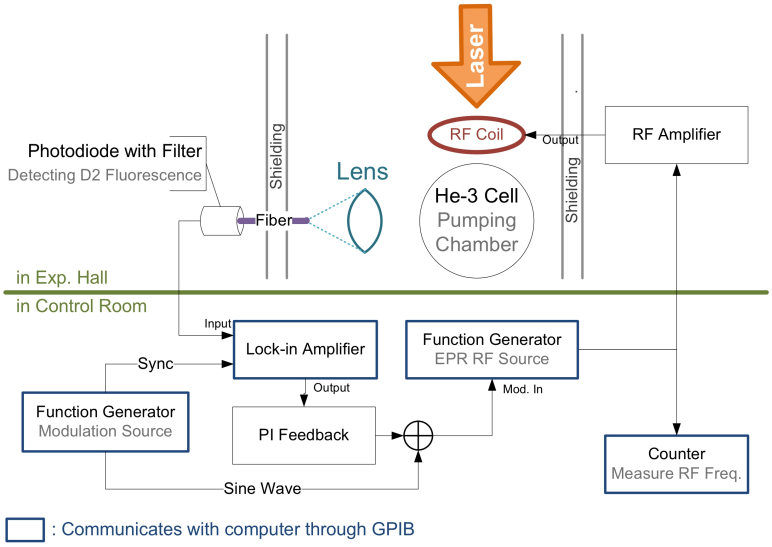

Figure 6.25: Schematic diagram for EPR setup. The proportional-integral (PI) was disabled during EPR FM sweeps, and switch on before EPR AFP sweeps. Figure reproduced from [102].

EPR transition frequency. Finally, the EPR frequency at each AFP was analyzed to extract the polarization in the pumping chamber [102]. A diagram of the EPR electronics setup is shown in Figure 6.25.

By exciting the EPR transition, an alkali metal (Rb or K chosen by central frequency) depolarizes. Once one of the metals (Rb or K) are depolarized, due to the fast spin exchange, the other metal (Rb or K) is also depolarized. The Rb atoms then start to repolarize, producing florescence at a wavelength of 780 nm. This florescence is from the decay of the $5P_{\frac{3}{2}}$ to the $5S_{\frac{1}{2}}$ state, and is known as the D2 transition. It was measured using photodiodes. During the EPR measurement, the RF frequency was modulated with a 100 Hz sine wave and the D2 transition was synchronized to the 100 Hz modulation and measured with a lock-in. The signal from the lock-in output is proportional to the derivative of the EPR florescence curve as a function of RF frequency. Therefore, the EPR resonance occurs when the derivative is equal to zero. During EPR FM sweeps, the central RF is scanned

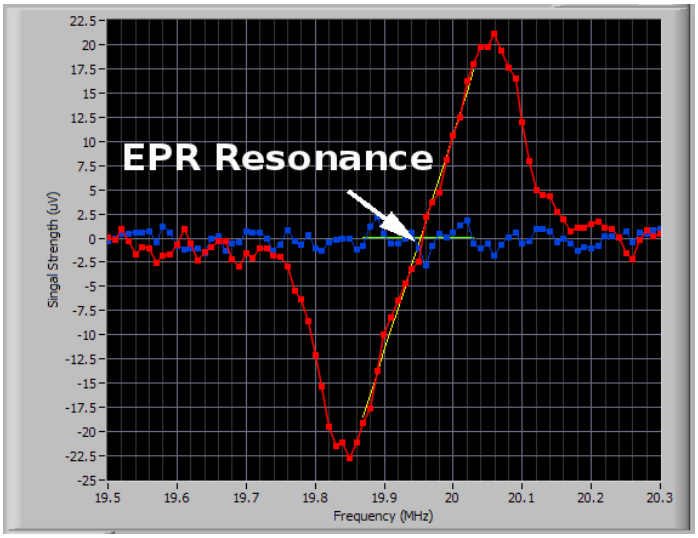

Figure 6.26: A typical EPR FM sweep for potassium when the pumping spin direction is anti-parallel to the holding field.

for resonance by finding the zero derivative point as shown in Figure 6.26. The EPR RF frequency is then locked to the resonance frequency by a proportional-integral (PI) feed back loop, which utilized the linear shape of the EPR FM curve around the resonance to lock on to the zero-point. Typically, four NMR AFP frequency sweeps were performed, with each sweep flipping the ^{3}He spin direction once. Figure 6.27 shows a typical EPR AFP sweep for three of the four sweeps.

6.5.3 EPR Calibration

Over the course of E06-014, about 10 EPR measurements were performed using ^{39}K alkali atoms. During each EPR AFP sweep, the corresponding NMR sweep was used to form a calibration constant, C_{EPR}, that was applied to the production NMR frequency sweep in order to obtain the ^{3}He polarization in the pumping chamber. An additional calibration constant (C_{dif}) is needed, due to the polarization gradient between the pumping and target chambers. This calibration constant was applied to the pumping chamber polarization in order to extract the ^{3}He polarization in the target chamber. C_{dif} is discussed in detail in

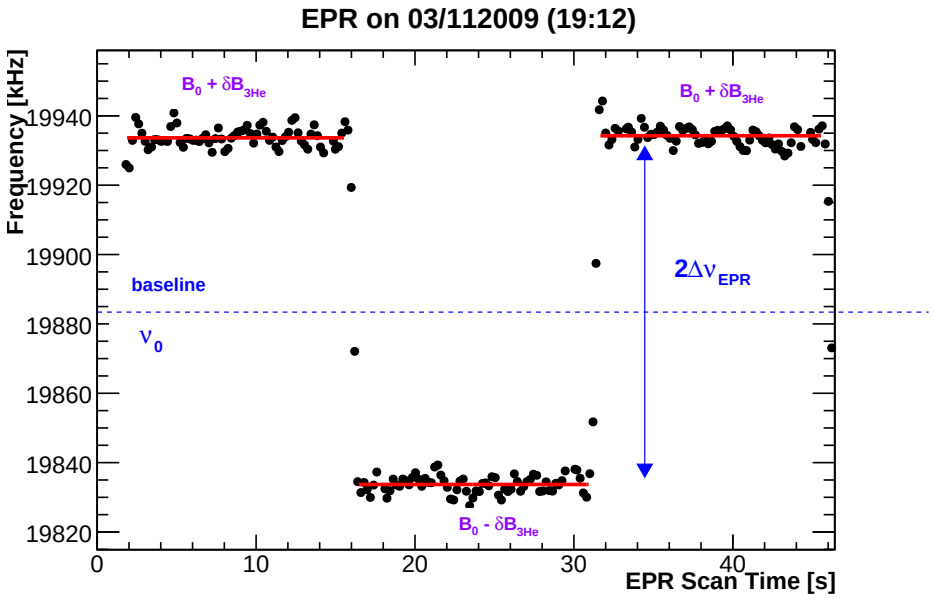

Figure 6.27: A typical EPR AFP sweep, showing three of the four sweeps. The distance between the splitting is equal to two times the frequency shift.

Section 6.5.4. In this section, the evaluation of the pumping chamber ^{3}He polarization via EPR polarimetry will be discussed.

As seen from Equation 6.45, the ^{3}He polarization is proportional to the EPR frequency shift,

$$P_{^3\mathrm{He}} = \frac{\Delta\nu_{EPR}}{\frac{2}{3}\mu_0 k_0 \frac{d\nu_{EPR}}{dB}\mu_{^3\mathrm{He}} n_{pc}}. \tag{6.46}$$

As mentioned earlier, κ_0 is a dimensionless constant that depends on the cell temperature. For the E06-014 target analysis, the κ_0 for ^{39}K was evaluated according to the expression [137]

$$\kappa_0 = (5.99 \pm 0.11) + (0.0086 \pm 0.002)\,(T_{pc} - T_0)\,, \tag{6.47}$$

where T_0 was the reference temperature of 200° C. The uncertainty in κ_0 at a temperature of 270°C is near 3%. The derivative of the EPR frequency change with respect to the

magnetic field can be expressed as [138]

$$\frac{d\nu_{EPR}}{dB} = \mp\frac{g_I\mu_N}{h} + \frac{g_I\mu_N - g_S\mu_B}{2h\,[I]}\left[\frac{2m_F + [I]\,x}{\sqrt{1+\frac{4m_F}{[I]}x+x^2}} - \frac{2m_F - 2 + [I]\,x}{\sqrt{1+\frac{4(m_F-1)}{[I]}x+x^2}}\right], \tag{6.48}$$

where the $\pm$ corresponds to the edge state $m_F = \pm\left(I+\frac{1}{2}\right)$. The derivative can be expanded in x at low field, in this case up to fith order as:

$$\frac{d\nu_{EPR}\pm}{dB} = \frac{g_I\mu_N - g_S\mu_B}{h\,[I]}\sum_{n=0}^{5} b_n\frac{x^n}{[I]^n}, \tag{6.49}$$

where,

- $x = (g_I\mu_N - g_S\mu_B)\,\frac{B}{h\nu_{hfs}}$,
- $[I] = 2I+1$,
- $b_0 = 1$,
- $b_1 = \mp 4I$,
- $b_2 = 6I\,(2I-1)$,
- $b_3 = \mp 8I\,(4I^2-6I+1)$,
- $b_4 = 10I\,(2I-1)\,(4I^2-10I+1)$,
- $b_5 = \mp 12I\,(16I^4-80I^3+80I^2-20I+1)$,

and a description of the parameters and there values can be found in Table 6.11

Finally, the EPR frequency shift was measured by fitting the parallel and anti-parallel spin states with a constant line and taking the difference between them. Equation 6.46 can

Table 6.11: List of parameters that go into calculating $\frac{d\nu_{EPR}}{dB}$.

Parameter	Description	Value	Unit
g_I	Nuclear g-factor (K)	0.2601	–
μ_N	Nuclear magnaton	5.051×10^{-27}	J/T
g_S	Electron g-factor	2.0023	–
μ_B	Bohr magnaton	9.275×10^{-24}	J/T
h	Plank's constant	6.626×10^{-34}	Js
I	Nuclear spin (K)	1.5	$\hbar$
ν_{hfs}	Hyperfine splitting frequency (K)	461.719	MHz

Table 6.12: Systematic uncertainty contributed to P^{EPR} for a longitudinally polarized target.

Parameter	Uncertainty [%]
n_{pc}	2.79
$\Delta\nu_{EPR}$	0.5
κ_0	2.92
Total	4.05

then be used to extract the ^{3}He polarization in the pumping chamber, $P^{EPR}_{^3\mathrm{He}}$. Figure 6.28 shows all of the EPR sweeps done throughout E06-014. The red closed markers are when the target spin was parallel relative to the electron beam, and the blue closed markers are when the target spin was transverse relative to the electron beam. The uncertainty on the EPR polarization is predominantly due to the uncertainty in the pumping chamber target density, n_{pc} and the κ_0 value. The total uncertainty on P^{EPR} is presented in Tables 6.12 and 6.13 for the longitudinal and transverse target orientations relative to the electron beam.

Once the EPR polarization is extracted, which is the absolute polarization of the ^{3}He in the pumping chamber, it can be used to calibrate the production NMR measurements. This was accomplished by taking the ratio of the EPR polarization and the amplitude of the NMR sweep that was taken at the same time as the EPR measurement. This ratio is known as the

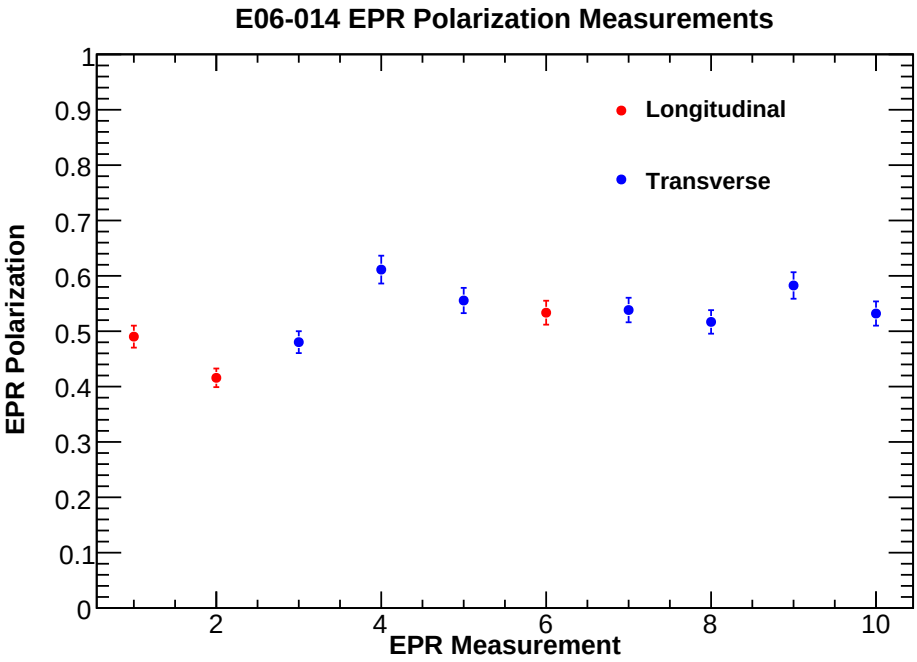

Figure 6.28: EPR polarization measured in the pumping chamber. The markers correspond to a longitudinally polarized target, and blue markers to a transversely polarized target.

Table 6.13: Systematic uncertainty contributed to P^{EPR} for a transversely polarized target.

Parameter	Uncertainty [%]
n_{pc}	2.74
$\Delta\nu_{EPR}$	0.5
κ_0	3.06
Total	4.10

Table 6.14: Results for EPR–NMR calibration constant C_{EPR}.

Target Direction	Value [%/mV]	Total Uncertainty [%]
Longitudinal	2.853	3.75
Transverse	1.719	3.84

EPR calibration constant, C_{EPR}:

$$C_{EPR} = \frac{P^{EPR}_{^3\mathrm{He}}}{S^{EPR}_{NMR}}. \tag{6.50}$$

The NMR amplitude was extracted by fitting the NMR signal with the functional form found in Equation 6.19. Figure 6.29 shows a typical NMR signal for each of the EPR spin states. The results of the EPR-NMR calibration can be seen in Figure 6.30 for each EPR measurement. The red solid marker represent EPR–NMR measurements when the target was longitudinally polarized and the blue solid markers correspond to a transversely polarized target. The EPR calibration constant calculated for the longitudinal target spin direction was found to be larger than that computed for the transverse target spin direction. The final C_{EPR} constant values were computed by taking the uncertainty weighted average of the individual C_{EPR} calculations for each target spin orientation, and are listed in Table 6.14. The ^{3}He pumping chamber polarization during production running can be extracted by multiplying the production NMR signal height (S_{NMR}) by C_{EPR}

$$P_{pc} = C_{EPR} \times S_{NMR}. \tag{6.51}$$

6.5.4 Polarization Gradient

During production running NMR polarimetry was used to measure the ^{3}He polarization in the pumping chamber, P_{pc}. However, the scattered electrons interacted with the ^{3}He gas in

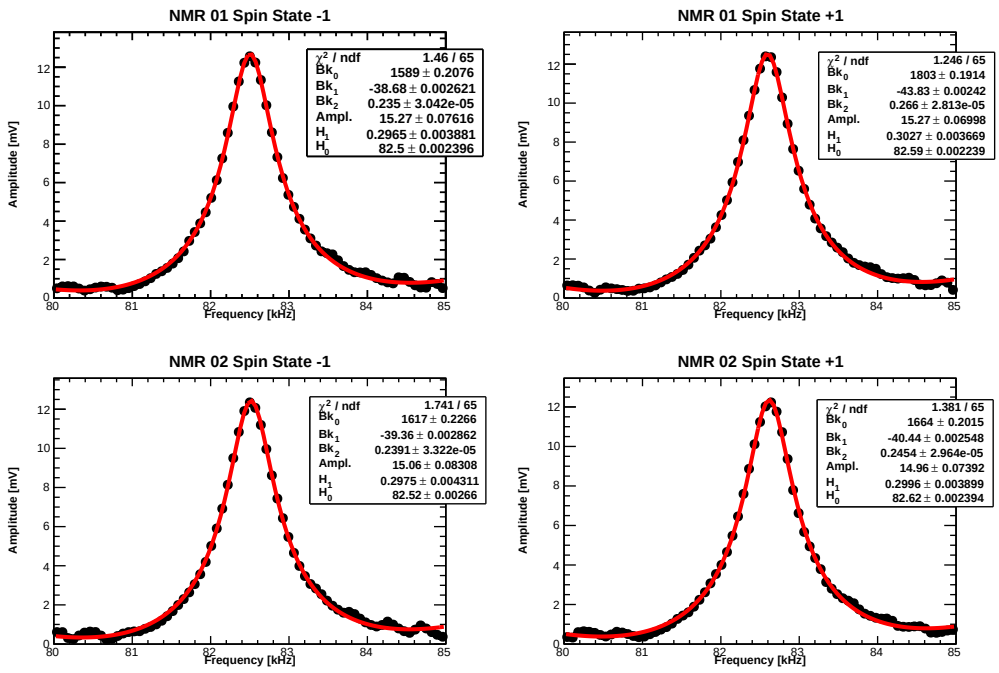

Figure 6.29: NMR signals taken during EPR sweep, used for EPR-NMR calibrations.

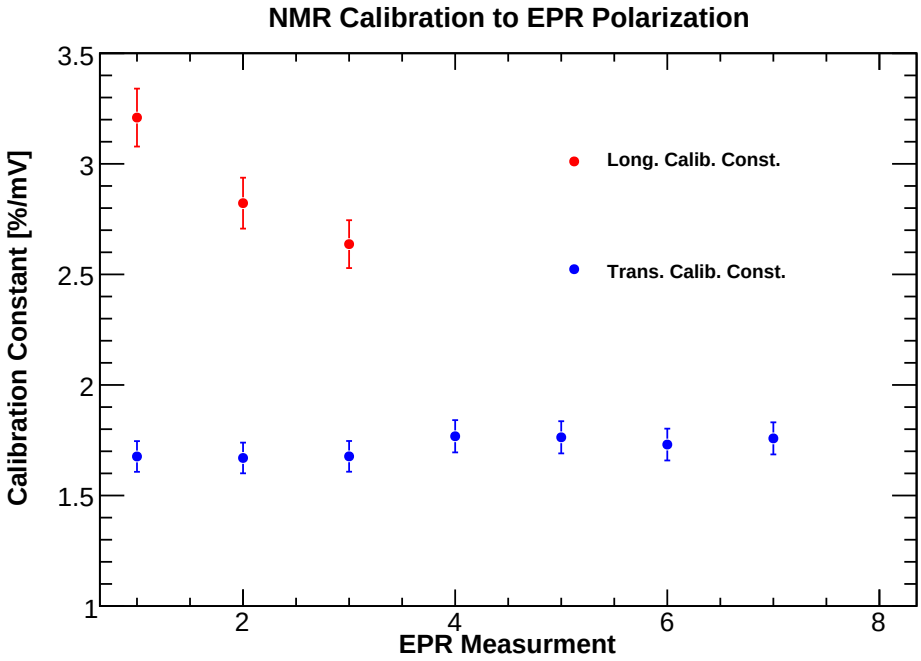

Figure 6.30: EPR–NMR calibration constant, C_{EPR}, for all EPR measurements.

the target chamber, which carried a polarization P_{tc}. Since the ^{3}He gas was polarized in the pumping chamber and diffused down through the transfer tube into the target chamber, there was a polarization gradient created between the pumping and target chambers. There are two methods by which to account for this. The first method was discussed in Section 6.4.4, and is associated with calibrating the ^{3}He polarization using the known polarization of protons in a water sample. The other method is through the use of a two-chamber polarization model, which will be discussed in this section.

6.5.4.1 Diffusion Rate

The ^{3}He target cells used at Jefferson Lab consist of a pumping chamber and a target chamber, which are connected by a small transfer tube (Figure 6.7). The ^{3}He is polarized in the pumping chamber and then diffuses into the target chamber via the transfer tube. The evolution of the polarization with time are described by a set of differential equations, consisting of spin relaxation, spin exchange and diffusion terms [139] [122]. When the diffusion is in the presence of a temperature gradient, the flux is given by [140]:

$$G_i = -n\left(z\right) D\left(z\right) \left(\frac{dc_i}{dz} - \frac{k_T}{T} \frac{dT}{dz} \right), i = 1, 2 \tag{6.52}$$

where c_i is the concentration of i's component in the mixture, with i = 1 corresponding to ^{3}He atoms with spin up and i = 2 with spin down. Since both types of atoms have the same mass, the diffusion ratio k_T vanishes [140]. If one assumes that the flux is constant along the transfer tube and that the temperature changes linearly with distance, then the temperature and density dependence of the diffusion constant D can be described with a model based on the classical gas of hard spheres [141]

$$D\left(T\right) = D\left(T_0\right) \frac{n_0}{n_{tc}} \left(\frac{T_{tc}}{T_0} \right)^{m-1}, \tag{6.53}$$

where $D\,(T_0)$ = 2.76 cm^2 at T_0 = 80° C, n_0 = 0.773 amg and m = 1.7 were obtained from fits experimental to data on ^{4}He [142] with a scale of ^{4}He to ^{3}He mass ratio [3, 122]. Given these assumptions, the rate of change of the polarization in the pumping and target chambers can be described by the dynamical equations [122, 141]

$$\frac{dP_{tc}}{dt} = d_{pc}\,(P_{tc} - P_{pc}) + \gamma_{SE}\,(P_{Rb} - P_{pc}) - \Gamma_{pc}P_{pc}, \tag{6.54}$$

$$\frac{dP_{pc}}{dt} = d_{tc}\,(P_{pc} - P_{tc}) + \Gamma_{tc}P_{tc}, \tag{6.55}$$

where P is the polarization of the target chamber (tc), pumping chamber (pc) or rubidium (Rb) respectively, Γ is the spin relaxation time and d is the reduced diffusion constant. For typical running conditions, the following rates were observed: $\gamma_{SE} \sim$ (4 hour)$^{-1}$, $\Gamma_{pc} \sim$ (10 hour)$^{-1}$, $\Gamma_{tc} \sim$ (10–20 hour)$^{-1}$ and both d_{pc} and $d_{tc} \sim$ (1–2 hour)$^{-1}$. If the target cell is brought to operating temperature before the pumping lasers are turned on, it can be assumed that the total nuclei in both chambers have reached equilibrium (i.e. $\frac{dP_{pc}}{dt}$ = $\frac{dP_{tc}}{dt}$ = 0), leading to the solutions of Equations 6.54 and 6.55 [141]

$$P_{pc} = P_{Rb}\left(\frac{\gamma_{SE}f_{pc}}{\gamma_{SE}f_{pc} + \Gamma_{pc}f_{pc} + \Gamma_{tc}f_{tc}\left(1 + \frac{\Gamma_{tc}}{d_{tc}}\right)^{-1}}\right), \tag{6.56}$$

$$P_{tc} = \left(\frac{1}{1 + \frac{\Gamma_{tc}}{d_{tc}}}\right)P_{pc} = C_{dif}P_{pc}, \tag{6.57}$$

where f is the ratio of ^{3}He atoms in a particular chamber to the total number of ^{3}He atoms in the target cell. The reduced diffusion constants d_{tc} and d_{pc} are given by:

Table 6.15: List of longitudinal parameters used to calculate d_T, where h = hours.

Parameter	Value	Units	Uncertainty [%]
A_{tt}	0.7543	cm^2	13.62
L_{tt}	9.398	cm	1.0
V_{tc}	75.514	mL	5.0
T_{tc}	342.95	K	1.46
T_{pc}	536.15	K	0.93
$D(T_0)$	2.76	cm^2/s	0.3
n_0	0.7733	amg	Neg.
n_{tc}	10.74	amg	3.99
m	1.7	-	Neg.
K	1.178	-	0.80
D	0.195	cm^2/s	3.84
d_{tc}	0.878	h^{-1}	15.11

$$d_{pc} = \frac{A_{tr}D}{V_{tc}L_{tr}}K, \tag{6.58}$$

$$d_{tc} = \frac{A_{tr}Dn_{tc}}{V_{pc}L_{tr}n_{pc}}k, \tag{6.59}$$

where sub-script tr refers to the transfer tube, k is a dimensionless constant [122] [3] given by Equation 6.60, A_{tr} is the area of the transfer tube and L_{tr} is the length of the transfer tube. A summary of the values used to compute d_{tc} when the target polarization was oriented longitudinally and transversely are found in tables 6.15 and 6.16.

$$k = \frac{(m-2)\,(T_{tc}-T_{pc})\,T_{tc}}{(T_{tc}/T_{pc})^m\,T_{pc}^2 - T_{tc}^2}, \tag{6.60}$$

Table 6.16: List of transverse parameters used to calculate d_T, where h = hours.

Parameter	Value	Units	Uncertainty [%]
A_{tt}	0.7543	cm^2	13.62
L_{tt}	9.398	cm	1.0
V_{tc}	75.514	mL	5.0
T_{tc}	342.71	K	1.46
T_{pc}	543.3	K	0.92
$D(T_0)$	2.76	cm^2/s	0.3
n_0	0.7733	amg	Neg.
n_{tc}	10.85	amg	3.90
m	1.7	-	Neg.
K	1.185	-	0.783
D	0.1926	cm^2/s	4.04
d_T	0.873	h^{-1}	15.09

6.5.4.2 Cell Lifetime

The target's lifetime, which is inversely proportional to the spin relaxation rate, is one of the main characteristics used to evaluate the quality of the target cell. During production conditions, there are several factors that contribute to the target chamber spin relaxation rate,

$$\Gamma_{tc} = \Gamma^{dip} + \Gamma^{wall} + \Gamma^{beam} + \Gamma^{AFP} + \Gamma^{\nabla B}, \tag{6.61}$$

where the spin relaxation mechanisms are:

- Γ^{dip} **(Nuclear dipolar interaction)** is a result of the direct coupling between two ^{3}He nuclei and can be parameterized as [143]

$$\Gamma^{dip} = \frac{n}{744\ amg \cdot hour} \tag{6.62}$$

at 23°C, where n is the ^{3}He density.

- Γ^{wall} **(Wall relaxation)** is the relaxation of ^{3}He nuclei due to collisions with the target cell glass wall. The wall relaxation rate can be expressed as

$$\Gamma^{wall} = 1/\tau_{lifetime} - \Gamma^{dip}, \tag{6.63}$$

where $\tau_{lifetime}$ is the lifetime of the target cell. The cell life time for the ^{3}He target cell Samantha was not measured for E06-014 at JLab; therefore, the measured average life time ($\tau_{lifetime}$ = 14 hours) of the target cells used during E06-010, was used to obtain a relaxation rate consisting of the wall and nuclear dipole interactions ($\Gamma^{dip} + \Gamma^{wall}$). The E06-010 target cells were very similar in geometry and design to the target cell used for E06-014, and the lifetime from each of the cells measured during E06-010 were found to agree to within 30% of each other [123].

- Γ^{beam} **(Beam depolarization)** increases nuclear spin relaxation in the target chamber through ionizing radiation. To estimate the relaxation time due to the beam, a parameterization done at JLab beam energies was used [141]

$$\Gamma^{Ion} = \left(0.0095\frac{cm^2}{\mu A \cdot h}\right)\frac{I}{A_{tc}} = \left(\frac{1}{21h}\right)\cdot\left(\frac{I}{10\mu A}\right)\cdot\left(\frac{2cm^2}{A_{tc}}\right), \tag{6.64}$$

where h is in units of hours, A_{tc} is the target chamber area, I is the electron beam current and Γ^{Ion} is the ionization relaxation rate. The ionization rate per atom of Equation6.64 was found to be within 5% over all JLab energies. The ionization relaxation rate can be related to the beam relaxation rate

Table 6.17: List of parameters used to model beam depolarization effects. Target cell wall thickness (0.166 cm) is subtracted from the target cell diameter.

Parameter	Value	Units	Uncertainty [%]
Parameterization	–	–	5
A_{tc}	1.919	cm^2	9.19
I	16.0	μA	–
Γ^{Beam}	0.0794	$(\text{hours})^{-1}$	10.46

$$\Gamma^{Beam} = \Gamma^{Ion}\left(n_a + n_m\right), \tag{6.65}$$

where n_a represents the number of atomic ions and n_m is the number of molecular ions. However, due to the nitrogen present in the target chamber, n_m is suppressed. n_a is constrained because an atomic ion can only depolarize at most on atomic nucleus, leading to $\Gamma^{beam} \leq \Gamma^{Ion}$. The results for the beam depolarization rate can be found in Table 6.17.

- Γ^{AFP} **(AFP loss)**: The spin loss resulting from an AFP spin flip was not measured during E06-014. However, the AFP spin loss was measured during E06-010 and found to be negligible [102]. During E06-010, an AFP spin flip was performed $\sim$ 20 min., where as during E06-014 it was roughly every 4 hours. Therefore, one would expect the AFP loss to be greater during E06-010.

- $\Gamma^{\nabla B}$ **(Gradient magnetic field relaxation)** is the relaxation due to the magnetic field gradient [144, 145]

$$\Gamma^{\nabla B} = D\frac{\left|\nabla B_x\right|^2 + \left|\nabla B_y\right|^2}{B_z^2}, \tag{6.66}$$

Table 6.18: List of spin relaxation mechanisms used in the two chamber polarization gradient model.

Parameter	Value	Units	Uncertainty [%]
$\Gamma^{dip} + \Gamma^{wall}$	0.0714	$(\text{hour})^{-1}$	35
Γ^{beam}	0.0794	$(\text{hour})^{-1}$	10.46
Γ^{AFP}	–	$(\text{hour})^{-1}$	–
$\Gamma^{\nabla B}$	–	$(\text{hour})^{-1}$	–
Γ_{tc}	0.151	$(\text{hour})^{-1}$	36.54

where $D \sim 0.2$ cm^2/s is ^{3}He self diffusion constant. The magnitude of $\Gamma^{\nabla B}$ was found to be $\sim$ 0.001/hour, which is a much smaller effect than the rest of the relaxation mechanisms and was therefore neglected.

The spin relaxation mechanisms are summarized in Table 6.18.

6.5.4.3 Polarization Gradient Results

Using the Equation 6.57, the calibration constant C_{dif} can be computed for the longitudinal and transverse target orientations (Table 6.19). The effect of the polarization gradient between the pumping and target chambers is fairly significant, losing $\sim 15\%$ relative to the pumping chamber polarization, which results in loosing an average of $\sim 9\%$ absolute polarization in going from the pumping to target chamber.

Table 6.19: Results for C_{dif} computed from the two chamber polarization gradient model.

Target Direction	Value	Units	Uncertainty [%]
Long.	0.853	$(\text{hour})^{-1}$	5.80
Trans.	0.846	$(\text{hour})^{-1}$	6.12

6.6 Target Performance

The pumping chamber ^{3}He polarization was extracted using Equation 6.51 at each BigBite production run. The target chamber ^{3}He polarization was computed using the extracted pumping chamber polarization and Equation 6.57. Figure 6.31 shows the pumping chamber (upper panel) and target chamber (lower panel) ^{3}He polarizations for each production BigBite run. There is a $\sim 9\%$ decrease in absolute polarization observed when going from the pumping chamber to the target chamber due to the polarization gradient along the transfer tube. The final average target polarizations achieved for E06-014 are summarized in Table 6.20.

As a cross check to the ^{3}He polarization obtained via EPR polarimetry, the longitudinal target chamber ^{3}He was compared to the polarization obtained through the water calibration (Section 6.4.4). Figure 6.24 shows the excellent agreement between the ^{3}He polarizations obtained by using the two independent polarimetry methods.

Table 6.20: Average target polarizations achieved during E06-014.

Chamber	$\langle P_{^3\mathrm{He}} \rangle$ [%]	Uncertainty (Absolute) [%]	Uncertainty (Relative) [%]
Pumping	59.60	2.31	3.88
Target	50.49	3.64	7.22

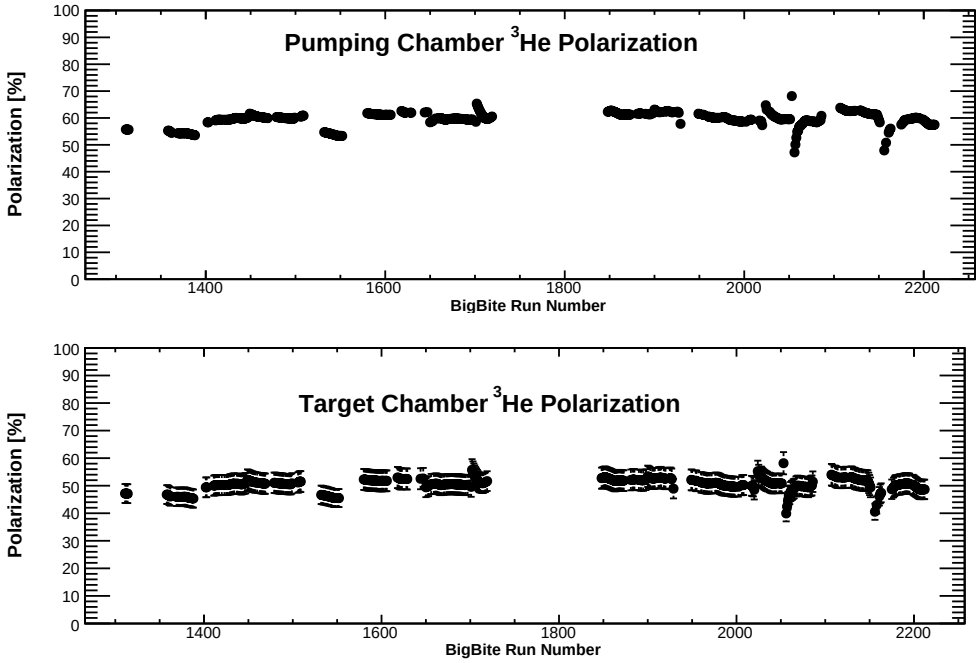

Figure 6.31: ^{3}He polarizations measured in the pumping (top panel) and target (bottom panel) chambers as a function of BigBite run number. These polarizations were calibrated using the EPR measurements discussed in Section 6.5.

CHAPTER 7

DETECTOR CALIBRATIONS

In this chapter a description of the methods used to calibrate the various components of the BigBite and LHRS subdetectors are presented. Section 7.1 discusses the calibration of the BigBite detector arm, while the LHRS calibration is discussed in Section 7.2.

7.1 BigBite Spectrometer Calibration

The BigBite spectrometer consists of several sub detectors: three sets of multi-wire drift chambers, a scintillator plane, a gas Čerenkov detector, a preshower calorimeter and a shower calorimeter. When these sub detectors are analyzed together, they provide the directions and momenta of scattered particles to a high accuracy. However in order to accurately use the sub detectors together they must each be calibrated first. This section provides details on the calibration procedure for all of the BigBite detector components.

7.1.1 Multi-Wire Drift Chambers

The three sets of multi-wire drift chambers, described in Section 4.4.4.2, record a pattern of hits as a charged particle makes its way through the MWDCs. The particle's trajectory

through the MWDCs can then be reconstructed from hit information recorded by the MWDCs. Knowing the particle's trajectory, or its *track*, allows behavior of the particle's trajectory before its interaction with the MWDCs to be inferred, and thus allowing the determination of the particle's point of origin and the direction of its bend when passing through the BigBite magnetic field (and in turn its momentum). Additionally, the particle's trajectory after its interaction with the MWDCs can be deduced, which allows information on where the particle interacts in the Čerenkov, preshower and shower detectors to be extracted. However, in order to accurately reconstruct the particle's track there are several calibrations that must be performed first. This generally consists of four parts: examination of the detector map, calibration of the t_0 timing, calibration of the drift time to drift distance functions, and the calibration of the wire positions.

7.1.1.1 Examining the Detector Map

Three MWDCs, consisting of over 3200 wires, were used in E06-014, with each wire connected to one FASTBUS TDC channel as described in Section 4.4.4.2. 1877 TDCs were used to record the timing information of each of the wire hits. When forming the reconstructed track, each TDC signal needs to be projected to the corresponding wire in the wire chamber. During the transversity experiment[86] the initial detector map was formed when different components of the wire chamber read out electronics were connected. However given the vast amount of channels in the MWDCs, it is essential to confirm the detector map. The wire hit distribution (Figure 7.1) in each plane can reveal issues with the detector map, such as swapped cables, dead channels, etc. If everything is properly connected, the hit distribution of each plane to be smooth and reflects the physical geometry of the wire chambers. The lower hit counts in Figure 7.1 are expected because the length of the wires in the *u* and *v* orientations are shorter at the edge of the chambers; while the slope seen is due to the BigBite acceptance.

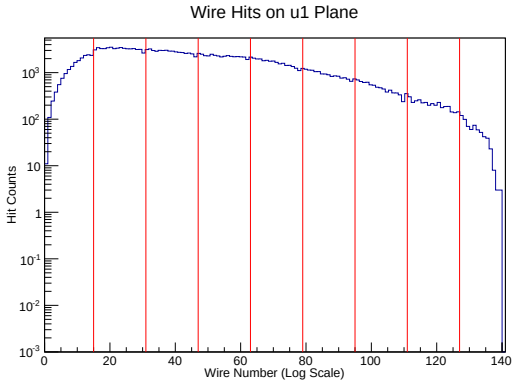

Figure 7.1: The wire hit distribution for the u-plane in the first wire chamber. The red lines separate different read-out amplified A/D cards. Generally each A/D card consists of sixteen wires.

One can further investigate the validity of the detector map by examining the reconstructed tracks projected onto the wire chambers. Plotted in Figure 7.2 is the vertical verses the horizontal track position for each of the three wire chambers. Again if everything is connected correctly, one would expect a uniform (no gaps) distribution that reflects the geometry of the wire chambers.

7.1.1.2 t_0

The wire chamber DAQ is designed to record the timing information, from which the particles position can be extracted. Therefore, the first and most crucial calibration of the wire chambers is the timing calibration know as the t_0 calibration. Each of the MWDC wires is connected to a TDC channel for which the BigBite trigger controls the common stop. The readout time $t_{TDC,i}$, for the i^{th} wire depends on two propagation times. The first is the time, $t_{sig,i}$, it takes a particle passing near the i^{th} wire to generate a signal in the TDC. The second is the propagation time, t_{trig}, that it takes for the trigger signal to reach the TDC and generate the common stop. Following the analysis of [86, 146], the propagation times can be expressed in more fundamental terms, in which $t_{sig,i}$ consists of two physical

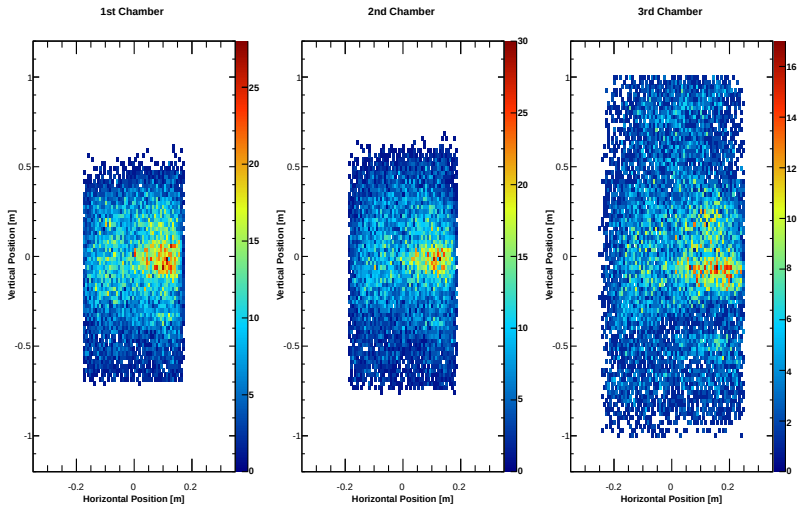

Figure 7.2: The reconstructed track projections on each of the three wire chambers. Note: These distributions are plotted in the tracking coordinate system (see Section 4.4.1).

processes: t_{drift}, which is the time it takes the electrons resulting from ionization with the gas to reach the nearest wire and generate a signal, and $t_{delay,i}$, which is the time it takes the signal produced in the i^{th} wire to propagate to the TDC. Thus

$$t_{sig,i} = t_{drift} + t_{delay,i}. \tag{7.1}$$

After the charged particle hits a wire in one of the wire chambers, it will take some finite time, t_{flight} to reach the trigger detector (in the case of E06-014 this is the BigBite shower calorimeter). Figure 7.3 shows the flight time of an electron traveling from the first wire chamber to the calorimeter. The timing differences are generally less than 1 ns, and with a wire chamber TDC resolution of 0.5 ns, one can safely neglect the t_{flight} time difference in further analyses. In addition to the time it takes the particle to reach the trigger detector, after the particle causes a trigger, there is a finite time, t_{logic}, in which it takes the trigger logic to operate and propagate to various electronics. The t_{trig} time can then be expressed as

$$t_{trig} = t_{flight} + t_{logic} \tag{7.2}$$

The time that gets recorded in the TDCs, $t_{TDC,i}$, is the difference between $t_{sig,i}$ and t_{trig}

$$t_{TDC,i} = t_{drift} + t_{delay,i} - t_{flight} - t_{logic} \approx t_{drift} + t_{0,i} \tag{7.3}$$

where all times except for the drift time have been combined into one offset, $t_{0,i}$. Determining the $t_{0,i}$ offset for each wire allows for the determination of the drift time from the TDC spectra. The $t_{0,i}$ offset is determined by aligning the rising edge of the drift time to zero, allowing the TDC spectrum of each wire to only be sensitive to the particles drift time. The t_0 was calibrated for each A/D card. There were generally 16 wires connected to one A/D card [86], with each wire in a particular A/D card having the same t_0 offset applied. The result of the t_0 calibration on the drift time spectrum of the second V plane in the first wire chamber can be seen in Figure 7.4. Plotted on the left is the drift time for all events, while the drift time plotted on the right shows only events that have a valid reconstructed track. Considering only valid tracks has two advantages, the background is suppressed and the rising edge of the drift time is enhanced.

7.1.1.3 Drift Time to Drift Distance Conversion

Continuing to follow the analysis procedure used by X. Qian [86], the drift time of each wire was used to extract a drift distance via a conversion function. The drift distance is defined as the distance between the reconstructed track projection on to the corresponding hit plane and the wire hit position. The drift distance is plotted in Figure 7.5 as a function of drift time. The conversion function was parameterized using an empirical function that consisted of several polynomial functions. The conversion function was parameterized over the entire drift time window (from 0 to 200 ns).

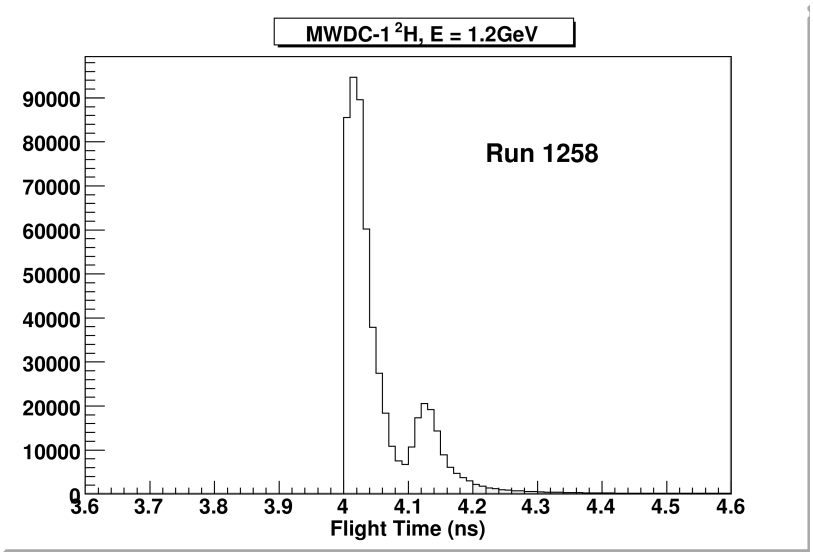

Figure 7.3: Flight of time of an electron traveling from the first wire chamber to the BigBite shower calorimeter.

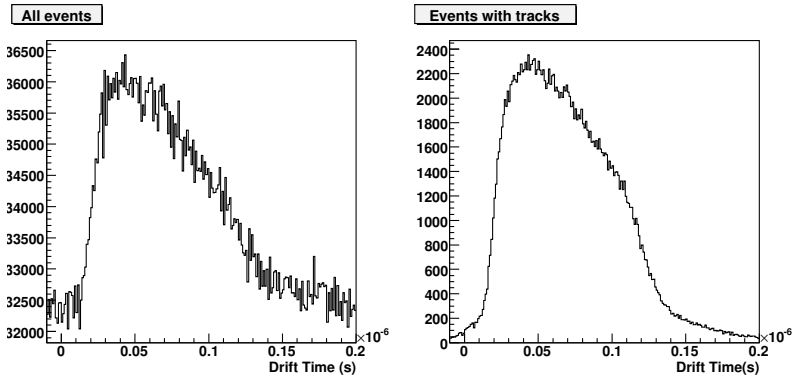

Figure 7.4: Drift time spectrum for the second V (V1p) plane in the first wire chamber is shown for all events (left) and events which had a valid reconstructed track (right). By requiring a valid track, the background is suppressed and the rising edge of the drift time spectrum is enhanced.

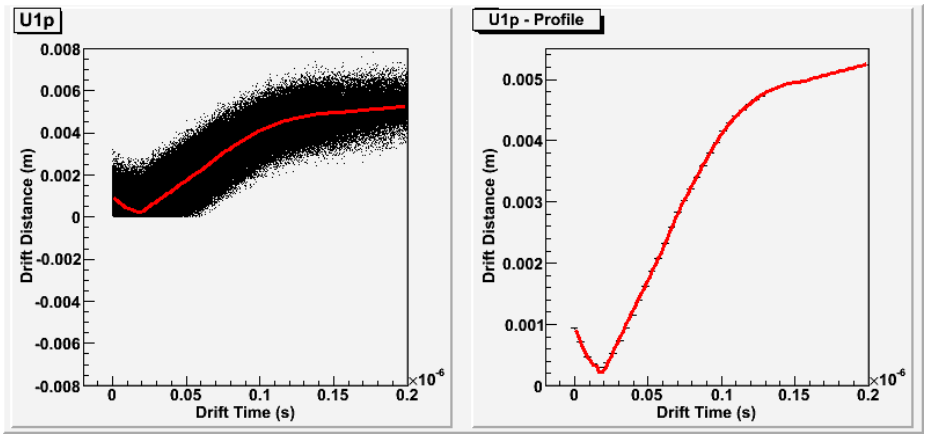

Figure 7.5: The drift distance of the second U plane (u') of the first wire chamber is plotted against the drift time (left panel). The profile of the 2-D histogram is plotted in the right panel. The red line is the conversion function.

7.1.1.4 Wire Positions

For reliable track reconstruction, precise knowledge of the wire positions is crucial. One can determine the position of the wire chambers from the survey report (Appendix A). The positions of the wires can be obtained from the wire chamber construction report [86]. The wire positions are then calibrated by shifting the positions, in order to minimize the difference between the reconstructed tracks projected to the hit wire plane and the wire positions, known as the track residuals. Figure 7.6 shows a representative result of the calibrated track residuals for the U planes in the three wire chambers for a selected production run.

7.1.1.5 Iteration Procedure

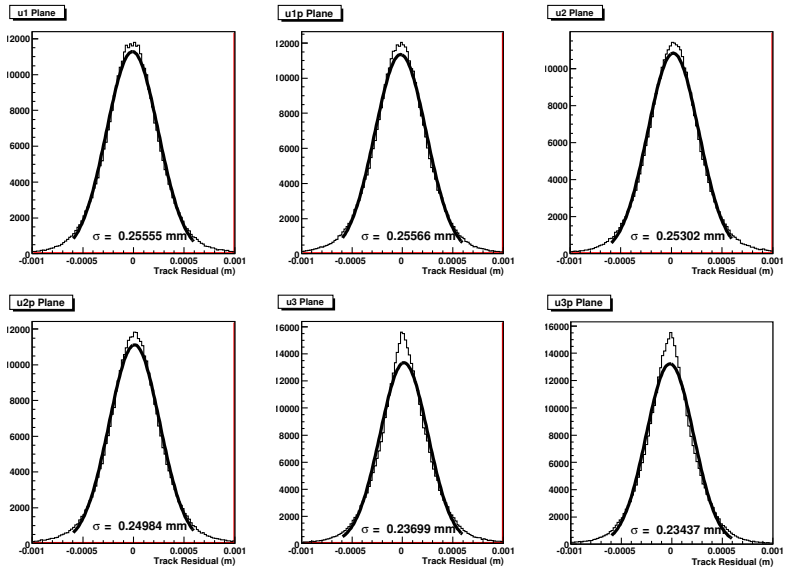

Figure 7.6: Track residuals of a particular run for the six U planes in the three MWDCs; The X and V planes follow a similar distribution for all runs.

The calibration of the MWDC depends on information from the reconstructed tracks, which in turn depend on the calibration of the t_0, drift time to drift distance conversion function and the wire positions. Therefore, an iterative procedure was adopted. Figure 7.7 shows the flow of the iteration procedure. There are three iteration loops in the procedure. The first loop is the global calibration of t_0 for each read out card. The second loop is the global calibration of vertical positioning of the wire chamber planes. The first two loops are done to provide a reasonable starting point for the final iteration loop. The final iteration loop is used to fine tune the MWDC calibrations at the individual wire level. While this is a time consuming process, due to the similarities of the BigBite set-up, the MWDC calibrations performed by X. Qian [86] during E06-010 were able to be used as an initial starting point for E06-014. This eliminated the need for the first two iteration loops and achieved a quick convergence of the final iteration loop.

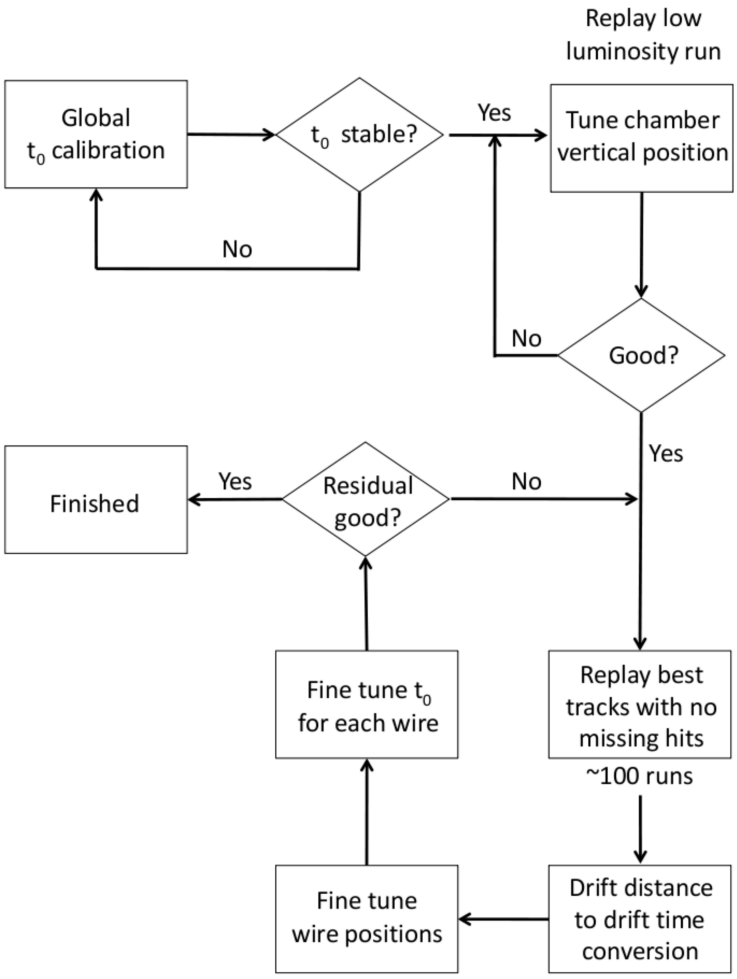

Figure 7.7: Iterative procedure to calibrate the MWDC. Image reproduced from [86]

7.1.1.6 Results

The MWDCs had to be calibrated for each target and electron beam energy. Listed in Tables 7.1, 7.2 and 7.3 are the average σ for the track residual peaks of each plane in the three wire chambers. The first row lists the results for elastic e-p scattering from an unpolarized hydrogen target at a beam energy of 1.23 GeV/c^2. The second and third rows list the results from 15 μA production runs on a polarized ^{3}He target. A resolution better than 300 μm was achieved on all wire chamber planes.

7.1.1.7 Tracking Software

In order to extract real particle tracks, software is needed to process all of the hit information recorded in the MWDCs. The tracking algorithm used in the BigBite spectrometer is the "Pattern Match Tree Search" algorithm, first proposed by Mauro Dell'Orso and Luciano Ristori in 1990 [147]. This algorithm uses increasing resolution to search for tracks. An illustration of the tree searching algorithm can be seen in figure 7.8. The first step uses a coarse resolution with a few templates. Within the templates that matched a hit pattern, the track searching resolution is increased by generating a set of daughter templates. The daughter templates are then compared with a finer hit pattern. This procedure is repeated until the desired matching resolution is achieved. The hits left after the tree searching algorithm is finished, are then fitted to reconstruct a track.

The BigBite tracking software was developed by O. Hansen (of JLab HallA). The 18 wire planes of the MWDC were divided into three groups based upon their orientations (U,V or X see 4.4.4.2. The tree search algorithm was then used to find two-dimensional tracks, or *roads*, in each wire plane orientation. The roads within a common orientations are then combined and fit to reconstruct three-dimensional tracks. In order to eliminate clone (or *ghost*) tracks, each of the roads is only able to contribute to one track. A successfully

Table 7.1: Chamber 1: Average track residuals for each plane in the first wire chamber.

E_{beam} [GeV]	Target	U [μm]	Up [μm]	V [μm]	Vp [μm]	X [μm]	Xp [μm]
1.23	^{2}H	215	216	209	209	206	208
4.74	^{3}He	270	271	263	261	247	250
5.89	^{3}He	286	287	273	272	258	261

Table 7.2: Chamber 2: Average track residuals for each plane in the second wire chamber.

E_{beam} [GeV]	Target	U [μm]	Up [μm]	V [μm]	Vp [μm]	X [μm]	Xp [μm]
1.23	^{2}H	213	211	216	214	203	198
4.74	^{3}He	267	265	262	261	245	240
5.89	^{3}He	283	279	275	273	255	250

Table 7.3: Chamber 3: Average track residuals for each plane in the third wire chamber.

E_{beam} [GeV]	Target	U [μm]	Up [μm]	V [μm]	Vp [μm]	X [μm]	Xp [μm]
1.23	^{2}H	164	161	161	159	145	141
4.74	^{3}He	248	245	246	245	202	199
5.89	^{3}He	250	247	244	242	203	199

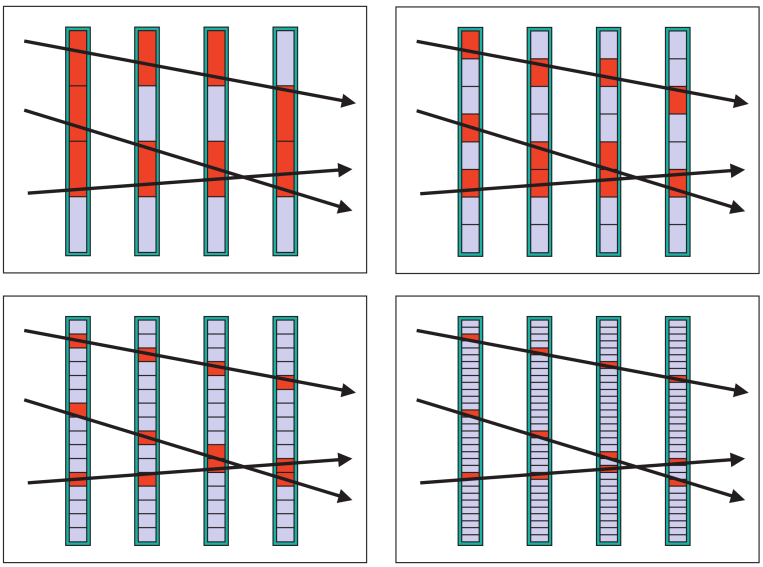

Figure 7.8: An schematic illustration of the tree-search tracking algorithm used for BigBite, image is taken from Ref. [148]. At each stage the track is matched with templates of increasing resolution.

reconstructed track must have a hits from at least fifteen of the eighteen wire planes. If the tree search algorithm finds two tracks, the track with the lower χ^2 is kept.

X. Qian [86] performed a software efficiency study of the E06-010 BigBite data using a GEANT3 Monte Carlo. He calculated a software tracking efficiency of 95%. Combining the software efficiency with the hardware efficiency of 98%, a total tracking efficiency of 93% [86] was estimated. Since E06-010 and E06-014 experiments use the same tracking software with the MWDCs in the same configuration, this tracking efficiency is applicable to E06-014.

7.1.2 Optics

After a particle's track is reconstructed using the hits recorded in the MWDCs and the tracking software, the particle's momentum, scattering angle and interaction vertex (location where the particle interacted with the target) needs to be determined by the BigBite optics

module. The under lying principle of the optics modal is that the trajectory of a charged particle through a known magnetic field is determined by its charge and momentum. Therefore if the particle's trajectory and the magnetic field are known, one can reconstruct all the particles kinematic information. Unfortunately, in reality the magnetic field is not known precise enough to reconstruct the particle's kinematics using only the particle's trajectory and the magnetic field. As a result the BigBite optics module had to be calibrated using an iterative algorithm and software package developed by X. Qian [86].

The BigBite optics module calibration consisted of several calibration runs on various targets in order to accurately reconstruct a particle's interaction vertex, angle and momentum. Below is a list of the different runs and targets the were used during the calibration:

1. **Survey Report:** The survey report is used to determine the positions of the target, magnet and MWDCs.

2. **No-Field Runs:** These runs are used to empirically determine the position of the MWDCs.

3. **Carbon Runs (Sieve OUT):** Carbon foils with known positions are used to calibrate the interaction vertex.

4. **Carbon Runs (Sieve IN):** Carbon foil targets are used, along with a sieve plate (a lead plate consisting of different sized slots to force a known scattering pattern) inserted in front of the magnet. The known geometry of the sieve plate slots are then used to calibrate the particle's scattering angles.

5. **Elastic Hydrogen Runs (Sieve OUT) Runs:** Elastic electron-proton scattering on hydrogen is used to calibrate the particle's momentum.

6. **Elastic Hydrogen Runs (Sieve IN) Runs:** A sieve-plate is inserted in front of the magnet and used to check and further refine the particle's scattering angles.

7.1.2.1 Survey Report and No Field Runs

The first step of the optics calibration is to determine the locations of the target, magnet, sieve plate, and MWDCs. This information was found from the survey report in appendix A. Next, the positions of the MWDCs are found empirically by having particles transverse through the BigBite detector with the BigBite magnet turned off. No magnetic field allows the MWDC to reconstruct tracks that are not bent and hence not altering the particle's kinematics. Both of these calibrations were performed for E06-014 by X. Qian [86]. The results after the no field calibration can be seen in figure 7.9, where the right plot shows the reconstructed interaction vertex of the carbon foil targets; the red lines mark the actual position of the carbon foils. The middle plot shows the BigBite sieve-plate that was used for the calibration of a particle's scattering angles. The reconstructed sieve pattern obtained when inserting the sieve-plate is shown in the left most plot; the red holes/slots in the left plot mark the center of the sieve holes/slots.

7.1.2.2 First Order Optics Model

The first order optics model treats the BigBite magnet as a perfect dipole magnet, with a uniform field throughout its volume, in order to extract a particle's kinematic information. When a charged particle transverses the magnetic field it will be bent by an arc of radius R. The bend radius is measured relative to an effective bend plane that passes through the center to the magnet. Figure 7.10 shows the first order optics model as implemented during E06-010 and E06-014. The particle enters the magnetic field at point A and exits at point D. The interaction point is modeled by a single point on the bend plane (thick dashed line), point C. The particle trajectory through the magnetic field is given by the line segments $\overline{AC}$ and $\overline{CD}$ (red dashed lines). The path length through the magnetic field is then given as $l = \overline{AC} + \overline{CD}$, noting that $l/2 = \overline{AC} = \overline{CD}$, because the bend plane bisects the

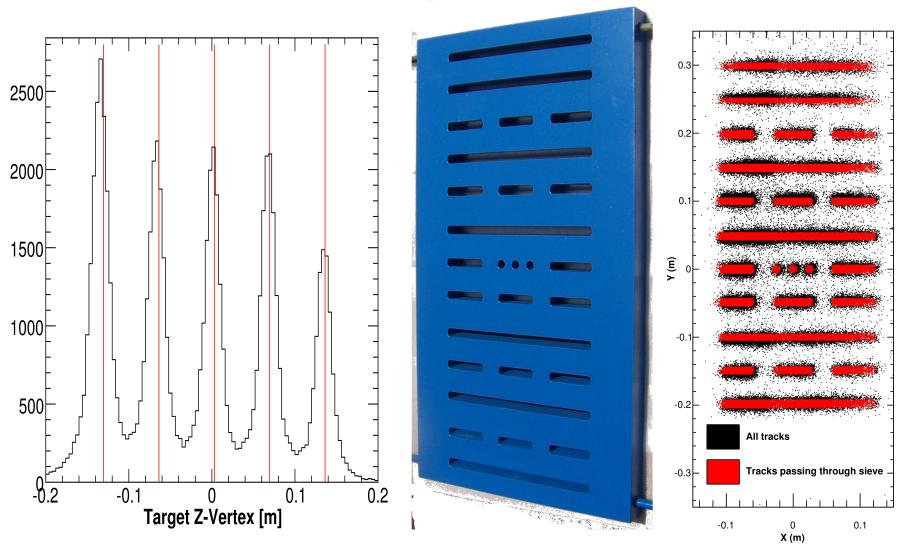

Figure 7.9: Results after no-field optics module calibration. The right plot shows the reconstructed scattering vertex of the carbon foils. The middle plot shows lead sieve-plate that was used in the optics calibrate. The left plot shows the reconstructed sieve pattern obtained with the BigBite magnet off.

bending arc. The angle $\angle$ BAC is 90 ° due to the line segment $\overline{AC}$ being tangent to the arc of curvature. The bend angle of the trajectory in the plane perpendicular to the magnetic field can be defined as θ_{bend} = $\angle$ ABD, with $\angle$ ABC = $\theta_{\text{bend}}/2$. Using the path length and the bend angle, the bend radius can be written as:

$$R = \frac{l}{2\tan\frac{\theta_{\text{bend}}}{2}}. \tag{7.4}$$

Using Equation 7.4, along with the charge of the particle and the magnetic filed information, the particle's transverse momentum can be calculated:

$$p_{\perp} = |q|RB = \frac{|q|lB}{2\tan\frac{\theta}{2}}. \tag{7.5}$$

In order to obtain the particle's total momentum, the angle between the momentum

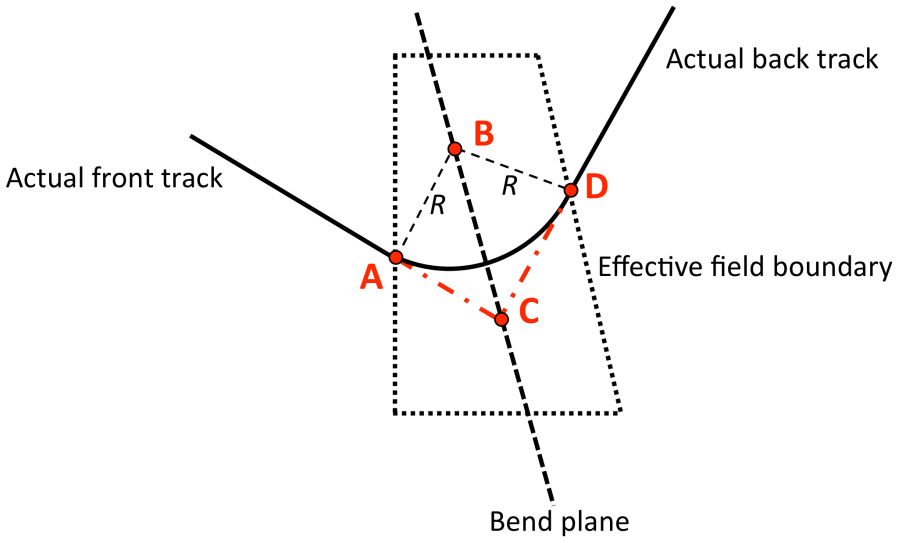

Figure 7.10: Illustration of the BigBite first order optics model as implemented in E06-010 and E06-014. Image reproduced from D. Parno [75].

vector and magnetic field are needed

$$\cos\phi = \frac{\vec{B}\cdot\vec{p}}{|\vec{B}||\vec{p}|}. \tag{7.6}$$

The angle ϕ remains fixed throughout the volume, because the BigBite magnet is being treated as a dipole magnet. Making use of Equation 7.6, the transverse component of the particle's momentum can be written in terms of the magnitude of the momentum vector

$$p_\perp = p\sin\phi. \tag{7.7}$$

Using Equations 7.4,7.5 and 7.7 the total momentum of the particle can then be computed from:

$$p = \frac{|q|lB}{2\sin\phi\tan\frac{\theta}{2}}. \tag{7.8}$$

The optics modual can be used to reconstruct the first order target vertex and scattering angles. The back track, which is reconstructed using the MWDCs, is extrapolated to find the point C, which is where the track intersects the bend plane. Because the BigBite magnet is modeled as a perfect dipole, the front track must also intersect the bend plane at point C, and have with the same angle ϕ with the magnetic field as the back track does. These constraints restrict the solutions of the front track to a cone that has its apex at point C and an opening angle of ϕ. The front track that gets reconstructed is the one that intersects with the beam line. The intersection of the front track and the beam line is the first order vertex position. The first order scattering angles can then be defined by the vector connecting the first order vertex point and mid point of the bend plane (point C) [75, 86].

7.1.2.3 Refinements to First Order Corrections

The first order optics calibration is just an approximation. In reality, the BigBite magnet is not a perfect dipole and therefore corrections must be made to account for deviations from the dipole model. These corrections are refereed to as higher order corrections. During E06-010 higher order corrections were performed at two incident electron beam energies of 1.231 GeV and 2.396 GeV [86]. During E06-014, there was not enough optics data taken to determine all of the higher order corrections. As a result, many of the higher order corrections had to be taken from E06-010 or neglected completely.

7.1.2.3.1 Correlation Variables Due to the inhomogeneous magnetic field produced by the BigBite magnet, a charged particle's trajectory depends on the region of the magnetic field that it is traversing. This position dependence can be seen in data when looking

at correlations between the target vertex position, reconstructed particle momentum, and several other reconstructed tracking variables that describe the location and direction of the charged particle. There are six *tracking* variables that are used to describe how and where a charged particle passes through the magnetic field.

The first pair of tracking variables used are the x and y (in detector coordinates) hit positions of the reconstructed track on the first wire chamber. The second pair are x' and y' (also refereed to as $\tan\theta$ and $\tan\phi$ [146]), which defines the reconstructed track's direction in detector coordinates.

$$x' = \frac{dx_{det}}{dz_{det}} \tag{7.9}$$

$$y' = \frac{dy_{det}}{dz_{det}} \tag{7.10}$$

The final tracking variable pair are x_{bend} and y_{bend}, which give the position where the reconstructed track intersects the bend plane (point C in figure 7.10). Unlike the first four tracking variables, x_{bend} and y_{bend} are defined in the HallA coordinate system. In summary, x, x' and y_{bend} are vertical, and y, y' and x_{bend} are horizontal.

7.1.2.3.2 Vertex Reconstruction From the first order interaction vertex $Z_v^{(0)}$, corrections were made to the interaction vertex by studying the difference between $Z_v^{(0)}$ and the expected iteration vertex, Z_v obtained from the survey information of the carbon multi foil target. The discrepancies found between $Z_v^{(0)}$ and Z_v can be associated with one of the six correlation variables. To correct the discrepancies, the interaction vertex difference is plotted against the correlation variables, leading to the first two higher order corrections:

$$Z_v^{(1)} = Z_v^{(0)} + b_1 + a_1 y \tag{7.11}$$

$$
\begin{aligned}
Z_v^{(2)} = Z_v^{(1)} \;&+\; \left(a_{20} + a_{21} Z_v^{(1)}\right) + x\left(b_{20} + b_{21} Z_v^{(1)}\right) \\
&+\; \left(a_{22} + a_{23} Z_v^{(1)}\right) + y\left(b_{22} + b_{23} Z_v^{(1)}\right) \\
&+\; \left(a_{24} + a_{25} Z_v^{(1)}\right) + x'\left(b_{24} + b_{25} Z_v^{(1)}\right) \\
&+\; \left(a_{26} + a_{27} Z_v^{(1)}\right) + y'\left(b_{26} + b_{27} Z_v^{(1)}\right) \\
&+\; \left(a_{28} + a_{29} Z_v^{(1)}\right) + x_{bend}\left(b_{28} + b_{29} Z_v^{(1)}\right) \\
&+\; \left(a_{30} + a_{31} Z_v^{(1)}\right) + y_{bend}\left(b_{30} + b_{31} Z_v^{(1)}\right)
\end{aligned}
\tag{7.12}
$$

It should be noted that the coefficients for each line of Equation 7.12 were determined independently (i.e. a separate calibration for each correlation variable.). Equation 7.12 was then repeated (with $Z_v^{(1)} \rightarrow Z_v^{(2)}$ and $Z_v^{(2)} \rightarrow Z_v^{(3)}$) until the fourth order interaction vertex $Z_v^{(3)}$ was obtained. After the fourth order corrections to the interaction vertex, discrepancies due to the six correlation variables were minimized. Next, the reconstructed momentum was used to correct $Z_v^{(3)}$ for momentum dependence. However, due to the broad momentum spectrum of scattering from a carbon-foil, the reconstructed momentum at this stage is only an approximation. The first order momentum $p^{(0)}$ was reconstructed using $Z_v^{(3)}$ based on Equation 7.8. Similar to the higher order corrections applied to the interaction vertex, the second and third momentum corrections were defined based on momentum variations with the six correlation variables

$$
\begin{aligned}
p^{(1)} = p^{(0)} \quad & \cdot \quad \left(c_0 + c_1 y_{bend} + c_2 y_{bend}^2\right) \\
& \cdot \quad \left(d_0 + d_1 x_{bend}\right) \\
& \cdot \quad \left(e_0 + e_1 Z_v^{(3)}\right) \\
& \cdot \quad \left(f_0 + f_1 x + f_2 x^2\right) \\
& \cdot \quad \left(g_0 + g_1 x' + g_2 x'^2\right) \\
& \cdot \quad \left(h_0 + h_1 y + h_2 y^2\right) \\
& \cdot \quad \left(i_0 + i_1 y' + i_2 y'^2\right)
\end{aligned}
\tag{7.13}
$$

$$
\begin{aligned}
p^{(2)} = p^{(1)} \quad & \cdot \quad \left(j_0 + j_1 x_{bend} + j_2 x_{bend}^2\right) \\
& \cdot \quad \left(k_0 + k_1 y_{bend} + k_2 y_{bend}\right) \\
& \cdot \quad \left(l_0 + l_1 p^{(3)}\right).
\end{aligned}
\tag{7.14}
$$

The momentum dependent vertex correction was then obtained as:

$$
\begin{aligned}
Z_v^{(4)} = Z_v^{(3)} \quad & - \quad x_{bend} Z_v^{(3)} \left(m_0 + m_1 p^{(2)}\right) \\
& + \quad \left(n_0 + n_1 Z_v^{(3)}\right) \left(o_0 + o_1 p^{(2)}\right) \\
& + \quad e^{\left[\left(p_0 + p_1 p^{(2)}\right)\left(q_0 + q_1 Z_v^{(3)}\right)\right]}.
\end{aligned}
\tag{7.15}
$$

$Z_v^{(5)}$ was computed using Equation 7.15 with $Z_v^{(3)} \rightarrow Z_v^{(4)}$ and $Z_v^{(4)} \rightarrow Z_v^{(5)}$. The field at the top and bottom of the BigBite magnet is weaker than at the center of the magnet. Such a

feature can lead to deviations in the reconstructed interaction vertex from the real one. To correct for this effect, a fiducial volume cut was added to the bend plane (x_{bend} and y_{bend}) to exclude the extreme regions of the magnet. The effect of the field in the extreme regions of the BigBite magnet can be seen in Figure 7.11. In addition to the fiducial cut, there were several corrections based on look up tables that were also implemented to further correct deviations specific to those particular regions of the magnet. The phase space defined by x_{bend}, y_{bend}, and Z_v was divided into small regions producing a fine grid that covered the entire phase space. Any point that lays within the phase space makes a cubical volume with eight corners defined by various values of x_{bend}, y_{bend}, and Z_v. A new interaction vertex was computed by performing a linear interpolation between the corners of the cubical volume. Two additional look up tables were created to correct for momentum dependence. The final three vertex corrections are defined by

$$Z_v^{(6)} = f_1\left(x_{bend}, y_{bend}, Z_v^{(5)}\right) \tag{7.16}$$

$$Z_v^{(7)} = f_2\left(x_{bend}, p^{(2)}, Z_v^{(6)}\right) \tag{7.17}$$

$$Z_v^{(8)} = f_3\left(y_{bend}, p^{(2)}, Z_v^{(7)}\right) \tag{7.18}$$

where f_1, f_2, and f_3 are the linear interpolation functions. The majority of the calibrations, including the look up tables were performed by X. Qian [86], and extended to E06-014 by applying some minor corrections (mostly to first order calibrations). Results for the interaction vertex calibration done on a carbon multi-foil target for 1.23 GeV incident electrons can be seen in Figure 7.12. A vertex resolution of about 1 cm was achieved. A check of the calibration was done with the carbon multi-foil target at the full production

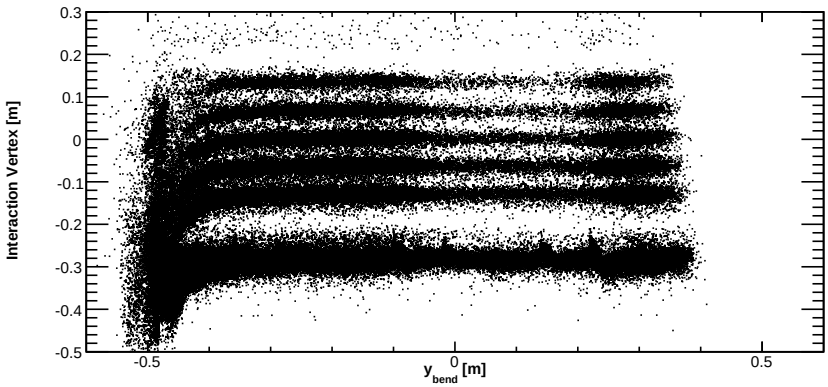

Figure 7.11: Reconstructed vertex is plotted against the y_{bend} tracking variable, which is the vertical position on the bend plane. The left side is corresponding to the bottom of the BigBite magnet. The extreme region can be seen at the bottom of the magnet.

energy using 5.9 GeV incident electrons (Figure 7.13), which resulted in a vertex resolution at the cm level. The red lines in Figures 7.12 and 7.13 show the actual locations of the carbon foils.

7.1.2.3.3 Angle Reconstruction The calibration of the angles ϕ and θ_{bend}, defined in Section 7.1.2.2, relied on the use of carbon and hydrogen targets, in addition to the sieve slit being inserted in front of the magnet. The initial angles were determined by connecting the final interaction vertex position to the middle point on the bend plane (point C in Figure 7.10). Similar to the procedure used for the interaction vertex, offsets and higher order corrections, including look up tables for the extreme regions, were implemented by X. Qian [86]. Figure 7.14 shows the results from the angle calibration performed on a carbon multi-foil target for 1.23 GeV incident electrons. The red points label where the sieve slit/hole should be. An angular reconstruction resolution of 10 mrad was achieved [86].

7.1.2.3.4 Momentum Reconstruction

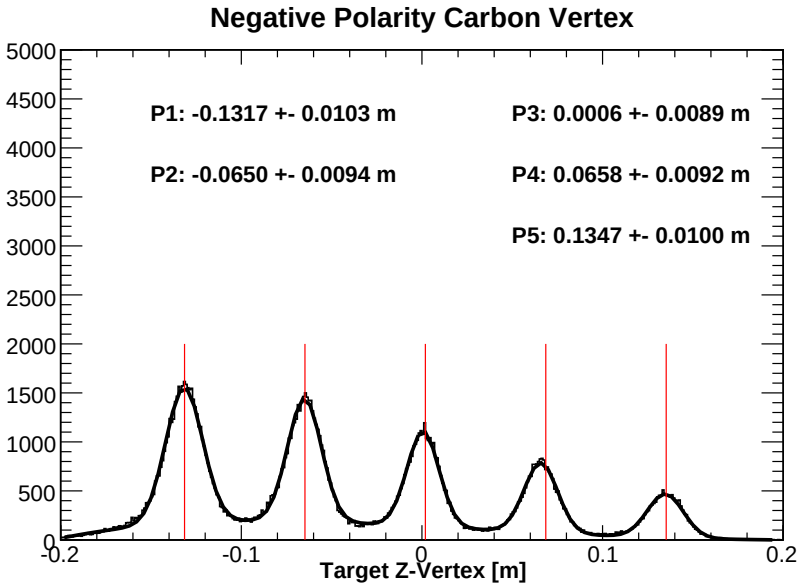

Figure 7.12: The final reconstructed interaction vertex of a carbon multi-foil target for 1.23 GeV incident electrons. The red lines mark the actual positions of the carbon foils.

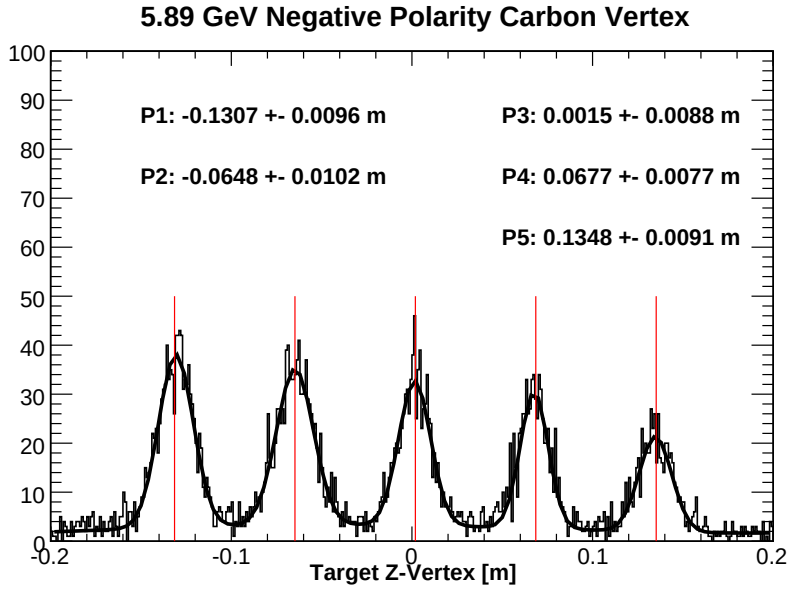

Figure 7.13: The reconstructed interaction vertex of a carbon multi-foil target at the full production energy of 5.9 GeV incident electrons. The lines mark the actual positions of the carbon foils.

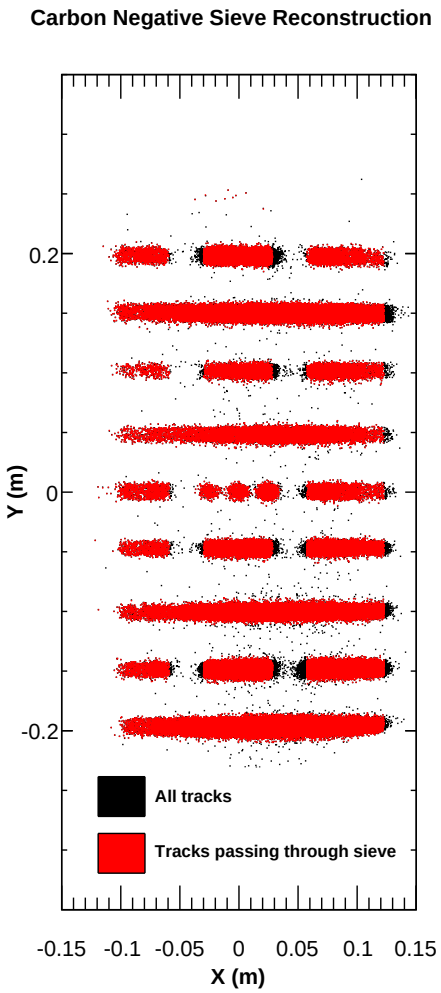

Figure 7.14: The sieve plate reconstruction for 1.23 GeV electrons scattering from a carbon multi-foil target. The red points show the locations of the sieve slits/holes.

Starting with accurate position reconstruction via the interaction vertex and angular reconstruction calibrations, the reconstructed momentum can now be reliably calibrated. The momentum calibration is done by elastically scattering electrons off a hydrogen target (proton). One can calculate the final momentum, $p_{elastic}$, in elastic e-p scattering if the initial momentum, p_i and scattering angle θ are known.

$$p_{elastic} = \frac{p_i M}{M + p_i \left(1 - \cos\left(\theta\right)\right)}, \tag{7.19}$$

were M is the target mass, in the case of ^{2}H the target mass is 0.938 GeV (the proton mass). Ignoring the electron mass (which is small compared to the proton mass), the initial momentum is then given by the incident electron beam energy of 1.23 GeV, and the scattering angle is known from the previous calibrations. The calculated momentum, $p_{elastic}$, can then be compared to the scattering momentum measured during elastic e-p scattering; discrepancies between the two momenta must then be corrected.

The E06-010 optics [86] applied their first correction to the first-order momentum, which was a linear correction applied to all momenta below 0.9 GeV

$$p = \begin{cases} p^{(0)} & p^{(0)} > 0.9\,\mathrm{GeV} \\ p^{(0)} + 0.148\left(p^{(0)} - 0.9\,\mathrm{GeV}\right) & p^{(0)} \leq 0.9\,\mathrm{GeV} \end{cases} \tag{7.20}$$

The purpose of this correction was to align the secondary peak in the invariant mass, to the Δ mass of 1.232 GeV. However, this leads to a discontinuity in the first derivative of the momentum. Applying further corrections that were based on look up tables failed to resolve the discontinuity.

Consequently, a simple Monte-Carlo simulation of BigBite showed that the inelastic peak in W, which is affected by Q^2 variations and the BigBite acceptance, does not coincide with the Δ mass of 1.232 GeV, but rather 1.215 ± 0.005 GeV [149]. As a result, the low

momentum and higher order corrections were removed from the E06-014 analysis, and only E06-010's first order momentum was kept. To determine the overall scale factor that needed to be applied in order to align the elastic and inelastic peaks of the first order momentum, five runs were taken with 1.23-GeV electrons incident on a hydrogen target. To insure that good elastic electrons were selected, cuts were applied to remove extreme regions of the magnet and select negatively charged particles, one-track events, and events that scattered within 17 cm from the target center (see Section 8). Finally, events were required to have fired the T1 trigger, because this trigger results in the most uniform BigBite acceptance. Figure 7.15 shows the invariant mass spectrum for 1.23 GeV electrons incident on a hydrogen target after the overall scale factor was adjusted to 1.041. The red line at $W = 0.938$ GeV is the proton peak and the red line for the inelastic peak falls at $W = 1.21$ GeV. The resolution of the reconstructed momentum can be measured by taking the difference of the predicted elastic momentum, given by Equation 7.19 and the measured elastic momentum

$$\frac{\delta p}{p} = \frac{p_{elastic} - p}{p}, \tag{7.21}$$

where p is the measured elastic momentum. Figure 7.16 shows the momentum difference used to measure the momentum resolution. E06-014 achieved a momentum resolution of 1%.

7.1.2.4 Positive Optics

The calibrations of Sections 7.1.2.2 and 7.1.2.3 used only electrons that were bent up when passing through the BigBite magnet. However, due to BigBite's large acceptance, charged particles that bend-down can also be detected. The kinematics between the particles that bend-up are not necessarily the same as those that bend-down. Therefore an independent optics calibration of the particles that bend down needed to be performed. This was achieved

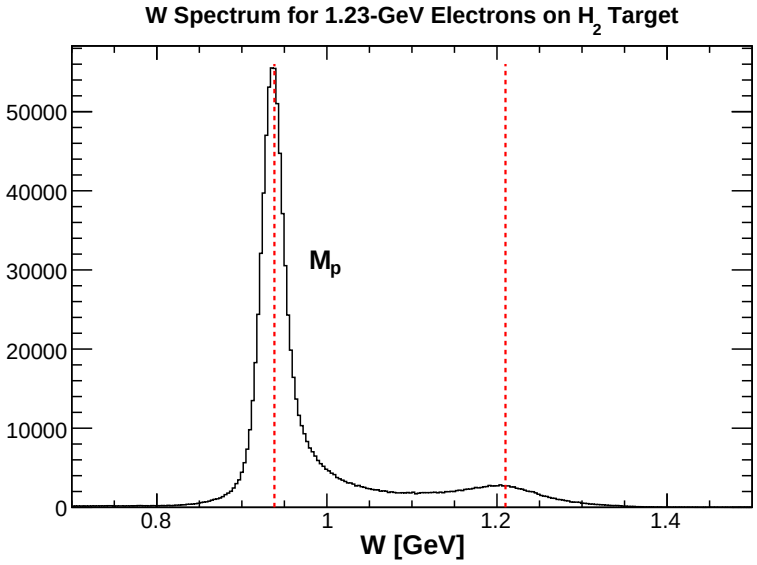

Figure 7.15: W spectrum for calibration events with 1.23 GeV electrons incident on ^{2}H target. The red line at $W = 0.938\,\mathrm{GeV}$ marks the proton peak, while the red line at $W = 1.21\,\mathrm{GeV}$ marks the location of the inelastic peak.

by switching the magnetic field of the BigBite magnet to positive polarity, which resulted in negatively charged particles being bent down when passing through the BigBite magnet and positively charged particles being bent up. Electrons bending down can now be selected and calibrated following the procedure of the last sections (Sections 7.1.2.2 and 7.1.2.3).

7.1.2.4.1 Calibration Results

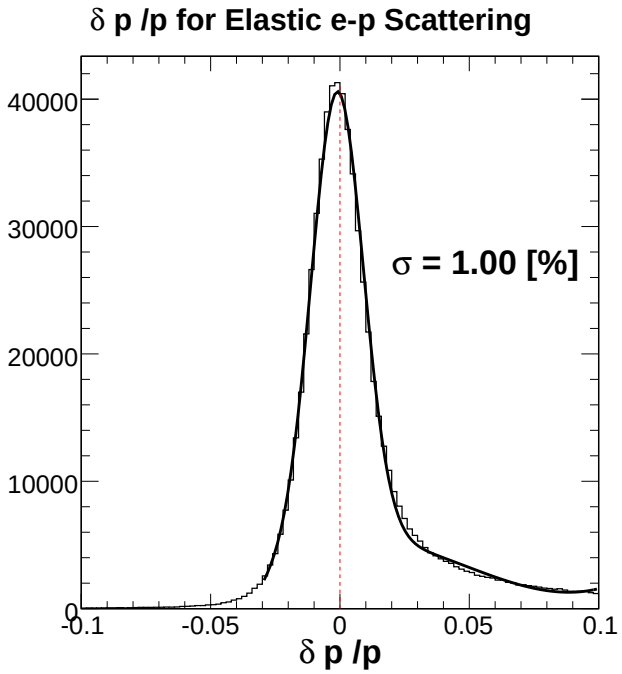

Figure 7.16: Momentum resolution for E06-014 optics package. The difference between the predicted momentum (Equation 7.19) and measured momentum for 1.23-GeV electrons indecent on a hydrogen target has been plotted. The fit function is the sum of a Gaussian and three degree polynomial. The red line is just a guide for the eye marking the zero location.

E06-014 used the positive optics calibrations performed by X. Qian [86], but opting to remove the low momentum and higher order momentum corrections, and applying a overall scale factor of 1.040 to the first order momentum, ala Section 7.1.2.3. The results of the interaction vertex and angular reconstructions are shown in Figures 7.17 and 7.18. The vertex reconstruction was measured by scattering 1.23-GeV electrons incident on carbon foils. The red lines in the Figure 7.17 mark the actual position of the carbon foils. A sub-centimeter resolution was achieved. Inserting the sieve plate in front of the BigBite magnet, and scattering 1.23-GeV electrons from a hydrogen target, the angular reconstruction can be calibrated. Figure 7.18 shows the sieve reconstruction using the positive optics package. The red holes/slits mark the location of the sieve holes/slits. Only half of the sieve plate is reconstructed, because only about half of the particles that bend-down make it into the BigBite acceptance.[1] The results of momentum calibration and resolution using elastic bend-down electrons, can be seen in Figures 7.19 and 7.20. The red lines in Figure 7.19 of the invariant mass fall at $W = 0.938\,\mathrm{GeV}$ and $W = 1.21\,\mathrm{GeV}$, marking the proton and inelastic peaks. The momentum resolution measured by using Equation 7.19 was found to be 1.17%. This is slightly worse than what was measured for the bend-up electrons.

[1] Figure 7.18 is in detector coordinates, where positive vertical direction is the physical bottom the the BigBite detector.

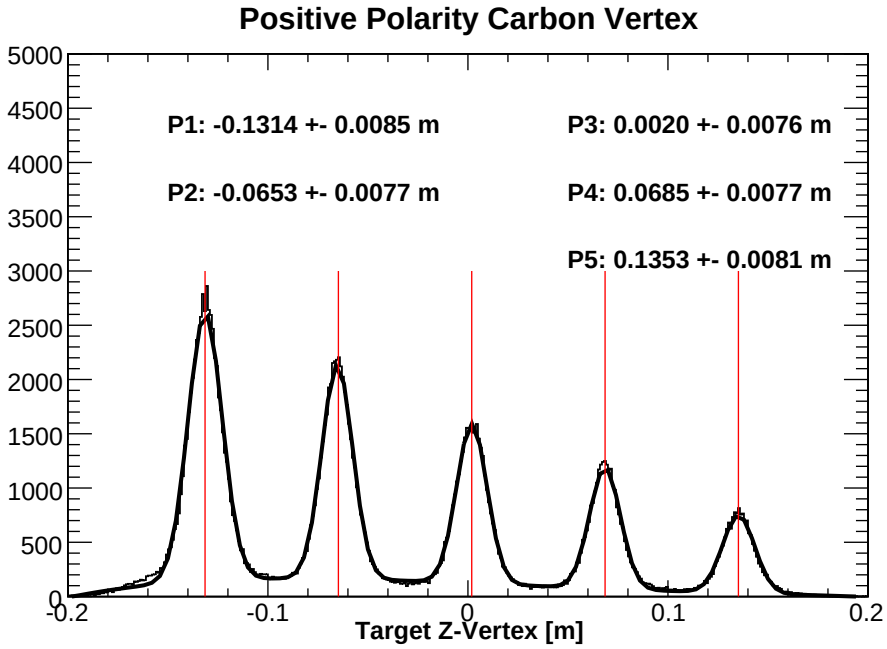

Figure 7.17: Interaction vertex reconstruction achieved for the positive optics calibration by scattering 1.23-GeV electrons incident on carbon foil targets. The red lines mark the actual location of the carbon foils.

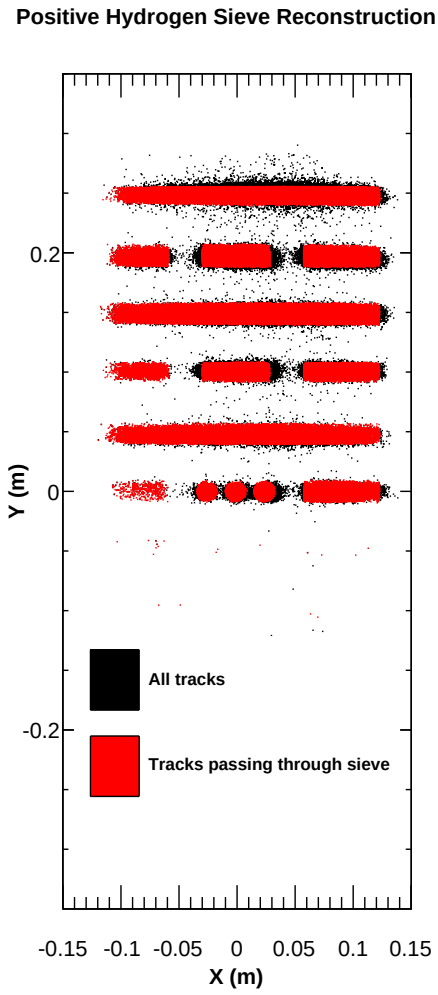

Figure 7.18: Angular reconstruction achieved for the positive optics calibration by scattering 1.23-GeV electrons incident on a hydrogen target, while a sieve plate was inserted in front of the magnet. Only half of the sieve plate is reconstructed due to acceptance. The red holes/slits mark the locations of the actual hole/slit locations.

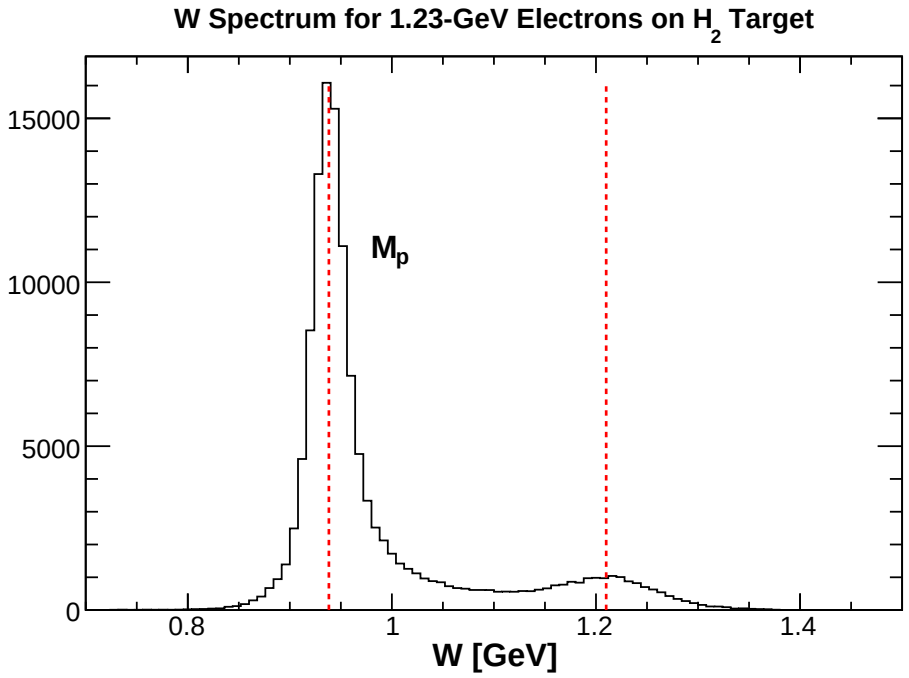

Figure 7.19: W spectrum for positive optics calibration events with 1.23 GeV electrons incident on ^{2}H target. The red line at $W = 0.938\,\mathrm{GeV}$ marks the proton peak, while the red line at $W = 1.21\,\mathrm{GeV}$ marks the location of the inelastic peak.

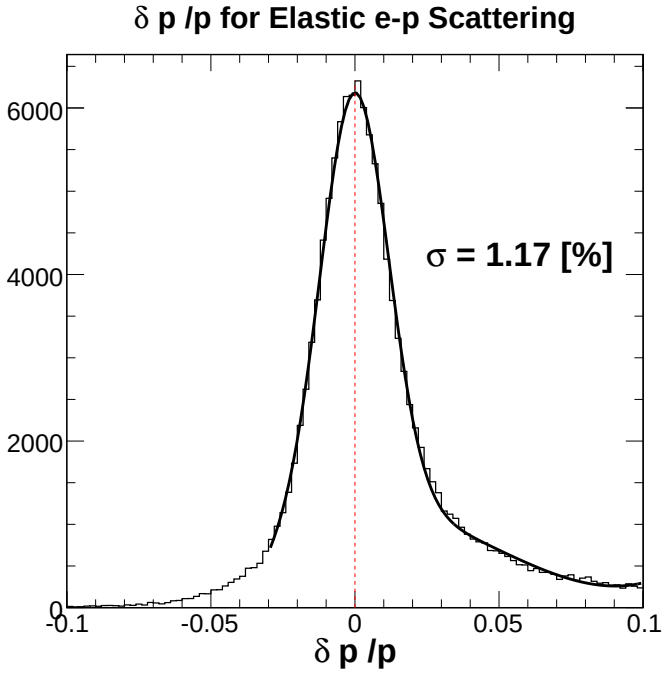

Figure 7.20: Momentum resolution for E06-014 positive optics package. The difference between the predicted momentum (Equation 7.19) and measured momentum for 1.23-GeV electrons incident on a hydrogen target has been plotted. The fit function is the sum of a Gaussian and three degree polynomial. The red line is just a guide for the eye marking the zero location.

7.1.3 Preshower and Shower

The BigBite calorimeter consists of a preshower and a shower detector, which are both made of lead-glass as described in Section 4.4.4.5. The calorimeter was used in triggering the BigBite spectrometer and played a central role in identifying electrons and pions through PID cuts (Chapter 8). The total scattering energy of the detected particles is approximately equal to the sum of the cluster amplitudes in the preshower and shower. In order to obtain an accurate energy from the BigBite calorimeter, it must be calibrated with an incident particle of known energy. The calibration was done by using a two step process. First, a rough hardware calibration was preformed using cosmic rays to gain match the detector responses[2]. The second step in the calibration uses the reconstructed momentum, discussed in Section 7.1.2.3.4, to refine the calorimeter energy resulting from the first step.

7.1.3.1 Energy Calibration

7.1.3.1.1 Calibration with Cosmic Rays With the BigBite calorimeter being used in the triggering of the BigBite spectrometer, it is important to have all the blocks making up the calorimeter give the same response for the same deposited energy. This is done by measuring high energy cosmic rays, which are primarily muons, passing vertically through the preshower and shower detectors. The muons behave as minimum ionizing particles and leave a well defined energy loss peak in each of the block's ADC spectra. The ADCs can then be aligned by adjusting the HV on the PMT. Cosmic rays were identified by using two plastic scintillators; one mounted at the top of the detector and the other at the bottom of the detector. Each of the scintillators had two PMTs one on each side. The cosmic ray trigger was then setup as a logical AND between the four PMTs. In an iterative procedure, the high voltage on the shower blocks were adjusted so the energy-loss peak populated ADC

[2]Gain matching the detector responses involves adjusting the HV applied to the PMTs so that the ADC amplitudes of each PMT gives the same response.

channel 120; while in the preshower the high voltage was adjusted so the energy-loss peak was at ADC channel 240 [82]. This rough calibration for E06-014 was performed by K. Allada [82].

7.1.3.1.2 Shower Cluster Reconstruction When an electron produces an electromagnetic shower in one of the shower or preshower blocks, its shower is not confined to just one block, but rather several blocks. To obtain the total energy deposited in the detectors, the amplitudes of several blocks need to be added together. The summing of several continuous blocks is known as a cluster. Each cluster has a central block, in which the most energy was deposited relative to the other near by blocks. The goal of the cluster reconstruction is to determine the energy and position of a particle that generated the electromagnetic shower in the detector. One complication in reconstructing clusters is that there can be more than one cluster per event which leads to issues in trying to determine which cluster is associated with a reconstructed track. During E06-010, the cluster reconstruction algorithm was updated to save and consider multiple clusters, as well as compare the cluster position to the position of the reconstructed track projected onto the shower and preshower planes [82]. However for E06-014, it was found that with the difference in particle triggering[3] and track quality cuts (discussed in Chapter 8), that there was minimal improvement when employing the updated reconstruction algorithm. As a result E06-014 chose not to use the updated reconstruction algorithm. A comparison between the reconstruction algorithm used in E06-014 and E06-010 can be found in Appendix B. The following cluster algorithm was used in E06-014 to identify a cluster in the shower and preshower:

- Search all blocks in the shower for the block with the largest energy, known as the central block.

[3]The main differences in the BigBite triggering for electron signals between E06-010 and E06-014 was the inclusion of the Čerenkov detector into the trigger and a higher shower energy threshold.

- Sum over the eight blocks surrounding the central block to get the cluster energy (nine total blocks in the sum.)
- This procedure is repeated for all possible clusters and the largest cluster is saved.
- Corresponding to the largest cluster in the shower detector, the preshower cluster is formed by finding the central block, and summing over the five surrounding blocks (six total blocks in the sum).

The energy E of a cluster is calculated as the sum of the energies deposited in all of the blocks in the cluster

$$E = \sum_{i=1}^{M} E_i, \tag{7.22}$$

and the X-Y position are calculated using an energy weighting method

$$X = \sum_{i=1}^{M} \frac{E_i X_i}{E},\ Y = \sum_{i=1}^{M} \frac{E_i Y_i}{E}, \tag{7.23}$$

where M is the number of blocks in the cluster and i is the i^{th} block in the cluster.

7.1.3.1.3 Energy Calibration The cosmic ray calibration is only a rough calibration; to use the calorimeter as a way to identify particles, a more precise energy calibration needs to be performed. Through the use of particles with known scattering energies, one can calibrate the ADC response of each block in the preshower and shower detectors to reproduce the known energies. This resulted in a set of 243 coefficients C_i (54 coefficients for the preshower and 189 coefficients for the shower), that transformed their ADC amplitudes into an energy in MeV, according to

$$E_i = C_i \left(A_i - P_i\right) = C_i A_{pi}, \tag{7.24}$$

where A_i is the raw amplitude of the i^{th} ADC, P_i the ADC pedestal[4] and A_{Pi} is the pedestal subtracted ADC. The coefficients for each block were determined by minimizing the χ^2, which is defined as the squared difference between a known energy, in the case of E06-014 this was the reconstructed momentum, and the measured energy in the calorimeter. A linear minimization method was used to solve for the block coefficients, C_i. Letting P_{trk} be the reconstructed momentum, calculated from tracking, C_j the coefficient of the j^{th} block, and A_j the pedestal subtracted ADC amplitude measured in the j^{th} block. Then for N electron events (selected using PID cuts discussed in Chapter 8), χ^2 is given as

$$\chi^2 = \sum_{i=1}^{N} \left(P^i_{trk} - \sum_{j=0}^{M} C_j A^i_j \right)^2 \tag{7.25}$$

$$= \sum_{i=1}^{N} \left[\left(P^i_{trk}\right)^2 + \left(\sum_{j=0}^{M} C_j A^i_j \right)^2 - 2P^i_{trk} \sum_{j=0}^{M} C_j A^i_j \right], \tag{7.26}$$

where M is the total number of blocks in the preshower and shower clusters. The set of linear equations can be obtained by setting the derivative of χ^2 with respect to C_k equal to zero:

$$\frac{\partial \chi^2}{\partial C_k} = 0, \tag{7.27}$$

$$2 \sum_{i=1}^{N} \left(\sum_{j=0}^{M} C_j A^i_j \right) A^i_k - 2 \sum_{i=1}^{N} P^i_{trk} A^i_k = 0, \tag{7.28}$$

$$\sum_{i=1}^{N} \left[C_j \left(\sum_{j=0}^{M} A^i_j A^i_k \right) \right] = \sum_{i=1}^{N} P^i_{trk} A^i_k. \tag{7.29}$$

[4]Electric noise leads to a non-zero signal in the ADC, even when there is no signal in the PMT. This non-zero ADC value is known as the pedestal.

The system of linear equations can now be expressed in matrix form as follows:

$$MC = B, \tag{7.30}$$

where

$$B = \begin{pmatrix} \sum_{i=1}^{N} P_{trk}^{i} A_{0}^{i} \\ . \\ . \\ . \\ \sum_{i=1}^{N} P_{trk}^{i} A_{M}^{i} \end{pmatrix}, \tag{7.31}$$

$$C = \begin{pmatrix} C_0 \\ . \\ . \\ . \\ C_M \end{pmatrix}, \tag{7.32}$$

and the matrix elements of matrix M can be written as

$$M_{lm} = \sum_{i=1}^{N} A_{l}^{i} A_{m}^{i}. \tag{7.33}$$

Then by inverting Equation 7.30

$$C = M^{-1}B, \tag{7.34}$$

the coefficients can be obtained.

Ideally the BigBite calorimeter would be calibrated using elastic electrons from electron-proton scattering, since the elastic scattering energy (ignoring the electron mass[5]) can be

[5]Electron mass of 0.511 MeV is much smaller relative to other masses and energies and can be neglected.

calculated from Equation 7.19. However, during E06-014 elastic data on a ^{2}H target was only taken at one beam energy setting (E = 1.23 GeV), which covered only a portion of the BigBite acceptance. Therefore, the calorimeter calibration was done at production beam energies of 4.74 GeV and 5.89 GeV on a ^{3}He target, and used electron PID cuts described in Section 8 to select electrons. During a portion of the early production running, one of the summing modules, which is responsible for adding the amplitudes of several blocks at the hardware was over loaded (see Sections 4.4.6.2 and 4.5), resulting in several blocks producing amplitudes lower than expected. These blocks did not have a significant impact on the measured asymmetries (Section 8.2.5) and were compensated by having a larger coefficient associated with them. Coefficients for blocks near the outer perimeter tended to be slightly smaller than the mean coefficient value. This can be seen in Figure 7.21, which shows the calibration coefficients of the preshower and shower blocks after the initial calibration. Figure 7.22 shows the calorimeter energy after using the initial calibration results seen in Figure 7.21. The top left panel shows the total energy deposited in the preshower and shower, the top right panel shows the difference between the total energy in the calorimeter and the reconstructed momentum, normalized by the momentum. This allows the resolution of the BigBite calorimeter to be calculated. For E06-014 the calorimeter resolution was measured to be between 8-9% throughout the experiment. The bottom left panel of Figure 7.22 shows the total calorimeter energy divided by the momentum. By calibrating the calorimeter with electrons and ignoring the electron mass (0.511 MeV), the reconstructed energy should be roughly equal the deposited energy in the calorimeter. Because of this the electrons will fall at E/p $\simeq$ 1 compared to minimum ionizing particles, such as pions, fall at lower E/p values; thus the quantity E/p can be used to identify particles. Finally in the bottom right panel the total calorimeter energy vs. the reconstructed momentum is plotted. The red line is a guide for the eye which traces out the values where the energy equals the momentum. For comparison, Figure 7.23 shows the results of the shower calibration after the summing

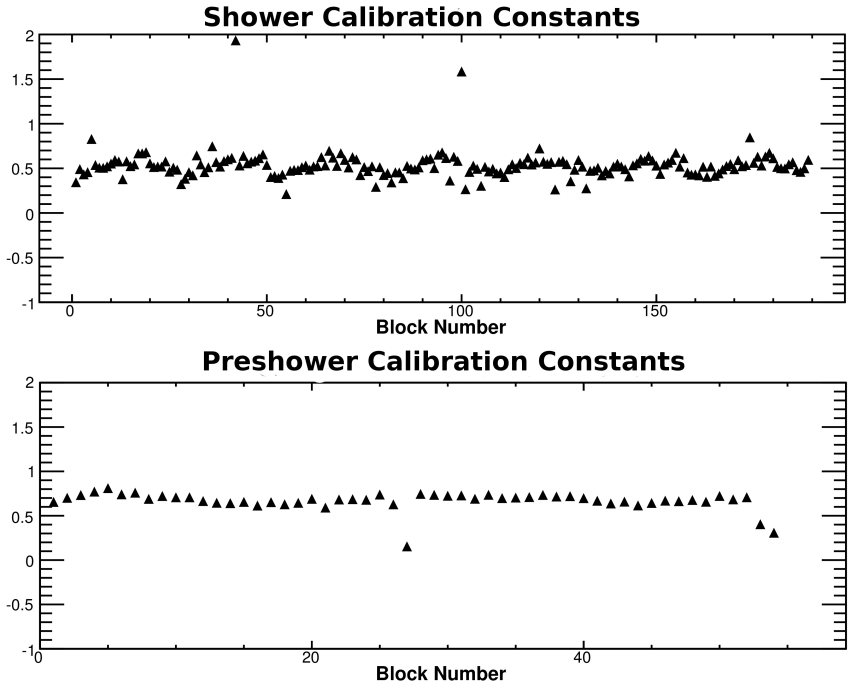

Figure 7.21: Energy coefficients for the initial calibration of the preshower and shower detectors, in which 5.89 GeV electrons were scattered from a ^{3}He target.

module was fixed.

7.1.3.1.4 Elastic e-p Cross-Check Although elastic electrons from e-p scattering could not be used to calibrate the full acceptance of the calorimeter, the initial calibrations coefficients obtained from production runs can be applied to the elastic data to check if the calibration coefficients lead to reasonable results. The elastic data provides a good consistency check because the elastically scattered electron energy is known (Equation 7.19). Figure 7.24 shows the results of the calorimeter calibration, after applying the calibration coefficients computed from the production runs (Figure 7.21) to the elastic data. In addition to applying the electron cuts described in Chapter 8, an additional cut was applied to select elastic scattering electrons by cutting on the proton invariant mass peak centered around W = 0.938 GeV. Applying the calibration coefficients to the elastic data results in a calorimeter

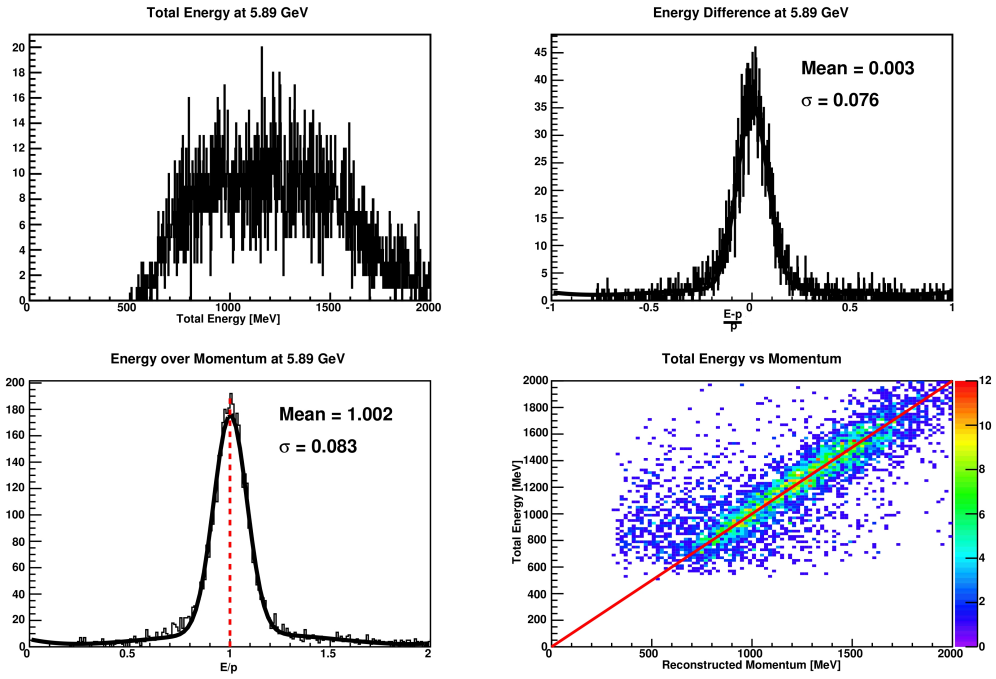

Figure 7.22: Results of the initial calorimeter calibration before the summing module was fixed. The top left panel shows the total energy deposited in the preshower + shower. The top right panel shows the difference of the total energy in the calorimeters and the reconstructed momentum normalized by the momentum. The bottom left panel shows the total calorimeter energy divided by the momentum. Finally in the bottom right panel the total calorimeter energy vs the reconstructed momentum is plotted. The red line is a guide for the eye which traces out the values where E = p.

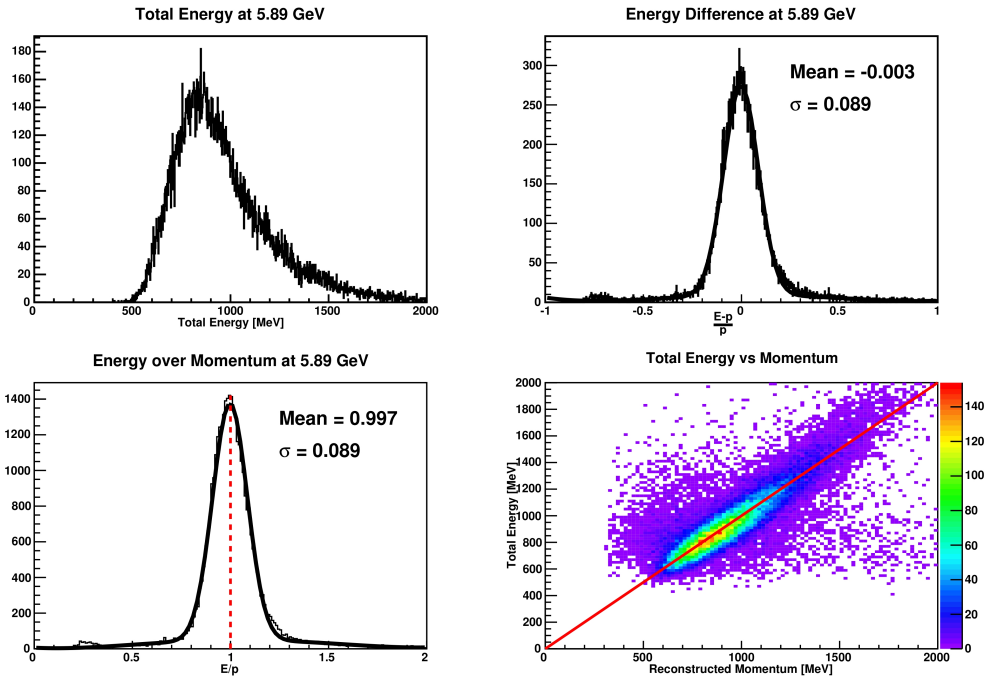

Figure 7.23: Results of the calorimeter calibration after the summing module was fixed. The top left panel shows the total energy deposited in the preshower + shower. The top right panel shows the difference of the total energy in the calorimeters and the reconstructed momentum normalized by the momentum. The bottom left panel shows the total calorimeter energy divided by the momentum. Finally in the bottom right panel the total calorimeter energy vs the reconstructed momentum is plotted. The red line is a guide for the eye which traces out the values where E = p.

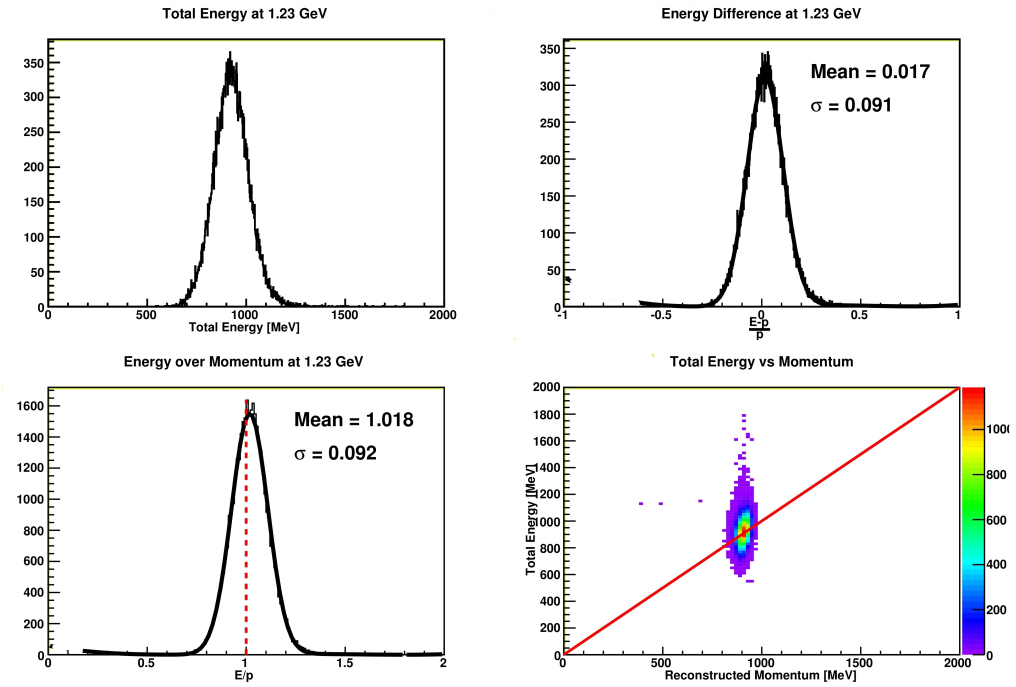

Figure 7.24: Results of applying the calibration coefficients from production data to elastic data. The top left panel shows the total energy deposited in the preshower + shower. The top right panel shows the difference of the total energy in the calorimeters and the reconstructed momentum normalized by the momentum. The bottom left panel shows the total calorimeter energy divided by the momentum. Finally in the bottom right panel the total calorimeter energy vs the reconstructed momentum is plotted. The red line is a guide for the eye which traces out the values where E = p.

response that is expected.

Due to the BigBite calorimeter being in the trigger, every time the trigger hardware is changed the energy needs to be re-calibrated. There were a total of five shower calibrations that needed to be done throughout the experiment. Table 7.4 lists the results for all of the shower calibrations that were performed. The initial calibration was done at the start of the experiment and cross-checked with elastic e-p data. The second calibration was performed after the shower summing module was repaired. The third and fourth calibrations were performed after the high voltages on the shower were changed. The final calibration was

performed when electron beam energy was changed from 5.89 GeV to 4.74 GeV[6].

7.1.3.2 Calorimeter Position

While the calorimeter's energy measurement is a powerful particle identification tool (Section 8.2.3.2), the energy deposited in the calorimeter must also have a valid track reconstructed in the MWDC associated with it. In order to ensure that the energy found in the calorimeter has a valid track, the difference between the reconstructed track projected onto the calorimeter planes and the calorimeter cluster positions (defined in Equations 7.35 and 7.36) can be studied. The vertical difference can be defined as

$$\Delta x = x_{cal} - \left(x_{trk} + dx'_{trk}\right), \tag{7.35}$$

where x_{cal} is the vertical calorimeter cluster position given by Equation 7.23, x_{trk} and x'_{trk} are the vertical position and the slope of the reconstructed track at the first MWDC, and d is the distance along the z-axis in detector coordinate units. Similarly the horizontal difference between the calorimeter and reconstructed track positions can be defined

$$\Delta y = y_{cal} - \left(y_{trk} + dy'_{trk}\right). \tag{7.36}$$

By minimizing Δx and Δy, one can assure that the energy cluster in the calorimeter has a valid reconstructed track. A precise location of the calorimeter position is difficult to determine due to the poor energy resolution of the calorimeter, however because of the good tracking resolution, the position d of the calorimeters can be adjusted to minimize the differences. A misalignment in d leads to large misalignments at larger angles. Figure 7.25 shows an example of using an inaccurate (left panel) and accurate (right panel) value for the

[6]The first run period with the electron beam at an energy of 4.74 GeV was mostly unpolarized (and not used in the analysis), therefore a calorimeter calibration was not performed.

Table 7.4: Summary of BigBite calorimeter calibration results.

Energy[GeV]	Calibration Reason	Calorimeter Resolution [%]	E/p Mean	E/p Resolution [%]
1.23	Elastic e-p check	9.10	1.02	0.92
5.89	Initial Calibration	7.60	1.00	8.30
5.89	Summing module fixed	8.90	1.00	8.90
5.89	HV change on calorimeter	9.10	0.99	9.10
5.89	HV change on calorimeter	8.40	0.98	8.40
4.74	Beam energy change	8.70	0.98	8.70

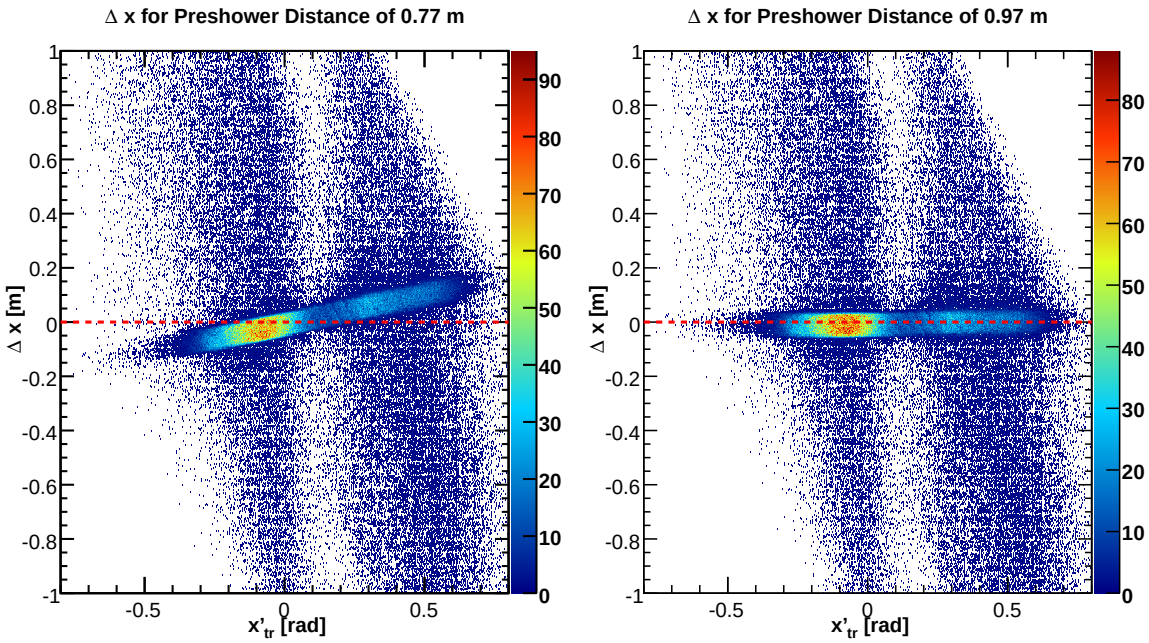

Figure 7.25: The difference between the reconstructed tracks projected onto the preshower plane and the preshower cluster position are plotted against the vertical slope of the track at the first MWDC are plotted for two different values of the detector position. The left plot, using an inaccurate value of d= 0.77 m, shows the large deviation from zero at the two extreme angles. Where as in the right plot, using an accurate value of d = 0.97 m, shows the alignment (no deviation from zero) of the reconstructed track and preshower cluster position.

preshower distance by plotting Δx as a function of x'_{trk}. For the inaccurate distance of d = 0.77m, there are large deviations from Δx = 0 (red dashed line) at the two extreme angles. However, when an accurate preshower distance of d = 0.97 m is used, the deviation from Δx at the extreme angles is greatly reduced showing that the projected track and cluster positions are in agreement with one another. A similar study was repeated by D. Parno [75] for the shower detector. The final calorimeter positions are listed in table 7.5.

Table 7.5: Calibrated distances d between first MWDC and calorimeter layers.

Layer	d [m]
Preshower	0.97
Shower	1.28

7.1.3.3 Energy Loss

As the electrons leave the beam pipe they interact with several materials before they scatter from the ^{3}He target, and then several more materials after they scatter from the target. As the electrons traverse materials they will loose energy through various process, primarily due to Bremsstrahlung radiation. The radiation length X_0, which is the characteristic length scale of these interactions with materials, can be defined as the mean distance in a material over which an electron's energy is reduced to $1/e$ of its initial value [150]. The materials encountered by the electrons on their way from the beam pipe to the target are summarized in Table 7.6, like wise, as the materials that the electrons encounter along their way from the target to the BigBite detector are summarized in Table 7.7. The total radiation length before scattering from the target is 0.0029 radiation lengths, where as the total radiation length from the target to the BigBite detector is 0.0298 radiation lengths. As can be seen in Table 7.7 the target cell side wall is the main contributor to the radiation length.

The energy loss of the electrons can be calculated and implemented into the optics package, allowing the reconstructed momentum to be corrected for energy loss. However, GEANT4 simulations of the E06-014 experiment showed that the most likely energy loss was about 0.1%, which corresponds to only a few MeV [75, 151]. Applying this correction on an event by event basis resulted in no significant change in the final momentum. Therefore no energy loss corrections are applied in this analysis.

Table 7.6: Materials in the path of incoming electrons.

Object	Material	X_0 [cm] [%]	Thickness [cm]	Thickness [X_0]
Beam pipe exit window	Be	35.28	0.0254	0.00072
Gas in target enclosure	^{4}He	5.281×10^5	22.86	0.00004
Target cell entrance window	GE-180 glass	7.038	0.0121	0.00172
Gas in first half of cell	^{3}He	4.342×10^4	19.8	0.00045
Total			42.70	0.0029

Table 7.7: Materials in the path of the scattered electrons. The thicknesses were calculated using a nominal scattering angle of 45°.The type of plastic in the yellow cover is unknown; values were taken for polycarbonate, which has relatively short radiation length compared to other plastics.

Object	Material	X_0 [cm] [%]	Thickness [cm]	Thickness [X_0]
Gas between vertex and sidewall	^{3}He	4.342×10^4	1.34	0.00003
Target sidewall	GE-180 glass	7.038	0.156	0.02216
Gas in target enclosure	^{4}He	5.281×10^5	79.05	0.00015
Yellow cover	Plastic	34.5	0.0889	0.00257
Open air	Air	3.042×10^5	150.0	0.00493
Total				0.0298

7.1.3.4 PreShower Sum TDCs

The final calibration that was performed on the BigBite calorimeter consisted of applying offsets to the TDCs corresponding the the 26 preshower sums[7], resulting in each of the 26 electron timing peaks being aligned to a common TDC channel (TDC channel zero). By aligning all of the timing peaks to a common channel, applying timing cuts on the preshower sums was simplified.

7.1.4 Scintillator Plane

In addition to having the BigBite calorimeter consisting of the preshower and shower layers for particle identification, there was also a scintillator layer that was positioned between the preshower and shower layers to provide additional particle identification. The BigBite scintillator consisted of 13 plastic scintillator bars, with two PMTs attached to each side. The signal in the scintillator is proportional to the energy deposited by the particle (i.e. hadrons, such as pions, will leave less energy in scintillator than electrons). The signals detected by the PMTs were sent to ADC and TDC modules to record energy and timing information.

The ADC signals were calibrated by gain matching the ADC responses, which involved adjusting the high voltage applied to each PMT so that all PMTs produce the same ADC response. The ADC responses were further calibrated by J. Huang during the E06-010 experiment [102]. These calibration coefficients were checked and found to be valid for E06-014. Additionally, the TDC signals were also found to be aligned to a common TDC channel across all 13 bars (also calibrated by J. Haung during E06-010 [102]). However the timing resolution of the TDCs were not precise enough to distinguish between hadrons (pions) and electrons. Therefore the TDC timing was not used during the E06-014 analysis.

[7]The BigBite triggers used the shower calorimeter as a common stop, resulting in the shower timing begin self-timed.

7.1.5 Čerenkov Detector

E06-014 served as the commissioning experiment for the new BigBite gas Čerenkov [87], consisting of two columns, each column containing 10 spherical and flat mirrors which reflected Čerenkov light into mirrors corresponding PMTs (20 PMTs total, 10 per column). Each PMT has associated with it an ADC and TDC. E06-014 originally began running with CAEN v792 VME ADCs, however due to high rate conditions, the ADCs exhibited a large pedestal instability. This would result in the ADC signal showing up well under the beam-off pedestal channel. This displacement was *not* caused by a rate induced DC bias at the PMT, but rather a failure to integrate the input signal correctly [87]. This issue was resolved by moving the signals to FASTBUS 1881 ADCs. Even with the 1881 ADCs there was a slight shift between the beam-on and beam-off pedestal positions on the small angle side of the detector, which are discussed in further detail in Appendix C. The TDCs used by the Čerenkov detector were 1877 TDCs. The Čerenkov detector was integrated into the main BigBite trigger (see section 4.4.6), with the primary purpose of increasing electron rates by rejecting pions from triggering the DAQ. An analysis of the Čerenkov performance is presented in Section 8.2.3.1. In this section an overview of the ADC calibration, used to measure the number of photo-electrons, and the TDC calibrations will be discussed. The ADC calibration consists of two parts: first, a calibration that was done near the end of the experiment using an LED setup, and then a cross calibration of the earlier production data to the later LED calibrated data was performed. As it will be shown the pedestals associated with small angle PMTs needed special attention due to the high rates.

7.1.5.1 ADC Calibrations

7.1.5.1.1 LED Calibrations The ADC signal is the integrated charge of electrons from Čerenkov radiation produced via the photo-electron effect. Thus, the ADC signal is pro-

portional to the number of photo-electrons produced, and must be calibrated to correctly quantify the number of photo-electrons measured. Similarly to the gain matching of the PMTs used in the BigBite calorimeter, the PMTs used in the Čerenkov detector also needed to be gain matched in order to give the same response across the detector. The gain matching is done in two steps: first, a rough calibration during the experiment, and then a more precise calibration was done after the experiment using software. Gain matching the PMTs was done by adjusting the HV so that the one photo-electron peak of each PMT fell at the same ADC channel. The one photo-electron peak was produced though the use of a LED flasher system that was installed in the Čerenkov tank. The set-up consisted of adding an LED, which is shrouded to reduce its light output, to each PMT. The LEDs are then powered/pulsed through a BNC connection on the PMT assembly's external flange. It was found that by pulsing only 2-3 of the LEDs (i.e. top, middle, bottom) on one side of the tank, that the one photo-electron signal was optimized in the correlated PMTs on the opposite side of the pulsed LEDs [152]. The average photo-electron response of the LED pulser system was found to be between about 1.5-2.5 photo-electrons. Figure 7.26 shows a typical ADC response measured using the LED pulser system, in which the pedestal ($\sim$ ADC channel 478) and one photo-electron peak ($\sim$ ADC channel 524) are clearly visible, as well as a bit of two photo-electron peak which presents it self as a shoulder ($\sim$ ADC channel 570).

While the gain matching during the experiment serves as a good first order calibration, a more stringent calibration can be done in software. The precise location of the one photo-electron peak can be extracted by fitting the entire ADC spectrum. The ADC signal from the LED runs were fitted with a convoluted Poisson-Gaussian and background function [153]

$$S(x)_{real} = \int S(x')B(x - x')dx', \tag{7.37}$$

where $S(x)$ is the ideal ADC signal and $B(x)$ is the background function.

$$S(x) = \sum_{n=1}^{7} \frac{\mu^n e^{-\mu}}{n!} \left(\frac{1}{\sigma_1 \sqrt{2\pi n}} \right) exp \left(- \frac{\left(x - Q_0 - Q_{sh} - nQ_1\right)^2}{2n\sigma_1^2} \right) \tag{7.38}$$

and

$$B(x) = \left[\left(\frac{(1-w)}{\sigma_0 \sqrt{2\pi}} \right) exp \left(- \frac{\left(x - Q_0\right)^2}{2\sigma_0^2} \right) + w\alpha\theta(x - Q_0) exp\left(-\alpha\left(x - Q_0\right)\right) \right] e^{-\mu}. \tag{7.39}$$

Equation 7.38, models a nearly ideal ADC signal, that corresponds to the Poisson-Gauss convolution with μ being defined as the mean number of photoelectrons collected by the first dynode, n is the number of photoelectrons, Q_1 is the average charge at the PMT output when one electron is collected by the first dynode, σ_1 is the standard deviation of the charge, Q_{sh} is the effective spectrum shift due to background and Q_0 is the position of the pedestal. Equation 7.39 is included in the fit to account for PMT pedestal, noise and other backgrounds that present themselves in the ADC spectrum. Associated with the pedestal position, Q_0 is the pedestal resolution σ_0, w is the probability that the measured signal will have background related to thermoemmission, noise initiated by the measured light, etc. [153], α is the coefficient of the exponential decrease of the fore-mentioned background and finally θ is the step function. Figure 7.26 shows a representative sample of the ADC response of PMT 4. The red line in the figure is the fit obtained from using Equations 7.38 and 7.39, from that fit values for the pedestal subtracted ADC, the one photo-electron ADC location was found to be at about 46 ADC channels. The ADC signal was then multiplied by a coefficient so that the one photo-electron peak was aligned to ADC channel 30[8]. This was repeated for all ADCs so that the one photo-electron for each PMT fell at ADC channel 30.

[8]The channel in which the one photo-electron peak is aligned is some what arbitrary. Channel 30 was selected for E06-014 because the one photo-electron peak was near this channel for most PMTs

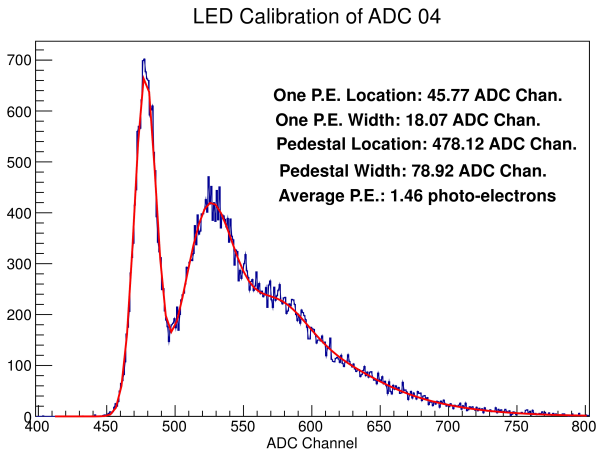

Figure 7.26: The ADC response of PMT 4 measured with the LED flasher system. The red line is the fit results to the ADC spectrum.

7.1.5.1.2 Cross-Calibration

Although the LED flasher was used to gain match the Čerenkov PMTs every time there was a change to the high voltage or when a PMT was swapped out, not all LED runs were saved for software calibration. As a result, the production ADCs that were calibrated with LED runs were used to cross-calibrate earlier production ADCs. In order to accurately compare the LED calibrated ADCs to the uncalibrated ADCs, the pedestals must first be removed from the uncalibrated ADCs. When removing the pedestals from the uncalibrated production ADCs, it was discovered that the pedestals of the PMTs located on the small angle side (closest to the beam) of the Čerenkov disagreed significantly with those given by the LED runs, when the electron beam was on. The pedestals with beam on were selected by looking at T8 trigger (1024 Hz pulser) which should select mostly uncorrelated background events. Figure 7.27 shows the discrepancy between the LED pedestals (represented by the blue histograms) and the pedestals measured with the electron beam on (represented by the red histograms) for the small angle side of the Čerenkov. It was determined that the pedestal discrepancy was due to the higher rates on the small angle PMTs, which caused the pedestals to broaden and shift. A more detailed discussion concerning the Čerenkov ADC pedestals can be found in Appendix C. Due to the shift in the beam-on pedestals, which in turn causes the ADC spectrum to shift to lower channels resulting in fewer photo-electrons, a correction offset needed to be applied to all PMTs located on the small angle side when the electron beam was turned on (even those calibrated with via LED runs). This correction was applied via a run-time stamped database that applied the correct pedestal correction depending on the beam current. Once the pedestals were corrected, the uncalibrated ADCs were multiplied by a coefficient so that the mean photoelectrons detected match those measured by the LED calibrated ADCs.

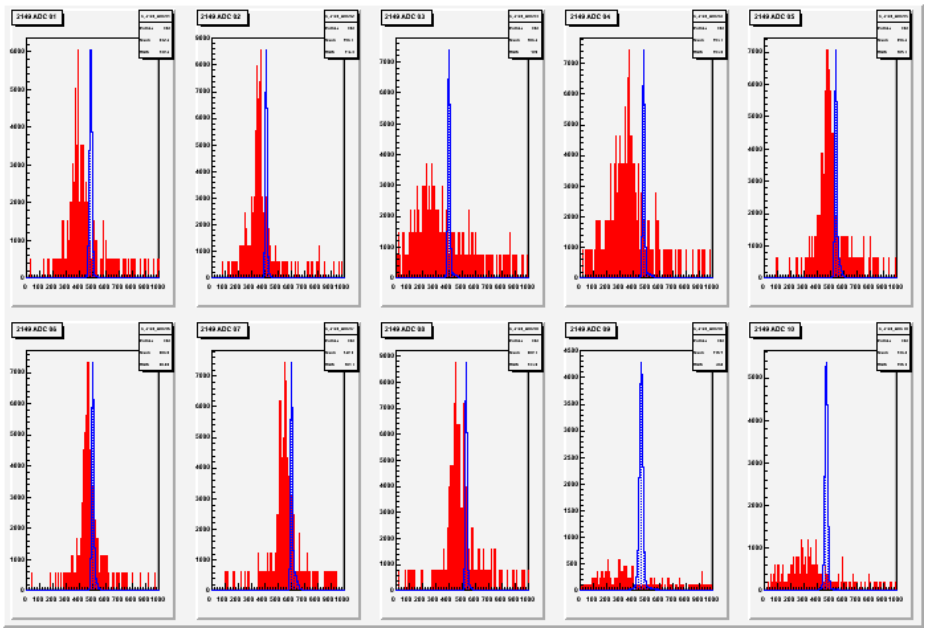

Figure 7.27: Pedestal positions for the small angle Čerenkov PMTs. The shift between the beam-on pedestals (red histograms) and LED pedestals (blue histograms) are due to the high rates at the small angle side.

7.1.5.2 TDC Calibration

Complimentary to measuring the produced photoelectrons using ADCs, the particle timing in the Čerenkov is also measured. The particle timing is recorded with TDCs that are associated with each PMT. The Čerenkov TDCs will provide another means to reject pions and in turn select electrons. The electron timing peak in each TDC is located at a different TDC channel, thus in order to make applying cuts to the TDCs more convenient, an offset is applied to each TDC spectrum so that the electron peak is aligned to a common TDC channel (channel 0). The location of the electron timing peak was extracted from a Gaussian fit to the TDC peak and its value was subtracted from the TDC spectrum, resulting in an overall shift in the TDC spectrum. Figure 7.28 shows an example of the fits used to obtain the position of the timing peak for the large angle side of the Čerenkov detector. PMTs at the bottom of the Čerenkov detector (PMTs 8, 9, 19 and 20) fell outside of the electron

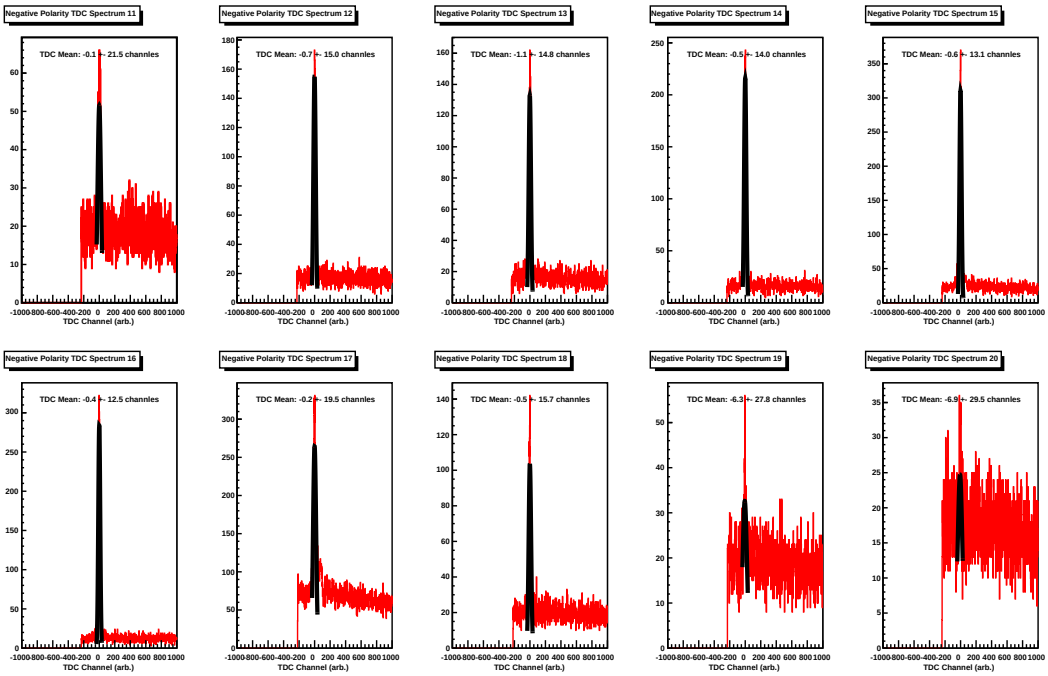

Figure 7.28: Fits used on large angle side PMTs to extract the mean TDC timing peak location.

acceptance, resulting in positron data being used to calibrate those regions. Figure 7.29 shows the final results of the TDC calibrations for PMT 3, in which the mean TDC value is plotted as a function of the BigBite run number. The upper and lower red lines show the location of the TDC cut window that was used in the E06-014 analysis of ± 50 TDC channels (or $\pm$ 25 ns).

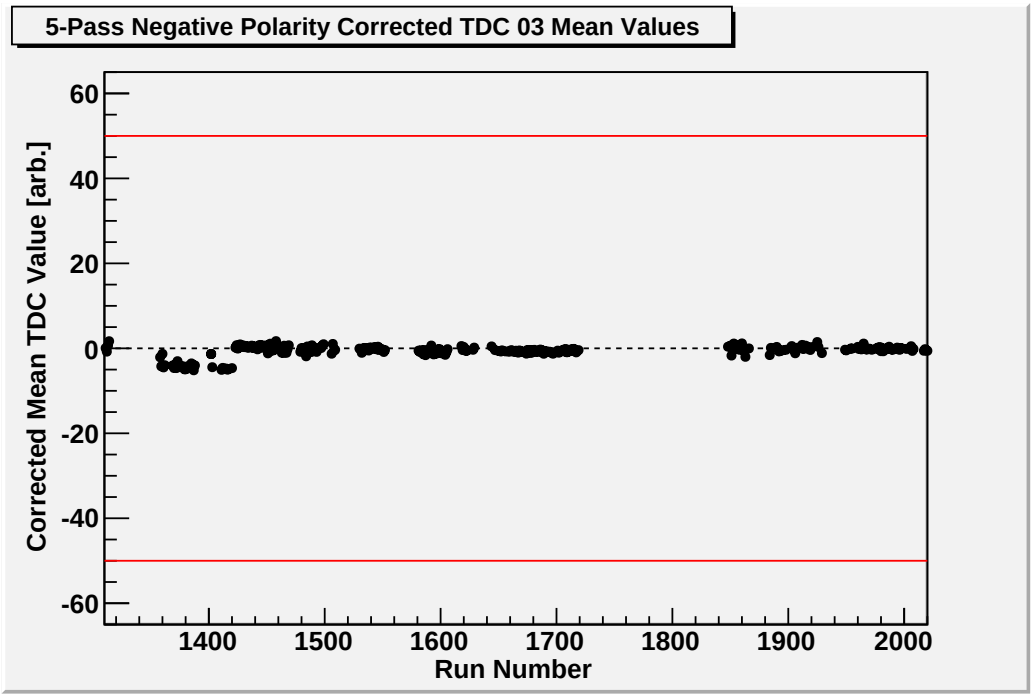

Figure 7.29: Mean TDC timing peak location for PMT 3 after correcting with TDC offset. The upper and lower red lines mark the production Čerenkov TDC cut positions at $\pm$ 50 TDC channels.

7.2 High Resolution Spectrometer Calibration

The LHRS, like the BigBite detector is made up of several sub-detectors that when combined produce highly accurate particle information. However before that information can be used the LHRS detector package first needs to be calibrated. As presented in Section 4.4.5, the LHRS consists of: VDCs, a scintillator, calorimeters, and a gas Čerenkov. This section will briefly summarize the LHRS calibrations, which except for the optics calibration (performed by J. Huang [102]), were performed by D. Flay [135].

7.2.1 Vertical Drift Chambers

The principle of the VDC calibration is similar to that used to calibrate the BigBite MWDCs discussed in Section 7.1.1. The LHRS VDCs are part of the standard Hall A equipment [78] and only required a t_0 calibration. The t_0 timing was extracted by identifying the rising edge of the drift time spectrum.

7.2.2 Optics

Time constraints during E06-014 resulted in not taking enough runs to do a proper independent optics calibration (no LHRS sieve slit runs were taken). However given E06-010's similar experimental setup,their optics calibration was able to be used in the E06-014 analysis. The validity of using E06-010's optics calibration was check through the use of the target vertex and momentum reconstruction.

The optics calibration during E06-010 was performed by J. Huang [102], following the general procedure of [154].

The Z target vertex reconstruction procedure was similar to that used in the BigBite target reconstruction (Section 7.1.2. Carbon foil targets with known positions were used to calibrate the reconstructed target; achieving a target vertex resolution of about 6 mm.

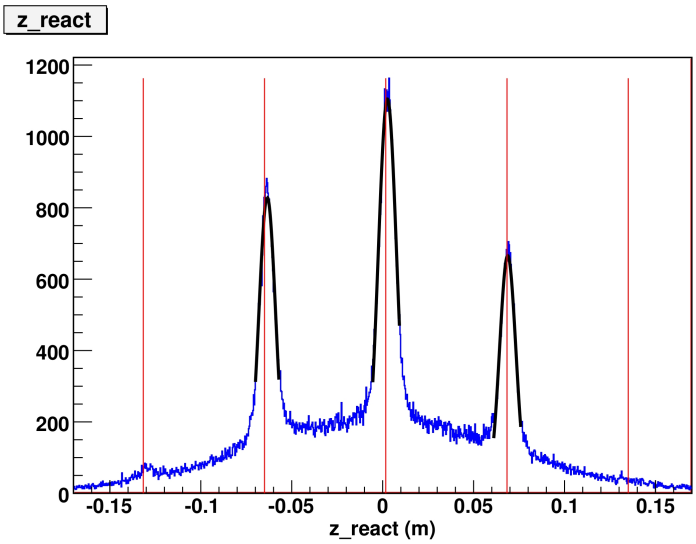

Figure 7.30: LHRS z-target vertex reconstruction of a carbon run taken during E06-014 using the optics calibration from E06-010. The red lines mark the positions of the carbon foils. The plot was produced by D. Flay [135].

The target vertex reconstruction of a carbon foil run taken during E06-014 can be seen in Figure 7.30.

The reconstructed out of plane (θ_{tg}) and in plane (ϕ_{tg}) angles were calibrated using carbon foil runs with the sieve slit positioned in front of the LHRS. Each good event detected in the LHRS corresponds to a particular carbon foil and one of the LHRS sieve holes. Using this information and the angle of the actual vertex trajectory (obtained from the survey reports [155]), the angles were optimized by minimizing the difference between the calculated and actual angles.

The momentum was calibrated using a run set similar to that which was used in the scattering angle calibrations. The full momentum range of the spectrometer was covered by moving the carbon elastic peak across the focal plane; where each settings chose a specific carbon ground or excited state. An optimization was then performed on all momentum setting simultaneously, achieving a final resolution of 5×10^{-4} [86, 102].

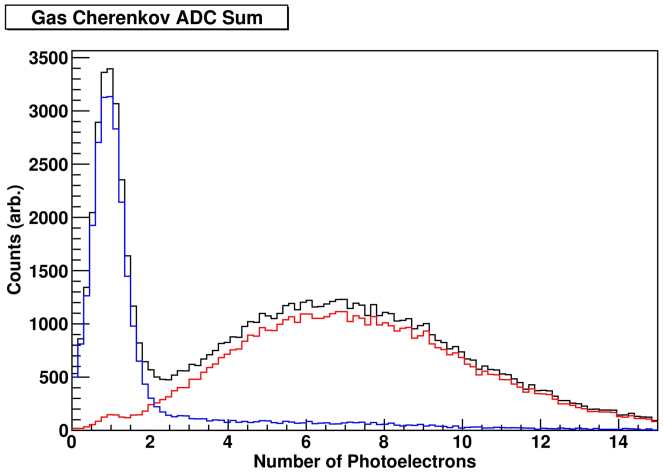

Figure 7.31: A typical LHRS Čerenkov ADC sum after calibration plotted against photoelectron number. Cuts on the pion rejector (Sections 7.2.5 and 8.3.2) reveal pion (blue histogram) and electron (red histogram) like events in the Čerenkov. Plot produced by D. Flay [135].

7.2.3 Gas Čerenkov Detector

The calibration of the LHRS gas Čerenkov was similar to that of the BigBite gas Čerenkov (discussed in Section 7.1.5). The single-photoelectron peak of each pedestal subtracted ADC was aligned to ADC channel 200, resulting in all of the PMTs giving the same ADC response. The Čerenkov ADC spectra from each PMT were then added together to form a Čerenkov ADC sum, providing a means by which to separate pion from electron like events. The results of the Čerenkov ADC sum are shown in Figure 7.31 for pion (blue histogram) and electron (red histogram) like events determined by cuts on the E/p distribution (discussed in Sections 7.2.5 and 8.3.2), and total events (black histogram).

7.2.4 Scintillators

A proper calibration of the scintillator is essential, since it was used in the main LHRS trigger. The TDC peaks in the right paddles of the S2m plane were first aligned to a common

arbitrary value. Then, the left paddles of the S2m plane were aligned to the same values as the right paddles. The final steps of the calibration involved repeating the procedure used on the S2m plane for the S1 plane TDC times. This calibration resulted in the proper timing of charged events.

7.2.5 Calorimeters

The LHRS Calorimeter, consisting of two pion rejection layers, also followed a similar calibration to that of the BigBite calorimeter calibration (discussed in Section 7.1.3. The ADC spectra for each block was gain-matched by aligning the pion peak to a common channel number. Pions were selected using a Čerenkov cut of less then 2.5 photoelectrons and aligning the pion peak in both pion rejection layers to ADC channel 100. The fact that the LHRS calorimeter is made up of two pion rejectors (partial shower calorimeters) and not a full shower, is reflected in the achieved energy resolution of $\sim 18\%$.

The ratio of the combined deposited energy from both layers to the reconstructed momentum of the track is shown in Figure 7.32, and reveals excellent pion (blue histogram with Čerenkov ADC sum < 2.5 photoelectrons) and electron (red histogram with Čerenkov > 2.5 photoelectrons) separation.

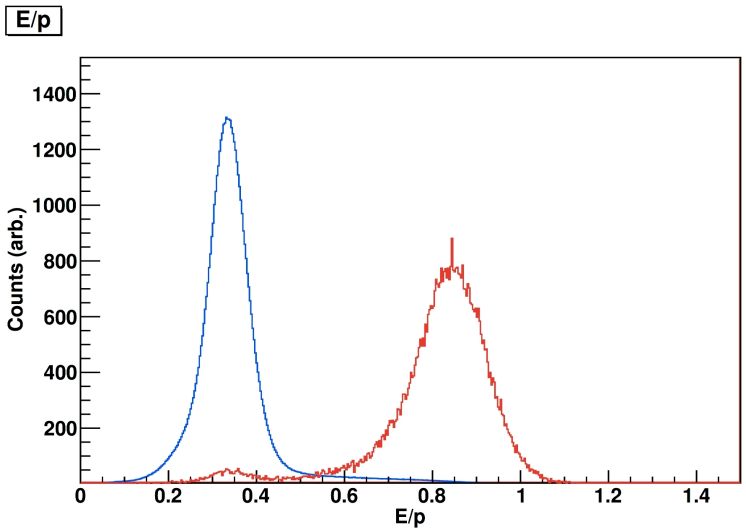

Figure 7.32: Typical LHRS E/p distribution for pions (blue histogram), selected with Čerenkov ADC sum < 2.5 photoelectrons and electrons (red histogram), selected with Čerenkov ADC sum $>$ 2.5 photoelectrons. The pion curve has been scaled down so it can be viewed with the electron curve. Plot produced by D. Flay [135].

CHAPTER 8

DATA ANALYSIS

With the detectors calibrated (Section 7), the frame work is now in place to begin to extract physics information from the collected data. This Section will discuss the analysis performed on the the data collected from indecent beam energies of 4.74 and 5.89 GeV. First, in Section 8.1, an overveiw of the analysis procedure, including how detected electronic signals are converted into physical quantities using the Hall A software (Section 4.4.9), will be presented. Sections 8.2.1 (8.3.1) and Sections 8.2.2 (8.3.2) will review the cuts used to select quality data and particular particle types for the BigBite (LHRS) detectors. Sections 8.2.3 and 8.3.3 will study the performance of the BigBite and LHRS detectors used during E06-014. Finally, Sections 8.3.5 and 8.2.5, will focus on how the data was used to construct the electron scattering cross-sections and double spin asymmetries.

8.1 Analysis Procedure

8.1.1 Data Processing

In order to analyze the data that was collected during E06-014, it first has to be converted from raw electronic signals stored in CODA files to organized physical quantities that are

stored in ROOT files. The conversion from raw CODA files to finalized ROOT files, was done using the Hall A *ANALYZER* (Section 4.4.9), through a two step process. The first step called the *replay* step, relied on the Hall A *ANALYZER* to process the raw CODA files. The *ANALYZER* included analysis packages for all of the Hall A detectors (those contained in LHRS and BigBite), and allows electronic signals to matched to their hardware sources through time stamped Database (DB) files. A small production data set and special calibration runs were then replayed to calibrate the various hardware components (Section 7), resulting in higher level DB files that transformed hardware signals into energy, currents, positions, etc. A full replay of all the calibrated production data was then performed on the JLab batch farm, taking advantage of the many cpu cores and memory contained on the batch farm [156].

The Hall A *ANALYZER* processes events during a replay in three stages [146]:

- The *decoding* stage converts raw CODA events into physical values. For example TDC values read from respected wires in the drift chamber are converted into drift times.

- The *course processing* stage reconstructs rough tracks and does quick calculations of various detector variables.

- The *fine processing* stage uses the detector variables produced during the *course processing* stage as initial inputs (i.e. beam position) to generate the final outputs (i.e. cluster positions, energy, hit times, etc.) for each detector.

The resulting BigBite ROOT files produced from the *replay* step are very large[1] and working with such large file sizes would make future analysis of the replayed data very slow. Thus to make more manageable sized BigBite ROOT files, a basic valid track cut, which

[1]The BigBite ROOT files were larger than the LHRS ROOT files due to BigBites open geometry, which resulted in higher rates.

required that any given event must have at least one valid reconstructed track associated with it, was applied to all the replayed ROOT files. The ROOT file size was reduced by $\sim$ 85%, due to the fact that on average, only 15% of BigBite events has a valid track associated with it.

The second step of the data processing was known as the *skim replay* step. The *skim replay* was used to compute kinematic variables (i.e. x, Q^2, etc.) and add flags to remove undesirable time periods (Sections 8.2.1 and 8.3.1). The *skim* ROOT files were copies of the final ROOT files produced during the *replay* step, with the additional kinematic variables and flags written to the file. The E06-014 physics analysis was done using the *skim* ROOT files.

8.1.2 Analysis Overview

The goal of E06-014 data analysis is to extract the neutron d_2 matrix element from double spin asymmetries and absolute cross sections. These quantities can also be used to form the polarized structure functions g_1 and g_2. Because a polarized ^{3}He target is used, results also needed to be corrected for nuclear effects in order to extract the neutron information. Data was taken at two incident beam energies, 4.74 and 5.89 GeV, with BigBite measuring the DSA and positioned at 45° towards beam-right; while the LHRS was position 45° to beam-left and measured the scattering electron-^{3}He cross-section. This setup allowed data to be measured in both the DIS and resonance regions. The scattered electrons fell in a momentum range of $p \sim$ 0.7–2.0 GeV, which corresponds to $x \sim$ 0.27–0.92 and $Q^2 \sim$ 2.0–6.9 GeV^2 depending on the incident energy. An overview of the analysis process is illustrated in Figure 8.1. First, raw data from the LHRS and BigBite detectors are supplemented with detector calibrations (Section 7), and are then processed using the Hall A analysis software (the *ANALYZER*). Next, data quality (Sections 8.2.1 and 8.3.1) and particle identification

(Sections 8.2.2 and 8.3.2) cuts are applied. Up to this point the BigBite and LHRS detector packages followed similar analysis procedures. Over the next several steps, the analysis procedures of the two detectors diverge. On the BigBite detector side, the target and electron beam polarization directions are taken into account to form the raw DSAs (Section 8.2.5). The DSAs are then normalized by the target and beam polarizations that were achieved, corrected for various contaminations, and radiation. These corrections result in producing what are refereed to as the Born DSAs. On the LHRS side, the raw cross sections are formed by considering the detector efficiencies, acceptance, and momentum (Section 8.3.5). The Born cross sections are then extracted by correcting for various contaminations and radiation. Once the Born DSAs and cross sections are extracted, the analysis once again converges. The polarized structure functions, g_1 and g_2 can now extracted using the Born DSA and cross sections, and the d_2 matrix element can be computed. Once d_2 is computed, the nuclear effects are accounted for, leading to the extraction of the neutron d_2.

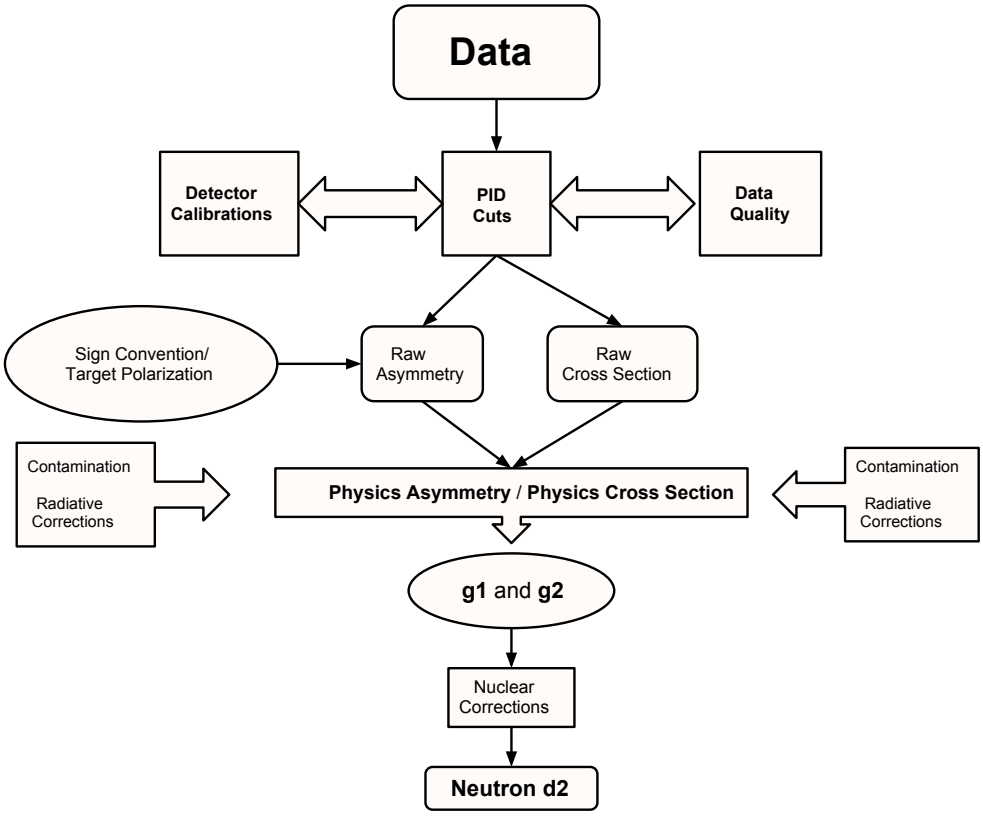

Figure 8.1: Illustration of the analysis procedure used to go from raw data to the neutron d_2 matrix element.

8.2 BigBite Data Analysis

In this section the analyses related to the BigBite detector stack will be discussed. The BigBite data quality and PID cuts that were were used in the analysis are defined first in Sections 8.2.1 and 8.2.2. These cuts were then used to study the performance of the BigBite detector and are presented in Section 8.2.3. Next, in Section 8.2.4, the BigBite acceptance was analyzed. Section 8.2.5 defines the asymmetry sign conventions used and forms the raw asymmetries from the BigBite data. An overview of the BigBite kinematics binning for both incident beam energies is then presented in Section 8.2.7. The physics asymmetries are then formed from the raw asymmetries (Section 8.2.8). Finally, various corrections are applied to the asymmetries, including: nitrogen dilution (Section 8.2.6), and pair-production and pion contaminations (Section 8.2.9).

8.2.1 Data Quality

Data quality cuts were used to remove any unwanted events from the data. These unwanted events included removing periods of unstable beam, scattering events from outside of the target volume, events passing through poorly understood regions of the magnet, and imposing checks on the reconstructed tracks to assure that a particle's position in the MWDC is consistent with its position in the calorimeter.

8.2.1.1 Beam Stability

During the running of E06-014, there were periods where the delivery of the beam into the hall was briefly interrupted. This resulted in the beam current dropping suddenly to zero and then recovering and ramping back up to the set-point current. These beam interruptions are know as beam trips. During a beam trip recovery, when the current is low and begins ramping back up to the production current, the beam position and charge asymmetry are

unstable [3], resulting in a non-linear BCM [86]. Thus these beam trips need to be removed from the data. The beam trips were identified using the $u3$ BCM readouts. The scaler values were written to the CODA data stream about once every 100 triggered events; meaning that 100 consecutive CODA events would share the same scaler value before being updated. The beam current can then be measured using the scaler rate, which is calculated from the count difference between two consecutive scaler readings. In principle, the procedure of defining beam trip cuts should be identical between the BigBite and LHRS (the LHRS procedure can be found in Section 8.3.1) detector packages. However, due to a lower readout rate of the LHRS compared to the BigBite detector, as seen in Figure 8.2, the LHRS beam current versus time appears to be more stable; effectively averaging over the noise to produce an average beam current reading within $1\mu A$ of the set-point current. Where as in the case of the BigBite detector, there is a relatively large variation of about $\pm$ 5 μA around the set-point current. This large variation in the beam current reading complicates the process of defining a beam trip cut for the BigBite detector, as one would like to remove the entire trip-and-recovery period from the data, and not the normal variation about the current set-point. As a result, the BigBite scaler readings were averaged over groups of fifty consecutive readouts. The beam current samples were then fit with a Gaussian distribution and any group of fifty readouts falling within 1.5σ of the high-current mean were accepted as belonging to a stable beam period, while those falling outside of that window were rejected. The beam trip edges were tagged with time stamps marking the transition between the rejected and accepted readout groups. Although the scaler readouts needed to be averaged together for the BigBite beam trip analysis, the resulting beam current still had a timing resolution of about 1.25 seconds per read out group.

The identification of beam trips in the BigBite detector was done by D. Parno [75] and was performed in two stages. In the first stage, the beam current fits and the identification of acceptable beam current windows were performed automatically, were a time-stamped

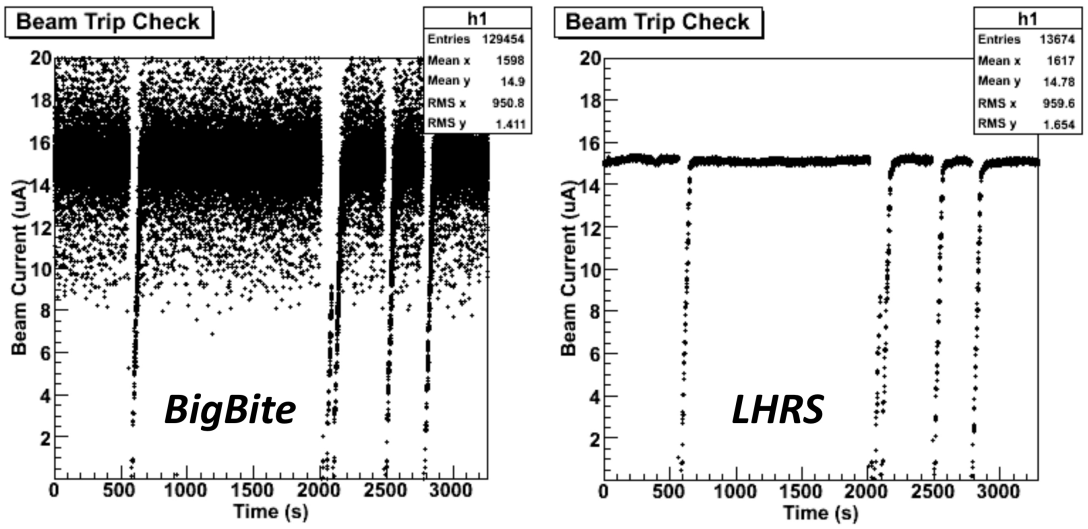

Figure 8.2: Beam current readouts in the BigBite (left) and LHRS (right) as a function of time. The slower scaler read out rate effectively averages out the noise. Figure reproduced from [75].

database defining each cut was created. This analysis was carried out on a run-by-run basis to account for all runs that may have different current set-points[2]. The results of the first stage are shown in Figure 8.3, where the red points were identified as beam trip (or recovery) periods and were rejected. Overlayed onto the beam trips are the accepted beam current readouts, identified as stable beam periods (green points). The second stage consists of a visual analysis, which consists of looking for beam trip periods that were mis-identified by the automated process, and modifying the corresponding times contained in the database.

During the skim stage of the global analysis, a flag is set for each event corresponding to a stable beam or a beam trip state determined by the time-stamped beam trip database. A cut on this flag allows one to remove beam trips from the analysis.

[2]The beam current setting may change from run to run for a number of reasons: a change in the trigger rates, prescales or to reduce online deadtime.

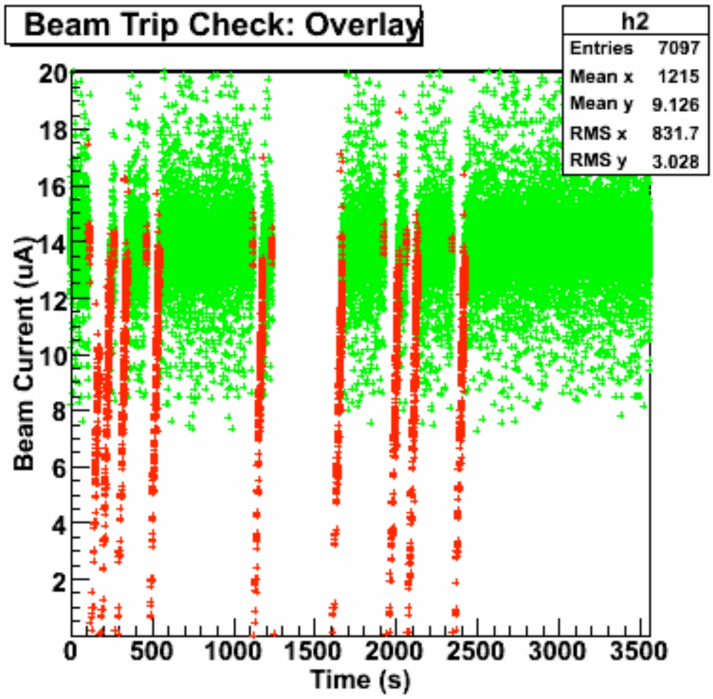

Figure 8.3: Identification of beam trips in the BigBite detector. The red points have been identified as beam trips and are rejected, and the green points are beam readouts identified as stable beam periods. Figure is reproduced from [75].

8.2.1.2 Vertex Cut

The electrons of interest to E06-014, are those that scattered from polarized ^{3}He nuclei contained with in the 40 cm target cell. Several steps were taken to ensure that the scattered electrons detected originated from with in the target volume. The first step was to place tungsten-powder collimators, with a 10 cm thickness, between each of the target windows and the BigBite spectrometer [86]. This resulted in lowering the background produced from electrons scattering off the target windows. The Second step involved using tracking and optics software (Section 7.1.2) to apply cuts on the reconstructed scattering vertex position (z_v). Figure 8.4 shows a typical distribution of the reconstructed scattering vertex for 5.89 GeV indecent electrons scattering from a polarized ^{3}He target. To ensure that the scattering electrons originated from within the target cell, a cut of $\pm$ 0.17 m from the nominal target center at z_v = 0 m (shown by the red dashed lines) was placed on the reconstructed vertex. The $\pm$ 0.17 m cut positions were found to be valid and applied to 4.74 GeV data set as well.

8.2.1.3 Particles Through the Magnet

The optics model used in E06-014 (7.1.2) assumes a uniform magnetic field throughout the BigBite magnet. However, in reality the field throughout the BigBite magnet is not uniform; this non-uniformity directly affects the path the particles take as they pass through the magnet, and hence their momenta. There are two ways to handle the non-uniformity of the magnetic field, one is to correct the particle's path dependent momentum as it passes through the BigBite magnet, and the other way is to remove regions where there are large field deviations. Given the production statistics of BigBite and the limited elastic calibration data, the problematic regions were removed from E06-014 analysis.

The tracking and optics reconstruction algorithms sometimes fail, and when doing so it is possible that a physical quantity may be set to either zero or a very large number. The

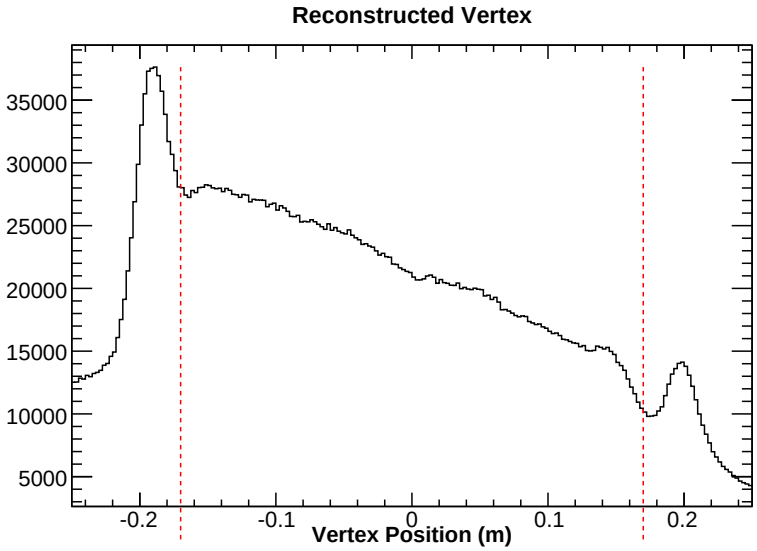

Figure 8.4: Scattering vertex reconstruction for 5.89 GeV incident electrons scattering from a polarized ^{3}He target. The two peaks at target vertex of $\pm$0.2 m, correspond to scattering from the target windows, which are located at the two ends of the target cell. Events that fall within the red lines ($\pm$ 0.17 m) are accepted by the target vertex cut.

failed tracks can be removed from the analysis by applying a loose cut on the reconstructed momentum

$$0.0 < p < 10.0\text{GeV}, \tag{8.1}$$

which corresponds to rejecting tracks that have no momentum and therefore should not be detected in the MWDCs, and tracks with momenta too large to have resulted from 6 GeV incident electrons scattering off a fixed target. Once the failed tracks were removed, the tracks that pass through portions of the BigBite magnet where the field gradient is large, also need to be removed. These tracks could result in an unreliable optics reconstruction, and were removed through the use of two geometric cuts. The first geometrical cut was based on where the front and back tracks intersect the bend plane, which bisects the BigBite magnet (Figure 7.10). Undesirable regions of the magnet volume were removed from the data by cutting out the corresponding region in the bend plane. This cut was set by X. Qian [86] during E06-010, whose optics model is the basis for E06-014. Figure 8.5 shows the distribution of the vertical and horizontal bend plane for all tracks in the left most panel, while in the center panel, the first geometrical cut is applied resulting in the removal of most extreme and non-uniform regions of the magnet. The first geometrical cut was further tightened by the addition of a second geometrical cut, which was applied to the vertical slope of the front track, $x^{'}_{trk}$. A study of the elastic scattering data lead to a cut value of [75]

$$x^{'}_{trk} < 0.2, \tag{8.2}$$

where this boundary was found to correspond to a sharp change in the reconstructed momentum. The right most panel of Figure 8.5 shows the bend plane distribution with both geometrical cuts applied.

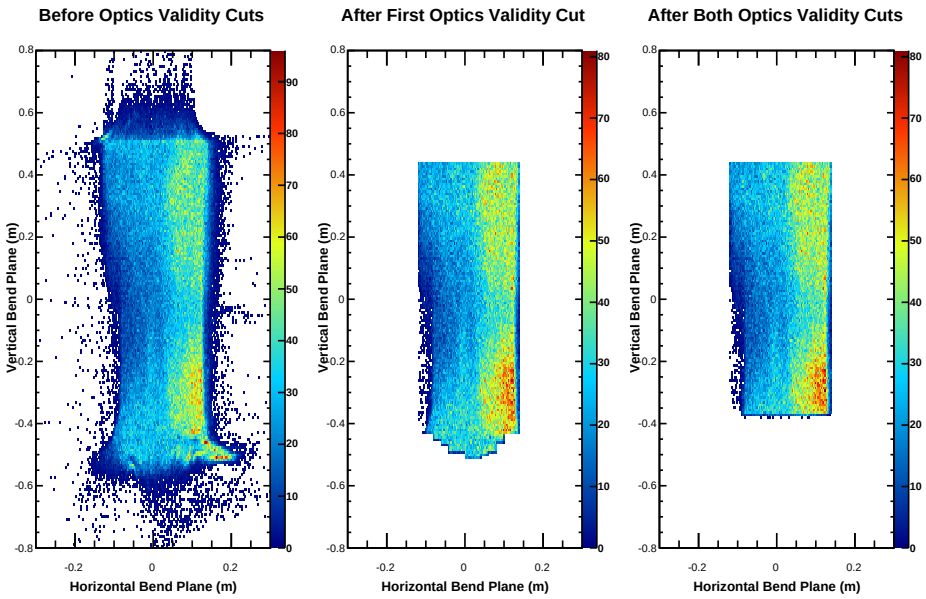

Figure 8.5: Geometrical optics validity cuts. The left panel shows the distribution of all tracks at the bend plane. The center panel shows the distribution of the tracks at the bend plane that pass the first optics validity cut, which are based on track intersections with the bend plane. The right panel shows all tracks at the bend plane that pass the first and second optics validity cuts. The second optics validity cut is based on the front-track slope. In these distributions, the bottom of the BigBite magnet is at the bottom of the plots.

8.2.1.4 Rescattering Cut

So far it has been assumed that particles pass unobstructed through the the BigBite magnet, unfortunately this may not always be the case. If an electron strikes an iron pole or coil housing, the result is a premature shower that can lead to an artificially low energy deposited in the calorimeter. Furthermore, if the electron rescatteres so as to strike the wire chambers, the reconstructed vertex position and momentum will also be affected. A study was carried out by D. Parno [75] where events with calorimeter energy $E < 1$ GeV and reconstructed momentum $p > 1.5$ GeV were selected. It was found the such particles were disproportionaly likely to intersect the bend plane at its horizontal edges. By measuring the correlation between the tracks horizontal positions on the bend plane and their horizontal slopes at the wire chamber, it was deduced that rescattering occurred about 0.23 m upstream of the bend plane. Figure 8.6 shows tracks projected onto a plane that is 0.23 m upstream of the bend plane, where the rescattering positions are seen from the peaks at the two ends of the histogram. The rescattering cut removed all events falling outside the red lines seen in Figure 8.6. The rescattering cut was defined as:

$$-0.097\text{ m} < 0.23\text{ m} \cdot y' - y_{bend} < 0.13\text{ m}\,, \tag{8.3}$$

where y' is the horizontal slope of the track in the wire chambers, and y_{bend} is the horizontal position of the tracks intersection point in the bend plane.

8.2.1.5 Track-Calorimeter Match

In order to compare quantities derived from measured energies (using the calorimeter) and reconstructed tracks, care must be taken to ensure that both quantities are the result of the same event. As mentioned in Section 7.1.3.1, this was done in E06-010 through the use of an updated shower reconstruction algorithm, which used tracking information to verify that

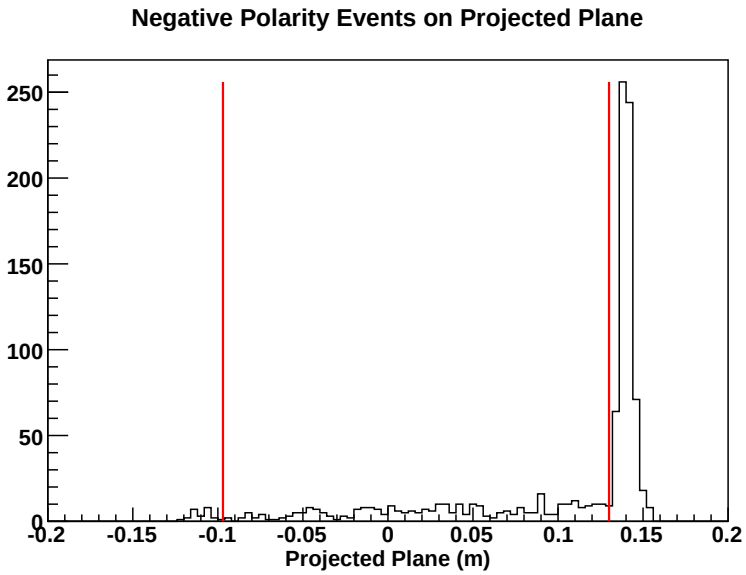

Figure 8.6: Projected horizontal position of low energy ($E < 1$ GeV) and high momentum ($p > 1.5$ GeV) particles on a plane 0.23 m upstream of the BigBite bend plane. The peaks at the ends correspond to the re-scattering positions. The rescattering cut rejects all events outside of the red lines.

the reconstructed track (from MWDC) and measured energy (from the calorimeter) were the result of the same particle. During E06-014, this updated algorithm was not used, thus a set of cuts known as the track-calorimeter alignment cuts were applied to ensure that measured energies and reconstructed tracks resulted from the same particle.

It can be verified that a measured energy and reconstructed track occurred from the same particle, by testing the distance between the central cluster position (as defined in Equation 7.23) in each calorimeter layer and the reconstructed track position projected onto that layer. Due to the fact that the shower and preshower cluster reconstructions are independent of each other, both the preshower and shower layers are treated separately when applying the track-calorimeter alignment cuts. Using the projected distances for the two layers defined in Table 7.5, the track-calorimeter alignment cuts take the form:

$$\Delta y_{sh} = |y_{sh} - (y_{trk} + d_{sh} \cdot y'_{trk}) - \text{offset}_{y_{sh}}| < 3\sigma_{y_{sh}}, \tag{8.4}$$

$$\Delta x_{sh} = |x_{sh} - (x_{trk} + d_{sh} \cdot x'_{trk}) - \text{offset}_{x_{sh}}| < 3\sigma_{x_{sh}}, \tag{8.5}$$

where y_{sh} (x_{sh}) are the central horizontal and vertical shower cluster positions, d_{sh} is the projected distance to the shower layer, defined in Table 7.5, y_{trk} (x_{trk}) are the horizontal (vertical) reconstructed tracks at the first wire chamber, and y'_{trk} (x'_{trk}) are the horizontal (vertical) track slopes at the first wire chamber; the offset centers the distribution at zero, and $\sigma_{y_{sh}}$ ($\sigma_{x_{sh}}$) was obtained by fitting a Gaussian to the Δy_{sh} (Δx_{sh}) distribution. A similar procedure was used to define the track-calorimeter alignment cuts for the preshower layer. However, due to the lack of resolution (54 blocks) compared to the shower (189 blocks), a Gaussian fit was not made to the Δx_{ps} and Δy_{ps} distributions. The track-calorimeter alignment cuts for the preshower layer took the form:

$$\Delta y_{ps} = \left|(y_{trk} + d_{ps} \cdot y'_{trk}) - y_{ps} - \text{offset}_{y_{ps}}\right| < \sigma_{y_{ps}}, \tag{8.6}$$

$$\Delta x_{ps} = \left|(x_{trk} + d_{ps} \cdot x'_{trk}) - x_{ps} - \text{offset}_{x_{ps}}\right| < \sigma_{x_{ps}}, \tag{8.7}$$

where y_{ps} (x_{ps}) are the central horizontal and vertical preshower cluster positions and d_{ps} is the projected distance to the preshower layer, defined in Table 7.5. Tables 8.1 and 8.2 summarize the values used in the analysis for both incident beam energies, and typical track-calorimeter alignment results can be seen in Figure 8.7 for the shower layer and Figure 8.8 for the preshower layer. In both figures the vertical direction is shown in the left panel, while the horizontal direction is shown in the right panel; events falling outside of the red lines are rejected from the analysis.

Table 8.1: Values that contribute to defining the track-calorimeter alignment cuts for the shower layer.

Parameter	E = 4.74 GeV	E = 5.89 GeV
$\sigma_{x_{sh}}$ [m]	3.33$\times$ 10^{-2}	3.53$\times$ 10^{-2}
offset$_{x_{sh}}$ [m]	1.01$\times$ 10^{-2}	9.74$\times$ 10^{-3}
$\sigma_{y_{sh}}$ [m]	3.33$\times$ 10^{-2}	3.49$\times$ 10^{-2}
offset$_{y_{sh}}$ [m]	-6.49$\times$ 10^{-3}	-4.92$\times$ 10^{-3}

Table 8.2: Values that contribute to defining the track-calorimeter alignment cuts for the preshower layer.

Parameter	E = 4.74 GeV	E = 5.89 GeV
$\sigma_{x_{ps}}$ [m]	0.081	0.071
offset$_{x_{ps}}$ [m]	-7.83$\times$ 10^{-3}	-6.64$\times$ 10^{-3}
$\sigma_{y_{ps}}$ [m]	0.19	0.24
offset$_{y_{ps}}$ [m]	0.01	-3.14$\times$ 10^{-3}

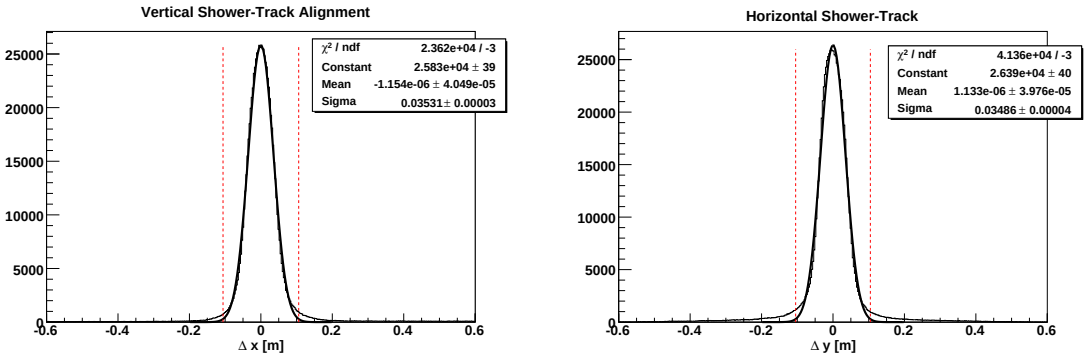

Figure 8.7: The difference between the vertical (left panel) and horizontal (right panel) shower detector cluster positions and the reconstructed tracks projected onto the shower detector plane are shown for a typical 5.89 GeV incident electron run. Events that fall outside of the red dashed lines are rejected by the shower-track alignment cuts.

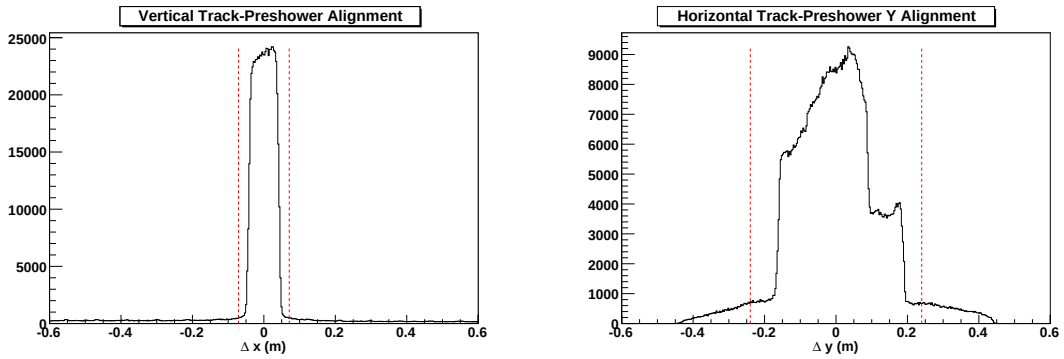

Figure 8.8: The difference between the vertical (left panel) and horizontal (right panel) reconstructed tracks projected onto the preshower detector plane and the preshower detector cluster positions are shown for a typical 5.89 GeV incident electron run. Events that fall outside of the red dashed lines are rejected by the preshower-track alignment cuts.

8.2.1.6 Track Quality Cut

The track quality can be determined by comparing how well a computed track positions in each wire plane agrees with the reconstructed hit position in the three planes. Accordingly, a χ^2 value can be defined for each track

$$\chi^2 = \sum_i \frac{\left(x_i^{reconstructed} - x_i^{track}\right)^2}{R_i^2}, \tag{8.8}$$

where the x values are the reconstructed track and hit positions in the i^{th} plane, and R is the plane resolution used in the tracking software [82]. The fit for each track has a certain number of degrees of freedom, N_{dof}, which is defined as the number of planes that fire minus the number of parameters used in the fit. Since each track fit contained four independent fit parameters x, y, x' and y', N_{dof} can be written as:

$$N_{dof} = N_{planes} - 4, \tag{8.9}$$

where N_{planes} are the number of wire chamber planes. The tracking algorithm is programed to incorporate data from at least fifteen planes into its analysis [86], leading to a majority of the tracks having $N_{dof} = 11$. Classically, one would expect $\chi^2/N_{dof} \sim 1$ to indicate a good fit. However, as can be seen in Figure 8.9, the quantity χ^2/N_{dof} given by the BigBite tracking software peaks well below a value of one. The low peaking value of χ^2/N_{dof} is due to an over estimate of the wire plane resolutions. Regardless of the low peaking value, this quantity is still useful as a measure of tracking quality, but to avoid confusion with the classical χ^2/N_{dof} quality fit, the BigBite track quality is redefined as k^2/N_{dof}. Figure 8.9 shows the k^2/N_{dof} distribution, with a cut being placed at $k^2/N_{dof} < 5$, represented in the figure by the red line, which removes all events with a χ^2 greater than 5 from the analysis.

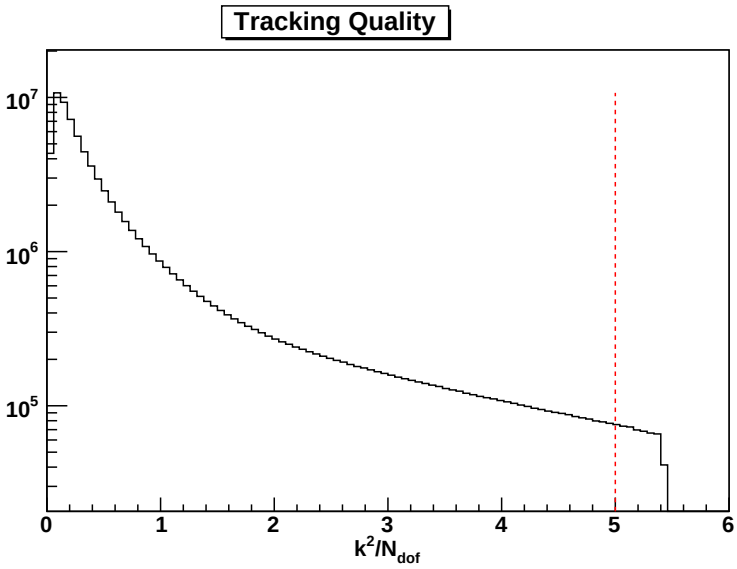

Figure 8.9: $k^2/\mathrm{N_{dof}}$ distribution for a typical production run. The track quality cut rejects all events above the red dashed line.

8.2.2 Particle Identification

The second group of cuts, particle identification (PID) cuts, are applied to tracks that are valid (i.e. passed all of the data quality cuts) in an attempt to select a particular particle type. Particles that pass the quality cuts tend to be pions, electrons, and positrons. While Sections 8.2.3 and 8.2.5 will use the PID cuts to select pions and positrons as well as electrons, for the majority of the analysis only electrons will want to be selected. This section will discuss the PID cuts used to select electrons in the analysis.

8.2.2.1 Charge Cut

With the BigBite magnet set to negative polarity[3], as a charged particle traverses the BigBite magnet, it will either bend-up (negatively charged) or bend-down (positively charged) into the BigBite spectrometer. Due to the large acceptance of BigBite, both particle trajectories

[3]By switching the magnet polarity to positive, negatively charged particles would bend-down and positively charged particles would bend-up into the BigBite spectrometer.

were able to be measured through the use of the BigBite optics package. If a particle's path was determined to bend upward into the spectrometer, it was tagged with a charge flag value of -1. On the other hand, if the particle's path was determined to bend downward into the spectrometer, it was assigned a charge flag value of +1. Figure 8.10 shows charge separate between positive (red points) and negative (blue points) particles by plotting the vertical track position (x) at the first wire chamber vs the slope of the vertical track ($x^{'}$) at the first wire chamber (as per BigBite detector coordinates, a negative vertical slope corresponds to a particle physically bending upward.). The black events in the center resulted from straight tracks, which were caused by the particle having a large momentum. Since the bend trajectory of particles with stiff tracks can not be determined, they are removed from the data. The charge cuts were set by X. Qian during E06-014 [86] and take the form:

$$x > 3.17x^{'} - 0.31, \tag{8.10}$$

for negativley charged particles bending up into the spectrometer and

$$x < 2.73x^{'} - 0.17, \tag{8.11}$$

for positively charged particles bending down into the spectrometer. By selecting events that were tagged with a charge flag value of -1 (blue points in Figure 8.10) negatively charged particles can be selected, eliminating any positively charged particles from the electron analysis.

8.2.2.2 Trigger Cut

Once the charge of the particles are determined, further discrimination can be applied through the use of the BigBite trigger. The T2 trigger was the main trigger used during production running. As seen in Section 4.4.6, the T2 trigger is formed from a geometrical

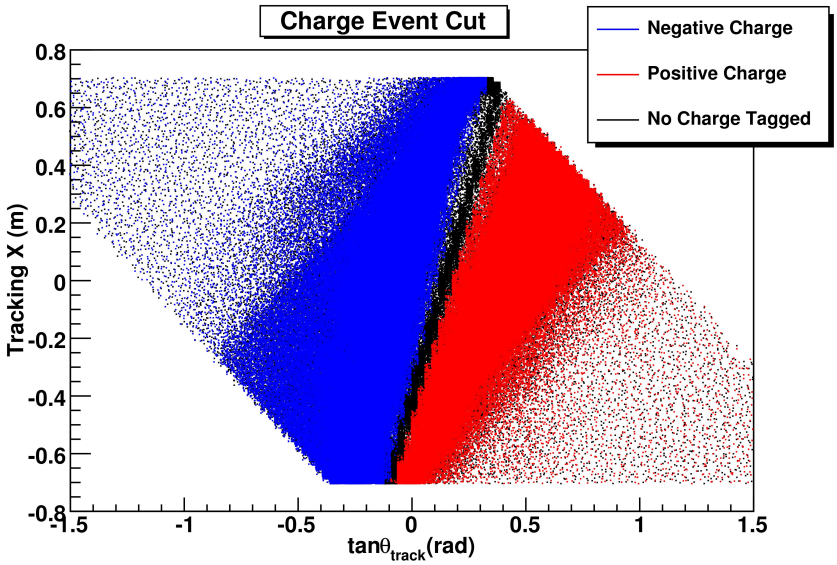

Figure 8.10: Charge separation measured in BigBite.

overlap between the shower and Čerenkov signals. Many of the pion events were removed from the on-line trigger by imposing a hardware thresholds on the shower signals (sensitive to the particle's energy) and the amount of light deposited in a group of four PMTs (sensitive to the particle's velocity).

During the off-line analysis, the electron sample was improved by requiring that the particle under consideration came from a T2 tagged event. This cut is applied through the means of the trigger word, a byte of information that encodes the value of each trigger (1 if the trigger had fired, 0 if it had not) as a single bit. By requiring the trigger bit corresponding to the T2 trigger was set to 1, T2 type trigger events were accepted, while all other trigger types were rejected.

8.2.2.3 Scintillator Cut

While the BigBite scintillator plane provides accurate timing information of the particles entering the detector, such timing information is not critical for single-arm experiments such as E06-014. However, in addition to the timing information being recorded via TDCs,

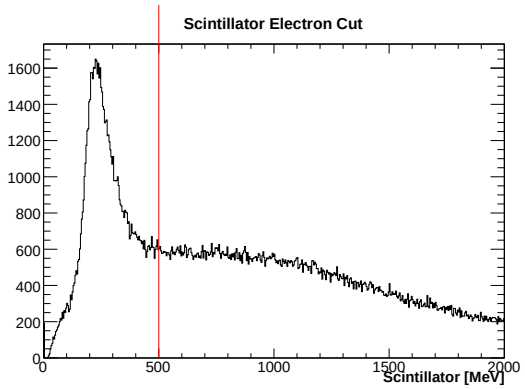

Figure 8.11: Typical energy distribution measured in the scintillator. The red line at 500 MeV marks the location of the scintillator electron energy cut used in the electron analysis.

a particle's deposited energy was also recorded in ADCs associated with the scintillator's PMTs. The deposited energy of the particles passing though the scintillator proved to be a very useful PID tool. Charged hadrons, such as $\pi^{\pm}$, will deposit less energy than electrons. This allows cuts to be applied to the energy distribution in the scintillator to select electrons or pion like events. By selecting the events that produced the maximum ADC signal, the energy distribution can be plotted, as shown in Figure 8.11. A cut was placed at 500 MeV on the scintillator energy distribution, thus all particles depositing less than 500 MeV in the scintillator were removed from the electron analysis.

8.2.2.4 Calorimeter Cuts

The two layers of the BigBite calorimeter, the preshower and shower, allows one to distinguish between electrons and non-showering particles (such as pions) by measuring the energy that each particle leaves in each of the layers. With the preshower layer having a depth of only 8.5 cm, particles that do not cause a shower deposit very little energy. If one considers the entire calorimeter (preshower and shower) for negatively charge particles, only electrons are expected to deposit nearly all of their energy.

8.2.2.4.1 Preshower The low energy deposit characteristic of non-showering particles, not only provides a powerful tool for studying pion contamination (which is discussed in Section 8.2.9), but also allows for a potent PID cut. The right panel of Figure 8.12 shows a typical preshower energy distribution for a 5.89 GeV incident electron beam, where there is a clear distinction between non-showering (hadrons) and showering (electrons) particles. The non-showering particles deposit most of there energy below 100 MeV, while the showering particles deposit most of their energy above 200 MeV. Near the end of the E06-014, the preshower energy was added into the main electron trigger (T2) as discussed in Section 4.4.6. The addition of the preshower energy into the T2 trigger, resulted in removing most of the non-showering particles as can be seen in the left panel of Figure 8.12, which shows a typical preshower energy distribution after the preshower is added to the trigger. It was found that setting the preshower energy cut at

$$E_{ps} > 200 \text{ MeV}, \tag{8.12}$$

resulted in removing the most non-showering particles, while retaining as many electrons as possible in the electron analysis. The same preshower energy cut position was used for both 4.74 and 5.89 GeV beam energies.

Additionally, a cut was placed on the preshower timing via the preshower sum TDCs. The TDC cut is given as

$$|PS_{TDC} - TDC_{mean}| < \sigma, \tag{8.13}$$

where PS_{TDC} is the preshower TDC time, TDC_{mean} is the mean of the TDC timing peak and σ is the TDC timing window cut set at 50 TDC Channels. This cut was applied to both the 4.74 and 5.89 GeV data sets. An example of a typical preshower TDC cut can be seen in Figure 8.13, where an offset has been applied (discussed in Section 7.1.3.4) to center

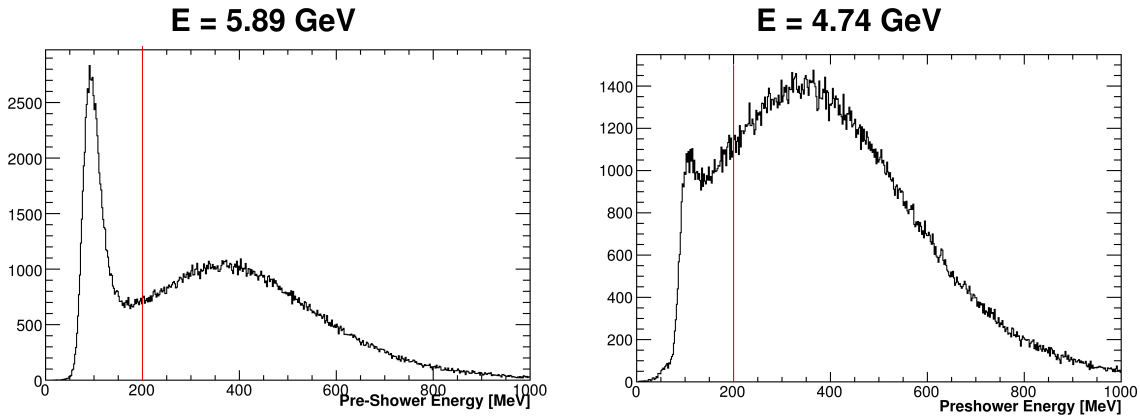

Figure 8.12: The left panel shows a typical energy distribution measured in the preshower before the preshower energy was added into the main trigger (A 5.89 GeV incident electron run). The right panel shows a typical energy distribution measured in the preshower after the preshower energy was added into the main trigger (A 4.74 GeV incident electron run). The red lines at 200 MeV mark the location of the preshower electron energy cut used in the electron analysis.

the timing peak at TDC channel 0. The red lines mark the TDC channels $\pm$ 50. All events falling outside the $\pm$ 50 TDC channel window were removed from the electron analysis.

8.2.2.4.2 E/p As a result of the electron depositing nearly all of its energy into the BigBite calorimeter, and the electron rest mass begin negligible in the kinematics of E06-014, one would expect that the electrons energy to be approximately equal to is momentum, or $E/p \sim 1$. On the other hand MIPs such as pions, will deposit little energy into the calorimeter, leading to an $E/p < 1$. This difference in E/p ratios can be exploited to further discriminate against particle types detected in BigBite by applying the cut

$$|E/p - \langle E/p \rangle| < 2\sigma, \tag{8.14}$$

where E/p is the measured E/p value, $\langle E/p \rangle$ is the mean E/p value obtained from

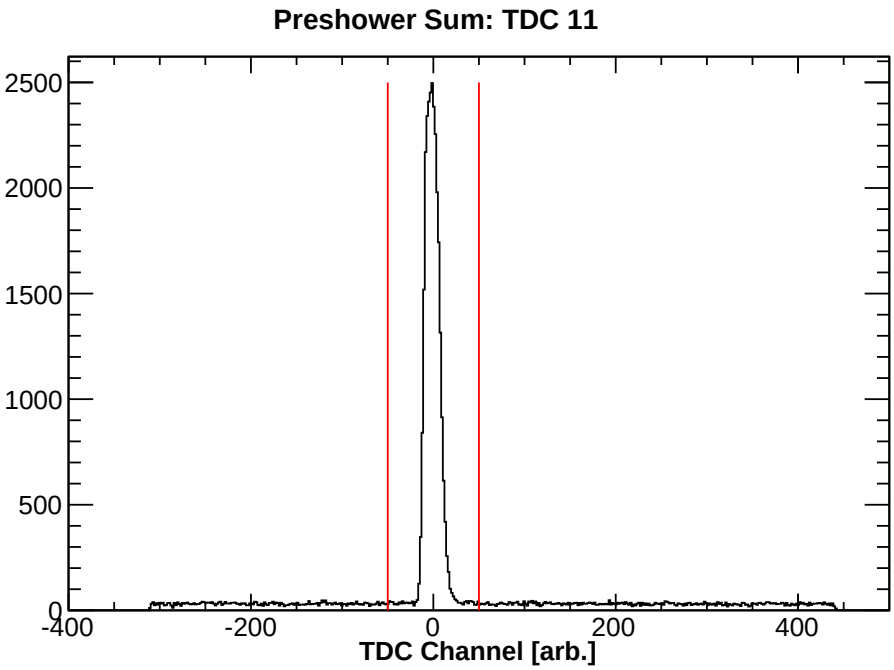

Figure 8.13: Typical TDC signal recorded using the preshower sum TDCs. The red lines define the TDC timing cut used in the electron analysis.

Table 8.3: Values that contribute to defining the 5.89 GeV incident electron E/p cut.

Run Period	$\langle E/p \rangle$	σ
1311–1447	0.963	0.090
1448–1475	0.998	0.089
1476–1742	0.987	0.091
1829–2020	0.985	0.084

a Gaussian fit to the data, and σ the resulting width. Due to changing triggers, detector thresholds and hardware issues throughout E06-014, the E/p cut had to be altered slightly from run period to run period (see Sections 4.5 and 7.1.3.1). Table 8.3 lists the various cuts values used during different run periods for the 5.89 GeV data set. For the 4.74 GeV data set the E/p cut was defined as

$$0.833 < E/p < 1.158. \tag{8.15}$$

Figure 8.14 shows the E/p distribution for 5.89 GeV incident electrons (right panel) with only data quality cuts applied. The main peak near E/p = 1 corresponds to electrons and the smaller peak near E/p = 0.6 corresponds to non-showering particles in the calorimeter. The left panel shows the E/p distribution for 4.74 GeV incident electrons. The red lines represent the cut windows used to select electrons. All of the events that fall outside the red lines are rejected from the electron analysis.

8.2.2.5 Čerenkov Cuts

The final detector that can be used to distinguish between particle types is the Čerenkov detector. Through its inclusion in the main electron trigger (T2), the Čerenkov detector was immediately put to use by rejecting pions in the on-line trigger (Section 4.4.6). Additional Čerenkov related cuts can be applied during the off-line analysis to remove even more pions

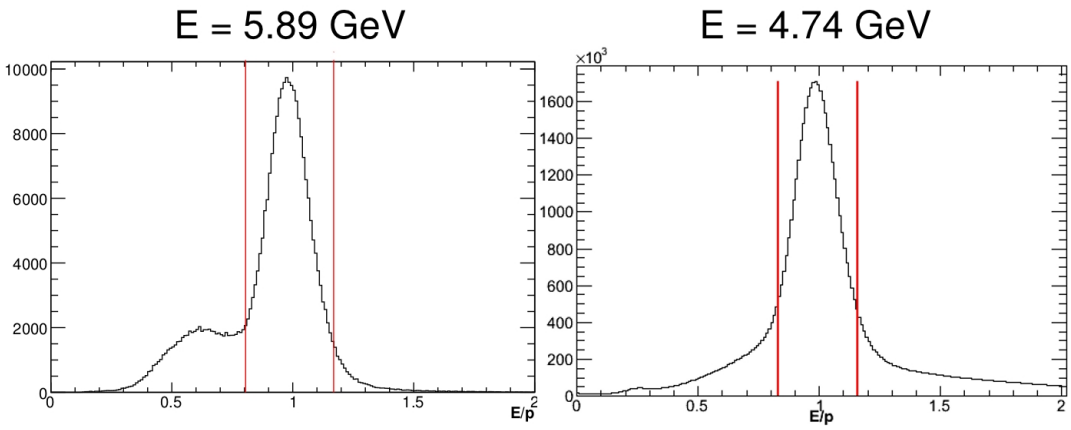

Figure 8.14: Typical E/p distribution for 5.89 GeV (right panel) and 4.74 GeV (left panel) incident electrons. The red lines define the E/p cut positions, in which any event outside of the red lines is removed from the analysis.

from the electron analysis by placing cuts on the Čerenkov timing and PMT acceptance.

8.2.2.5.1 TDC Timing Timing information for hits in each Čerenkov PMT, relative to the shower timing, were recorded in multi-hit TDCs. Each TDC was capable of recording information for up to 16 hits. However, it was found that only the first hit carried any useful timing information, as all subsequent hits resulted in times far from the electron timing peak. A hit can be recorded in the TDC in one of two ways: either it was a hit that formed the trigger for that event, or it was an accidental. In order to distinguish between the two types of hits, the Čerenkov TDC spectrum can be used. Figure 8.15 shows a representative sample of the TDC spectrum associated with PMT 17. The spectrum in black, only requires that the recorded event have at least one track associated with it; while the blue TDC spectrum requires that all recorded events pass the data quality cuts defined in Section 8.2.1. There are two clear structures present in the black TDC spectrum: a sharp peak centered at TDC channel 0 (electron timing peak) and a square-shaped shoulder, whose width is approximately equal to the width of the logic signal generated by the T6 (a hit in the shower).

The shoulder arises from the fact that the T2 timing is set by the shower hit rather than by the hit in the Čerenkov. This allows for accidentals that fall within the T6 window to possibly cause a T2 trigger. If the shoulder consists of accidentals, then by applying cuts to remove accidental events the shoulder should decrease. This is in fact seen when the data quality cuts are applied to the black TDC spectrum, which produces the blue TDC spectrum. The shoulder is almost non-existent in the TDC spectrum that contains the data quality cuts. The red dashed lines in Figure 8.15 mark the TDC timing window cut, whose width is 100 TDC channels (50 ns), that was used in the electron analysis. Because the electron timing peak location varies from PMT to PMT, a TDC offset was applied to each PMT in order to align the main timing peak to TDC channel zero (Section 7.1.5.2). Even with the Čerenkov timing cuts, there are still a significant percentage of hits within the timing window cut that are associated with accidentals.

8.2.2.5.2 PMT Acceptance One way to attempt to remove more of the accidentals is to associate a particle track in the MWDCs with a hit in the Čerenkov. By relating the geometry of the Čerenkov to the trajectories of the tracks measured in the MWDCs, it can be determined which PMT should have observed a particular track. As mentioned in Section 4.4.4.3, the Čerenkov acceptance is determined by twenty spherical mirrors arranged in two columns. For the E06-014 analysis, the *Čerenkov plane*, or effective mirror position was defined to be 0.8 m downstream of the first MWDC. The track positions projected forward from the MWDC to the Čerenkov plane, reveal the effective PMT acceptances on this plane. Figure 8.16 shows the projected vertical and horizontal track positions on the Čerenkov plane. The rate difference between the small-angle side and large-angle side is obvious. There are also the several *dead regions*, associated with bad shower and preshower blocks (Section 8.2.4), near the top of the magnet (negative vertical track positions in the plot). The distinction between the two columns is also evident due to the sparsely populated

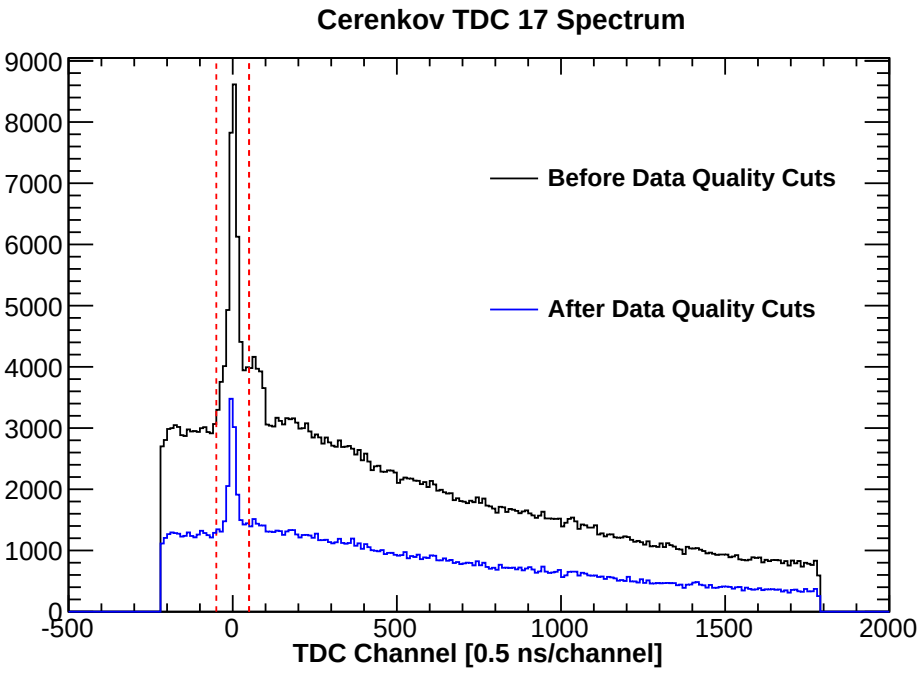

Figure 8.15: Čerenkov TDC spectrum of PMT 17 for a typical run. The black histogram shows events that require at least one track to be reconstructed. The blue histogram corresponds to events that pass all data quality cuts (defined in Section 8.2.1). The region between the red dashed lines is the TDC timing window cut that is used in the electron analysis.

region running up and down the center of the plane.

The various regions in Figure 8.16 can be associated with a particular PMT by requiring that the TDC for that PMT have a hit. For this study a hit is defined as having a TDC time that falls within the timing window cut, and has a corresponding ADC signal of least three photoelectrons. By isolating the acceptance to that of a single PMT, one can study the vertical acceptance position on the Čerenkov plane for each PMT. Figure 8.17 shows the vertical acceptance for each PMT using the conditions stated above, where each PMT is associated with a colored histogram. The black histogram represents all PMTs that fired over the entire Čerenkov detector acceptance. The left side of Figure 8.17 shows the small-angle PMT vertical acceptances, while the right panel corresponds to the large-angle side acceptances. Although there are still accidentals that trigger the Čerenkov, there is a clear vertical position associated with each PMT, as well as a few centimeter overlap of the low-efficiency edges between neighboring PMTs. Using the histograms in Figure 8.17, loose vertical position cuts were placed on each of the PMT acceptances. These cuts were loose enough to retain the neighboring PMT overlaps, but restrictive enough to reject a considerable amount of accidentals. Table 8.4 lists the high (x_{high}) and low (x_{low}) cut vertical positions used for each PMT. The lower portion of the Čerenkov PMTs (9,10,19 and 20) were excluded from the analysis as they fell outside of the BigBite electron acceptance.

Accompanying the vertical PMT acceptance cuts, are a set of cuts that define the horizontal PMT acceptances. However, because the horizontal plane only consists of two columns of mirrors, the cuts on the horizontal acceptance can not be as precise as those applies to the vertical acceptance. By combining the PMTs that make up the small and large-angle sides of the Čerenkov and applying the same the conditions used to study the vertical acceptance, the horizontal acceptance can be analyzed. Figure 8.18 shows the horizontal acceptance for the small-angle (red) and the large-angle (blue) sides of the Čerenkov. There is an apparent overlap of a few centimeters between the inner mirror edges of the two sides

Table 8.4: PMT cut positions on the vertical Čerenkov plane.

PMT	x_{high} [m]	x_{low} [m]	PMT	x_{high} [m]	x_{low} [m]
01	-0.815	-0.950	11	-0.815	-0.950
02	-0.610	-0.890	12	-0.610	-0.890
03	-0.395	-0.680	13	-0.395	-0.680
04	-0.190	-0.475	14	-0.190	-0.475
05	0.025	-0.250	15	0.025	-0.250
06	0.250	-0.050	16	0.250	-0.050
07	0.450	0.180	17	0.450	0.180
08	0.600	0.390	18	0.600	0.390
09	1.000	0.550	19	1.000	0.550
10	1.000	0.550	20	1.000	0.550

Table 8.5: PMT cut positions on the horizontal Čerenkov plane.

Čerenkov Side	y_{high} [m]	y_{low} [m]
Small-Angle	–	-0.03
Large-Angle	0.016	–

of the detector. The dip near the center (0 m) of the horizontal acceptance is as result of the rate difference between the two Čerenkov sides. The cut positions used to define the horizontal PMT acceptance is shown in Figure 8.18 with the red line defining the upper limit on the large-angle acceptance and the blue line defining the lower limit associated with the small-angle acceptance. The horizontal cut positions are also defined in Table 8.5.

The inclusion of the PMT acceptance cuts in the analysis removes a considerable amount of accidentals from the data. Figure 8.19 shows the TDC spectrum associated with PMT 07 without the PMT acceptance cut (also referred to as the mirror cut), as the black histogram, and with the PMT acceptance cut as the red histogram. The red lines mark where the TDC timing window cuts would fall. It is evident form the plot, that the accidental trigger rate is greatly reduced with the application of the PMT acceptance cuts.

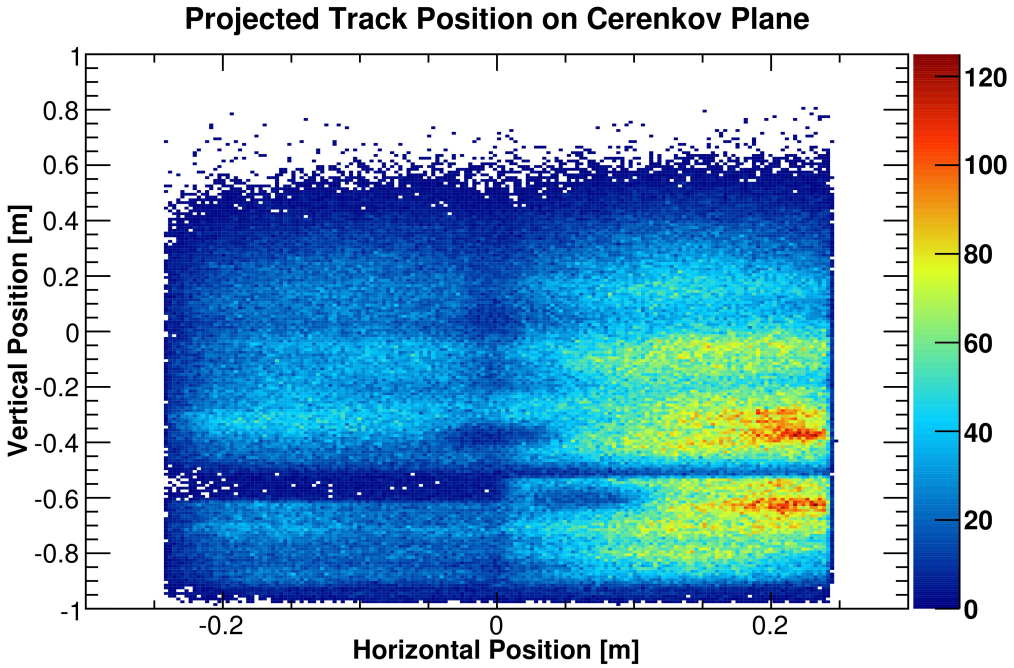

Figure 8.16: Projected track positions on the Čerenkov plane. These tracks passed all data quality cuts and are associated with negative charged particles and T2 triggers. In accordance with Hall A convention, the top of the plot corresponds to the bottom of the BigBite detector stack and vise versa. The right side of the plot is towards the beam (small-angle side), while the left side is away from the beam (large-angle side).

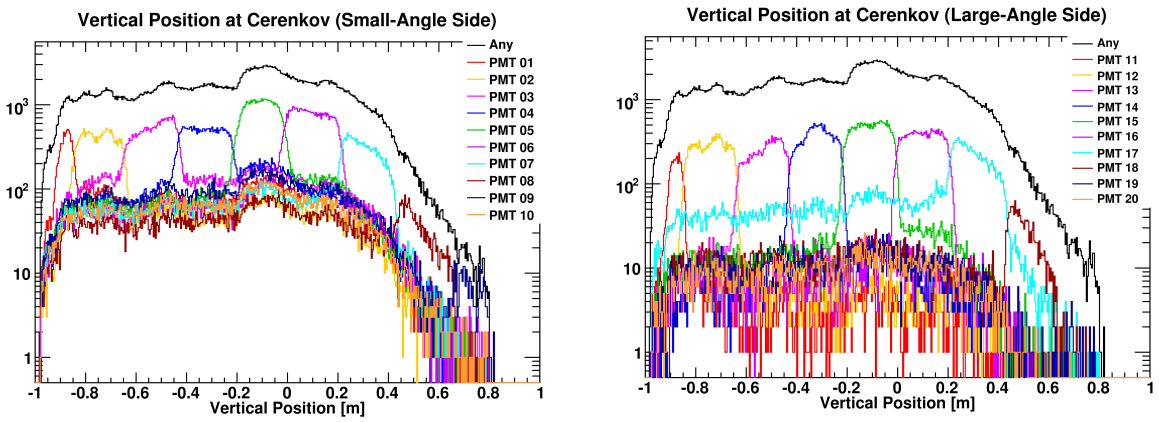

Figure 8.17: Reconstructed tracks projected onto the vertical Čerenkov plane, which were used to define the Čerenkov PMT acceptances. The small-angle side acceptances (PMTs 1–10) are shown in the right panel and the large-angle side acceptances (PMTs 11–20) are shown in the left panel.

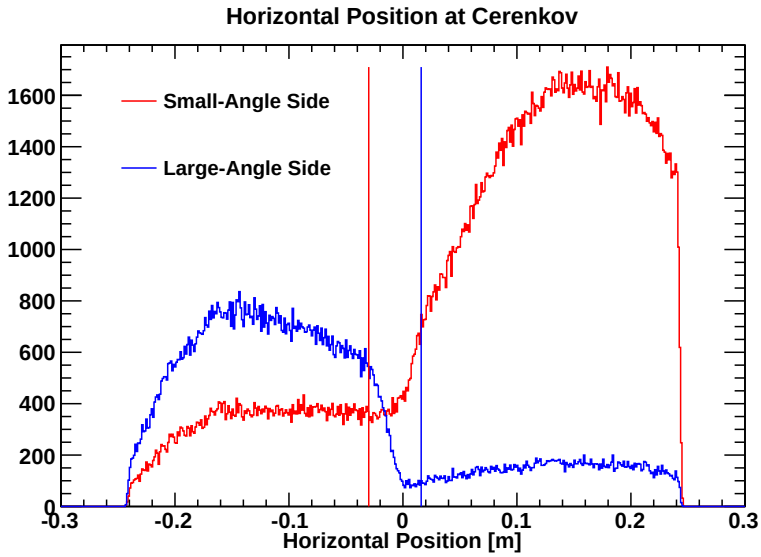

Figure 8.18: Reconstructed tracks projected onto the horizontal Čerenkov plane, which were used to define the Čerenkov PMT acceptances. The small-angle side (PMTs 1–10) acceptance corresponds to the red histogram, and the blue histogram corresponds to the large-angle side acceptance (PMTs 11–20). The red (small-angle side) and blue (large-angle side) lines mark the lower and upper horizontal cut positions.

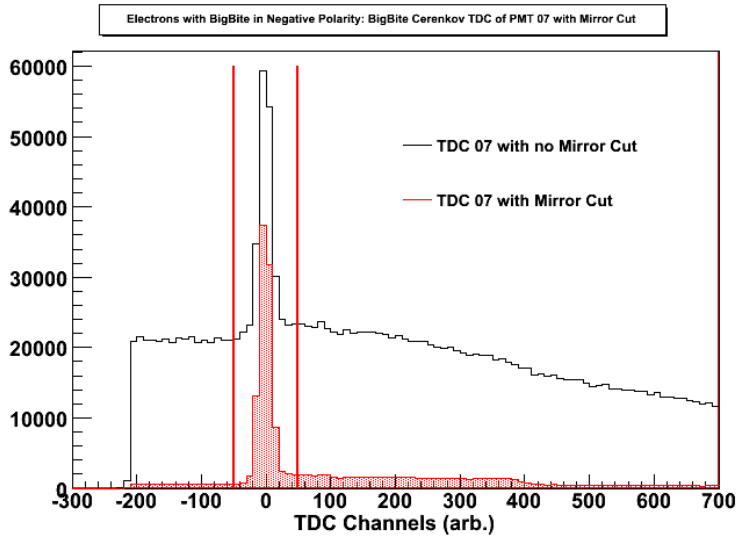

Figure 8.19: The TDC spectrum associated with PMT 07. The black histogram shows the TDC signal before applying the Čerenkov PMT acceptance cuts (also known as the Čerenkov mirror cuts), and after applying the acceptance cuts (red histogram). The red lines show the locations that defines the TDC timing window cut.

8.2.2.5.3 Čerenkov Electron Cut The final Čerenkov cut used to select electrons, involved a combination of several cuts. Each event had to meet the following criteria:

1. Did the PMT record a hit in its TDC?

2. Did the hit in the TDC fall within the defined TDC timing window for that PMT? (Defined in Section 8.2.2.5.1)

3. Does the projected track onto the Čerenkov plane fall within the geometrical acceptance of that PMT? (Defined in Section 8.2.2.5.2)

If all three of the above criteria are met, then the event passes the Čerenkov electron cut. There was no Čerenkov ADC condition used in the off-line analysis, as such a cut was found to reduce statistics uniformly across the acceptance and not improve the characteristics of the electron sample. The Čerenkov cut proved to be a powerful analysis tool. Figure 8.20 shows

a typical Čerenkov ADC from PMT 07, in which the ADC is plotted with no Čerenkov cuts applied (the black histogram). The Čerenkov TDC (green histogram) and PMT acceptance (blue histogram) cuts are applied to the same ADC. With the application of each Čerenkov cut, the background can be seen to reduce and the electron signal is enhanced. When the final Čerenkov cut is applied (the red histogram), most of the background is removed leaving only the electron signal. The dashed blue line in Figure 8.20 marks the ADC channel which corresponds to five photoelectrons.

8.2.3 Detector Performance

Through the use of PID cuts, particular event types (i.e. electrons and pions) can be chosen which can be used to study the performance of the BigBite detector. With E06-014 serving as the commissioning experiment for the gas Čerenkov, Section 8.2.3.1 provides an analysis of the Čerenkov detector performance, which includes its photoelectron yields, electron efficiencies, and pion-rejection factors. For E06-014, the main background contamination consists of pions. Therefore Section 8.2.3.2 summarizes the results of the BigBite spectrometer's ability to reject pions.

8.2.3.1 Čerenkov Performance

During the running of E06-014, the two sides of the gas Čerenkov detector experienced different rates. The small-angle side (closest to the beam line) saw rates below 1 MHz, with most experiencing 400-500 kHz. On the other hand, the large-angle side (farthest from the beam line) measured rates below 100 kHz [87]. The higher rate experienced on the small-angle side resulted in a poorer performance relative to the large-angle side of the Čerenkov detector.

The performance of the Čerenkov detector can be measured through several different

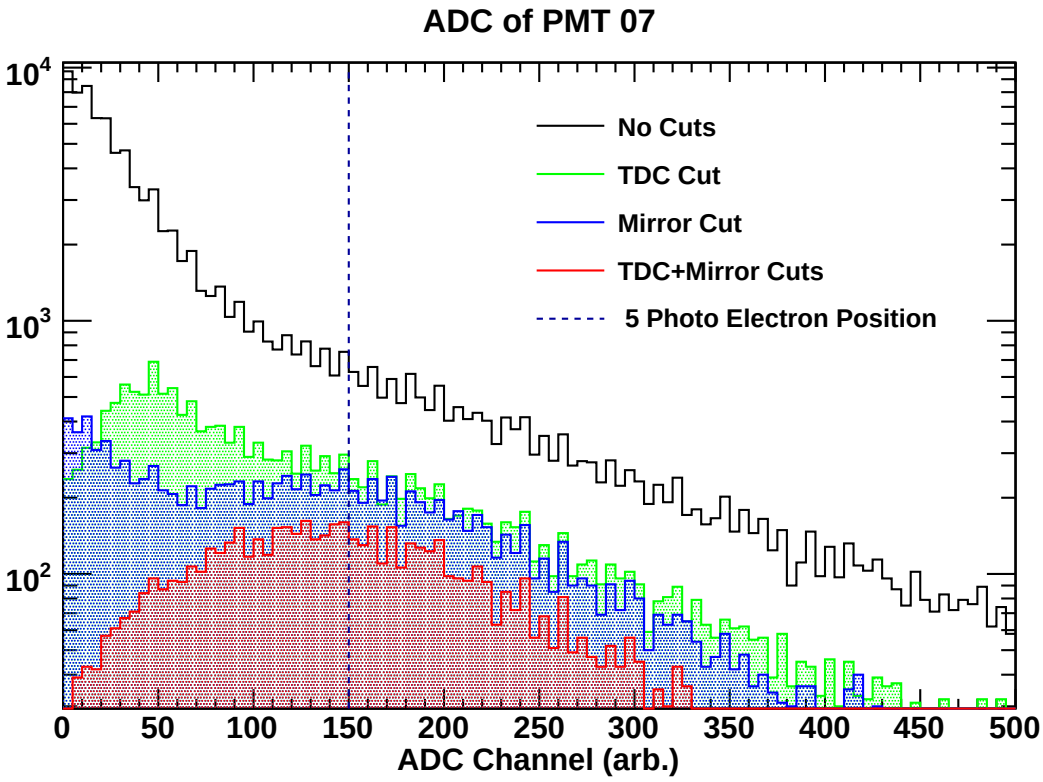

Figure 8.20: The effect of the Čerenkov cuts on the ADC signal from PMT 07. The black histogram does not have any Čerenkov cuts applied, the green histogram shows events passing the Čerenkov TDC timing cuts. The blue histogram shows events passing the Čerenkov PMT acceptance cuts. Finally, events that pass all Čerenkov cuts correspond to the red histogram. The dashed line marks the location of the ADC channel corresponding to five photoelectrons.

quantities: the number of photoelectrons produced per electron track, how well the Čerenkov detector can detect electrons, and how well it can reject pions from being misidentified as electrons.

8.2.3.1.1 Photoelectron Yields The photoelectron yield allows for a way to distinguish electron like events from non-electron like events. Knock-on electrons, which are low energy electrons produced by pions interacting with the medium, and other background events tend to produce low ADC signals (a couple photoelectrons). Whereas electrons that originated from the target produce a larger ADC signal (more than a couple photoelectrons). The larger the photoelectron yield, the cleaner one distinguished good electron events from background events.

The photoelectron yield was measured in each of the Čerenkov PMTs (with the exception of PMTs 09,10,19 and 20 because they were outside the electron acceptance) by applying the data quality cuts (defined in Section 8.2.1) and PID cuts (defined in Section 8.2.2) to the Čerenkov ADCs. Figure 8.21 shows a representative sample of the Čerenkov ADC spectra corresponding to PMTs 03, 04 ,13 and 14. The dashed line marks the location of the ADC channel corresponding to the one photoelectron position. The average photoelectron yield that was measured during E06-014 was found to be 5–7 photoelectrons [87]. Table 8.6 summarizes the approximate photoelectron yield for each PMT.

8.2.3.1.2 Electron Efficiency The electron efficiency, the ability for the Čerenkov to identify an electron as an electron, is another important quantity that is used to characterize the performance of the Čerenkov detector. To measure the electron efficiency (ϵ_{e^-}) an electron sample ($N^0_{e^-}$) needs to be selected. This was done by applying the already discussed data quality (defined in Section 8.2.1) and PID cuts (defined in Section 8.2.2) to the preshower energy distribution, with the following modifications made to the cuts to better

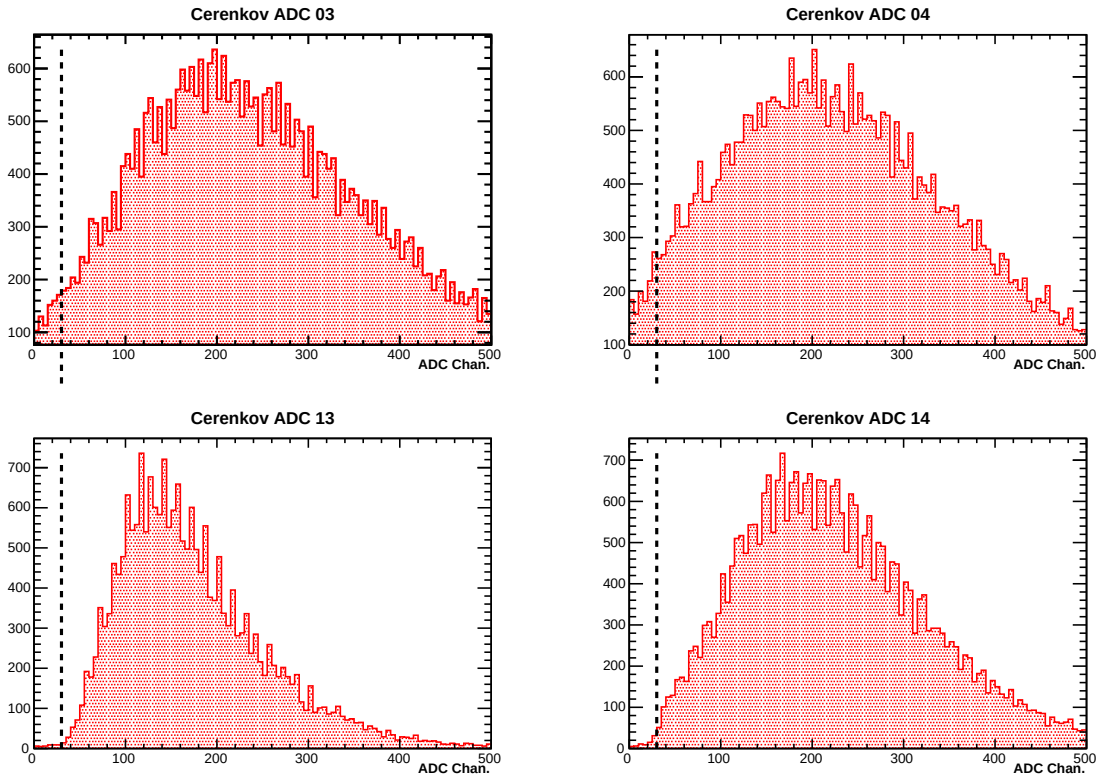

Figure 8.21: Representative sample of the Čerenkov ADCs. This particular plot shows the ADC spectrum corresponding to PMTs 03 (upper left), 04 upper right, 05 lower left, and 06 lower right. The dashed line marks the location of the single photoelectron position.

Table 8.6: Approximate photoelectron yield for each Čerenkov PMT. PMTs 9,10,19 and 20 are not listed because they were outside the electron acceptance.

PMT	Photoelectrons	PMT	Photoelectrons
01	6.0	11	5.0
02	5.0	12	6.0
03	7.0	13	5.0
04	7.0	14	6.0
05	5.0	15	8.0
06	5.0	16	5.0
07	4.0	17	5.0
08	3.0	18	5.0

insure that there was no contamination within the electron sample:

- The Čerenkov PMT acceptance cuts were made tighter in order to select more of the center of the acceptance for a given PMT.
- The target vertex cut was tightened to select the target center, at $\pm$ 10 cm from the nominal target center.
- Only events that fell into the 0.8–1.5 GeV momentum rage were selected.
- All events were required to deposit more than 400 MeV of their energy into the preshower.

To see how many of the $N^0_{e^-}$ electrons were detected by the Čerenkov, the number of $N^0_{e^-}$ events producing an Čerenkov ADC signal ($N^{'}_{e^-}$) were counted and the electron efficiency was computed as

$$\epsilon = \frac{N^{'}_{e^-}}{N^0_{e^-}}. \tag{8.16}$$

The electron efficiencies were computed using various ADC thresholds to compute $N^{'}_{e^-}$. The thresholds chosen ranged from applying no software threshold (zero photoelectrons, also known as the detection efficiency) up to four photoelectrons. The electron efficiency was computed for both T6 and T2 triggered events[4]. When computing the BigBite Čerenkov electron efficiencies for E06-014, there was an inherent photoelectron threshold applied to all Čerenkov ADCs due to the Čerenkov hardware threshold[5]. Thus the real Čerenkov detection efficiency could not be measured, because all events leaving a signal in the Čerenkov ADC would have had to be above the hardware threshold, which leads to an efficiency that is lower

[4]The electron efficiency could not be computed from T1 triggered events because of low T1 statistics, which resulted from a high prescale setting.

[5]During E06-014, the average Čerenkov threshold (sum of four adjacent ADCs) was set to around 1–1.5 photoelectrons [87].

than the actual efficiency. In order to determine a more realistic measurement of the electron efficiency, a photoelectron cut of 0.5 photoelectrons was applied to the electron sample $N^0_{e^-}$, effectively removing the Čerenkov threshold effect from the electron sample. Computing the electron efficiency using this method yields higher electron efficiencies (about 10% higher). The upper left (small-angle side) and right (large-angle side) panels of Figure 8.22 show the T6 electron efficiencies for each PMT as a function of photoelectron cut, without applying a photoelectron cut to $N^0_{e^-}$. Where as the bottom panels of Figure 8.22 show the T6 electron efficiencies for each PMT as a function of photoelectron cut, after applying the photoelectron cut to $N^0_{e^-}$.

Since the Čerenkov is in the T2 trigger and an event needs to pass the Čerenkov threshold in order to produce the trigger (so all $N^0_{e^-}$ events need to pass T2 trigger thresholds), the Čerenkov hardware threshold should be effectively removed from the $N^0_{e^-}$ events. Thus the Čerenkov threshold effect does not need to be considered when studying the T2 triggered events. This can be seen in Figure 8.23 where the detection efficiency (zero photoelectron cut) is higher in the T2 triggered events ($\sim$ 90–95%) than in the T6 triggered events ($\sim$ 85–90%, seen in the upper panels of Figure 8.22), but lower than the T6 triggered events ($\sim$ 95–100%) that had the Čerenkov threshold effect removed (lower panels of Figure 8.22). However at the three photoelectron cut, where the ADC signals are well above the Čerenkov threshold, both the T2 and Čerenkov threshold removed T6 triggered events have consistent electron efficiencies at roughly 80%.

8.2.3.1.3 Pion Rejection Factors Complementary to the Čerenkov electron efficiency is the pion rejection factor, which measures the amount of pions that are removed due to the Čerenkov detector. Pion rejection was the primary purpose of the BigBite gas Čerenkov during E06-014 and thus is an important performance characteristic. The pion rejection study was done in a similar manner to that of the electron efficiency study. Data quality and

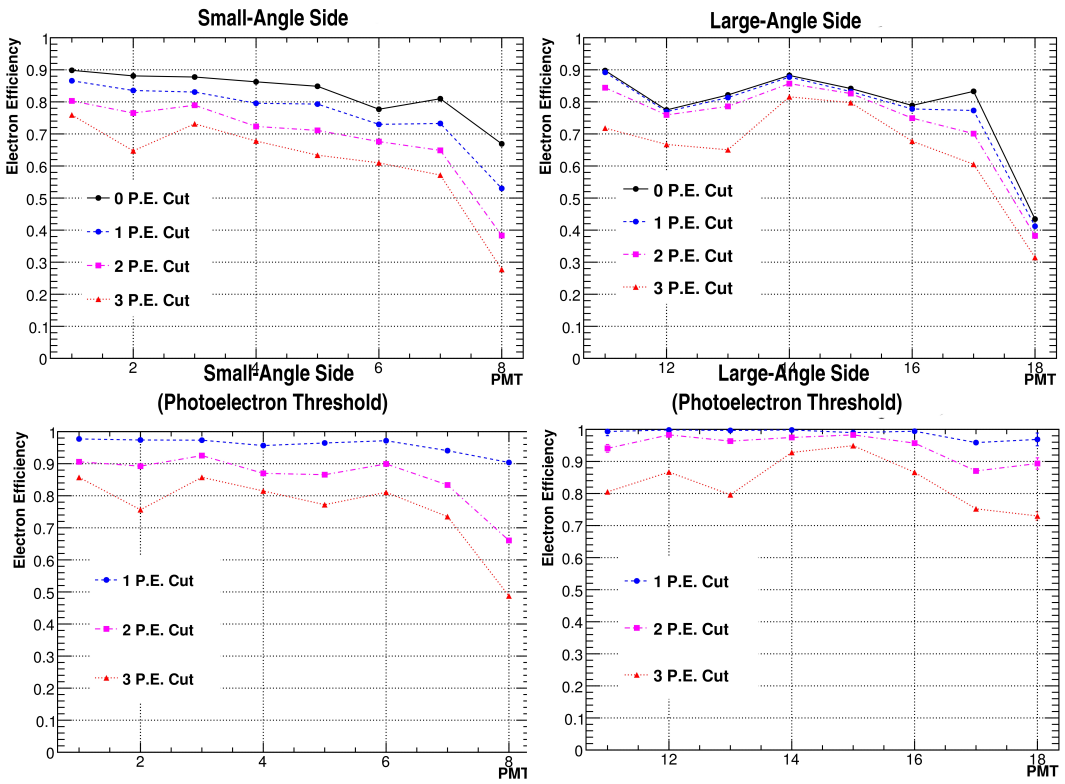

Figure 8.22: Čerenkov electron efficiency calculated using the T6 trigger at 15 μA as a function of photoelectron cut. The top two panels compute the efficiency without a software threshold placed on the Čerenkov ADCs, while the bottom two panels used a software imposed threshold of 0.5 photoelectrons on the Čerenkov ADCs.

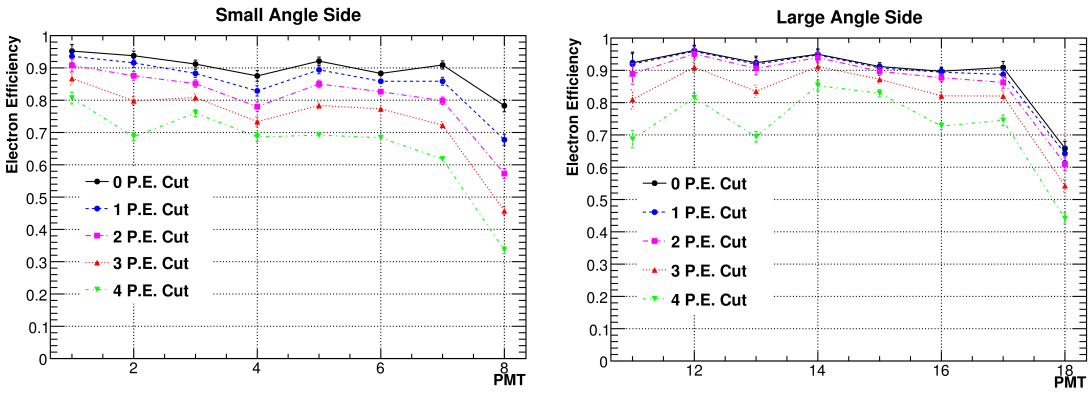

Figure 8.23: Čerenkov electron efficiency calculated using the T2 trigger at 15 μA as a function of photoelectron cut.

PID (modified to select pions rather than electrons) cuts were used to select an initial pion sample (N_π^0) in the preshower energy distribution. The following PID cuts were altered to select non contaminated pions:

- Tighter Čerenkov PMT acceptance cuts were used to select the center of the PMT acceptance.
- Events had to deposit energy in the preshower between 50 and 80 MeV.
- Events depositing less than 450 MeV in the scintillator were selected.
- Required events falling in the E/p range of 0.6 to 0.9.

The Čerenkov electron cuts, consisting of a hit in the TDC, the TDC timing window cut, and an ADC cut corresponding to several different photoelectron cuts were applied to the N_π^0 sample. The number of N_π^0 events surviving the Čerenkov cuts ($N_\pi^{'}$) were used to compute the pion rejection factor (ϵ_π) as:

$$\epsilon_\pi = \frac{N_\pi^0}{N_\pi^{'}}. \tag{8.17}$$

The pion rejection factors were computed at two beam currents, a low background producing 1 μA current (using T1 triggered events), and the production current of 15 μA (using T6 triggered events). Pion rejection factors were computed for the full Čerenkov acceptance (consisting of the small and large angle sides), as well as for the individual small and large angle sides. The pion rejection factor results can be seen in Figure 8.24. The left panel corresponding to the 1 μA beam current, while the right panel corresponds to the 15 μA beam current. The resulting pion rejection factors corresponding to the zero and three photoelectron cut positions are shown in Tables 8.7 (1 μA) and 8.8 (15 μA). From Figure 8.24, it is clear that the Čerenkov detector performs better in the lower beam

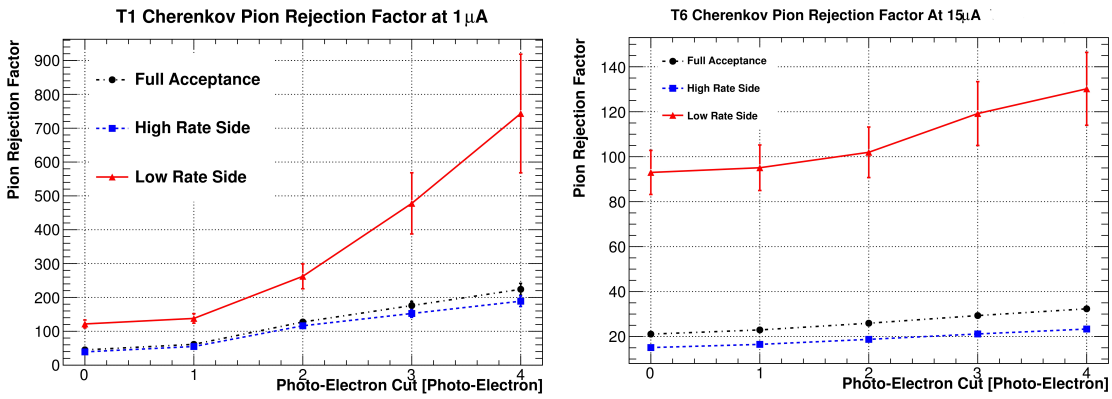

Figure 8.24: Čerenkov pion rejection factors computed using the T1 trigger at a beam current of 1 μA (left panel), and using the T6 trigger at 15 μA (right panel).

Table 8.7: Čerenkov pion rejection factors computed using the T1 trigger at a beam current of 1 μA for zero and three photoelectrons.

Čerenkov Side	0 PE. Cut	3 PE. Cut
Small-Angle	37.05 ± 2.00	100.57 ± 14.51
Large-Angle	102.00 ± 51.5	204.00 ± 205.00
Full Acceptance	39.91 ± 1.95	104.75 ± 13.22

current environment than it does at the higher production beam current. At both beam currents, the large-angle side performs much better than the small-angle side, which is due to their respective rate difference. As a result of the higher rates on the small-angle side, its contribution when studying the full acceptance of the Čerenkov is greater than that of the large-angle side, leading to the pion rejection factor over the whole acceptance being weighted towards the small-angle value. The final pion rejection factor measured over the entire Čerenkov range using a 15 μA beam was 21.09 ± 0.019.

8.2.3.2 BigBite Performance

Due to the inclusive nature of E06-014, much of the produced background were pions. As a result, many of the BigBite sub detectors were used to reject pions from the data. In

Table 8.8: Čerenkov pion rejection factors computed using the T6 trigger at a beam current of 15 μA for zero and three photoelectrons.

Čerenkov Side	0 PE. Cut	3 PE. Cut
Small-Angle	15.10 ± 0.01	21.16 ± 0.03
Large-Angle	93.00 ± 1.03	119.20 ± 1.70
Full Acceptance	21.09 ± 0.019	29.34 ± 0.036

addition to the BigBite gas Čerenkov pion rejection factor, the pion rejection factor of the other detecors were also studied. When the pion rejection factors from all of the detectors are combined, a total BigBite pion rejection factor could be computed. The pion rejection factors computed here follow the same definition as that given in Section 8.2.3.1.3.

The following summerizes how the pion rejection factor was computed in each of the BigBite sub detectors:

- **Preshower:** To study the pion rejection of the preshower, pions were selected using PID cuts on the Čerenkov and scintillator. The Čerenkov pion cut requires a particle to pass through one of the PMT acceptances and not have that event register a hit in the corresponding PMT's TDC. In addition to the Čerenkov pion cut, the particle must also deposit less than 450 MeV of its energy into the scintillator. The pion rejection factor was then evaluated by applying a varying cut on the preshower energy, requiring the particle to deposit at least that much energy into the preshower layer. The counting of the events in the pion sample, before (N_{π}^{0}) and after ($N_{\pi}^{'}$) the preshower energy cuts, was done on the E/p distribution in the range of $0.2 < E/p < 0.8$. Figure 8.25 shows in the upper left panel the preshower pion rejection factor as a function of preshower energy cut position for T1 triggered events at an electron beam current of 1 μA.

- **Scintillator:** The pion sample used to study the scintillator pion rejection, was

selected using pion PID cuts on the Čerenkov and preshower. The Čerenkov pion cut here is the same as that used for the preshower pion rejection analysis. The preshower cut required a particle to deposit less than 120 MeV of its energy in the preshower. The pion rejection factor was then evaluated by applying a varying cut on the scintillator energy, requiring the particle to deposit at least that much energy into the scintillator. The counting of the events in the pion sample, before (N_{π}^{0}) and after ($N_{\pi}^{'}$) the scintillator energy cuts, was done on the E/p distribution in the range of $0.2 < E/p < 0.8$. Figure 8.25 shows in the upper right panel, the preshower pion rejection factor as a function of preshower energy cut position for T1 triggered events at an electron beam current of 1 μA.

- **E/p:** The pion sample used to study the E/p pion rejection was identical to that used in the preshower pion rejection analysis. The pion rejection factor was then evaluated by applying a varying σ (σ = 0.091) cut on the E/p distribution, where events within a certain σ width of the mean E/p peak are chosen and compared to the initial pion sample. The counting of the events in the pion sample, before (N_{π}^{0}) and after ($N_{\pi}^{'}$) the E/p cuts, was done using the preshower energy distribution in the range of 20 to 160 MeV. Figure 8.25 shows in the lower left panel the E/p pion rejection factor as a function of E/p σ cut position for T1 triggered events at an electron beam current of 1 μA.

Table 8.9 lists the pion rejection factors evaluated on T6 triggered events at the cut positions used during the electron analysis, resulting in a total pion rejection factor better than 10^{4}. The effectiveness of the PID cuts to remove pion contamination can be seen when studying the preshower energy distribution. Because pions are minimal ionizing particles, they will deposit less energy ($\sim$ 80 MeV) relative to electrons in the preshower layer. This makes the preshower energy distribution a great tool for studying pion contamination.

Table 8.9: Pion rejection factors measured using T6 triggered events at a beam current of 15 μA.

Detector	Cut	Pion Rejection
Preshower	Energy $>$ 200 MeV	176.19 ± 0.41
Scintillator	Energy $>$ 500 MeV	7.21 ± 0.00
E/p	2 σ	2.59 ± 0.00
Čerenkov	TDC + PMT Acceptance	21.09 ± 0.019
Total	–	$6.94 \times 10^4 \pm 0.41$

Figure 8.26 shows the preshower energy distribution for T2 triggered events without any PID cuts applied (the black histogram). Each of the PID cuts is then applied individually, which are represented by the various colored histograms. When each of the PID cuts applied, the pion population (the peak near 80 MeV) decreases relative to the pion population without any PID cuts applied. When all PID cuts are used together, nearly all of the pions are removed (the red histogram). There is one more additional PID cut that was not applied in this plot, the preshower energy cut, whose location is marked by the black dashed line in Figure 8.26. These PID cuts served as powerful tools for removing nearly all of the pions from the electron sample, rendering the asymmetry contamination due to pions negligible (discussed in Section 8.2.9).

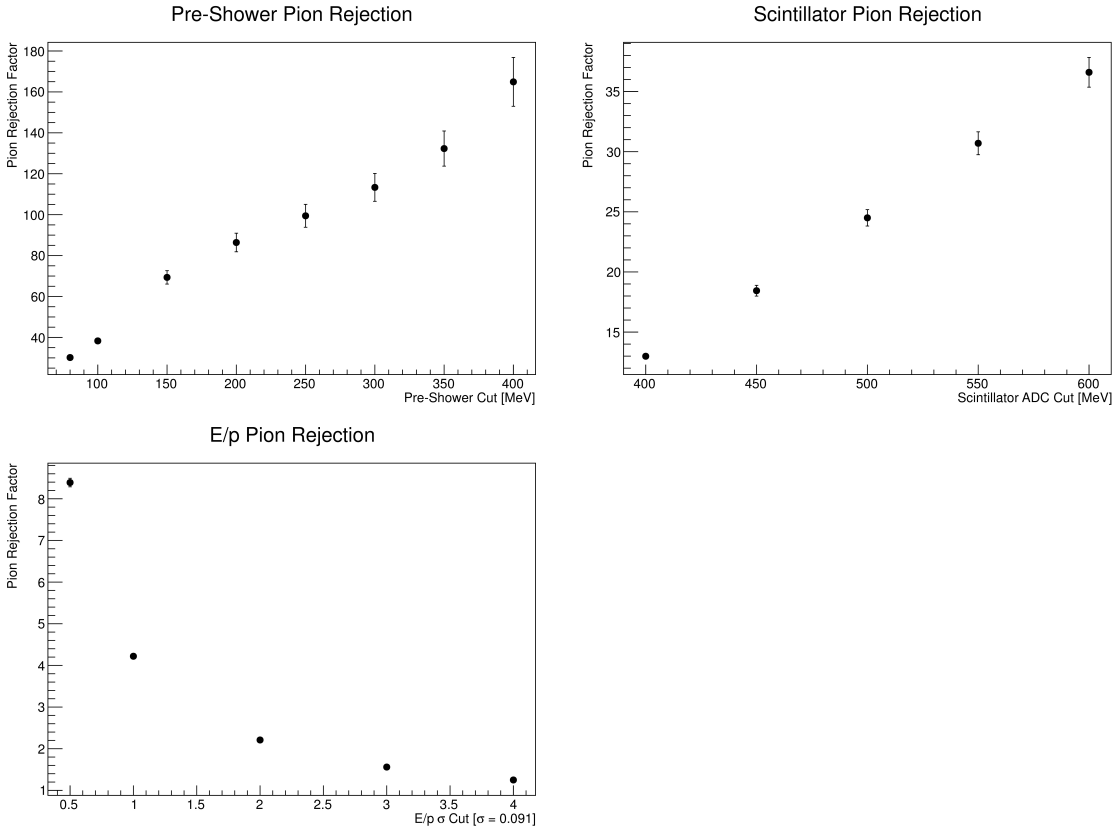

Figure 8.25: Pion rejection factors computed using the T1 trigger at a beam current of 1 μA for the preshower (top left panel), scintillator (top right panel) and the E/p cut (bottom left panel) as a function of cut position.

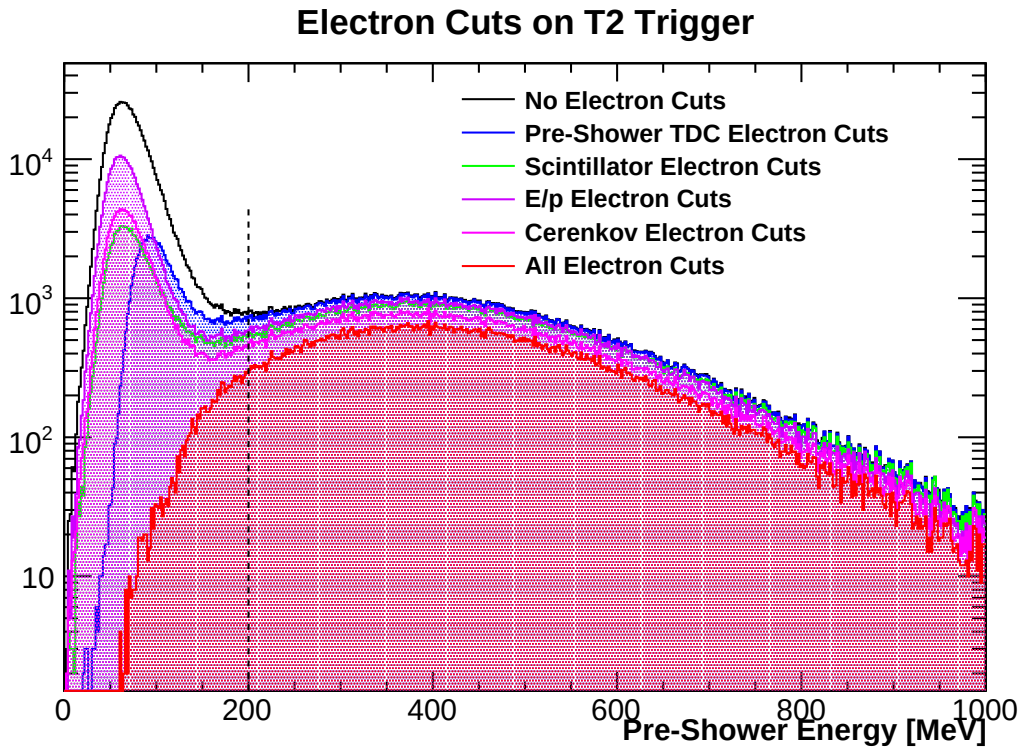

Figure 8.26: Preshower energy spectrum in which the removal of pions can be seen through the use of the electron PID cuts.

8.2.4 BigBite Acceptance

Throughout the running of E06-014, there were several periods during which hardware components failed. One failure in particular, the over loading of the summing modual associated with the BigBite calorimeter mentioned in Section 4.5, took place at the beginning of the experiment. The over-loaded modual resulted in events not passing energy thresholds that were set on the shower energy, resulting in many events not being able to produce one of the electron triggers (T1,T2 or T6). The effect of the over-loaded summing modual can be seen when looking at the reconstructed tracks from the MWDCs projected onto the shower layer as gaps in the acceptance. The difference in the acceptance at the shower plane can be seen in Figure 8.27, where the acceptance before the summing modual fix is shown in the left panel and after the fix in the right panel. It is obvious that many more events were gained after the fix, which also lead to a much more uniform acceptance.

Shortly after the summing modual fix, it was discovered that there were still several gaps in the BigBite acceptance. These gaps were traced back to being caused by inadequate calorimeter blocks, corresponding to preshower block 21, and shower blocks 100 and 130.[6]. Figure 8.28 shows the which calorimeter block is associated with a particular acceptance gap. If a calorimeter block is faulty, then its ADC signal will appear lower than the other ADC signals from adjacent blocks. Figure 8.29 shows the preshower ADC corresponding to the dead preshower block in the left panel as the red histogram, and several ADCs from surrounding blocks (from the large and small angle sides). There is a clear reduction that can be seen in the ADC gain of preshower block 21 relative to the properly functioning preshower blocks. Checking the ADC signals corresponding to the faulty shower blocks, seen in Figure 8.30, reveals a smaller discrepancy between the ADCs of the malfunctioning and the properly functioning blocks than what was seen with the preshower blocks. But

[6]The first physical block counting starts with block 1. However, in the plots, the ADC arrays start counting blocks from 0, i.e. ADC[0] is the ADC of block 1.

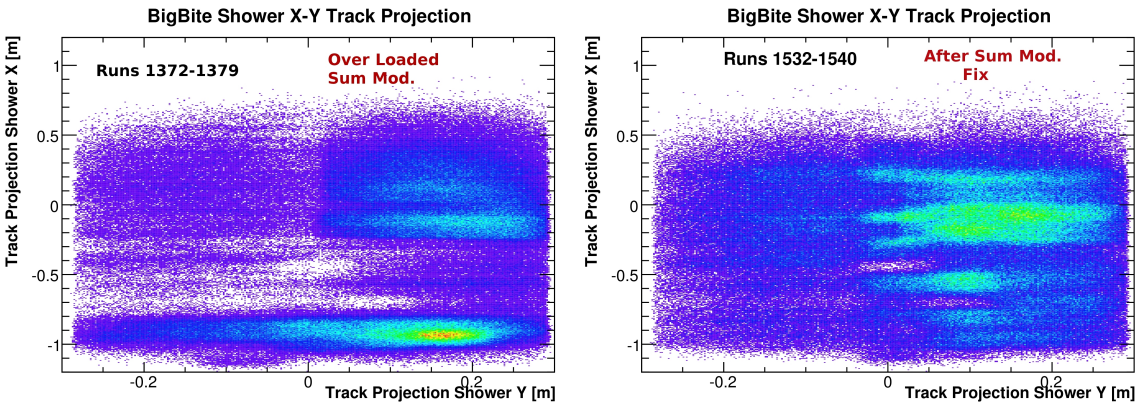

Figure 8.27: BigBite acceptance before and after the summing modual fix.

none the less the ADCs correlated to the inadequate shower blocks are still lower than the surrounding blocks.

While studying the acceptance effects, it was found that the gaps in the acceptance did not significantly affect the off-line analysis. During the calibration of the calorimeter energy, a larger calibration constant was applied to the faulty blocks to counteract the their low signals. Furthermore, since the BigBite spectrometer was measuring asymmetries, any acceptance effects should drop out of the asymmetry calculations (discussed in Section 8.2.5.4).

8.2.5 Asymmetry Analysis

The experimental raw asymmetries were determined through the observed asymmetry in the counts measured in the BigBite detector

$$A_{raw} = \frac{N^{\downarrow S} - N^{\uparrow S}}{N^{\downarrow S} + N^{\uparrow S}}, \tag{8.18}$$

where N is the number of counts (the number of electrons counted after applying data quality and electron PID cuts) in a particular configuration, $\downarrow$ represents negative electron

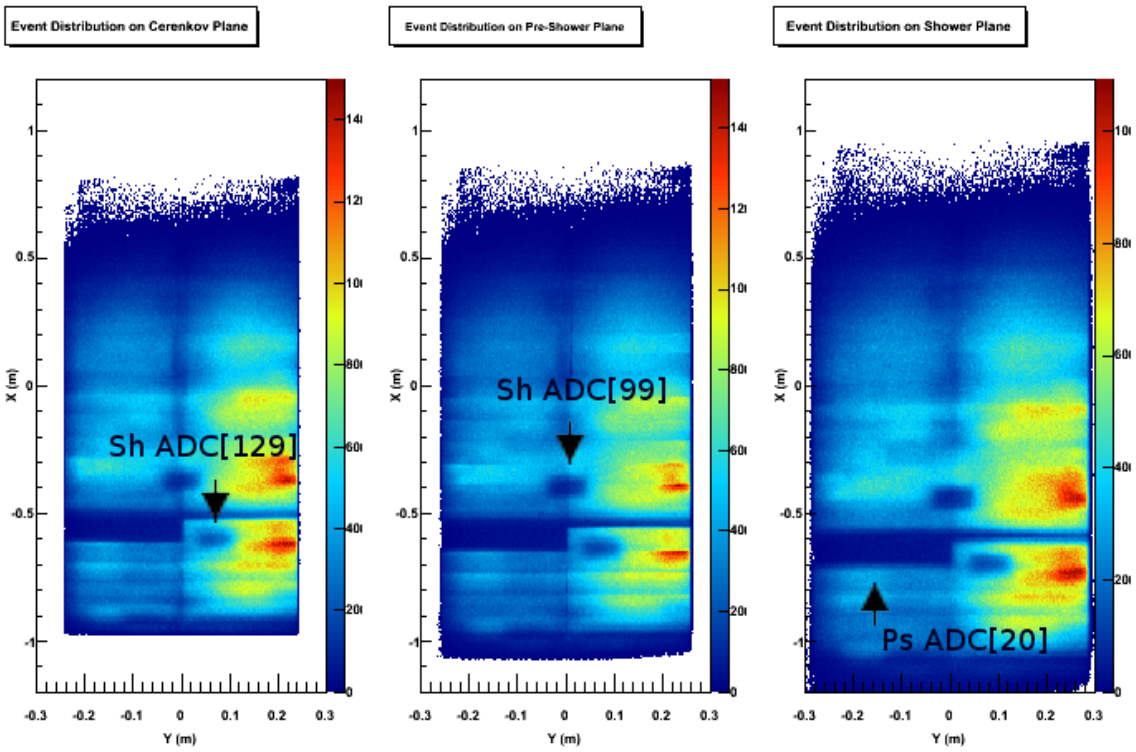

Figure 8.28: Reconstructed tracks projected onto the vertical and horizontal shower plane; each of the acceptance gaps are labeled with the associated bad calorimeter block.

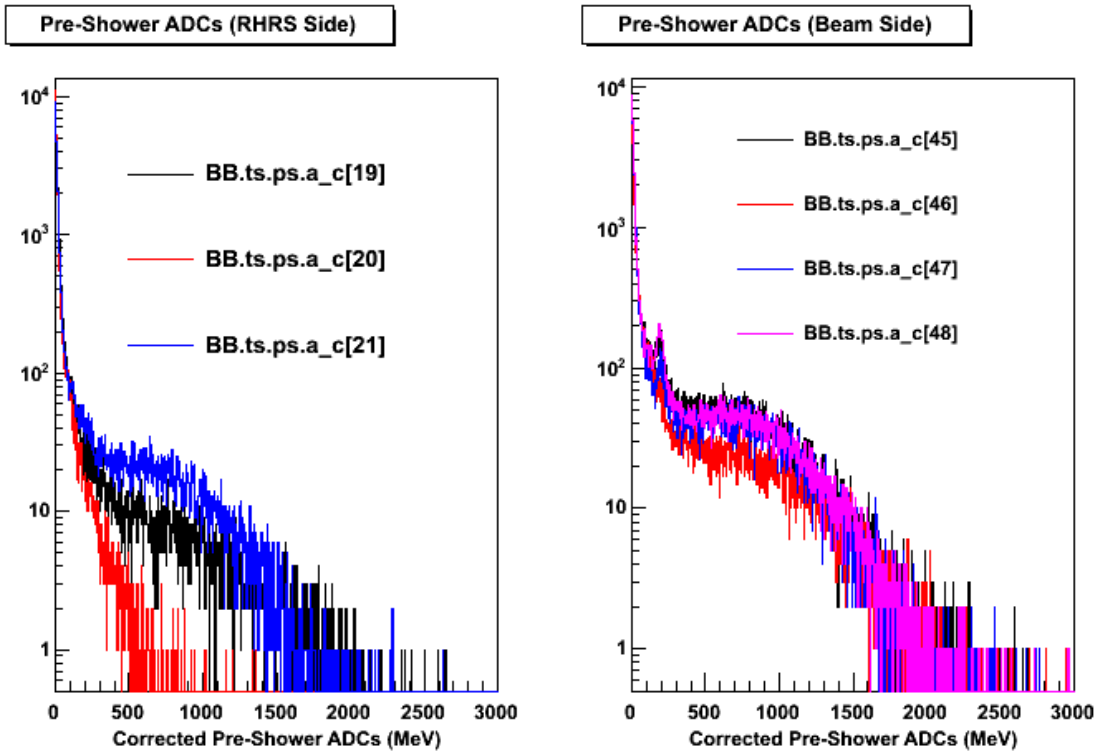

Figure 8.29: Preshower ADCs. Left panel shows preshower ADCs associated with blocks on the large angle side (column furthest from the beam), where the red histogram (preshower block 21) is the faulty preshower block. The right panel shows preshower ADC signals from blocks on the small angle side (closest to the beam).

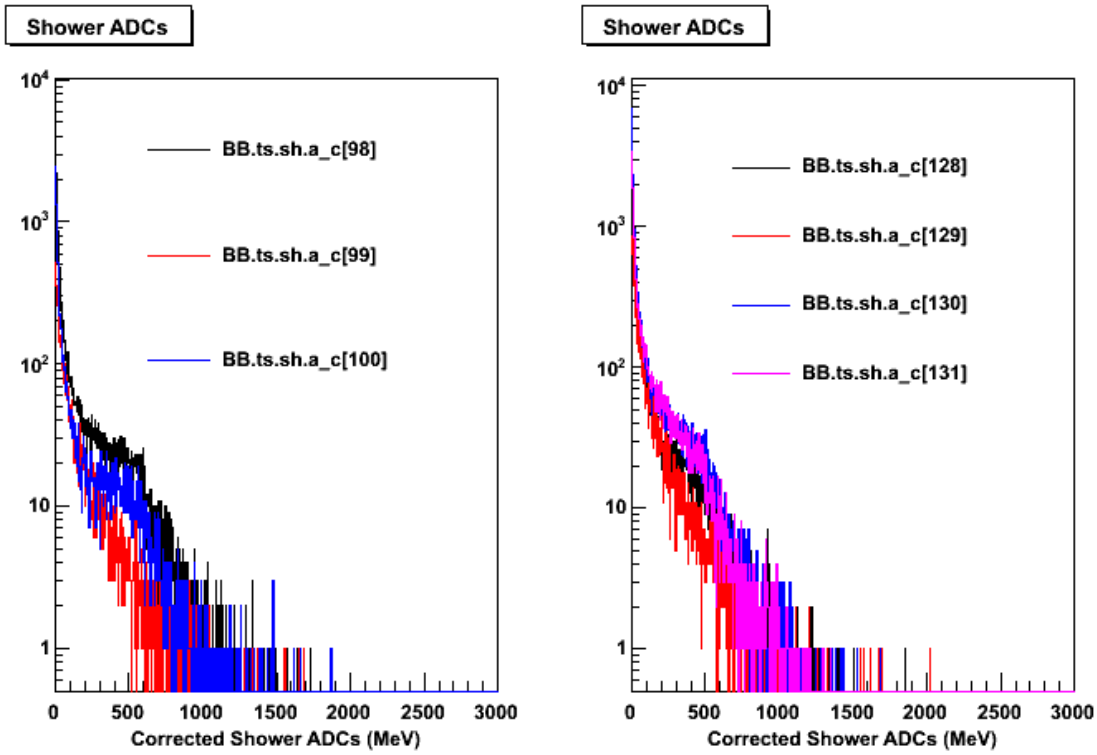

Figure 8.30: Shower ADCs. The shower blocks 100 (red histogram in the left panel) and 130 (red histogram in the right panel) are known to be the blocks responsible for producing gaps in the BigBite acceptance.

helicity (electron's spin is anti-parallel to it's momentum), $\uparrow$ represents positive electron helicity (electron's spin is parallel to it's momentum), and S is the target spin direction. A detailed description of the target spin configurations and sign conventions are discussed in Section 8.2.5.1.

The raw counting asymmetries fail to account for several factors, which results in a different asymmetry from the physics asymmetries defined in Equations 1.32 and 1.33. The raw asymmetries do not consider the imperfect polarization of the ^{3}He target and electron beam. They also include unpolarized scattering contributions. Although the contributions from unpolarized scattering will cancel in the numerator of the asymmetry, it will add in the denominator causing a suppression (dilution) of the overall asymmetry. Since the target used in E06-014 contained a small amount of unpolarized nitrogen, its dilution (D_{N_2}) to the asymmetries also needs to be included. Considering such effects, one can recover the physics asymmetries as

$$A_{phys}^{^3\text{He}} = \frac{A_{raw}}{P_b P_t D_{N_2}}, \tag{8.19}$$

where, P_b is the beam polarization (given in Table 5.2), P_t is the ^{3}He polarization of the nuclei inside the target chamber (given in Figure 6.31), and dilution factor D_{N_2} is calculated according to Section 8.2.6.

Up to this point, the physics asymmetry have assumed that the particle detection efficiencies are uncorrelated to the spin configurations. In reality, however this is may not be the case. The charge and detector deadtime are correlated to the rates, therefore an asymmetry in one spin configuration could have more or less collected charge or deadtime than the other. Both of these effects were found to be negligible in E06-014, and are discussed in Section 8.2.5.2. In addition to how quantities correlated to rate affect the asymmetries, the effect of the acceptance gaps on the asymmetries were also studied in Section 8.2.5.4.

8.2.5.1 Asymmetry Sign

In order to define a consistent sign convention, one needs to know the physical direction of the electron beam helicity and the target spin. As shown in Figure 8.31, E06-014 ran with three target spin configurations, one longitudinal and two transverse, all of which were in the horizontal scattering plane. The LHRS was positioned 45° to the left of the electron beam and the BigBite detector was positioned 45° to the right of the beam. The "Target Spin" portion of Figure 8.31 shows the definition of the target spin configuration used in the asymmetry analysis. When the target spin direction is at 0°, it is parallel to the electron beam momentum. The transverse target spin configurations correspond to the target spin pointing to 90°($+X$, towards the LHRS detector stack in Figure 6.6) and 270°($-X$, towards the BigBite detector stack in Figure 6.6). E06-014 ran in an anti-parallel optical pumping configuration, meaning that the target spin was always oriented opposite to that of the magnetic holding field. The magnetic field information was recorded during each configuration change and could be used to determine the target spin orientation.

8.2.5.1.1 Longitudinal Asymmetry When the electron beam and target spin are longitudinally polarized, the electron spin may be either parallel or anti-parallel to the target spin direction. Following the convention of previous experiments (*e.g.* E99-117[3]), the asymmetry is given in general as

$$A = \frac{N^{\downarrow\Uparrow} - N^{\uparrow\Uparrow}}{N^{\downarrow\Uparrow} + N^{\uparrow\Uparrow}}, \tag{8.20}$$

where $\Uparrow$ corresponds to a target spin towards 0°, and $\Downarrow$ towards 180°.

When the E06-014 ^{3}He target was longitudinally polarized, it was always oriented so that the spin pointed towards 0° (the target spin pointed down stream), therefore as shown in Equation 8.20, counts with negative helicity ($N^{\downarrow}$) are given a positive sign, where as counts

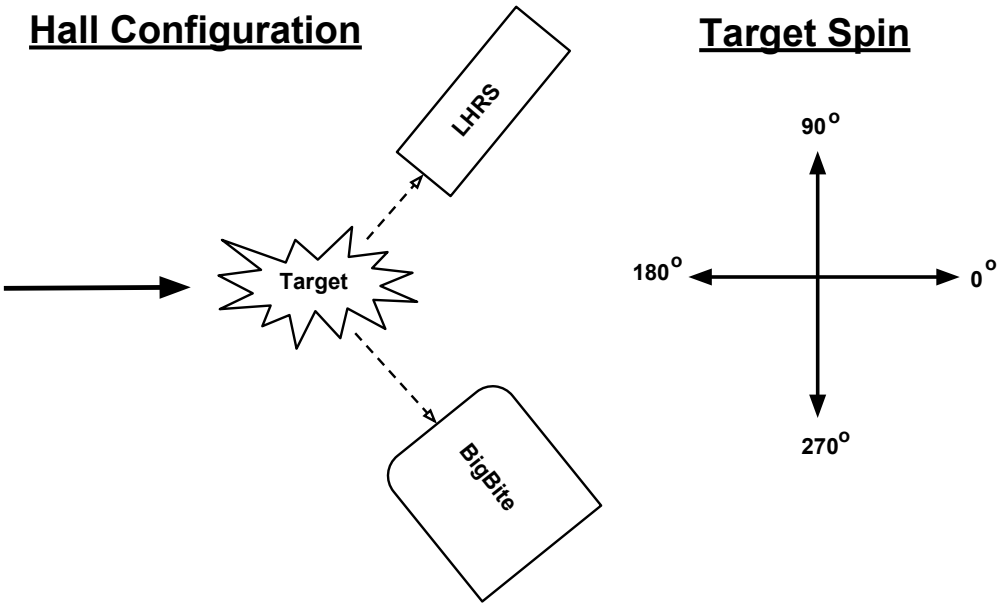

Figure 8.31: Definition of the three target spin directions used for E06-014. Looking down at the hall, a target spin of 0° is the longitudinal target spin direction, and 90° and 270° are the two transverse target spin directions. Image modified from[75].

with positive helicity ($N^{\uparrow}$) are assigned a negative sign.

8.2.5.1.2 Beam Helicity Changes in the beam configuration, such as a change to the number of passes through the linacs, can alter the spin precession angle. This could lead to a reversal in the observed beam helicity relative to the helicity logic signal used in the DAQ, which assigns a spin direction to the electron [77]. Møller polarimetry measurements were performed after each beam configuration change, allowing for the beam polarization and absolute electron helicity in Hall A to be measured[7]. If an insertable half wave plate (IHWP) is placed at the electron source, it would invert the relationship of the helicity logic to the helicity of the emitted electron, which is not considered in the Møller measurements. Therefore in order to find the relationship between the helicity recorded in the BigBite DAQ and the Møller helicity standard, the raw ^{3}He longitudinal asymmetry in the quasielastic scattering region can be calculated and compared to the measured value. The raw quasielastic asymmetry at a beam energy of 1.23 GeV and scattering angle of 45° was found to be $A_{raw}^{QE} \approx +0.02$[149].

Several runs were taken at a beam energy of 1.23 GeV on polarized ^{3}He , which resulted in electrons quasielasticly scattering from ^{3}He nuclei. In order to select electrons, data quality and PID cuts defined in Sections 8.2.1 and 8.2.2 were applied to the data, with a slight modification to the E/p and scintillator energy cuts. The E/p cut was changed to

$$0.7 < E/p < 1.3, \tag{8.21}$$

and the scintillator cut was changed to

$$\text{Scintillator Energy} > 200\text{MeV}. \tag{8.22}$$

[7]The sign of the Møller polarization measurement provides a relationship between the actual helicity and the Møller standard[75].

An additional cut was applied to the invariant mass, $W < 3.1GeV$, in order to ensure that the electrons being analyzed were quasielastic electrons. The measured asymmetry can be seen in Figure 8.32 and was found to be

$$A_{raw}^{QE} = \frac{N^{\downarrow\Uparrow} - N^{\uparrow\Uparrow}}{N^{\downarrow\Uparrow} + N^{\uparrow\Uparrow}} = +0.012 \pm 0.0026. \tag{8.23}$$

The measured result is within a factor of two to the calculated estimate, but is clearly positive.

During the quasielastic measurement, with the IHWP OUT, the helicity logic signal measured in BigBite (as well as the LHRS) accurately reflected the helicity of the electron arriving at the Hall A target. Meanwhile, the Møller measurement done for this beam configuration, but with the IHWP IN, gave a negative beam polarization. Thus to correct for the IHWP being IN, the results measured with the IHWP IN need to be multiplied by -1, to give the correct beam polarization sign as when the IHWP was OUT[75]. Thus one can conclude that when the IHWP is OUT of the beamline, a positive Møller measurement means that the electrons detected in BigBite; which are tagged as having positive (negative) helicities, actually do have positive (negitive) helicities. This helicity dependence on the IHWP state (IN = -1 or OUT = +1) was consistent throughout the entire experiment, with the exception of the last 4.74 GeV data set, where the helicity dependence on the IHWP was reversed (IN = +1 or OUT = -1). This reversal was the result of a change in the electron's spin percession, caused by the unbalanced running of the linacs during this period of the experiment [75].

8.2.5.1.3 Transverse Asymmetry Following from Section 8.2.5.1.1, a positive sign is applied to events with negative helicity electrons and a negative sign is applied to events having a positive electron helicity when forming the transverse asymmetry. However, unlike

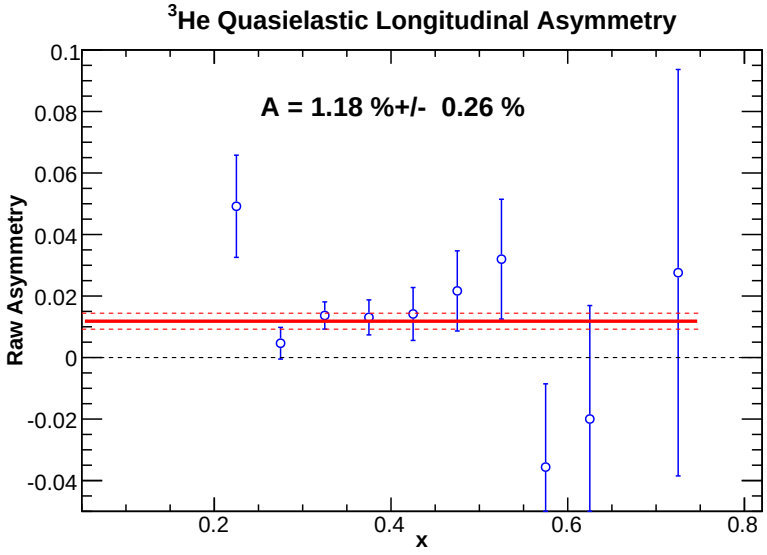

Figure 8.32: Measured quasieleastic longitudinal asymmetry on ^{3}He at a beam energy of 1.23 GeV. The red solid line shows a constant fit to the asymmetry plotted against x. The two dashed red lines mark the upper and lower statistical error in the total asymmetry.

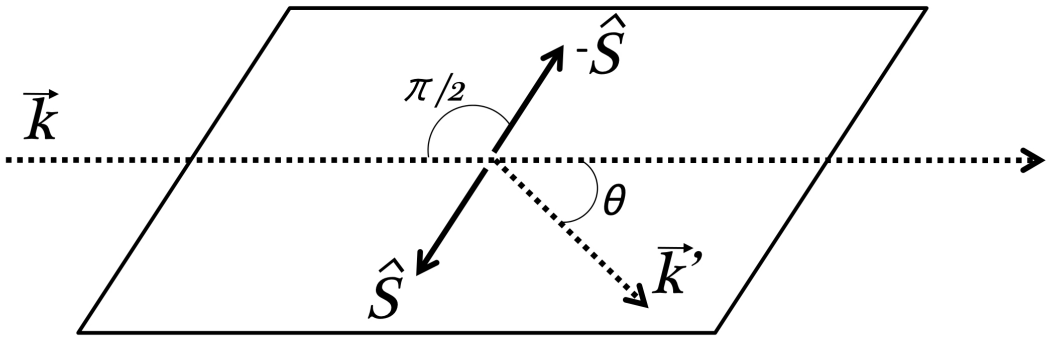

Figure 8.33: Convention for transverse target spin $\hat{S}$. The spin of the incident electron is parallel or anti-parallel to its momentum $\vec{k}$. Figure reproduced from [75].

the longitudinally polarized target, there are two orientations for the transverse configuration: one pointing towards 90° and the other towards 270°. The asymmetry measured in each configuration will have an opposite sign relative to the other. To determine which target configuration should carry which sign, one can consider the momentum-spin vectors. As seen in Section 1.5.2, $\vec{k} \cdot \hat{S} = 0$ for both transverse spin configurations, meaning that the target spin only enters the cross section through $\vec{k}' \cdot \hat{S} = E \sin\cos\phi$, where θ is the scattering angle and ϕ the angle between the scattering and polarization planes, defined in Figure 1.4. E06-014 only polarized the target transverse to the electron beam in the scattering plane, which results in $\phi = 0$, illustrated in Figure 8.33. The positive sense of the target spin is then the direction that points to the side of the beamline where the scattering electron is detected (consistent E99-117[3]). Asymmetries measured during E06-014, were done using the BigBite detector, therefore the target spin pointing towards 270° was assigned a positive sign and a negative sign was assigned to the target spin direction pointing towards 90°. Transverse asymmetries that were measured in the LHRS[8] would follow a sign convention opposite to that of BigBite.

8.2.5.2 False Asymmetries

When measuring an asymmetry, care must be taken to ensure that the asymmetry is due to electron spin-dependent scattering, and not helicity-correlated changes in the electron beam, known as *false asymmetries*. One of the most problematic sources of false asymmetries arises from a difference in the electron beam intensity between the two helicity states, resulting in a charge asymmetry. The beam-charge asymmetry during E06-014 was limited to about 100 ppm. This was accomplished through the use of a feedback loop controlled by a specialized DAQ[157], and was also verified by D. Parno [75] by measuring the charge

[8] Statistics were too low in the LHRS to measure any meaningful electron DSAs. However, the LHRS was able to measure precise pion DSAs.

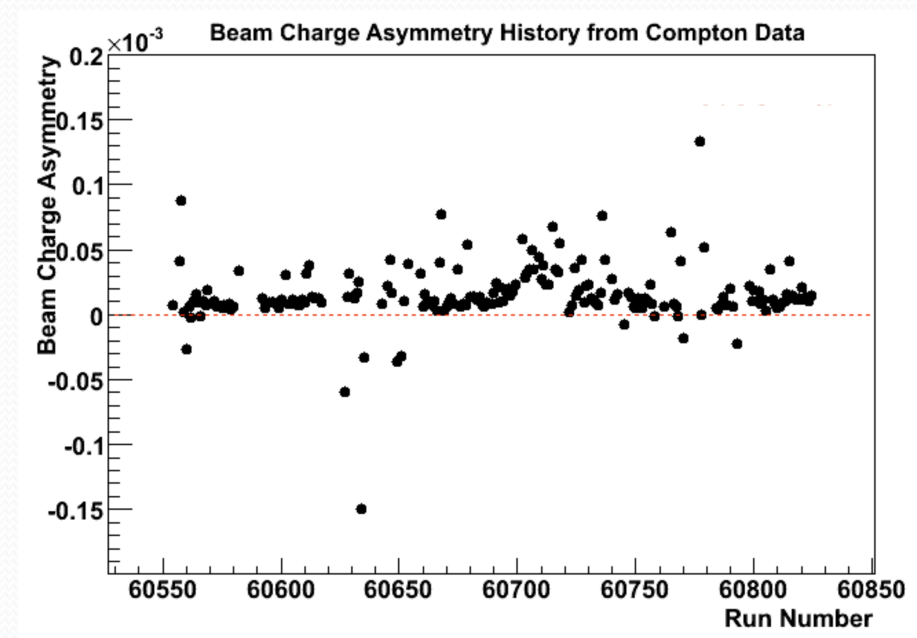

Figure 8.34: Beam-charge asymmetry history measured using the Compton detector. Plot taken from reference [75].

asymmetry using the Compton detector. Figure8.34 shows the beam-charge asymmetry history (beam-charge asymmetry as a function of Compton run number) measured using the Compton detector[75]. The beam-charge asymmetry size is negligible compared to the precision of the electron asymmetry measurements, thus beam-charge corrections did not need to be applied.

Helicity dependent DAQ changes can also generate false asymmetries. Such a dependency can be seen through the detector's livetime[9]. A helicity dependent rate could lead to one helicity state having a longer livetime than the other helicity state, resulting in an asymmetry. To check the size of this asymmetry, the BigBite detector livetimes were recorded for each of the BigBite helicity gates (as defined in Section 4.4.7). Figure 8.35 shows the BigBite helicity dependent livetimes measured at both electron beam energy settings. The

[9] A detectors livetime is $1 -$ deadtime, where the deadtime is the amount of time that a detector cannot accept any new information, because it is busy processing the previous event.

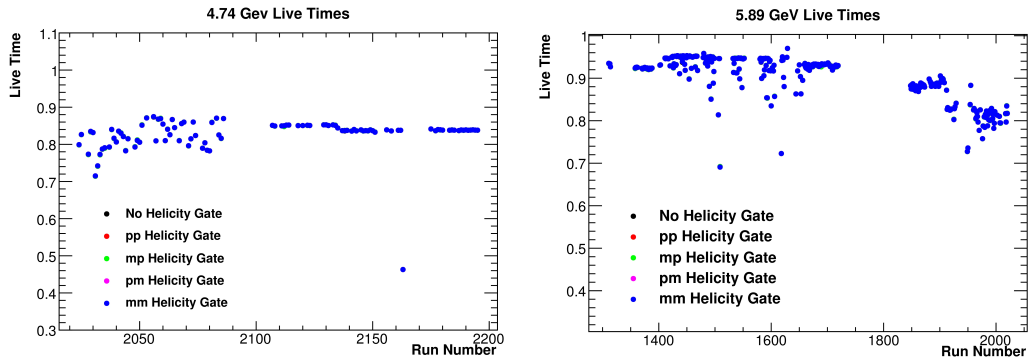

Figure 8.35: Measured BigBite livetimes for incident beam energy of 4.74 GeV (left panel) and 5.89 GeV (right panel).

difference between the helicity dependent livetimes is too small to be seen in plot. The change in the livetimes (near run 1800) from $\sim 90\%$ to $\sim 80\%$, seen in the right panel of Figure 8.35, is due to changes in the main BigBite trigger (T2), in particular, the addition of the preshower energy into the T2 trigger. The second livetime change seen in the right panel (near run 1900), is due to altering the trigger prescales and optimizing the trigger. The 4.74 GeV beam energy setting ran with the optimized (preshower energy included) trigger, and hence had the same average livetime (left panel of Figure 8.35) as the end of the 5.89 GeV data set. The varying livetime seen in the early running of the 4.74 GeV data set was due to unstable beam, which resulting from the faulty linac described in Section 4.5. After the linac fix (around run 2100), the livetime becomes stable.

The helicity dependent livetime asymmetry can be written as

$$A_{lt} = \frac{N^{mm} - N^{pp}}{N^{mm} + N^{pp}} = \frac{N^{pm} - N^{mp}}{N^{pm} + N^{mp}}, \tag{8.24}$$

where N are the event counts for the different helicity gates used during E06-014 (Section 4.4.7). The live time asymmetry results are shown in Figure 8.36 for the 4.74 (top row) and 5.89 (bottom row) GeV data sets. The plots in the left columns show the asymmetry as a function of run number with a constant fit (the red line), and in the columns on the

right, show the histogrammed asymmetries with a Gaussian fit. In both cases (constant and Gaussian fits) the live time asymmetry is small, $<$ 100ppm for both beam energies and therefore they are not considered in the E06-014 analysis.

In addition to the charge and DAQ induced false asymmetries, software can also introduce an artificial asymmetry. For example, if rates are high enough, it may be more difficult to reconstruct good tracks related to the higher rate helicity state, than for the lower one, resulting in an asymmetry [146]. However, E06-014 had a very low track multiplicity ($\sim$ 4%) and therefore, the rates were not high enough for such an asymmetry to have a significant contribution to the measured electron asymmetries. Other potential false asymmetries can be limited through the 30 Hz helicity flipping of the electron beam. Furthermore, any false asymmetry that does not change sign with respect to the IHWP state, such as those due to electronic cross-talk [158], would be canceled when combining the IHWP states.

8.2.5.3 Raw Asymmetries

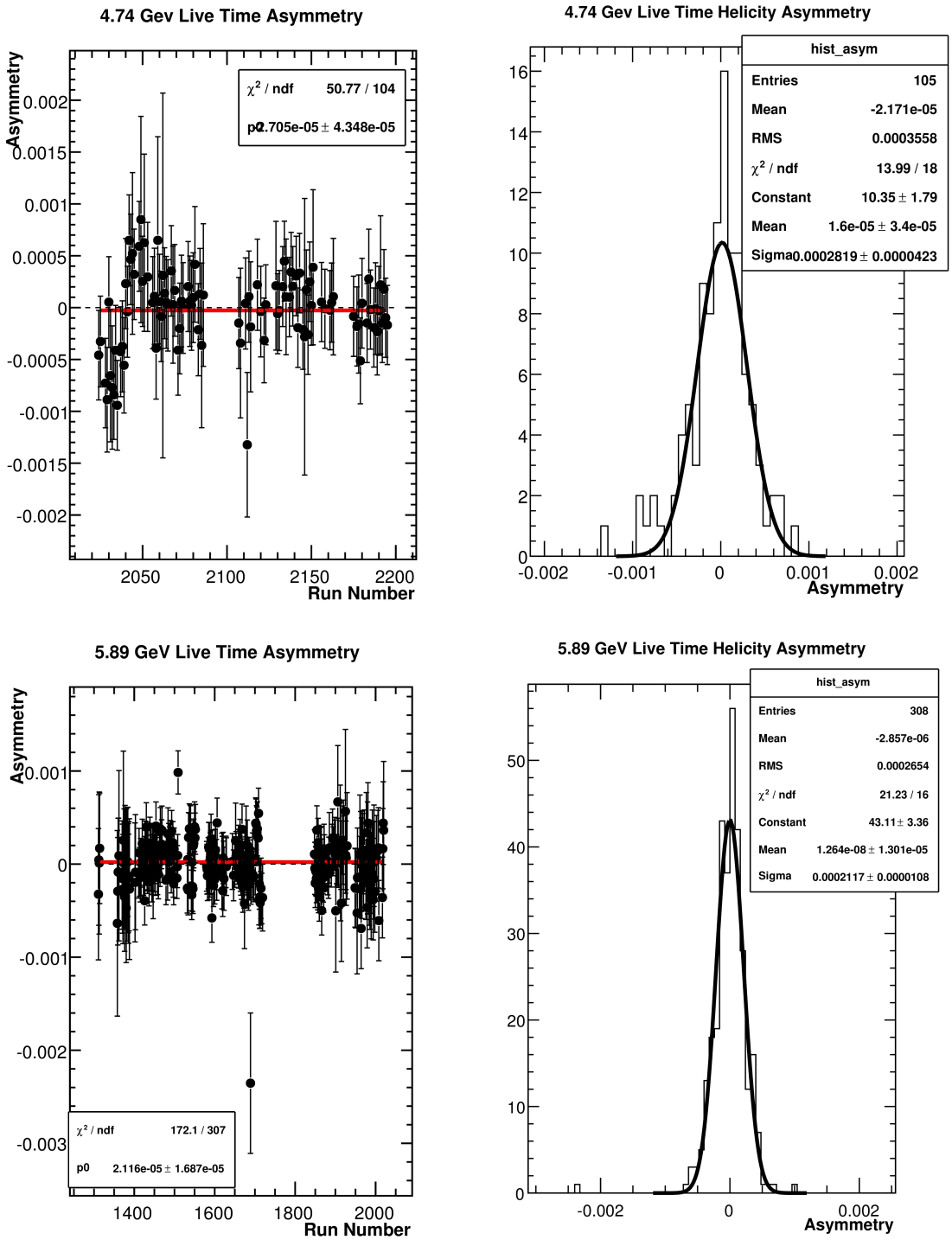

Figure 8.36: Measured BigBite live time asymmetries for incident beam energy of 4.74 GeV (upper panel) and 5.89 GeV (lower panel). Left panel shows live time asymmetries with a constant fit, while the right panels show Gaussian fit to the live time asymmetries.

In order to begin evaluating the raw electron asymmetries on a polarized ^{3}He target, the three target spin configurations used during E06-014 needed to be separated. This was accomplished by collecting runs that shared the same target spin direction and applying the correct sign for IHWP status. The IHWP changes were recorded during the experiment in both the electronic logbook and EPICS data stream. Since these transitions only occurred between runs, a definite IHWP status could be assigned to each run. Tables 8.10 and 8.11 show the collected data divided into each of the target spin directions for the 4.74 GeV and 5.89 GeV data sets. These tables list the total number of production runs, the number runs taken for each IHWP configuration, and the total collected charge incident on the target[10] for each of the spin configurations.

The asymmetries were binned into equally spaced x bins covering the range of $0 \leq x \leq 1$, with a bin width of 0.05. For each target spin configuration (S) the raw asymmetry for each x-bin was formed on a run-by-run basis as

[10]When computing the total charge on target, the data quality and PID cuts described in Sections 8.2.1 and 8.2.2 were not applied.

Table 8.10: E06-014 run statistics for 4.74 GeV data set. With the exception of the beam trip cut, data quality and PID cuts were not applied when computing the incident charge.

Target Spin	Runs	IHWP IN (Runs)	IHWP OUT (Runs)	Total Q [C]
0°	24	11	13	0.69
90°	26	21	5	0.80
270°	51	22	29	1.90
Total	101	54	47	3.39

Table 8.11: E06-014 run statistics for 5.89 GeV data set. With the exception of the beam trip cut, data quality and PID cuts were not applied when computing the indcident charge.

Target Spin	Runs	IHWP IN (Runs)	IHWP OUT (Runs)	Total Q [C]
0°	35	18	17	1.06
90°	141	76	65	4.22
270°	130	54	76	3.85
Total	306	148	158	9.13

$$A_i^S = \frac{N_i^{\downarrow,S} - N_i^{\uparrow,S}}{N_i^{\downarrow,S} + N_i^{\uparrow,S}}, \tag{8.25}$$

$$\begin{aligned} \delta A_i^S &= \sqrt{\frac{\left(2N_i^{\downarrow,S}\delta N_i^{\uparrow,S}\right)^2 + \left(2N_i^{\uparrow,S}\delta N_i^{\downarrow,S}\right)^2}{\left(N_i^{\downarrow,S} + N_i^{\uparrow,S}\right)^4}} \\ &= \sqrt{\frac{4N_i^{\downarrow,S}N_i^{\uparrow,S}}{\left(N_i^{\downarrow,S} + N_i^{\uparrow,S}\right)^3}}, \end{aligned} \tag{8.26}$$

where A_i^S is the asymmetry for the i^{th} run corresponding to target spin direction S and δA_i^S is the statistical uncertainty of the A_i^S. The counts ($N_i^{\uparrow,S}$ and $N_i^{\downarrow,S}$) for a given target spin direction in the asymmetries were evaluated by applying the electron data quality and PID cuts. A helicity flag cut, set by the helicity logic signal [11], was also used to select either the negative ($\downarrow$) or positive ($\uparrow$) electron helicity states. The statistical uncertainty in the counts is given by $\delta N_i^{\downarrow,S} = \sqrt{N_i^{\downarrow,S}}$ and likewise $\delta N_i^{\uparrow,S} = \sqrt{N_i^{\uparrow,S}}$.

The total (helicity summed) electron counts for each x-bin used in the evaluation of the E = 4.74 GeV and E = 5.89 GeV raw asymmetries are shown in Figures 8.37 and 8.38. There values can also be found in Table 8.12. The x-bins that were considered in the analysis

[11] some events were detected during an MPS transition, and thus had an indeterminate helicity state; these were removed by requiring a definite helicity state.

Table 8.12: E06-014 electron counts (after passing data-quality and PID cuts) per target state.

Beam Energy [GeV]	S = 0°	S = 90°	S = 270°	Total
4.74	2380893	5168892	11876138	19425923
5.89	1205433	7587803	12787087	21580323

began at the bin with its center at 0.225. While bins with centers below 0.225 typically only contained a couple of counts and were therefore discarded.

The asymmetries for each x-bin were then combined over all runs i, for a given target orientation S, using a statistical uncertainty weighted sum

$$A^S_{raw} = \frac{\sum_i A^S_i \left(\delta A^S_i\right)^{-2}}{\sum_i \left(\delta A^S_i\right)^{-2}} \tag{8.27}$$

$$\delta A^S_{raw} = \sqrt{\frac{1}{\sum_i \left(\delta A^S_i\right)^{-2}}}. \tag{8.28}$$

The E = 4.74 GeV (red triangles) and E = 5.89 GeV (blue circles) raw asymmetries for each of the ^{3}He target spin configurations are plotted in Figure 8.39 as a function of x. Their values are also listed in Tables 8.13 and 8.14. From Figure 8.39, it is evident that A^{90}_{raw} and A^{270}_{raw} do in fact have opposite signs, which corresponds to the target spin direction that the asymmetry was measured at. It should be noted that only data at $x < 0.519$ when E = 4.74 GeV, and $x < 0.623$ when E = 5.89 GeV, corresponds to deep inelastic electron scattering.

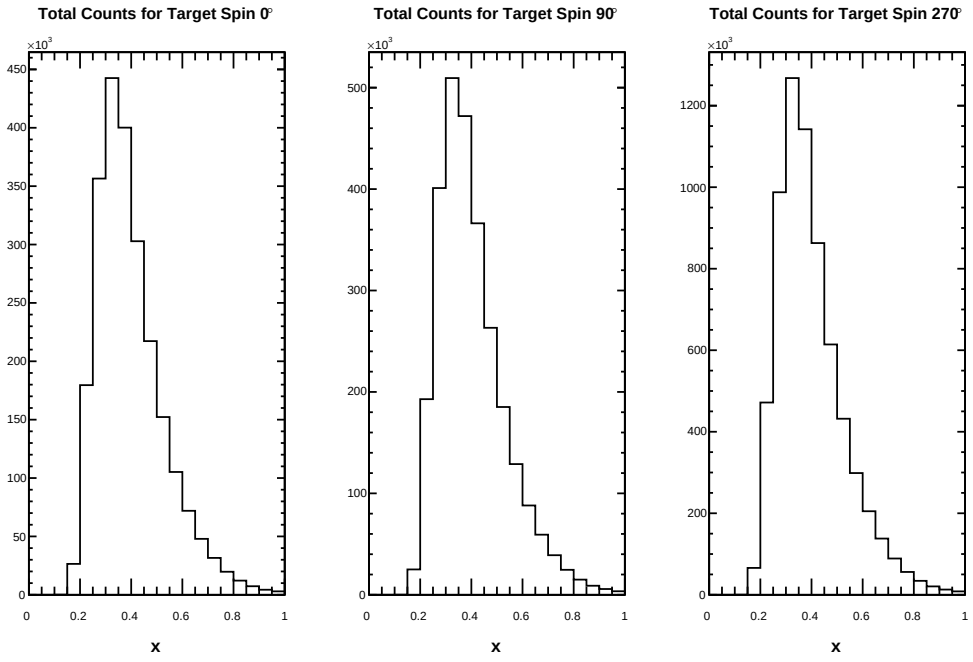

Figure 8.37: Total electron counts (helicity summed) detected in each x bin at E = 4.74 GeV for each of the three target spin configurations.

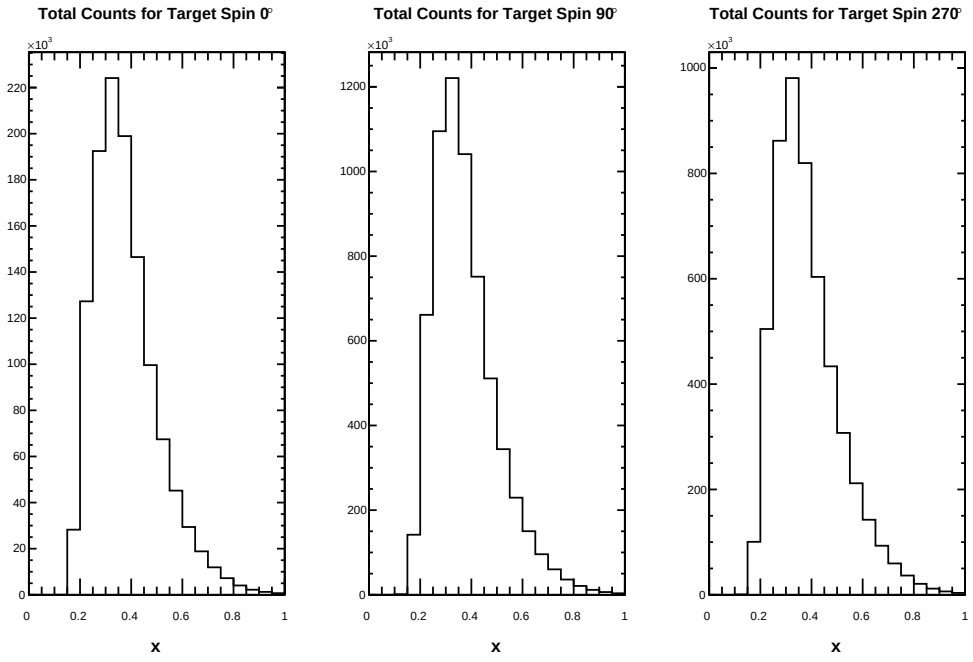

Figure 8.38: Total electron counts (helicity summed) detected in each x bin at E = 5.89 GeV for each of the three target spin configurations.

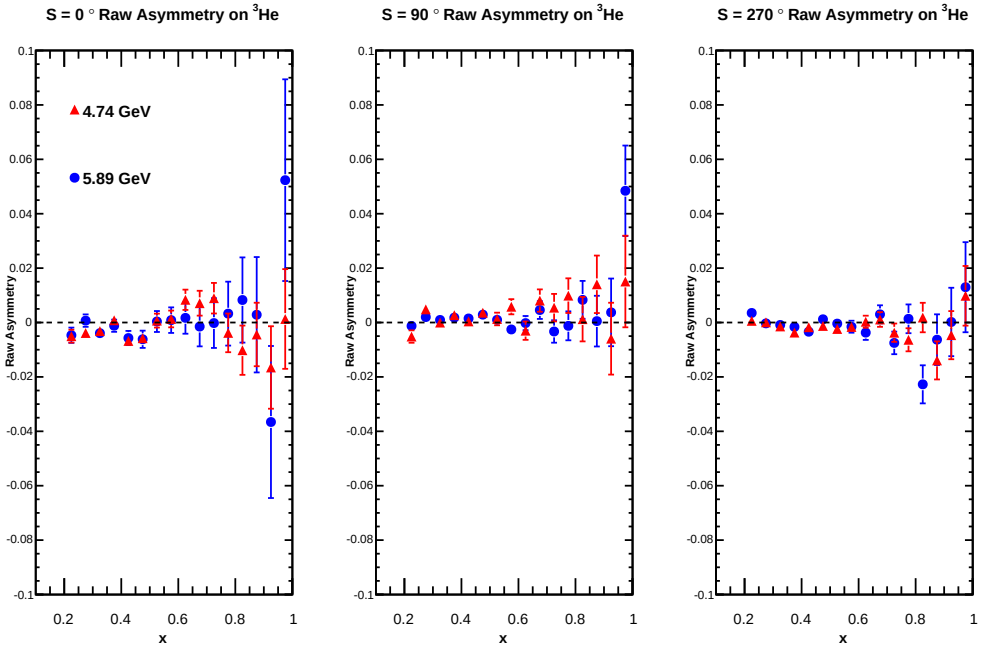

Figure 8.39: Raw asymmetries measured at E = 4.74 GeV (red triangles) and E = 5.89 GeV (blue circles) for each of the three target spin configurations as defined by Equation 8.18. Only statistical uncertainties are shown.

Table 8.13: Raw asymmetries on ^{3}He binned in x, and computed from Equation 8.27 for E = 4.74 GeV.

	Target Spin = 0°	Target Spin = 90°	Target Spin = 270°
Central x Bin Value	A^0_{raw}	A^{90}_{raw}	A^{270}_{raw}
0.225	-0.0050 $\pm$ 0.0024$_{stat}$	-0.0052 $\pm$ 0.0023$_{stat}$	0.0006 $\pm$ 0.0015$_{stat}$
0.275	-0.0039 $\pm$ 0.0017$_{stat}$	0.0048 $\pm$ 0.0016$_{stat}$	0.0001 $\pm$ 0.0010$_{stat}$
0.325	-0.0032 $\pm$ 0.0015$_{stat}$	-0.0000 $\pm$ 0.0014$_{stat}$	-0.0014 $\pm$ 0.0009$_{stat}$
0.375	0.0008 $\pm$ 0.0016$_{stat}$	0.0027 $\pm$ 0.0015$_{stat}$	-0.0037 $\pm$ 0.0009$_{stat}$
0.425	-0.0068 $\pm$ 0.0018$_{stat}$	0.0004 $\pm$ 0.0016$_{stat}$	-0.0017 $\pm$ 0.0011$_{stat}$
0.475	-0.0058 $\pm$ 0.0022$_{stat}$	0.0036 $\pm$ 0.0019$_{stat}$	-0.0013 $\pm$ 0.0013$_{stat}$
0.525	0.0007 $\pm$ 0.0026$_{stat}$	0.0013 $\pm$ 0.0023$_{stat}$	-0.0024 $\pm$ 0.0015$_{stat}$
0.575	0.0013 $\pm$ 0.0031$_{stat}$	0.0058 $\pm$ 0.0028$_{stat}$	-0.0016 $\pm$ 0.0018$_{stat}$
0.625	0.0084 $\pm$ 0.0037$_{stat}$	-0.0030 $\pm$ 0.0034$_{stat}$	0.0003 $\pm$ 0.0022$_{stat}$
0.675	0.0071 $\pm$ 0.0046$_{stat}$	0.0081 $\pm$ 0.0041$_{stat}$	0.0011 $\pm$ 0.0027$_{stat}$
0.725	0.0089 $\pm$ 0.0056$_{stat}$	0.0055 $\pm$ 0.0051$_{stat}$	-0.0037 $\pm$ 0.0034$_{stat}$
0.775	-0.0038 $\pm$ 0.0071$_{stat}$	0.0099 $\pm$ 0.0064$_{stat}$	-0.0063 $\pm$ 0.0042$_{stat}$
0.825	-0.0102 $\pm$ 0.0091$_{stat}$	0.0012 $\pm$ 0.0082$_{stat}$	0.0018 $\pm$ 0.0054$_{stat}$
0.875	-0.0044 $\pm$ 0.0117$_{stat}$	0.0140 $\pm$ 0.0106$_{stat}$	-0.0139 $\pm$ 0.0070$_{stat}$
0.925	-0.0165 $\pm$ 0.0152$_{stat}$	-0.0059 $\pm$ 0.0132$_{stat}$	-0.0046 $\pm$ 0.0089$_{stat}$
0.975	0.0013 $\pm$ 0.0183$_{stat}$	0.0151 $\pm$ 0.0168$_{stat}$	0.0098 $\pm$ 0.0110$_{stat}$

Table 8.14: Raw asymmetries on ^{3}He binned in x, and computed from Equation 8.27 for E = 5.89 GeV.

	Target Spin = 0°	Target Spin = 90°	Target Spin = 270°
Central x Bin Value	A^0_{raw}	A^{90}_{raw}	A^{270}_{raw}
0.225	-0.0047 $\pm$ 0.0028$_{stat}$	-0.0013 $\pm$ 0.0012$_{stat}$	0.0035 $\pm$ 0.0014$_{stat}$
0.275	0.0007 $\pm$ 0.0023$_{stat}$	0.0020 $\pm$ 0.0010$_{stat}$	-0.0003 $\pm$ 0.0011$_{stat}$
0.325	-0.0039 $\pm$ 0.0021$_{stat}$	0.0009 $\pm$ 0.0009$_{stat}$	-0.0009 $\pm$ 0.0010$_{stat}$
0.375	-0.0012 $\pm$ 0.0022$_{stat}$	0.0018 $\pm$ 0.0010$_{stat}$	-0.0016 $\pm$ 0.0011$_{stat}$
0.425	-0.0057 $\pm$ 0.0026$_{stat}$	0.0015 $\pm$ 0.0012$_{stat}$	-0.0034 $\pm$ 0.0013$_{stat}$
0.475	-0.0062 $\pm$ 0.0032$_{stat}$	0.0029 $\pm$ 0.0014$_{stat}$	0.0012 $\pm$ 0.0015$_{stat}$
0.525	0.0004 $\pm$ 0.0039$_{stat}$	0.0010 $\pm$ 0.0017$_{stat}$	-0.0004 $\pm$ 0.0018$_{stat}$
0.575	0.0009 $\pm$ 0.0047$_{stat}$	-0.0026 $\pm$ 0.0021$_{stat}$	-0.0015 $\pm$ 0.0022$_{stat}$
0.625	0.0017 $\pm$ 0.0058$_{stat}$	-0.0002 $\pm$ 0.0026$_{stat}$	-0.0037 $\pm$ 0.0027$_{stat}$
0.675	-0.0015 $\pm$ 0.0073$_{stat}$	0.0046 $\pm$ 0.0033$_{stat}$	0.0030 $\pm$ 0.0033$_{stat}$
0.725	-0.0002 $\pm$ 0.0092$_{stat}$	-0.0033 $\pm$ 0.0041$_{stat}$	-0.0075 $\pm$ 0.0042$_{stat}$
0.775	0.0033 $\pm$ 0.0118$_{stat}$	-0.0012 $\pm$ 0.0053$_{stat}$	0.0014 $\pm$ 0.0053$_{stat}$
0.825	0.0083 $\pm$ 0.0157$_{stat}$	0.0083 $\pm$ 0.0070$_{stat}$	-0.0227 $\pm$ 0.0070$_{stat}$
0.875	0.0029 $\pm$ 0.0212$_{stat}$	0.0005 $\pm$ 0.0093$_{stat}$	-0.0063 $\pm$ 0.0093$_{stat}$
0.925	-0.0366 $\pm$ 0.0279$_{stat}$	0.0037 $\pm$ 0.0124$_{stat}$	0.0002 $\pm$ 0.0126$_{stat}$
0.975	0.0523 $\pm$ 0.0371$_{stat}$	0.0484 $\pm$ 0.0166$_{stat}$	0.0130 $\pm$ 0.0166$_{stat}$

8.2.5.4 Acceptance Gap

During the running of E06-014, one of the preshower blocks had failed, which resulted in a visible gap in the BigBite acceptance. Since the BigBite was used to measure the electron DSA, which is a relative measurement, the acceptance factor should cancel out when computing the asymmetry; to verify this a study was done in which the raw longitudinal electron asymmetry (at E = 4.74 GeV) was computed for different positions along the vertical shower plane. The shower plane was split into three regions, shown in Figure 8.28, in which region one selected electrons detected in the lower portion of the acceptance[12]. Region two selects electrons in the upper portion of the acceptance, while region three selects electrons falling into a region of the acceptance corresponding to the gap. Figure 8.41 shows the resulting asymmetry for each of the three defined acceptance regions compared to the asymmetry computed over the full acceptance. Because the x distribution changes with the vertical position, an x range of 0.175 to 0.625 was chosen for comparison, to optimized the x distribution overlap between the three acceptance regions being compared. Within this x range, all of the asymmetries are consistent (within the measured precision) with each other, as a result there was no correction included for the acceptance gap.

[12] As per HallA detector coordinate convention, the -X (vertical) position points to the top of the BigBite detector.

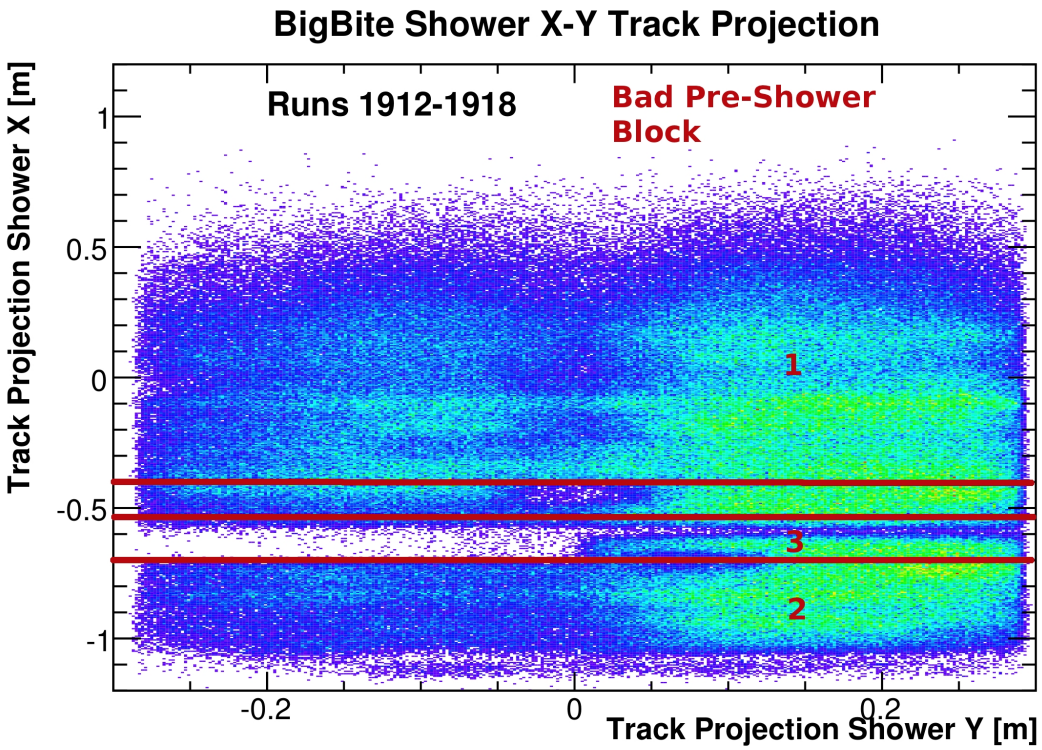

Figure 8.40: BigBite acceptance regions used to study electron asymmetries. Region 1 selects events falling in the lower (in HallA coordinates -X points up) portion of the BigBite acceptance, region 2 selects the events that occupy the upper region of the detector, and region 3 selects events that fall in the acceptance gap region.

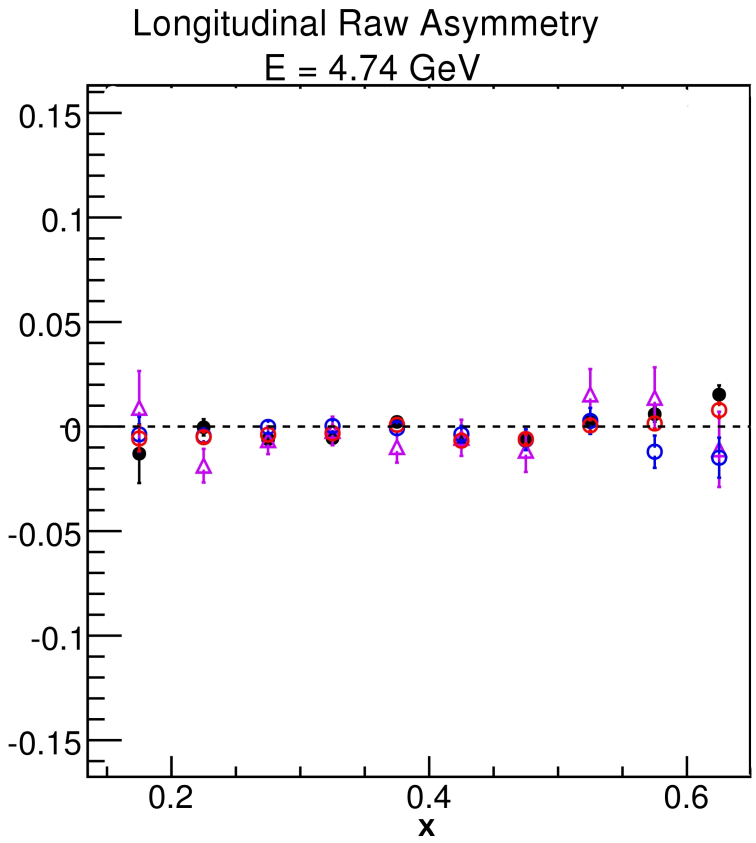

Figure 8.41: Longitudinal electron asymmetries at E = 4.74 GeV, corresponding to particular regions of the BigBite acceptance. The black markers correspond to region 1 (higher momentum particles). The open blue markers correspond to the asymmetries in region 2 (lower momentum particles). The Asymmetries measured in region 3 (the BigBite acceptance associated to the acceptance gap) are shown as the magenta open triangles. Finally the open red circles show the asymmetry computed over the entire BigBite acceptance.

8.2.6 Nitrogen Dilution

Since the ^{3}He target has a small percentage of N_2 present (Chapter 6), the unpolarized N_2 gas will tend to dilute the measured asymmetries. In order to correct for this in BigBite, the counting rates from a pure N_2 target were measured. Comparing the N_2 target counting rates to the ^{3}He production cell scattering rates, a dilution factor can be formed and applied to the measured asymmetry. The dilution factor is given as:

$$D_{\mathrm{N}_2} = 1 - \frac{\Sigma_{\mathrm{N}_2}(\mathrm{N}_2) \cdot ps\,(\mathrm{N}_2)}{\Sigma_{total}(^3\mathrm{He}) \cdot ps\,(^3\mathrm{He})} \frac{Q(^3\mathrm{He}) \cdot t_{LT}\,(^3\mathrm{He}) \cdot n_{\mathrm{N}_2}(^3\mathrm{He})}{Q(\mathrm{N}_2) \cdot t_{LT}\,(\mathrm{N}_2) \cdot n_{\mathrm{N}_2}(\mathrm{N}_2)}, \tag{8.29}$$

where Σ_{N_2} and Σ_{total} are the total scattering counts that pass data-quality and PID cuts detected during the N_2 and ^{3}He target runs and $n_{\mathrm{N}_2}(\mathrm{N}_2)$ and $n_{\mathrm{N}_2}(^3\mathrm{He})$ are the nitrogen number densities present in the two targets. Due to the nitrogen and ^{3}He production runs having different characteristics (*i.e.* scattering rates, running time, etc.) the measured electrons must be normalized by taking into account the total charge, Q(N_2) and Q(^{3}He) deposited on the two targets; the prescale factor, $ps\,(\mathrm{N}_2)$ and $ps\,(^3\mathrm{He})$ that the T2 trigger had for that run; and the livetime, $t_{LT}\,(\mathrm{N}_2)$ and $t_{LT}\,(^3\mathrm{He})$ of the T2 trigger for the given run.

While the nitrogen reference cell was in the beam, the number densities, $n_{\mathrm{N}2}\,(\mathrm{N}_2)$, were extracted using the measured pressure and temperature of the cell. A systematic uncertainty of 2.2% was estimated by calculating the number densities for pressure and temperature excursions of up to 2 psig and 2°C. Whereas, for the nitrogen number density in the ^{3}He production cell, $n_{\mathrm{N}_2}\,(^3\mathrm{He})$, a density of 0.113 amg was used, recorded as the target was initially filled. Pressure-curve analysis performed during E06-010 confirms that this value is accurate to within about 3% [123]. A summary of the nitrogen reference cell density parameters used in the nitrogen dilution factor calculation can be found in Table 8.15.

Table 8.15: Temperatures, pressures, and densities of the nitrogen reference cell used in nitrogen dilution calculation.

Run	Beam Energy [GeV]	Temperature [°C]	Pressure [psig]	Density [amg]
1529	5.89	41.7	22.0	2.17
1696	5.89	42.0	100.0	6.77
1923	5.89	41.6	113.0	7.54
1962	5.89	41.9	120.0	7.95
2055	4.74	41.7	119.0	7.89
2186	4.74	42.2	116.0	7.70

The dilution factor was computed at each of the x bins corresponding to the asymmetry binning defined in Section 8.2.5.3, and are listed in Tables 8.16, 8.17 and 8.18. Figure 8.42 shows the results of the nitrogen dilution calculations. The 5.89 GeV data set was separated into two time periods, before and after the preshower was added to the main trigger. Nitrogen dilution factors that correspond to the time period before the preshower was added into the main trigger are shown in blue in Figure 8.42, whereas nitrogen dilution factors that correspond to the time period after the preshower was added to the main trigger are shown in red. Comparing the two time periods of the E = 5.89 GeV data set, it is clear that the latter (having the preshower in the trigger) agree better with the E = 4.74 GeV data set.

In addition to the statistical uncertainty, which is just the counting uncertainty given by

$$\left(\delta D_{\mathrm{N}_2}\right)_{stat} = \frac{Y\left(\mathrm{N}_2\right)}{Y\left(^3\mathrm{He}\right)}\sqrt{\frac{1}{Y\left(\mathrm{N}_2\right)} + \frac{1}{Y\left(^3\mathrm{He}\right)}}, \tag{8.30}$$

where $Y = \frac{\Sigma \cdot ps}{Q \cdot t_{LT} \cdot n_{\mathrm{N}_2}}$ for the reference $\left(\mathrm{N}_2\right)$ and production $\left(^3\mathrm{He}\right)$ cells, there is a systematic uncertainty that arises from the density measurements, and is given as

$$\left(\delta D_{\mathrm{N}_2}\right)_{sys} = \frac{Y\left(\mathrm{N}_2\right)}{Y\left(^3\mathrm{He}\right)}\sqrt{\left(\delta n_{\mathrm{N}_2}\left(N_2\right)\right)^2 + \left(\delta n_{\mathrm{N}_2}\left(^3\mathrm{He}\right)\right)^2}, \tag{8.31}$$

where δn_{N_2} is the relative uncertainty of 2.2% for the reference cell and 3% for the

Table 8.16: Nitrogen dilution factors for 4.74 GeV data set. The statistical uncertainty for the nitrogen dilution factor is at the 10^{-5} level.

Central x Value	D_{N_2}
0.225	$0.9223 \pm 0.0000_{stat} \pm 0.0028_{sys}$
0.275	$0.9173 \pm 0.0000_{stat} \pm 0.0030_{sys}$
0.325	$0.9160 \pm 0.0000_{stat} \pm 0.0031_{sys}$
0.375	$0.9162 \pm 0.0000_{stat} \pm 0.0031_{sys}$
0.425	$0.9167 \pm 0.0000_{stat} \pm 0.0031_{sys}$
0.475	$0.9177 \pm 0.0000_{stat} \pm 0.0030_{sys}$
0.525	$0.9196 \pm 0.0000_{stat} \pm 0.0029_{sys}$
0.575	$0.9194 \pm 0.0000_{stat} \pm 0.0030_{sys}$
0.625	$0.9216 \pm 0.0000_{stat} \pm 0.0029_{sys}$
0.675	$0.9213 \pm 0.0000_{stat} \pm 0.0029_{sys}$
0.725	$0.9225 \pm 0.0000_{stat} \pm 0.0028_{sys}$
0.775	$0.9231 \pm 0.0000_{stat} \pm 0.0028_{sys}$
0.825	$0.9174 \pm 0.0000_{stat} \pm 0.0030_{sys}$
0.875	$0.9190 \pm 0.0000_{stat} \pm 0.0030_{sys}$
0.925	$0.9226 \pm 0.0000_{stat} \pm 0.0028_{sys}$
0.975	$0.9283 \pm 0.0000_{stat} \pm 0.0026_{sys}$

production cell.

Table 8.17: Nitrogen dilution factors for the 5.89 GeV data set before the preshower was added to the main electron trigger. Most of the bins have their statistical uncertainty for the nitrogen dilution factor at the 10^{-5} level.

Central x Value	D_{N_2}
0.225	$0.8382 \pm 0.0000_{stat} \pm 0.0059_{sys}$
0.275	$0.8809 \pm 0.0000_{stat} \pm 0.0044_{sys}$
0.325	$0.8888 \pm 0.0000_{stat} \pm 0.0041_{sys}$
0.375	$0.8932 \pm 0.0000_{stat} \pm 0.0039_{sys}$
0.425	$0.9006 \pm 0.0000_{stat} \pm 0.0036_{sys}$
0.475	$0.9059 \pm 0.0000_{stat} \pm 0.0034_{sys}$
0.525	$0.9056 \pm 0.0000_{stat} \pm 0.0035_{sys}$
0.575	$0.9097 \pm 0.0000_{stat} \pm 0.0033_{sys}$
0.625	$0.9099 \pm 0.0000_{stat} \pm 0.0033_{sys}$
0.675	$0.9116 \pm 0.0000_{stat} \pm 0.0032_{sys}$
0.725	$0.9122 \pm 0.0000_{stat} \pm 0.0032_{sys}$
0.775	$0.9181 \pm 0.0000_{stat} \pm 0.0030_{sys}$
0.825	$0.9095 \pm 0.0000_{stat} \pm 0.0033_{sys}$
0.875	$0.9212 \pm 0.0001_{stat} \pm 0.0029_{sys}$
0.925	$0.8975 \pm 0.0002_{stat} \pm 0.0038_{sys}$
0.975	$0.9058 \pm 0.0004_{stat} \pm 0.0035_{sys}$

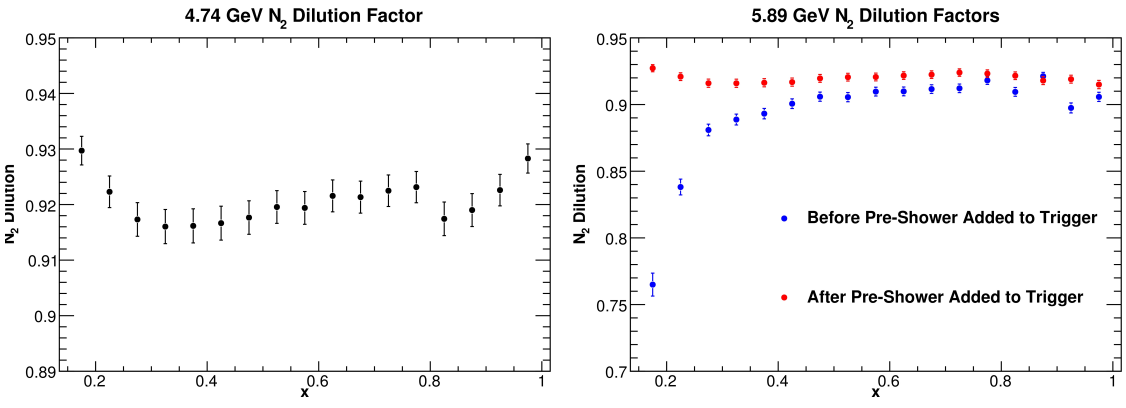

Figure 8.42: Nitrogen dilution factor is shown as a function of x for the 4.74 GeV (left panel) and the 5.89 GeV (right panel) data sets. The error bars represents the statistical and systematic uncertainties added in quadrature. The systematic uncertainty makes up nearly the entire error bar.

Table 8.18: Nitrogen dilution factors for the 5.89 GeV data set after the preshower was added to the main electron trigger. Most of the bins have their statistical uncertainty for the nitrogen dilution factor at the 10^{-5} level.

Central x Value	D_{N_2}
0.225	$0.9209 \pm 0.0000_{stat} \pm 0.0029_{sys}$
0.275	$0.9160 \pm 0.0000_{stat} \pm 0.0031_{sys}$
0.325	$0.9159 \pm 0.0000_{stat} \pm 0.0031_{sys}$
0.375	$0.9164 \pm 0.0000_{stat} \pm 0.0031_{sys}$
0.425	$0.9168 \pm 0.0000_{stat} \pm 0.0030_{sys}$
0.475	$0.9196 \pm 0.0000_{stat} \pm 0.0029_{sys}$
0.525	$0.9205 \pm 0.0000_{stat} \pm 0.0029_{sys}$
0.575	$0.9207 \pm 0.0000_{stat} \pm 0.0029_{sys}$
0.625	$0.9217 \pm 0.0000_{stat} \pm 0.0029_{sys}$
0.675	$0.9225 \pm 0.0000_{stat} \pm 0.0028_{sys}$
0.725	$0.9240 \pm 0.0000_{stat} \pm 0.0028_{sys}$
0.775	$0.9232 \pm 0.0000_{stat} \pm 0.0028_{sys}$
0.825	$0.9216 \pm 0.0000_{stat} \pm 0.0029_{sys}$
0.875	$0.9180 \pm 0.0000_{stat} \pm 0.0030_{sys}$
0.925	$0.9190 \pm 0.0001_{stat} \pm 0.0030_{sys}$
0.975	$0.9150 \pm 0.0001_{stat} \pm 0.0031_{sys}$

8.2.7 Kinematic Parameters Binned in x

The computation of the kinematic parameters in the BigBite spectrometer depend heavily on the optics package (Section 7.1.2). The particle scattering momentum $\vec{k'}$, the scattering angle θ, and the azimuthal angle ϕ between the scattering and scattering and polarization planes are all derived from the optics package. The incident energy E of the electron beam is measured to 0.05% using Tiefenback monitoring (Section 4.4.2); the electron beam direction and momentum are measured through beam position monitors (Section 4.4.2). The information of the incident electron momentum $\vec{k}$ can be used with $\vec{k'}$, θ, and ϕ to compute additional kinematic quantities such as: ν (according to Equation 1.1), Q^2 (according to Equation 1.2), x (according to Equation 1.4), and W^2 according to Equation 1.3). The distributions of the kinematic quantities within each x-bin can be found in Appendix E.

The mean kinematic value for each x-bin was determined by plotting the kinematic distribution within a given x-bin (Appendix E) and evaluating its mean, where the RMS of the distribution was assigned as the statistical uncertainty. A systematic uncertainty was also assigned to the kinematic parameters through the error propagation of the most fundamental kinematic parameters θ, ϕ, $\vec{k'}$ and $\vec{k}$. The angular measurements θ and ϕ were computed via the BigBite survey report (Appendix A), which gives the position of the wire chambers relative to the nominal target center to mm-level precision. This lead to a systematic uncertainty of about 0.4 mrad on the angular measurements, which is negligible compared to the 10 mrad systematic uncertainty due to the angular reconstruction [86] (Section 7.1.2.3.3). The systematic uncertainty associated with the reconstructed momentum ($\vec{k'}$) was determined to be 1% of its value (Section 7.1.2.3.4). By varying θ, ϕ, and $\vec{k'}$ within their respective systematic uncertainties, a systematic uncertainty can be applied to all of the kinematic factors that were computed. The mean kinematic quantities measured in each x-bin, along with their respective statistical and systematic uncertainties are listed in

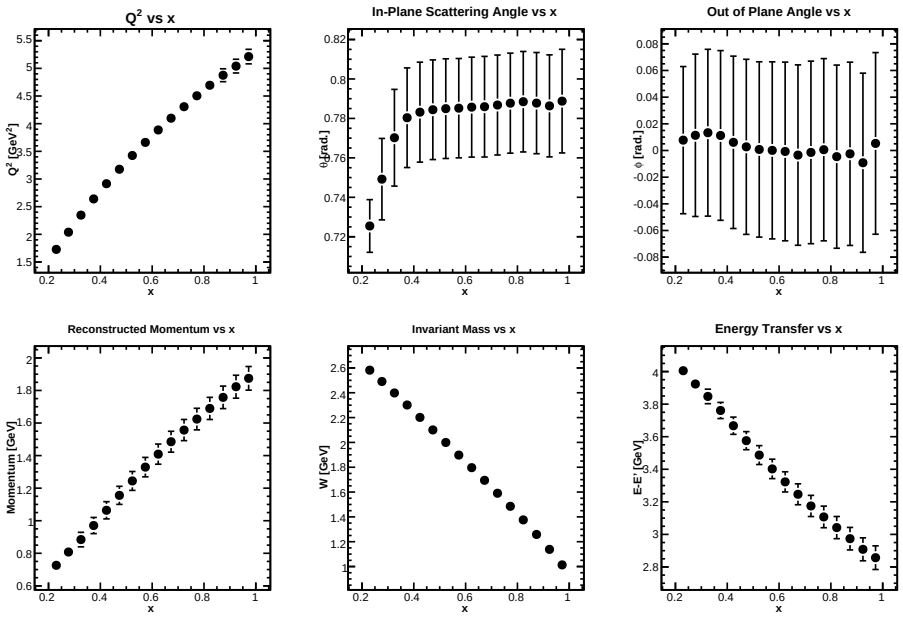

Figure 8.43: Mean kinematic factors for each x-bin at an incident electron energy of 4.74 GeV. Error bars are statistical only.

Tables 8.19 and 8.21. Figures 8.43 and 8.44 show the mean kinematic variables plotted against x. In addition to the kinematic variables listed in Tables 8.19 and 8.21, kinematic factors that went into forming the physics asymmetry and the polarized structure functions ($\cos\theta$, $\sin\theta$, $\tan\frac{\theta}{2}$, $\cos\phi$, and y) are plotted as a function of x in Figures 8.45 and 8.46 for the 4.74 GeV and 5.89 GeV data sets respectively.

8.2.8 Physics Asymmetry

Correcting for the dilution effects arising from the imperfect target and beam polarizations, and scattering from unpolarized nitrogen, the physics asymmetries are formed according to Equation 8.19. The physics asymmetry was computed on a run-to-run basis for each x bin; runs were then combined in the same manner as that which was used to combine the raw asymmetries (Section 8.2.5.3). In the case of the asymmetry measured at the 0° target spin direction,

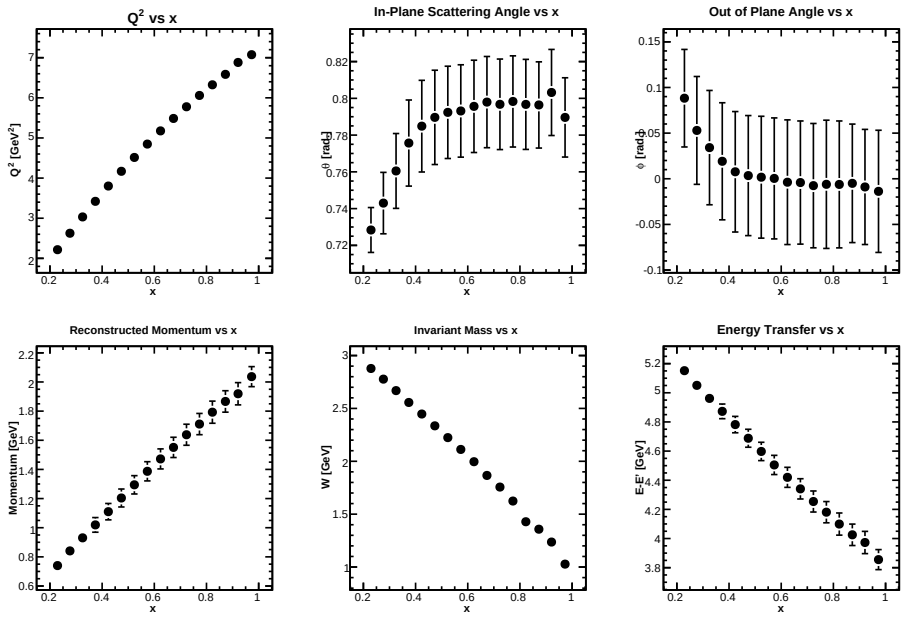

Figure 8.44: Mean kinematic factors for each x-bin at an incident electron energy of 5.89 GeV. Error bars are statistical only.

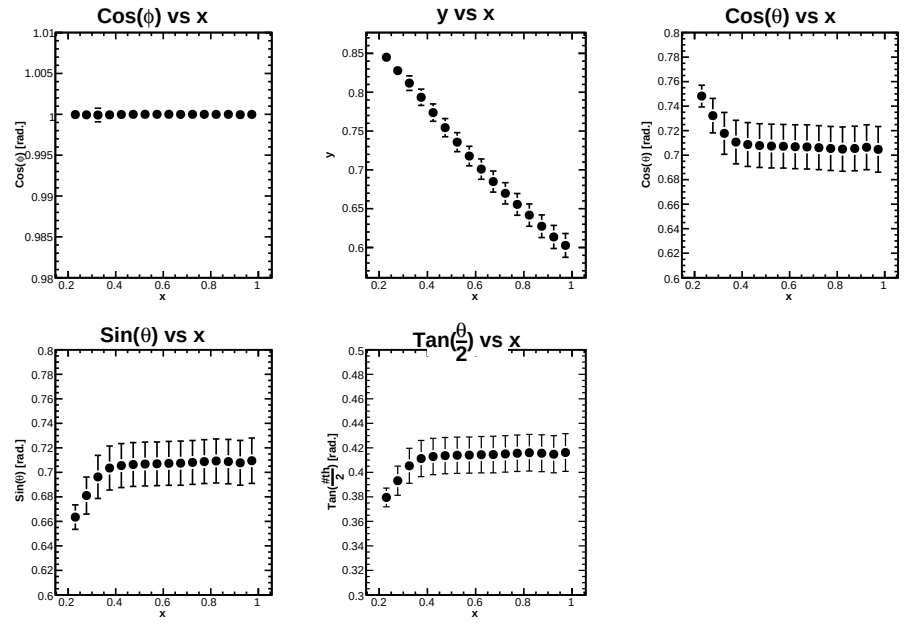

Figure 8.45: Mean kinematic factors that go into evaluating the polarized structure functions for each x-bin at an incident electron energy of 4.74 GeV. Error bars are statistical only.

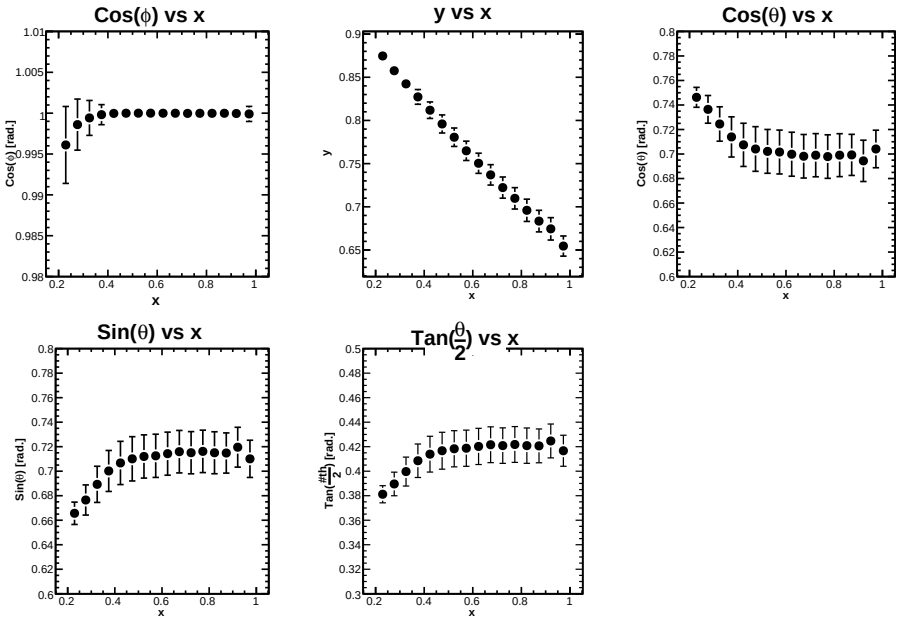

Figure 8.46: Mean kinematic factors that go into evaluating the polarized structure functions for each x-bin at an incident electron energy of 5.89 GeV. Error bars are statistical only.

$$A^0_{phys} = \frac{\sum_i \frac{(A^0_i)}{P_{bi}P_{ti}D_{\mathrm{N}_2 i}} \left(\frac{\delta A_i}{P_{bi}P_{ti}D_{\mathrm{N}_2 i}} \right)^{-2}}{\sum_i \left(\frac{\delta A_i}{P_{bi}P_{ti}D_{\mathrm{N}_2 i}} \right)^{-2}}, \tag{8.32}$$

where (A^0_i) is the raw asymmetry for the i^{th} run, defined in Equation 8.25, with the target spin direction pointing toward 0° (S = 0); δA_i is defined in Equation 8.26; P_{bi} is the beam polarization of the i^{th} run, which corresponds to the values given in Table 5.2; P_{ti} is the target polarization of the i^{th} run shown in Figure 6.31, and $D_{\mathrm{N}_2 i}$ is the nitrogen dilution factor of the i^{th} run given in Tables 8.16, 8.17, and 8.18. The statistical uncertainty in the physics asymmetry was defined as

$$\delta A^0_{phys} = \sqrt{(\delta A^0)^2 + \left(\frac{\partial A^0_{phys}}{\partial D_{\mathrm{N}_2}} \right)^2 (\delta D_{\mathrm{N}_2})^2_{stat}}, \tag{8.33}$$

where $\left(\delta D_{\mathrm{N}_2}\right)_{stat}$ is defined in Equation 8.30 and

$$\delta A^0 = \sqrt{\frac{1}{\sum_i \left(\frac{\delta A_i}{P_{bi} P_{ti} D_{\mathrm{N}_2 i}}\right)^{-2}}}. \tag{8.34}$$

Uncertainties from the target and beam polarizations enter later through the systematic uncertainty. Similarly, the physics asymmetry and the uncertainties of the transverse target spin configurations are

$$A^{90,270}_{phys} = \frac{\sum_i \frac{\left(A_i^{90,270}\right)}{P_{bi} P_{ti} D_{\mathrm{N}_2 i} \langle \cos\phi \rangle} \left(\frac{\delta A_i}{P_{bi} P_{ti} D_{\mathrm{N}_2 i} \langle \cos\phi \rangle}\right)^{-2}}{\sum_i \left(\frac{\delta A_i}{P_{bi} P_{ti} D_{\mathrm{N}_2 i} \langle \cos\phi \rangle}\right)^{-2}}, \tag{8.35}$$

and

$$\delta A^{90,270}_{phys} = \sqrt{\left(\delta A^{90,270}\right)^2 + \left(\frac{\partial A^{90,270}_{phys}}{\partial D_{\mathrm{N}_2}}\right)^2 \left(\delta D_{\mathrm{N}_2}\right)^2_{stat} + \left(\frac{\partial A^{90,270}_{phys}}{\partial \langle \cos\phi \rangle}\right)^2 \left(\delta \langle \cos\phi \rangle\right)^2_{stat}}, \tag{8.36}$$

where

$$\delta A^{90,270} = \sqrt{\frac{1}{\sum_i \left(\frac{\delta A_i}{P_{bi} P_{ti} D_{\mathrm{N}_2 i} \langle \cos\phi \rangle}\right)^{-2}}}, \tag{8.37}$$

where the target spin direction is either S = 90° or 270°. The mean $\cos\phi$ value for each x-bin, where ϕ is listed in Tables 8.19 and 8.21 for the appropriate data set, divides the perpendicular asymmetries in order to account for the azimuthal angle's variation over the acceptance. Figures 8.45 and 8.46 show that the azimuthal variation ($\cos\phi$) was ~ 1 for all x bins. Tables 8.23 and 8.24 list the physics asymmetries, calculated from Equations 8.32

and 8.35, for each of the three target spin orientations at beam energies of 4.74 and 5.89 GeV respectivly.

At this stage in the analysis it is beneficial to combine the two transverse spin configurations to form one transverse asymmetry. Following the sign convention laid out in Section 8.2.5.1

$$A_{\perp}^{phys} = \frac{A_{phys}^{270} \cdot \left(\delta A_{phys}^{270}\right)^{-2} - A_{phys}^{90} \cdot \left(\delta A_{phys}^{90}\right)^{-2}}{\left(\delta A_{phys}^{90}\right)^{-2} + \left(\delta A_{phys}^{90}\right)^{-2}}, \tag{8.38}$$

and the statistical uncertainty becomes

$$\delta A_{\perp}^{phys} = \frac{1}{\left(\delta A_{phys}^{90}\right)^{-2} + \left(\delta A_{phys}^{90}\right)^{-2}}. \tag{8.39}$$

Due to the fact that there is only one longitudinal target spin direction, the longitudinal asymmetry is simply

$$A_{\parallel}^{phys} = A_{phys}^{0}, \tag{8.40}$$

with a statistical uncertainty of

$$\delta A_{\parallel}^{phys} = \delta A_{phys}^{0}. \tag{8.41}$$

The longitudinal and transverse ^{3}He asymmetries are plotted as function of x in Figure 8.47 and are listed in Tables 8.25 and 8.26 for incident electron beam energies of 4.74 GeV and 5.89 GeV data sets.

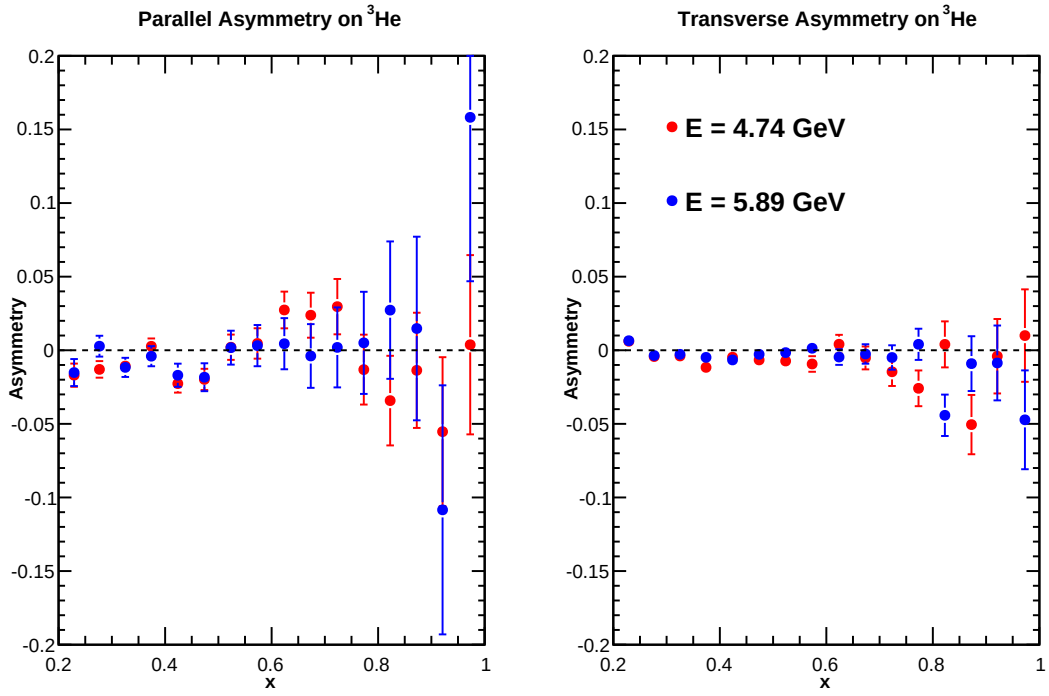

Figure 8.47: Longitudinal (left panel) and transverse (right panel) ^{3}He asymmetries verses x for both the E = 4.74 GeV(red markers) and E = 5.89 GeV (blue markers) data sets. The error bars are statistical uncertainties only.

Table 8.19: Mean kinematic quantities reconstructed from software at incident electron energy of 4.74 GeV for each x-bin. Listed uncertainties are absolute.

$\langle k' \rangle$ [GeV]	$\langle \theta \rangle$ [rad]	$\langle \phi \rangle$ [rad]
$0.726 \pm 0.026_{stat} \pm 0.007_{sys}$	$0.7255 \pm 0.0134_{stat} \pm 0.0100_{sys}$	$0.0078 \pm 0.0552_{stat} \pm 0.0100_{sys}$
$0.808 \pm 0.036_{stat} \pm 0.008_{sys}$	$0.7492 \pm 0.0206_{stat} \pm 0.0100_{sys}$	$0.0114 \pm 0.0609_{stat} \pm 0.0100_{sys}$
$0.884 \pm 0.045_{stat} \pm 0.009_{sys}$	$0.7702 \pm 0.0245_{stat} \pm 0.0100_{sys}$	$0.0133 \pm 0.0625_{stat} \pm 0.0100_{sys}$
$0.970 \pm 0.050_{stat} \pm 0.010_{sys}$	$0.7803 \pm 0.0253_{stat} \pm 0.0100_{sys}$	$0.0113 \pm 0.0636_{stat} \pm 0.0100_{sys}$
$1.064 \pm 0.053_{stat} \pm 0.011_{sys}$	$0.7832 \pm 0.0253_{stat} \pm 0.0100_{sys}$	$0.0061 \pm 0.0646_{stat} \pm 0.0100_{sys}$
$1.156 \pm 0.055_{stat} \pm 0.012_{sys}$	$0.7844 \pm 0.0253_{stat} \pm 0.0100_{sys}$	$0.0027 \pm 0.0656_{stat} \pm 0.0100_{sys}$
$1.244 \pm 0.058_{stat} \pm 0.012_{sys}$	$0.7849 \pm 0.0253_{stat} \pm 0.0100_{sys}$	$0.0008 \pm 0.0657_{stat} \pm 0.0100_{sys}$
$1.329 \pm 0.060_{stat} \pm 0.013_{sys}$	$0.7852 \pm 0.0252_{stat} \pm 0.0100_{sys}$	$0.0001 \pm 0.0664_{stat} \pm 0.0100_{sys}$
$1.409 \pm 0.062_{stat} \pm 0.014_{sys}$	$0.7857 \pm 0.0253_{stat} \pm 0.0100_{sys}$	$-0.0007 \pm 0.0670_{stat} \pm 0.0100_{sys}$
$1.485 \pm 0.064_{stat} \pm 0.015_{sys}$	$0.7859 \pm 0.0255_{stat} \pm 0.0100_{sys}$	$-0.0034 \pm 0.0676_{stat} \pm 0.0100_{sys}$
$1.557 \pm 0.065_{stat} \pm 0.016_{sys}$	$0.7868 \pm 0.0253_{stat} \pm 0.0100_{sys}$	$-0.0014 \pm 0.0684_{stat} \pm 0.0100_{sys}$
$1.624 \pm 0.066_{stat} \pm 0.016_{sys}$	$0.7877 \pm 0.0254_{stat} \pm 0.0100_{sys}$	$0.0006 \pm 0.0683_{stat} \pm 0.0100_{sys}$
$1.690 \pm 0.068_{stat} \pm 0.017_{sys}$	$0.7885 \pm 0.0255_{stat} \pm 0.0100_{sys}$	$-0.0046 \pm 0.0687_{stat} \pm 0.0100_{sys}$
$1.758 \pm 0.069_{stat} \pm 0.018_{sys}$	$0.7878 \pm 0.0257_{stat} \pm 0.0100_{sys}$	$-0.0025 \pm 0.0687_{stat} \pm 0.0100_{sys}$
$1.823 \pm 0.070_{stat} \pm 0.018_{sys}$	$0.7864 \pm 0.0259_{stat} \pm 0.0100_{sys}$	$-0.0092 \pm 0.0672_{stat} \pm 0.0100_{sys}$
$1.875 \pm 0.073_{stat} \pm 0.019_{sys}$	$0.7888 \pm 0.0263_{stat} \pm 0.0100_{sys}$	$0.0053 \pm 0.0681_{stat} \pm 0.0100_{sys}$

Table 8.20: Mean kinematic quantities constructed using Table 8.19 at incident electron energy of 4.74 GeV for each x-bin. Listed uncertainties are absolute.

$\langle x \rangle$	$\langle Q^2 \rangle$ [GeV^2]	$\langle W \rangle$ [GeV]	$\langle \nu \rangle$ [GeV]
$0.230 \pm 0.008_{stat} \pm 0.009_{sys}$	$1.728 \pm 0.053_{stat} \pm 0.066_{sys}$	$2.582 \pm 0.029_{stat} \pm 0.001_{sys}$	$4.005 \pm 0.026_{stat} \pm 0.007_{sys}$
$0.277 \pm 0.008_{stat} \pm 0.011_{sys}$	$2.039 \pm 0.057_{stat} \pm 0.076_{sys}$	$2.491 \pm 0.018_{stat} \pm 0.001_{sys}$	$3.924 \pm 0.036_{stat} \pm 0.008_{sys}$
$0.325 \pm 0.008_{stat} \pm 0.013_{sys}$	$2.347 \pm 0.058_{stat} \pm 0.085_{sys}$	$2.398 \pm 0.020_{stat} \pm 0.001_{sys}$	$3.847 \pm 0.045_{stat} \pm 0.009_{sys}$
$0.374 \pm 0.008_{stat} \pm 0.014_{sys}$	$2.640 \pm 0.058_{stat} \pm 0.095_{sys}$	$2.302 \pm 0.021_{stat} \pm 0.002_{sys}$	$3.761 \pm 0.050_{stat} \pm 0.010_{sys}$
$0.424 \pm 0.008_{stat} \pm 0.017_{sys}$	$2.915 \pm 0.060_{stat} \pm 0.105_{sys}$	$2.201 \pm 0.021_{stat} \pm 0.002_{sys}$	$3.667 \pm 0.053_{stat} \pm 0.011_{sys}$
$0.473 \pm 0.008_{stat} \pm 0.019_{sys}$	$3.176 \pm 0.063_{stat} \pm 0.114_{sys}$	$2.101 \pm 0.021_{stat} \pm 0.002_{sys}$	$3.576 \pm 0.055_{stat} \pm 0.012_{sys}$
$0.523 \pm 0.008_{stat} \pm 0.021_{sys}$	$3.425 \pm 0.068_{stat} \pm 0.123_{sys}$	$2.000 \pm 0.021_{stat} \pm 0.002_{sys}$	$3.487 \pm 0.058_{stat} \pm 0.012_{sys}$
$0.574 \pm 0.008_{stat} \pm 0.023_{sys}$	$3.662 \pm 0.074_{stat} \pm 0.131_{sys}$	$1.898 \pm 0.021_{stat} \pm 0.003_{sys}$	$3.402 \pm 0.060_{stat} \pm 0.013_{sys}$
$0.623 \pm 0.008_{stat} \pm 0.025_{sys}$	$3.886 \pm 0.080_{stat} \pm 0.139_{sys}$	$1.797 \pm 0.021_{stat} \pm 0.003_{sys}$	$3.323 \pm 0.062_{stat} \pm 0.014_{sys}$
$0.673 \pm 0.008_{stat} \pm 0.027_{sys}$	$4.099 \pm 0.086_{stat} \pm 0.147_{sys}$	$1.695 \pm 0.021_{stat} \pm 0.003_{sys}$	$3.246 \pm 0.064_{stat} \pm 0.015_{sys}$
$0.723 \pm 0.008_{stat} \pm 0.030_{sys}$	$4.307 \pm 0.093_{stat} \pm 0.154_{sys}$	$1.590 \pm 0.020_{stat} \pm 0.003_{sys}$	$3.175 \pm 0.065_{stat} \pm 0.016_{sys}$
$0.773 \pm 0.008_{stat} \pm 0.032_{sys}$	$4.504 \pm 0.100_{stat} \pm 0.161_{sys}$	$1.485 \pm 0.020_{stat} \pm 0.000_{sys}$	$3.107 \pm 0.066_{stat} \pm 0.016_{sys}$
$0.823 \pm 0.008_{stat} \pm 0.034_{sys}$	$4.695 \pm 0.107_{stat} \pm 0.168_{sys}$	$1.376 \pm 0.021_{stat} \pm 0.000_{sys}$	$3.042 \pm 0.068_{stat} \pm 0.017_{sys}$
$0.874 \pm 0.008_{stat} \pm 0.037_{sys}$	$4.876 \pm 0.116_{stat} \pm 0.175_{sys}$	$1.258 \pm 0.021_{stat} \pm 0.000_{sys}$	$2.974 \pm 0.069_{stat} \pm 0.018_{sys}$
$0.924 \pm 0.008_{stat} \pm 0.039_{sys}$	$5.040 \pm 0.124_{stat} \pm 0.181_{sys}$	$1.138 \pm 0.021_{stat} \pm 0.003_{sys}$	$2.908 \pm 0.070_{stat} \pm 0.018_{sys}$
$0.972 \pm 0.008_{stat} \pm 0.041_{sys}$	$5.213 \pm 0.132_{stat} \pm 0.186_{sys}$	$1.013 \pm 0.037_{stat} \pm 0.003_{sys}$	$2.857 \pm 0.073_{stat} \pm 0.019_{sys}$

Table 8.21: Mean kinematic quantities reconstructed from software at incident electron energy of 5.89 GeV for each x-bin. Uncertainties listed are absolute.

$\langle k' \rangle$ [GeV]	$\langle \theta \rangle$ [rad]	$\langle \phi \rangle$ [rad]
$0.740 \pm 0.028_{stat} \pm 0.007_{sys}$	$0.7284 \pm 0.0122_{stat} \pm 0.0100_{sys}$	$0.0882 \pm 0.0534_{stat} \pm 0.0100_{sys}$
$0.841 \pm 0.035_{stat} \pm 0.008_{sys}$	$0.7430 \pm 0.0167_{stat} \pm 0.0100_{sys}$	$0.0530 \pm 0.0591_{stat} \pm 0.0100_{sys}$
$0.931 \pm 0.043_{stat} \pm 0.009_{sys}$	$0.7605 \pm 0.0204_{stat} \pm 0.0100_{sys}$	$0.0341 \pm 0.0626_{stat} \pm 0.0100_{sys}$
$1.019 \pm 0.050_{stat} \pm 0.010_{sys}$	$0.7757 \pm 0.0234_{stat} \pm 0.0100_{sys}$	$0.0191 \pm 0.0641_{stat} \pm 0.0100_{sys}$
$1.110 \pm 0.056_{stat} \pm 0.011_{sys}$	$0.7849 \pm 0.0249_{stat} \pm 0.0100_{sys}$	$0.0076 \pm 0.0660_{stat} \pm 0.0100_{sys}$
$1.204 \pm 0.062_{stat} \pm 0.012_{sys}$	$0.7896 \pm 0.0257_{stat} \pm 0.0100_{sys}$	$0.0035 \pm 0.0658_{stat} \pm 0.0100_{sys}$
$1.294 \pm 0.063_{stat} \pm 0.013_{sys}$	$0.7924 \pm 0.0251_{stat} \pm 0.0100_{sys}$	$0.0017 \pm 0.0667_{stat} \pm 0.0100_{sys}$
$1.387 \pm 0.066_{stat} \pm 0.014_{sys}$	$0.7931 \pm 0.0251_{stat} \pm 0.0100_{sys}$	$0.0004 \pm 0.0663_{stat} \pm 0.0100_{sys}$
$1.472 \pm 0.069_{stat} \pm 0.015_{sys}$	$0.7956 \pm 0.0251_{stat} \pm 0.0100_{sys}$	$-0.0038 \pm 0.0683_{stat} \pm 0.0100_{sys}$
$1.551 \pm 0.070_{stat} \pm 0.016_{sys}$	$0.7980 \pm 0.0248_{stat} \pm 0.0100_{sys}$	$-0.0041 \pm 0.0674_{stat} \pm 0.0100_{sys}$
$1.638 \pm 0.072_{stat} \pm 0.016_{sys}$	$0.7968 \pm 0.0246_{stat} \pm 0.0100_{sys}$	$-0.0075 \pm 0.0681_{stat} \pm 0.0100_{sys}$
$1.711 \pm 0.073_{stat} \pm 0.017_{sys}$	$0.7983 \pm 0.0248_{stat} \pm 0.0100_{sys}$	$-0.0061 \pm 0.0702_{stat} \pm 0.0100_{sys}$
$1.793 \pm 0.076_{stat} \pm 0.018_{sys}$	$0.7967 \pm 0.0245_{stat} \pm 0.0100_{sys}$	$-0.0062 \pm 0.0695_{stat} \pm 0.0100_{sys}$
$1.866 \pm 0.074_{stat} \pm 0.019_{sys}$	$0.7964 \pm 0.0235_{stat} \pm 0.0100_{sys}$	$-0.0050 \pm 0.0649_{stat} \pm 0.0100_{sys}$
$1.919 \pm 0.076_{stat} \pm 0.019_{sys}$	$0.8032 \pm 0.0234_{stat} \pm 0.0100_{sys}$	$-0.0090 \pm 0.0631_{stat} \pm 0.0100_{sys}$
$2.037 \pm 0.069_{stat} \pm 0.020_{sys}$	$0.7896 \pm 0.0216_{stat} \pm 0.0100_{sys}$	$-0.0138 \pm 0.0669_{stat} \pm 0.0100_{sys}$

Table 8.22: Mean kinematic quantities constructed using Table 8.21 at incident electron energy of 5.89 GeV for each x-bin. Listed uncertainties are absolute.

$\langle x \rangle$	$\langle Q^2 \rangle$ [GeV^2]	$\langle W \rangle$ [GeV]	$\langle \nu \rangle$ [GeV]
$0.229 \pm 0.005_{stat} \pm 0.009_{sys}$	$2.216 \pm 0.068_{stat} \pm 0.084_{sys}$	$2.878 \pm 0.018_{stat} \pm 0.001_{sys}$	$5.152 \pm 0.028_{stat} \pm 0.007_{sys}$
$0.277 \pm 0.005_{stat} \pm 0.011_{sys}$	$2.626 \pm 0.072_{stat} \pm 0.098_{sys}$	$2.777 \pm 0.019_{stat} \pm 0.001_{sys}$	$5.051 \pm 0.035_{stat} \pm 0.008_{sys}$
$0.325 \pm 0.005_{stat} \pm 0.013_{sys}$	$3.032 \pm 0.072_{stat} \pm 0.111_{sys}$	$2.668 \pm 0.020_{stat} \pm 0.001_{sys}$	$4.961 \pm 0.043_{stat} \pm 0.009_{sys}$
$0.374 \pm 0.005_{stat} \pm 0.014_{sys}$	$3.421 \pm 0.073_{stat} \pm 0.124_{sys}$	$2.556 \pm 0.021_{stat} \pm 0.001_{sys}$	$4.873 \pm 0.050_{stat} \pm 0.010_{sys}$
$0.424 \pm 0.005_{stat} \pm 0.016_{sys}$	$3.802 \pm 0.076_{stat} \pm 0.136_{sys}$	$2.447 \pm 0.022_{stat} \pm 0.002_{sys}$	$4.782 \pm 0.056_{stat} \pm 0.011_{sys}$
$0.474 \pm 0.005_{stat} \pm 0.018_{sys}$	$4.169 \pm 0.080_{stat} \pm 0.149_{sys}$	$2.335 \pm 0.022_{stat} \pm 0.002_{sys}$	$4.688 \pm 0.062_{stat} \pm 0.012_{sys}$
$0.524 \pm 0.005_{stat} \pm 0.020_{sys}$	$4.515 \pm 0.084_{stat} \pm 0.161_{sys}$	$2.224 \pm 0.023_{stat} \pm 0.002_{sys}$	$4.598 \pm 0.063_{stat} \pm 0.013_{sys}$
$0.573 \pm 0.005_{stat} \pm 0.022_{sys}$	$4.848 \pm 0.089_{stat} \pm 0.173_{sys}$	$2.112 \pm 0.021_{stat} \pm 0.002_{sys}$	$4.505 \pm 0.066_{stat} \pm 0.014_{sys}$
$0.624 \pm 0.005_{stat} \pm 0.024_{sys}$	$5.176 \pm 0.094_{stat} \pm 0.184_{sys}$	$1.996 \pm 0.021_{stat} \pm 0.002_{sys}$	$4.420 \pm 0.069_{stat} \pm 0.015_{sys}$
$0.674 \pm 0.005_{stat} \pm 0.026_{sys}$	$5.486 \pm 0.101_{stat} \pm 0.195_{sys}$	$1.866 \pm 0.019_{stat} \pm 0.000_{sys}$	$4.341 \pm 0.070_{stat} \pm 0.016_{sys}$
$0.723 \pm 0.005_{stat} \pm 0.029_{sys}$	$5.777 \pm 0.105_{stat} \pm 0.205_{sys}$	$1.756 \pm 0.020_{stat} \pm 0.000_{sys}$	$4.254 \pm 0.072_{stat} \pm 0.016_{sys}$
$0.773 \pm 0.005_{stat} \pm 0.031_{sys}$	$6.060 \pm 0.115_{stat} \pm 0.215_{sys}$	$1.624 \pm 0.018_{stat} \pm 0.000_{sys}$	$4.181 \pm 0.073_{stat} \pm 0.017_{sys}$
$0.823 \pm 0.005_{stat} \pm 0.033_{sys}$	$6.325 \pm 0.121_{stat} \pm 0.225_{sys}$	$1.428 \pm 0.000_{stat} \pm 0.000_{sys}$	$4.099 \pm 0.076_{stat} \pm 0.018_{sys}$
$0.873 \pm 0.005_{stat} \pm 0.035_{sys}$	$6.585 \pm 0.123_{stat} \pm 0.234_{sys}$	$1.358 \pm 0.042_{stat} \pm 0.000_{sys}$	$4.026 \pm 0.074_{stat} \pm 0.019_{sys}$
$0.921 \pm 0.005_{stat} \pm 0.037_{sys}$	$6.882 \pm 0.115_{stat} \pm 0.243_{sys}$	$1.236 \pm 0.013_{stat} \pm 0.000_{sys}$	$3.973 \pm 0.076_{stat} \pm 0.019_{sys}$
$0.973 \pm 0.004_{stat} \pm 0.040_{sys}$	$7.075 \pm 0.131_{stat} \pm 0.253_{sys}$	$1.027 \pm 0.052_{stat} \pm 0.002_{sys}$	$3.855 \pm 0.069_{stat} \pm 0.020_{sys}$

Table 8.23: Physics asymmetries, as defined in Equations 8.32-8.36, measured using electron beam of E = 4.74 GeV.

	Target Spin = 0°	Target Spin = 90°	Target Spin = 270°
Central x Bin Value	A^0_{phys}	A^{90}_{phys}	A^{270}_{phys}
0.225	-0.0169 $\pm$ 0.0079$_{stat}$	-0.0179 $\pm$ 0.0081$_{stat}$	0.0017 $\pm$ 0.0050$_{stat}$
0.275	-0.0130 $\pm$ 0.0056$_{stat}$	0.0171 $\pm$ 0.0057$_{stat}$	0.0005 $\pm$ 0.0034$_{stat}$
0.325	-0.0107 $\pm$ 0.0051$_{stat}$	-0.0001 $\pm$ 0.0050$_{stat}$	-0.0053 $\pm$ 0.0031$_{stat}$
0.375	0.0027 $\pm$ 0.0053$_{stat}$	0.0090 $\pm$ 0.0052$_{stat}$	-0.0126 $\pm$ 0.0032$_{stat}$
0.425	-0.0227 $\pm$ 0.0061$_{stat}$	0.0018 $\pm$ 0.0059$_{stat}$	-0.0058 $\pm$ 0.0037$_{stat}$
0.475	-0.0198 $\pm$ 0.0072$_{stat}$	0.0128 $\pm$ 0.0070$_{stat}$	-0.0041 $\pm$ 0.0044$_{stat}$
0.525	0.0021 $\pm$ 0.0086$_{stat}$	0.0046 $\pm$ 0.0083$_{stat}$	-0.0084 $\pm$ 0.0052$_{stat}$
0.575	0.0046 $\pm$ 0.0103$_{stat}$	0.0209 $\pm$ 0.0100$_{stat}$	-0.0048 $\pm$ 0.0063$_{stat}$
0.625	0.0274 $\pm$ 0.0125$_{stat}$	-0.0109 $\pm$ 0.0120$_{stat}$	0.0014 $\pm$ 0.0075$_{stat}$
0.675	0.0238 $\pm$ 0.0153$_{stat}$	0.0293 $\pm$ 0.0146$_{stat}$	0.0042 $\pm$ 0.0092$_{stat}$
0.725	0.0296 $\pm$ 0.0188$_{stat}$	0.0181 $\pm$ 0.0180$_{stat}$	-0.0132 $\pm$ 0.0114$_{stat}$
0.775	-0.0132 $\pm$ 0.0237$_{stat}$	0.0355 $\pm$ 0.0227$_{stat}$	-0.0220 $\pm$ 0.0144$_{stat}$
0.825	-0.0342 $\pm$ 0.0304$_{stat}$	0.0027 $\pm$ 0.0293$_{stat}$	0.0067 $\pm$ 0.0185$_{stat}$
0.875	-0.0136 $\pm$ 0.0391$_{stat}$	0.0538 $\pm$ 0.0378$_{stat}$	-0.0492 $\pm$ 0.0238$_{stat}$
0.925	-0.0553 $\pm$ 0.0506$_{stat}$	-0.0231 $\pm$ 0.0471$_{stat}$	-0.0150 $\pm$ 0.0300$_{stat}$
0.975	0.0037 $\pm$ 0.0609$_{stat}$	0.0448 $\pm$ 0.0596$_{stat}$	0.0310 $\pm$ 0.0369$_{stat}$

Table 8.24: Physics asymmetries, as defined in Equations 8.32-8.36, measured using electron beam of E = 5.89 GeV.

	Target Spin = 0°	Target Spin = 90°	Target Spin = 270°
Central x Bin Value	A^0_{phys}	A^{90}_{phys}	A^{270}_{phys}
0.225	-0.0152 $\pm$ 0.0092$_{stat}$	-0.0038 $\pm$ 0.0037$_{stat}$	0.0101 $\pm$ 0.0043$_{stat}$
0.275	0.0028 $\pm$ 0.0071$_{stat}$	0.0058 $\pm$ 0.0028$_{stat}$	-0.0007 $\pm$ 0.0031$_{stat}$
0.325	-0.0116 $\pm$ 0.0065$_{stat}$	0.0029 $\pm$ 0.0026$_{stat}$	-0.0026 $\pm$ 0.0029$_{stat}$
0.375	-0.0040 $\pm$ 0.0068$_{stat}$	0.0051 $\pm$ 0.0028$_{stat}$	-0.0045 $\pm$ 0.0032$_{stat}$
0.425	-0.0170 $\pm$ 0.0079$_{stat}$	0.0042 $\pm$ 0.0033$_{stat}$	-0.0095 $\pm$ 0.0037$_{stat}$
0.475	-0.0183 $\pm$ 0.0095$_{stat}$	0.0081 $\pm$ 0.0040$_{stat}$	0.0036 $\pm$ 0.0044$_{stat}$
0.525	0.0018 $\pm$ 0.0115$_{stat}$	0.0026 $\pm$ 0.0049$_{stat}$	-0.0005 $\pm$ 0.0052$_{stat}$
0.575	0.0032 $\pm$ 0.0140$_{stat}$	-0.0069 $\pm$ 0.0060$_{stat}$	-0.0048 $\pm$ 0.0063$_{stat}$
0.625	0.0044 $\pm$ 0.0174$_{stat}$	-0.0004 $\pm$ 0.0074$_{stat}$	-0.0100 $\pm$ 0.0077$_{stat}$
0.675	-0.0039 $\pm$ 0.0216$_{stat}$	0.0133 $\pm$ 0.0092$_{stat}$	0.0089 $\pm$ 0.0095$_{stat}$
0.725	0.0019 $\pm$ 0.0272$_{stat}$	-0.0090 $\pm$ 0.0116$_{stat}$	-0.0194 $\pm$ 0.0118$_{stat}$
0.775	0.0050 $\pm$ 0.0347$_{stat}$	-0.0031 $\pm$ 0.0149$_{stat}$	0.0050 $\pm$ 0.0150$_{stat}$
0.825	0.0273 $\pm$ 0.0467$_{stat}$	0.0235 $\pm$ 0.0197$_{stat}$	-0.0658 $\pm$ 0.0201$_{stat}$
0.875	0.0148 $\pm$ 0.0624$_{stat}$	0.0006 $\pm$ 0.0262$_{stat}$	-0.0177 $\pm$ 0.0265$_{stat}$
0.925	-0.1084 $\pm$ 0.0846$_{stat}$	0.0156 $\pm$ 0.0353$_{stat}$	-0.0011 $\pm$ 0.0366$_{stat}$
0.975	0.1582 $\pm$ 0.1113$_{stat}$	0.1370 $\pm$ 0.0472$_{stat}$	0.0445 $\pm$ 0.0477$_{stat}$

Table 8.25: $A_{\parallel}^{phys}$ and $A_{\perp}^{phys}$, defined by Equations 8.38- 8.41, for each x bin at an electron beam energy of 4.74 GeV.

Central x Bin Value	$A_{\parallel}^{phys}$	$A_{\perp}^{phys}$
0.225	-0.0169 $\pm$ 0.0079$_{stat}$	0.0061 $\pm$ 0.0042$_{stat}$
0.275	-0.0130 $\pm$ 0.0056$_{stat}$	-0.0043 $\pm$ 0.0029$_{stat}$
0.325	-0.0107 $\pm$ 0.0051$_{stat}$	-0.0039 $\pm$ 0.0026$_{stat}$
0.375	0.0027 $\pm$ 0.0053$_{stat}$	-0.0116 $\pm$ 0.0027$_{stat}$
0.425	-0.0227 $\pm$ 0.0061$_{stat}$	-0.0047 $\pm$ 0.0031$_{stat}$
0.475	-0.0198 $\pm$ 0.0072$_{stat}$	-0.0066 $\pm$ 0.0037$_{stat}$
0.525	0.0021 $\pm$ 0.0086$_{stat}$	-0.0073 $\pm$ 0.0044$_{stat}$
0.575	0.0046 $\pm$ 0.0103$_{stat}$	-0.0093 $\pm$ 0.0053$_{stat}$
0.625	0.0274 $\pm$ 0.0125$_{stat}$	0.0041 $\pm$ 0.0064$_{stat}$
0.675	0.0238 $\pm$ 0.0153$_{stat}$	-0.0052 $\pm$ 0.0078$_{stat}$
0.725	0.0296 $\pm$ 0.0188$_{stat}$	-0.0146 $\pm$ 0.0096$_{stat}$
0.775	-0.0132 $\pm$ 0.0237$_{stat}$	-0.0259 $\pm$ 0.0121$_{stat}$
0.825	-0.0342 $\pm$ 0.0304$_{stat}$	0.0040 $\pm$ 0.0156$_{stat}$
0.875	-0.0136 $\pm$ 0.0391$_{stat}$	-0.0505 $\pm$ 0.0201$_{stat}$
0.925	-0.0553 $\pm$ 0.0506$_{stat}$	-0.0041 $\pm$ 0.0253$_{stat}$
0.975	0.0037 $\pm$ 0.0609$_{stat}$	0.0100 $\pm$ 0.0314$_{stat}$

Table 8.26: $A_{\parallel}^{phys}$ and $A_{\perp}^{phys}$, defined by Equations 8.38- 8.41, for each x bin at an electron beam energy of 5.89 GeV.

Central x Bin Value	$A_{\parallel}^{phys}$	$A_{\perp}^{phys}$
0.225	-0.0152 $\pm$ 0.0092$_{stat}$	0.0065 $\pm$ 0.0028$_{stat}$
0.275	0.0028 $\pm$ 0.0071$_{stat}$	-0.0036 $\pm$ 0.0021$_{stat}$
0.325	-0.0116 $\pm$ 0.0065$_{stat}$	-0.0028 $\pm$ 0.0019$_{stat}$
0.375	-0.0040 $\pm$ 0.0068$_{stat}$	-0.0048 $\pm$ 0.0021$_{stat}$
0.425	-0.0170 $\pm$ 0.0079$_{stat}$	-0.0066 $\pm$ 0.0025$_{stat}$
0.475	-0.0183 $\pm$ 0.0095$_{stat}$	-0.0028 $\pm$ 0.0030$_{stat}$
0.525	0.0018 $\pm$ 0.0115$_{stat}$	-0.0016 $\pm$ 0.0036$_{stat}$
0.575	0.0032 $\pm$ 0.0140$_{stat}$	0.0013 $\pm$ 0.0043$_{stat}$
0.625	0.0044 $\pm$ 0.0174$_{stat}$	-0.0046 $\pm$ 0.0053$_{stat}$
0.675	-0.0039 $\pm$ 0.0216$_{stat}$	-0.0025 $\pm$ 0.0066$_{stat}$
0.725	0.0019 $\pm$ 0.0272$_{stat}$	-0.0049 $\pm$ 0.0083$_{stat}$
0.775	0.0050 $\pm$ 0.0347$_{stat}$	0.0040 $\pm$ 0.0106$_{stat}$
0.825	0.0273 $\pm$ 0.0467$_{stat}$	-0.0442 $\pm$ 0.0141$_{stat}$
0.875	0.0148 $\pm$ 0.0624$_{stat}$	-0.0091 $\pm$ 0.0186$_{stat}$
0.925	-0.1084 $\pm$ 0.0846$_{stat}$	-0.0086 $\pm$ 0.0254$_{stat}$
0.975	0.1582 $\pm$ 0.1113$_{stat}$	-0.0472 $\pm$ 0.0336$_{stat}$

8.2.9 Contamination

The main sources of background contamination for E06-014 were from pions and pair-production. Despite applying PID cuts, electrons originating from these two processes were still misidentified in the electron sample as being electrons scattering inelastically from the ^{3}He nuclei. The next two sections will examine how much of the electron sample was a result of these background processes and how the asymmetry was corrected for their contributions.

8.2.9.1 Pion

In the BigBite spectrometer, one of the main sources of contamination to the electron sample was from charged pions. With the Čerenkov detector threshold set relatively high (1-1.5 photoelectrons), it was difficult to use the Čerenkov detector as a way by which to detect pions. As a result, following in the foot steps of the E06-010 [82] pion contamination analysis, the Pb-glass calorimeter was used to analyze the pion contamination. Although the pions and electrons are fairly well separated in the preshower detector (see Figure 8.12), it is important to determine the level of pion background in the electron sample, as it will dilute the electron asymmetry.

8.2.9.1.1 Pion Background The pion background contamination was determined by summing over particle helicity states and using the preshower energy spectrum (E_{ps}) to determine pion to electron ratios. The minimum ionization peak around channel 200 was modeled as a convoluted Gaussian Landau function, f_{LG}. While the electron peak, which was above channel 200 was modeled as a Gaussian function, f_G. The pion contamination, f_π, could then be determined

$$f_{\pi} = \frac{\int_{200}^{1000} f_{LG}\left(x\right) dx}{\int_{200}^{1000} f_{G}\left(x\right) dx} = \frac{\pi}{e}, \tag{8.42}$$

where x is the preshower energy channel and the integrals run from preshower energies of 200 to 1000 MeV. Ideally, the pion contamination factor given in Equation 8.42 would be computed using the preshower energy spectrum with all electron PID cuts (described in Section 8.2.2) applied, except the preshower energy cut. However, in the case of E06-014 applying all the PID electron cuts results in the removal of nearly the entire minimum ionization peak (see Figure 8.26). While this result allows one to conclude that many of the pions are being removed by the electron PID cuts, it does not reveal what is happening to the pion distribution laying underneath electron peak (E_{ps} channel 400). In order determine the amount of pions laying in the electron portion of the preshower energy spectrum when all PID cuts are applied (with the exception of the preshower energy cut), a three step process was used.

1. Applying the data quality cuts defined in Section 8.2.1 and only the Čerenkov electron cut (Section 8.2.2.5), the preshower energy spectrum is fitted using the Landau-Gaussian and Gaussian functions for the minimum ionization and electron peaks. The number of pions and electrons are extracted through Equation 8.42. Figure 8.48 shows the preshower energy modeling of the minimum ionization (blue fit) and electron (red fit) peaks. The solid line shows the fit region of the curves, while the dashed line is the extension of the functions resulting from the solid line fits.

2. The difference between the preshower energy spectrum described in the first step, and the preshower energy spectrum obtained by applying data quality cuts and all the electron PID cuts is computed. This difference allows one to see the energy distribution of the events that are removed by applying the electron cuts. The resulting energy spectrum's minimum ionization and electron peaks are fitted with Landau-Gaussian

and Gaussian functions, and the number of pions and electrons are computed according to Equation 8.42. The preshower energy modeling of the minimum ionization (blue fit) and electron (red fit) peaks is shown in Figure 8.49. The solid line shows the fit region of the curves, while the dashed line is the extension of the functions resulting from the solid line fits.

3. Finally, the pion contamination contained in the electron sample with all electron PID cuts applied can be determined as

$$f'_{\pi} = \frac{\pi^{(1)} - \pi^{(2)}}{e^{(1)} - e^{(2)}} \tag{8.43}$$

where the superscripts 1 and 2 refer to the number pions and electrons computed in steps 1 and 2 through the use of Equation 8.42.

The three preshower energy spectra types (Čerenkov electron cut only, all electron PID cuts and the energy spectra difference) can be seen in Figure 8.50, which reveals the energy distribution of the events removed by the electron PID cuts (black histogram). This three step process was performed for all x bins up to the x bin where there were not enough statistics, due to low pion rates, to accurately compute a pion contamination factor. These x bins were assumed to have a negligible pion contamination. In addition to measuring the negative pion contamination, by flipping the BigBite magnet polarity to positive polarity (so that positively charged particles bend up into the BigBite spectrometer) and applying the same cut sets described above, with the exception of selecting positively rather than negatively charged particles[13],the positive pion contamination to the positron sample (using the same

[13]This cut has a misleading name; in the software this cut is defined based on the bend direction of the particles through the BigBite magnet and not the physical charge of the particle. Therefore with the BigBite magnet in negative polarity a charge flag value of -1 selects negative particles that bend up through the magnet; while in positive polarity a charge flag value of -1 selects positively charged particles that bend up through the magnet.

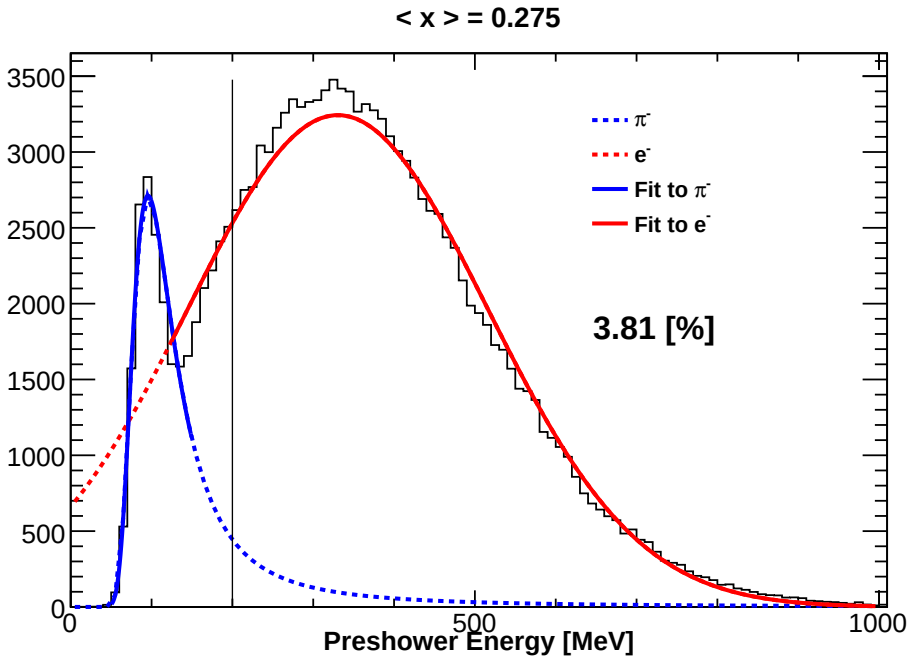

Figure 8.48: Preshower energy spectrum with only the Čerenkov electron PID cut applied for the bin $x = 0.275$. The preshower energy modeling of the minimum ionization and electron peaks are the solid lines. Extending the fit to a wider preshower energy range is shown by the dashed lines.

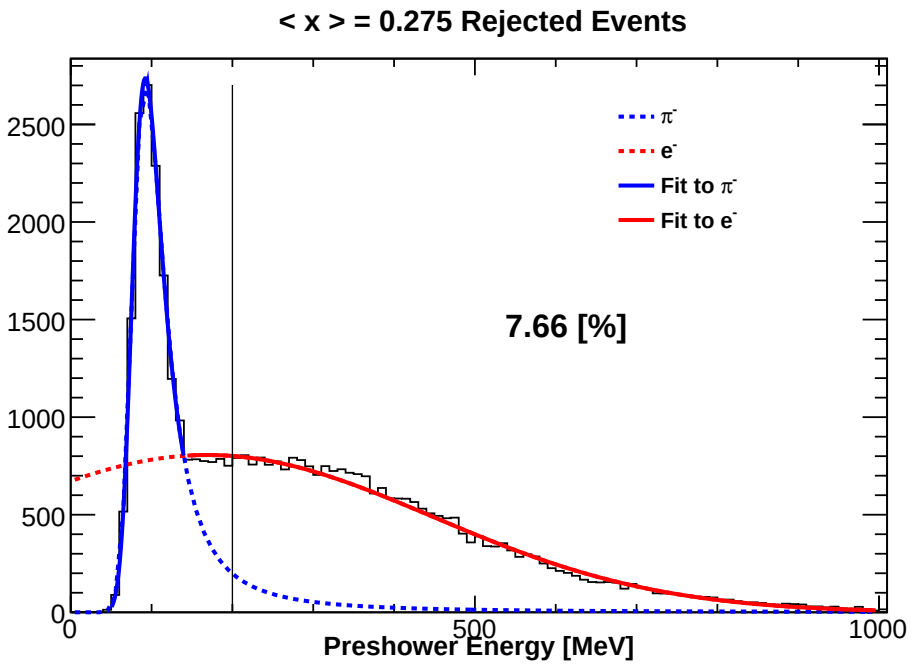

Figure 8.49: Preshower energy spectrum resulting from the difference of the preshower energy spectrum with only the Čerenkov electron PID cut applied and with all the electron PID cuts applied for the bin $x = 0.275$. The preshower energy modeling of the minimum ionization and electron peaks are the solid lines. Extending the fit to a wider preshower energy range is shown by the dashed lines.

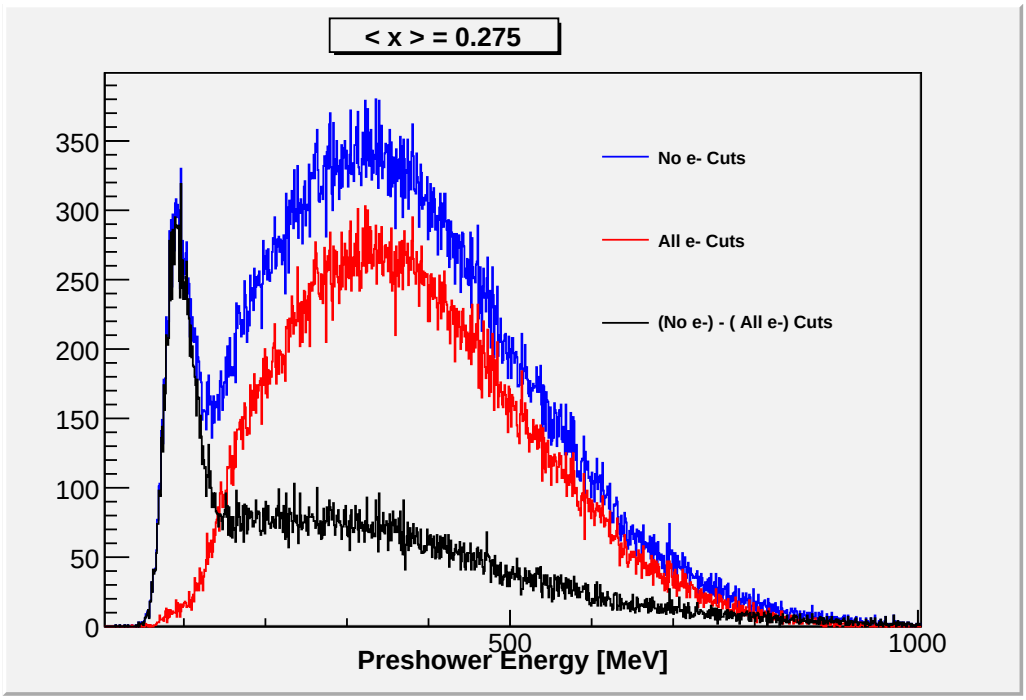

Figure 8.50: The preshower energy spectra used to compute the pion contamination. The blue histogram has only the electron Čerenkov cut applied, the red histogram has all if the electron PID cuts applied, and the black is the difference of the blue and red histograms, which shows the energy distribution of the events that are removed when applying all electron PID cuts.

cuts that defined the electrons) was measured. Table 8.27 lists the measured BigBite pion contamination for each x bin. The largest negative pion contamination of about 3% was found at the smallest x bin (x = 0.225), and quickly fell off to under 1% by x = 0.425. The positive pion contamination was found to be larger, around 5%, and more constant over x than the negative pion contamination. Towards the end of the experiment running, which coincided with data taking at an electron beam energy of 4.74 GeV, the main electron trigger was optimized to remove a significant portion of the minimum ionization peak and trigger primarily on electrons. As a result there preshower energy minimum ionization peak could not be used to extract a pion contamination. However, the data taken at a beam energy of 5.89 GeV should have a larger pion contamination and hence serve as an upper bound on the lower beam energy pion contamination. E06-010 measured the BigBite pion contamination following a similar method to the one that was just discussed [82], however E06-010 was also able to evaluate the pion contamination through a second method involving a coincidence between electrons in BigBite and pions in the LHRS. Using these two methods, a systematic uncertainty was assigned to the pion contamination computed from a similar method to the one discussed above. For E06-014 there is not a second way in which to directly measure the pion contamination, as a result the largest systematic uncertainty, of 2.5%, found in E06-010 is assigned as the uncertainty for E06-014's measurements.

8.2.9.1.2 Pion Asymmetry Since the BigBite detector is being used to measure electron asymmetries, the contamination to the asymmetry due to the pion asymmetry also needs to be considered. The $\pi^{\pm}$ asymmetries were measured in BigBite at an incident electron energy of 5.89 GeV using the data quality cut defined in Section 8.2.1 and altering the PID cuts as follows:

- Preshower energy cut was changed to select events that deposit less than 150 MeV into the preshower.

Table 8.27: The $\frac{\pi^-}{e^-}$ and $\frac{\pi^+}{e^+}$ ratios extracted using the preshower energy spectrum at an incident electron energy of 5.89 GeV.

x Bin Center	π^-/e^- [%]	π^+/e^+ [%]
0.225	3.00	3.76
0.275	2.70	5.73
0.325	1.60	4.33
0.375	1.00	3.70
0.425	0.90	4.34
0.475	0.70	6.47
0.525	0.40	4.11
0.575	0.70	—

- The scintillator energy cut was changed to select events that deposit less than 450 MeV into the scintillator.
- The Čerenkov cut was removed from the analysis.
- Finally, the energy over momentum cut was changed to $E/p < 0.8$.

The π^- events were selected with the BigBite magnet set to negative polarity using the charge cut to select particles that bent up when traversing the magnet. Whereas the π^+ events were selected with the BigBite magnet again set to negative polarity, however the charge cut was now used to select the particles that bent down when passing through the magnet. Although the *bend-up* and *bend-down* particles have different acceptances, as it will be shown in Section 8.2.9.2.2, the acceptance effects cancel out when computing the asymmetry.

Given the high pion rates, the LHRS was able to accumulate enough $\pi^\pm$ statistics to measure the DSA for several x values, which served as a convenient way to cross check the BigBite asymmetries. Plotted in Figures 8.51 and 8.52 are the negative and positive pion raw asymmetries on polarized ^{3}He nuclei measured in the BigBite (blue markers) and the LHRS (red markers). In Figure 8.51, the two transverse target spin configurations were

Table 8.28: π^- longitudinal and transverse asymmetries measured in the BigBite spectrometer, as defined in Equations 8.38- 8.41, at an incident electron energy of 5.89 GeV.

x Bin Center	$A_{\parallel}^{\pi^-} \pm \delta A_{\parallel}^{\pi^-}$	$A_{\perp}^{\pi^-} \pm \delta A_{\perp}^{\pi^-}$
0.225	-0.0111 $\pm$ 0.0161$_{stat}$	-0.0169 $\pm$ 0.0069$_{stat}$
0.275	-0.0126 $\pm$ 0.0109$_{stat}$	-0.0152 $\pm$ 0.0051$_{stat}$
0.325	-0.0470 $\pm$ 0.0113$_{stat}$	-0.0183 $\pm$ 0.0053$_{stat}$
0.375	-0.0732 $\pm$ 0.0134$_{stat}$	-0.0114 $\pm$ 0.0062$_{stat}$
0.425	-0.0877 $\pm$ 0.0168$_{stat}$	0.0139 $\pm$ 0.0076$_{stat}$
0.475	-0.0949 $\pm$ 0.0221$_{stat}$	0.0222 $\pm$ 0.0098$_{stat}$
0.525	-0.1026 $\pm$ 0.0296$_{stat}$	0.0409 $\pm$ 0.0130$_{stat}$
0.575	-0.0690 $\pm$ 0.0405$_{stat}$	0.0481 $\pm$ 0.0175$_{stat}$
0.625	-0.0299 $\pm$ 0.0548$_{stat}$	0.0598 $\pm$ 0.0232$_{stat}$
0.675	0.0374 $\pm$ 0.0736$_{stat}$	0.0649 $\pm$ 0.0313$_{stat}$
0.725	0.0141 $\pm$ 0.0990$_{stat}$	0.0519 $\pm$ 0.0421$_{stat}$
0.775	-0.1187 $\pm$ 0.1258$_{stat}$	0.1045 $\pm$ 0.0560$_{stat}$
0.825	-0.2998 $\pm$ 0.1693$_{stat}$	-0.0663 $\pm$ 0.0754$_{stat}$
0.875	0.2351 $\pm$ 0.2372$_{stat}$	0.0787 $\pm$ 0.1043$_{stat}$
0.925	0.5229 $\pm$ 0.4270$_{stat}$	0.1360 $\pm$ 0.1795$_{stat}$
0.975	0.3357 $\pm$ 1.0321$_{stat}$	0.1738 $\pm$ 0.2522$_{stat}$

combined to produce one transverse raw asymmetry. In Figure 8.52, only the transverse target spin pointing towards 90°is shown because the LHRS did not take positron data in any other target spin configuration with the electron beam energy set to 5.89 GeV. As can be seen in Figures 8.51 and 8.52, the LHRS, having more precision due to a looser online trigger than BigBite spectrometer, agrees well with the asymmetry measured in the BigBite spectrometer. Through the use of Equations 8.38- 8.41, the raw $\pi^{\pm}$ asymmetries measured in BigBite can be converted to physics asymmetries and are shown in Figures 8.53 and 8.54, and listed in Tables 8.28 and 8.29.

The contribution of the negative(positive) pion asymmetry to the electron(positron) asymmetry was determined by multiplying the pion asymmetry by the pion background contamination. The π^- asymmetry contamination was found to be less than 5% of the

Table 8.29: π^+ longitudinal and transverse asymmetries measured in the BigBite spectrometer, as defined in Equations 8.38- 8.41, at an incident electron energy of 5.89 GeV.

x Bin Center	$A_{\parallel}^{\pi^+} \pm \delta A_{\parallel}^{\pi^+}$	$A_{\perp}^{\pi^+} \pm \delta A_{\perp}^{\pi^+}$
0.225	$0.0011 \pm 0.0322_{stat}$	$0.0127 \pm 0.0164_{stat}$
0.275	$-0.0177 \pm 0.0214_{stat}$	$0.0106 \pm 0.0112_{stat}$
0.325	$-0.0158 \pm 0.0202_{stat}$	$-0.0046 \pm 0.0106_{stat}$
0.375	$0.0028 \pm 0.0219_{stat}$	$0.0094 \pm 0.0116_{stat}$
0.425	$-0.0085 \pm 0.0259_{stat}$	$0.0088 \pm 0.0136_{stat}$
0.475	$-0.0436 \pm 0.0330_{stat}$	$-0.0215 \pm 0.0172_{stat}$
0.525	$-0.0183 \pm 0.0432_{stat}$	$0.0007 \pm 0.0224_{stat}$
0.575	$-0.0369 \pm 0.0560_{stat}$	$0.0044 \pm 0.0289_{stat}$
0.625	$0.0091 \pm 0.0752_{stat}$	$0.0428 \pm 0.0369_{stat}$
0.675	$0.3122 \pm 0.0977_{stat}$	$-0.0288 \pm 0.0467_{stat}$
0.725	$-0.1272 \pm 0.1201_{stat}$	$-0.1030 \pm 0.0575_{stat}$
0.775	$0.1230 \pm 0.1417_{stat}$	$0.1318 \pm 0.0711_{stat}$
0.825	$-0.0344 \pm 0.1845_{stat}$	$0.0387 \pm 0.0916_{stat}$
0.875	$0.0899 \pm 0.2086_{stat}$	$0.0171 \pm 0.1215_{stat}$
0.925	$0.0999 \pm 0.3480_{stat}$	$-0.1608 \pm 0.1655_{stat}$
0.975	$-0.1892 \pm 0.3887_{stat}$	$-0.2423 \pm 0.2241_{stat}$

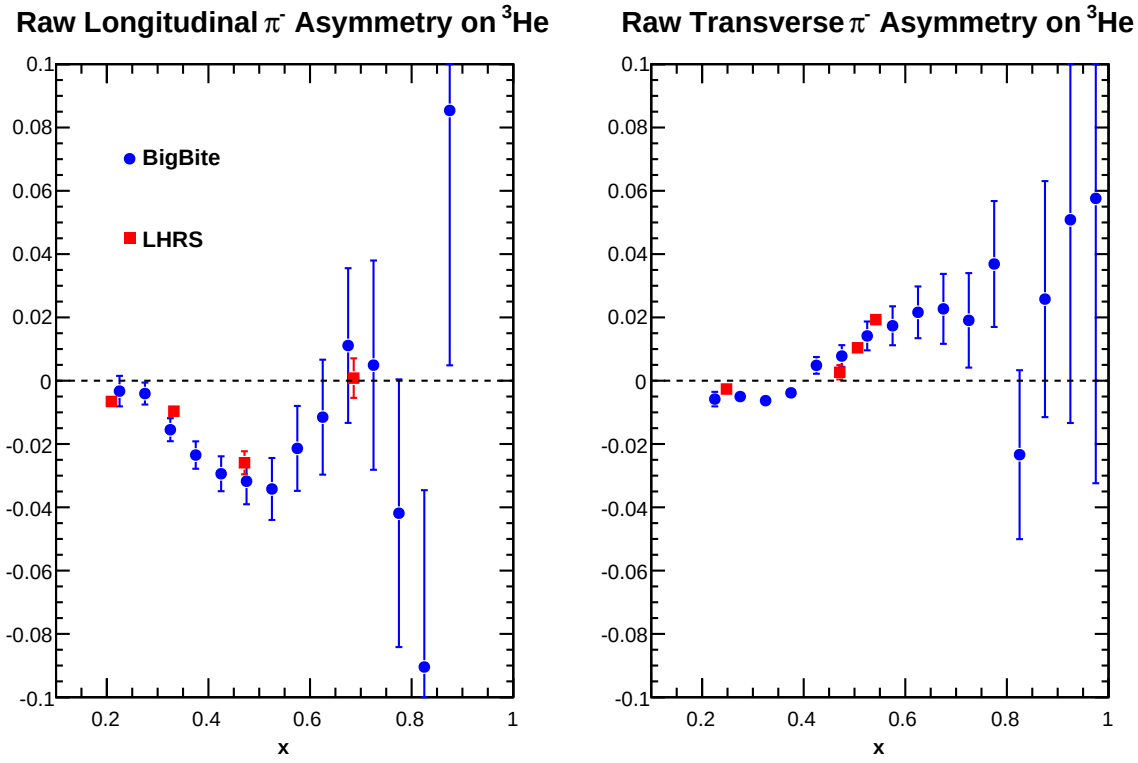

Figure 8.51: Raw longitudinal (left panel) and transverse (right panel) π^- asymmetries measured in the BigBite spectrometer (blue markers) and LHRS (red markers) as a function of x at an incident electron energy of 5.89 GeV.

total electron longitudinal and transverse asymmetry uncertainties ($\pm\delta A_{\parallel}^{phys}$ and $\pm\delta A_{\perp}^{phys}$), while the π^+ asymmetry contamination was less than 3% of the total positron asymmetry uncertainty. For both charged hadrons, the π^- asymmetry had negligible effects on the electron asymmetry and the π^+ asymmetry had negligible effects on the positron asymmetry. Therefore no π^- or π^+ asymmetry correction needed to be applied to the measured electron asymmetries.

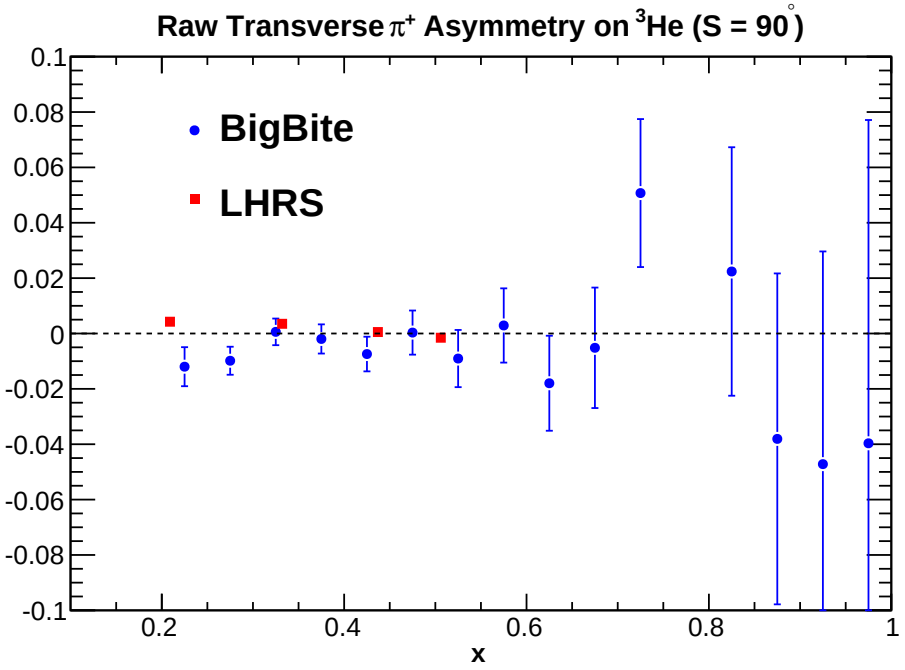

Figure 8.52: Raw transverse (target spin direction = 90°) π^+ asymmetry measured in the BigBite spectrometer and LHRS at an incident electron energy of 5.89 GeV.

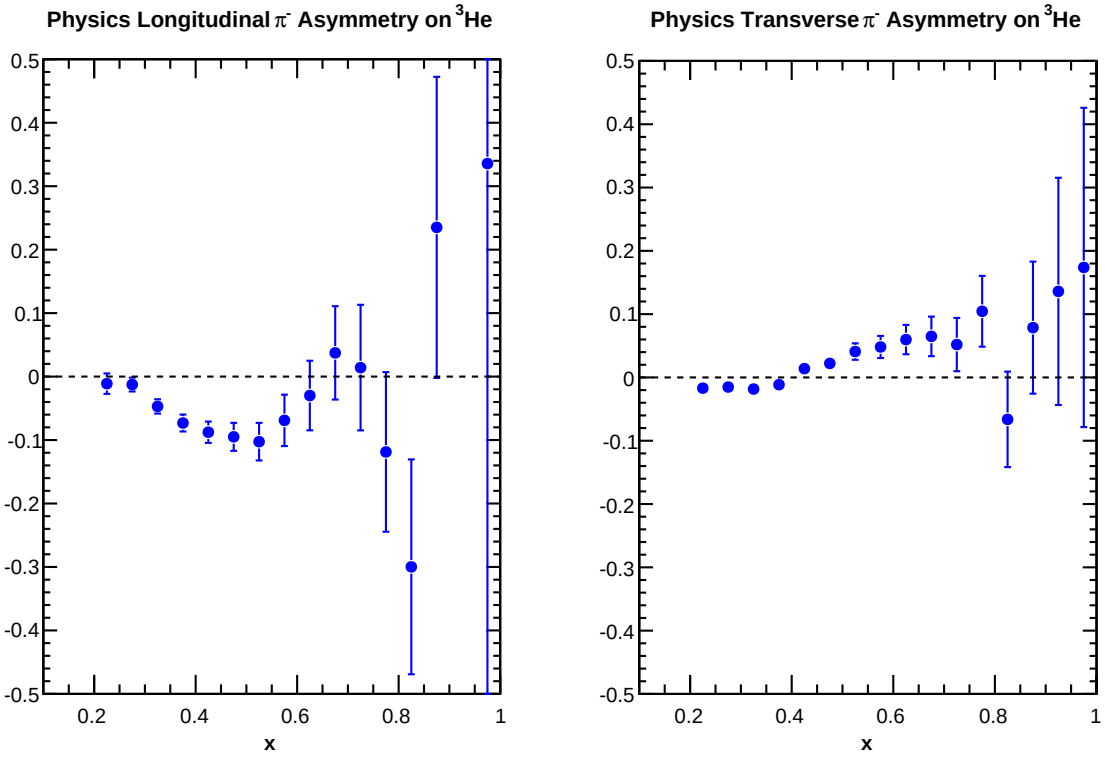

Figure 8.53: Longitudinal (left panel) and transverse (right panel) π^- physics asymmetries measured in the BigBite spectrometer at an incident energy of 5.89 GeV.

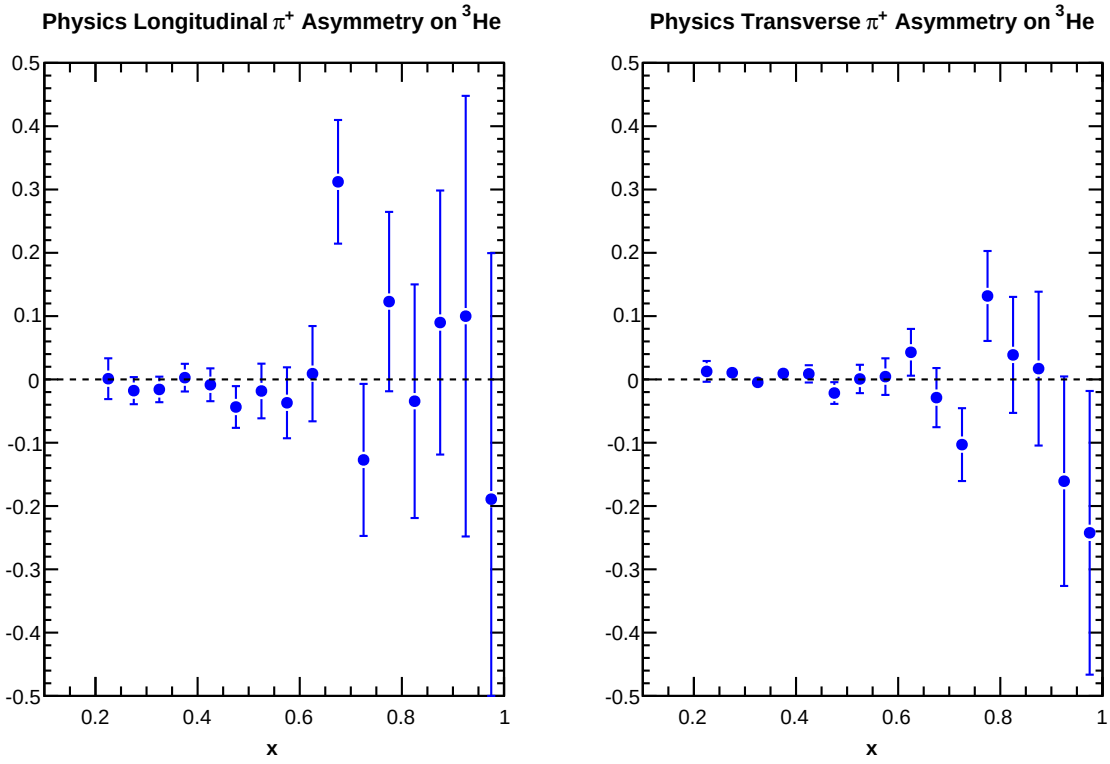

Figure 8.54: Longitudinal (left panel) and transverse (right panel) π^+ physics asymmetries measured in the BigBite spectrometer at an incident energy of 5.89 GeV.

8.2.9.2 Pair-Production

8.2.9.2.1 Pair Produced Background Another significant source of background contamination in the BigBite spectrometer were electrons produced via pair production. π^0 events were produced at the target and due to its short lifetime, would decay before leaving the target region. These decays were dominated by high energy photons, which would pass through materials, such as the target cell wall, and have a probability of producing an e^+e^- pair. In addition to this, there is also about a 1% branching ratio of $\pi^0 \rightarrow \gamma e^+ e^-$ decay. The resulting electrons from such decays can be misidentified in the BigBite spectrometer as originating from ^{3}He nuclei.

Pair production is a charge symmetric process (*i.e.* for every electron produced in a pair production decay, there is also a positron produced.), thus the amount of pair produced electrons in the total electron sample can be determined by summing over particle helicity states and measuring the positron to electron ratio. In E06-014 the positrons were measured in the BigBite spectrometer by changing the magnet to positive polarity, which resulted in positive particles bending up through the magnet into the spectrometer, and provided the positrons with the same acceptance coverage as the electrons[14] that were used in the d_2^n analysis. The positrons were selected by applying all of the BigBite data quality (Section 8.2.1) and electron PID cuts (Section 8.2.2), with the exception that the E/p cut was widened slightly to account for a wider E/p distribution[15]

$$0.779 < E/p < 1.187. \tag{8.44}$$

[14] Analysis showed that the bend-down particles in BigBite have a different acceptance from those that bend-up, thus like particle trajectories should be compared (i.e. bend-up to bend-up or bend-down to bend-down).

[15] The E/p for positrons has a wider distribution than for electrons for two reasons: one, the momentum resolution of negatively charged particles is higher than that of the positively charged particles (Section 7.1.2; secondly, the ADCs that measure the energy deposited in the BigBite calorimeter were calibrated for negatively charged particles, and thus would provide better resolution for negatively charged particles than positively charged particles, which would take a slightly different trajectory when entering the PMTs [152].

Unfortunately, because of time constraints resulting from issues with the linac, the bend-up positrons were only able to be measured at one electron beam energy, 4.74 GeV. Therefore an indirect measurement was employed to compute the e^+/e^- ratio at an electron beam energy of 5.89 GeV. The e^+/e^- ratios measured using the BigBite spectrometer at incident electron energy of 4.74 GeV, LHRS at incident electron energies of 4.74 GeV and 5.89 GeV, and from CLAS EG1b [159] at an incident energy of 5.7 GeV and scattering angle of 41.1°, were used to plot $\left(\frac{e^+}{e^-}\right) \cdot \frac{1}{E_0^2}$ versus the transverse momentum $p_t = p \sin\theta$, where E_0 is the electron beam energy. This data showed a fairly universal trend, which was fitted with a function of the form

$$f\left(p_t\right) = \exp\left(a + b \cdot p_t\right), \tag{8.45}$$

where a and b were free parameters. Figure8.55 shows the fit to the data (red line), with the gray band representing the systematic uncertainty in the fit, which was determined through varying the fit function within the fit uncertainty. Using the fit results, the positron-electron ratio can be extracted at E_0 = 5.89 GeV and θ = 45°. Comparing the measured e^+/e^- ratios used in the fitting and the extracted ratios (at both BigBite energies) as a function of x, one can see from Figure 8.56 that there is very good agreement at high x and decent agreement at low x. Given that the three detectors used to measure the e^+/e^- ratios are very different from one another, some disagreement was expected. One thing that all the data have in common is the trend to more positron counts as x becomes smaller. Furthermore, all three detectors show a positron contamination greater than 50% at $x = 0.2$, with data taken with a 5.89 GeV and 5.7 GeV electron beam showing a positron contamination larger than 60% at $x = 0.2$. This consistent high positron contamination resulted in removeing the lowest x bin (x bin center = 0.225) for the remainder of the E06-014 analysis. Table 8.30 lists the BigBite positron-electron ratios and their uncertainties.

Table 8.30: Positron to electron ratios extracted from fit given in Equation 8.45 and their systematic uncertainty (absolute) for incident electron energies of 4.74 GeV and 5.89 GeV.

	E = 4.74 GeV	E = 5.89 GeV
$\langle x \rangle$	$e^+/e^- \pm \delta\,(e^+/e^-)_{sys}$	$e^+/e^- \pm \delta\,(e^+/e^-)_{sys}$
0.230	0.8072 ± 0.0383	1.1491 ± 0.0554
0.277	0.4848 ± 0.0244	0.6512 ± 0.0335
0.325	0.2977 ± 0.0158	0.3793 ± 0.0207
0.374	0.1806 ± 0.0101	0.2211 ± 0.0127
0.424	0.1087 ± 0.0064	0.1305 ± 0.0079
0.473	0.0666 ± 0.0041	0.0772 ± 0.0049
0.523	0.0416 ± 0.0027	0.0470 ± 0.0031
0.574	0.0266 ± 0.0018	0.0286 ± 0.0020
0.623	0.0174 ± 0.0012	0.0178 ± 0.0013
0.673	0.0116 ± 0.0008	0.0115 ± 0.0009
0.723	0.0079 ± 0.0006	0.0073 ± 0.0006
0.773	0.0055 ± 0.0004	0.0049 ± 0.0004
0.823	0.0000 ± 0.0000	0.0000 ± 0.0000
0.874	0.0000 ± 0.0000	0.0000 ± 0.0000
0.924	0.0000 ± 0.0000	0.0000 ± 0.0000
0.972	0.0000 ± 0.0000	0.0000 ± 0.0000

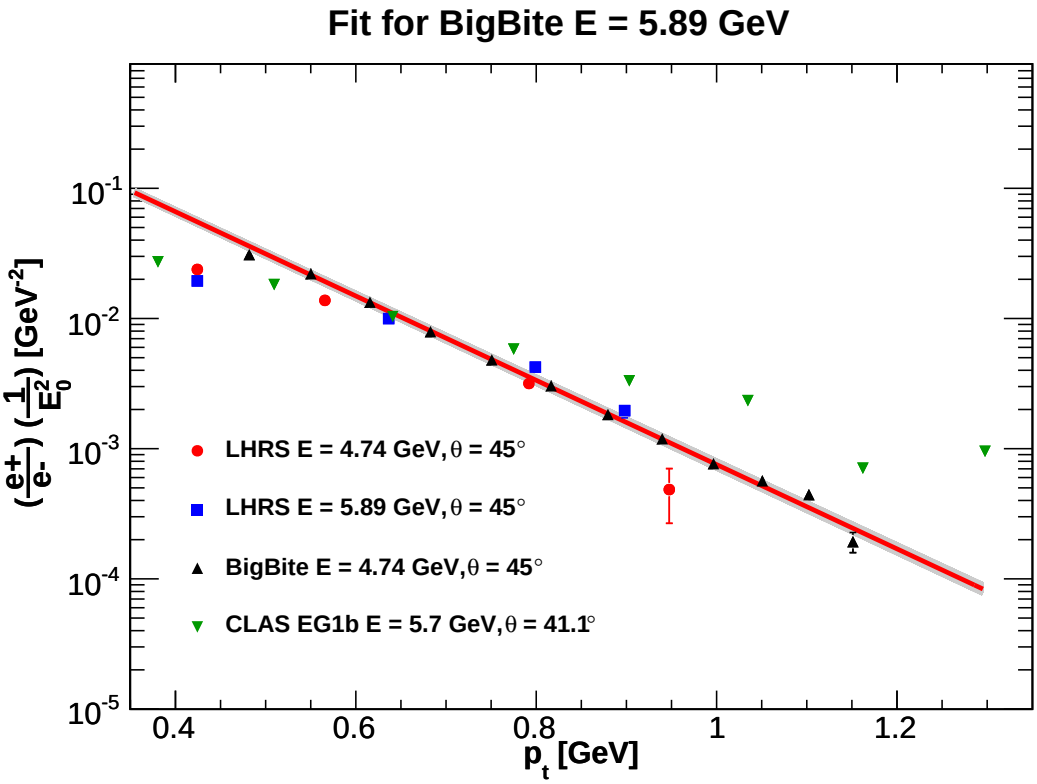

Figure 8.55: $\left(\frac{e^+}{e^-}\right) \cdot \frac{1}{E_0^2}$ plotted on Log scale against p_t for several independent measurements of the positron-electron ratio. The fit to the data is represented by the red line and the uncertainty in the fit is contained in the gray band.

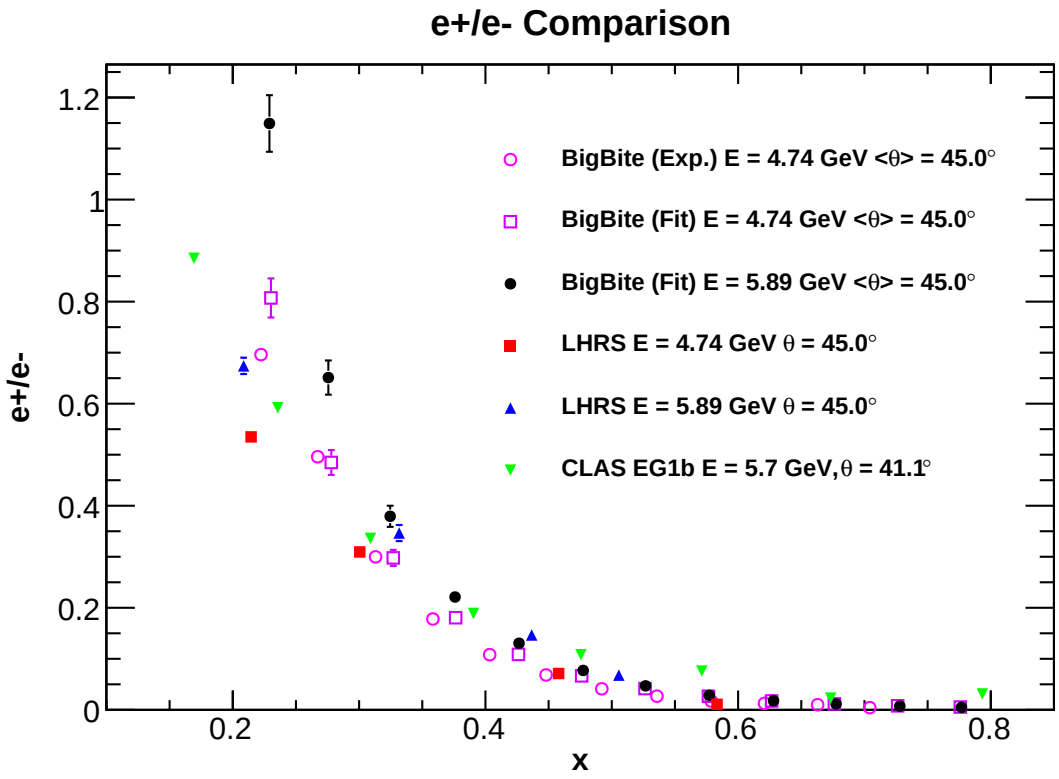

Figure 8.56: $\frac{e^-}{e^-}$ ratios measured in the BigBite spectrometer at an incident energy, E_0 = 4.74 GeV (open magenta circle), LHRS at E_0 = 4.74 GeV (solid red square) and 5.89 GeV (solid blue up triangle), and CLAS EG1b at E_0 = 5.7 GeV (solid green down triangle), along with ratios extracted from using the fit given in Equation 8.45 for the BigBite spectrometer at E_0 = 4.74 GeV (open magenta square) and 5.89 GeV (solid black circle).

8.2.9.2.2 Pair Produced Asymmetry As was the case with the pion contamination (Section 8.2.9.1), one must worry not only about the background contamination, but also the asymmetry contamination from the background. Ideally, the pair produced asymmetry would be measured through the positron asymmetry, by changing the BigBite magnet setting to positive polarity assuring that the positron and electron acceptances match. However due to time constraints mentioned previously, the positron asymmetry was measured (with BigBite in positive polarity) for only one target spin configuration (270°) and one indecent electron energy (4.74 GeV). Fortunately, since an asymmetry is being formed any acceptance dependence should be minimal.[16] This allowed the positron asymmetry to be measured by altering the charge cut to select bend-down positrons, and applying the data quality and PID cuts described Section 8.2.9.2.1 [17]. As a cross check, the asymmetry for the bend-down positrons were compared to the asymmetry of the bend-up positrons. Both positron samples were taken at an incident electron energy of 4.74 GeV, with the target spin oriented at 270°. Figure 8.57 shows that within the precision of the measurement, the bend-up (red markers) and the bend-down (blue markers) positron asymmetries are consistent with each other. The bend-down positron asymmetry measurements did not achieve as good a precision as the bend-up electron asymmetries (only about 40% of a run's total events before cuts bent-down through the magnet.). As a result, the longitudinal and transverse physics asymmetries were plotted against x and fitted with a constant value to eliminate any large central value fluctuations, which may result from poor precision. Figures 8.58 and 8.59 show the bend-down positron asymmetry fit results for incident electron energies of 4.74 GeV and 5.89 GeV. As was the case with the pions, to determine contamination contribution from the pair produced asymmetry, the positron asymmetry is multiplied by the positron background.

[16] The acceptance factor of the total counts in the denominator is the same acceptance factor associated with the helicity count difference in the numerator, and thus cancels in the ratio.

[17] The E/p cut for bend-down positrons, at an incident electron energy of 5.89 GeV was the same as that defined in Section 8.2.2. Whereas at an incident electron energy of 4.89 GeV, the bend-down positron E/p was altered according to Equation 8.44.

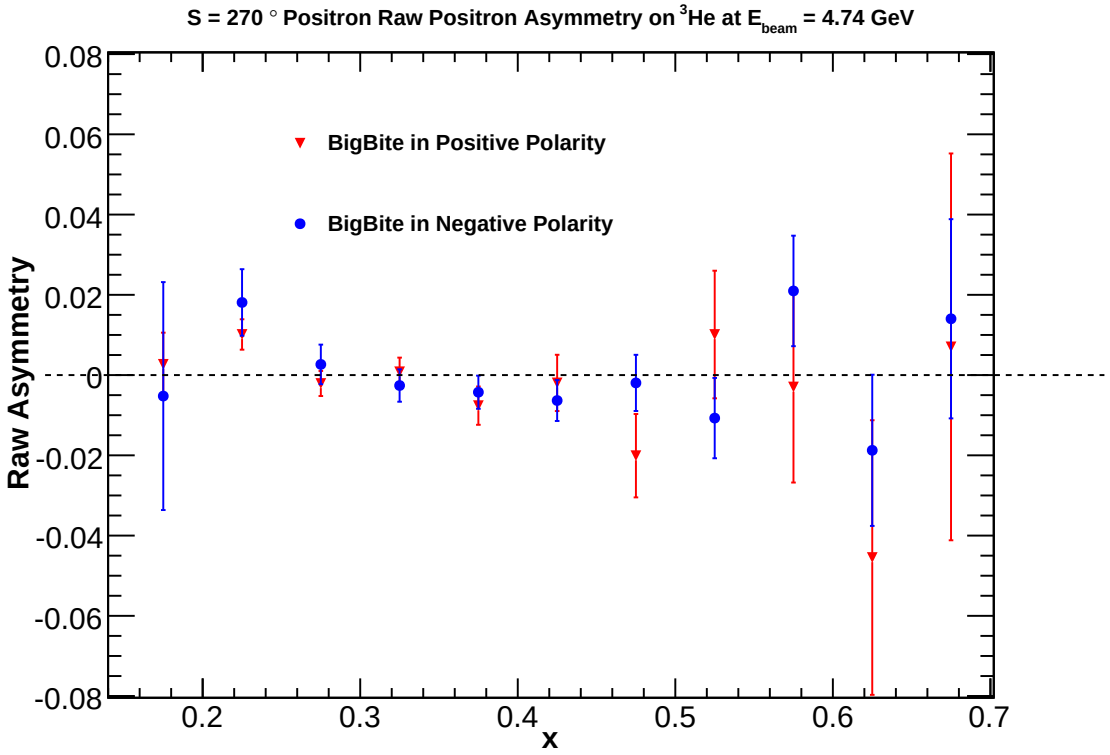

Figure 8.57: Comparison of the bend-up positron asymmetries (solid red down triangle) and bend-down positron asymmetries (solid blue circle) measured in the BigBite spectrometer as a function of x at a beam energy of 4.74 GeV and the target spin is oriented at 270°.

However, unlike pion asymmetries, the pair produced asymmetries was found to have a significant effect on the electron asymmetries. The decision to include the pair production asymmetry correction in the electron asymmetry was made based on the size of the positron asymmetry relative to the electron asymmetry, as well as a GEANT4 [160] simulation in which a π^0 asymmetry was created and the e^+e^- pairs resulting from pair production were found to have an asymmetry (Section 9).

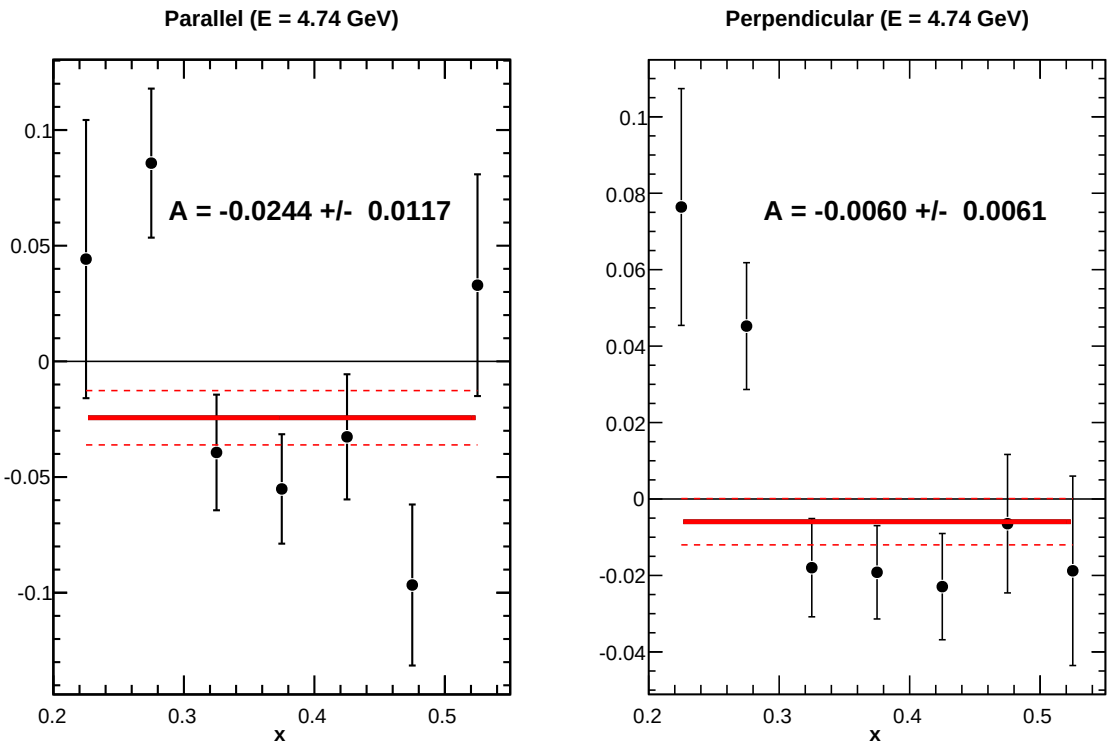

Figure 8.58: Constant fit to the longitudinal (left panel) and transverse (right panel) positron asymmetries measured in BigBite at an incident electron energy of 4.74 GeV. The solid red line is the fit result and the dashed lines are the upper and lower uncertainties on the fit.

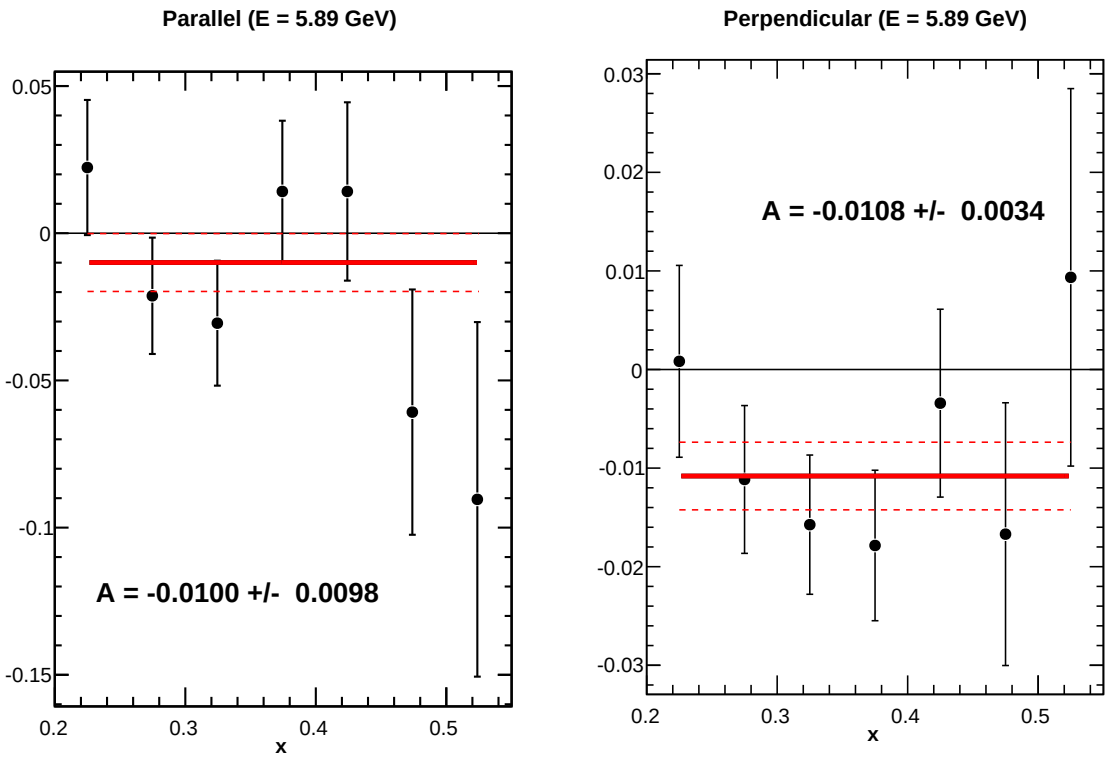

Figure 8.59: Constant fit to the longitudinal (left panel) and transverse (right panel) positron asymmetries measured in BigBite at an incident electron energy of 5.89 GeV. The solid red line is the fit result and the dashed lines are the upper and lower uncertainties on the fit.

8.2.9.3 Asymmetry Contamination Corrections

As the previous sections have shown, the measured electron asymmetry does not simply contain contributions from electrons scattering from ^{3}He nuclei, but also various background events. Therefore to obtain the electron portion that is due to e^- - ^{3}He scattering the other contributions need to be removed. This results in the electron counts for a particular helicity state being

$$N^{e-} = N_m^{e^-} - N^{\pi^-} - N_m^{e^+} + N^{\pi^+}, \tag{8.46}$$

where N_m^{e-} is number of electron counts measured in the BigBite spectrometer, N^{π^-} is the number of π^- counts leaking into the electron sample, $N_m^{e^+}$ is the number of bend-up positron counts in the BigBite spectrometer, which represent the pair produced electrons contaminating the e^--^{3}He sample, and N^{π^+} are the π^+ counts that are contaminating the positron sample, which need to be removed from the positron counts because they are not present in the pair produced electrons. Using Equation 8.46, the contamination corrected electron asymmetry, A^{e^-} can be written as

$$A^{e^-} = \frac{A_m^{e^-} - f_1 A^{\pi^-} - f_3 A_m^{e^+} + f_2 f_3 A^{\pi^+}}{1 - f_1 - f_3 + f_2 f_3}, \tag{8.47}$$

where $A_m^{e^-}$ is the asymmetry given by Equations 8.38- 8.41, $f_1 = \frac{\pi^-}{e^-}$ (Table 8.27), $f_2 = \frac{\pi^+}{e^+}$ (Table 8.27), $f_3 = \frac{e^+}{e^-}$ (Table 8.30), $A^{\pi^\pm}$ are the $\pi^\pm$ asymmetries (Tables 8.29 and 8.28) and finally A_m^{e+} is the measured positron asymmetry (Figures 8.58 and 8.59). For E06-014, Equation 8.47 can be simplified by neglecting the pion asymmetries

$$A^{e^-} = \frac{A_m^{e^-} - f_3 A_m^{e^+}}{1 - f_1 - f_3 + f_2 f_3} \equiv A^{cor}. \tag{8.48}$$

The $\frac{\pi^\pm}{e^\pm}$ ratios evaluated at an incident electron energy of 5.89 GeV were used in

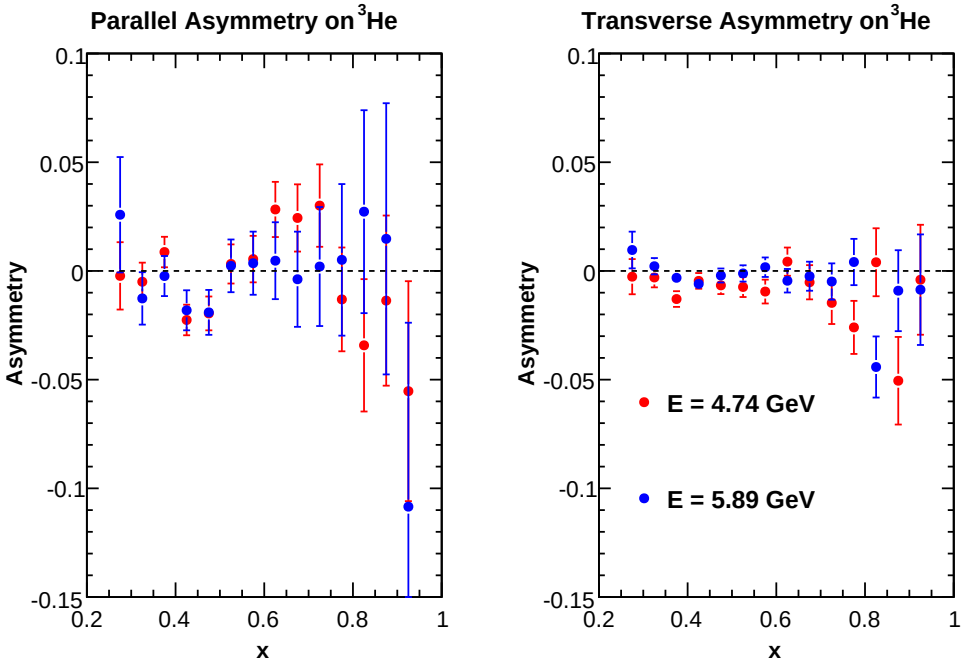

Figure 8.60: Physics asymmetries from Tables 8.25 (red markers) and 8.26(blue markers) corrected for background contaminates according to Equation 8.48 plotted against x. Error bars are statistical only.

correcting the 4.74 GeV incident energy data. In both cases the effects of pion corrections were very small. The electron asymmetries corrected for background contributions can be seen in Figure 8.60 with values listed in Tables 8.31 and 8.32 for incident electron energies of 4.74 GeV and 5.89 GeV. The systematic uncertainty associated with the asymmetries in Tables 8.31 and 8.32 are discussed in Section 8.7. At this stage in the highest x bin was removed from the analysis due to low statistics, which rendered its measurement insignificant and being on the edge of the BigBite electron acceptance. The main contributor to the difference between the background corrected asymmetries and the asymmetries listed in Tables 8.25 and 8.26 is due to the pair produced electrons.

Table 8.31: Longitudinal and transverse physics asymmetries from Tables 8.25 corrected for background contamination via Equation 8.48 for an incident electron energy of 4.74 GeV.

x Center	$A_{\parallel}^{cor}$	$A_{\perp}^{cor}$
0.275	-0.0023 $\pm$ 0.0155$_{stat}$	-0.0026 $\pm$ 0.0081$_{stat}$
0.325	-0.0050 $\pm$ 0.0088$_{stat}$	-0.0030 $\pm$ 0.0045$_{stat}$
0.375	0.0087 $\pm$ 0.0070$_{stat}$	-0.0129 $\pm$ 0.0036$_{stat}$
0.425	-0.0226 $\pm$ 0.0070$_{stat}$	-0.0046 $\pm$ 0.0036$_{stat}$
0.475	-0.0195 $\pm$ 0.0078$_{stat}$	-0.0066 $\pm$ 0.0040$_{stat}$
0.525	0.0032 $\pm$ 0.0090$_{stat}$	-0.0074 $\pm$ 0.0046$_{stat}$
0.575	0.0055 $\pm$ 0.0107$_{stat}$	-0.0095 $\pm$ 0.0055$_{stat}$
0.625	0.0283 $\pm$ 0.0127$_{stat}$	0.0043 $\pm$ 0.0065$_{stat}$
0.675	0.0244 $\pm$ 0.0155$_{stat}$	-0.0052 $\pm$ 0.0079$_{stat}$
0.725	0.0301 $\pm$ 0.0189$_{stat}$	-0.0147 $\pm$ 0.0097$_{stat}$
0.775	-0.0131 $\pm$ 0.0239$_{stat}$	-0.0260 $\pm$ 0.0122$_{stat}$
0.825	-0.0342 $\pm$ 0.0304$_{stat}$	0.0040 $\pm$ 0.0156$_{stat}$
0.875	-0.0136 $\pm$ 0.0391$_{stat}$	-0.0505 $\pm$ 0.0201$_{stat}$
0.925	-0.0553 $\pm$ 0.0506$_{stat}$	-0.0041 $\pm$ 0.0253$_{stat}$

Table 8.32: Longitudinal and transverse physics asymmetries from Tables 8.26 corrected for background contamination via Equation 8.48 for an incident electron energy of 5.89 GeV.

x Center	$A_{\parallel}^{cor}$	$A_{\perp}^{cor}$
0.275	0.0258 $\pm$ 0.0265$_{stat}$	0.0096 $\pm$ 0.0084$_{stat}$
0.325	-0.0126 $\pm$ 0.0121$_{stat}$	0.0022 $\pm$ 0.0038$_{stat}$
0.375	-0.0023 $\pm$ 0.0092$_{stat}$	-0.0032 $\pm$ 0.0029$_{stat}$
0.425	-0.0181 $\pm$ 0.0092$_{stat}$	-0.0060 $\pm$ 0.0029$_{stat}$
0.475	-0.0191 $\pm$ 0.0103$_{stat}$	-0.0021 $\pm$ 0.0032$_{stat}$
0.525	0.0023 $\pm$ 0.0121$_{stat}$	-0.0011 $\pm$ 0.0037$_{stat}$
0.575	0.0036 $\pm$ 0.0145$_{stat}$	0.0017 $\pm$ 0.0045$_{stat}$
0.625	0.0047 $\pm$ 0.0177$_{stat}$	-0.0045 $\pm$ 0.0054$_{stat}$
0.675	-0.0038 $\pm$ 0.0219$_{stat}$	-0.0024 $\pm$ 0.0067$_{stat}$
0.725	0.0020 $\pm$ 0.0274$_{stat}$	-0.0049 $\pm$ 0.0084$_{stat}$
0.775	0.0051 $\pm$ 0.0349$_{stat}$	0.0041 $\pm$ 0.0106$_{stat}$
0.825	0.0273 $\pm$ 0.0467$_{stat}$	-0.0442 $\pm$ 0.0141$_{stat}$
0.875	0.0148 $\pm$ 0.0624$_{stat}$	-0.0091 $\pm$ 0.0186$_{stat}$
0.925	-0.1084 $\pm$ 0.0846$_{stat}$	-0.0086 $\pm$ 0.0254$_{stat}$

8.3 LHRS Data Analysis

In this section the analysis related to the LHRS detector package will be discussed, from cuts (Sections 8.3.1 and 8.3.2) to detector performances (Section 8.3.3) to final unpolarized cross sections (Section 8.3.5). The LHRS analysis was performed by D. Flay. One can refer to Reference [135] for a more detailed discussion of the analysis presented here.

8.3.1 Data Quality

Data quality cuts used in the LHRS, which are comparable to those used in the BigBite detector (Section8.2.1), are used in order to remove unwanted events from the data. This includes removing beam trips and applying cuts to the target and VDCs to ensure that only valid events are kept.

8.3.1.1 Beam Trip

The removal of time periods where the beam was interrupted, resulting in a drop of the beam current, were removed using the same procedure defined in Section 8.2.1.1. The only slight difference here is that the LHRS rates were much lower than those seen in BigBite, as a result the beam current did not need to be averaged in order to reduce noise.

8.3.1.2 Acceptance Cut

To remove events that originated from the target end caps and magnet edges, cuts were applied to the LHRS acceptance ensuring that detected events had scattered from the target center. Cuts on y_{tg}, θ_{tg}, ϕ_{tg} and $\delta p/p$ distributions were used to define the acceptance cuts. These variables are defined in the target coordinate system (Section 4.4.1). The y_{tg} variable is the target's y coordinate, θ_{tg} is the out of plane scattering angle, ϕ_{tg} is the in plane

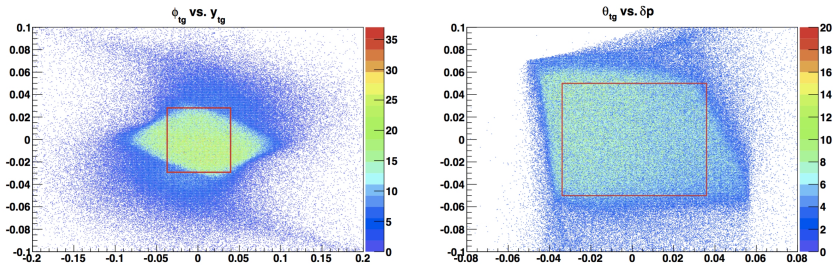

Figure 8.61: Graphical representation of LHRS acceptance cuts. The left panel shows $\phi_t g$ (y-axis) vs. y_{tg} (x-axis). The right panel shows θ_{tg} (y-axis) vs. δp (x-axis). The red boxes indicate the cut (these cuts are slightly different than the final cuts in Equation 8.49. Events that fall within the boxes pass the acceptance cut. Plot produced by D. Flay.

scattering angle, and $\delta p/p$ ensures that the particle had a good momentum. The following cuts are combined to form the acceptance cut:

$$\begin{aligned} |y_{tg}| &< 0.045 \\ |\frac{\delta p}{p}| &< 0.035 \\ |\theta_{tg}| &< 0.04 \\ |\phi_{tg}| &< 0.02 \end{aligned} \tag{8.49}$$

A graphical representation of the acceptance cuts, with values close to the final cut values, are shown in Figure 8.61.

8.3.1.3 Track Quality

Tracking cuts were also used to help define valid events. Only one-track reconstruction from one particle is required, with all secondary tracks being disgarded. In addition to the one-track cut, cuts are applied to each of the VDC planes (U_1, V_1, U_2, V_2) requiring that

only one cluster fires as the particle passes through it.

8.3.2 Particle Identification

Analogous to the BigBite analysis (Section 8.2.2), a second set of cuts were used to identify specific particle types. These include cuts on the Čerenkov ADC, energy deposited in the pion rejector layers and trigger types. The PID cut positions were chosen based on optimization of the electron efficiency and the pion rejection factors, which are discussed in Section 8.3.3.

8.3.2.1 Trigger Cuts

As was the case in the BigBite detector (Section 8.2.2), the LHRS trigger type can serve as a way identify the detected particle type. The LHRS's main electron trigger was the T3. The T3 trigger was formed through a coincidence between the S1 and S2m scintillator planes. While the T3 trigger is not as aggressive as some of BigBite's triggers, it was used an initial cut to identify electrons, by requiring detected events to be tagged with a T3 trigger type.

8.3.2.2 Čerenkov Cut

Unlike the BigBite detector, the LHRS had its Čerenkov detector completely independent of any trigger and a relatively low threshold level. This allowed a clear separation between pion and electron like particle types, as can be seen in Figure 7.31. The pions cause knock-on electrons (δe^{-}) to fire the Čerenkov, which populate the one photoelectron channel. On the other hand, electrons scattering from the target will populate higher photoelectron channels. Thus pion events in the Čerenkov were chosen by requiring no signal in the ADC sum, while electron events were chosen by requiring a Čerenkov ADC sum $>$ 400 ADC channels and that they be in time with the Čerenkov TDC timing.

8.3.2.3 E/p and Pion Rejector Cuts

Further particle discrimination was possible by applying cuts to the E/p distribution, where E is the total energy deposited in the both pion rejector layers and p is the reconstructed momentum. The separation between pion and electron like events, seen in Figure 7.32, allows for the E/p distribution to be used as a PID tool. For E06-014 analysis the electron cut $E/p > 0.54$ was determined to be the best cut position. In addition to the E/p cut, a separate cut was also placed on the first pion rejector layer, which required that electrons deposit an energy greater than 200 MeV.

8.3.2.4 β Cut

The final PID cut that the LHRS took advantage of was the time of flight between the two scintillating planes, S1 and S2m. The timing differences between S1 and S2m are used in defining the variable $\beta \propto \frac{1}{t_2 - t_1}$, where t_1 is the S1 timing and t_2 referees to the S2m timing. The β distribution can be seen in Figure 8.62. By using the cut $\beta > -0.15$, cosmic events ($\beta < 0$) are excluded from the analysis. The cut on β is not at zero because the pile-up at zero consists of good events, which are due to the TDC times in the paddles not properly setting the timing of the events [135, 161].

8.3.3 Detector Performance

Knowing the cut and detector efficiencies of the contributions that make up the cross section is vital, as the LHRS is used to obtain an absolute measurement. Applying cuts to the data will ultimately end up changing the efficiency of the detectors. Therefore, choosing the optimal cuts for an absolute measurement is balancing act between the maximizing the electron efficiencies (the amount of detected events that are electrons) and the pion rejection factors (the amount of events identified as pions and thrown out of the analysis). All of the

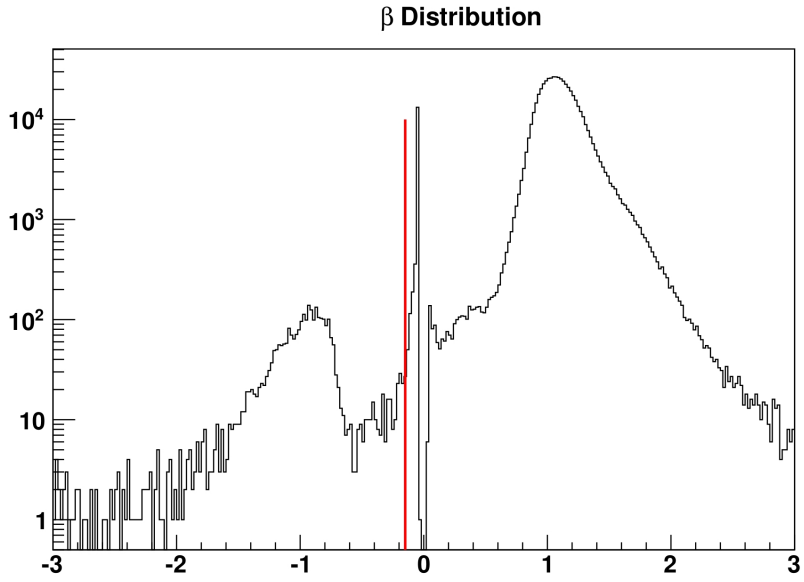

Figure 8.62: A typical β distribution in the LHRS. The events that have a value greater than the red line (-0.15) are kept in the analysis. Plot produced by D. Flay [135].

LHRS PID cut positions were determined by D. Flay [135]. How the electron efficiency (ϵ) and pion rejection factors (ϵ_π) are formed have been discussed in Sections 8.2.3.1.2 and 8.2.3.1.3 respectively. As the following sections will show, the total electron efficiency of the LHRS detector was better than 97% and achieved a pion rejection factor better than 10^4 [135].

8.3.3.1 Čerenkov

The results of the LHRS Čerenkov electron efficiency (red markers) and the pion rejection factors (blue markers) are shown in Figure 8.63. The overall electron efficiency of the LHRS Čerenkov was $\sim$ 97% [135], while obtaining a pion rejection factor of approximately 10^2.

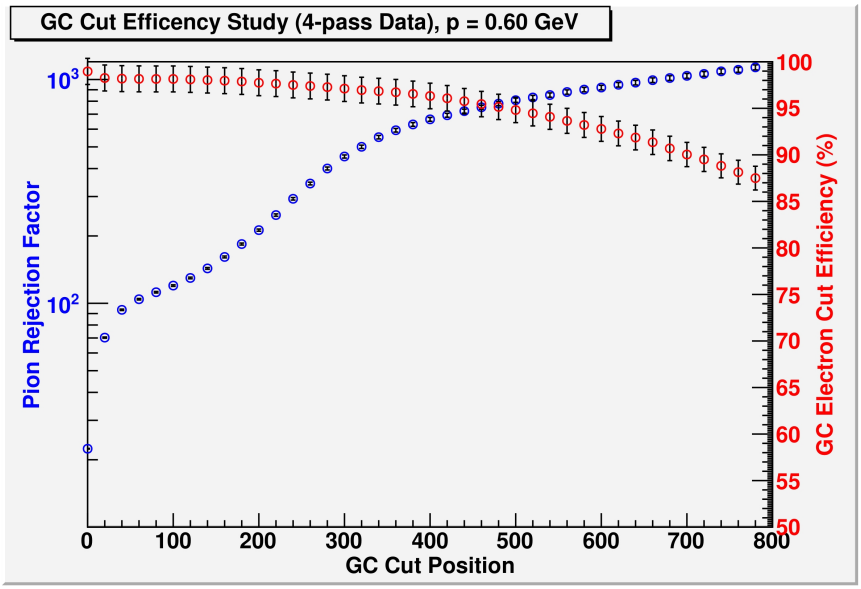

Figure 8.63: Gas Čerenkov cut efficiency study results. Plot produced by D. Flay [135].

8.3.3.2 Pion Rejector

The results of the LHRS pion rejector E/p electron efficiency (red markers) and the pion rejection factors (blue markers) are shown in Figure 8.64. The overall electron efficiency of the pion rejector was $\sim 99\%$, while obtaining a pion rejection factor of roughly 10^2 [135].

8.3.3.3 β Cut

The efficiency of the β cut was determined by evaluating the ratio of events that pass the β cut ($\beta > -0.15$) to the number of events that pass all PID and data quality cuts. The efficiency of this cut was evaluated to be $\sim 99\%$ [135].

8.3.3.4 Tracking

The VDC one-track efficiency is determined through a multi-track analysis. The number of one track events is compared to the number of multi- and no-track events:

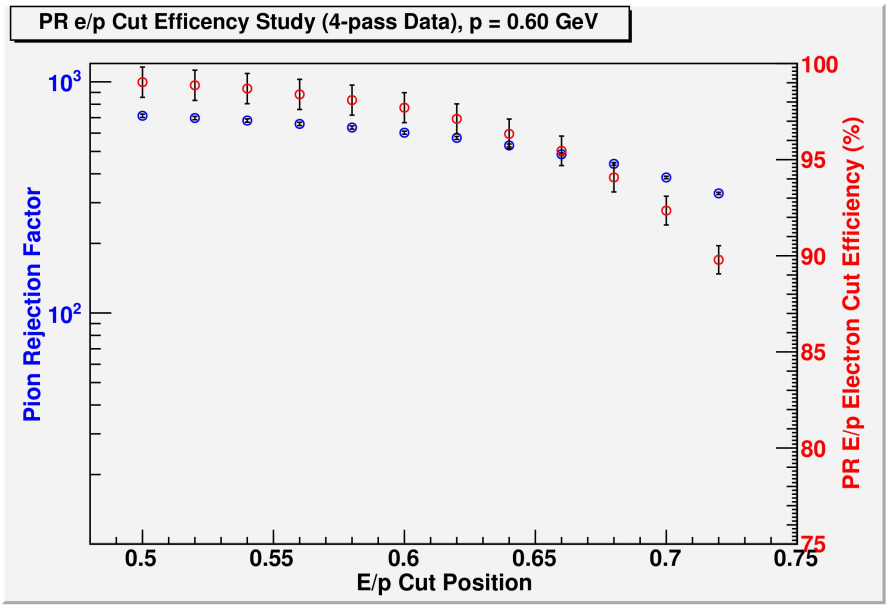

Figure 8.64: Pion rejector E/p cut efficiency study results. Plot produced by D. Flay [135].

$$\epsilon_1 = \frac{N_1}{\sum_{i=0}^{4} N_i}, \tag{8.50}$$

where N_1 is the number of one track events, and N_i is the number of i-track events ($i = 0, ...4$)[18]. An one-track efficiency of $\sim 99\%$ was achieved [135].

8.3.3.5 Trigger

The main LHRS electron trigger (T3) efficiency was computed using the T4 trigger. By considering all events from the T3 and T4 one can define a T3 efficiency as

$$\epsilon_{T3} = \frac{N_{T3}}{N_{T3} + N_{T4}}, \tag{8.51}$$

where N_{Ti} is the number events identified as being a trigger Ti event, after the triggers

[18]The maximum number of reconstructed tracks per event is 4.

were adjusted for prescaling. This efficiency was determined to be better than 99% [135].

8.3.3.6 Live Time

The final efficiency that needs to be calculated is the livetime. The livetime calculation follows a procedure similar to that discussed in Section 8.2.5.2 for the ungated livetime. The livetime is defined as

$$t_{LT} = \frac{T3_{event}}{T3c}, \tag{8.52}$$

where $T3_{event}$ are the recorded T3 tagged events that were accepted by the TS, and $T3c$ are the T3 scaler counts that are always recorded regardless of TS. Equation 8.52 then allows one to calculate how many T3 triggers the TS rejected because it was busy processing other data [19]. The livetime for the LHRS was a bit larger, at $\geq 90\%$ [135], than that achieved for the BigBite detector (Section 8.2.5.2) because the LHRS saw lower rates.

8.3.4 Acceptance

The effective acceptance of the LHRS describes the solid angle that is seen by the opening of the spectrometer. It is defined as the product of $d\Omega_{\text{eff}} = w\Delta\theta\Delta\phi$, where the angular distribution is given by $\Delta\theta$ for the vertical (dispersive) and $\Delta\phi$ for the horizontal (transverse) directions. The weight factor w was determined through Monte Carlo simulations.

The calculation of the effective acceptance utilized the use of a single-arm Monte Carlo (SAMC), which determined how the geometrical acceptance of the LHRS differs from an ideal square acceptance. SAMC generates a uniform distribution of events in a kinematic phase space (θ, ϕ) that is larger than the nominal LHRS values. Events are then transported through the LHRS magnet apertures to the focal plane via a HRS optical model [162].

[19] 1 - t_{LT} is known as the dead time, the amount of time that the TS could not receive any new T3 triggers.

The events that pass the magnet aperture openings and make it to the focal plane are then compared to the initial sample to obtain the effective acceptance. For E06-014 it was found that $d\Omega_{\text{eff}}$ was roughly constant at $\approx$ 3msr over all momentum bins [135].

8.3.5 Cross-Section Analysis

The unpolarized raw cross section, σ_{raw} can be calculated from data

$$\frac{d^2\sigma_{raw}}{d\Omega dE'} = \frac{ps_{T3}N_{cut}}{(Q/e)\,\rho t_{TL}\epsilon}\left(\frac{1}{\Delta E'\Delta\Omega\Delta z}\right), \tag{8.53}$$

where each quantity in Equation 8.53 is as follows: ps_{T3} is the prescale factor associated with the T3 trigger; N_{cut} is the number of electrons that pass the LHRS electron production cuts defined in Sections 8.3.1 and 8.3.2; Q/e is the number of beam electrons, with Q being the accumulated charge collected on the target; ρ is the target density; t_{LT} is the T3 live time; ϵ is the product of all detector and cut efficiencies; $\Delta E'$ is the energy width in MeV for a given momentum bin; $\Delta\Omega$ is the effective angular acceptance; Δz is the effective target length see by the spectrometer.

After the cross section was computed for each run, common momentum were then combined over all n runs using a weighted average

$$\sigma = \frac{\sum_{i=1}^{n}\sigma_i\left(\frac{1}{\delta\sigma_i}\right)^2}{\sum_i\left(\frac{1}{\sigma_i}\right)^2}, \tag{8.54}$$

where $\delta\sigma_i$ is the statistical uncertainty of the i^{th} cross section

$$\delta\sigma = \sigma\sqrt{\sum_{j=1}^{n}\left(\frac{\delta a_j}{a_j}\right)^2},$$

where a_j corresponds to each component in the cross section calculation. This includes Q/e, N_{cut}, t_{LT} and ϵ. However, because ϵ is a product sum, its uncertainty is computed as

$$\frac{\delta\epsilon}{\epsilon} = \sqrt{\sum_{k=1}^{p}\left(\frac{\delta\epsilon_k}{\epsilon_k}\right)^2}, \tag{8.56}$$

where k referees to the k^{th} efficiency factor.

8.3.5.1 Background Corrections

The measured cross sections contain electrons that did not scatter from the target, but rather from pair production processes and from nitrogen nuclei. The nitrogen background ($\sigma^{e^-}_{N_2}$) was measured using a nitrogen reference cell (with similar geometry as the production cells, see Appendix D), while the pair production background was determined from positron measurements. The position cross section (σ_{e^+}) was measured by switching the LHRS detector magnets to positive polarity, which resulted in positive charges being detected in the LHRS. In addition to the nitrogen background due to electron scattering from nitrogen nuclei, positrons will also scatter from nitrogen nuclei ($\sigma^{e^+}_{N_2}$) and need to be accounted for. Each of these background contributions was subtracted from the raw cross section

$$\sigma_{rad} = \sigma_{raw} - \sigma_{e^+} - \sigma^{dil}_{N_2}, \tag{8.57}$$

where

$$\sigma^{dil}_{N_2} = \frac{n_{N_2}}{n_{N_2} + n_{^3\text{He}}}\left(\sigma^{e-}_{N_2} - \sigma^{e^+}_{N_2}\right), \tag{8.58}$$

where n is the number density of nitrogen (N_2) or ^{3}He and σ_{rad} is the radiated cross section.

Due to time constraints and problems encountered during E06-014, measurements of the

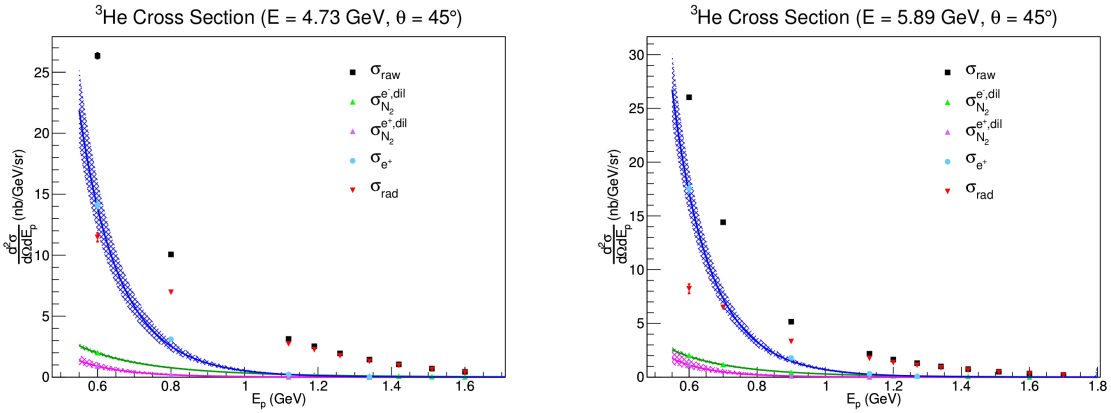

Figure 8.65: Electron (green markers and bands) and positron (purple/magenta markers/band) nitrogen dilution, and positron (blue markers and band) background contributions with their fits (colored lines) and uncertainties (colored bands) compared to the raw (black markers) and radiated (red markers) ^{3}He cross sections for E = 4.74 Gev (left panel) and 5.89 GeV (right panel) data sets. Plots produced by D. Flay.

backgrounds at all of the production kinematic bins could not be made. As a result measured nitrogen and pair production backgrounds were fitted as a function of scattering energy by D. Flay [135] with the function

$$f\left(E_p\right) = \frac{1}{E_p^2} Exp\left(p_0 + p_1 E_p\right), \tag{8.59}$$

and used to determine the backgrounds at each production kinematic bin. The uncertainty of the fit was determined by varying each fit parameter within its uncertainty and observing the change in the fit. The largest change was taken as the final uncertainty in the fit.

The measured background contributions compared to raw and radiated cross sections computed by D. Flay [135] can be seen in Figure 8.65, along with the background fits and their uncertainties (colored bands).

The radiated ^{3}He cross sections and their uncertainties are listed in Tables 8.33 and 8.34

Table 8.33: The experimental (radiated) cross section for E = 4.74 GeV [135]. Uncertainties listed are absolute.

E_p [GeV]	ν [GeV]	y	W [GeV]	x	$\frac{d^2\sigma_{rad}}{d\Omega dE_p}$ [nb/GeV/sr]
0.6	4.13	0.873	2.64	0.215	$11.470 \pm 0.365_{stat} \pm 0.894_{sys}$
0.8	3.93	0.831	2.46	0.301	$6.961 \pm 0.178_{stat} \pm 0.362_{sys}$
1.12	3.61	0.763	2.13	0.458	$2.722 \pm 0.048_{stat} \pm 0.129_{sys}$
1.19	3.54	0.748	2.06	0.496	$2.250 \pm 0.034_{stat} \pm 0.105_{sys}$
1.26	3.47	0.734	1.97	0.536	$1.747 \pm 0.026_{stat} \pm 0.084_{sys}$
1.34	3.39	0.717	1.88	0.584	$1.301 \pm 0.027_{stat} \pm 0.062_{sys}$
1.42	3.31	0.7	1.78	0.634	$0.948 \pm 0.018_{stat} \pm 0.046_{sys}$
1.51	3.22	0.681	1.65	0.693	$0.633 \pm 0.012_{stat} \pm 0.031_{sys}$
1.6	3.13	0.662	1.52	0.755	$0.390 \pm 0.012_{stat} \pm 0.019_{sys}$

for the E = 4.74 GeV and 5.89 GeV data sets respectively.

Table 8.34: The experimental (radiated) cross section for E = 5.89 GeV [135]. Uncertainties listed are absolute.

E_p [GeV]	ν [GeV]	y	W [GeV]	x	$\frac{d^2\sigma_{rad}}{d\Omega dE_p}$ [nb/GeV/sr]
0.6	5.29	0.898	2.96	0.209	$8.221 \pm 0.441_{stat} \pm 0.844_{sys}$
0.7	5.19	0.881	2.86	0.248	$6.486 \pm 0.116_{stat} \pm 0.460_{sys}$
0.9	4.99	0.847	2.67	0.332	$3.318 \pm 0.099_{stat} \pm 0.171_{sys}$
1.13	4.76	0.808	2.43	0.437	$1.749 \pm 0.038_{stat} \pm 0.086_{sys}$
1.2	4.69	0.796	2.35	0.471	$1.352 \pm 0.030_{stat} \pm 0.068_{sys}$
1.27	4.62	0.784	2.27	0.506	$1.107 \pm 0.020_{stat} \pm 0.054_{sys}$
1.34	4.55	0.772	2.19	0.542	$0.859 \pm 0.016_{stat} \pm 0.043_{sys}$
1.42	4.47	0.759	2.09	0.584	$0.655 \pm 0.012_{stat} \pm 0.031_{sys}$
1.51	4.38	0.744	1.97	0.634	$0.445 \pm 0.010_{stat} \pm 0.021_{sys}$
1.6	4.29	0.728	1.85	0.686	$0.297 \pm 0.007_{stat} \pm 0.014_{sys}$
1.7	4.19	0.711	1.7	0.746	$0.181 \pm 0.006_{stat} \pm 0.009_{sys}$

8.3.5.2 Final Cross Section

The total uncertainty of the cross sections depend on several contributions, the target density, beam charge, analysis cuts and efficiencies. The uncertainties on the analysis cuts were determined using the same method that was used to determine the BigBite cut systematic uncertainties (Section 8.7). This involved changing a single cut slightly and studying the resulting change in the cross section. The systematic contributions were evaluated by D. Flay [135], and are listed in Table 8.35.

Applying the radiative corrections discussed in Section 8.5 to the radiated cross sections, one can extract the Born cross sections. This results in an uncertainty given as

$$\delta\sigma^2_{Born} = \left(\frac{\sigma_{rad}}{\sigma_{Born}}\right)^2 \delta\sigma^2_{rad} + \left(\frac{\sigma_{Born} - \sigma_{rad}}{\sigma_{Born}}\right)^2 \delta\sigma^2_{RC}, \tag{8.60}$$

where $\delta\sigma_{RC}$ contains the uncertainty on the experimental cross section, and $\delta\sigma_{RC}$ is the uncertainty due to radiative corrections.

Tables 8.36 and 8.37 lists the final Born ^{3}He cross sections [135] measured during

Table 8.35: The systematic errors on the Born cross section. The PID efficiencies entry is the in quadrature sum of contributions from the gas Čerenkov, pion rejector, β cuts and the trigger efficiency. The largest contributions come from the radiative corrections and the target density.

Type	Proposal [%]	Experiment [%]
PID Efficiency	≈ 1	1
Background Rejection Efficiency	≈ 1	1
Beam Charge	< 1	≈ 0.3
Acceptance Cut	2–3	2.7
Target Density	2–3	3.94
Dead Time	< 1	< 1
Radiative Corrections	≤ 10	≈ 6

E06-014 for the E = 4.74 GeV and 5.89 GeV data sets, and are displayed in Figure 8.66.

Table 8.36: The final Born cross section for E = 4.74 GeV [135]. Uncertainties listed are absolute.

E_p [GeV]	ν [GeV]	y	W [GeV]	x	$\frac{d^2\sigma}{d\Omega dE_p}$ [nb/GeV/sr]
0.6	4.13	0.873	2.64	0.215	$6.191 \pm 0.365_{stat} \pm 0.561_{sys}$
0.8	3.93	0.831	2.46	0.301	$5.374 \pm 0.178_{stat} \pm 0.281_{sys}$
1.12	3.61	0.763	2.13	0.458	$2.544 \pm 0.048_{stat} \pm 0.121_{sys}$
1.19	3.54	0.748	2.06	0.496	$2.223 \pm 0.034_{stat} \pm 0.103_{sys}$
1.26	3.47	0.734	1.97	0.536	$1.762 \pm 0.026_{stat} \pm 0.084_{sys}$
1.34	3.39	0.717	1.88	0.584	$1.353 \pm 0.027_{stat} \pm 0.065_{sys}$
1.42	3.31	0.7	1.78	0.634	$1.021 \pm 0.018_{stat} \pm 0.049_{sys}$
1.51	3.22	0.681	1.65	0.693	$0.716 \pm 0.012_{stat} \pm 0.035_{sys}$
1.6	3.13	0.662	1.52	0.755	$0.536 \pm 0.012_{stat} \pm 0.028_{sys}$

Table 8.37: The final Born cross section for E = 5.89 GeV [135]. Uncertainties listed are absolute.

E_p [GeV]	ν [GeV]	y	W [GeV]	x	$\frac{d^2\sigma}{d\Omega dE_p}$ [nb/GeV/sr]
0.6	5.29	0.898	2.96	0.209	$4.069 \pm 0.441_{stat} \pm 0.473_{sys}$
0.7	5.19	0.881	2.86	0.248	$4.322 \pm 0.156_{stat} \pm 0.308_{sys}$
0.9	4.99	0.847	2.67	0.332	$2.488 \pm 0.992_{stat} \pm 0.130_{sys}$
1.13	4.76	0.808	2.43	0.437	$1.596 \pm 0.038_{stat} \pm 0.079_{sys}$
1.2	4.69	0.796	2.35	0.471	$1.234 \pm 0.030_{stat} \pm 0.067_{sys}$
1.27	4.62	0.784	2.27	0.506	$1.067 \pm 0.020_{stat} \pm 0.052_{sys}$
1.34	4.55	0.772	2.19	0.542	$0.846 \pm 0.016_{stat} \pm 0.043_{sys}$
1.42	4.47	0.759	2.09	0.584	$0.679 \pm 0.012_{stat} \pm 0.033_{sys}$
1.51	4.38	0.744	1.97	0.634	$0.473 \pm 0.010_{stat} \pm 0.022_{sys}$
1.6	4.29	0.728	1.85	0.686	$0.331 \pm 0.007_{stat} \pm 0.016_{sys}$
1.7	4.19	0.711	1.7	0.746	$0.250 \pm 0.006_{stat} \pm 0.013_{sys}$

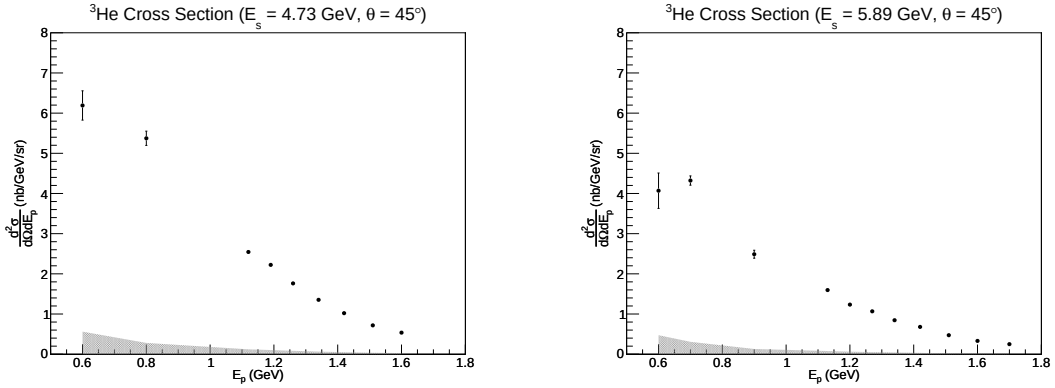

Figure 8.66: Final E06-014 Born cross sections measured in the LHRS at beam energies of E = 4.74 (left panel) and 5.89 (right panel) GeV. Error bars represent statistical uncertainties and gray bands represent systematic uncertainties. Plots produced by D. Flay [135].

8.4 Polarized Structure Functions

The polarized spin structure functions g_1 and g_2, which are defined in Equations 1.28 and 1.31, can be written in terms of the longitudinal and transverse doulbe spin asymmetries $A_{\parallel}$ and $A_{\perp}$

$$g_1 = \frac{MQ^2}{4\alpha^2}\frac{2y\sigma_0}{(1-y)(2-y)}\left[A_{\parallel} + \tan\frac{\theta}{2}A_{\perp}\right] \tag{8.61}$$

$$g_2 = \frac{MQ^2}{4\alpha^2}\frac{y^2\sigma_0}{(1-y)(2-y)}\left[-A_{\parallel} + \frac{1+(1-y)\cos\theta}{(1-y)\sin\theta}A_{\perp}\right]. \tag{8.62}$$

The statistical uncertainty for the polarized structure functions were determined through error propagation

$$\delta\left(g_i\right)_{stat} = \sqrt{\sum_j \left(\partial_j \cdot \delta j\right)^2}, \tag{8.63}$$

where $i = 1, 2$ corresponding to g_1 or g_2, $\partial_j = \frac{\partial g_i}{\partial j}$, where j runs over the quantities: x,

Q^2, y, $A_{\parallel}$, and $A_{\perp}$, with its statistical uncertainty given by δj. The systematic uncertainties associated with the polarized spin structure functions are discussed in Section 8.7.

8.4.1 Cross Section Interpolation and Extrapolation

As was discussed in Section 4.2.1, the kinematic coverage of the BigBite detector and the LHRS were not the same. The BigBite detector covered a much wider range in x and Q^2 than the LHRS. Even by changing the LHRS's central momentum to better match BigBite's kinematics, it does not perfectly coincide with BigBite's kinematics. As a result, the Born cross section measurements discussed in Section 8.5.1 and listed in Tables 8.36 and 8.37, were interpolated and extrapolated inorder to obtain the correct cross section values for a given x bin that matched the BigBite kinematics. The extrapolation provided cross section values at higher x bins where the BigBite detector recorded data, but the LHRS could not reach. The extrapolated results were found to be in agreement with the F1F209 model [163].

The interpolation and extrapolation was done using a common function, which took the form

$$f\left(x\right) = Exp\left[A + Bx + Cx^2\right], \tag{8.64}$$

where A, B and C were free parameters and were determined by fitting the measured LHRS Born cross section (Tables 8.36 and 8.37) results as a function of x. Figure 8.67 shows the fits to the Born cross sections that were used to carry out the interpolation and extrapolation, while Table 8.38 lists the values of the fit parameters used.

The uncertainty of using the interpolated and extrapolated cross sections was determined by randomly varying the fit results (listed in Table 8.38) within the fit parameter uncertainties. For each random variation (5,000 of them) the percent difference between the initial cross section fit (σ_{fit}, determined by using the fit parameters in Table 8.38) and the randomly varied

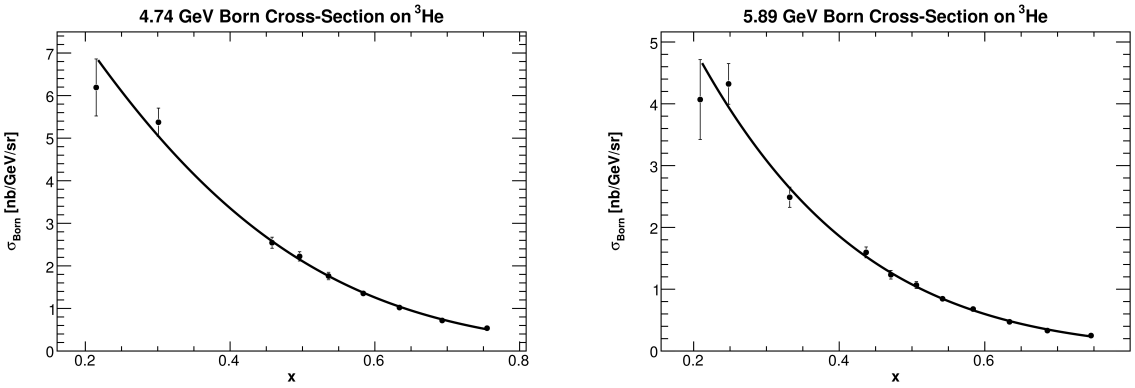

Figure 8.67: Fits to the Born ^{3}He cross sections measured by LHRS. The fits are used to interpolate and extrapolate over x to match BigBite x coverage. The error bars represent the quadrature sum of the statistical and systematic LHRS cross section uncertainties.

Table 8.38: Fit parameters used in cross section extrapolations and interpolations.

Energy Data Set [GeV]	A	B	C
4.74	2.542 ± 0.201	-2.279 ± 0.802	-2.625 ± 0.776
5.89	2.397 ± 0.203	-3.619 ± 0.827	-2.051 ± 0.811

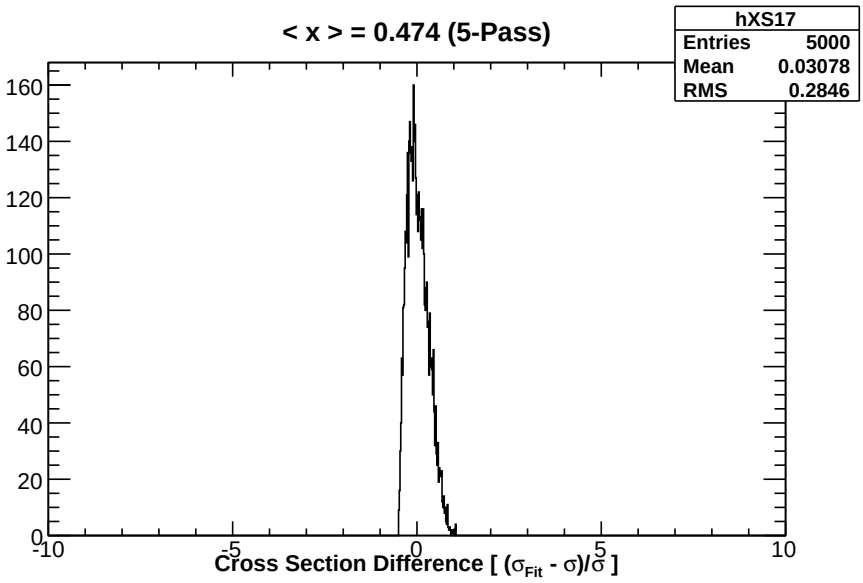

Figure 8.68: Example of the cross section difference obtained by varying the fit function at $\langle x \rangle$ = 0.474. The mean value of the histogram is taken as the systematic uncertainty.

cross section (σ) was calculated for each x bin. The mean percent difference resulting from the 5,000 random variations was then taken as the systematic uncertainty that was applied to the cross sections. A representative example of the cross section percent difference, determined by the random variations, for x = 0.474 of the E = 5.89 GeV data set can be seen in Figure 8.68. The final Born cross sections that go into Equations 8.61 and 8.62 are listed in Tables 8.39 and 8.40 for the E = 4.74 and 5.89 GeV data sets.

Table 8.39: ^{3}He Born cross sections determined at BigBite x-bins from fits to measured LHRS cross sections for E = 4.74 GeV data set.

$\langle x \rangle$	σ_0 [nb/GeV/sr]	$\delta\sigma_0^{\text{sys}}$ [%]
0.229	6.571	1.332
0.277	5.534	1.585
0.325	4.589	1.911
0.374	3.753	2.317
0.424	3.019	2.822
0.474	2.395	3.434
0.524	1.876	4.166
0.573	1.452	5.037
0.624	1.104	6.083
0.674	0.832	7.294
0.723	0.619	8.719
0.773	0.454	10.379
0.823	0.330	12.299
0.873	0.236	14.547
0.921	0.168	17.066
0.973	0.115	20.186

Table 8.40: ^{3}He Born cross sections determined at BigBite x-bins from fits to measured LHRS cross sections for E = 5.89 GeV data set.

$\langle x \rangle$	σ_0 [nb/GeV/sr]	$\delta\sigma_0^{\text{sys}}$ [%]
0.229	4.306	0.896
0.277	3.450	1.161
0.325	2.726	1.500
0.374	2.129	1.921
0.424	1.639	2.443
0.474	1.248	3.078
0.524	0.941	3.836
0.573	0.703	4.737
0.624	0.517	5.822
0.674	0.379	7.079
0.723	0.274	8.559
0.773	0.196	10.286
0.823	0.140	12.286
0.873	0.098	14.631
0.921	0.069	17.263
0.973	0.047	20.528

8.4.2 Forming Polarized Structure Functions

Now that each BigBite x bin has a corresponding cross section (Tables 8.39 and 8.40, they can be combined with the asymmetries $A_{\parallel}$ and $A_{\perp}$ (Tables 8.31 and 8.32) through Equations 8.61 and 8.62 to obtain the polarized structure functions. The ^{3}He polarized structure functions for both energies are plotted in Figure 8.69 and their values are listed in Tables 8.41 and 8.42.

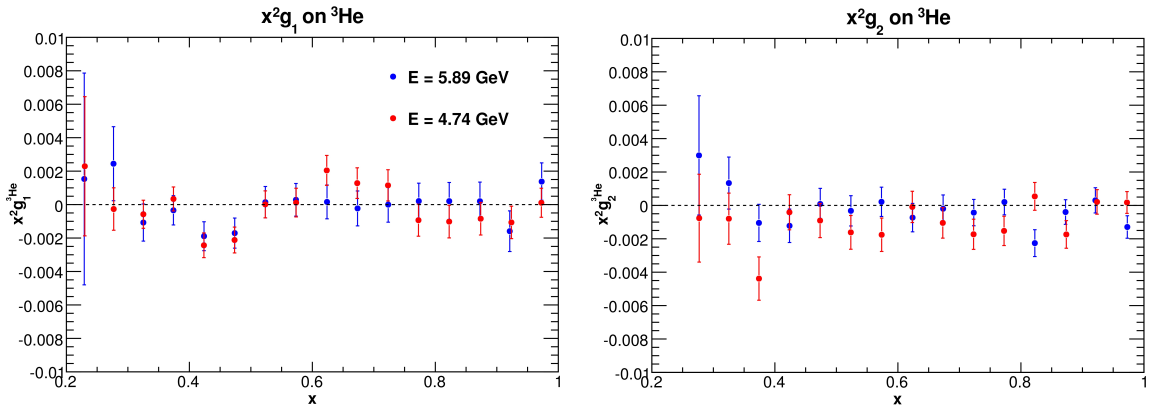

Figure 8.69: Radiated ^{3}He polarized structure functions $x^2 g_1$ (left panel) and $x^2 g_2$ (right panel) for E = 4.74 (red markers) and 5.89 (blue markers) GeV data sets. Error bars represent the statistical uncertainty.

Table 8.41: $g_1^{^3\mathrm{He}}$ and $g_2^{^3\mathrm{He}}$ radiated spin structure functions, at incident an electron energy of 4.74 GeV, corrected for background contaminates.

$\langle x \rangle$	$g_1^{^3\mathrm{He}}$	$g_2^{^3\mathrm{He}}$
0.229	$0.0434 \pm 0.0787_{stat}$	$0.3069 \pm 0.1916_{stat}$
0.277	$-0.0035 \pm 0.0165_{stat}$	$-0.0100 \pm 0.0343_{stat}$
0.325	$-0.0055 \pm 0.0079_{stat}$	$-0.0075 \pm 0.0145_{stat}$
0.374	$0.0024 \pm 0.0051_{stat}$	$-0.0313 \pm 0.0093_{stat}$
0.424	$-0.0136 \pm 0.0041_{stat}$	$-0.0023 \pm 0.0059_{stat}$
0.474	$-0.0094 \pm 0.0034_{stat}$	$-0.0040 \pm 0.0046_{stat}$
0.524	$0.0001 \pm 0.0029_{stat}$	$-0.0059 \pm 0.0037_{stat}$
0.573	$0.0004 \pm 0.0026_{stat}$	$-0.0053 \pm 0.0030_{stat}$
0.624	$0.0053 \pm 0.0023_{stat}$	$-0.0002 \pm 0.0024_{stat}$
0.674	$0.0028 \pm 0.0020_{stat}$	$-0.0023 \pm 0.0020_{stat}$
0.723	$0.0022 \pm 0.0018_{stat}$	$-0.0033 \pm 0.0017_{stat}$
0.773	$-0.0016 \pm 0.0016_{stat}$	$-0.0026 \pm 0.0015_{stat}$
0.823	$-0.0015 \pm 0.0014_{stat}$	$0.0008 \pm 0.0012_{stat}$
0.874	$-0.0011 \pm 0.0013_{stat}$	$-0.0023 \pm 0.0011_{stat}$
0.921	$-0.0012 \pm 0.0011_{stat}$	$0.0002 \pm 0.0009_{stat}$
0.973	$0.0001 \pm 0.0009_{stat}$	$0.0002 \pm 0.0007_{stat}$

Table 8.42: $g_1^{^3\mathrm{He}}$ and $g_2^{^3\mathrm{He}}$ radiated spin structure functions, at incident an electron energy of 5.89 GeV, corrected for background contaminates.

$\langle x \rangle$	$g_1^{^3\mathrm{He}}$	$g_2^{^3\mathrm{He}}$
0.229	$0.0292 \pm 0.1207_{stat}$	$0.9059 \pm 0.2474_{stat}$
0.277	$0.0319 \pm 0.0289_{stat}$	$0.0391 \pm 0.0467_{stat}$
0.325	$-0.0102 \pm 0.0105_{stat}$	$0.0126 \pm 0.0147_{stat}$
0.374	$-0.0024 \pm 0.0063_{stat}$	$-0.0075 \pm 0.0079_{stat}$
0.424	$-0.0105 \pm 0.0048_{stat}$	$-0.0068 \pm 0.0056_{stat}$
0.474	$-0.0076 \pm 0.0040_{stat}$	$0.0004 \pm 0.0042_{stat}$
0.524	$0.0005 \pm 0.0034_{stat}$	$-0.0012 \pm 0.0033_{stat}$
0.573	$0.0009 \pm 0.0030_{stat}$	$0.0007 \pm 0.0027_{stat}$
0.624	$0.0004 \pm 0.0026_{stat}$	$-0.0019 \pm 0.0022_{stat}$
0.674	$-0.0005 \pm 0.0023_{stat}$	$-0.0004 \pm 0.0018_{stat}$
0.723	$-0.0000 \pm 0.0020_{stat}$	$-0.0008 \pm 0.0015_{stat}$
0.773	$0.0003 \pm 0.0018_{stat}$	$0.0003 \pm 0.0013_{stat}$
0.823	$0.0003 \pm 0.0016_{stat}$	$-0.0033 \pm 0.0012_{stat}$
0.873	$0.0003 \pm 0.0015_{stat}$	$-0.0005 \pm 0.0010_{stat}$
0.921	$-0.0019 \pm 0.0014_{stat}$	$0.0004 \pm 0.0009_{stat}$
0.973	$0.0015 \pm 0.0012_{stat}$	$-0.0014 \pm 0.0007_{stat}$

8.4.3 Q^2 Dependence

The spin structure functions g_1 and g_2 in general depend on Q^2, which result in d_2 also depending on Q^2. Thus a proper evaluation of d_2 should be performed by integrating the spin structure functions over the entire x range at a constant Q^2 value. However, E06-014 only took data at two beam energies, which made a proper interpolation to constant Q^2 impossible. As a result, three approaches were used to estimate the size of the polarized structure functions' Q^2 dependence; which in all cases was found to be small relative to the measured precision of g_1 and g_2.

One way in which to gauge the polarized structure functions' dependence on Q^2 is to compare their measured values at fixed x. Using the ^{3}He data from E06-014's two beam energies (E = 4.74 GeV and E = 5.89 GeV), E99-117 [3, 57], and E142 [50] at $\langle x \rangle = 0.33$, g_1 and g_2 were plotted against Q^2 (Figure 8.70). Taking into account the precision of the measurements in Figure 8.70, the Q^2 dependence appears to be minimal.

In addition to comparing with experimental data, one could also use models and fits to world data to investigate the Q^2 dependence of the polarized structure functions. The global analysis fits to polarized parton densities from DSSV [164] were used to evaluate

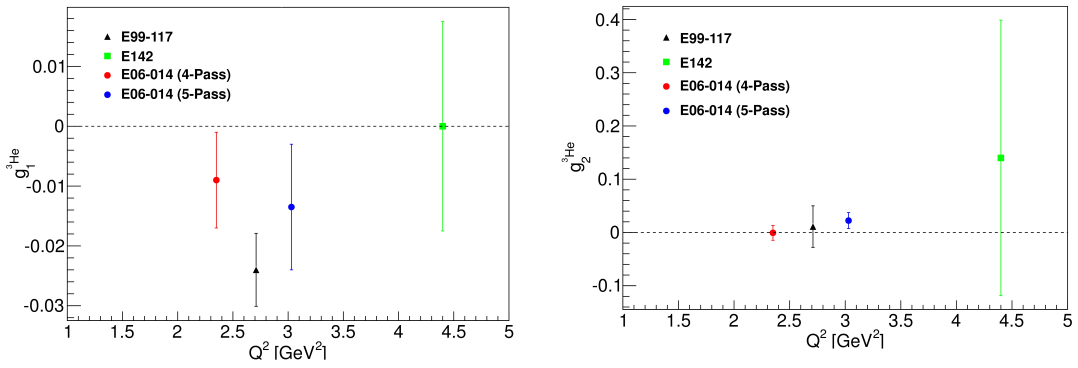

Figure 8.70: Polarized structure functions g_1 (left panel) and g_2 (right panel) on ^{3}He at mean x of 0.33 as a function of Q^2.

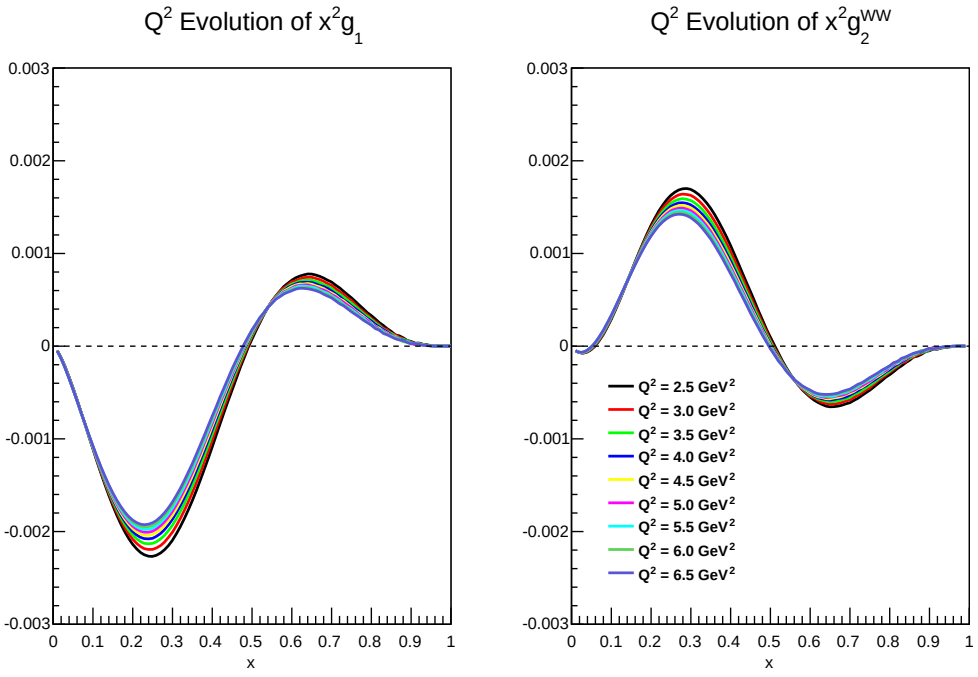

Figure 8.71: Polarized structure functions $x^2 g_1$ (left panel) and $x^2 g_2^{WW}$ (right panel) on ^{3}He evaluated from DSSV [164] plotted against x for a range of Q^2 values.

g_1 and g_2^{WW} [20] for a range of fixed Q^2 values[21]. Figure 8.71 shows $x^2 g_1$ and $x^2 g_2^{WW}$ on ^{3}He as a function of x at constant Q^2 values ranging from Q^2 = 2.5 to 6.5 GeV^2. The Q^2 dependence seen in DSSV is largest around x = 0.25 and x = 0.65. Although, compared to the precision of the g_1 and g_2 measured by E60-014, the Q^2 variation is small.

The final method used to assess the Q^2 dependence, also used by SLAC E143 [51], is to assume that g_1/F_1 is Q^2 independent. Then g_1 at a fixed Q^2 value (Q_0^2) can be determined as

[20] g_1 is formed from polarized quark distributions, whereas g_2 does not have a simple parton interpretation and can not be formed from the polarized quark distributions. As a result g_1 is used to calculate g_2^{WW} rather than g_2.

[21] Several other global analyses (BBS [165, 166], LSS [167], DNS [168], and GS [169]) were also checked and found to give similar results as DSSV.

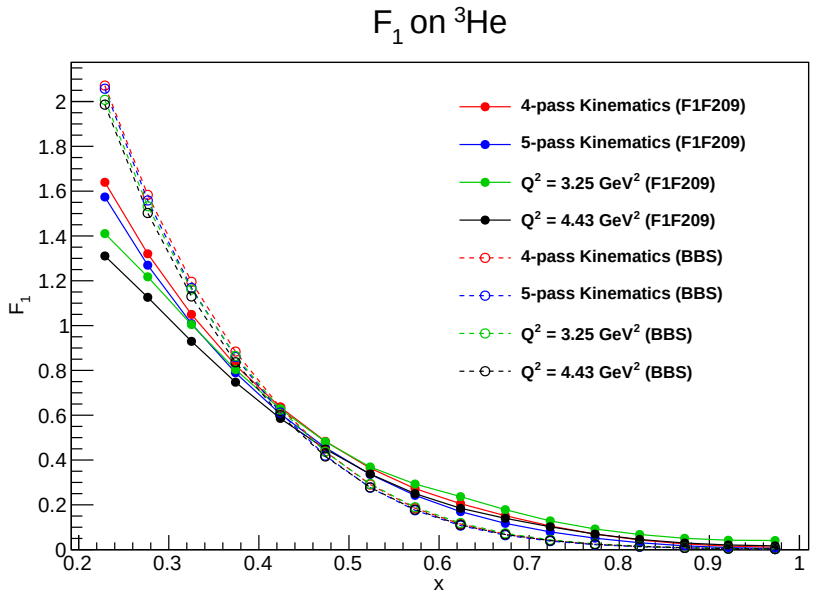

Figure 8.72: Unpolarized structure function F_1 evaluated using F1F209 [163] and BBS [165, 166] for Q^2 values matching measured E06-014 kinematics and for two constant Q^2 values on ^{3}He

.

$$g_1\left(x, Q_0^2\right) = \frac{g_1\left(x, Q^2\right)}{F_1\left(x, Q^2\right)} \cdot F_1\left(x, Q_0^2\right). \tag{8.65}$$

The ^{3}He polarized structure function $g_1\left(x, Q^2\right)$ are the measured E06-014 values. The ^{3}He unpolarized structure function F_1, was computed at Q^2 values matching the measured $g_1\left(x, Q^2\right)$ data, in addition to F_1 at Q_0^2 = 3.25 and 4.43 GeV^2. To evaluate F_1 two different global fits, F1F209 [163] and BBS [165, 166] were used. F1F209 uses fits to world data to determine F_1 and F_2, and BBS uses a statistical quark model to determine polarized and non-polarized parton distributions. Figure 8.72 shows the results of F_1 as a function of x for both the F1F209 (solid circles, solid lines) and BBS (open circles, dashed lines) fits. The red and blue markers give the F_1 values for x and Q^2 values matching E06-014's E = 4.74 and 5.89 GeV E06-014 datasets. The green and black markers show F_1 values calculated at a constant Q_0^2 of 3.25 and 4.43 GeV^2.

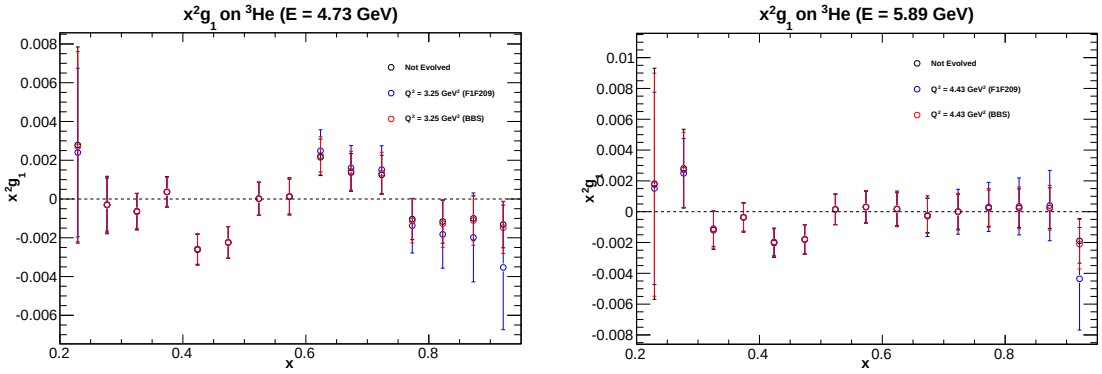

Figure 8.73: Compares the evolved x^2g_1 from F1F209 [163] and BBS [165, 166] fits to the measured E06-014 x^2g_1 on ^{3}He for E = 4.74 and 5.89 GeV data sets.

Applying the values of F_1 to the measured g_1, following Equation 8.65, g_1 can be evolved to a constant Q^2. A comparison of the evolved x^2g_1 data using F1F209 (blue markers) and BBS (red markers) to the measured x^2g_1 (black marker) can be seen in Figure 8.73, which clearly show a negligible Q^2 dependence within the experimental precision. If one assumes that the Q^2 dependence of g_2 is similar to that of g_1, then the Q^2 dependence on g_2 is also small.

Considering the size of the Q^2 dependence from the three methods presented above, the Q^2 dependence was neglected in E06-014, and a mean Q^2 value was used when computing d_2 and other Q^2 dependent quantities. While the quantities were not computed at a constant Q^2 for E06-014, the upcoming JLab experiment E12-06-121 [170, 171] will be able to compute the spin structure functions and d_2^n at constant Q^2, in addition to providing an extension of the E06-014 measured d_2^n to higher Q^2 values.

8.5 Radiative Corrections

An electron's interaction with materials before and after scattering, as well as with the target itself, will cause it to loose energy. These interactions lead to an alteration of the electron's

true scattering angle and energy. One can characterize these effects through ionization and bremsstrahlung (also refereed to as external radiation), in addition to higher order processes at the interaction vertex (known as internal radiation). The removal of the aforementioned effects are known as radiative corrections.

The measured radiated cross section (σ_{rad}) is given as

$$\sigma_{rad}\left(E_s, E_p\right) = \int_0^T \frac{dt}{T} \int_{E_s^{min}}^{E_s} dE_s^{'} \int_{E_p}^{E_p^{max}} dE_p^{'} I\left(E_s, E_s^{'}, t\right) \sigma_r\left(E_s^{'}, E_p^{'}\right) I\left(E_p, E_p^{'}, T-t\right), \tag{8.66}$$

where σ_r is the internally radiated cross section, E_s is the incident energy, E_p is the scattered energy, and $I\left(E_0, E, t\right)$ is the probability of finding an electron with incident energy E_0 that has undergone bremsstrahlung with energy E at a depth t inside the material [172, 173].

8.5.1 Born Cross Sections

Before preceding with the radiative corrections, both the elastic and quasi-elastic tails need to be removed, as they affect all states of higher W [172]. The elastic tail was computed using the Amroun form factors [174], and the quasi-elastic tail was modeled by D. Flay using a quasi-free scattering model, QFS [175]. Figure 8.74 shows the sizes of the elastic and quasi-elastic tails compared to measured E06-014 radiated cross sections. The elastic tail was found to be extremely small, while the quasielastic tail had a sizable effect on the radiated cross section.

Beginning with the elastic and quasi-elastic tail subtracted data, the cross sections obtained after applying radiative corrections (known as the Born cross sections) were computed using an iterative procedure carried out in RADCOR [176]. E06-014 took data at two beam energies, equating to having only two E_s values (4.74 and 5.89 GeV). In order to

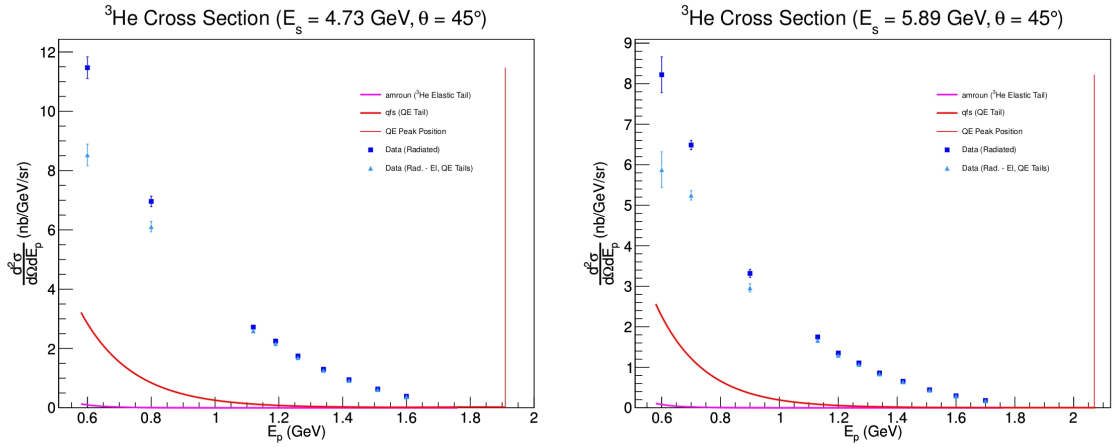

Figure 8.74: Size of elastic (magenta line) and quasi-elastic (red line) tails at E06-014 kinematics compared to measured radiated cross sections (dark blue markers) and quasi-elastic tail subtracted radiated ^{3}He cross sections (light blue markers) for E = 4.74 GeV and 5.89 GeV data sets. The vertical line represents the location of the quasi-elastic peak. Plots produced by D. Flay flay.

accurately compute the integrals of Equation 8.66, more input energies were needed. As a result, the unpolarized cross section was modeled using F1F209 [163] to fill in the remaining phase space (E_s,E_p). This analysis was done by D. Flay and a detailed discussion of the procedure can be found in Reference [135].

8.5.2 Born Asymmetries

The extraction of the of the Born asymmetries (the asymmetries obtained after radiative corrections) proved to be a bit more complicated than extracting the Born cross sections. Using the radiated asymmetries (Tables 8.31 and 8.32) and Born cross sections from F1F209, the polarized cross section differences ($\Delta\sigma_{\parallel,\perp}$) were formed. The elastic tail (computed using Amroun form factors [174]) was found to be small compared to the data and could be neglected. The Born cross section differences were computed using RADCOR and integrating Equation 8.66 beginning from 5 MeV below the elastic threshold. This

integration limit (elastic peak - 5 MeV) insured that the elastic peak was excluded, while including the entire quasielastic peak. The born asymmetries were then extracted using the relation

$$A_{Born} = \frac{\Delta\sigma_{Born}}{2\sigma_{0,Born}}. \tag{8.67}$$

As was the case with the Born cross section analysis, the phase space of E06-014 needed to be filled in. The phase space was divided into the following three regions in order to accurately model the behavior of the asymmetries:

- **DIS**

  The DIS region used g_1 and g_2 structure functions calculated from DSSV [164] to model the polarized cross section differences. The radiative corrections were also studied using other global analyses such as BBS, GS, DNS and LSS [165–169], rather than DSSV and were found to have minimal model dependence.

- **Resonance**

  MAID2007 [48] fits were used to model the cross section differences in the resonance region. Reasonable agreement was found between the MAID modeled cross section differences and real data [135].

- **Quasi-Elastic**

  The quasielastic region was modeled by applying a smearing function defined in Reference [177] to quasiealstic form factors defined in Reference [178]. This quasielastic model was found to reproduce measured data reasonably well [135].

The modeling of the cross sections, asymmetries, and extraction of the Born data was performed by D. Flay. A more detailed account of the radiative corrections can be found in Reference [135]. The Born asymmetry results are listed in Tables 10.1 and 10.2, and

Table 8.43: Lists the systematic uncertainties assigned to the parallel and perpendicular asymmetries (E = 4.74 and 5.89 GeV^2 data sets), due to the radiative corrections. The uncertainties here are absolute values.

	E = 4.74 GeV		E = 5.89 GeV	
x	$A_\parallel$	$A_\perp$	$A_\parallel$	$A_\perp$
0.225	0.00028	0.00083	0.00055	0.00173
0.275	0.00025	0.00010	0.00036	0.00018
0.325	0.00022	0.00011	0.00028	0.00011
0.375	0.00013	0.00018	0.00012	0.00008
0.425	0.00037	0.00007	0.00031	0.00009
0.475	0.00031	0.00009	0.00031	0.00004
0.525	0.00005	0.00010	0.00004	0.00004
0.575	0.00009	0.00013	0.00007	0.00005
0.625	0.00043	0.00008	0.00010	0.00006
0.675	0.00038	0.00007	0.00009	0.00003
0.725	0.00047	0.00021	0.00008	0.00007
0.775	0.00019	0.00038	0.00011	0.00007
0.825	0.00050	0.00008	0.00042	0.00065
0.875	0.00022	0.00074	0.00022	0.00012
0.925	0.00084	0.00008	0.00163	0.00012

are plotted in Figure 10.1. The systematic uncertainties associated with $A_\parallel^{Born}$ and $A_\perp^{Born}$ were found by randomly varying the model inputs within 10%, and varying the target thickness [135]. The resulting systematic uncertainties for the 4.74 and 5.89 GeV^2 electron energy data sets are listed in Table 8.43.

8.6 Neutron Extraction

The properties of protons and neutrons contained within nuclei differ from those in free space, which lead to structure functions with no nuclear corrections, such as $g_1^{^3\mathrm{He}}$, to be different from structure functions describing a nucleon, such as g_1^n. These differences arise

due to nuclear effects, which consist of Fermi motion, spin depolarization, nuclear binding, off-shell, nuclear shadowing, and nuclear anti-shadowing effects.

Neutron information was extracted from the ^{3}He wave function following the model described in Reference [179]. This model accounts for the off-shellness of the nucleons, the presence of non-nucleonic degrees of freedom, nuclear shadowing and anti-shadowing effects, and for $g_1^{^3He}$ gives

$$\begin{aligned} g_1^{^3He} &= \int_x^3 \frac{dy}{y} \Delta f_{n/^3\mathrm{He}}(y)\, \tilde{g}_1^n\left(x/y, Q^2\right) \\ &+ \int_x^3 \frac{dy}{y} \Delta f_{p/^3\mathrm{He}}(y)\, \tilde{g}_1^p\left(x/y, Q^2\right) \\ &- 0.014\left(\tilde{g}_1^p(x) - 4\tilde{g}_1^n(x) + a(x)\, g_1^n(x) + b(x)\, g_1^p(x)\right), \end{aligned} \tag{8.68}$$

where $\tilde{g}_1^N$ are the off-shell nucleon spin structure functions, y is the ratio of the struck nucleon to the nucleus momentum, and $\Delta f_{N/^3\mathrm{He}}$ is the spin dependent nucleon light-cone momentum distribution. The third term on the rhs of Equation 8.68 has terms with contributions from Δ isobars and nuclear shadowing (anti-shadowing) effects represented by $a(b)$.

Nuclear shadowing effects describe the observation that the ratio $2F_2^A/AF_2^d < 1$, where A is the mass number and d is the deuteron. This effect is present in the range 0.0035 $\leq x \leq$ 0.03 $\sim$ 0.07. Anti-shadowing effects, which show that $2F_2^A/AF_2^d > 1$, are present in the range of 0.03 $\sim$ 0.07 $\leq x \leq$ 0.2 [3, 180, 181].

8.6.1 Extracting Neutron from Data

From Equation 8.68 and assuming that $\tilde{g}_1^N$ can be replaced by its on-shell counterpart, $g_1^{^3\mathrm{He}}$ can be given as

$$g_1^{^3\mathrm{He}} = P_n g_1^n + 2P_p g_1^p - 0.014\left(g_1^p(x) - 4g_1^n(x)\right) + a(x)\, g_1^n(x) + b(x)\, g_1^p(x). \quad (8.69)$$

Since E06-014 is at high enough x that there are no nuclear shadowing or anti-shadowing effects, Equation 8.69 simplifies to become

$$\begin{aligned} g_1^{^3\mathrm{He}} &= P_n g_1^n + 2P_p g_1^p - 0.014\left(g_1^p(x) - 4g_1^n(x)\right) \quad (8.70) \\ &= \left(P_n + 0.056\right) g_1^n + \left(2P_p - 0.014\right) g_1^p. \end{aligned}$$

(8.71)

Similarly, $g_2^{^3\mathrm{He}}$ can be written as

$$g_2^{^3\mathrm{He}} = \left(P_n + 0.056\right) g_2^n + \left(2P_p - 0.014\right) g_2^p. \quad (8.72)$$

8.6.2 Inputs

In order to extract the neutron information from ^{3}He data, proton data is needed to serve as inputs to the neutron extraction procedure. The proton spin structure function g_1^p was obtained using an assortment of global analyses, which include DSSV [164], BBS [165, 166], DNS2005 [168], GS [169] and LSS [167]. The g_2^p structure function was then determined through the Wandzura–Wilczek relation (Equation 2.15). This relation is valid if the higher twist is assumed to be small, which seems to be a reasonable assumption based on the results

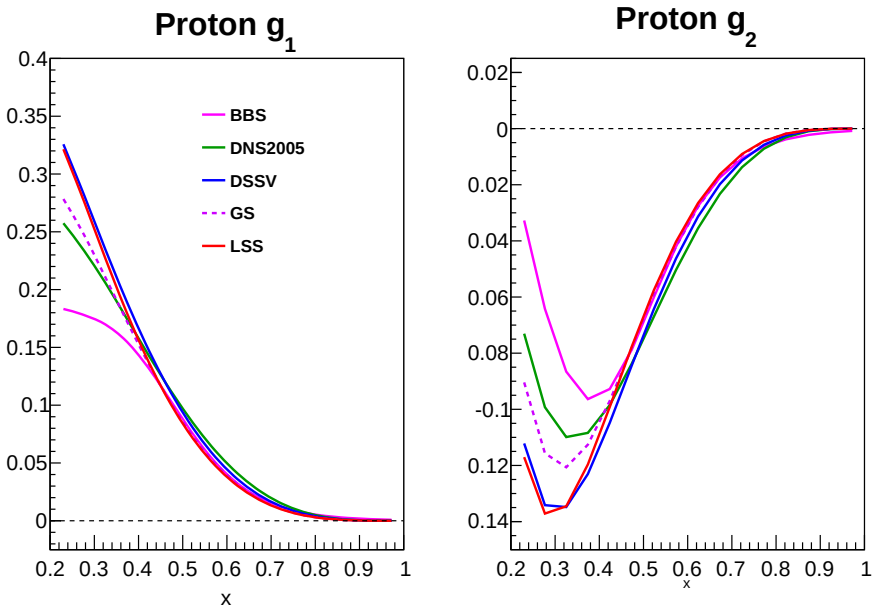

Figure 8.75: Comparison of g_1^p (left panel) and $g_2^{p,WW}$ (right panel) computed at E06-014 E = 4.74 GeV kinematics from the following global analysis: BBS [165, 166] (magenta line), DNS2005 [168] (green line), DSSV [164] (blue line), GS [169] (magenta dashed line), and LSS [167] (red line).

of E155 [54], who found g_2^p to be in good agreement with $g_2^{p,WW}$. The proton spin structure functions were computed at the same x and Q^2 values as the corresponding E06-014's measured data. Because there are several global analysis fits, the final proton value that went into the neutron extraction was the average value of all of the global fits, with an uncertainty given as the spread in the proton values. Figure 8.75 shows the results for g_1^p and $g_2^{p,WW}$ used in the neutron extraction, with Tables 8.44 and 8.45 listing their values.

Neutron corrections were done on the d_2 moment, rather than each contribution to the integrand. The matrix element d_2^p was evaluated using the proton spin structure functions g_1^p and $g_2^{p,WW}$ evaluated from the global analyses. The integral over the measured x region yielded two mean Q^2 values, one for each beam energy. The data for each beam energy was also divided into two more sets, one for the DIS region and another for the resonance region.

Table 8.44: Average g_1^p and $g_2^{p,WW}$ values from various global analysis fits. The structure functions were evaluated at kinematics matching the E06-014 E = 4.74 GeV data set. The systematic uncertainties listed represent the difference between the largest and smallest structure function values for that particular bin.

$< x >$	$g_1^p \pm \delta\left(g_1^p\right)_{sys}$	$g_2^{p,WW} \pm \delta\left(g_2^{p,WW}\right)_{sys}$
0.230	0.2732 $\pm$ 0.1425	-0.0851 $\pm$ 0.0843
0.277	0.2433 $\pm$ 0.1036	-0.1101 $\pm$ 0.0729
0.325	0.2095 $\pm$ 0.0647	-0.1173 $\pm$ 0.0483
0.374	0.1739 $\pm$ 0.0342	-0.1120 $\pm$ 0.0267
0.424	0.1387 $\pm$ 0.0156	-0.0984 $\pm$ 0.0120
0.473	0.1057 $\pm$ 0.0116	-0.0805 $\pm$ 0.0067
0.523	0.0767 $\pm$ 0.0135	-0.0616 $\pm$ 0.0094
0.574	0.0528 $\pm$ 0.0129	-0.0442 $\pm$ 0.0101
0.623	0.0344 $\pm$ 0.0107	-0.0298 $\pm$ 0.0090
0.673	0.0211 $\pm$ 0.0080	-0.0188 $\pm$ 0.0070
0.723	0.0119 $\pm$ 0.0052	-0.0108 $\pm$ 0.0047
0.773	0.0061 $\pm$ 0.0029	-0.0057 $\pm$ 0.0027
0.823	0.0027 $\pm$ 0.0023	-0.0026 $\pm$ 0.0020
0.874	0.0010 $\pm$ 0.0019	-0.0010 $\pm$ 0.0017
0.924	0.0004 $\pm$ 0.0013	-0.0003 $\pm$ 0.0013
0.972	0.0002 $\pm$ 0.0008	-0.0002 $\pm$ 0.0008

Table 8.45: Average g_1^p and $g_2^{p,WW}$ values from various global analysis fits. The structure functions were evaluated at kinematics matching the E06-014 E = 5.89 GeV data set. The systematic uncertainties listed represent the difference between the largest and smallest structure function values for that particular bin.

$< x >$	$g_1^p \pm \delta\left(g_1^p\right)_{sys}$	$g_2^{p,WW} \pm \delta\left(g_2^{p,WW}\right)_{sys}$
0.229	0.2719 ± 0.1382	-0.0875 ± 0.0858
0.277	0.2398 ± 0.0975	-0.1105 ± 0.0708
0.325	0.2046 ± 0.0585	-0.1160 ± 0.0449
0.374	0.1686 ± 0.0290	-0.1095 ± 0.0233
0.424	0.1331 ± 0.0114	-0.0951 ± 0.0091
0.474	0.1005 ± 0.0120	-0.0769 ± 0.0067
0.524	0.0724 ± 0.0134	-0.0584 ± 0.0095
0.573	0.0497 ± 0.0124	-0.0417 ± 0.0098
0.624	0.0320 ± 0.0101	-0.0277 ± 0.0085
0.674	0.0194 ± 0.0073	-0.0173 ± 0.0064
0.723	0.0109 ± 0.0047	-0.0099 ± 0.0043
0.773	0.0055 ± 0.0026	-0.0051 ± 0.0024
0.823	0.0025 ± 0.0022	-0.0023 ± 0.0020
0.873	0.0009 ± 0.0018	-0.0009 ± 0.0017
0.921	0.0004 ± 0.0013	-0.0003 ± 0.0012
0.973	0.0002 ± 0.0008	-0.0002 ± 0.0008

Table 8.46: Average d_2^p and a_2^p values computed using several global fits (DSSV, BBS, DNS, GS and LSS). The uncertainties are given as the difference between the smallest and largest d_2^p values.

Region	Q^2 [GeV^2]	x Integration Range	$d_2^p \times 10^{-3}$	$a_2^p \times 10^{-3}$
DIS(4-pass)	2.59	0.25-0.50	0.49 ± 0.65	5.71 ± 1.21
DIS(5-pass)	3.67	0.25-0.60	-0.50 ± 0.52	7.36 ± 1.13
Res(4-pass)	4.17	0.57-0.95	-1.61 ± 0.51	2.59 ± 0.88
Res(5-pass)	5.99	0.65-0.95	-0.72 ± 0.30	1.00 ± 0.41
DIS+Res(4-pass)	3.21	0.25-0.95	-1.75 ± 0.53	9.41 ± 1.37
DIS+Res(5-pass)	4.32	0.25-0.95	-1.69 ± 0.47	8.92 ± 1.15

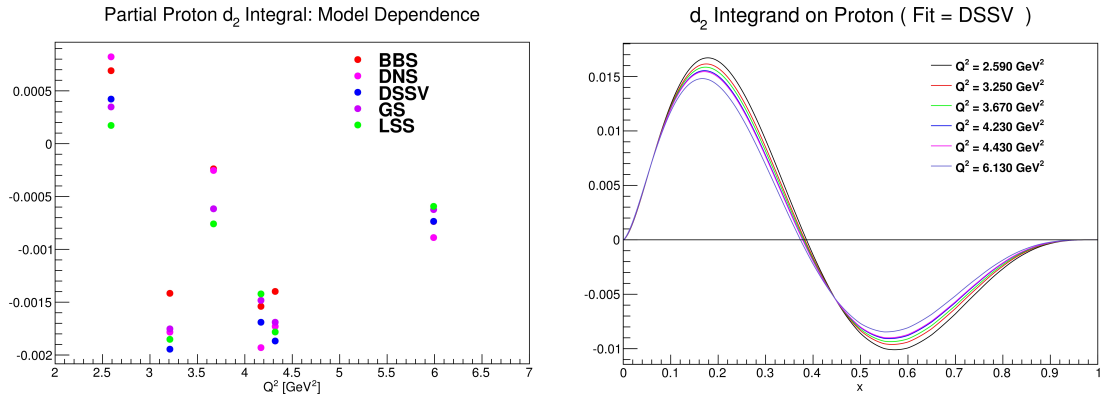

Figure 8.76: Left panel: d_2^p calculations from DSSV, GS, BBS, DNS and LSS global analyses computed using Q^2 values and x integration limits. Right panel: The resulting d_2^p integrand from the DSSV calculations at various Q^2 values.

This yielded two additional mean Q^2 values for each beam energy, resulting in a total of six Q^2 values. The six mean Q^2 values are listed in Table 8.46, along with their associated integration limits, a_2^p (computed using the same method as that used for d_2^p), and the d_2^p matrix elements for each region. The left panel of Figure 8.76 shows the d_2^p computation from various models at the six Q^2 values of interest to E06-014. The d_2^p integrands resulting from the DSSV calculation at various Q^2 values are shown in the right panel of Figure 8.76. For the range covered in x by E06-014 ($0.25 \leq x \leq 0.9$), the d_2^p integrand is dominated by negative contributions, which lead to negative d_2^p values.

8.6.3 Effective Polarization

The neutron (P_n) and proton (P_p) polarization can be calculated form various calculations given by [3]

$$P_p = p^+ - p^- = -\frac{1}{3}\left[P\left(D\right) - P\left(S'\right)\right] \tag{8.73}$$

$$P_n = n^+ - n^- = 1 - \frac{2}{3}\left[P\left(S'\right) - 2P\left(D\right)\right] \tag{8.74}$$

where $n^{\pm}(p^{\pm})$ is the probability of finding a neutron (proton) with momentum fraction y of a nucleous with spin aligned (+) or anti-aligned (-) along the spin of the nucleous.

The average over world calculations [182] gives

$$P_n = 0.86 \pm 0.002 \quad \text{and} \quad P_p = -0.028 \pm 0.004. \tag{8.75}$$

In addition to Equation 8.75, nine more models [3, 179, 183] can be considered to obtain the full uncertainty on the effective polarizations

$$P_n = 0.86^{+0.036}_{-0.020} \quad \text{and} \quad P_p = -0.028^{+0.009}_{-0.004}. \tag{8.76}$$

8.7 Systematic Uncertainty

The systematic uncertainties associated with various parameters (target and beam polarizations, dilution factors and various kinematics) were propagated to each of the measured spin dependent quantities (i.e. $A_\perp$, g_1, etc.), inorder to determine the systematic uncertainty associated with it. Each of the contributions that contained a systematic uncertainty were

varied within its uncertainty range and the resulting change in the spin dependent quantity was studied. The difference between the initial production spin dependent quantity and the varied spin dependent quantity was assigned as the systematic uncertainty. For example consider $A_\perp$, which depends on the target polarization P_t, and has an uncertainty range of $\pm\delta P_t$. $A_\perp$ would then be recomputed using $P_t \pm P_t \cdot \delta P_t$, where $\pm$ was determined based on which sign produces the largest change (for most cases the difference between $\pm$ was negligible), resulting in a value $A_\perp^{'}$. The systematic uncertainty of $A_\perp$ due to P_t is then $|A_\perp - A_\perp^{'|}$. To evaluate the P_t systematic uncertainty on say g_1 or g_2, the asymmetries $A_\parallel^{'}$(defined in similar way as $A_\perp^{'}$) and $A_\perp^{'}$ would be used to compute $g_1^{'}$ or $g_2^{'}$, with the systematic uncertainty on g_1 or g_2 due to the target polarization given as the difference of $|g_1 - g_1^{'}|$ or $|g_2 - g_2^{'}|$. This procedure was followed for each contribution to a spin dependent quantity (including d_2) that had a systematic uncertainty associated with it.

In this section the measured asymmetries sensitivity to the data quality and PID cuts will be discussed in Section 8.7.1. The systematic uncertainty due to contributions from the dilution factors, beam and target polarizations, cross section, and kinematics will then be discussed in Section 8.7.2. The systematic uncertainties assigned to d_2^n however, can be found in Section 10.2.1.

8.7.1 Asymmetry Cut Systematics

If an asymmetry is sensitive to a particular cut, then variations on the cut threshold will cause the central value of the asymmetry to shift. For E06-014 the asymmetry sensitivity to electron cuts was analyzed by slightly varying particular data quality and PID cuts, and computing the asymmetries with the new cut threshold. The difference between the asymmetry computed with the original cut threshold (Tables 8.25 and 8.26) and the new cut threshold was assigned to the original asymmetry as the systematic uncertainty for that cut.

The total systematic uncertainty due to the asymmetry's sensitivity to the cut thresholds was computed by adding the uncertainties assigned to each cut in quadrature. This procedure was applied to data from both electron beam energies (E = 4.74 and 5.89 GeV). The cut variations used in the systematic study (only one cut at time was varied) were as follows:

- Cer TDC: Čerenkov TDC window $<$ 60 TDC channels
- Preshower energy: Preshower energy $>$ 150 MeV
- E/p : 0.788 $< E/p <$ 1.203
- Scintillator energy: Scintillator energy $>$ 450 MeV
- Multi-track: Multiple track cut was set to select only one track events
- Track-cluster (for E = 4.74 GeV data set): $\Delta x_{sh} <$ 0.118 m, $\Delta y_{sh} <$ 0.117 m, $\Delta x_{ps} <$ 0.212 m, and $\Delta y_{ps} <$ 0.200 m
- Track-cluster (for E = 5.89 GeV data set): $\Delta x_{sh} < 3.5\sigma_{x_{sh}}$, $\Delta y_{sh} < 3.5\sigma_{y_{sh}}$, $\Delta x_{ps} <$ 0.081 m, and $\Delta y_{ps} <$ 0.250 m
- Track quality: $\frac{k^2}{N_{dof}} < 4$
- Target vertex: $|z_v| <$ 0.19 m

The differences between the asymmetries (top two panels) and polarized structure functions (bottom two panels) defined using the final data quality and PID cuts, and those using the varied cuts listed above, can be seen in Figures 8.77 and 8.78. Each of the colored markers in Figures 8.77 (E = 4.74 GeV data) and 8.78(E = 5.89 GeV data) represents a particular cut that was varied, with the green circle marker being the total systematic uncertainty due to the cuts. The black marker shows the statistical uncertainty (for comparison) that is associated with the given asymmetry or structure function.

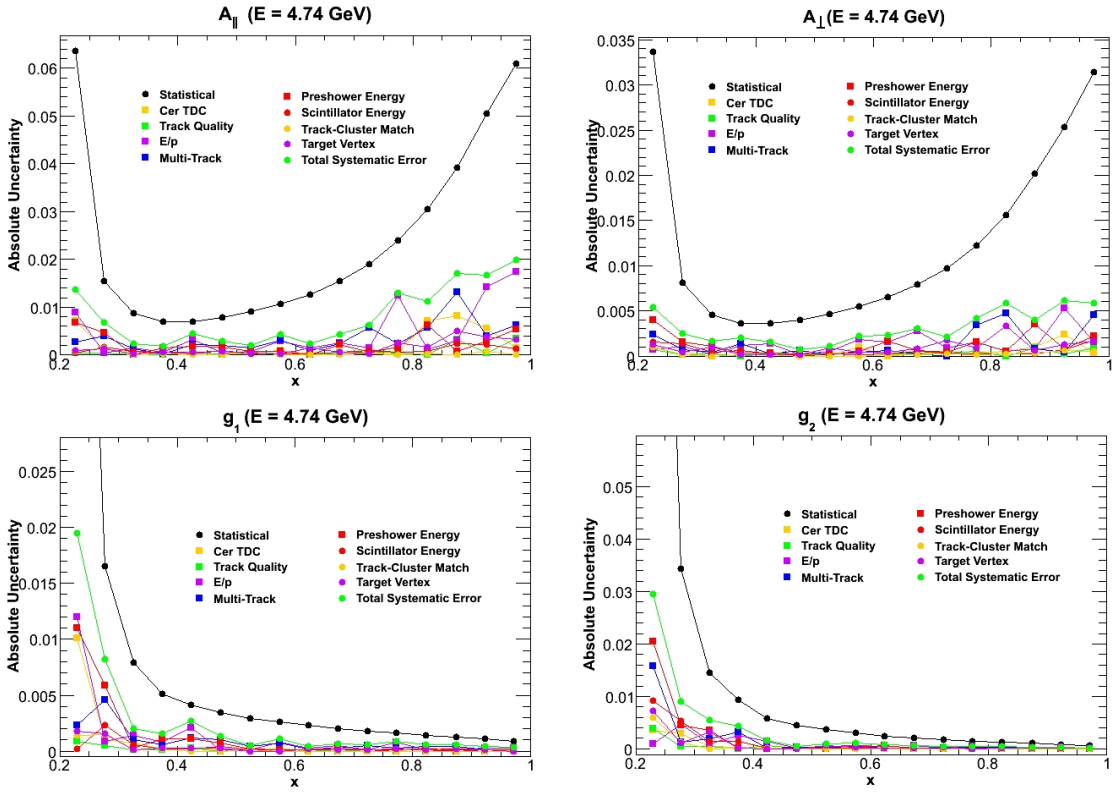

Figure 8.77: Systematic uncertainties due to electron cuts, determined for $A_{\parallel}$ and $A_{\perp}$ (top panels), and g_1 and g_2 (bottom panels) on ^{3}He , at an electron beam energy of E = 4.74 GeV.

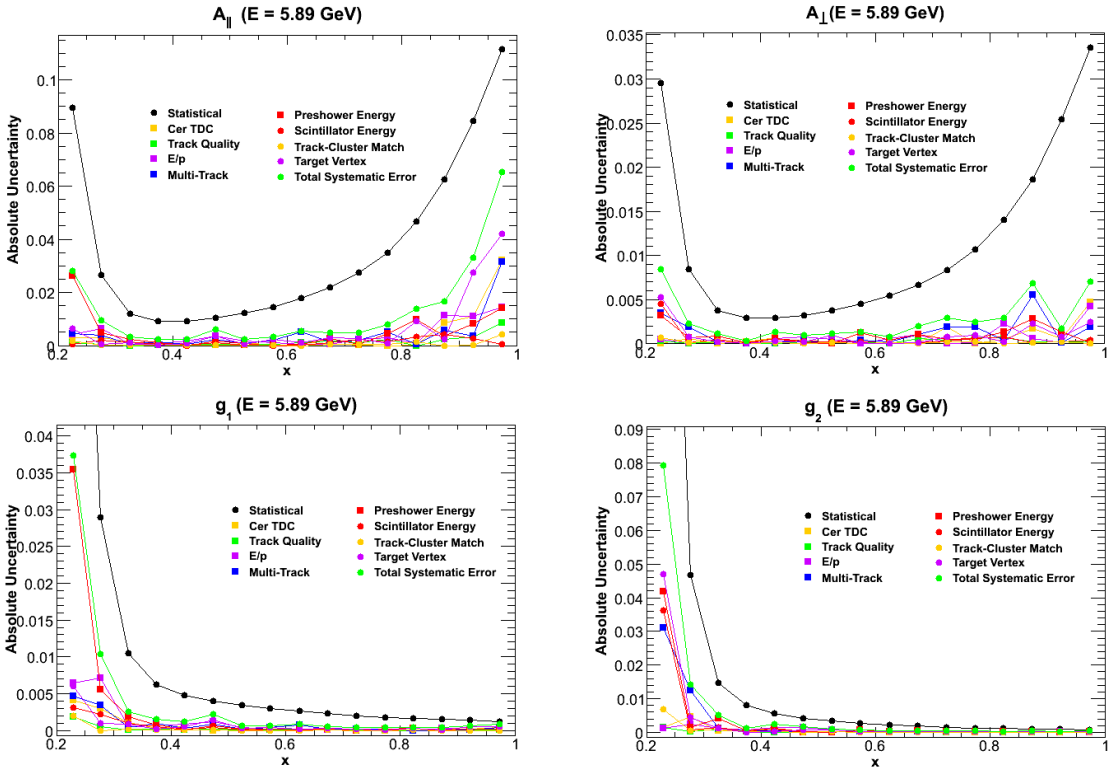

Figure 8.78: Systematic uncertainties due to electron cuts, determined for $A_{\parallel}$ and $A_{\perp}$ (top panels), and g_1 and g_2 (bottom panels) on ^{3}He , at an electron beam energy of E = 5.89 GeV.

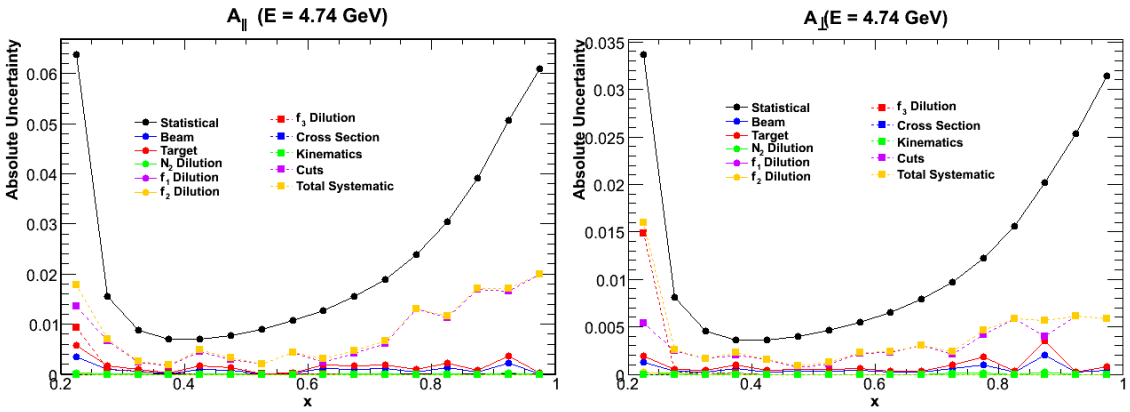

Figure 8.79: Systematic uncertainties determined for $A_{\parallel}$ and $A_{\perp}$ on ^{3}He , at an electron beam energy of E = 4.74 GeV.

8.7.2 Other Systematics

In addition to the cut systematic uncertainties, the systematic uncertainties resulting from variations in the kinematics (x, Q^2, ϕ, ν, p, and θ), beam and target polarizations (P_b and P_t), dilution factors (D_{N_2},f_1,f_2, and f_3), radiative corrections and cross sections (for g_1 and g_2) were also studied. Figures 8.79 and 8.80 show the systematic uncertainty assigned to the double spin asymmetries, resulting from various contributions. For comparison, the statistical uncertainty associated with the asymmetries is also drawn in the plots (the black markers). Appendix F lists the systematic uncertainties calculated for all of the contributions that were used in the evaluation of the double spin asymmetries and polarized structure functions.

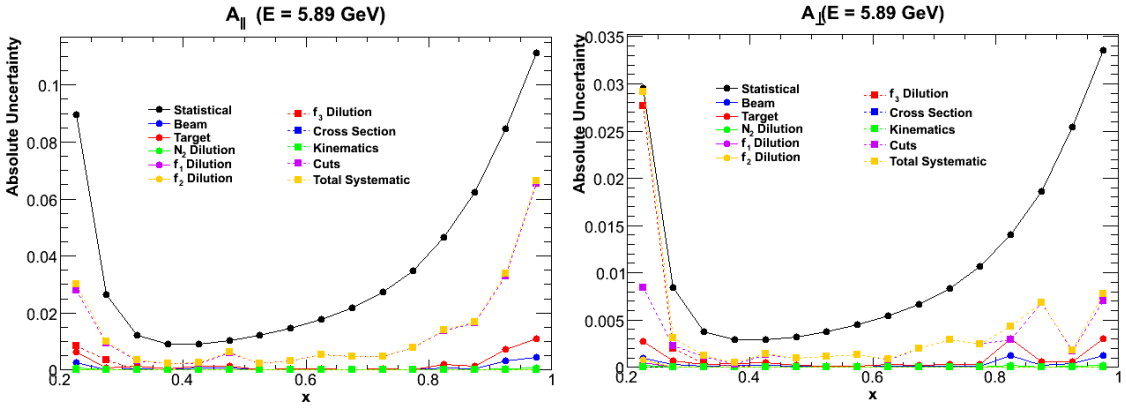

Figure 8.80: Systematic uncertainties determined for $A_{\parallel}$ and $A_{\perp}$ on ^{3}He , at an electron beam energy of E = 5.89 GeV.

CHAPTER 9

GEANT4 SIMULATION

Monte Carlo (MC) simulations can be used to help understand experimental factors such as background, detector acceptance, detector responses, etc.

In this Section the BigBite GEANT4 simulation is discussed. It was used to verify calorimeter calibrations, electron re-scattering effects and investigate the size of the pair-production asymmetry.

9.1 GEANT4 Setup

GEANT4 [160] is a tool kit for simulating and analyzing the passage of particles through matter. A BigBite GEANT4 simulation code was developed for E06-014 by V. Mamyan. The simulation was designed to study the energy deposited into the BigBite calorimeter. Accurate simulation of the shower and preshower responses required that all materials that were present during the real experiment were also included in the simulation, since the particles will interact with materials. To this end, all of the materials present between the target and shower calorimeter were considered, including several materials that were used for shielding purposes. Figure 9.1 shows all of the materials considered in the simulation.

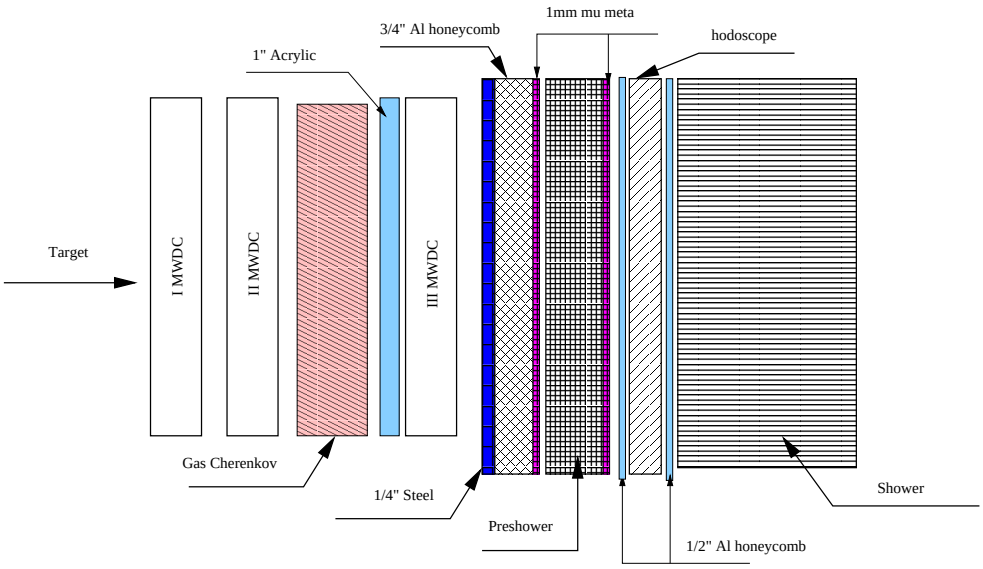

Figure 9.1: Illustration of the materials included in the GEANT4 simulation. Figure produced by V. Mamyan.

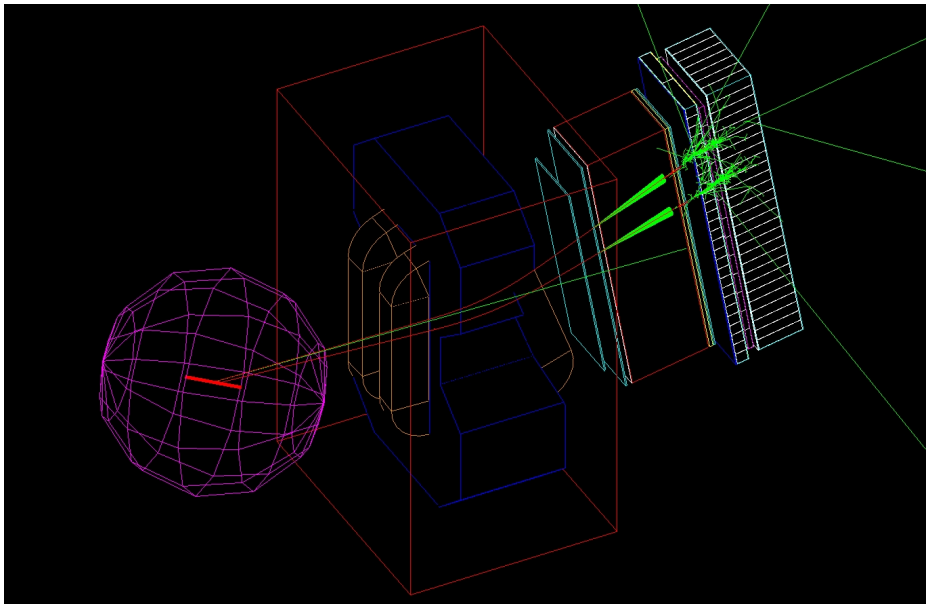

Figure 9.2: Simulated event in BigBite GEANT4 simulation. The red tracks represent electrons, while green tracks represent photons. Figure produced by V. Mamyan.

While all materials were defined, not all of the detectors were implemented in the simulation. The MWDCs were not digitized and were used only to provide primitive particle tracking; the Čerenkov was defined as a box filled with C_4F_8O gas, but no mirrors or efficiencies were defined. The BigBite magnet, scintillator, preshower and shower were fully implemented, however there were no efficiencies were considered in the simulation.

Another aspect of the simulation that needed to be defined was the event generator, in particular how often a particle type (such as electron or pion) is thrown from the target. The frequency at which each particle type is thrown was determined through cross section weighting, where the electron cross section was determined through the used of F1F209 [163] and the pion cross section from Wiser fits [184], as a function of scattering angle and momentum. An example of a simulated event in the BigBite simulation is shown in Figure 9.2, where the red tracks correspond to electrons and the green tracks correspond to photons.

9.2 Cuts

The simulation must have the same cuts applied as the measured data, in order to directly compare the simulation to the experimental data. The following cuts were applied to the GEANT4 simulation in order to match it to the measured data:

- **Charge Cut**: Used tracking to reproduce charge cut used in E06-014 (defined in Section 8.2.2.1).
- **Target Vertex**: Used tracking to reconstruct the target vertex and apply the same cut used by E06-014 (defined in Section 8.2.1.2).
- **Geometrical Cuts**: Tracking was used to apply the E06-014 geometrical cuts (defined in Section 8.2.1.3).
- **Re-scattering Cut**: Applied via tracking to reproduce the cut used in E06-014 (defined in Section 8.2.1.4
- **Čerenkov Mirror Cuts**: Tracking was used to apply cuts to match the geometrical Čerenkov acceptance used in E06-014 (defined in Section 8.2.2.5)
- **Momentum**: E06-014 momentum cuts (defined in Section 8.2.1.3 were applied to the simulated reconstructed momentum.
- **Scintillator**: Scintillator cut equivalent to that used in E06-014 (defined in Section 8.2.2.3) was used.
- **Preshower**: Preshower energy cut matching the cut used in E06-014 (defined in Section 8.2.2.4) was applied.
- **E/p**: An E/p range consistent with that used in E06-014 (defined in Section 8.2.2.4) was used.

In addition to the cuts above, a cut needs to be formed that will mimic the trigger that was used in E06-014. The main T2 trigger consisted of a shower + Čerenkov signal, however because the Čerenkov was not implemented in the simulation, the T2 could not be fully simulated. As a result the trigger was simulated by applying cuts to the calorimeter energy distributions in order to match the distributions seen in the T2 data. The first cut that was defined is a two dimensional cut that is applied to the preshower vs shower energy, as seen in Figure 9.3. The top panel shows the energy distribution of the preshower (this distribution has a preshower cut requiring an event deposit more than 200 MeV into the preshower layer) plotted against the shower for T2 events recorded during production running, and the bottom panel shows the energy distributions of the preshower (no preshower cuts applied) versus the shower produced from simulation. The blue line in both panels defines the threshold of the two dimensional cut that makes up one part of the simulated T2 trigger cut. Everything above the threshold is accepted, which can be seen is the bottom panel, where the black markers are all simulated events and the red markers represent the events passing this cut.

There was also an additional cut on the total calorimeter energy that was defined for the simulated T2 trigger. This cut is shown in Figure 9.4, which compares the simulated (black histogram) total calorimeter energy to the measured energy (red histogram). The dashed line defines the cut position that was used to try and match the calorimeter energies between the experiment and simulation.

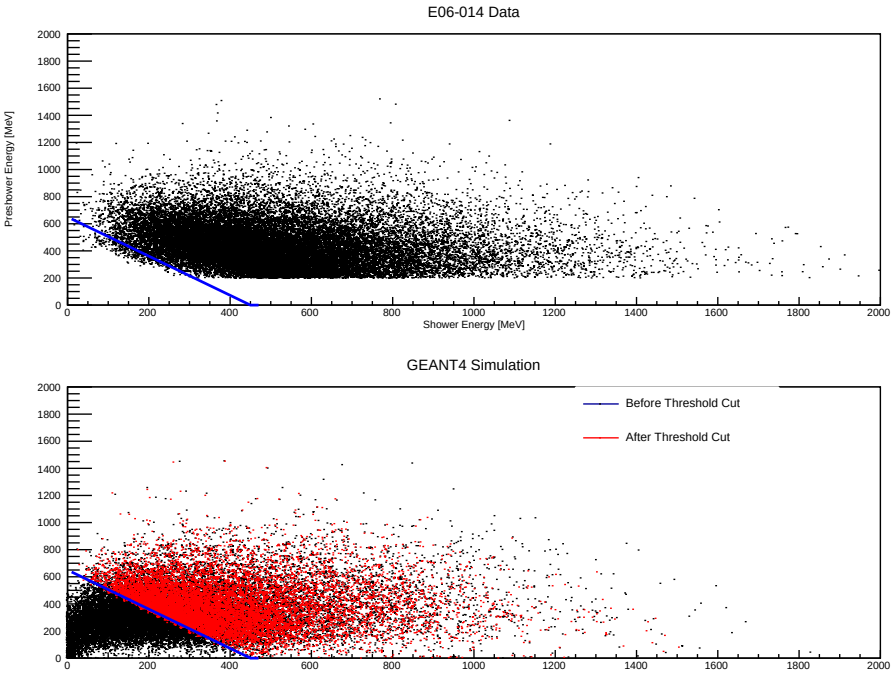

Figure 9.3: Two dimensional cut on preshower and shower energy that goes into forming the GEANT4 T2 trigger cut. Top panel shows T2 data taken during E06-014, while the bottom panel shows simulated data before (black markers) and after (red markers) the two dimensional cut. Everything above the blue line is accepted by the cut.

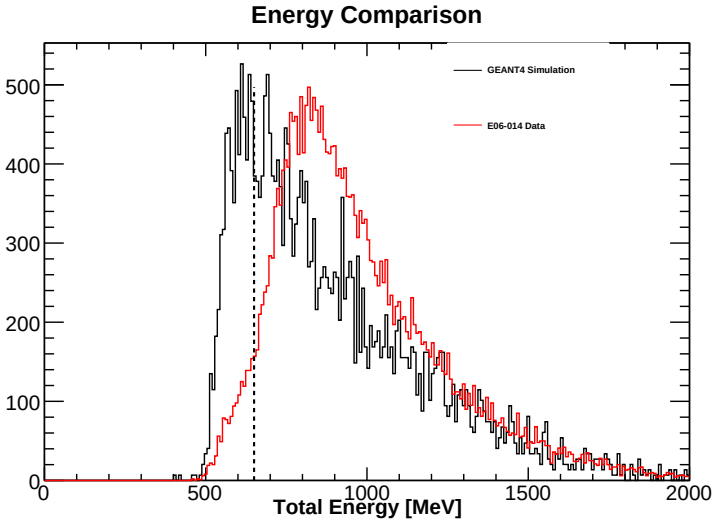

Figure 9.4: Comparison total energy from T2 data taken during E06-014 and GEANT4 simulation. The second part of the GEANT4 T2 trigger cut is everything greater than the dashed line.

9.3 Calorimeter Response

9.3.1 Electrons

Using the electron cuts defined in Section 9.2, the measured and simulated distributions can be compared and gain insight in to how well the calorimeters are understood and the validity of the calorimeter calibrations. Before proceeding with such a comparison, it is important to make sure that the simulation reproduces the experimental parameters, for example the electron scattering angle and target vertex. Figure 9.5 shows that even using a primitive tracking algorithm and partially implemented MWDCs and Čerenkov detector, that the target vertex (left panel) and scattering angle (right panel) reproduced from the simulation (blue histogram) agrees very well with data (red histogram). The differences in the scattering angle can be contributed to the exclusion of the Čerenkov detector, BigBite efficiencies and the simple tracking algorithm.

Once the simulation was verified that it was reproducing the experimental parameters, a

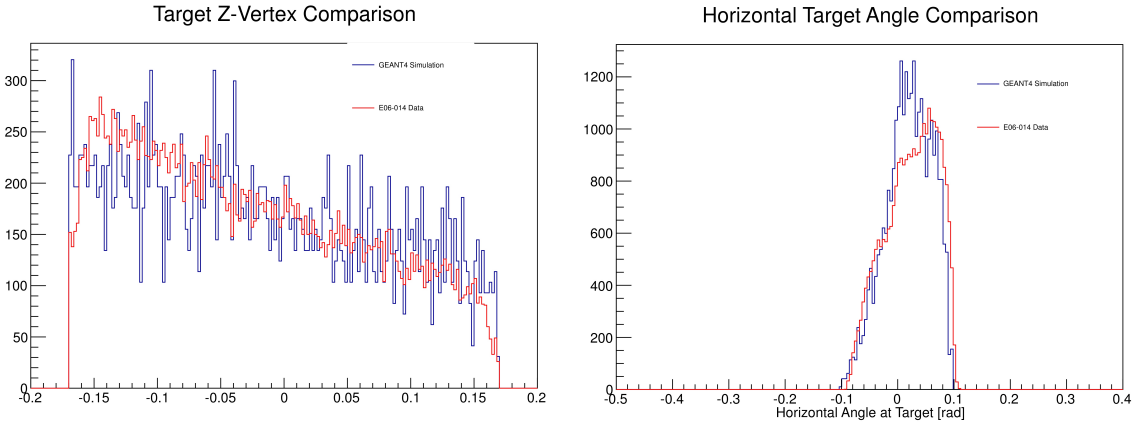

Figure 9.5: Comparison between simulation (blue histogram) and data (red histogram). The left panel shows the reconstructed target vertex, while the right panel shows the electron scattering angle.

comparison of the energy distributions can be made. Figure 9.6 shows comparisons between data (red histograms) and simulation (blue histograms) for the preshower energy (top-left panel), shower energy (top-right panel), reconstructed momentum (bottom-left panel) and E/p (bottom-right panel) distributions. The simulation matches the data very well for all four distributions, and provides confidence that the measured electrons were correctly calibrated and understood.

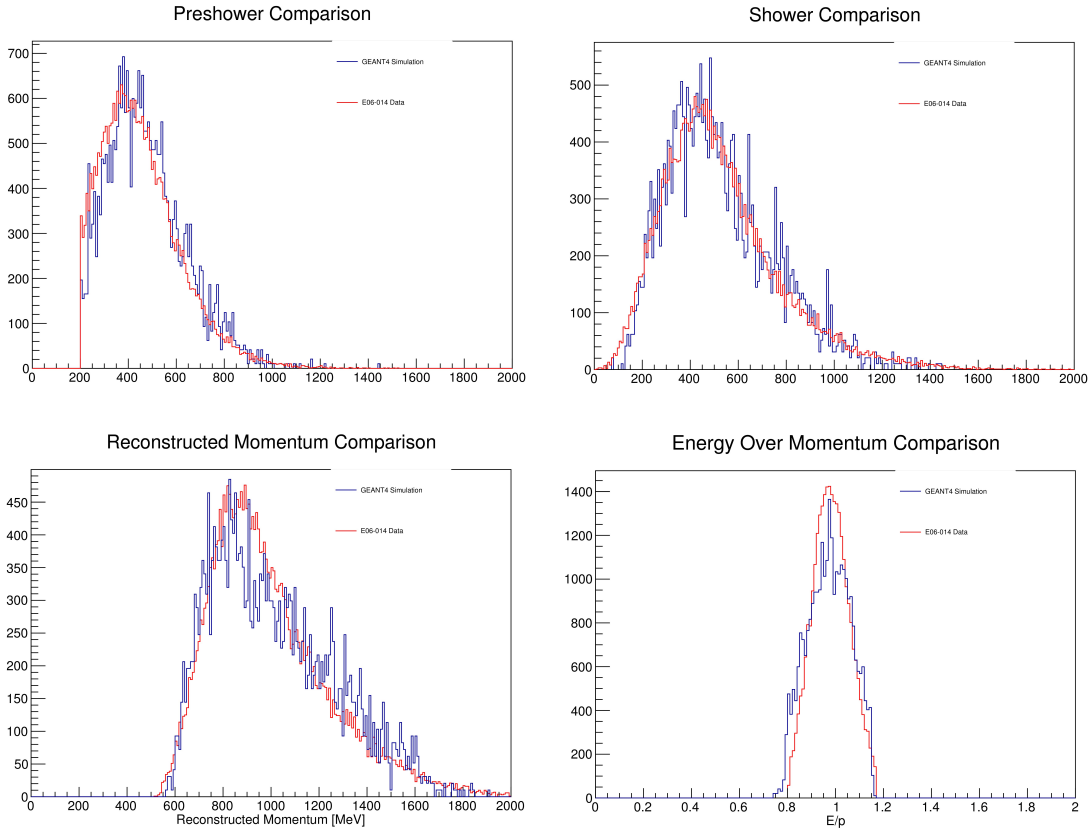

Figure 9.6: Comparison between simulation (blue histogram) and data (red histogram) of the following electron distributions: preshower energy (top-left panel), shower energy (top-right panel), reconstructed momentum (bottom-left panel) and E/p (bottom-right panel).

9.3.2 Pions

Not only is it important to verify and understand the electron distributions, but also the pion distributions, which are one of the main background sources. The pion distribution was investigated by removing the PID cuts (preshower energy, scintillator energy and E/p cuts) from the simulation and data and studying the preshower energy distribution. The preshower energy distribution for electrons and negatively charged pions are can be seen in Figure 9.7. The distinction between MIP peak ($\sim$ 82 MeV) of the pions and the peak ($\sim$400 MeV) corresponding to electrons is clearly visible. While the electron peaks between simulation (red histogram) and data (blue histogram) agree well with each other, the simulated pion peak is shifted to a slightly lower energy than the data.

The shift in the preshower energy was further investigated by studying each particle type's preshower energy distribution. The pions and electrons were selected by applying E/p and scintillator cuts to select the desired particle type. The resulting preshower energy distributions (red histograms) are shown in Figure 9.8 and are compared to their measured counter parts (blue histograms). The preshower energy for pions (the left panel) shows a shift in the energy peak between the simulation and data (The dashed line marks E = 82 MeV). If one now considers the electron preshower energy distribution (shown in the right panel of Figure 9.8) produced from the simulation (red histogram) and measured data (blue histogram), it is evident that while the electron peaks ($\sim$ 400 MeV) agree fairly well with each other, there is a glaring discrepancy at the lower energy near where the pion peak would be. The simulation shows pion events contaminating the lower electron preshower energy distribution, whereas the measured data shows no such peak. Considering these two observations, one can conclude that the trigger defined in the simulation is not as stringent as the trigger used in the experiment. The experimental trigger cuts into part of the pion energy distribution, causing the pion energy peak to appear shifted relative to the simulation.

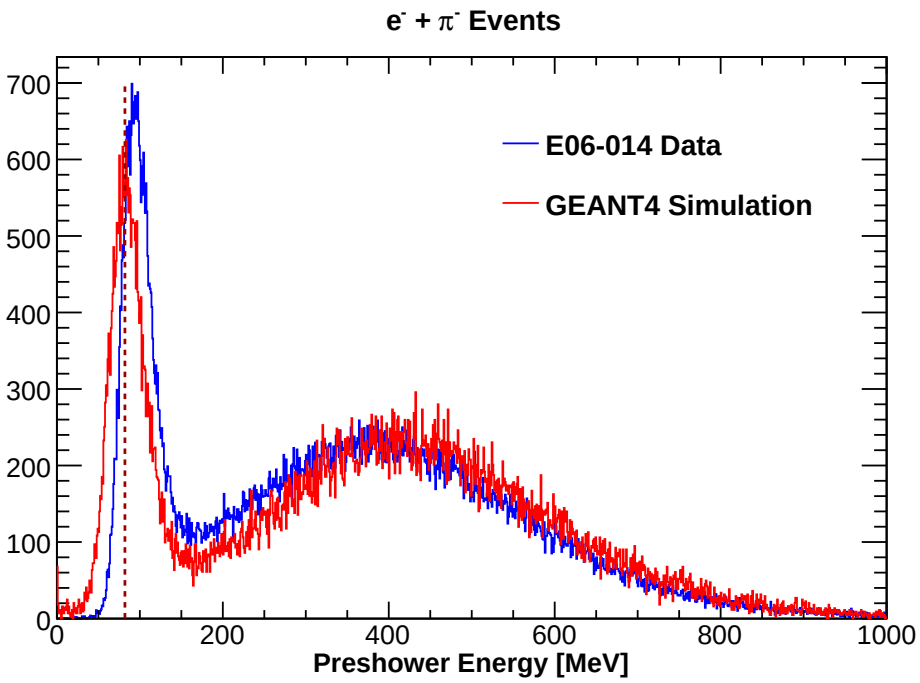

Figure 9.7: Preshower energy comparison between simulation (red histogram) and data (blue histogram) when considering both negatively charged pions and electrons.

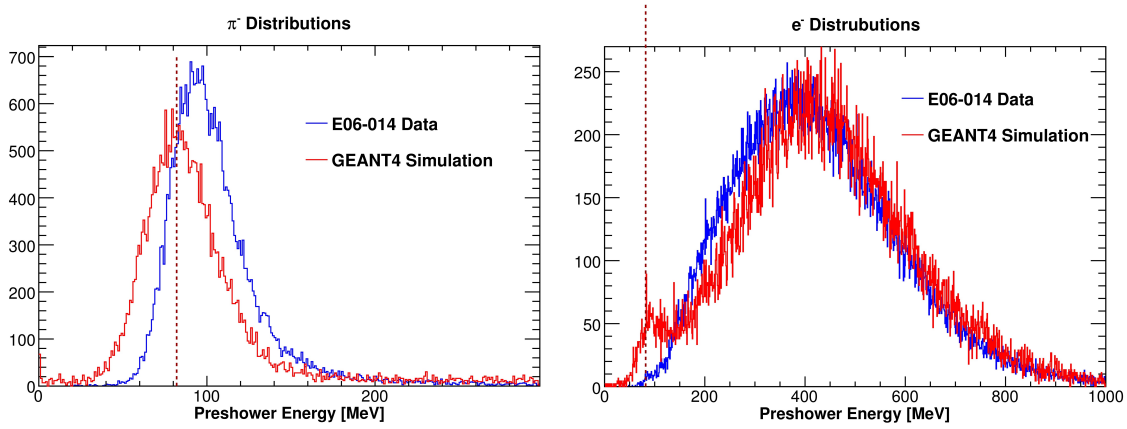

Figure 9.8: Preshower energy comparison between simulation (red histogram) and data (blue histogram) for π^- (left panel) and e^- (right panel) events.

This conclusion also supports why the electron energy distribution for the simulation shows the existence of a pion peak at low energy, whereas the measured energy distribution has no pion peak present, yet the electron peaks between the simulation and data are in agreement.

Thus through the use of GEANT4 MC simulations, an understanding of how particles interact in the BigBite calorimeters was achieved, as well as verifying the use of the energy calibration used for E06-014.

9.4 Pair-Production Asymmetry

Besides using GEANT4 to verify calibrations and study detector responses, it can also be used to predict behaviors. One such behavior that was seen in E06-014 data was that the pair-produced positrons had a significant (relative to the electron asymmetry) non-zero asymmetry (discussed in Section 8.2.9.2). The GEANT4 simulation was used to study how the π^0 asymmetry propagated to the pair-produced e^+e^- pairs.

The GEANT4 code was modified to include π^- longitudinal and perpendicular asymmetries measured from E06-014 (values found in Table 8.28), which were parameterized

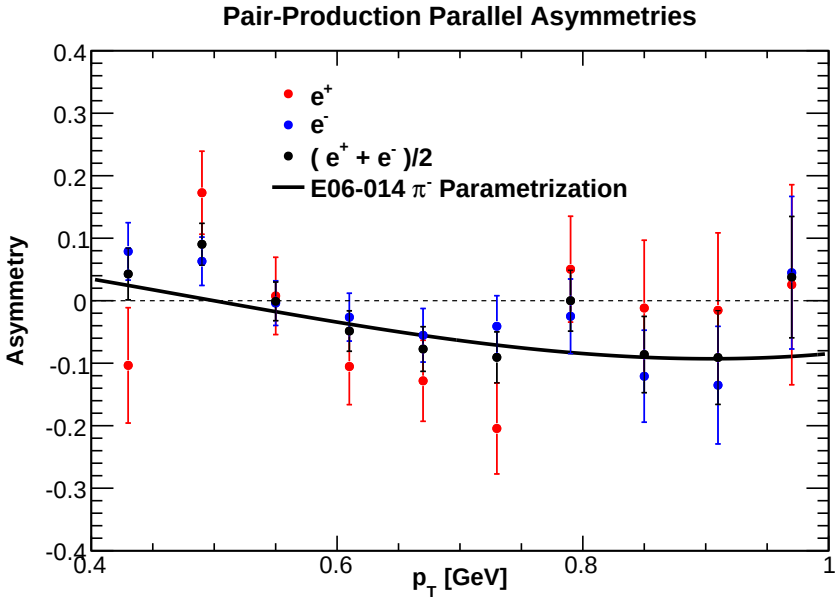

Figure 9.9: Longitudinal pair produced asymmetry results from GEANT4 based on parameterization of π^- data (black line).

with a third order polynomial, as a function of the transverse momentum p_T. The simulation was then ran so that only π^0 events were thrown at the target, and a spin helicity (+ or -) was assigned to the particle based on the parameterized asymmetry. When the pion decays into high energy photons, which then decay into e^+e^- pairs, the e^+e^- pairs will have a helicity associated with them and an asymmetry can be formed. Figures 9.9 and 9.10 show the results for the longitudinal and transverse asymmetries, where the red markers are the positron asymmetries, the blue markers are the electron asymmetries, the black markers are the average positron and electron asymmetry, and the black line represents the values used in the π^- parameterization of the data. In both target spin configurations GEANT4 seems to show a non-zero pair produced asymmetry, which supports what is seen in the data.

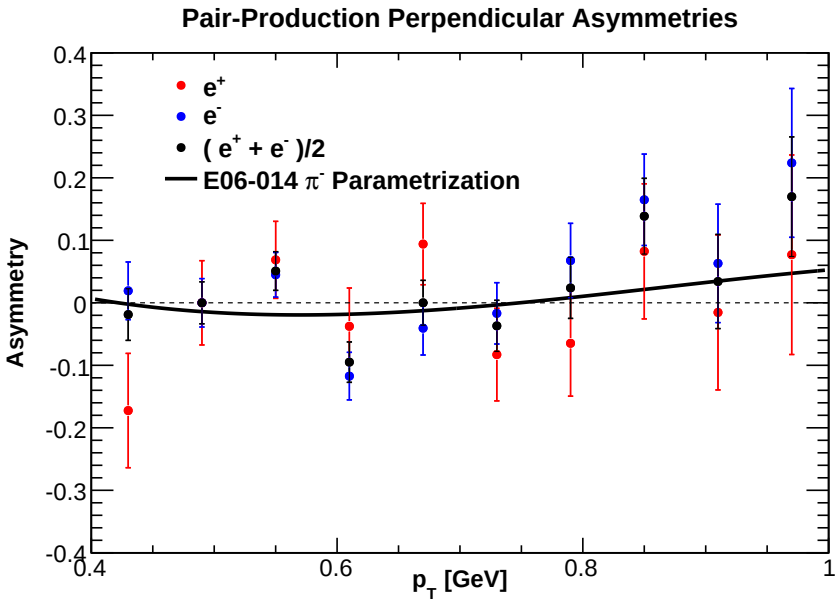

Figure 9.10: Transverse pair produced asymmetry results from GEANT4 based on parameterization of π^- data (black line).

CHAPTER 10

RESULTS

In this section, the results of the E06-014 experiment will be discussed. Section 10.1, begins by showing the final double spin asymmetries and polarized structure functions. These results are then used in Section 10.2 to evaluate the d_2^n matrix elements, which in turn are used to extract the f_2^n matrix elements. Finally, the d_2^n and f_2^n results are used in Section 10.3 to compute the color electric and magnetic color forces.

10.1 Polarized Structure Functions

10.1.1 Asymmetries

Applying the radiative corrections (Section 8.5) to the measured asymmetries listed in Tables 8.31 and 8.32, the final Born asymmetries on ^{3}He were extracted, are shown in Figure 10.1. The Born asymmetries are also listed in Tables 10.1 and 10.2 for the 4.74 and5.89 GeV data sets, respectively. The systematic uncertainty associated with the asymmetries is the quadratic sum of all the contributing uncertainties discussed in Section 8.7 and Appendix F, which are represented by the band at the bottom the the plots in Figure 10.1.

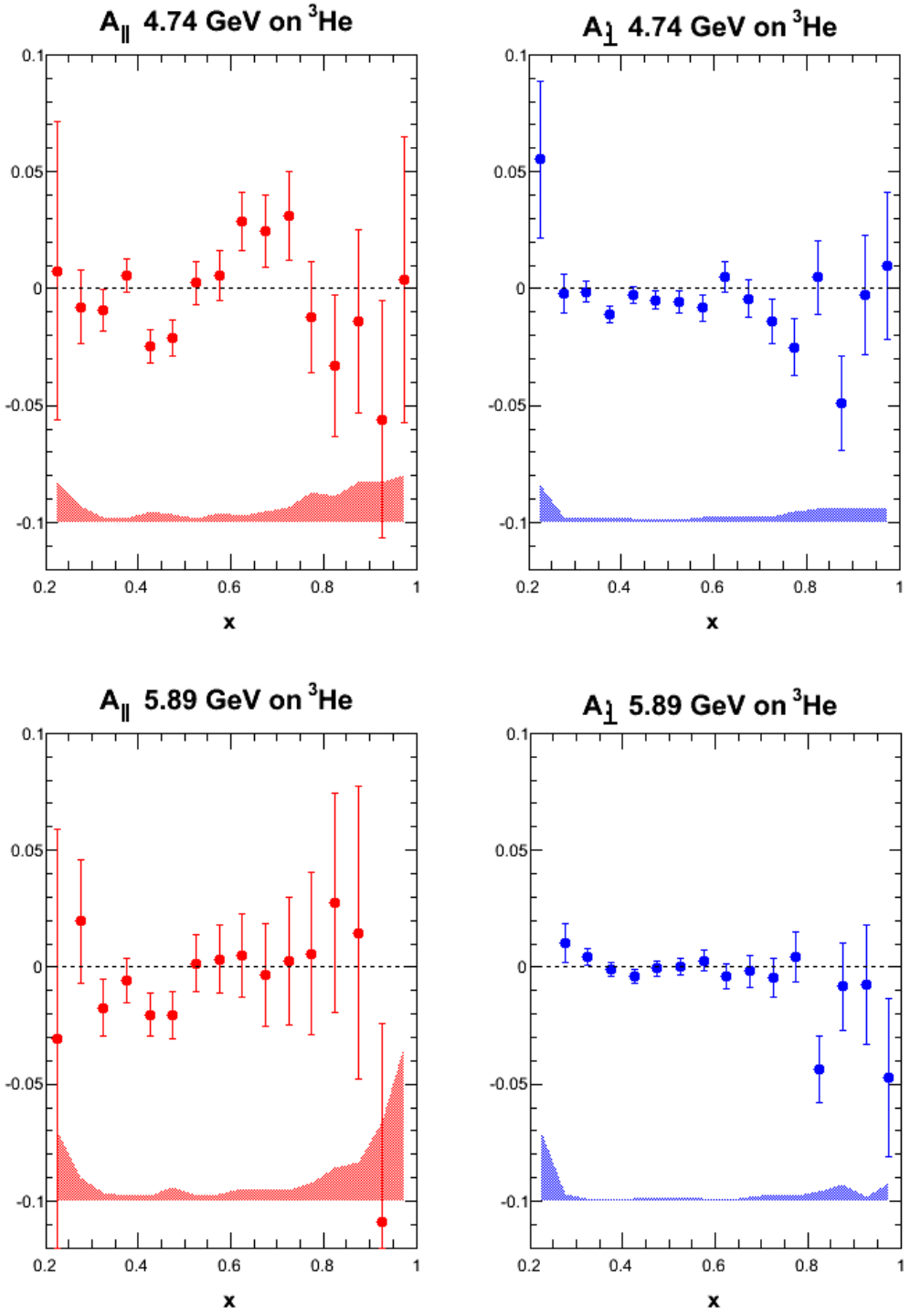

Figure 10.1: The longitudinal (left panels) and transverse (right panels) Born DSAs measured on a ^{3}He target are plotted against x. The top (bottom) two panels correspond to the E = 4.74 (5.89) GeV data set. The systematic uncertainty is $\pm$ the value given by the colored bands at the bottom of each plot.

Table 10.1: Final Born longitudinal and transverse asymmetries measured on ^{3}He at an incident electron energy of 4.74 GeV.

E = 4.74 GeV		
x Bin Center	$A_{\parallel}^{^3\mathrm{He}}$	$A_{\perp}^{^3\mathrm{He}}$
0.225	$0.00745 \pm 0.06368_{stat} \pm 0.01791_{sys}$	$0.05521 \pm 0.03362_{stat} \pm 0.01594_{sys}$
0.275	$-0.00780 \pm 0.01549_{stat} \pm 0.00709_{sys}$	$-0.00220 \pm 0.00809_{stat} \pm 0.00260_{sys}$
0.325	$-0.00929 \pm 0.00879_{stat} \pm 0.00265_{sys}$	$-0.00131 \pm 0.00455_{stat} \pm 0.00167_{sys}$
0.375	$0.00547 \pm 0.00701_{stat} \pm 0.00181_{sys}$	$-0.01082 \pm 0.00361_{stat} \pm 0.00230_{sys}$
0.425	$-0.02478 \pm 0.00704_{stat} \pm 0.00488_{sys}$	$-0.00256 \pm 0.00361_{stat} \pm 0.00157_{sys}$
0.475	$-0.02089 \pm 0.00778_{stat} \pm 0.00336_{sys}$	$-0.00492 \pm 0.00400_{stat} \pm 0.00093_{sys}$
0.525	$0.00238 \pm 0.00900_{stat} \pm 0.00202_{sys}$	$-0.00582 \pm 0.00462_{stat} \pm 0.00123_{sys}$
0.575	$0.00535 \pm 0.01069_{stat} \pm 0.00440_{sys}$	$-0.00827 \pm 0.00548_{stat} \pm 0.00232_{sys}$
0.625	$0.02869 \pm 0.01269_{stat} \pm 0.00318_{sys}$	$0.00523 \pm 0.00650_{stat} \pm 0.00236_{sys}$
0.675	$0.02473 \pm 0.01546_{stat} \pm 0.00463_{sys}$	$-0.00426 \pm 0.00787_{stat} \pm 0.00307_{sys}$
0.725	$0.03102 \pm 0.01895_{stat} \pm 0.00658_{sys}$	$-0.01402 \pm 0.00972_{stat} \pm 0.00240_{sys}$
0.775	$-0.01233 \pm 0.02387_{stat} \pm 0.01302_{sys}$	$-0.02508 \pm 0.01221_{stat} \pm 0.00465_{sys}$
0.825	$-0.03295 \pm 0.03044_{stat} \pm 0.01158_{sys}$	$0.00481 \pm 0.01563_{stat} \pm 0.00583_{sys}$
0.875	$-0.01406 \pm 0.03913_{stat} \pm 0.01704_{sys}$	$-0.04924 \pm 0.02015_{stat} \pm 0.00572_{sys}$
0.925	$-0.05593 \pm 0.05059_{stat} \pm 0.01722_{sys}$	$-0.00265 \pm 0.02529_{stat} \pm 0.00611_{sys}$
0.975	$0.00375 \pm 0.06089_{stat} \pm 0.01993_{sys}$	$0.00997 \pm 0.03140_{stat} \pm 0.00589_{sys}$

Table 10.2: Final Born longitudinal and transverse asymmetries measured on ^{3}He at an incident electron energy of 5.89 GeV.

E = 5.89 GeV		
x Bin Center	$A_{\parallel}^{^3\mathrm{He}}$	$A_{\perp}^{^3\mathrm{He}}$
0.225	-0.03050 $\pm$ 0.08951$_{stat}$ $\pm$ 0.03004$_{sys}$	0.11501 $\pm$ 0.02956$_{stat}$ $\pm$ 0.02917$_{sys}$
0.275	0.01960 $\pm$ 0.02654$_{stat}$ $\pm$ 0.01008$_{sys}$	0.01042 $\pm$ 0.00844$_{stat}$ $\pm$ 0.00312$_{sys}$
0.325	-0.01731 $\pm$ 0.01205$_{stat}$ $\pm$ 0.00343$_{sys}$	0.00431 $\pm$ 0.00376$_{stat}$ $\pm$ 0.00128$_{sys}$
0.375	-0.00569 $\pm$ 0.00922$_{stat}$ $\pm$ 0.00230$_{sys}$	-0.00078 $\pm$ 0.00289$_{stat}$ $\pm$ 0.00054$_{sys}$
0.425	-0.02039 $\pm$ 0.00921$_{stat}$ $\pm$ 0.00268$_{sys}$	-0.00386 $\pm$ 0.00290$_{stat}$ $\pm$ 0.00141$_{sys}$
0.475	-0.02051 $\pm$ 0.01033$_{stat}$ $\pm$ 0.00618$_{sys}$	-0.00040 $\pm$ 0.00322$_{stat}$ $\pm$ 0.00099$_{sys}$
0.525	0.00154 $\pm$ 0.01212$_{stat}$ $\pm$ 0.00226$_{sys}$	0.00019 $\pm$ 0.00375$_{stat}$ $\pm$ 0.00117$_{sys}$
0.575	0.00331 $\pm$ 0.01452$_{stat}$ $\pm$ 0.00329$_{sys}$	0.00276 $\pm$ 0.00448$_{stat}$ $\pm$ 0.00132$_{sys}$
0.625	0.00495 $\pm$ 0.01769$_{stat}$ $\pm$ 0.00541$_{sys}$	-0.00370 $\pm$ 0.00541$_{stat}$ $\pm$ 0.00083$_{sys}$
0.675	-0.00324 $\pm$ 0.02189$_{stat}$ $\pm$ 0.00489$_{sys}$	-0.00179 $\pm$ 0.00668$_{stat}$ $\pm$ 0.00202$_{sys}$
0.725	0.00276 $\pm$ 0.02737$_{stat}$ $\pm$ 0.00473$_{sys}$	-0.00434 $\pm$ 0.00835$_{stat}$ $\pm$ 0.00292$_{sys}$
0.775	0.00582 $\pm$ 0.03486$_{stat}$ $\pm$ 0.00793$_{sys}$	0.00462 $\pm$ 0.01064$_{stat}$ $\pm$ 0.00244$_{sys}$
0.825	0.02758 $\pm$ 0.04667$_{stat}$ $\pm$ 0.01399$_{sys}$	-0.04355 $\pm$ 0.01406$_{stat}$ $\pm$ 0.00441$_{sys}$
0.875	0.01473 $\pm$ 0.06237$_{stat}$ $\pm$ 0.01669$_{sys}$	-0.00822 $\pm$ 0.01862$_{stat}$ $\pm$ 0.00686$_{sys}$
0.925	-0.10895 $\pm$ 0.08460$_{stat}$ $\pm$ 0.03399$_{sys}$	-0.00748 $\pm$ 0.02543$_{stat}$ $\pm$ 0.00184$_{sys}$
0.975	0.15823 $\pm$ 0.11134$_{stat}$ $\pm$ 0.06644$_{sys}$	-0.04725 $\pm$ 0.03357$_{stat}$ $\pm$ 0.00776$_{sys}$

10.1.2 Polarized Structure Functions

Using the unpolarized cross sections listed in Tables 8.39 and 8.40, and the asymmetries listed in Tables 10.1 and 10.2, the Born spin dependent structure functions were formed. Figure 10.2 shows $g_1^{^3\mathrm{He}}$ and $g_2^{^3\mathrm{He}}$ results, with their values listed in Tables 10.3(E = 4.74 GeV) and 10.4 (E = 5.89 GeV). The $g_1^{^3\mathrm{He}}$ ($g_2^{^3\mathrm{He}}$) results of the E06-014 experiment are represented by the red (blue) markers, with the systematic uncertainty (the quadrature sum of the contributions discussed in Section 8.7 and Appendix F) being represented by $\pm$ the colored band at the bottom of the plots. Overlayed on the E06-014 results in Figure 10.2 are selected world ^{3}He data and ^{3}He structure functions calculated using various global analyses [164–166, 168, 169] (gray band).

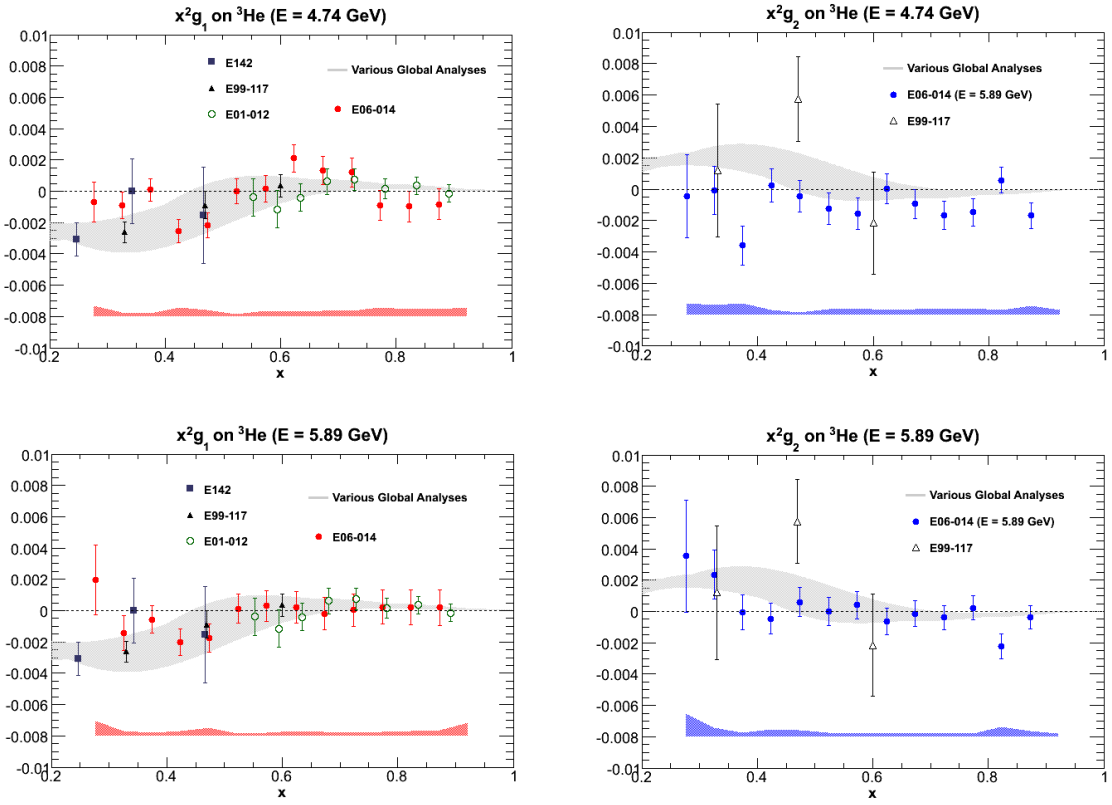

Figure 10.2: Born g_1 (left panels) and g_2 (right panels) polarized structure functions measured on a ^{3}He target plotted against x. The top (bottom) two panels correspond to the E = 4.74 (5.89) GeV data set. The systematic uncertainty is $\pm$ the value given by the colored bands at the bottom of each plot. Overlayed on the g_1 results are ^{3}He data from SLAC E142 [50] (dark blue squares), JLab E99-117 [3] (black triangles), and JLab E01-012 [185] (open green circles). Overlayed on the g_2 results are the results from E99-117 [3] (open triangles). For both the g_1 and g_2 data, the ^{3}He results calculated from various global analyses [164–166, 168, 169] are represented by the gray band.

Table 10.3: Final Born g_1 and g_2 spin structure functions measured on ^{3}He at an incident electron energy of 4.74 GeV.

E = 4.74 GeV		
$\langle x \rangle$	$g_1^{^3\mathrm{He}}$	$g_2^{^3\mathrm{He}}$
0.277	-0.00906 $\pm$ 0.01655$_{stat}$ $\pm$ 0.00861$_{sys}$	-0.00577 $\pm$ 0.03429$_{stat}$ $\pm$ 0.00924$_{sys}$
0.325	-0.00867 $\pm$ 0.00795$_{stat}$ $\pm$ 0.00230$_{sys}$	-0.00074 $\pm$ 0.01445$_{stat}$ $\pm$ 0.00560$_{sys}$
0.374	0.00073 $\pm$ 0.00511$_{stat}$ $\pm$ 0.00162$_{sys}$	-0.02570 $\pm$ 0.00897$_{stat}$ $\pm$ 0.00524$_{sys}$
0.424	-0.01433 $\pm$ 0.00413$_{stat}$ $\pm$ 0.00311$_{sys}$	0.00132 $\pm$ 0.00583$_{stat}$ $\pm$ 0.00162$_{sys}$
0.473	-0.00972 $\pm$ 0.00345$_{stat}$ $\pm$ 0.00179$_{sys}$	-0.00198 $\pm$ 0.00453$_{stat}$ $\pm$ 0.00065$_{sys}$
0.523	-0.00001 $\pm$ 0.00294$_{stat}$ $\pm$ 0.00053$_{sys}$	-0.00463 $\pm$ 0.00366$_{stat}$ $\pm$ 0.00120$_{sys}$
0.574	0.00046 $\pm$ 0.00261$_{stat}$ $\pm$ 0.00112$_{sys}$	-0.00471 $\pm$ 0.00302$_{stat}$ $\pm$ 0.00124$_{sys}$
0.623	0.00540 $\pm$ 0.00231$_{stat}$ $\pm$ 0.00084$_{sys}$	0.00008 $\pm$ 0.00241$_{stat}$ $\pm$ 0.00078$_{sys}$
0.673	0.00293 $\pm$ 0.00203$_{stat}$ $\pm$ 0.00078$_{sys}$	-0.00210 $\pm$ 0.00202$_{stat}$ $\pm$ 0.00074$_{sys}$
0.723	0.00232 $\pm$ 0.00179$_{stat}$ $\pm$ 0.00065$_{sys}$	-0.00323 $\pm$ 0.00173$_{stat}$ $\pm$ 0.00064$_{sys}$
0.773	-0.00149 $\pm$ 0.00160$_{stat}$ $\pm$ 0.00093$_{sys}$	-0.00248 $\pm$ 0.00147$_{stat}$ $\pm$ 0.00070$_{sys}$
0.823	-0.00143 $\pm$ 0.00144$_{stat}$ $\pm$ 0.00071$_{sys}$	0.00084 $\pm$ 0.00123$_{stat}$ $\pm$ 0.00040$_{sys}$
0.873	-0.00110 $\pm$ 0.00128$_{stat}$ $\pm$ 0.00064$_{sys}$	-0.00221 $\pm$ 0.00108$_{stat}$ $\pm$ 0.00074$_{sys}$
0.921	-0.00125 $\pm$ 0.00114$_{stat}$ $\pm$ 0.00067$_{sys}$	0.00029 $\pm$ 0.00086$_{stat}$ $\pm$ 0.00033$_{sys}$

Table 10.4: Final Born g_1 and g_2 spin structure functions measured on ^{3}He at an incident electron energy of 5.89 GeV.

E = 5.89 GeV		
$\langle x \rangle$	$g_1^{^3\mathrm{He}}$	$g_2^{^3\mathrm{He}}$
0.277	$0.02553 \pm 0.02891_{stat} \pm 0.01224_{sys}$	$0.04620 \pm 0.04674_{stat} \pm 0.01927_{sys}$
0.325	$-0.01345 \pm 0.01052_{stat} \pm 0.00285_{sys}$	$0.02233 \pm 0.01486_{stat} \pm 0.00559_{sys}$
0.374	$-0.00404 \pm 0.00626_{stat} \pm 0.00158_{sys}$	$-0.00044 \pm 0.00789_{stat} \pm 0.00168_{sys}$
0.424	$-0.01125 \pm 0.00482_{stat} \pm 0.00170_{sys}$	$-0.00260 \pm 0.00550_{stat} \pm 0.00258_{sys}$
0.473	$-0.00788 \pm 0.00401_{stat} \pm 0.00242_{sys}$	$0.00263 \pm 0.00417_{stat} \pm 0.00174_{sys}$
0.523	$0.00045 \pm 0.00343_{stat} \pm 0.00062_{sys}$	$-0.00001 \pm 0.00331_{stat} \pm 0.00098_{sys}$
0.574	$0.00091 \pm 0.00297_{stat} \pm 0.00066_{sys}$	$0.00123 \pm 0.00267_{stat} \pm 0.00068_{sys}$
0.623	$0.00049 \pm 0.00260_{stat} \pm 0.00079_{sys}$	$-0.00160 \pm 0.00218_{stat} \pm 0.00052_{sys}$
0.673	$-0.00042 \pm 0.00230_{stat} \pm 0.00051_{sys}$	$-0.00031 \pm 0.00182_{stat} \pm 0.00057_{sys}$
0.723	$0.00007 \pm 0.00201_{stat} \pm 0.00042_{sys}$	$-0.00076 \pm 0.00151_{stat} \pm 0.00042_{sys}$
0.773	$0.00040 \pm 0.00179_{stat} \pm 0.00040_{sys}$	$0.00038 \pm 0.00128_{stat} \pm 0.00037_{sys}$
0.823	$0.00032 \pm 0.00165_{stat} \pm 0.00046_{sys}$	$-0.00330 \pm 0.00119_{stat} \pm 0.00090_{sys}$
0.873	$0.00027 \pm 0.00150_{stat} \pm 0.00044_{sys}$	$-0.00048 \pm 0.00097_{stat} \pm 0.00045_{sys}$
0.921	$-0.00188 \pm 0.00143_{stat} \pm 0.00096_{sys}$	$0.00039 \pm 0.00089_{stat} \pm 0.00026_{sys}$

10.2 Matrix Elements

10.2.1 d_2^n

Rather than extracting the neutron information from the asymmetries or spin structure functions and then evaluating d_2^n, E06-014 opted to extract the neutron information from the ^{3}He d_2 integral. When integrating nuclear target quantities (such as d_2), one must be sure not to include the quasielastic region (which for E06-014 kinematics, the quasielastic peak was near $x \approx 0.90$). Thus, the x integration range considered for the d_2 integral covered $0.25 \leq x \leq 0.90$ (the first and last x values at the bin edges), which correspond to a mean x range of $0.277 \leq \langle x \rangle \leq 0.873$. In addition to evaluating d_2 over the entire measured x range, the data could also be split into the DIS and resonance regions.

The d_2 integrand was formed for each x-bin using the unpolarized cross sections (Tables 8.39 and 8.40) and double spin asymmetries (Tables 10.1 and 10.2) as shown in Equation 4.1. The d_2 integrand was then integrated over the different x ranges to produce two ^{3}He d_2 measurements (one for each beam energy) in the three regions described above (DIS+resonance, DIS, and resonance). The neutron d_2 was then extracted using the method defined in Section 8.6 and values listed in Table 8.46. The polarization of the proton and neutron, which make up the ^{3}He nucleus, that was used in the neutron extraction is given by Equation 8.76. The $d_2^{^3\mathrm{He}}$ and d_2^n results obtained for the various x integration ranges are listed in Table 10.5. The systematic uncertainty associated with the values in Table 10.5 are the quadrature sum of the individual contributions listed in Table F.9(with the exception of the low-x contribution), which are discussed further in Appendix F.

Figure 10.3 shows the DIS and resonance d_2^n data listed in Table 10.5, where the DIS (solid blue circles) and resonance contributions (open red circles) are plotted against Q^2. Plotted for comparison are world d_2^n data from E155x [54], E155x and E99-117 combined data [54, 57], E01-012 [58], E94010 [56], and RSS [39]. Additionally, the MAID 2007

Table 10.5: Results of $d_2^{^3\mathrm{He}}$ and d_2^n.

Region	$\langle Q^2 \rangle$ [GeV^2]	x Range	$\langle x \rangle$ Range	$d_2^{^3\mathrm{He}}$	d_2^n
DIS + Res.	3.21	0.25-0.90	0.277-0.873	-0.00227 $\pm$ 0.00072$_{stat}$	-0.00261 $\pm$ 0.00079$_{stat}$ $\pm$ 0.00048$_{sys}$
DIS + Res.	4.32	0.25-0.90	0.277-0.873	0.00015 $\pm$ 0.00076$_{stat}$	0.00004 $\pm$ 0.00083$_{stat}$ $\pm$ 0.00037$_{sys}$
DIS	2.59	0.25-0.50	0.277-0.473	-0.00127 $\pm$ 0.00057$_{stat}$	-0.00135 $\pm$ 0.00063$_{stat}$ $\pm$ 0.00037$_{sys}$
DIS	3.67	0.25-0.50	0.277-0.574	0.00061 $\pm$ 0.00069$_{stat}$	0.00063 $\pm$ 0.00075$_{stat}$ $\pm$ 0.00029$_{sys}$
Res	4.17	0.55-0.90	0.574-0.873	-0.00080 $\pm$ 0.00040$_{stat}$	-0.00100 $\pm$ 0.00044$_{stat}$ $\pm$ 0.00023$_{sys}$
Res	5.99	0.65-0.90	0.673-0.873	-0.00039 $\pm$ 0.00028$_{stat}$	-0.00048 $\pm$ 0.00031$_{stat}$ $\pm$ 0.00012$_{sys}$

model [48] and lattice QCD prediction [66] are also plotted. The d_2^n values measured in the resonance region are displayed as open markers, whereas d_2^n measured in the DIS region are displayed as filled markers. The E06-014 measured d_2^n central values in the DIS region tended to be slightly larger in magnitude than those measured in the resonance region. The DIS measurements were found to straddle zero, while the resonance measurements surrounded the lattice QCD prediction.

10.2.1.1 Complete d_2^n Integral

Splitting the d_2^n measurements into its DIS and resonance contributions, results in much of the integral being unaccounted for. Therefore to accurately compare to the world data and the lattice QCD prediction, the full d_2^n integral needed to be evaluated. A majority of the d_2^n integral was covered by E06-014 when combining the DIS and resonance data, which corresponds to covering an x range of 0.25 to 0.90 (Table 10.5). In order to compute the unmeasured low-x contribution to the d_2^n integral, which should be small due to the x^2 weighting of the d_2^n integrand, $x^2 g_1^n$ and $x^2 g_2$ world data was fit over a x range of 0.02 $\leq x \leq 0.25$, with a third order polynomial. These fits were then combined to form the d_2^n integrand and were then integrated over to compute $(d_2^n)_{low-x}$. Data from E142 [50], E143 [51], E154 [52], and E97-103 [55] was used to parameterize $x^2 g_1$ as a function x. The determination of $x^2 g_2$ parameterized as a function of x was determined by fitting data from E97-103, E155[53], and E155x [54]. The fit results are shown in Figure 10.4. Although the SLAC E155 g_2^n data have large uncertainties, they played a minimal role in determining the $x^2 g_2$ parameterization, due to uncertainty weighted fitting (smaller uncertainties contribute more than large uncertainties). These parameterizations were then combined and integrated over to evaluate the low x d_2^n contribution according to:

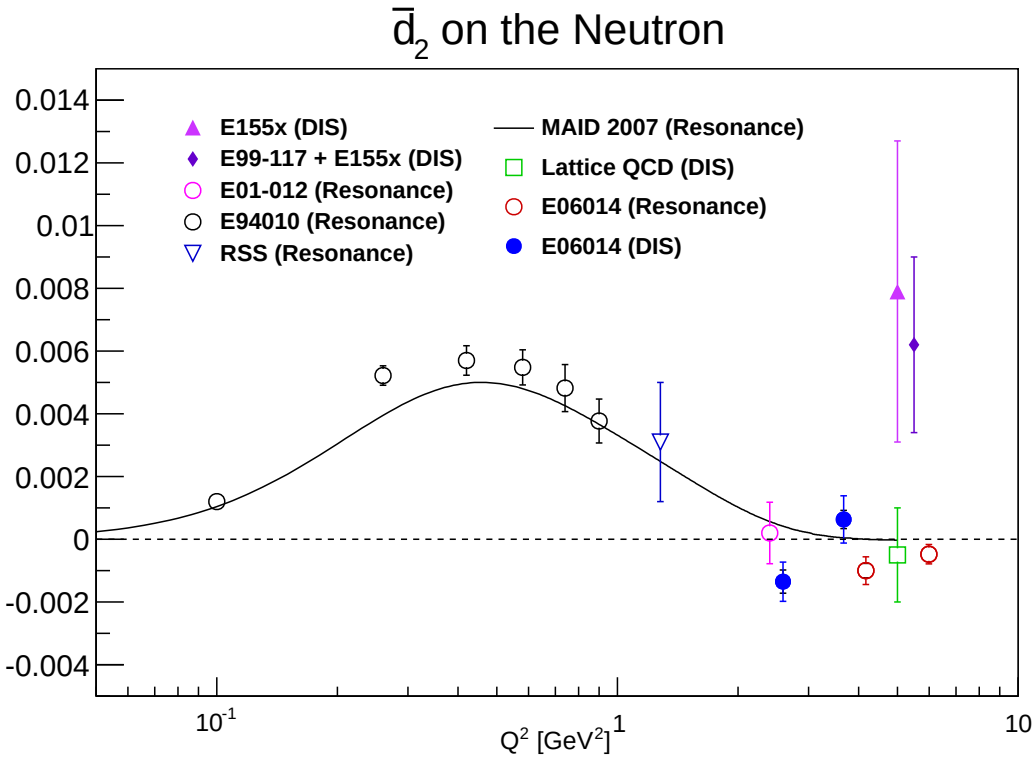

Figure 10.3: E06-014 measured partial d_2^n in the DIS (filed blue circles) and resonance (open red circles) regions plotted against Q^2. The black error bar ticks on the E06-014 measurements represents the systematic uncertainty, while the colored error bar ticks represent the statistical uncertainties. The open markers represent d_2^n measured in the resonance region and filled markers represent DIS measurements. The world data error bars are the quadratic sum of the statistical and systematic uncertainties. There are no elastic contributions included in these data or models.

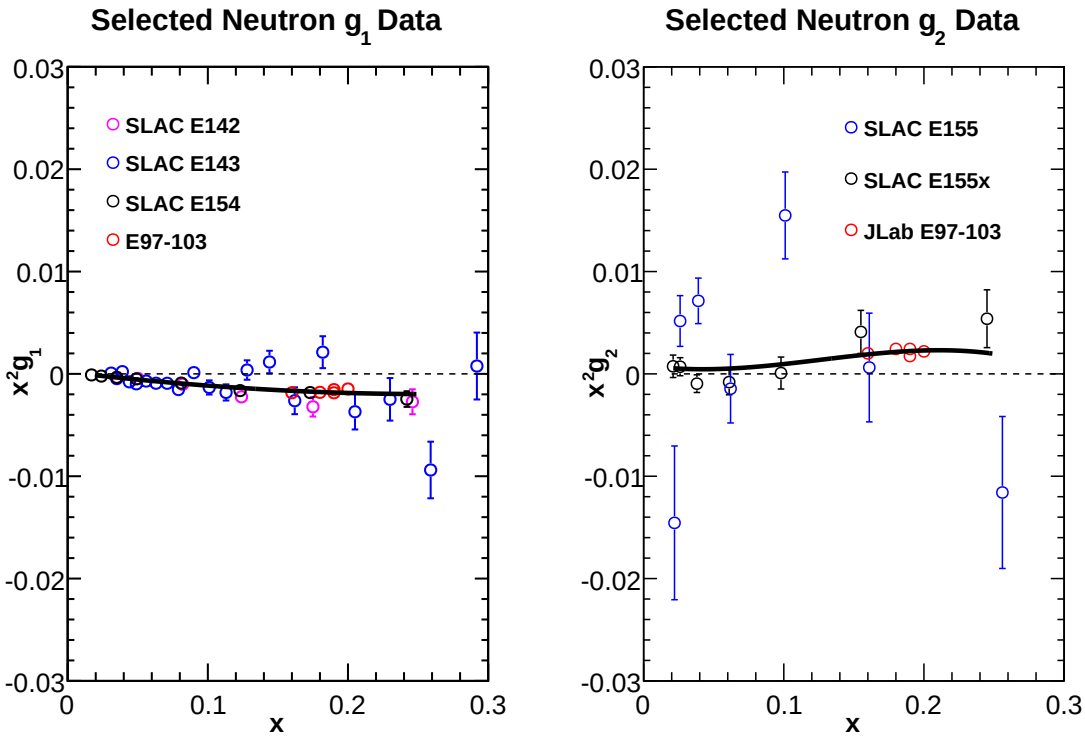

Figure 10.4: Fit results to world g_1 and g_2 data at low x used to evaluate d_2^n over the x range of 0.02 to 0.25.

$$\left(d_2^n\right)^{low-x} = \int_{0.02}^{0.25} 2\left(x^2 g_1\right)^{fit} + 3\left(x^2 g_2\right)^{fit} dx, \tag{10.1}$$

were $\left(x^2 g_1\right)^{fit}$ and $\left(x^2 g_2\right)^{fit}$ are the parameterized fits to world data.

The computation of the d_2^n contribution at low x is listed in Table 10.6, along some of the characteristics from the g_1 and g_2 world data fits. The uncertainty on the low x d_2^n contribution was computed by considering the world data's statistical and systematic uncertainties. The statistical uncertainty was computed as

$$\delta\tilde{g}_{k\,stat}^2 = \left(\sum_i \frac{1}{\delta\tilde{g}_{ki}^{\,2}}\right)^{-1}, \tag{10.2}$$

where the sum runs over all data points from all of the experiments that were included in the fits, $\tilde{g}_k = x^2 g_k$, with $k = 1$ or 2 corresponding to the either g_1 or g_2 structure functions, and δg_k is the experimental statistical uncertainty. The systematic uncertainties for the fits were determined by taking the average systematic uncertainty of data for each experiment that was included in the fits, which can be expressed as

$$\left(\delta\left\langle\tilde{g}_k\right\rangle_{sys}\right)_l = \frac{1}{N}\sum_{j=1}^{N}\left(\tilde{g}_k\right)_j^{sys}, \tag{10.3}$$

where N is number of data points in experiment l, and $\left(\tilde{g}_k\right)_j^{sys}$ is the systematic uncertainty of the j^{th} data point from experiment l. Since the systematic uncertainties from experiment to experiment are independent, they can be combined as

$$\left(\delta\tilde{g}_k\right)_{sys}^2 = \frac{\sum_i w_i^2\left(\left\langle\delta\tilde{g}_k\right\rangle_{sys}\right)_i}{\sum_i w_i^2}, \tag{10.4}$$

where w_i is the total statistical uncertainty defined in Equation 10.2 for experiment i. The statistical and systematic uncertainties on $x^2 g_1$ and $x^2 g_2$ are listed in Table 10.6 and

were then propagated to the low x d_2^n contribution through the following equations:

$$(\delta d_2^n)^{stat}_{low-x} = \sqrt{4\left(\delta\tilde{g}_1\right)^2_{stat} + 9\left(\delta\tilde{g}_2\right)^2_{stat}} \quad (10.5)$$

$$(\delta d_2^n)^{sys}_{low-x} = \sqrt{4\left(\delta\tilde{g}_1\right)^2_{sys} + 9\left(\delta\tilde{g}_2\right)^2_{sys}} \quad (10.6)$$

$$(\delta d_2^n)^{total}_{low-x} = \sqrt{\left[(\delta d_2^n)^{stat}_{low-x}\right]^2 + \left[(\delta d_2^n)^{sys}_{low-x}\right]^2}. \quad (10.7)$$

As it turns out, one of the largest systematic uncertainties ($\approx 5 \times 10^{-4}$) applied to the d_2^n matrix element is due to the uncertainty on the low x contribution (Appendix F).

In addition to computing the contribution to d_2^n from the unmeasured low x region (0.02 $\leq$ x $\leq$ 0.25), the contribution to d_2^n from the high x region also needs to be included. E06-014 was able to measure up to x = 0.90 (corresponds to $< x >$ = 0.873 bin). As a result, only the elastic contribution at $x = 1$ was added to d_2^n integral. The elastic form factors were evaluated using the Galster parameterization and the dipole model, which allowed for the elastic d_2^n contribution ($(d_2^n)^{el}$) to be computed. A more detailed analysis of the elastic d_2^n contribution can be found in Appendix G. The elastic contribution to d_2^n was found to be negative and on the same order of magnitude as the measured values listed in Table 10.5. The elastic contribution to the d_2^n integral can be found in Table G.1 of Appendix G.

Adding the calculated low (Table 10.6) and high (Table G.1) x contributions to the measured d_2^n (Table 10.5) matrix elements, the full d_2^n integral can be computed for each of the two electron beam energies, which are listed in Table 10.7. Note that when adding the low x contribution to the E06-014 measured d_2^n matrix element, the Q^2 of the low x contribution is not considered (i.e. adding the low x contribution does not change E06-014 measured d_2^n mean Q^2 value). The top panel of Figure 10.5 shows the d_2^n matrix element results with no elastic contributions. E06-014's measured d_2^n matrix elements in the combined DIS and

Table 10.6: Results of low x contributions to d_2^n. The uncertainties on $x^2 g_1$ and $x^2 g_2$ are given by Equations 10.2 and 10.4. The uncertainties listed for d_2^n are given by Equations 10.5 and 10.6. The total uncertainty listed in the table is the quadrature sum of the statistical and systematic uncertainties.

Quantity	$\langle Q^2 \rangle\ [GeV^2]$	χ^2/N_{dof}	Value	Stat. Error	Sys. Error	Total
$\left(x^2 g_1\right)^{low-x}$	2.46	1.29	NA	2.16×10^{-5}	2.50×10^{-4}	2.51×10^{-4}
$\left(x^2 g_2\right)^{low-x}$	1.08	2.69	NA	1.30×10^{-4}	3.50×10^{-4}	3.73×10^{-4}
$(d_2^n)^{low-x}$	1.77	NA	3.77×10^{-4}	$3.90 \times 10^{-4}_{stat}$	$4.30 \times 10^{-4}_{sys}$	5.80×10^{-4}

Table 10.7: E06-014 results for the full d_2^n integral. This includes contributions from the unmeasured low (Table 10.6) and high (Table G.1) x regions.

Beam Energy [GeV]	$\langle Q^2 \rangle$ [GeV^2]	d_2^n (full integral)
4.74	3.21	-0.00331 $\pm$ 0.00079$_{stat}$ $\pm$ 0.00075$_{sys}$
5.89	4.32	-0.00027 $\pm$ 0.00083$_{stat}$ $\pm$ 0.00069$_{sys}$

resonance regions are shown by the blue filled circles, and the red filled circles show the combined DIS and resonance data with the low x contribution included. However, for a proper comparison to the lattice QCD prediction, the high x contribution also needs to be included. Adding the elastic contribution (shown by dashed red line in bottom panel of Figure 10.5) to all of the data and the MAID results (lattice QCD prediction already has $x = 1$ contribution built into its prediction) shown in the upper panel of Figure 10.5, the bottom panel of Figure 10.5 is produced. The elastic contribution is clearly the dominate effect, especially at lower Q^2 ($\approx< 1GeV^2$), resulting in all (but the SLAC E155x data) data becoming negative. The E06-014 d_2^n data seems to follow the MAID trend, even though the MAID model includes only resonance contributions. E06-014's d_2^n measurements are also consistent with E01-012's d_2^n measurement and the lattice QCD prediction. The d_2^n matrix elements measured by E06-014 are smaller than those measured by SLAC E155x. The d_2^n value measured by E06-014 at $\langle Q^2 \rangle$ = 4.32 GeV^2 was found to be consistent with zero, while d_2^n measured at $\langle Q^2 \rangle$ = 3.21 GeV^2 was found to be slightly negative.

10.2.1.2 Target Mass Correction Effect

The final contribution that must be considered are the target mass corrections (Section 2.5), which arise from having a finite Q^2. The effect of including TMC in the d_2 evaluation was studied by comparing the $d_2^{^3\mathrm{He}}$ values evaluated using the CN and Nachtmann moments (Equation 2.43). Table 10.8 lists the results of the measured $d_2^{^3\mathrm{He}}$ using both the CN and

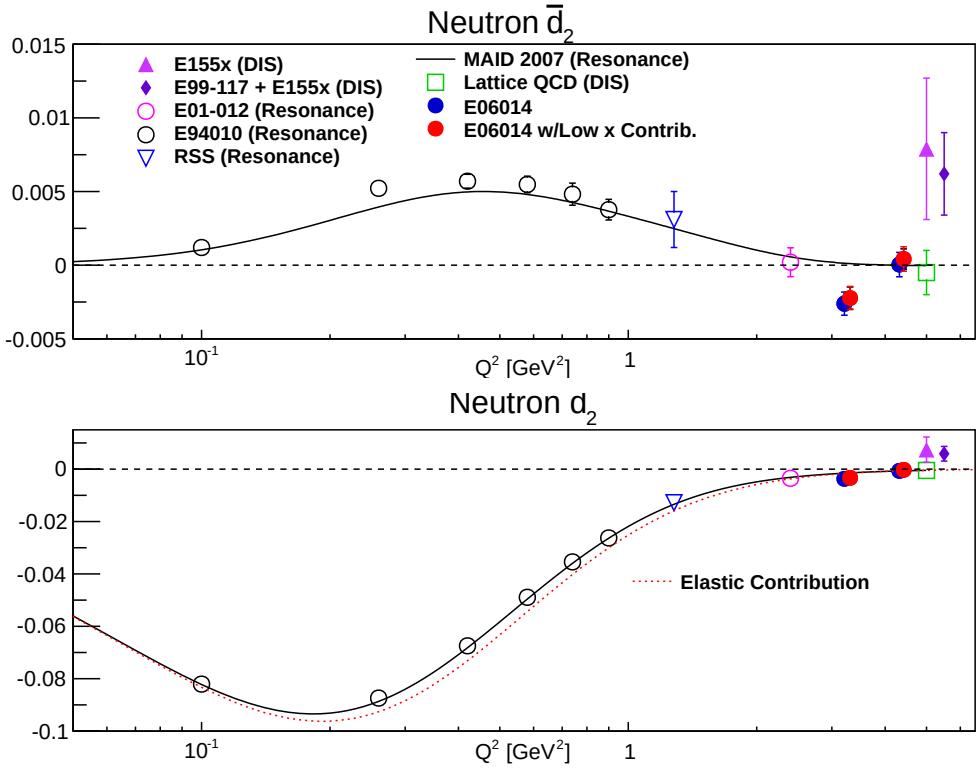

Figure 10.5: Top panel: World $\bar{d}_2^n$ (no elastic contribution) data plotted against Q^2. The E06-014 measured d_2^n with the low x contribution added (red markers) are offset by +0.5 GeV^2 in Q^2 for clarity. The black error bar ticks on the E06-014 measurements represents the systematic uncertainty, while the colored error bar ticks represent the statistical uncertainties. The world data error bars represent the quadrature sum of the statistical and systematic uncertainties. Bottom panel: This plot shows the effect of adding the elastic contribution to the all data (including the MAID model, but excluding the lattice QCD prediction).

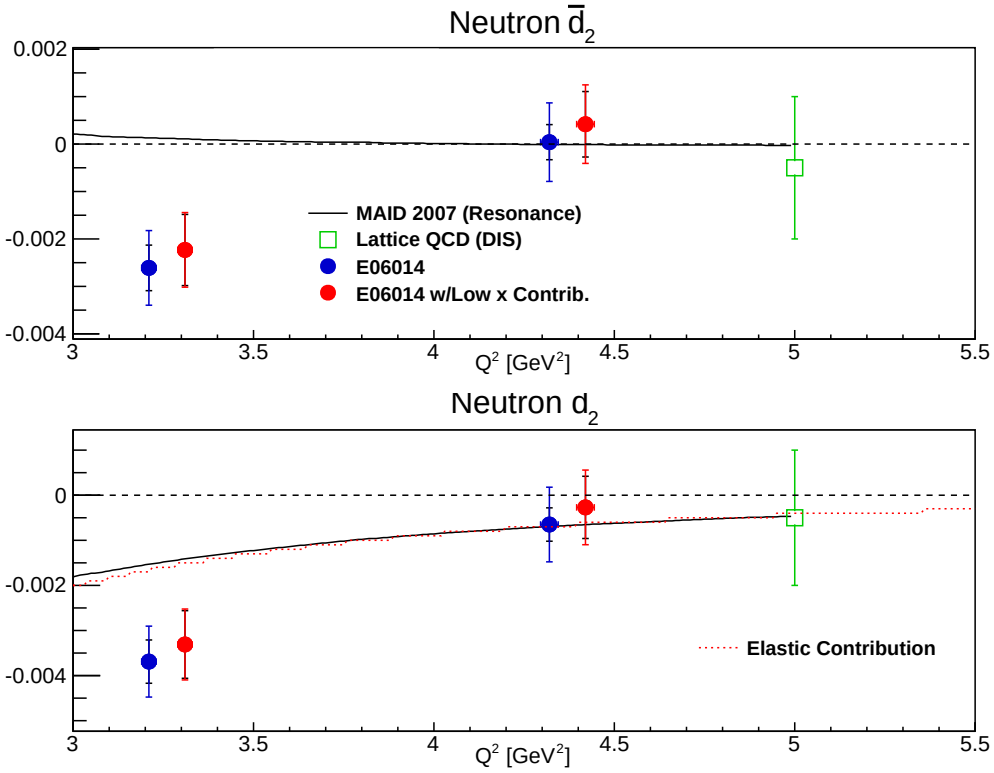

Figure 10.6: Zoomed in plot of Figure 10.5.

Nachtmann moments. In general, when using the Nachmann moments, the absolute size of $d_2^{^3\mathrm{He}}$ tends to be smaller than that found using the CN moments. The difference between the CN and Nachmann computed d_2 turns out to be rather small, about an order of magnitude smaller than the measured $d_2^{^3\mathrm{He}}$ matrix element using the CN moments, and well within the the experiment's measured precision (statistical and systematic). As a result the TMC were not implemented in this analysis.

10.2.2 a_2^n

As was discussed in Section 2.4, the twist-2 matrix element a_2^n is needed if one wants to extract f_2^n, and ultimately decompose the Lorentz color force into its electric and magnetic components, as given by Equation 2.41. The a_2^n matrix element was computed by integrating various global analyses (DSSV, BBS, GS, DNS and LSS [164–169]) over the x range of 0.02-0.90[1], at Q^2 values of 3.21 and 4.32 GeV^2. The average of the results from the five global analyses for each Q^2, was taken as the a_2^n result. The spread of the a_2^n results from the global analyses was assigned as the uncertainty of the calculation. Table 10.9 summarizes the a_2^n results at each of E06-014's mean Q^2 values.

The elastic contribution to a_2^n, found in Table G.1, was added to the average a_2^n results listed in Table 10.9. The final values of a_2^n used in the E06-014 color force analysis can be found in Table 10.10.

10.2.3 f_2^n

With a_2^n and d_2^n matrix elements evaluated, one can now proceed to extract the twist-4 matrix element, f_2^n, as discussed in Section 2.4.3. An updated analysis following in the footsteps of the analysis done by Z.E. Meziani *et al.* [26] and Xiangdong Ji and W. Melnitchouk [186]

[1] a_2^n was also computed at other integral ranges of x = 0.001-0.90 and 0.001-0.99, both ranges showed consistent results relative to the a_2^n value computed in the x range of 0.02-0.90.

Table 10.8: Effect of target mass corrections on the d_2 matrix element computed from ^{3}He structure functions.

$\langle Q^2 \rangle$ [GeV^2]	$d_2^{^3\mathrm{He}}$ (CN Moment)	$d_2^{^3\mathrm{He}}$ (Nachtmann Moment)	$\Delta d_2^{^3\mathrm{He}}$ [CN - Nachtmann]
3.21	-0.00227	-0.00196	0.00031
4.32	0.00015	0.00012	0.00003

Table 10.9: a_2^n results from various analyses.

Q^2 = 3.21 GeV^2	
Global Analysis	a_2^n
DSSV	0.00024
BBS	0.00001
GS	-0.00096
DNS	0.00003
LSS	-0.00038
Average	-0.00021 $\pm$ 0.00120$_{sys}$
Q^2 = 4.32 GeV^2	
DSSV	0.00023
BBS	0.00001
GS	-0.00090
DNS	0.00003
LSS	-0.00035
Average	-0.00020 $\pm$ 0.00113$_{sys}$

Table 10.10: a_2^n values, with elastic contributions added, that were used in E06-014's extraction of f_2^n.

Q^2 [GeV^2]	a_2^n (with elastic contribution)
3.21	0.00057 $\pm$ 0.00120$_{sys}$
4.32	0.00015 $\pm$ 0.00113$_{sys}$

was performed. Γ_1^n results from HERMES [187], SMC [49], JLAB RSS [39], JLAB E94-010 [13, 56], SLAC E143 [51], SLAC E142 [50], and SLAC E154 [52] were used in the updated E06-014 f_2^n extraction analysis. Γ_1^n depends on the integration over the entire x range ($0 \leq x \leq 1$), as a result the measured results from the experiments above needed to be extrapolated to the lower and higher unmeasured x regions. These extrapolations can be carried out in several different ways, as discussed in Reference [51]. To ensure consistent results amongst the data, the low and high x extrapolations were reanalyzed using the same method for each experiment, with the exception of HERMES and JLab data, which already used the extrapolation method that is discussed below.

To calculate the Γ_1 low x contribution, the lowest three x bins of the experiment's measured g_1^n data was fitted with a constant line. The constant fit result (A) was then integrated from the lowest measured g_1^n x bin (x') to a minimum x value (x_{min}). Thus the low x contribution was defined as

$$(\Gamma_1^n)_{low-x} = \int_{x_{min}}^{x'} A dx = A \cdot (x' - x_{min}) \,, \tag{10.8}$$

where x_{min} is defined for each Q^2 by W^2 = 1000 GeV^2. However for the SMC data, which is above W^2 = 1000 GeV^2, x_{min} = 0.003.

The high x Γ_1^n contribution was evaluated by fitting the experiments two highest measured g_1^n x bins with the function $f = A\,(1-x)^3$, where A was free to float. The high x contribution to Γ_1^n was then evaluated as

$$(\Gamma_1^n)_{high-x} = \int_{x'}^{x_{max}} A\,(1-x)^3\,dx = \frac{A}{4}\left[(1-x')^4 - (1-x_{max})^4\right], \tag{10.9}$$

where x' is the experiments highest measured g_1^n x bin, and x_{max} is defined for each Q^2

by evaluating x at the pion production threshold (W = 1.12 GeV).

The final contribution that needed to be added to the measured Γ_1^n, was the elastic contribution at $x = 1$. The elastic Γ_1^n contribution $\left(\Gamma_1^n\right)_{el}$ was determined using elastic form factors, which were evaluated using the Galster parameterization and the dipole model (Appendix G). The size of the elastic contribution can be seen in Figure G.1, and was added to all of the world data. The left panel of Figure 10.7 shows the reanalyzed Γ_1^n world data, which includes the low and high x extrapolations, and the elastic contributions.

If one hopes to extract the higher twist contributions, the twist-2 contribution must first be removed. Using Equation 2.37, the Γ_1^n data can be expanded in a power series of Q^{-2}, revealing higher twist contributions. The twist-2 contribution (μ_2) can be calculated and subtracted from Γ_1^n, where the difference $\Gamma_1^n - \mu_2 \equiv \Delta\Gamma_1^n$ leaves only higher twist contributions. Plotting $\Delta\Gamma_1^n$ as a function of $\frac{1}{Q^2}$ and fitting the data, allows for the extraction of the higher twist contributions μ_4 and μ_6.

The twist-2 contribution was calculated using Equation2.38. The Wilson coefficients [29] depend on the strong coupling constant $\alpha_s\left(Q^2\right)$. The parameterization of α_s as a function of Q^2 depends on a few parameters, such as the number of colors (N_f), the number of α_s loop corrections (N_{loop}), and the QCD energy (Λ_{QCD}). The parameterization of α_s used in the E06-014 analysis followed that used by Reference [186], which included:

- N_f = 3
- N_{loop} = 3
- $\alpha_s\left(1GeV^2\right)$ = 0.45 $\pm$ 0.05, this corresponds to Λ_{QCD} = 315 MeV.

In addition to the Wilson coefficients, the axial charges were also needed to calculate the twist-2 contributions. The axial charges g_A [188] and a_8 [188] were measured in neutron β and weak hyperon decay experiments, respectively. The flavor singlet axial charge, however

Table 10.11: List of charges used in the E06-014 f_2^n extraction.

Charge	Value	Uncertainty
g_A	1.2670	0.0035
a_8	0.579	0.025
$\Delta\Sigma$	0.375	0.052

needed to be extracted. At large Q^2 the higher twist contributions to Γ_1^n should be small or negligible, due to the Q^{-2} suppression. Thus at large Q^2 only the twist-2 contribution should contribute significantly to Γ_1^n, leading to

$$\Gamma_1^n\left(Q^2\right) = \mu_2 = C_{ns}\left(Q^2\right)\left(-\frac{1}{12}g_A + \frac{1}{36}a_8\right) + C_s\left(Q^2\right)\frac{1}{9}\Delta\Sigma, \tag{10.10}$$

where the singlet axial charge ($\Delta\Sigma$) can then extracted. $\Delta\Sigma$ was determined by combining the three highest Q^2 Γ_1^n measurements. These included measurements form E154 (Q^2 = 5 GeV^2), SMC (Q^2 = 10 GeV^2), and HERMES (Q^2 = 6.5 GeV^2), resulting in a statistically weighted combined Q^2 of 5.77 GeV^2 and Γ_1^n = -0.03851 $\pm$ 0.00535. These values were then used in Equation 10.10 to extract $\Delta\Sigma$, which was found to be 0.375 $\pm$ 0.052. This $\Delta\Sigma$ value is in excellent agreement with that found in Reference [189]. The list of the axial charge values and their uncertainties used in the E06-014 f_2^n extraction analysis can be found in Table 10.11.

With all of the axial charges calculated, the twist-2 contribution can now be calculated as a function of Q^2. The left panel of Figure 10.7 shows the Γ_1^n measurements that were used in the extraction analysis. The error bars on these measurements are the quadrature sums of the experiments statistical and systematic uncertainties. The red line within the yellow band is the central value of the twist-2 contribution, and the band width represents the uncertainty in the twist-2 contribution, resulting from the uncertainties associated with

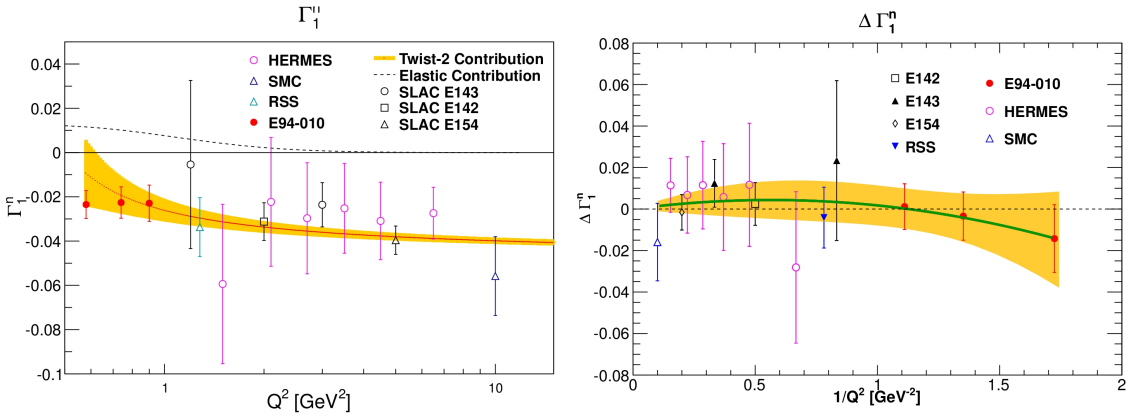

Figure 10.7: Left panel: World Γ_1^n data with unmeasured low and high x, and elastic contributions. The world data error bars include the statistical and systematic uncertainties summed in quadrature. The yellow band shows the calculated twist-2 contribution, with the red central line representing the central value. The band is due to uncertainties on the flavor charges and α_s. Right panel: Plots the twist-2 subtracted world Γ_1^n data against $\frac{1}{Q^2}$. The green line shows the two parameter fit that was used to extract f_2^n, with the yellow band representing the uncertainty in the fit.

the axial charges and α_s. The dashed line shows the size of the Γ_1^n elastic contribution.

The twist-2 contribution was then subtracted from the Γ_1^n data leaving behind only the higher twist contributions. $\Delta\Gamma_1^n$ was then plotted against $\frac{1}{Q^2}$. This distribution was then fitted using a two parameter fit. The two parameter fit was given as

$$f\left(\frac{1}{Q^2}\right) = \frac{M_n^2}{9}\left(a_2^n + 4d_2^n + 4A\right)\frac{1}{Q^2} + \frac{B}{Q^4}, \tag{10.11}$$

where the fit parameters $A = f_2^n$ and $B = \mu_6$ were allowed to float. This fit was done on both the $\langle Q^2 \rangle$ = 3.21 and 4.32 GeV^2 data sets, with a neutron mass value of M_n = 0.939 GeV, a_2^n values taken from Table 10.10, and d_2^n values taken from Table 10.7. The $\Delta\Gamma_1^n$ plotted against Q^{-2} is shown in Figure 10.7, with the two parameter fit shown by the green line. The results of the fit and f_2^n extraction are summarized in Table 10.12. The

Table 10.12: Summary of E06-014's f_2^n extraction.

$\langle Q^2 \rangle = 3.21 GeV^2$	
Quantity	Value
μ_4 [GeV^2]	0.01546 ± 0.01543
μ_6 [GeV^4]	-0.01372 ± 0.01183
f_2^n	$0.04263 \pm 0.00079_{stat} \pm 0.03938_{sys}$
$\langle Q^2 \rangle = 4.32 GeV^2$	
Quantity	Value
μ_4 [GeV^2]	0.01546 ± 0.01543
μ_6 [GeV^4]	-0.01372 ± 0.01183
f_2^n	$0.03970 \pm 0.00083_{stat} \pm 0.03938_{sys}$

statistical uncertainty associated with f_2^n contains the statistical uncertainty from d_2^n, and the systematic uncertainties contain the contributions from the f_2^n fit, and the a_2^n and d_2^n systematic uncertainties. The uncertainty due to the f_2^n fit is the dominate uncertainty, which is about an order of magnitude larger than the other uncertainties. The uncertainties on μ_4 and μ_6 are due to the fitting only. It was found that f_2^n is significantly larger than d_2^n at both $\langle Q^2 \rangle$ = 3.21 and 4.32 GeV^2.

10.3 Color Forces

With the d_2^n matrix elements measured (Table 10.7) and f_2^n matrix elements extracted (Table 10.12), the Lorentz color force can be decomposed into its color electric and magnetic components via Equation 2.41. Table 10.13 lists the evaluated color forces. The uncertainties in Table 10.13 include the d_2^n and f_2^n matrix elements' statistical and systematic uncertainties. At both $\langle Q^2 \rangle$ measured by E06-014, it was found that the electric and magnetic color forces were approximately equal with opposite sign. This relationship between F_E and F_B will lead to a small Lorentz color force (sum of color electric and magnetic components), which was seen through the measurment of a small d_2^n matrix element, and a relatively large

extracted f_2^n matrix element.

Table 10.13: Results of the magnetic and electric Lorentz color force components extracted from E06-014 data.

$\langle Q^2 \rangle$ [GeV^2]	F_E [GeV^2]	F_B [GeV^2]
3.21	-0.0053 $\pm$ 0.0003$_{stat}$ $\pm$ 0.0058$_{sys}$	0.0082 $\pm$ 0.0005$_{stat}$ $\pm$ 0.0058$_{sys}$
4.32	-0.0058 $\pm$ 0.0003$_{stat}$ $\pm$ 0.0058$_{sys}$	0.0060 $\pm$ 0.0005$_{stat}$ $\pm$ 0.0058$_{sys}$

CHAPTER 11

CONCLUSION

The E06-014 experiment scattered longitudinally polarized electrons from a longitudinally and transversely polarized ^{3}He target. The DSAs and unpolarized cross sections were measured by detecting the scattered electrons. Through the use of the cross sections and DSAs, the neutron d_2 matrix elements were evaluated. The Q^2 = 3.21 GeV^2 measurement was found to be slightly negative, while the Q^2 = 4.32 GeV^2 measurement was found to be consistent with zero. Both of the measurements were found to be consistent with the lattice QCD prediction [66]. Using the newly measured d_2^n matrix elements, the twist-4 matrix elements (f_2^n) were extracted and found to be much larger than the d_2^n matrix elements at both $\langle Q^2 \rangle$. Through the combinations of d_2^n and f_2^n, the electric and magnetic color forces were extracted. The color forces were found to be on the order of 10^{-3} GeV^2, and were roughly the same magnitude with opposite signs.

REFERENCES

[1] D. Binosi and L. TheuBl. Jaxodraw: A graphical user interface for drawing Feymman diagrams. *Comp. Phys. Comm.*, 161:76, (2004).

[2] F. Halzen and A. D. Martin. *Quarks and Leptons*. John Wiley and Sons Inc., (1984).

[3] X. Zheng. *Precision Measurement of Neutron Spin Asymmetry A_1^n at Large x_{Bj} Using CEBAF at 5.7 GeV*, Ph.D. thesis, Massachusetts Institute of Technology, (2002).

[4] Anthony W. Thomas and Wolfram Weise. *The Structure of the Nucleon*. Wiley-VCH, Berlin, (2001).

[5] A. deShalit and H. Feshbach. *Theoretical Nuclear Physics Volume I: Nuclear Structure*. Wiley Classics Library Edition, (1990).

[6] A. Efremov M. Anselmino and E. Leader. The theory and phenomenology of polarized deep inelastic scattering. *Phys. Rep.*, 261:1, (1995).

[7] J. D. Bjorken and E. A. Paschos. Inelastic electron-proton and γ-proton scattering and the structure of the nucleon. *Phys. Rev.*, 185:1975, (1969).

[8] C. G. Callon and D. J. Gross. High-energy eelctroproduction and the constitution of the eelctric current. *Phys. Rev. Lett.*, 22:156, (1969).

[9] J. Beringer et al.(Particle Data Group). *Phys. Rev. D*, 86:010001, (2012).

[10] R. P. Feynman. *Phys. Rev. Lett.*, 23:1415, (1969).

[11] K. G. Wilson. *Phys. Rev.*, 179:1499, (1969).

[12] A. V. Manohar. *hep-ph/9204208*, (1992).

[13] K. Slifer. *Spin structure of ^{3}He and the neutron at low Q^2; a measurment of the extended GDH integral and the Burkhardt-Cottingham sum rule*, Ph.D. thesis, Temple University, (2004).

[14] R. L. Jaffe. Comments. *Nucl. Part. Phys.*, 19:239, (1990).

[15] B. W. Filippone and X Ji. The spin structure of the nucleon. *arXiv:hep-ph/010122v4*, (2008).

[16] R. Ent W. Melnitchouk and C. E. Keppel. *Phys. Rep.*, 406:127, (2005).

[17] H. Burkhardt and W. N. Cottingham. *Annals Phys.*, 56:453, (1970).

[18] S. Wandzura and F. Wilczek. *Phys. Lett. B*, 72:195, (1977).

[19] J. P. Chen *et al.* X. Zheng, P. Bertin. Precision measurement ofthe neutron d_2: Towards the electric χ_e and magnetic χ_b color polarizabilities. *Proposal for Jefferson Lab PAC 29*, (2005).

[20] M. Burkardt. The g_2 structure function. *arXiv:hep-ph/0905.4079v1*, (2009).

[21] B .Pasquini D. Drechsel and M. Vanderaeghen. *Phys. Rep.*, 378:99, (2003).

[22] B. W. Filippone and X. Ji. *Adv. Nucl. Phys.*, 26:1, (2001).

[23] D. W. Sivers. *Phys. Rev. D*, 43:261, (1991).

[24] J. Qiu and G. Sterman. *Phys. Rev. Lett.*, 67:2264, (1991).

[25] S. J. Brodsky. Transversity from first principles in qcd. *arXiv:1112.0626v2 [hep-ph]*, (2011).

[26] Z. E. Meziani *et al. Phys. Lett. B*, 613:148, (2005).

[27] X. Ji. *arXiv:he-ph/9510362*, (1995).

[28] L. Mankiewicz E. Stein, P. Gornicki and A. Schfer. *Phys. Lett. B*, 353:107, (1995).

[29] T.van Ritbergen S. A. Larin and J. A. M. Vermaseren. *Phys. Lett. B*, 404:153, (1997).

[30] X. Ji and P. Unrau. *Phys. Lett. B*, 333:228, (1994).

[31] *Phys. Rev. C*, 77:015201, (2008).

[32] O. Nachtmann. *Nucl. Phys. B*, 63:237, (1973).

[33] S. Wandzura. *Nucl. Phys. B*, 122:412, (1977).

[34] H. Georgi and H. D. Politzer. *Phys. Rev. D*, 14:1829, (1976).

[35] S. Matsuda and T. Uematsu. *Nucl. Phys. B*, 168:181, (1980).

[36] A. V. Sidorov and D. B. Stamenov. *Mod. Phys. Lett. A*, 21:1991, (2006).

[37] A. Accardi and W. Melnitchouk. *Phys. Lett. B*, 670:114, (2008).

[38] A. Piccione and G. Ridolfi. *Nucl. Phys. B*, 513:301, (1998).

[39] K. Slifer *et al. Phys. Rev. Lett.*, 105:101601, (2010).

[40] A. I. Vainshtein M .A Shifman and V. I. Zakharov. *Nucl. Phys. B*, 58:333, (1979).

[41] M. Creutz. *Quarks Gluons and Lattices*. Cambridge Univ. Press, Cambridge, (1983).

[42] I. Montvay and G. Mnster. *Quantum Fields on a Lattice*. Cambridge Univ. Press, Cambridge, (1994).

[43] H. J. Rothe. *Lattice Gauge Theories: An Intorduction*. World Scientific Lecture Notes in Physics- Vol.59, World Scientific, Singapore, (1997).

[44] P. N. Bogoliubov. *Ann. Inst. Henri Poincare*, 8:163, (1967).

[45] K. Johnson A. Chodos, R. J. Jaffe and C. B. Thorne. *Phys. Rev. D*, 10:2599, (1974).

[46] K. Johnson T. DeGrand, R. J. Jaffe and J. Kiskis. *Phys. Rev. D*, 12:2060, (1975).

[47] Ta-Pei Cheng and Ling-Fong Li. *Gauge Theory of Elementary Particle Physics*. Oxford, (1984).

[48] S. S. Kamalov D. Drechsel and L. Tiator. *Eur. Phys. J.*, A34:69, (2007).

[49] (SMC) D. Adams *et al. Phys. Lett. B*, 336:125, (1994).

[50] (E142) P. Anthony *et al. Phys. Rev. D*, 54:6620, (1996).

[51] (E143) K. Abe *et al. Phys. Rev. D*, 58:112003, (1998).

[52] (E154) K. Abe *et al. Phys. Lett. B*, 404:377, (1997).

[53] (E155) P. Anthony *et al. Phys. Lett. B*, 458:529, (1999).

[54] (E155) P. Anthony *et al. Phys. Lett. B*, 553:18, (2003).

[55] (E97-103) K. Kramer *et al. Phys. Rev. Lett.*, 95:142002, (2005).

[56] (E94-010) M. Amerian *et al. Phys. Rev. Lett.*, 92:022301, (2004).

[57] (E99-117) X. Zheng *et al. Phys. Rev. C*, 70:065207, (2004).

[58] (E01-012) P. Solvignon *et al. (in Press.)*, arXiv:1304.4497v2 [nucl-ex], (2013).

[59] X. Song. *Phys. Rev. D*, 54:1955, (1996).

[60] M. Stratmann. *Z. Phys. C*, 60:763, (1993).

[61] X. Ji and P. Unrau. *Phys. Lett. B*, 333:228, (1994).

[62] E. Stein. *Phys. Lett. B*, 343:369, (1995).

[63] V. M. Braun I. Balitsky and A. V. Kolesnicher. *Phys. Lett. B*, 242:245, (1990).

[64] V. M. Braun I. Balitsky and A. V. Kolesnicher. *Phys. Lett. B*, 318:648, (1993).

[65] B. Ehrsperger and A. Schfer. *Phys. Rev. D*, 52:2709, (1995).

[66] M. Gckeler *et al. Phys. Rev. D*, 72:054507, (2005).

[67] L. Gamberg H. Weigel and H. Reinhart. *Phys. Rev. D*, 55:6910, (1997).

[68] H. Weigel and L. Gamberg. *Nucl. Phys. A*, 680:48, (2000).

[69] S. Galster *et al. Nucl. Phys. B*, 32:221, (1971).

[70] D. Douglas C. Leemann and G. Krafft. *Ann. Rev. of Nucl. and Part. Sci.*, 51:413–450, (2001).

[71] A. Alley *et al. Nucl. Inst. and Meth. in Phys. Res.*, A365:1, (1995).

[72] R. Prepost and T. Maruyama. *Ann. Rev. of Nucl. and Part. Sci.*, 45:41, (1995).

[73] R. L. Sutherland. *Handbook of Non Linear Optics*. CRC Press, 2nd edition, (2003).

[74] J. Hansknect and M. Poelker. Synchronous photoinjection using a frequency-double gain switch fiber coupled seed laser and eryb-doped fiber amplifier. *Phys. Rev. Spec. Top. Accel. Beams*, 9:063501, (2006).

[75] D. Parno. *Measurments of the double-spin asymmetry A_1 on helium-3: towards a precise measurment of the neutron A_1.*, Ph.D. thesis, Carnegie Mellon University, (2011).

[76] B. M. Dunham *et al.* C. K. Sinclair, P. A. Adderley. Development of a high average current polarized electron source with long cathode operational lifetime. *Phys. Rev. Spec. Top. Accel. Beams*, 10:023501, (2007).

[77] J. Mitchell *et. al* J.M. Grames, C.K. Sinclair. *Phys. Rev. Spec. Top. Accel. Beams*, 7:042802, (2004).

[78] Hall A collaboration. *JLab Hall A general operations manual, Technical report.* http://hallaweb.jlab.org/news/minutes/OSP/osp-27feb2011.pdf, (2011).

[79] M. Pitt and G^0 Collaboration. Helicity control requests form the G^0 experiment. *Technical Report*, Jefferson Lab:http://www.jlab.org/ rom/gohelicity.pdf, (2001).

[80] J. Alcorn *et al.* Basic instrumentation for Hall A at Jefferson Lab. *Nucl. Inst. Meth. A*, 522:294, (2004).

[81] R. Kazimi *et al.* Precision intercomparison of beam current monitors at CEBAF. *Proceedings of the 1995 Particle Accelerator Conference and International Conference on High-Eenrgy Accelrators*, 4:2610–2612, IEEE Operations Center (1995).

[82] K. Allada. *Measurment of single target-spin asymmetry in semi-inclusive deep inelastic scattering reaction $n^{\uparrow}\left(e, e'\pi^{\pm}\right)$ at Jefferson Lab*, Ph.D. thesis, University of Kentucky, (2010).

[83] M. G. Tiefenback and D. Douglas. Proposal for a beam profile monitor using a static wire pickup. *Technical Report*, TN92-061, JLab (1992).

[84] D. Marchand. *Calculation of Radiative Corrections for Virtual Compton Scattering, and Absolute Electron Beam Measurement at Jefferson Lab (Hall A) by a Magnetic Method: The Arc Project*, Ph.D. thesis, Universite Blais Pascal, JLab (1998).

[85] C. Dutta. *Measurment of single target-spin asymmetries in electroproduction of negative pions in semi-inclusive* $n^{\uparrow}\left(e,e'\pi^{+}\right)X$ *on a transversely polarized* ^{3}*He target*, Ph.D. thesis, University of Kentucky, (2010).

[86] X. Qian. *Measurment of single target-spin asymmetry in semi-inclusive* $n^{\uparrow}\left(e,e'\pi^{\pm}\right)$ *reaction on a transversely polarized* ^{3}*He target*, Ph.D. thesis, Duke University, (2010).

[87] W. Armstrong et al. Čerenkov detector construction for the d_2^n experiment in Hall A. *Tech. Note*, (2013).

[88] W. R. Leo. *Techniques for Nuclear and Particle Physics Experiments*. Springer-Verlag, 2nd edition, (1994).

[89] R. Winston. Light collection within the framework of geometrical optics. *J. Opt. Soc. Am.*, 60:245, (1970).

[90] Richard C. Fernow. *Introduction to Experimental Physics*. Cambridge University Press, (1986).

[91] G. Bathow et al. Measurements of the longitudinal and lateral development of electromagnetic cascades in leab, copper and aluminum at 6 GeV. *Nucl. Phys. B*, 20:592, (1970).

[92] D. Green. *The Physics of Particle Detectors*. Cambridge University Press, (2000).

[93] L. M. Mikhailov and Z. S. Aref'eva. Tables and design of lead glass shielding for a broad beam of gamma rays. *Atomic Eenrgy*, 12:58, (1962).

[94] B. D. Anderson *et al. Nucl. Inst. and Meth.*, A 522:294, (2004).

[95] R. Michales. Hall A HRS triggers. http://hallaweb.jlab.org/equipment/daq/trigger.html, (2003).

[96] VME International Trade Association. http://www.vita.com/specifications.htlm.

[97] J. Chen *et al.* W. A. W. III. CODA: A scalable, distributed data acquisition system. *IEEE Trans. Nucl. Sci.*, 41:61, (1994).

[98] S. A. Lewis. Overview of the Experimental Physics and Industrial Control System: EPICS. *Technical Report*, Lawrence Berkeley National Laboratory:http://epics.org/overview.pdf, (1998).

[99] R. Brun and F. Rademakers. ROOT- an object oriented data analysis framework. *Nucl. Inst. Meth. in Phys. Res. A*, 389:81, (1997).

[100] Hall A Analyzer. http://hallaweb.jlab.org/podd/.

[101] D. Dutta *et al.* D. J. Maraziotis, W .Chen. Measurement of a single target-spin asymmetry in semi-inclusive $n^{\uparrow}(e, e', \pi^-)$ reaction on a transversely polarized target. *Proposal for Jefferson Lab PAC 29*.

[102] J. Huang. *Double spin asymmetry A_{LT} in charged pion production from deep inelastic scattering on a transversely polarized ^{3}He target*, Ph.D. thesis, Massachusetts Institute of Technology, (2012).

[103] A. A. Kresnin and L. N. Rozentsveig. *Phys. JETP*, 5:288, (1957).

[104] L. G. Levchuk *et. al.* A. V. Glamazdin, V. G. Gorbenko. *Fiz B*, 8:91, (1999).

[105] F. W. Lipps and H. A. Tolhock. *Physica*, 20:85, (1954).

[106] F. W. Lipps and H. A. Tolhock. *Physica*, 20:395, (1954).

[107] C. Y. Prescott. *Technical Report*, TN-73-1 SLAC, (1973).

[108] (SLD collaboration) M. Woods. *SLAC-PUB-7319*, (1996).

[109] D. P. Barber *et a. Nucl. Inst. Meth. in Phys. Rev. A*, 239:79, (1993).

[110] M. Beckmann *et a. Nucl. Inst. Meth. in Phys. Rev. A*, 479:334, (2002).

[111] I. Passchier *et a. Nucl. Inst. Meth. in Phys. Rev. A*, 414:446, (1998).

[112] G.L. Payne A.M. Berstein J.L. Friar, B.F. Gibson and T.E. Chupp. *Phys. Rev. C*, 42,:2310, (1990).

[113] B. Blankleider and R.M. Woloshyn.

[114] W. Happer. *Rev. Mod. Phys.*, 44(2),:169–249, (1972).

[115] S. Applet et al. *Phys. Rev. A*, 58:1412, (1998).

[116] H. Kopfermann. *Nuclear Moments*. Academic Press, New York, USA, (1959).

[117] M. A. Bouchiat, T. R. Carver, and C. M. Varnum. Nuclear polarization in he^3 gas induced by optical pumping and dipolar exchange. *Phys. Rev. Lett.*, 5:373, (1960).

[118] Thad G. Walker. Estimates of spin-exchange parameters for alkali-metal-noble-gas pairs. *Phys. Rev. A*, 40:4959–4964, 1989.

[119] Earl Babcock, Ian Nelson, Steve Kadlecek, Bastiaan Driehuys, L. W. Anderson, F. W. Hersman, and Thad G. Walker. Hybrid spin-exchange optical pumping of $^3\mathrm{He}$. *Phys. Rev. Lett.*, 91:123003, 2003.

[120] A. Ben-Amar Baranga, S. Appelt, M. V. Romalis, C. J. Erickson, A. R. Young, G. D. Cates, and W. Happer. Polarization of ^{3}He by spin exchange with optically pumped Rb and K vapors. *Phys. Rev. Lett.*, 80, 1998.

[121] W. C. Chen, T. R. Gentile, T. G. Walker, and E. Babcock. Spin-exchange optical pumping of 3he ^{3}He with Rb-K mixtures and pure K. *Phys. Rev. A*, 75:013416, 2007.

[122] M. V. Romalis. *Laser polarized ^{3}He target used for a precision measurment of the neutron spin structure*, Ph.D. thesis, Prinction University, (1997).

[123] Y. Qiang. Private communication.

[124] J. Singh. *AIP Conf. Proc.*, 1149:823, (2009).

[125] Y. Qiang J. Huang and C. Dutta. *Hall A Weekly Meeting*. Sept 16 (2008).

[126] I. Kominis. *Measurment of the neutron (^{3}He) spin structure at low Q^2 and the extended Gerasimov-Drell-Hearn sum rule*, Ph.D. thesis, Princton University, (2001).

[127] L. El Fassi. *JLab Hall A E06-014*, https://userweb.jlab.org/ẽlfassi/d2n/targ_ana.html, (2009).

[128] Y. W. Zhang. Private communication.

[129] J. Jensen. *Measurment of the neutron (^{3}He) spin structure at low Q^2: a connection between the Bjorken and Gerasimov-Drell-Hearn sum rules*, Ph.D. thesis, Princton University, (2000).

[130] A. Abragam. *Principles of Nuclear Magnetism. Internaltional Series of Monographs on Physics*. Oxford Science Publications, (1961).

[131] W. Lorenzon et al. *Phys. Rev. A*, 47:468, (1993).

[132] D. Gill S. Meiboom, Z Luz. *J. Chem. Phys.*, 27:1411, (1957).

[133] D. Gill S. Meiboom, Z Luz. *J. Chem. Phys.*, 34:375, (1961).

[134] K.C. Tewari R.E. Glick. *J. Chem. Phys.*, 44:546, (1966).

[135] D. Flay. Ph.D. thesis, Temple University, (2013).

[136] M. V. Romalis and G. D. Cates. *Phys. Rev. A*, 58:3004, (1998).

[137] S. Kadlecek E. Babcock, I. A. Nelson and T. G. Walker. *Phys. Rev. A.*, 71:013414, (2005).

[138] J. Singh. Ph.D. Thesis, University of Virginia, (2010).

[139] A. K. Thompson A. M. Bernstein T. E. Chupp, R .A. Lovemann and D. R. Tieger. *Phys. Rev. C*, 45:915.

[140] C. F. Curtiss J. O. Hirshfelder and R. B. Bird. *Molecular Theory of Gases and Liquids*. John Wiley, (1954).

[141] A. M. Kelleher J. Singh and P. H. Solvignon. Polarization gradients in a two chamber cell. *Tech. Rep.*, (2008).

[142] J. Kestin *et. al. J. Phys. Chem. Ref. Data*, 13:229, (1984).

[143] G. D. Cates W. Happer N. R. Newbury, A. S. Barton and H. Middleton. *Phys. Rev. A*, 48:4411, (1993).

[144] T. R. Chien S. R. Schaefer G. D. Cates, D. J. White and W. Happer. *Phys. Rev. A*, 38:5092, (1988).

[145] S. Schaefer G. D. Cates and W. Happer. *Phys. Rev. A*, 37:2877, (1988).

[146] S. Riodan. *Measurments of the electric form factor of the neutron at Q^2 = 1.7 and 3.5 GeV^2.*, Ph.D. thesis, Carnegie Mellon University, (2008).

[147] M. Dell'Orso and L. Ristori. A highly parallel algorithm for track finding. *Nucl. Inst. & Meth. in Phys. Res A*, 287:436, (1990).

[148] R. Mankel. Pattern recognition and event reconstruction in particle physics experiments. *Rep. Prog. Phys.*, 67:553, (2004).

[149] G. Franklin. Private communication.

[150] J.D. Jackson. *Classical Electrodynamics.* John Wiley and Sons, Inc., New York, USA, 3rd edition, (1999).

[151] V. Mamyan. Private communication.

[152] B. Sawatzky. Private communication.

[153] E.H. Bellamy et al. *Nucl. Inst. & Meth. in Phys. Res A*, 339:468–476, (1994).

[154] N. Liyanage. *Jefferson Lab Tech Note*, JLAB-TN-02-012.

[155] C. Curtis *et al. Jefferson Lab Alignment Group Data Transmittal*, A1189, A1197, A1198 and A1208.

[156] JLab Batch Farm. *https://wiki.jlab.org/cc/external/wiki/index.php/Scientific_Computing*, (2013).

[157] R. Michales and B. Moffit. Parity daq for charge asymmetry feed back. *http://hallaweb.jlab.org/experiment/HAPPEX/HAPPEXII/paritydaq/partiy_daq.html*.

[158] G. W. Miller. *Parity Violation in forward angle elastic-proton scattering*, Ph.D. thesis, Princeton University, (2001).

[159] P. Bosted. Pair-symmetric and pion backgrounds for EG1b. *CLASNOTE*, 2004-005, (2004).

[160] S.Agostinelli et al. (Geant 4 Collaboration). *Nucl. Inst. Meth. Phys. Res. A*, 506:250, (2003).

[161] D. Flay. E06014 Progress Report. https://hallaweb.jlab.org/wiki/images/b/b1 /DF_LHRS_1_28_11.pdf, (2011).

[162] J.J. LeRose. Snake Transfer Functions. https://hallaweb.jlab.org/news/minutes /tranferfuncs.html.

[163] P. E. Bosted and V. Mamyan. *arXiv:1203.2262v2 [nucl-th]*, (2012).

[164] M. Stratmann D. de Florian, R. Sassot and W. Vogelsang. *Phys. Rev. Lett.*, 101:072001, (2008).

[165] F. Buccella C. Bourrely and J. Soffer. *Eur. Phys. J. C*, 23:487, (2002).

[166] F. Buccella C. Bourrely and J. Soffer. *Phys. Lett. B*, 648:39, (2007).

[167] A. V. Sidorov E. Leader and D. B. Stamenov. *Phys. Rev. D*, 73:034023, (2006).

[168] G. A. Navarro D. de Florian and R. Sassot. *Phys. Rev. D*, 71:094018, (2005).

[169] T. Gehrmann and W. J. Stirling. *Phys. Rev. D*, 63:6100, (1996).

[170] S. Zhou *et al.* Probing quark-gluon correlations in the neutron: A precision measurement of the neutron g_2 and d_2 at high q^2 in hall a. *Proposal for Jefferson Lab PAC 30*, (2006).

[171] S. Zhou *et al.* A path to color polarizabilities in the neutron: A precision measurement of the neutron g_2 and d_2 at high q^2 in hall c. *Proposal for Jefferson Lab PAC 36 (Update to PAC30)*, (2010).

[172] L. W. Mo and Y. S. Tsai. *Rev. Mod. Phys.*, 41:205, (1969).

[173] S. Stein *et al*. *Phys. Rev. D*, 12:1884, (1975).

[174] Amroun *et al*. *Nucl. Phys. A*, 579:596, (1994).

[175] J. W. Lightbody Jr. and J. S. O'Connell. *Comp. in Phys*, 57, (1988).

[176] Roy Whitney. radcor.f. *Fortran Analysis Code*, (2012).

[177] J. E. Amaro, M. B. Barbaro, J. A. Caballero, T. W. Donnelly, A. Molinari, and I. Sick. *Phys. Rev. C*, 71:015501, (2005).

[178] P. Bosted. *Phys. Rev. C*, 51:409, (1995).

[179] F. Bissey *et al. Phys. Rev. C*, 65:064137, (2002).

[180] P. Amaudruz *et al. Nucl. Phys. B*, 144:3, (1995).

[181] M. Arneodo *et al. Nucl. Phys. B*, 144:12, (1995).

[182] F. Bissey *et al. Phys. Rev. C*, 64:024004, (2001).

[183] A. Nogga. *Ph. D. Thesis, Ruhr-Univerität Bochum*, Bochum, Germany, (2001).

[184] D. E. Wiser. *Ph.D. Thesis*, University of Wisconsin, (1977).

[185] P. Solvignon. *Measurment of the ^{3}He Spin Structure Functions in the Resonance Region: A Test of Quark-Hadron Duality on the Neutron*, Ph.D. thesis, Temple University, (2004).

[186] Xiandong Ji and W. Melnitchouk. *Phys. Rev. D*, 56:1, (1997).

[187] A. Airapetian *et al. Eur. Phys. J. C*, 26:527, (2003).

[188] K. Hagiwara *et al.* (Particle Data Group Collaboration). *Phys. Rev. D*, 66:010001, (2002).

[189] A. Accardi *et al. arXiv:*, 1212.1701, (2013).

[190] UVa Helium-3 Target Lab. http://galileo.phys.virginia.edu/research/groups/spinphysics /transversity/transcells.html, (2009).

[191] L. El Fassi. Geometry of ^{3}he, reference and water cells. *JLab Hall A E06-014*, http://www.jlab.org/ẽlfassi/d2n/wall_thick/cells_geometry.pdf, (2009).

[192] Y. W. Zhang. Cell geometry measurement summary. *JLab Hall A E06-014*, https://hallaweb.jlab.org/wiki/images/7/77/Cell_geometry_03192012.pdf, (2011).

[193] W. Melnichouk. *hep-ph/0006170*, (1999).

APPENDIX A

SURVEY REPORTS

Figure A.1 shows the survey report listing the position of the BigBite detector at 30° and 45° relative to the beam line. The BigBite sieve and detector stack locations used during the BigBite optics calibration can be found in Figure A.2.

Jefferson Lab Alignment Group

Data Transmittal

TO: J. P. Chen, J. LeRose, D. Higinbotham | **DATE:** 11 Feb 2009

FROM: J. Dahlberg | **Checked:** | **# :** A1219

DETAILS: Data: Step2b\HallA\BigBite_Detector\090206a, 090206b

Below are the results from the surveys performed on the BigBite detector stack at 30º and 45º. The coordinates (in millimeters) are based on the ideal Hall A target center and straight ahead beam. A +X is to the beam left, a +Z is downstream, and a +Y is up. The corner points on the detectors are to the upstream of the detector frames, derived from fiducial data. Accuracy is estimated to be around 1mm due to deformation of the detector stack as noted in DT# A1191.

30 º

DETECTOR CENTERS

LOC.	Z	X	Y
1CL	2395.3	-1357.9	68.0
2CL	2507.0	-1421.8	80.5
3CL	3099.6	-1763.4	218.7

DETECTOR CORNERS

LOC.	Z	X	Y
1TOPBR	2055.4	-1628.9	953.0
1TOPBL	2459.6	-923.9	950.9
1BOTBR	2330.8	-1791.9	-814.6
1BOTBL	2735.2	-1086.8	-817.2
2TOPBR	2070.3	-1749.1	1272.2
2TOPBL	2573.6	-874.2	1269.7
2BOTBR	2440.1	-1970.0	-1108.7
2BOTBL	2944.1	-1093.9	-1111.1
3TOPBR	2662.9	-2090.2	1409.6
3TOPBL	3165.1	-1214.5	1408.5
3BOTBR	3034.1	-2312.4	-971.0
3BOTBL	3536.4	-1436.5	-972.1

DETECTOR FIDUCIALS

LOC.	Z	X	Y
E	1952.3	-2166.7	1428.7
F	3056.8	-2743.5	1645.6
G	3155.6	-2811.4	-1019.2
H	2356.3	-2404.4	-1158.3

45º

DETECTOR CENTERS

LOC.	Z	X	Y
1CL	1956.9	-1934.1	68.4
2CL	2048.2	-2025.0	81.0
3CL	2531.3	-2509.2	219.4

DETECTOR CORNERS

LOC.	Z	X	Y
1TOPBR	1557.2	-2108.0	952.8
1TOPBL	2131.1	-1532.5	951.7
1BOTBR	1782.7	-2335.8	-814.7
1BOTBL	2356.7	-1760.3	-816.2
2TOPBR	1540.0	-2228.1	1272.0
2TOPBL	2253.7	-1514.4	1270.8
2BOTBR	1842.1	-2536.0	-1108.9
2BOTBL	2556.9	-1821.3	-1110.0
3TOPBR	2023.3	-2711.9	1409.5
3TOPBL	2736.1	-1997.1	1409.7
3BOTBR	2326.4	-3021.3	-971.0
3BOTBL	3039.4	-2306.4	-970.8

DETECTOR FIDUCIALS

LOC.	Z	X	Y
E	1317.2	-2600.8	1428.0
F	2233.2	-3445.3	1645.2
G	2313.9	-3534.7	-1019.5
H	1648.2	-2933.6	-1158.9

Figure A.1: Survey report showing various BigBite detector locations at 30° and 45° relative to the electron beam line.

Jefferson Lab Alignment Group

Data Transmittal

TO: J. P. Chen, J. LeRose, D. Higinbotham		**DATE:** 28 Oct 2008
FROM: J. Dahlberg	**Checked:**	**# :** A1191

DETAILS: Data: Step2b\HallA\BigBite_Detector\080916A, 080916B

Below are the results from the survey performed on the BigBite detectors and sieve. The coordinates (in millimeters) are based on the ideal Hall A target center and straight ahead beam. A +X is to the beam left, a +Z is downstream, and a +Y is up. The corner points on the detectors are to the upstream of the detector frames. **Note:** The detector package was fiducialized in a vertical position on the floor. During this survey in the installed location, as much as 2 millimeters of deformation was seen on the fiducial points. The detector centers and corner points are derived from the fiducial points.

	LOCATION	Z	X	Y
	SIEVE	943.84	-555.84	0.65
DETECTOR CENTERS	**LOCATION**	**Z**	**X**	**Y**
	1CL	2472.12	-1401.24	68.02
	2CL	2583.87	-1465.18	80.59
	3CL	3176.39	-1806.91	219.00
DETECTOR CORNERS	**LOCATION**	**Z**	**X**	**Y**
	1TOPBR	2131.91	-1672.18	952.92
	1TOPBL	2536.33	-967.20	950.87
	1BOTBR	2407.86	-1835.29	-814.59
	1BOTBL	2812.39	-1130.29	-817.12
	2TOPBR	2146.70	-1792.30	1272.20
	2TOPBL	2650.24	-917.50	1269.77
	2BOTBR	2517.17	-2013.47	-1108.66
	2BOTBL	3021.39	-1137.42	-1110.96
	3TOPBR	2739.26	-2133.55	1409.74
	3TOPBL	3241.61	-1257.96	1408.73
	3BOTBR	3111.11	-2355.96	-970.74
	3BOTBL	3613.57	-1480.15	-971.74
DETECTOR FIDUCIALS	**LOCATION**	**Z**	**X**	**Y**
	HABBDTA	4008.92	-1267.36	1650.27
	HABBDTB	2953.59	-603.80	1431.14
	HABBDTC	3362.88	-846.39	-1180.33
	HABBDTD	4101.87	-1331.23	-1023.07
	HABBDTE	2028.62	-2209.90	1428.66
	HABBDTF	3132.90	-2786.91	1645.84
	HABBDTG	3232.47	-2854.95	-1018.89
	HABBDTH	2433.28	-2447.86	-1158.24

Figure A.2: Survey report showing various BigBite sieve and detector locations at 30° relative to the beam line. These locations were initally used when calibrating the BigBite optics for E06-010 and E06-014 by X. Qian [86]

APPENDIX B

SHOWER CLUSTER RECONSTRUCTION

Shower reconstruction is used to determine the energy and position of a particle that generates an electromagnetic shower in the shower. During E06-010 the calorimeter clustering algorithm of the BigBite calorimeter class was updated. The following conditions are included in the updated cluster algorithm which were not found in the algorithm used in E06-014:

- Searches multiple clusters in the shower detector and saves them in order of decreasing energy.
- Corresponding to the largest cluster in the shower, finds its matching cluster in the preshower to within a certain distance. If no cluster is found then the next shower cluster is considered and so on until a match is found.
- Track projection on shower X and Y coordinates are matched with the reconstructed position of the cluster within a certain distance (the size of two blocks). If no match is found then the procedure is repeated until all conditions are met.

In the updated calorimeter class, the shower and preshower energy clusters are indexed on track number, which allows an energy cluster to be reconstructed for each reconstructed track. The difference between the updated calorimeter class relative to the older calorimeter class was studied by replaying a run from E06-014 that used both versions of the calorimeter class. First the total number of reconstructed tracks were checked between the different calorimeter class versions, and found to be identical. Figure B.1 shows the track counts from the old calorimeter class in the upper panel (a) and updated calorimeter class in the lower panel (b). Next, a comparison of the preshower and shower energies were compared. Results for the preshower and shower energy comparisons can be found in Figures B.2 and B.3, with the reconstructed energy from the older calorimeter class shown on the panel a, while the reconstructed energy from the updated calorimeter class is shown in panel b. The three segments in panel b correspond to one (top-left), two (top-right) and three (bottom-left) track events. Comparing the events between the two class versions, the updated calorimeter class sees $< 1\%$ more events than the older calorimeter class. More importantly, comparing the mean preshower and shower energies between the two algorithm versions, one finds a mean discrepancy less than $\sim 2\%$, which is well within the resolution ($\sim$8% defined in 7.1.3.1) of the calorimeter. As a result the older algorithm was used in the analysis of E06-014. Furthermore, analysis using the older algorithm had cuts applied after the replay that are very similar to the track-cluster position conditions found in the updated algorithm (Section 8).

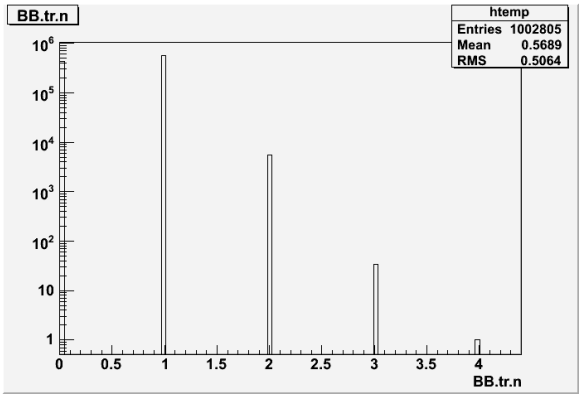

(a) Old algorithm

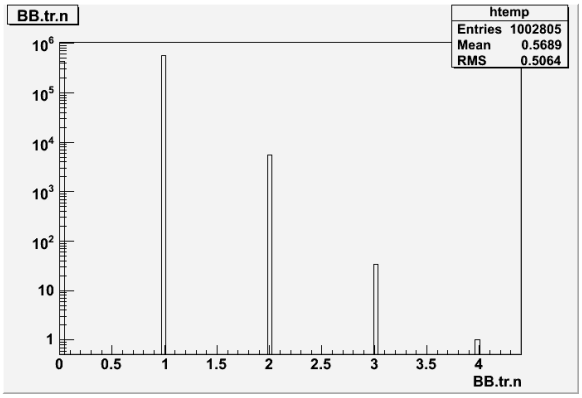

(b) Updated algorithm

Figure B.1: Total number of reconstructed tracks (including no tracks)

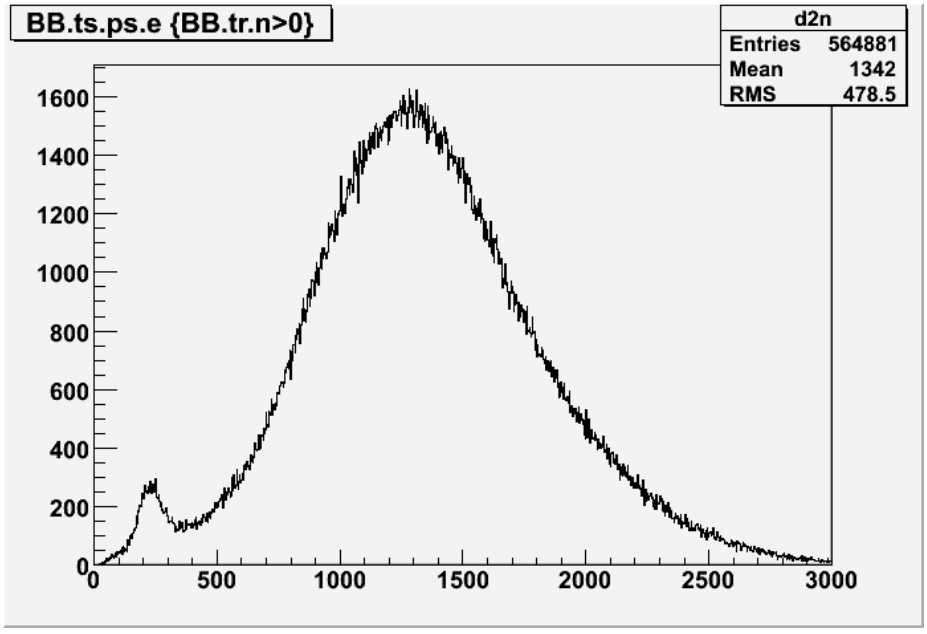

(a) Old algorithm

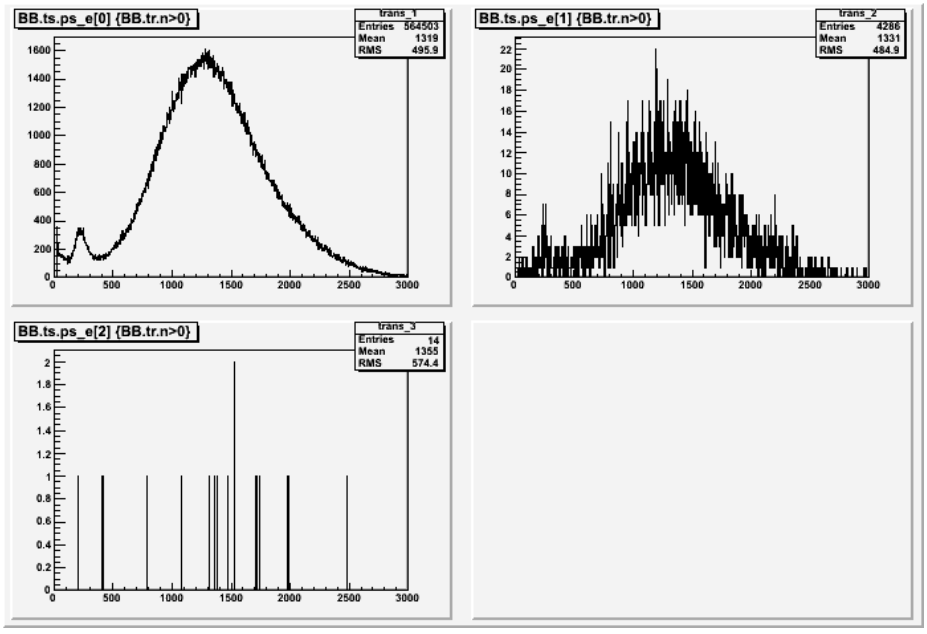

(b) Updated algorithm

Figure B.2: Preshower energy

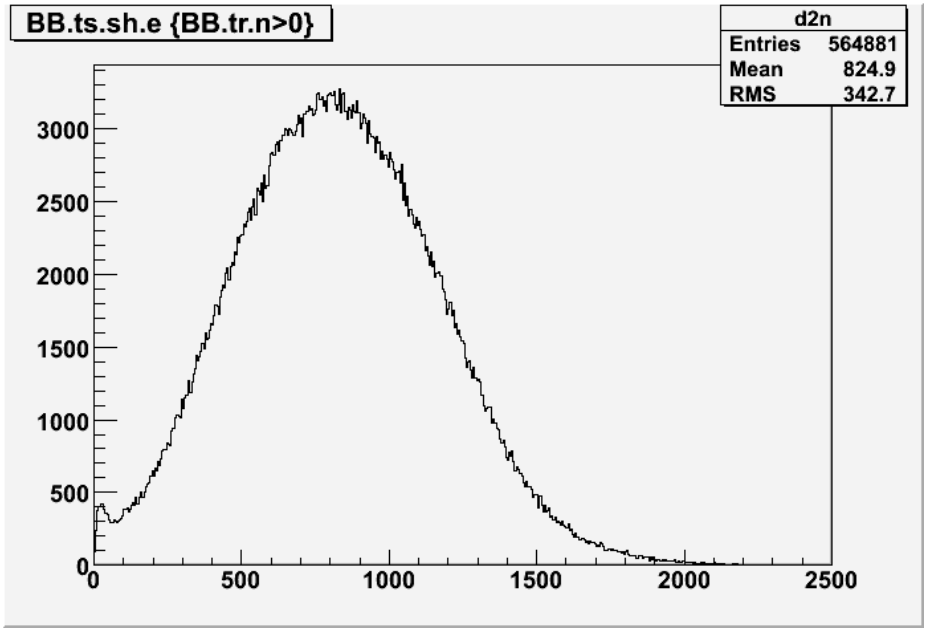

(a) Old algorithm

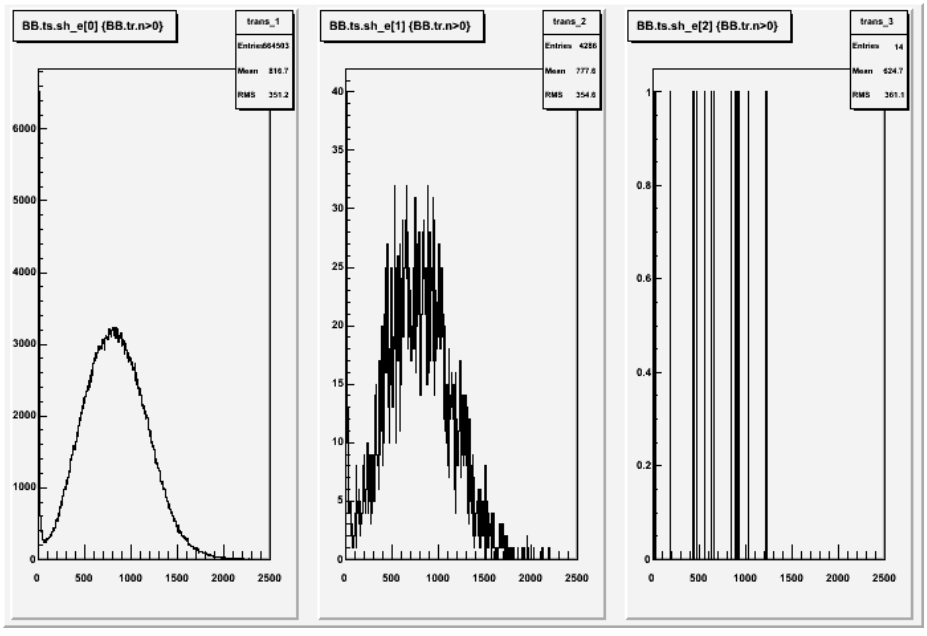

(b) Updated algorithm

Figure B.3: Shower energy

APPENDIX C

ČERENKOV PEDESTALS

The ADC pedestal is a result of electric noise in the ADC that leads to a non-zero value, and can be measured by applying a high voltage to the PMT with no signal. The result is a sharp peak in the ADC, which can later be subtracted from the ADC values obtained with a signal. This pedestal subtraction is necessary when comparing different ADC so that all ADCs have a common starting ADC channel. Ideally, the pedestal value of an ADC should not shift when measuring it with or without a signal. However, when analyzing the E06-014 production ADCs, the photo-electron yields were found to be lower than what was expected for PMTs on the small angle side of the Čerenkov detector. After some investigation it was found that the low photo-electron yields were due to the pedestal broadening and shifting to lower ADC channels relative to the pedestal values measured during LED runs (beam-off pedestals). The beam-on pedestals (pedestal measured when the electron beam was on) were selected during production like conditions by using the T8 trigger, which was a 1024 Hz pulser, and should sample uncorrelated events (i.e. background). Figures C.1 and C.2 show the pedestal values of the beam-on pedestals (red histograms) and beam-off pedestal values (blue histograms) for the PMTs on the small and large angle sides of the Čerenkov detector. It is clear from the figures, that only the pedestals on the small angle side of the

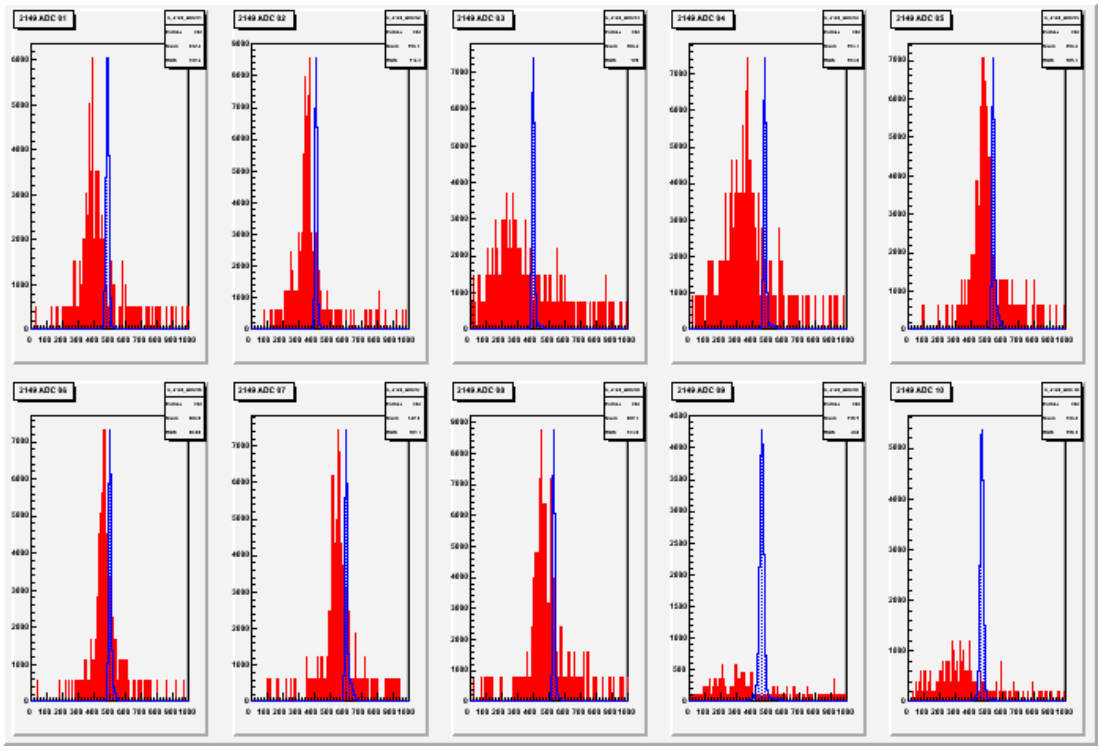

Figure C.1: Pedestal positions for the small angle side Čerenkov PMTs. The shift between the beam-on pedestals(red histograms) and LED pedestals (blue histograms) are due to the high rates at the small angle side.

Čerenkov experienced a pedestal shift.

The fact that the pedestal shift is only seen in the small angle side ADCs, which have a much higher rate than the large angle side, suggests that the pedestal shift my be related to high rates. This theory was investigated by studying the pedestal response as a function of beam current. Applying cuts to the beam trips, events with a range of different beam currents could be selected. Figure C.3 shows the beam current as a function of time for a given run that was used to select events with different currents. The pedestals for the events corresponding to various currents were then plotted in Figure C.4, with each colored histogram representing a different beam current range. The black histogram shows the pedestal for an ADC (on the small angle side) with no cut on the beam current, which shows

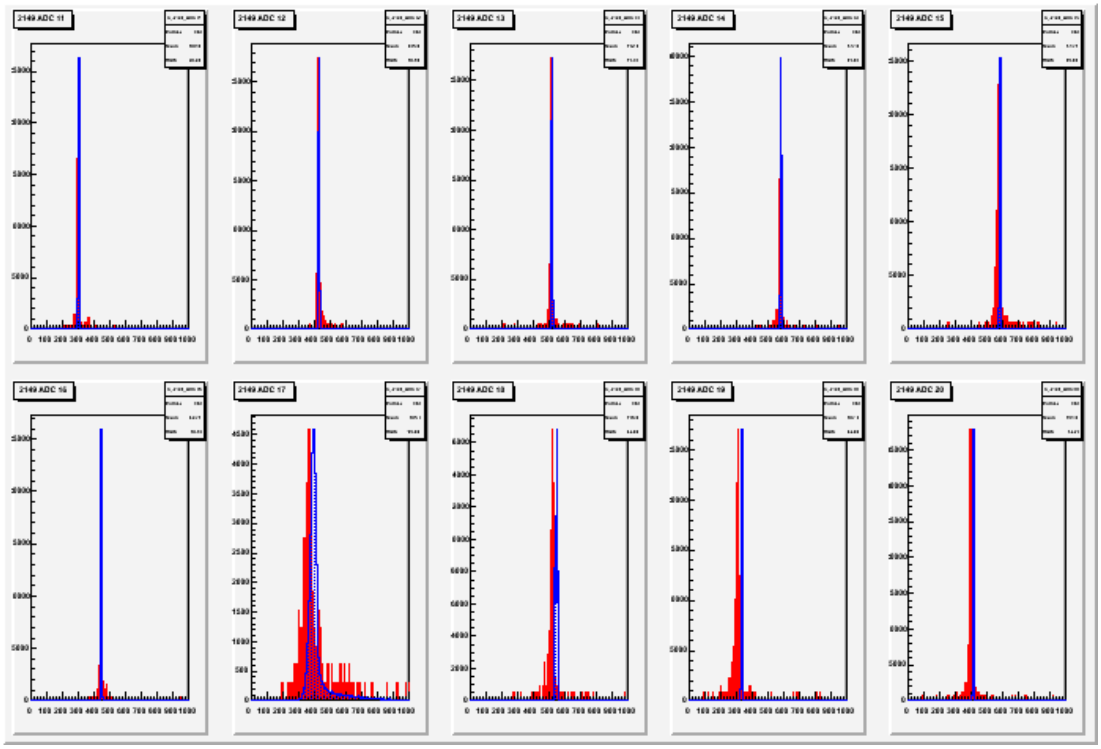

Figure C.2: Pedestal positions for the large angle side Čerenkov PMTs. The shift between the beam-on pedestals(red histograms) and LED pedestals (blue histograms) are not seen on the large angle side.

two pedestal distributions. One is a broad peak centered at channel 400, while the other peak is more narrow and centered near channel 475 which is consistent with the LED pedestal value. If only low beam current (0-2 μA) events are selected (magenta histogram), all events tend to populate the narrow pedestal peak. On the other hand, if events at higher beam current ($\geq$ 2 μ A) events are selected they are seen to populate the broad pedestal peak. So it seems that on the small angle side, the Čerenkov pedestal has a strong beam current dependence, which is most likely due to the higher rates experienced on the small angle side relative to the large angle side of the Čerenkov detector. The beam currents used for E06-014 can be roughly separated into three current ranges: low beam (0-2 μA), moderate beam (2-10 μA) and high beam (10-16 μA) currents[1]. The beam-on pedestal was measured at each beam current range for each of the small angle PMTs and were recorded into a time-stamped directory. Thus when a ROOT file is replayed depending on the time of the run, the correct pedestal value was applied based on the beam current for that given run.

[1] All production runs took place at beam currents of 10-16 μA

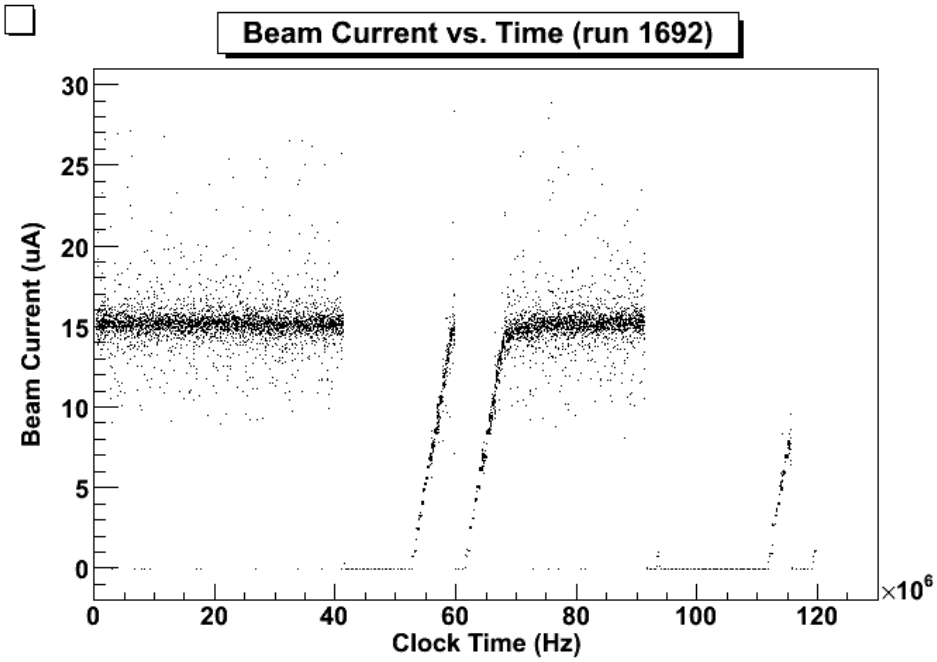

Figure C.3: The beam current as a function of clock frequency (time), that is used to apply cuts to select events with various beam currents.

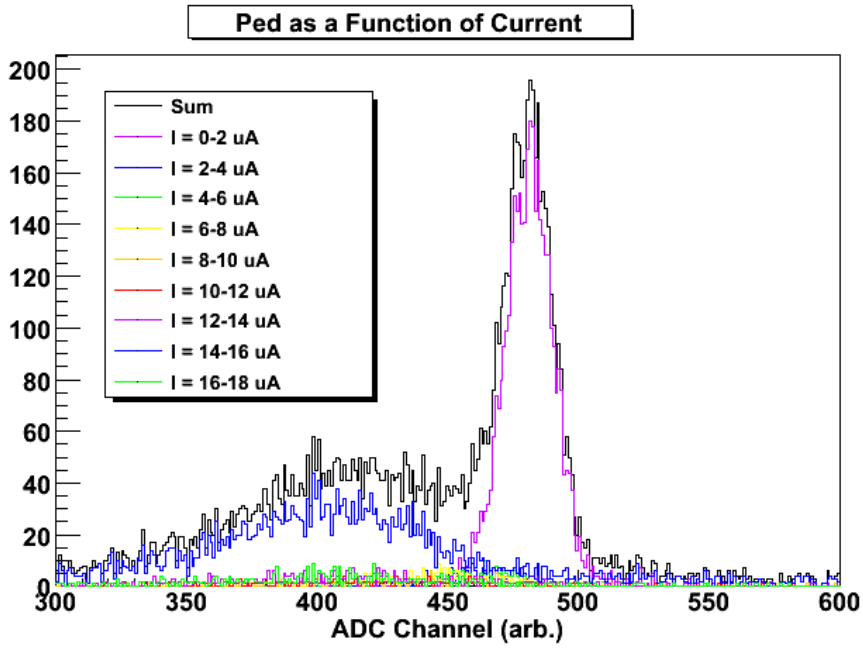

Figure C.4: Čerenkov pedestal evolution as a function of beam current.

APPENDIX D

TARGET CELL GEOMETRY

When calculating target densities to extract target polarization (Section 6) and applying radiative corrections (Section 8.5), knowledge of the target cell geometry is critical in order to obtain accurate results. The geometry of the target cells used during E06-014 were measured by UVa [190], Lamiaa El Fassi [191] and Yawei Zhang [192]. There were three cells in all that were used, with each cell given its own unique name. The cell named Samantha was the production target cell used during E06-014 (filled with polarized ^{3}He). The cell named Aqua contained water that was used for target polarization calibrations. The cell named GMA was a reference cell, whose geometry was very similar the Samantha, but was installed in a gas system that allowed various gases to be filled or evacuated from the cell. This allowed the GMA cell to act as several different targets that were used in calibrations and contamination studies (see Sections 7.1 and 8.2.6). Tables D.1 and D.2 list some measurements of the different target regions for the Aqua and Samantha cells. In these tables, the pull-off volume was computed as the volume of a truncated cone,

$$V_{pull\_off} = \frac{1}{3}\pi \left[r_{bottom}^2 h_0 - r_{top}^2 \left(h_0 - h \right) \right], \tag{D.1}$$

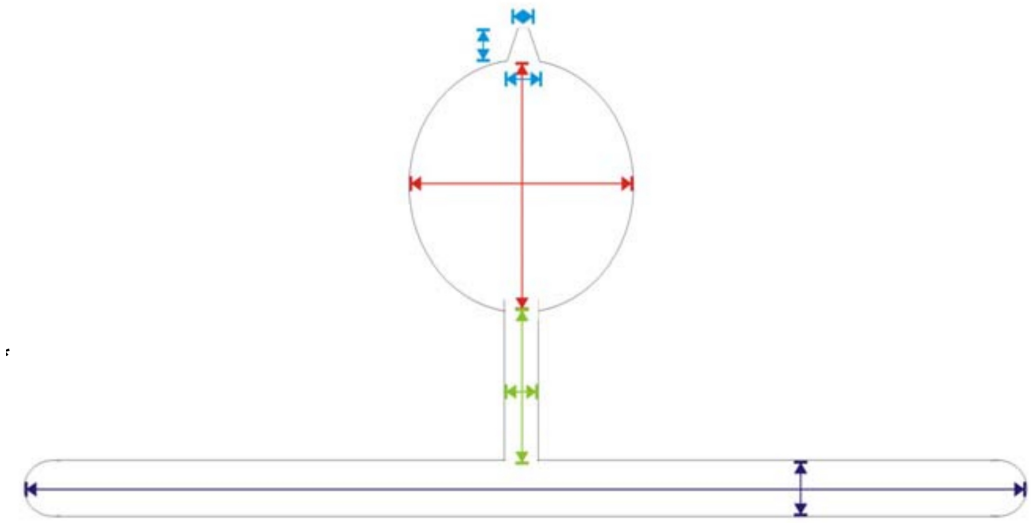

Figure D.1: ^{3}He target cell geometry measured by Yawei Zhang. Blue arrows correspond to the *pull-off* tab, red arrows to pumping chamber, green arrows to the transfer tube and purple arrows to the target chamber.

where h is the measured height, h_0 is the measured height plus an additional 5 mm for the truncation. The pumping chamber volume was given as

$$V_{pc} = \frac{4}{3}\pi r^3, \tag{D.2}$$

where r^3 is the mean value of the measured height and width of the pumping chamber. The transfer tube volume was computed using a cylindrical volume,

$$V_{tt} = \pi r^2 h, \tag{D.3}$$

and finally the target chamber volume was computed using a combination of a cylindrical volume whose length decreases by two times its radius and the volume of a sphere of the same radius

$$V_{tc} = \pi r^2 (h - 2r) + \frac{4}{3}\pi r^3. \tag{D.4}$$

The additions to the cylindrical volume were to account for the target chamber windows being spherical and thinner than the chamber walls. Table D.4 which lists the entrance (up stream) and exit (down stream) window thicknesses along with the wall thicknesses for the GMA and Samantha cells.

The volume computed from Equations D.1 - D.4 for Samantha can be compared to the volumes measured at UVa, which measured the volume through a buoyancy technique [190], whose results are listed in Table D.3. During the analysis of E06-014, the volumes measured by UVa were used.

Table D.1: Lists the various cell dimensions for the Aqua cell, which was used for target polarization calibrations. Values quoted here are from Reference [192], which are shown in Figure D.1

	Pull-off	**Pumping Chamber**	**Target Chamber**	**Transfer Tube**
Height [mm]	40.0	74.5	19.0	98.0
Width/Length [mm]	–	76.4	393.0	11.9
Width (top) [mm]	7.9	–	–	–
Width (bottom) [mm]	15.5	–	–	–
Wall Thickness [mm]	2.5	4.0	1.00	2.3
Volume [ml]	1.29	160.67	87.92	4.10

Table D.2: Lists the various cell dimensions for Samantha. Values quoted here are from Reference [192], which are shown in Figure D.1.

	Pull-off	**Pumping Chamber**	**Target Chamber**	**Transfer Tube**
Height [mm]	36.8	78.3	19.0	94.0
Width/Length [mm]	–	76.2	398.8	12.8
Width (top) [mm]	6.0	–	–	–
Width (bottom) [mm]	13.3	–	–	–
Wall Thickness [mm]	2.5	2.9	1.66	1.5
Volume [ml]	0.75	191.4	75.5	7.0

Table D.3: Volume measurements of Samantha from UVa [190].

Chamber	Volume [ml]
Pumping Chamber	176.9
Target Chamber	75.47
Transfer Tube	6.51

Table D.4: Lists the entrance and exit window thicknesses, as well as the average cell wall thicknesses. Values quoted here are from References [191] and [192].

Cell	Entrance Window [mm]	Exit Window [mm]	Average Wall Thickness [mm]
GMA	0.129	0.134	1.71
Samantha	0.121	0.125	1.66

APPENDIX E

BIGBITE X-BINNED KINEMATICS

The asymmetries measured during E06-014, were binned into equally spaced x-bins ranging between $0 \leq x \leq 1$, resulting in a bin width of 0.05. In order to go from the measured raw asymmetry, which depends on the counting asymmetry between electron helicities and target spin directions, to physics quantities of interest (g_1, g_2 and d_2), kinematic factors need to be applied to the asymmetries. Therefore it is important to check and understand the kinematic distributions in each of the x-bins before applying them to the corresponding asymmetries. Several kinematic distributions, which included: x (Bjorken variable), θ (electron scattering angle), ϕ (angle between the scattering and polarization planes), Q^2 (four momentum transfer), W (invariant mass), k' (scattering momentum), and ν (energy transfer), were plotted for each of the x-bins used in the analysis. Shown in Figures E.1-E.6 are the kinematic distributions from a typical ^{3}He production run (run 2037), which corresponds to the E = 4.74 GeV data set. Typical distributions obtained for the E = 5.89 GeV data set are shown in Figures E.7-E.12 for a polarized ^{3}He production run (run 1479).

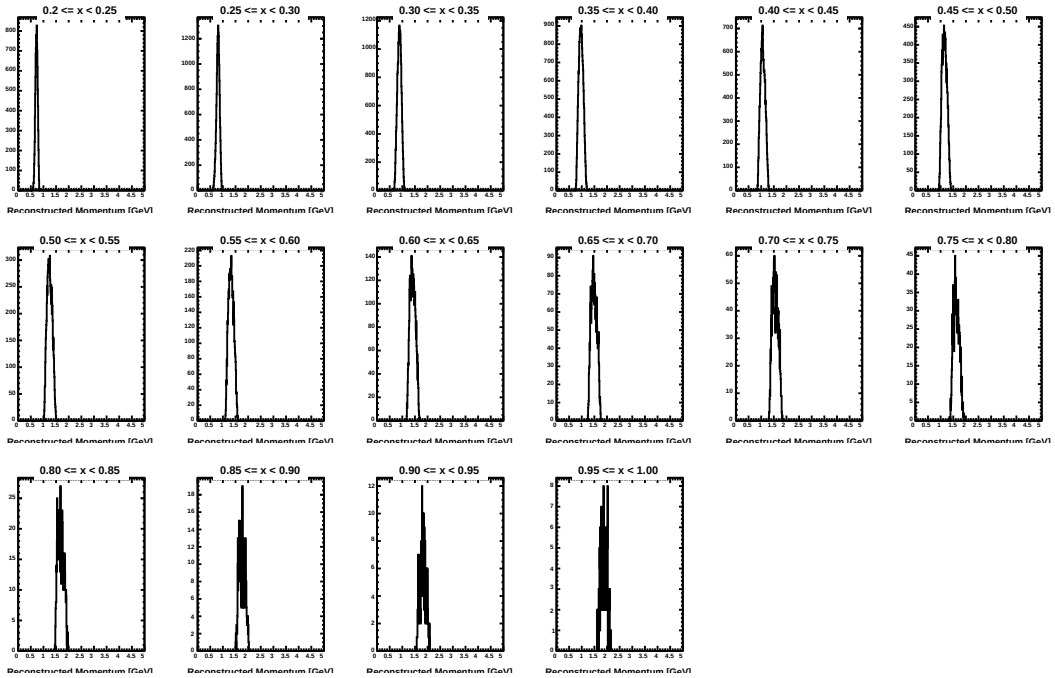

Figure E.1: Measured k' distribution in each x bin at incident electron beam energy of 4.74 GeV. Distributions are shown in order of increasing x from left to right.

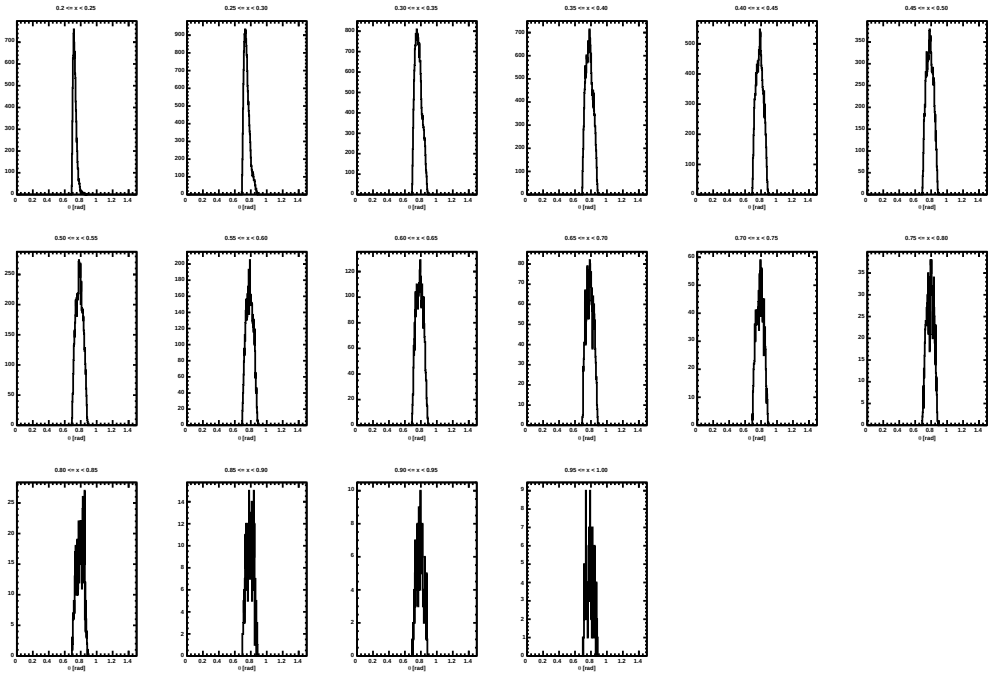

Figure E.2: Measured θ distribution in each x bin at incident electron beam energy of 4.74 GeV. Distributions are shown in order of increasing x from left to right.

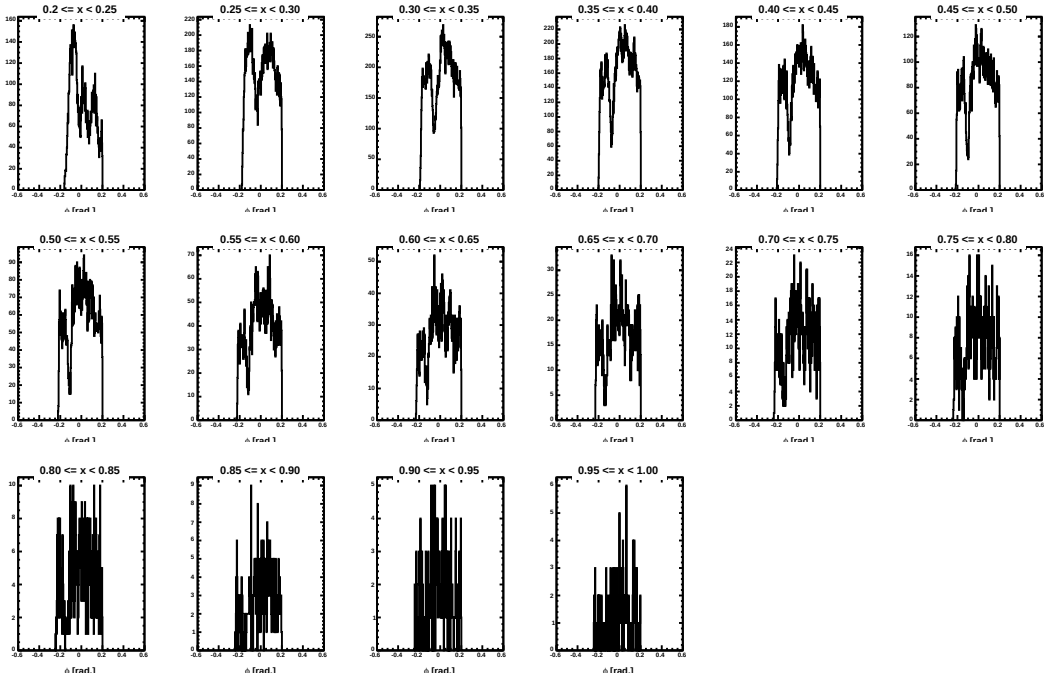

Figure E.3: Measured ϕ distribution in each x bin at incident electron beam energy of 4.74 GeV. Distributions are shown in order of increasing x from left to right. The BigBite acceptance hole is clearly visible, but was found not to affect the asymmetries (Section 8.2.5.4.

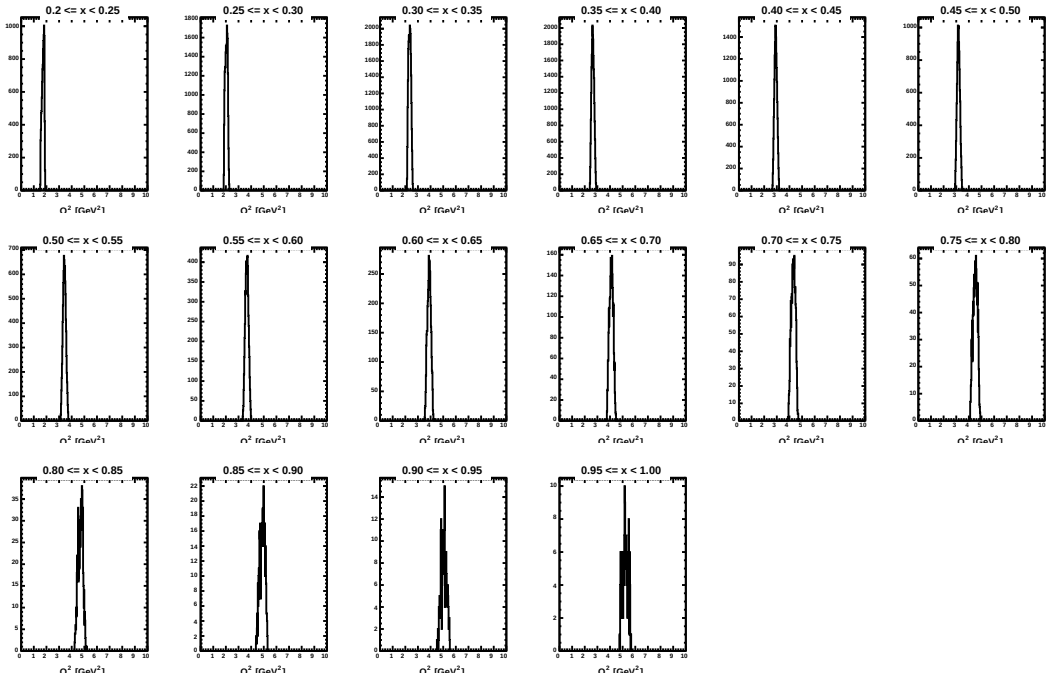

Figure E.4: Measured Q^2 distribution in each x bin at incident electron beam energy of 4.74 GeV. Distributions are shown in order of increasing x from left to right.

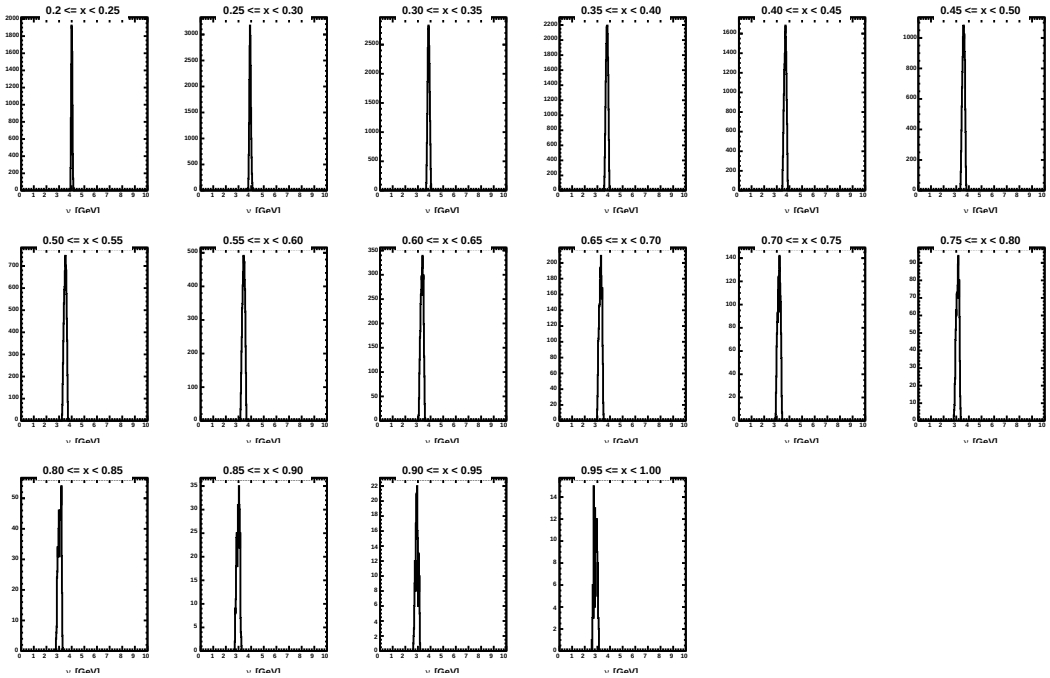

Figure E.5: Measured ν distribution in each x bin at incident electron beam energy of 4.74 GeV. Distributions are shown in order of increasing x from left to right.

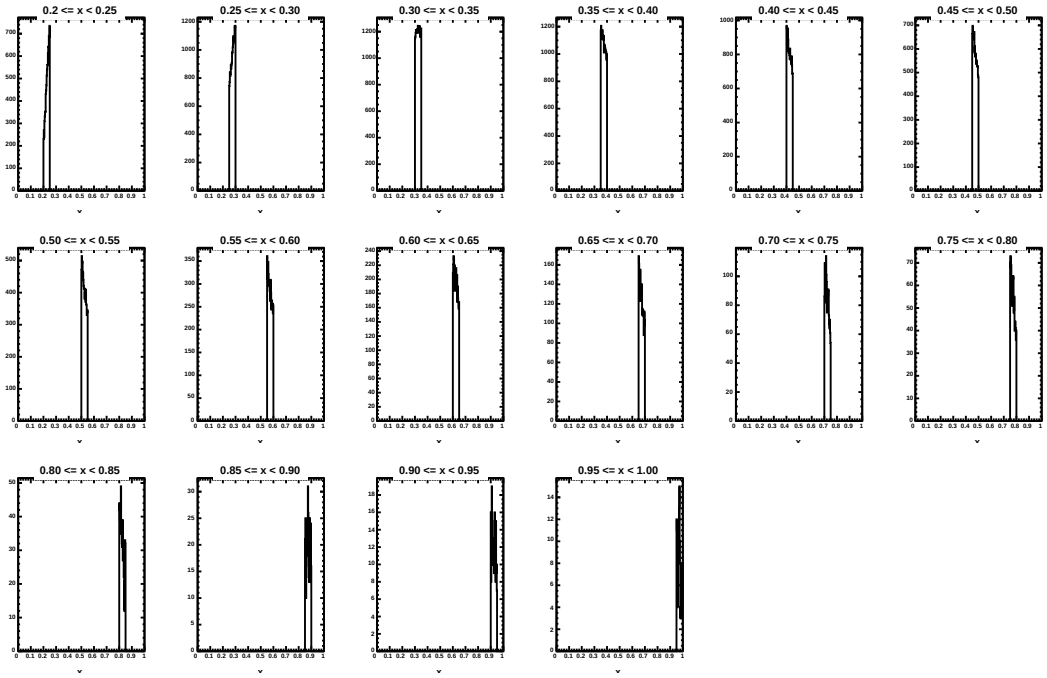

Figure E.6: Measured x distribution in each x bin at incident electron beam energy of 4.74 GeV.

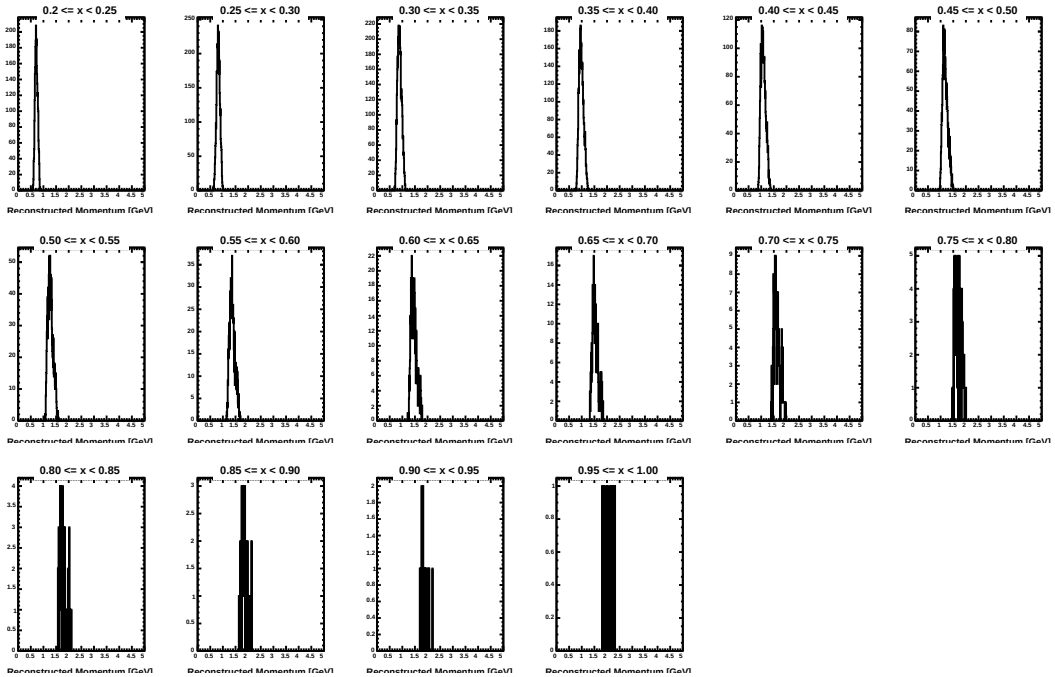

Figure E.7: Measured k' distribution in each x bin at incident electron beam energy of 5.89 GeV. Distributions are shown in order of increasing x from left to right.

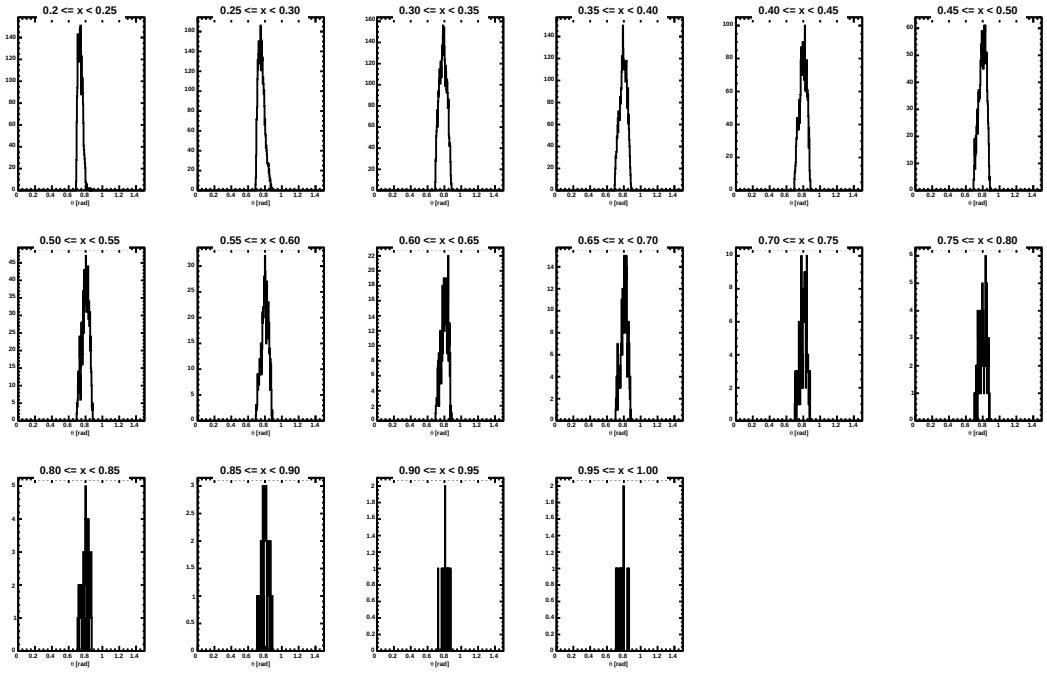

Figure E.8: Measured θ distribution in each x bin at incident electron beam energy of 5.89 GeV. Distributions are shown in order of increasing x from left to right.

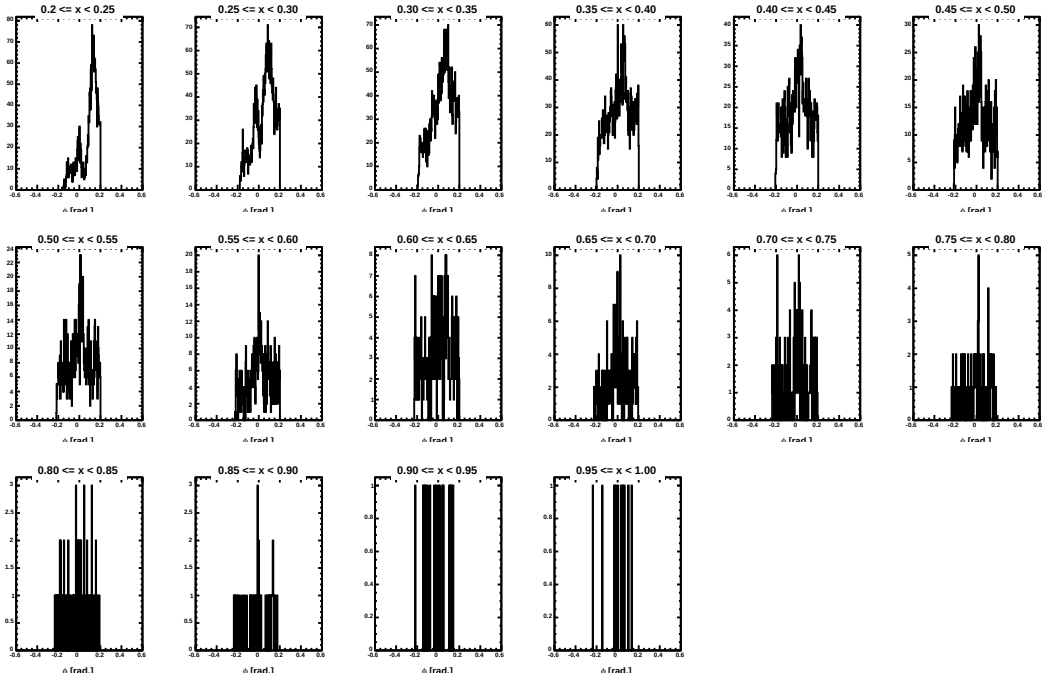

Figure E.9: Measured ϕ distribution in each x bin at incident electron beam energy of 5.89 GeV. Distributions are shown in order of increasing x from left to right. The acceptance hole is clearly visible, but was found not to affect the asymmetries (Section 8.2.5.4.

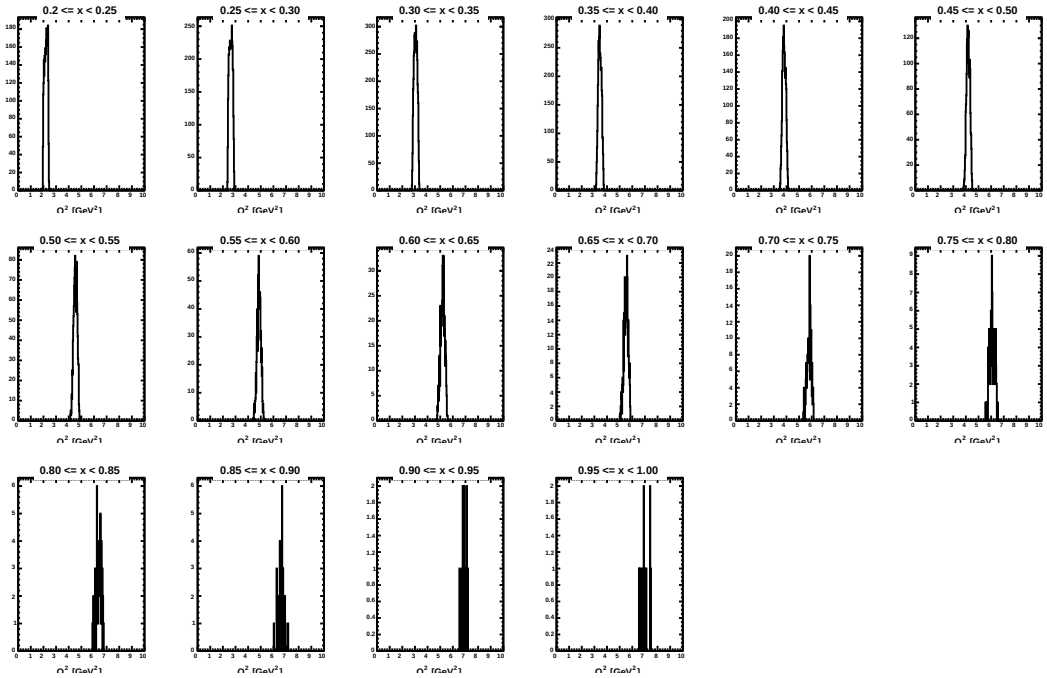

Figure E.10: Measured Q^2 distribution in each x bin at incident electron beam energy of 5.89 GeV. Distributions are shown in order of increasing x from left to right.

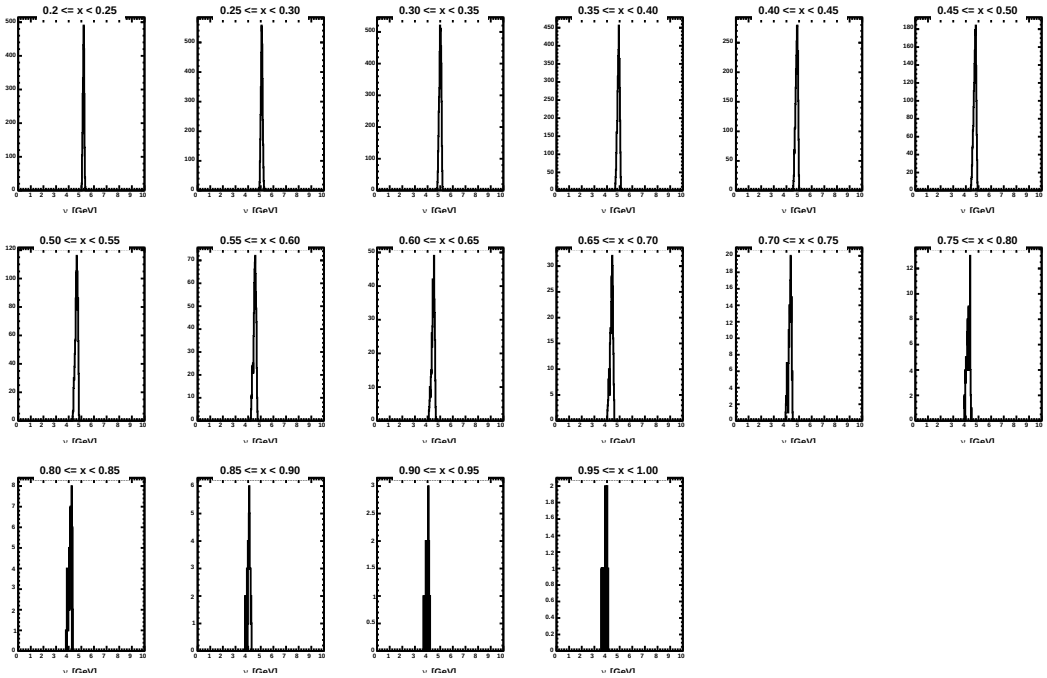

Figure E.11: Measured ν distribution in each x bin at incident electron beam energy of 5.89 GeV. Distributions are shown in order of increasing x from left to right.

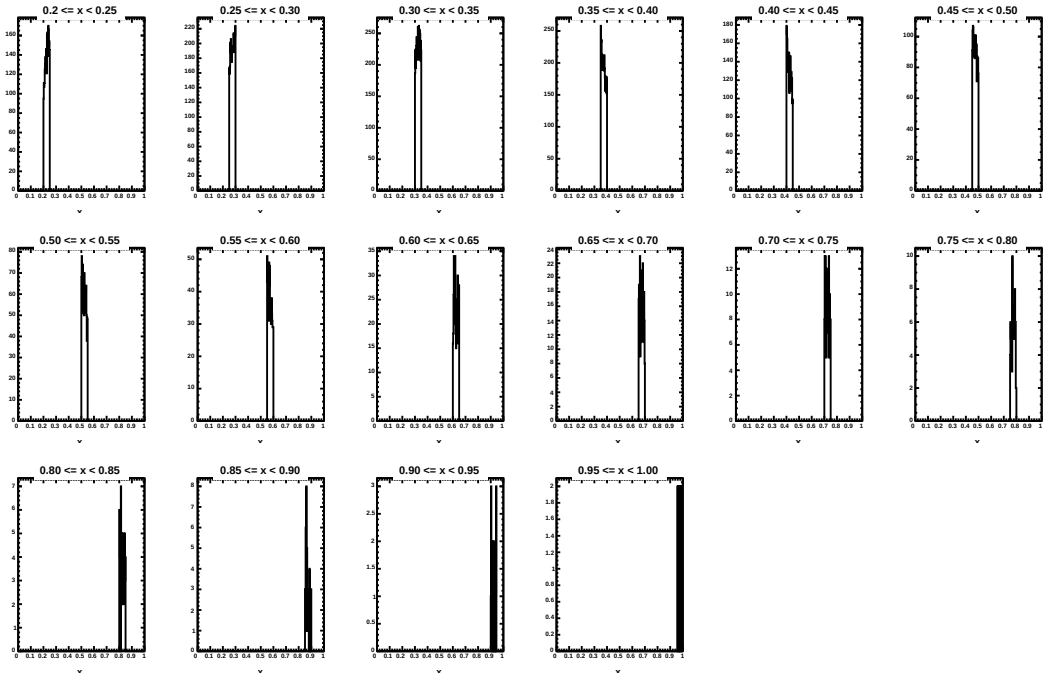

Figure E.12: Measured x distribution in each x bin at incident electron beam energy of 5.89 GeV.

APPENDIX F

SYSTEMATIC UNCERTAINTY TABLES

This section lists the systematic uncertainties assigned to the DSAs, spin structure functions, and the d_2^n matrix elements due to various contributions. The kinematic uncertainties were determined by studying how the computed quantities (i.e. DSAs, g_1, g_2, d_2^n, etc) change when the kinematic variables it depends on are varied within their uncertainty (defined in Section 8.2.5). Furthermore, additional contributions from the electron beam polarization (P_b, discussed in Section 5.3), ^{3}He target polarization (P_t, described in Section 6.6), nitrogen dilution (D_{N2}, discussed in Section 8.2.6), contaminations in the BigBite analysis including: π^- (f_1), π^+ (f_2), and e^+ (f_3) dilutions (discussed in Section 8.2.9), cross sections (σ, discussed in Section 8.4.1), and the uncertainties introduced through the data quality and PID cuts (Section 8.7.1). The column listed as "Total" in the tables below is the quadrature sum of the individual systematic contributions. For comparison, the statistical uncertainty of each quantity was also included in the tables. The final total systematic uncertainty for each quantity was then formed by adding the uncertainty in the "Total" column in quadrature with the systematic effects from radiative corrections (Section 8.5.2).

Table F.1: Systematic uncertainties assigned to parallel DSAs at incident beam energy of 4.74 GeV.

$A_{\parallel}^{^3\mathrm{He}}$ Systematics (E = 4.74 GeV)											
x	Stat.	P_b	P_t	D_{N2}	f_1	f_2	f_3	σ	Kinematics	Cuts	Total
0.225	0.06368	0.00350	0.00580	0.00030	0.00010	.0.000100	0.00940	0.00000	0.00000	0.01365	0.01790
0.275	0.01549	0.00100	0.00170	0.00010	0.00000	.0.000000	0.00110	0.00000	0.00000	0.00671	0.00708
0.325	0.00879	0.00060	0.00100	0.00010	0.00000	.0.000000	0.00050	0.00000	0.00000	0.00231	0.00264
0.375	0.00701	0.00010	0.00020	0.00000	0.00000	.0.000000	0.00040	0.00000	0.00000	0.00175	0.00181
0.425	0.00704	0.00100	0.00170	0.00010	0.00000	.0.000000	0.00000	0.00000	0.00000	0.00444	0.00486
0.475	0.00778	0.00080	0.00140	0.00010	0.00000	.0.000000	0.00000	0.00000	0.00000	0.00292	0.00334
0.525	0.00900	0.00010	0.00010	0.00000	0.00000	.0.000000	0.00010	0.00000	0.00000	0.00201	0.00202
0.575	0.01069	0.00020	0.00030	0.00000	0.00000	.0.000000	0.00010	0.00000	0.00000	0.00438	0.00440
0.625	0.01269	0.00110	0.00180	0.00010	0.00000	.0.000000	0.00010	0.00000	0.00000	0.00233	0.00315
0.675	0.01546	0.00090	0.00160	0.00010	0.00000	.0.000000	0.00000	0.00000	0.00000	0.00423	0.00461
0.725	0.01895	0.00120	0.00190	0.00010	0.00000	.0.000000	0.00000	0.00000	0.00000	0.00617	0.00656
0.775	0.02387	0.00050	0.00090	0.00000	0.00000	.0.000000	0.00000	0.00000	0.00000	0.01298	0.01302
0.825	0.03044	0.00130	0.00220	0.00010	0.00000	.0.000000	0.00000	0.00000	0.00000	0.01128	0.01157
0.875	0.03913	0.00050	0.00080	0.00000	0.00000	.0.000000	0.00000	0.00000	0.00000	0.01702	0.01704
0.925	0.05059	0.00220	0.00360	0.00020	0.00000	.0.000000	0.00000	0.00000	0.00000	0.01667	0.01720
0.975	0.06089	0.00010	0.00020	0.00000	0.00000	.0.000000	0.00000	0.00000	0.00000	0.01991	0.01991

Table F.2: Systematic uncertainties assigned to transverse DSAs at incident beam energy of 4.74 GeV.

$A_{\perp}^{^3\mathrm{He}}$ Systematics (E = 4.74 GeV)											
x	Stat.	P_b	P_t	D_{N2}	f_1	f_2	f_3	σ	Kinematics	Cuts	Total
0.225	0.03362	0.00130	0.00190	0.00010	0.00020	.0.000200	0.01480	0.00000	0.00000	0.00540	0.01592
0.275	0.00809	0.00030	0.00050	0.00010	0.00000	.0.000000	0.00020	0.00000	0.00000	0.00252	0.00259
0.325	0.00455	0.00020	0.00040	0.00000	0.00000	.0.000000	0.00010	0.00000	0.00000	0.00161	0.00167
0.375	0.00361	0.00060	0.00100	0.00010	0.00000	.0.000000	0.00010	0.00000	0.00000	0.00197	0.00229
0.425	0.00361	0.00020	0.00040	0.00000	0.00000	.0.000000	0.00000	0.00000	0.00000	0.00150	0.00157
0.475	0.00400	0.00030	0.00050	0.00000	0.00000	.0.000000	0.00000	0.00000	0.00000	0.00072	0.00093
0.525	0.00462	0.00030	0.00050	0.00000	0.00000	.0.000000	0.00000	0.00000	0.00000	0.00108	0.00123
0.575	0.00548	0.00040	0.00060	0.00000	0.00000	.0.000000	0.00000	0.00000	0.00000	0.00220	0.00231
0.625	0.00650	0.00020	0.00030	0.00000	0.00000	.0.000000	0.00000	0.00000	0.00000	0.00233	0.00236
0.675	0.00787	0.00020	0.00030	0.00000	0.00000	.0.000000	0.00000	0.00000	0.00000	0.00304	0.00307
0.725	0.00972	0.00060	0.00100	0.00010	0.00000	.0.000000	0.00000	0.00000	0.00000	0.00208	0.00239
0.775	0.01221	0.00100	0.00180	0.00010	0.00000	.0.000000	0.00000	0.00000	0.00000	0.00415	0.00464
0.825	0.01563	0.00020	0.00030	0.00000	0.00000	.0.000000	0.00000	0.00000	0.00000	0.00581	0.00583
0.875	0.02015	0.00200	0.00350	0.00020	0.00000	.0.000000	0.00000	0.00000	0.00000	0.00398	0.00567
0.925	0.02529	0.00020	0.00020	0.00000	0.00000	.0.000000	0.00000	0.00000	0.00000	0.00610	0.00611
0.975	0.03140	0.00040	0.00080	0.00000	0.00000	.0.000000	0.00000	0.00000	0.00000	0.00583	0.00589

Table F.3: Systematic uncertainties assigned to the parallel DSA at incident beam energy of 5.89 GeV.

$A_{\parallel}^{^3\mathrm{He}}$ Systematics (E = 5.89 GeV)											
x	Stat.	P_b	P_t	D_{N2}	f_1	f_2	f_3	σ	Kinematics	Cuts	Total
0.225	0.08951	0.00270	0.00630	0.00080	0.00010	.0.000100	0.00840	0.00000	0.00000	0.02800	0.03003
0.275	0.02654	0.00020	0.00060	0.00010	0.00000	.0.000100	0.00350	0.00000	0.00000	0.00943	0.01008
0.325	0.01205	0.00050	0.00120	0.00010	0.00000	.0.000000	0.00010	0.00000	0.00000	0.00316	0.00342
0.375	0.00922	0.00020	0.00040	0.00000	0.00000	.0.000000	0.00010	0.00000	0.00000	0.00225	0.00229
0.425	0.00921	0.00060	0.00130	0.00010	0.00000	.0.000000	0.00010	0.00000	0.00000	0.00224	0.00266
0.475	0.01033	0.00060	0.00130	0.00010	0.00000	.0.000000	0.00000	0.00000	0.00000	0.00600	0.00617
0.525	0.01212	0.00010	0.00020	0.00000	0.00000	.0.000000	0.00000	0.00000	0.00000	0.00225	0.00226
0.575	0.01452	0.00010	0.00030	0.00000	0.00000	.0.000000	0.00000	0.00000	0.00000	0.00327	0.00329
0.625	0.01769	0.00010	0.00030	0.00000	0.00000	.0.000000	0.00000	0.00000	0.00000	0.00540	0.00541
0.675	0.02189	0.00010	0.00020	0.00000	0.00000	.0.000000	0.00000	0.00000	0.00000	0.00488	0.00489
0.725	0.02737	0.00010	0.00030	0.00000	0.00000	.0.000000	0.00000	0.00000	0.00000	0.00472	0.00473
0.775	0.03486	0.00020	0.00010	0.00000	0.00000	.0.000000	0.00000	0.00000	0.00000	0.00793	0.00793
0.825	0.04667	0.00080	0.00200	0.00010	0.00000	.0.000000	0.00000	0.00000	0.00000	0.01382	0.01399
0.875	0.06237	0.00040	0.00140	0.00000	0.00000	.0.000000	0.00000	0.00000	0.00000	0.01662	0.01668
0.925	0.08460	0.00310	0.00720	0.00050	0.00000	.0.000000	0.00000	0.00000	0.00000	0.03303	0.03395
0.975	0.11134	0.00450	0.01080	0.00070	0.00000	.0.000000	0.00000	0.00000	0.00000	0.06538	0.06642

Table F.4: Systematic uncertainties assigned to transverse DSAs at incident beam energy of 5.89 GeV.

$A_{\perp}^{^3\mathrm{He}}$ Systematics (E = 5.89 GeV)											
x	Stat.	P_b	P_t	D_{N2}	f_1	f_2	f_3	σ	Kinematics	Cuts	Total
0.225	0.02956	0.00100	0.00270	0.00020	0.00050	.0.000800	0.02770	0.00000	0.00000	0.00847	0.02912
0.275	0.00844	0.00030	0.00070	0.00000	0.00000	.0.000000	0.00200	0.00000	0.00000	0.00226	0.00312
0.325	0.00376	0.00010	0.00030	0.00000	0.00000	.0.000000	0.00040	0.00000	0.00000	0.00117	0.00127
0.375	0.00289	0.00020	0.00040	0.00000	0.00000	.0.000000	0.00010	0.00000	0.00000	0.00026	0.00053
0.425	0.00290	0.00020	0.00050	0.00000	0.00000	.0.000000	0.00000	0.00000	0.00000	0.00130	0.00140
0.475	0.00322	0.00010	0.00020	0.00000	0.00000	.0.000000	0.00000	0.00000	0.00000	0.00096	0.00098
0.525	0.00375	0.00000	0.00010	0.00000	0.00000	.0.000000	0.00000	0.00000	0.00000	0.00117	0.00117
0.575	0.00448	0.00000	0.00010	0.00000	0.00000	.0.000000	0.00000	0.00000	0.00000	0.00131	0.00132
0.625	0.00541	0.00010	0.00030	0.00000	0.00000	.0.000000	0.00000	0.00000	0.00000	0.00077	0.00083
0.675	0.00668	0.00010	0.00020	0.00000	0.00000	.0.000000	0.00000	0.00000	0.00000	0.00200	0.00202
0.725	0.00835	0.00010	0.00030	0.00000	0.00000	.0.000000	0.00000	0.00000	0.00000	0.00290	0.00292
0.775	0.01064	0.00010	0.00030	0.00000	0.00000	.0.000000	0.00000	0.00000	0.00000	0.00242	0.00244
0.825	0.01406	0.00120	0.00300	0.00020	0.00000	.0.000000	0.00000	0.00000	0.00000	0.00293	0.00436
0.875	0.01862	0.00020	0.00060	0.00000	0.00000	.0.000000	0.00000	0.00000	0.00000	0.00683	0.00686
0.925	0.02543	0.00040	0.00060	0.00010	0.00000	.0.000000	0.00000	0.00000	0.00000	0.00168	0.00183
0.975	0.03357	0.00120	0.00300	0.00020	0.00000	.0.000000	0.00000	0.00000	0.00000	0.00706	0.00776

Table F.5: Systematic uncertainties assigned to g_1 at incident beam energy of 4.74 GeV.

$g_1^{^3\mathrm{He}}$ Systematics (E = 4.74 GeV)											
x	Stat.	P_b	P_t	D_{N2}	f_1	f_2	f_3	σ	Kinematics	Cuts	Total
0.230	0.07871	0.00780	0.01050	0.00420	0.00400	.0.003600	0.02360	0.00180	0.00194	0.01945	0.03406
0.277	0.01654	0.00100	0.00190	0.00010	0.00020	.0.000200	0.00110	0.00010	0.00010	0.00825	0.00861
0.325	0.00794	0.00050	0.00090	0.00010	0.00020	.0.000200	0.00030	0.00020	0.00022	0.00198	0.00229
0.374	0.00512	0.00010	0.00020	0.00000	0.00000	.0.000000	0.00030	0.00010	0.00014	0.00156	0.00161
0.424	0.00412	0.00070	0.00110	0.00010	0.00010	.0.000100	0.00010	0.00050	0.00054	0.00271	0.00311
0.473	0.00345	0.00060	0.00080	0.00020	0.00020	.0.000200	0.00020	0.00040	0.00032	0.00133	0.00178
0.523	0.00294	0.00000	0.00000	0.00000	0.00000	.0.000000	0.00000	0.00000	0.00000	0.00053	0.00053
0.574	0.00261	0.00000	0.00000	0.00000	0.00000	.0.000000	0.00000	0.00000	0.00000	0.00112	0.00112
0.623	0.00230	0.00030	0.00040	0.00010	0.00010	.0.000100	0.00010	0.00040	0.00022	0.00045	0.00084
0.673	0.00203	0.00010	0.00020	0.00000	0.00000	.0.000000	0.00000	0.00030	0.00010	0.00068	0.00078
0.723	0.00179	0.00010	0.00010	0.00000	0.00000	.0.000000	0.00000	0.00030	0.00010	0.00055	0.00065
0.773	0.00160	0.00000	0.00010	0.00000	0.00010	.0.000100	0.00010	0.00020	0.00010	0.00088	0.00093
0.823	0.00144	0.00000	0.00000	0.00010	0.00010	.0.000100	0.00010	0.00030	0.00010	0.00060	0.00071
0.873	0.00128	0.00010	0.00000	0.00010	0.00010	.0.000100	0.00010	0.00020	0.00000	0.00057	0.00064
0.921	0.00114	0.00010	0.00010	0.00020	0.00020	.0.000200	0.00020	0.00030	0.00010	0.00041	0.00067
0.973	0.00092	0.00000	0.00000	0.00000	0.00000	.0.000000	0.00000	0.00000	0.00000	0.00035	0.00035

Table F.6: Systematic uncertainties assigned to g_2 at incident beam energy of 4.74 GeV.

$g_2^{^3\mathrm{He}}$ Systematics (E = 4.74 GeV)											
x	Stat.	P_b	P_t	D_{N2}	f_1	f_2	f_3	σ	Kinematics	Cuts	Total
0.230	0.19162	0.01740	0.01230	0.02610	0.02840	.0.025800	0.11140	0.01270	0.01561	0.02951	0.12765
0.277	0.03430	0.00050	0.00100	0.00030	0.00060	.0.000600	0.00030	0.00040	0.00051	0.00909	0.00923
0.325	0.01449	0.00030	0.00070	0.00020	0.00020	.0.000200	0.00020	0.00030	0.00037	0.00550	0.00559
0.374	0.00927	0.00100	0.00190	0.00020	0.00030	.0.000300	0.00060	0.00110	0.00139	0.00435	0.00522
0.424	0.00585	0.00010	0.00020	0.00000	0.00000	.0.000000	0.00000	0.00010	0.00017	0.00158	0.00161
0.473	0.00456	0.00020	0.00030	0.00010	0.00010	.0.000100	0.00010	0.00020	0.00017	0.00041	0.00064
0.523	0.00369	0.00040	0.00050	0.00010	0.00010	.0.000100	0.00010	0.00030	0.00030	0.00089	0.00120
0.574	0.00304	0.00030	0.00040	0.00010	0.00010	.0.000100	0.00010	0.00030	0.00024	0.00105	0.00124
0.623	0.00241	0.00000	0.00000	0.00000	0.00000	.0.000000	0.00000	0.00000	0.00000	0.00078	0.00078
0.673	0.00202	0.00010	0.00020	0.00000	0.00000	.0.000000	0.00000	0.00020	0.00014	0.00066	0.00074
0.723	0.00173	0.00010	0.00020	0.00000	0.00000	.0.000000	0.00000	0.00040	0.00014	0.00042	0.00064
0.773	0.00147	0.00000	0.00010	0.00010	0.00010	.0.000100	0.00010	0.00040	0.00014	0.00051	0.00070
0.823	0.00123	0.00000	0.00000	0.00000	0.00000	.0.000000	0.00000	0.00010	0.00000	0.00039	0.00040
0.873	0.00108	0.00010	0.00000	0.00020	0.00020	.0.000200	0.00020	0.00050	0.00014	0.00033	0.00074
0.921	0.00086	0.00000	0.00000	0.00000	0.00000	.0.000000	0.00000	0.00010	0.00000	0.00032	0.00033
0.973	0.00069	0.00000	0.00000	0.00000	0.00000	.0.000000	0.00000	0.00010	0.00000	0.00017	0.00020

Table F.7: Systematic uncertainties assigned to g_1 at incident beam energy of 5.89 GeV.

$g_1^{^3\mathrm{He}}$ Systematics (E = 5.89 GeV)											
x	Stat.	P_b	P_t	D_{N2}	f_1	f_2	f_3	σ	Kinematics	Cuts	Total
0.229	0.12068	0.00500	0.00920	0.00270	0.00180	.0.001500	0.00140	0.00070	0.00155	0.03732	0.03899
0.277	0.02891	0.00100	0.00070	0.00110	0.00120	.0.001000	0.00590	0.00090	0.00127	0.01036	0.01223
0.325	0.01052	0.00030	0.00100	0.00010	0.00020	.0.000200	0.00010	0.00040	0.00041	0.00256	0.00284
0.374	0.00626	0.00010	0.00040	0.00000	0.00000	.0.000000	0.00010	0.00010	0.00010	0.00151	0.00157
0.424	0.00482	0.00040	0.00090	0.00020	0.00010	.0.000100	0.00010	0.00060	0.00041	0.00114	0.00169
0.473	0.00401	0.00040	0.00070	0.00020	0.00010	.0.000100	0.00010	0.00050	0.00032	0.00219	0.00242
0.523	0.00343	0.00000	0.00000	0.00000	0.00000	.0.000000	0.00000	0.00000	0.00000	0.00062	0.00062
0.574	0.00297	0.00000	0.00010	0.00000	0.00000	.0.000000	0.00000	0.00010	0.00000	0.00065	0.00066
0.623	0.00260	0.00000	0.00000	0.00000	0.00000	.0.000000	0.00000	0.00000	0.00000	0.00079	0.00079
0.673	0.00230	0.00000	0.00000	0.00000	0.00000	.0.000000	0.00000	0.00010	0.00000	0.00050	0.00051
0.723	0.00201	0.00000	0.00000	0.00000	0.00000	.0.000000	0.00000	0.00000	0.00000	0.00042	0.00042
0.773	0.00179	0.00000	0.00000	0.00000	0.00000	.0.000000	0.00000	0.00010	0.00000	0.00039	0.00040
0.823	0.00165	0.00000	0.00000	0.00000	0.00000	.0.000000	0.00000	0.00010	0.00000	0.00045	0.00046
0.873	0.00150	0.00000	0.00000	0.00000	0.00000	.0.000000	0.00000	0.00010	0.00000	0.00042	0.00044
0.921	0.00143	0.00010	0.00000	0.00020	0.00020	.0.000200	0.00020	0.00060	0.00010	0.00062	0.00096
0.973	0.00118	0.00010	0.00010	0.00020	0.00020	.0.000200	0.00020	0.00060	0.00010	0.00081	0.00110

Table F.8: Systematic uncertainties assigned to g_2 at incident beam energy of 5.89 GeV.

$g_2^{^3\mathrm{He}}$ Systematics (E = 5.89 GeV)											
x	Stat.	P_b	P_t	D_{N2}	f_1	f_2	f_3	σ	Kinematics	Cuts	Total
0.229	0.24712	0.04210	0.02640	0.05010	0.05660	.0.045800	0.17790	0.02060	0.04413	0.07920	0.22488
0.277	0.04674	0.00300	0.00530	0.00160	0.00140	.0.001300	0.01090	0.00110	0.00196	0.01425	0.01924
0.325	0.01486	0.00050	0.00090	0.00030	0.00020	.0.000200	0.00190	0.00050	0.00059	0.00506	0.00557
0.374	0.00789	0.00040	0.00100	0.00010	0.00000	.0.000000	0.00030	0.00030	0.00037	0.00114	0.00167
0.424	0.00550	0.00030	0.00070	0.00010	0.00010	.0.000100	0.00020	0.00040	0.00030	0.00240	0.00258
0.473	0.00417	0.00000	0.00000	0.00000	0.00000	.0.000000	0.00010	0.00000	0.00000	0.00174	0.00174
0.523	0.00331	0.00010	0.00010	0.00000	0.00000	.0.000000	0.00000	0.00010	0.00000	0.00096	0.00098
0.574	0.00267	0.00000	0.00000	0.00000	0.00000	.0.000000	0.00000	0.00010	0.00000	0.00067	0.00068
0.623	0.00218	0.00010	0.00020	0.00000	0.00000	.0.000000	0.00000	0.00020	0.00010	0.00041	0.00052
0.673	0.00182	0.00000	0.00000	0.00000	0.00000	.0.000000	0.00000	0.00010	0.00000	0.00056	0.00057
0.723	0.00151	0.00000	0.00010	0.00000	0.00000	.0.000000	0.00000	0.00010	0.00000	0.00040	0.00042
0.773	0.00128	0.00000	0.00000	0.00000	0.00000	.0.000000	0.00000	0.00010	0.00000	0.00036	0.00037
0.823	0.00119	0.00000	0.00010	0.00010	0.00010	.0.000100	0.00010	0.00080	0.00014	0.00032	0.00090
0.873	0.00097	0.00000	0.00000	0.00000	0.00000	.0.000000	0.00000	0.00010	0.00000	0.00044	0.00045
0.921	0.00089	0.00000	0.00000	0.00000	0.00000	.0.000000	0.00000	0.00010	0.00000	0.00024	0.00026
0.973	0.00071	0.00010	0.00010	0.00020	0.00020	.0.000200	0.00020	0.00050	0.00010	0.00036	0.00075

A break down of the d_2^n systematic uncertainties are given in Table F.9, for each of the measured mean Q^2 points. This table includes the effect of all the uncertainties found in the above tables (i.e. P_p, P_t, etc.), referred to as detector systematics, in addition to radiative corrections (Section 8.5.2), d_2^p (Section 8.6.2), the proton and neutron polarizations (P_p and P_n, Section 8.6.3), and the unmeasured low x contributions (Section 10.2.1.1). The two sources of uncertainty that dominate the d_2^n systematic uncertainty, are from the detector and low x contribution uncertainties. However, the final d_2^n measurement's statistical uncertainties are larger than its systematic uncertainties.

Table F.9: Systematic uncertainties assigned to different regions of d_2^n. The column labeled "Total" is the quadrature sum of all of the contributions listed in the table.

Region	$\langle Q^2 \rangle$ [GeV^2]	Detector Sys.	Rad. Cor.	d_2^p	P_p, P_n (high error)	P_p, P_n (low error)	Low x	Total
DIS+Res	3.21	0.00047	0.00002	0.00004	0.00006	0.00010	0.00058	0.00075
DIS+Res	4.32	0.00037	0.00002	0.00004	0.00002	0.00004	0.00058	0.00069
DIS	2.59	0.00036	0.00001	0.00005	0.00003	0.00005	–	0.00037
DIS	3.67	0.00029	0.00002	0.00004	0.00002	0.00002	–	0.00029
Res	4.71	0.00022	0.00000	0.00004	0.00003	0.00005	–	0.00023
Res	5.99	0.00011	0.00000	0.00002	0.00001	0.00003	–	0.00012

APPENDIX G

ELASTIC CONTRIBUTIONS

For elastic scattering the structure functions W_1 and W_2 can be written in terms of the electromagnetic form factors G_E and G_M as

$$W_1\left(\nu, Q^2\right) = \delta\left(\nu - \frac{Q^2}{2M}\right)\tau G_M^2\left(Q^2\right) \quad \text{(G.1)}$$

$$W_2\left(\nu, Q^2\right) = \delta\left(\nu - \frac{Q^2}{2M}\right)\frac{G_E^2\left(Q^2\right) + \tau G_M^2\left(Q^2\right)}{1+\tau}, \quad \text{(G.2)}$$

where $\tau = \frac{Q^2}{4M^2}$. The elastic contribution at x = 1 to the ploarized structure functions is [193]

$$g_1^{el} = \frac{1}{2}G_M\left(Q^2\right)G_E\left(Q^2\right) + \tau G_M\left(Q^2\right)\delta\left(x-1\right) \quad \text{(G.3)}$$

$$g_2^{el} = \frac{\tau}{2}\frac{G_M\left(Q^2\right)G_E\left(Q^2\right) - G_M\left(Q^2\right)}{1+\tau}\delta\left(x-1\right). \quad \text{(G.4)}$$

Intergrating Equations G.3 and G.4 over x one finds

$$\Gamma_1^{el} = \frac{1}{2} G_M\left(Q^2\right) \frac{G_E\left(Q^2\right) + \tau G_M\left(Q^2\right)}{1+\tau} \quad \text{(G.5)}$$

$$\Gamma_2^{el} = \frac{\tau}{2} G_M\left(Q^2\right) \frac{G_E\left(Q^2\right) - G_M\left(Q^2\right)}{1+\tau}. \quad \text{(G.6)}$$

Equations G.5 and G.6 then lead to the matrix elements d_2 and a_2 being expressed as

$$d_2^{el} = 2\Gamma_1^{el} + 3\Gamma_2^{el} \quad \text{(G.7)}$$

$$a_2^{el} = \Gamma_1^{el}. \quad \text{(G.8)}$$

For E06-014 the eleastic contributions were determined using the Dipole form factors for G_E^p, G_M^p and G_M^n. However, the Galster [69] parameterization was used for G_E^n. The Dipole form factors can be defined as follows:

$$\frac{G_M^p\left(Q^2\right)}{\mu_p} = \frac{G_M^n\left(Q^2\right)}{\mu_n} = G_D\left(Q^2\right) = \left(1 + \frac{Q^2}{0.71\text{GeV}^2}\right)^{-2} \quad \text{(G.9)}$$

$$G_E^p\left(Q^2\right) = G_D\left(Q^2\right), \quad \text{(G.10)}$$

where $G_D\left(Q^2\right)$ is the dipole form factor, μ_p (= 2.79) and μ_n (= -1.91) are the proton and neutron magnetic moments respectivly.

The Galster parameterized G_E^n is defined as

$$G_E^n\left(Q^2\right) = -\frac{\mu_n \tau}{1 + 5.6\tau} G_D\left(Q^2\right). \quad \text{(G.11)}$$

The left panel of Figure G.1 shows the elastic form factors used to compute the elastic contributions to d_2^n and a_2^n. The right panel shows the elastic Γ_1^n, Γ_2^n, and d_2^n moments as a

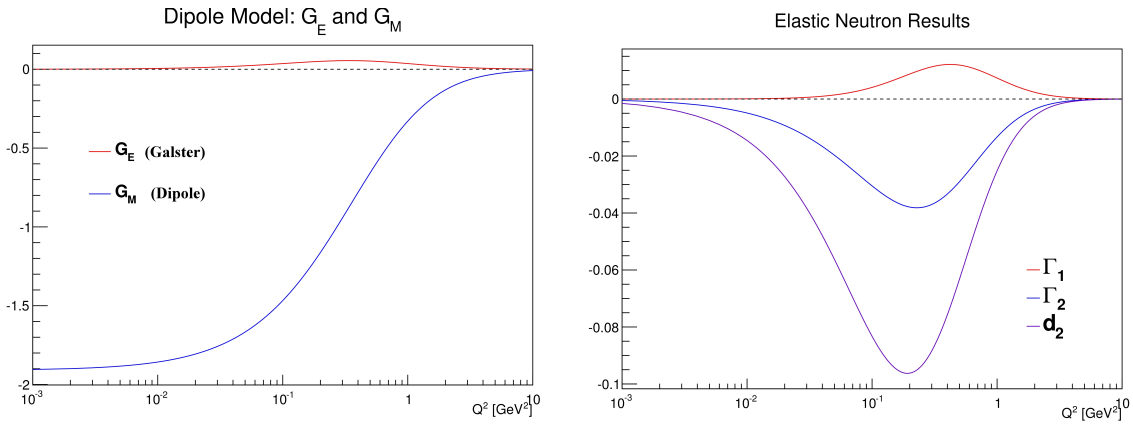

Figure G.1: Left panel:Elastic G_E^n (computed using the Galster parameterization) and G_M^n (computed using the dipole model) form factors. Right panel: Elastic d_2^n, Γ_1^n and Γ_2^n plotted as a function of Q^2.

Table G.1: Elastic d_2^n and a_2^n values computed from Equations G.7 and G.7.

Exp.	Q^2 [GeV^2]	Elastic d_2^n	Elastic a_2^n
E06-014 (DIS)	2.59	-3.02$\times 10^{-3}$	1.33$\times 10^{-3}$
E06-014 (DIS)	3.67	-1.12$\times 10^{-3}$	5.50$\times 10^{-4}$
E06-014 (Res)	4.17	-7.70$\times 10^{-4}$	3.90$\times 10^{-4}$
E06-014 (Res)	5.99	-2.40$\times 10^{-4}$	1.30$\times 10^{-4}$
E06-014 (DIS+Res)	3.21	-1.08$\times 10^{-3}$	7.80$\times 10^{-4}$
E06-014 (DIS+Res)	4.32	-6.90$\times 10^{-4}$	3.50$\times 10^{-4}$

function of Q^2. At low Q^2 ($< 1GeV^2$), it is clear that the elastic contribution will dominate the d_2^n matrix element. Table G.1 lists the elastic d_2^n and a_2^n contributions, for the various Q^2 values of inerest for E06-014.